SLAC-167
Volume I
(T/E)
UC-34d

PROCEEDINGS OF SUMMER INSTITUTE

ON PARTICLE PHYSICS

(In Two Volumes)

July 9-28, 1973

Volume I

Deep Inelastic Electroproduction

Program Directors

D.W.G.S. Leith

S. D. Drell

PREPARED FOR THE U. S. ATOMIC ENERGY
COMMISSION UNDER CONTRACT NO. AT(04-3)-515

November 1973

Printed in the United States of America. Available from National Technical Information Service, U. S. Department of Commerce, 5285 Port Royal Road, Springfield, Virginia 22151
Price: Printed Copy $10.60.

TABLE OF CONTENTS

Vol. I: DEEP INELASTIC ELECTROPRODUCTION — PAGE

Part A: Lectures

"Hadron Production in Deep Inelastic Processes"
J. D. Bjorken 1

"Hadron Production in the Collision of Virtual Photons with Nucleons - an Experimental Review"
M. Perl 35

"Phenomenological Analysis"
F. Gilman 71

"Asymptotic Behavior and Short Distance Singularities"
Y. Frishman 93

Part B: Topical Conference

"Results on Electro-Rho Production at Cornell"
K. Berkelman 101

"Inclusive Electroproduction of Hadrons from Protons and Neutrons and Tests of the Quark-Parton Model"
G. Feldman 119

"Results on Electroproduction Experiments from DESY"
H. Meyer 137

"Hadronic Final States from Inelastic Muon Scattering in a Hybrid Bubble Chamber Experiment"
T. Carroll 157

"Forward Electroproduction Experiments at Cornell"
F. Pipkin 177

PAGE

"Results on High Energy Neutrino Scattering at NAL"
D. Shields 227

"Quarks, Partons, Triality, Exotics and Colored Glue"
H. Lipkin 239

"Results on e^+e^- Reactions at the CEA (2.0 and 2.5 GeV per Beam)"
H. Newman 255

"Analytic Continuation from the Scattering to the Annihilation Region"
J. Sullivan 289

"Recent e^+e^- Colliding Beam Results"
R. Schwitters 313

"Hadronic Final States in Inclusive Lepto-Production and Colliding Beams, i. e. Features of Current Fragmentation"
W. Colglazier 327

"Scattering at Not-so-large Momentum Transfers"
R. Blankenbecler 347

"Study of the Multiplicity as a Function of q^2 in Deep Inelastic Electron Scattering"
K. Berkelman 355

List of Lectures Delivered During Sessions on Deep Inelastic Electroproduction 371

LECTURES DELIVERED DURING SESSIONS ON

DEEP INELASTIC ELECTROPRODUCTION

Several lectures and conference papers which were delivered during the school do not appear in these proceedings. The following is a complete list of the relevant talks.

H. DeStaebler
"Experimental Review of Single Arm Studies"

J. D. Bjorken
"Parton Picture and Discussion of Fragmentation Features"

M. Perl
"Experimental Review of 'Other Vertex Studies'"

F. Gilman
"Phenomenological Analysis"

Y. Frishman
"Formal Theory: Light Cone and Short Distance Methods"

K. Berkelman
"Results on Electro-Rho Production at Cornell"

G. Feldman
"Inclusive Electroproduction of Hadrons from Protons and Neutrons and Tests of the Quark Parton Model"

H. Meyer
"Results on Electroproduction Experiments from DESY"

T. Carroll
"Hadronic Final States from Inelastic Muon Scattering in a Hybrid Bubble Chamber Experiment"

F. Pipkin
"Forward Coincidence Electroproduction Experiments at Cornell"

D. Shields
"Results on High Energy Neutrino Scattering at NAL"

D. Cline
"Preliminary Results on High Energy Neutrino Interactions at NAL"

H. Lipkin
"Triality, Exotics and the Dynamical Basis of the Quark Model"

H. Newman
"Recent Results on e^+e^- Reactions at CEA (2 GeV; 2.5 GeV per Beam)"

J. Sullivan
"Analytic Continuation from the Scattering to the Annihilation Region"

R. Schwitters
"Recent Results in e^+e^- Annihilation"

M. Greco
"Deep Inelastic Processes"

W. Colglazier
"Hadronic Final States in Lepto-Production and Colliding Beams"

R. Blankenbecler
"Not-so-large Momentum Transfer Scattering"

K. Berkelman
"Study of the Multiplicity as a Function of q^2 in Deep Inelastic Electron Scattering"

J. D. Bjorken
"Large Transverse Momentum Production"

PREFACE

The first SLAC Summer Institute on Particle Physics was held at Stanford on July 9-28, 1973. The motivation for such a meeting derives from the need for continuing the education of young people who are working in the field and the desire of the SLAC faculty to contribute to this post-graduate educational process. Because of the rapid progress in the field and its concentration at fewer and fewer research centers, it is important to offer the opportunities both for critical review of recent major progress and for the continuing education of the post Ph.D. research community.

To achieve these goals, SLAC invited both theoretical and experimental physicists to join a program combining summer school and topical conference formats. Two consecutive ten-day periods were scheduled, each consisting of a one week school of highly pedagogic nature followed by an intense 2-1/2 day topical conference in which experts in the field described their current work. The topics for this first school, deep inelastic lepton scattering and the weak interactions, were chosen as being particularly exciting and timely subjects.

The proceedings, which have been collected and prepared by Martha C. Zipf, the Institute Coordinator, represent most of the material discussed during the meetings. We felt that rapid publication of the material was more important than completeness.

David W. G. S. Leith and Sidney D. Drell

Program Chairmen

HADRON PRODUCTION IN DEEP INELASTIC PROCESSES

J. D. Bjorken

SLAC

I. General Features of the Final States

In this lecture, we try to look at the expectations for hadron final states for the deep-inelastic processes $e^- p \to e^-$ + hadrons, $\nu_\mu p \to \mu^-$ + hadrons, and $e^+e^- \to$ hadrons in a general way, with as little recourse to models as possible. The purpose will be to try to develop a qualitative, and perhaps semiquantitative, idea of what might be "reasonable" experimental results. The strategy is to assume that the phenomena in the high - Q^2 unknown regions are smoothly connected to the known regions, and that there is no discontinuity in the dynamics. An example is the connection between inclusive and exclusive channels in electroproduction developed by Drell, Yan[1], West[2], Bloom, and Gilman[3] and the analogous Feynman[4] connection $(1-x)^{1-2\alpha(0)}$ in strong interaction processes. Duality is another example, where Regge and resonance regions become intimately connected to each other.

This assumption of smoothness in the dynamics John Kogut and I call "correspondence". It is analogous to Bohr's requirement that phenomena in the unknown (for him, quantum) region go smoothly into the known (classical) region, thereby constraining the properties of the phenomena in the unknown region. The way we apply the general idea, however, is much less precise than what Bohr did. In this lecture, I will not use quite the same tactics as Kogut and I did[5], which was to proceed from process to process and find so many interlocking connections between them that surprisingly little freedom in the answers was possible. Instead, I will start with our conclusion, which can be stated succinctly: The smoothest consistent extrapolation of electroproduction final states at $Q^2 = 0$ is simply that all quantities (e. g. multiplicities, prong distributions, particle ratios, exclusive non-diffractive channels) show no systematic variation with Q^2 at fixed W provided they are normalized to the total cross section at that Q^2 and W.

Such a solution evidently satisfies the correspondence idea, but did not, at least to me, seem a priori obvious. What must be made clear is that this hypothesis gives "reasonable" results for exclusive cross-sections, form-factors, etc. as well. We shall see that this is so.

However, the diffractive channels, for which the prototype is $e^- p \to e^- \rho^0 p$, must be considered separately. These present on the one hand some puzzles and on the other hand the opportunity to connect phenomena in e^+e^- annihilation to electroproduction (as determined by the "correspondence" ideas) through a generalization of the vector dominance concept.[6] Speculations about this question comprise the second half of this lecture.

A. Electroproduction and Neutrinoproduction

To begin, we write down the cross-section for producing some final state n or group of final states $\{n\}$. The invariant amplitude for the lepton-induced process is[7]

$$M = \begin{cases} \dfrac{e^2}{q^2}\ \bar{u}\,\gamma_\mu u\ \langle n \mid J^\mu(0) \mid P\rangle & e^- p \to e^- + \text{hadrons} \\ \dfrac{G}{\sqrt{2}}\ \bar{u}\,\gamma_\mu(1-\gamma_5)u\ \langle n \mid J^\mu(0) \mid P\rangle & \mu^- p \to \mu^- + \text{hadrons} \end{cases} \qquad (1.1)$$

Rather than directly squaring M and doing the traces, much can be seen by directly evaluating the lepton transition current for a given helicity of incident lepton. We approximate $\nu \gg 1$ GeV and $m_\ell = 0$ (so that $\nu^2 \gg Q^2$ and kinematics cleans up). For a left-handed lepton incident, we get

$$M = \left(\frac{e^2}{q^2} \text{ or } G\sqrt{2}\right) \sum_{i=L,R,S} \left(\frac{E'}{2E}\right)^{p_i} \langle n \mid \epsilon_i \cdot J \mid P\rangle \qquad (1.2)$$

where the normalized polarization vectors of the exchanged current are

$$\begin{aligned} \epsilon_L &= \frac{1}{\sqrt{2}}\ (0,\ 1,\ -i,\ 0) & p_L &= -\tfrac{1}{2} \\ \epsilon_S &= \frac{1}{\sqrt{Q^2}}\ (\sqrt{\nu^2+Q^2},\ \nu,\ 0,\ 0) & p_S &= 0 \\ \epsilon_R &= \frac{1}{\sqrt{2}}\ (0,\ 1,\ +i,\ 0) & p_R &= +\tfrac{1}{2} \end{aligned} \qquad (1.3)$$

The matrix elements $< n | \epsilon_i \cdot J | P >$ are what we are after (assuming we are not stalking big game, such as breakdown of conventional weak-interaction theory or quantum electrodynamics). Putting in all the phase-space factors gives us, for electroproduction

$$\frac{d\sigma}{dQ^2 d\nu d\Gamma} = \frac{\pi}{EE'} \frac{d\sigma}{d\Omega' dE' d\Gamma} = \frac{\alpha}{\pi Q^2 \nu} \frac{E'}{E} \left(1 - \frac{Q^2}{2M\nu}\right) \sum_{i=L,R,S} \left(\frac{E'}{2E}\right)^{2p_i} \frac{d\sigma_i}{d\Gamma} \quad (1.4)$$

with

$$\frac{d\sigma_i}{d\Gamma} = \frac{4\pi^2 \alpha}{\nu - \frac{Q^2}{2M}} \sum_{\text{Nind}\Gamma} | < n | \epsilon_i \cdot J | P > |^2 (2\pi)^3 \delta^4 (P_n - P - q) \quad (1.5)$$

The interference terms between L - R and L - S or R - S can be eliminated by an average over azimuthal angles ϕ of the lepton system relative to the direction of the momentum transfer $\underline{q}$. Or they can be isolated by taking a weighted integral over ϕ. The biggest such effects would be expected in exclusive channels such as $e p \to e n \pi^+$ or $e p \to e \rho^0 p$, and for those cases a very comprehensive kinematical formalism already exists.[8,9] Also, in electroproduction, an average over initial polarizations suffices to average $d\sigma_L$ and $d\sigma_R$ into $d\sigma_T = d\sigma_L + d\sigma_R$.

Features of the total virtual photoabsorption that we want to keep in mind are

1) Scaling; for $Q^2 > 1 - 2$ GeV.^{2} $Q^2 \sigma_T \approx F(\omega')$. This is good to ~10% for $2 < Q^2 < 10$.

2) $\sigma_S / \sigma_T \lesssim 0.2$. We will generally neglect σ_S. Indications for neutrino reactions are $\sigma_L > \sigma_R$; σ_S small (ν incident), at least at $\omega \lesssim 5$.

3) $\sigma_n / \sigma_p \approx 0.3 - 0.4$ at $\omega' \sim 1.2$ increasing smoothly to 0.85 at $\omega' \sim 20$.

4) $F(\omega') \approx (\omega' - 1)^3$ for ω' near 1.

5) $F(\omega') \approx$ constant for $5 < \omega' < 30$.

6) As $Q^2 \to 0$, $\sigma_T (Q^2, \nu) \to \sigma_\gamma (\nu)$

7) ρ, ω, ϕ dominance works quite well for real photon processes.

We now want to look into the partial cross-sections and see what is reasonable to expect. The natural experimental question is: At fixed W = total hadron mass, what is the dependence upon Q^2 (if any) of the nature of the final states? We will want to know the Q^2-dependence (at fixed W^2) of such things as

a) Topological cross-sections

b) Multiplicity

c) Inclusive distribution functions

d) Particle - ratios

e) Properties of explicit exclusive channels, such as $\gamma p \to \pi^+ n$, $K^+ \Lambda$, $\rho^0 p$, ϕp, etc.

As mentioned in the introduction, it turns out that a very reasonable behavior for all these quantities (with the possible exception of diffractive channels) is that, once normalized to the total cross-section $\sigma_i(Q^2, W^2)$, the partial cross-sections possess little or no systematic dependence on Q^2. For the purpose of keeping things simple, we shall describe the consequences of the extreme assumption of no change in these quantities with Q^2. This may be extreme and unrealistic as far as quantitative behavior is concerned. In the second lecture, we shall explore the nature of what kind of changes in Q^2 might be expected. But the simple hypothesis of no change does afford insight into qualitative behavior.

We start at low W, say at the 33 resonance. Looking at photoproduction, we see that the ratio $\sigma_{33}(0, W^2) / \sigma_\gamma (0, W^2)$ is large, 50% or so. Then, if $\sigma_{33}(Q^2, W^2) / \sigma_T (Q^2, W^2)$ is likewise a similar constant, we get

$$\sigma_{33}(Q^2, W^2) \sim \frac{1}{Q^2} (\omega' - 1)^3 \approx \frac{1}{Q^2} \left(\frac{M^2}{Q^2}\right)^3 \quad (1.6)$$

To see that this is "reasonable", notice that a pointlike (scale-invariant) behavior occurs if

$$\sigma \approx \frac{1}{Q^2} \delta (\omega' - 1) \quad (1.7)$$

This is in accord with dimensional analysis and gives $d\sigma / dQ^2 \sim Q^{-4}$, just the behavior of Rutherford scattering. Thus for a point particle

$$\int \sigma (Q^2, W^2) \, dW^2 \sim \text{constant} \quad (1.8)$$

over resonance

and for an extended particle

$$\int \sigma\ (Q^2, W^2)\, dW^2 \ \sim\ F^2\ (Q^2) \qquad (1.9)$$

over resonance

where F is its form factor. Comparing with Eqn. (1.6), we see that $F_{(33)}{}^2 \sim Q^{-8}$, or

$$F_{(33)}\ (Q^2) \sim Q^{-4} \qquad (1.10)$$

So, the threshold-behavior of the total cross-section σ_T is consistent with resonances taking a major fraction of the yield at low W^2. This is just the Drell, Yan, West, Bloom, Gilman connection argued in the reverse direction.

Look now at high W^2 at some two-body channel, such as $\gamma^* p \to \pi^+ n$. By high W^2 for a given Q^2, we shall mean the Regge region, defined as the kinematic region where the minimum momentum transfer for typical two-body processes is small (<< 350 MeV). This occurs when ω is large (>> 10 ?). To see this, consider electroproduction of a particle of mass m in the forward direction. Then, in the laboratory frame

$$\Delta_{min} = \sqrt{\nu^2 + Q^2} - \sqrt{\nu^2 - m^2} \approx \frac{Q^2 + m^2}{2\nu} \approx \frac{M}{\omega} \qquad (1.11)$$

Hence, large ω defines the Regge region.

Returning to our two-body process, by the "no change" hypothesis

$$\frac{\sigma(Q^2, W^2)\,\gamma p \to \pi^+ n}{\sigma_T(Q^2, W^2)\,\text{tot}} = \left(\begin{matrix}\text{independent} \\ \text{of } Q^2\end{matrix}\right) \cong (W^2)^{-2} \qquad (1.12)$$

The (W^2) dependence is what is observed at $Q^2 = 0$ in photoproduction: $s^{2\alpha_{eff}-2}; \alpha_{eff} \approx 0$.

Thus,

$$\sigma_{\gamma^* p \to \pi^+ n} \approx \frac{1}{Q^2}\ (W^2)^{-2} = \frac{1}{Q^2}\ (\omega')^{-2}\ (Q^2)^{-2} \quad (\omega' >> 1) \qquad (1.13)$$

Also, recall from Equ. (1.6) that we can write

$$\sigma_{\gamma^* p \to \pi^+ n} = \frac{1}{Q^2}\ (\omega' - 1)\ (Q^2)^{-2} \quad (\omega' \approx 1) \qquad (1.14)$$

We conclude that $Q^6 \sigma_{\gamma^* p \to \pi^+ n}$ should approximately scale; the scaling function is shown schematically in Fig. 1. Both in the threshold region and asymptotically the systematic behavior is reasonable. We have already argued the case for the threshold region. And for large ω' we expect the Regge structure to be

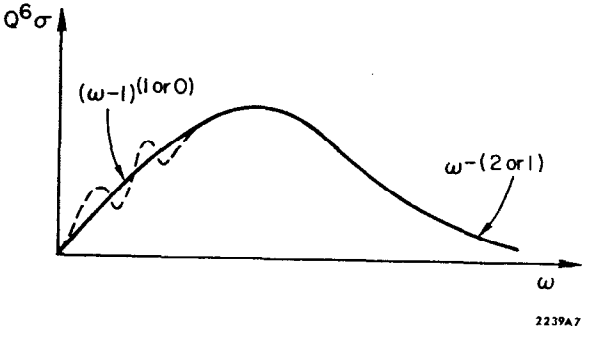

Fig. 1

Schematic behavior of the cross-section for electroproduction of a single π (or $\nu p \to \mu^- \pi^+ p$).

$$\sigma \approx \frac{1}{Q^2} \quad \omega^{2\alpha-2} \quad F^2 \ (Q^2) \tag{1.15}$$

with F_π the form factor at the upper photon-reggeon-pion vertex. With

$$F_\pi \ (Q^2) \approx (Q^2)^{\alpha_\pi(0)-1} \tag{1.16}$$

we reconstruct the behavior we wanted. Such a behavior for F_π is reasonable from the point of view of data, but its theoretical origin is more obscure.

For the backward small-u electroproduction of a fast nucleon, we can repeat the argument; now

$$F_N \ (Q^2) \approx (Q^2)^{\alpha_N(0)-1} \tag{1.17}$$

suggesting that nucleon form factors should fall with a greater power of Q^2 than meson form factors. This in turn would imply that the deep-inelastic structure function for electroproduction from a pion target should rise from threshold as a small power of $(\omega' - 1)$, e.g. linearly if indeed $F_\pi \sim (Q^2)^{-1}$ as suggested by Equ. (1.16).

We now leave the two-body channels and consider the amorphous mass of multi-body channels. In our "no change" idealization, the topological cross-sections, when normalized to $\sigma_T(Q^2, W^2)$ should depend only on W. We again get

$$\sigma_n(Q^2, W^2) \quad \alpha \frac{1}{Q^2} \ F \ (\omega') \ \sigma_{\gamma_L}(0, W^2) \tag{1.18}$$

Prong distributions should be independent of Q^2, and thus $\bar{n} = f(W^2) \sim A + B \log W^2$ as it is in photoproduction. The normalized inclusive hadron distributions again would not be expected to possess systematic change with Q^2; consequently

$$\frac{dN}{dZ} \sim \begin{cases} (1-z) & \pi\text{'s (K's ??)} \\ (1-z)^3 & \text{Baryons} \end{cases} \tag{1.19}$$

for leading particles: $z = P^{lab}/\nu$. This follows from data (in the case of pions) for photoproduction processes. Equ. (1.19) is consistent with the Feynman inclusive-exclusive connection at $Q^2 = 0$; hence that connection will be satisfied at all Q^2, according to the "no change" hypothesis.

Actually, the situation may well be more complex. Given the picture of short-range correlation in rapidity, which is reasonably successful in hadron physics, correspondence suggests we apply it to virtual photons as well. For sufficiently large W^2 and small Q^2/W^2, we expect three regions in rapidity-space, as shown in Figure 2. We should keep in mind that we are speaking of idealizations. It takes laboratory photon energies of hundreds of GeV to begin to develop the three distinguishable regions. But, setting such inconveniences aside, as Q^2 increases at these large W^2, we expect only the photon-fragmentation region to change. In particular its length changes. To see this, keep Q^2 fixed (thereby keeping the structure of the photon fragmentation region fixed) and decrease W^2 until the hadron plateau disappears. This happens when Regge-poles no longer control the dynamics, namely when ω becomes small ($\omega \sim 3$??, 10 ??, 50 ??). Thus the photon region has length $\sim \log W^2 = \log W^2/Q^2 + \log Q^2 = \log \omega' + \log Q^2 \approx \log Q^2$ under these circumstances. Even on general grounds (and certainly in the context of models, as discussed in the next lecture) we can expect special structure at the two boundaries of the photon fragmentation region. The boundary between the current-fragmentation region and the hadron plateau is called the hole-fragmentation region (a name inspired by the parton model). Likewise, the leading particles with their assumed Feynman-scaling behavior lie in a special region which we shall call the parton-fragmentation region. This is all illustrated in Fig. 3 for an enormous W^2 ($\gtrsim 10^4$ GeV^2). The current plateau, located between hole and parton fragmentation regions, has in our idealized no-change world the same height as the hadron plateau. This may well not be the case, although Kogut and I found an argument that this is preferred. The gist of the argument is that if the current plateau is lower, $\bar{n}$ decreases and the prong distribution shifts toward zero; hence two-prong and exclusive channels should be more important at high Q^2 than low at fixed W^2 (when normalized to $\sigma(Q^2, W^2)_{tot}$). However, for a lower current plateau, the inclusive spectrum at the high energy end is depressed; duality would suggest that the exclusive contributions do the same, i.e. go down with Q^2 instead of up.

To summarize, we have found a consistent zeroth-order picture of nondiffractive

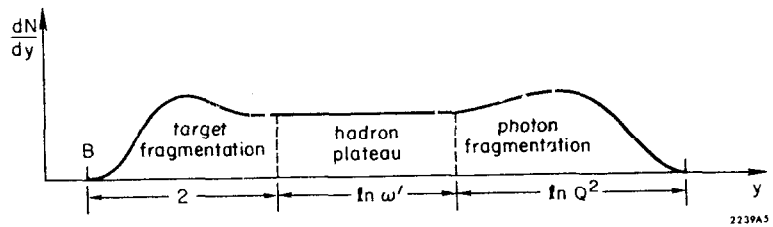

Fig. 2

Inclusive distribution function for hadron electroproduction

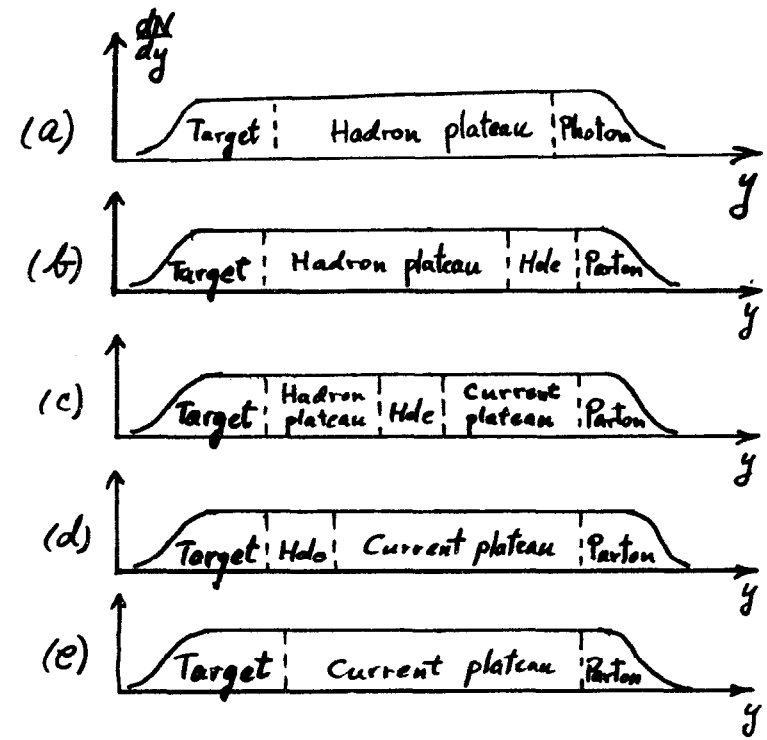

Fig. 3

Fragmentation regions in Q^2, ν space for W^2 very large: (a) $Q^2 = 0$. (b) $Q^2 \sim 5\text{-}30\ \mathrm{GeV}^2$ (?) (c) $Q^2 \gg 30\ \mathrm{GeV}^2$ and $\omega \gg 50$ (?) (d) $Q^2 \gg 30\ \mathrm{GeV}^2$; $\omega \sim 10\text{-}50$ (e) $Q^2 \gg 30\ \mathrm{GeV}^2$; $\omega < 10$.

inclusive and exclusive electroproduction processes by assuming no change with Q^2, at fixed W, of quantities which are normalized to the total cross section at that Q^2 and W. This is an extreme view; we must at the least expect (1) a finite readjustment as Q^2 increases from zero into the scaling region, (2) some additional dependence on ω as the hole-fragmentation region moves from the region of leading particles at large ω and small Q^2 to the target fragmentation region at large Q^2. To describe such changes in any detail probably requires more committment to a model of the dynamics.

B. Vector Dominance

The role of vector dominance at large Q^2 appears to be a rich and subtle problem, worthy of a great deal of experimental and theoretical study. The discussion here will only scratch the surface. Let us begin by speculating about vector dominance for very high energy photoproduction. From the ISR data on $pp \to p + \text{hadrons}$[16] we have a reasonable firm expectation of what we should see in $\pi + p \to \text{hadrons} + p$ at sufficiently high energy ($E_\pi >> 100$ GeV ??). The inclusive spectrum of slow protons will very likely again show a peak near $x = 1$ corresponding to diffraction excitation of the pion projectile into a state X of mass M_X, with a cross-section

$$\frac{d\sigma}{dM_X^2} \approx .01 \frac{\sigma_{tot}}{M_X^2} \qquad (1.20)$$

The factor .01 makes this a moderately small effect at foreseeable energies.

We should likewise expect a similar effect for $\rho^o p$ scattering (arguing from SU(6) or the quark model). Then, if pure ρ^o (plus ω, ϕ) dominance were correct, the same conclusion would follow for γp processes. This is still a small effect ($\lesssim 6\%$ of σ_{tot}, even at $E_\gamma \sim 10^3$ GeV); hence the main channel for diffraction dissociation of a real photon should be the ρ^o (plus ω, ϕ), giving 15 - 20% of σ_{tot} even at ISR energies. This is analogous to elastic pp scattering being more important than the diffraction excitation, at least for $E < 1$ TeV.

For virtual photons, the relative contribution of the ρ^o to the total $\sigma_T(Q^2, W^2)$ rapidly goes away, both experimentally and in accord with theoretical expectations (here, we ignore the problem of what to do about σ_S). We expect

$$\sigma(Q^2, W^2)^{\rho^o\text{-dominant}} \cong \sigma(0, W^2) \left(\frac{M_\rho^2}{M_\rho^2 + Q^2}\right)^2 \qquad (1.21)$$

Take $\sigma(0, W^2) \approx 100$ μb. Then that contribution to $\sigma_T + \sigma_S$ is shown in Fig. 4. Guessing $\sigma_S/\sigma_T \sim 0.2$ for $Q^2 \gtrsim 0.2$ and also removing it gives the remainder, shown shaded, which varies rather slowly with Q^2. Generalized vector dominance interprets that remainder as the contribution of higher mass states. Note that already at $Q^2 \sim 0.5$ GeV^2 these contribute half the total.

The simplest version of a generalized vector-dominance picture states that for very large ω, we may write

$$\sigma(Q^2, W^2)_{tot} \sim \int \frac{dm^2 \rho(m^2)}{(Q^2 + m^2)^2} \sigma(m^2, W^2) \qquad (1.22)$$

Here ρ defines the spectrum of vector states in the incident photon. With $\sigma(m^2, W^2) \sim$ constant and $\rho(m^2) \approx$ constant for $m^2 > m_1^2 \sim 2$ GeV^2 [actually more like Fig. 5] we get (ignoring the ϕ and effects of nonvanishing t_{min})

$$\sigma(Q^2, W^2)_{tot} \approx \sigma_\gamma^{\rho\text{-dom}}(W^2)\left(\frac{m_\rho^2}{m_\rho^2 + Q^2}\right)^2 + \sigma_\gamma^{\text{Direct}}(W^2)\left(\frac{m_1^2}{Q^2 + m_1^2}\right) \qquad (1.23)$$

With $m_1^2 \sim 2$ GeV^2 and $\sigma_\gamma^{\text{Direct}}/\sigma_\gamma^{tot} \sim 0.2 - 0.3$ this works pretty well. This kind of thing has been done much more professionally by Sakurai and Schildknecht.[6]

What do we now expect for diffraction-excitation? We guess that the cross-section for a component in the incident photon with mass m to interact and make mass $m_x \neq m$ should be

$$\frac{d\sigma}{dm_x^2} \approx .01 \sigma_{tot}^{(\text{Strong})}(m^2) \frac{\theta(m_x^2 - m^2)}{m_x^2} \qquad (1.24)$$

with $\sigma_{tot}^{(\text{Strong})}$ a constant in W^2. [Actually, we might also have guessed $m_x^2 - m^2$ in the denominator instead of m_x^2; this seems to make little difference in the results

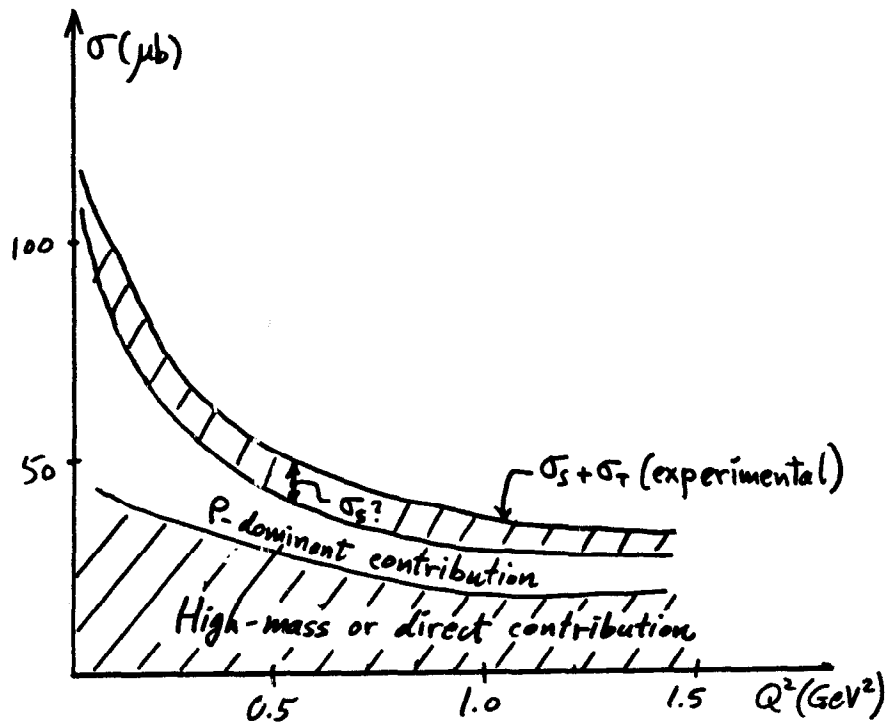

Fig. 4

$\sigma_T + \sigma_S$ as function of Q^2 for large W^2

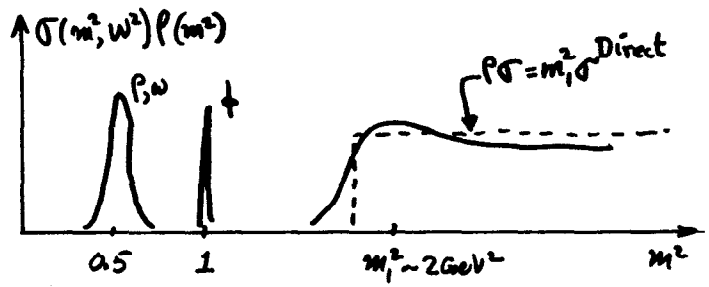

Fig. 5

Spectral functions for a vector dominant description of electroproduction

to be obtained.] The step function is included, because we assume that a state of low m is somehow "simpler" than one of high m. That is, in a collision simple states like ρ can be converted into complicated ones X but not vice versa; there is irreversibility here.

For better or worse, Equ. (1.24) gives, for $m_x^2 >> m_1^2$

$$\frac{d\sigma(Q^2, W^2)}{dm_x^2} \sim \int_0^{m_x^2} \frac{dm^2\, \rho(m^2)}{(Q^2 + m^2)^2} \frac{0.01}{m_x^2} \sigma_{tot}^{strong}(m^2) \approx \frac{.01}{m_x^2 + Q^2} \sigma(Q^2, W^2)_{tot} \quad (1.25)$$

In other words, for $m_x^2 >> Q^2$

$$\frac{1}{\sigma_{tot}(Q^2)} \frac{d\sigma(Q^2)}{dm_x^2} \sim \frac{.01}{m_x^2} \quad (1.26)$$

is again independent of Q^2; for $m_x^2 \lesssim Q^2$ the forward spike may well be cut off.

There is an additional contribution to the spectrum of diffractively produced massive states. It is analogous to elastic scattering of the various components of the incident photon: the virtual γ converts into state m which emerges intact; $m_x = m$. If $\sigma_{el}(m_x^2, s) \approx 0.2\, \sigma_{tot}(m_x^2, s)$ as is commonly the case in hadron physics, we find (again assuming $m_x^2 >> m_1^2$)

$$\frac{d\sigma(Q^2, m_x^2)}{dm_x^2}^{"elastic"} \approx \frac{0.2\, \rho(m_x^2)}{(Q^2 + m_x^2)^2} \sigma(m_x^2, s) = 0.2\, \sigma_\gamma^{Direct} \frac{m_1^2}{(Q^2 + m_x^2)^2} \quad (1.27)$$

where Equ. (1.22) and (1.23) have been used. Thus for $Q^2 >> 0.5\ GeV^2$

$$\frac{1}{\sigma(Q^2)_{tot}} \frac{d\sigma}{dm_x^2} \approx 0.2 \frac{(Q^2 + m_1^2)}{(Q^2 + m_x^2)^2} \quad (1.28)$$

Thus this "elastic" contribution dominates over the "inelastic" given in Equ. (1.25) if and only if

$$20\,(Q^2 + m_1^2) \gtrsim m_x^2 \quad (1.29)$$

This will be true provided only that $m_x^2 \lesssim 40\ GeV^2$. Even at ISR energies, one doesn't see diffractively-excited states with masses much larger than that. Thus once Q^2 is inside the deep inelastic region ($Q^2 >> 0.5\ GeV^2$) we expect this "elastic" contribution to be the most prominent. However, for $Q^2 \cong 0$, equation (1.28) should be replaced by

$$\frac{1}{\sigma_{tot}} \frac{d\sigma}{dm_x^2} \cong 0.2 \frac{\sigma_\gamma^{Direct}}{\sigma_\gamma^{total}} \frac{m_1^2}{(m_x^2)^2} \approx \frac{.05}{m_x^2} \left(\frac{m_1^2}{m_x^2}\right) \quad (1.30)$$

So even for the ρ' ($m_x^2 \simeq m_1^2 \sim 2\ GeV^2$) this "elastic" contribution does not tremendously overwhelm the estimated diffraction excitation of the virtual ρ^0 ($\approx .01\ m_x^{-2}$). And it disappears with increasing mass m_x.

To add to the confusion, we must here add some words of caution. One credible option for the dynamics, discussed in the next section, is that as the mass m of the virtual hadron in the photon increases its absorption cross-section on the nucleon decreases,[11] as m^{-2}. If this is the case, then eventually the nucleon becomes transparent to the incident virtual state and no shadow is cast; in other words, the "elastic" contribution should be omitted. However, in the "aligned jet" option discussed in Section C, the opposite is the case; the elastic contribution is present.

The frequent use of the verb "guess" in the above speculations shows how confusing I, at least, find this situation. This section is presented only as an introduction to the questions and as a stimulus for trying to understand what really is going on in this cryptic region of very large ω. In particular, we haven't even considered the question of the relevance of off-diagonal contributions to the virtual Compton amplitude (Fig. 6a), and they may be important. We also have not entertained the interesting and related question of whether the transverse size of the hadron cloud coupled to a virtual photon decreases with increasing Q^2. Yennie has recently considered this question in some detail[12], and I recommend his paper as an introduction into that subject. Nor have we mentioned the A-dependence of coherent production on nuclei. But even with these omissions and simplifications, we have identified three mechanisms (Figure 6) for coherent production of massive states X, all of which could play significant roles in var-

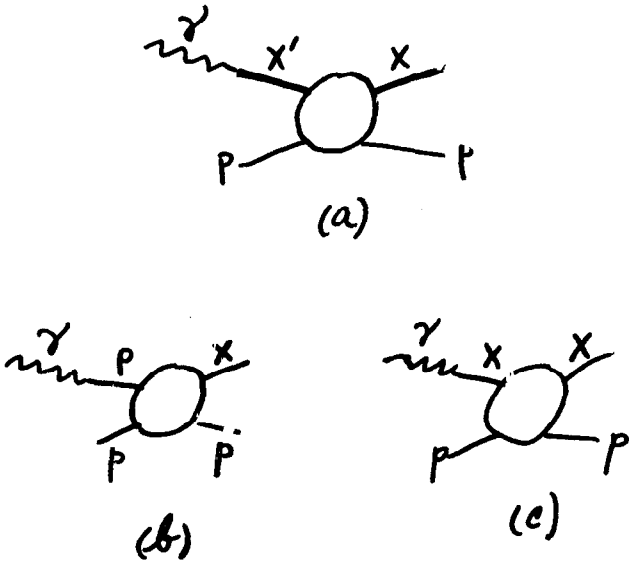

Fig. 6

Three mechanisms for coherent production of massive states X by real and/or virtual photons.

ious ranges of Q^2. This whole set of phenomena cannot help but give us a rich source of insight into deep inelastic dynamics.

C. Connection of Electroproduction to e^+e^- Annihilation

It is natural to try to connect the properties of the photon-fragmentation region in electroproduction to the properties of the hadron final states in e^+e^- annihilation. To do this requires a closer look into the generalized vector-dominance picture. We shall in fact encounter a paradox. To see the problem most simply,[13] we calculate the probability that a real γ-ray fluctuates into a hadron system, and then multiply by the cross section for the hadron system to interact with the target. Inasmuch as Z_3, the charge renormalization constant, is the probability of finding a bare photon in a real photon, $1 - Z_3$ is the probability it is something else, such as virtual hadrons. To get the normalization right, take first the case for which the only possible virtual transition is to a muon pair. From the books we get

$$(1 - Z_3)_{\mu\mu} \approx \frac{\alpha}{3\pi} \log \frac{\Lambda^2}{m_\mu^2} = \frac{\alpha}{3\pi} \int_{4m_\mu^2}^{\Lambda^2} \frac{dm^2}{m^2} \sim \int dm^2 \sigma(m^2)_{e^+e^- \to \mu^+\mu^-} \quad (1.31)$$

We infer immediately

$$(1 - Z_3)_{had} = \text{Probability } \gamma \text{ is a hadron system} = \frac{\alpha}{3\pi} \int \frac{dm^2}{m^2} R(m^2) \quad (1.32)$$

where

$$R(Q^2) = \frac{\sigma(Q^2)_{e^+e^- \to \text{hadrons}}}{\sigma(Q^2)_{e^+e^- \to \mu^+\mu^-}} , \quad (1.33)$$

and thus, according to vector dominance for real γ's

$$\sigma_{\gamma p}(W^2) = \frac{\alpha}{3\pi} \int \frac{dm^2}{m^2} R(m^2) \sigma^{had}(m^2, W^2) \quad (1.34)$$

For virtual transverse γ-rays, we modify the vector-dominant energy denominator or propagator, and get

$$\sigma_T(Q^2, W^2) \cong \frac{\alpha}{3\pi} \int \frac{dm^2 m^2}{(Q^2 + m^2)^2} R(m^2) \sigma(m^2, W^2)^{(\text{strong})}_{had} \quad (1.35)$$

Let us calculate the contribution from $2GeV^2 \cong m_1^2 < m^2 < 10\ GeV^2$, where $R \sim 1.5$ as measured at Frascati. Ignoring the ρ-dominant contribution and setting $\sigma_{had} = 27$ mb., we get

$$\sigma_T(Q^2) \approx 20\ \mu b. \times 1.5 \int_{m_1^2}^{\Lambda^2} \frac{dm^2\, m^2}{(Q^2 + m^2)^2} \approx 30\ \mu b. \left\{ \log \frac{\Lambda^2}{m_1^2 + Q^2} - \frac{Q^2}{Q^2 + m_1^2} \right\} \quad (1.36)$$

Numerically, this is not bad at all, and nicely accounts for the shaded region in Fig. 4. However, in principle, setting $\Lambda^2 \sim W^2$ (as follows from t_{min} arguments; m^2 cannot exceed $O(W^2)$ without increasing t_{min} unacceptably) we get

$$\sigma_T(Q^2) \rightarrow 30\ \mu b. \left[\log(\omega' + 1) - 1 \right] \quad (1.37)$$

This violates dimensional scaling by a full power of Q^2. And at $Q^2 \sim 20\ GeV^2$, R is reported by CEA to be still bigger, as large as 5. It would seem we have a problem of principle.

Other than abandoning scaling (which at large ω isn't ruled out), there are at least three ways out of the difficulty:

1) $R(Q^2) \sim Q^{-2}$ as $Q^2 \rightarrow \infty$ This looks bad experimentally.

2) The nucleon becomes transparent to the massive virtual states: $\sigma(m^2, s) \sim m^{-2}$ for very large s. This seems strange physically, but is tenable from the point of view of experiment. One of the most dramatic in principle predictions here is that all the states found in the $e^+e^- \rightarrow$ hadrons reaction will contribute uniformly to the vector dominant electroproduction. Thus, if the mean momentum of a secondary hadron increases in the annihilation process (e.g. roughly linearly with $\sqrt{Q^2}$) so also does the transverse momentum because the angular distribution must be nearly isotropic. Therefore, the $p_\perp$ distribution should likewise broaden (e.g. linearly with $\sqrt{Q^2}$) in the photon- fragmentation region as Q^2 increases. But to test this requires $Q^2 >> 2GeV^2$ since neither ρ nor ρ' make high $p_\perp$ secondaries. Conversely low $p_\perp$ in e^+e^- annihilation implies a multiplicity increase $\bar{n} \sim \sqrt{Q^2}$, and vector dominance would then imply the same in electroproduction, in conflict with the correspondence arguments.

3) In this case, we take over directly the hadron distribution, inferred from correspondence arguments, in the photon fragmentation region for electroproduction (hole-fragmentation, current plateau, parton fragmentation). At high Q^2 this region of phase-space is elongated along the beam direction ($< p_{\parallel}^* > \sim \sqrt{Q^2}$; $< p_\perp > \sim 0.3$ GeV). In e^+e^- annihilation this jet can point, in a given event, in a random direction. Averaged over events the angular distribution should be nearly isotropic (in the parton model $(1 + \cos^2\Theta)$, the same as for $\mu^+\mu^-$). Now thinking in reverse and going from this picture in e^+e^- annihilation to the electroproduction case via vector dominance a natural supposition is that only jets aligned along the beam direction (therefore leaving low $p_\perp$) can get absorbed by the target. The probability of that happening is a solid angle factor

$$\Delta\Omega \sim \frac{< p_\perp^2 >}{< p_{\parallel}^2 >} \sim \frac{\text{const}}{Q^2} \quad (1.38)$$

Putting such a pure fudge-factor $\Lambda^2 / (m^2 + \Lambda^2)$ with $\Lambda^2 \sim 1\ GeV^2$ fixes everything up. As $W^2 \rightarrow \infty$

$$\sigma_T(Q^2) \approx \frac{\alpha}{3\pi} \int \frac{dm^2\, m^2 R(m^2)}{(Q^2 + m^2)^2} \left(\frac{\Lambda^2}{\Lambda^2 + m^2} \right) \sigma_{had}(m^2) \approx 30\ \mu b. \left(\frac{\Lambda^2}{Q^2} \right) \quad (1.39)$$

This gives $\nu W_2 \sim 0.25$ asymptotically.

We repeat that this line of argument then implies that e^+e^- - annihilation leads to a hadron distribution characterized by a double-jet structure; in short, like the products of a $\pi\pi$ collision at $s \sim Q^2$ (except that the jet axis is distributed roughly isotropically). We expect fragmentation regions near the boundaries (where for the completely analogous process $W^+ \rightarrow$ hadrons the original charge of the W would most likely be found), as shown in Fig. 7. Furthermore, the dependence of the inclusive spectra near the boundary should be similar to inclusive electroproduction of leading hadrons. That in turn, using correspondence, is similar to photoproduction, namely $(1 - x)$ for pions and $(1 - x)^{2-3}$ for nucleons. Thus in colliding beams, we would expect scaling functions similar in shape to those found in deep-inelastic processes. They are exhibited in Fig. 8.

Finally, the logical circle can be closed by using the inclusive-exclusive connection

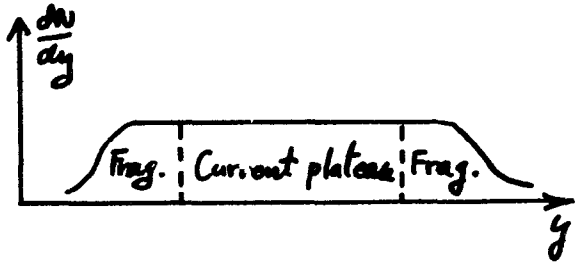

Fig. 7

Expected rapidity distribution for "jet" description of e^+e^- annihilation.

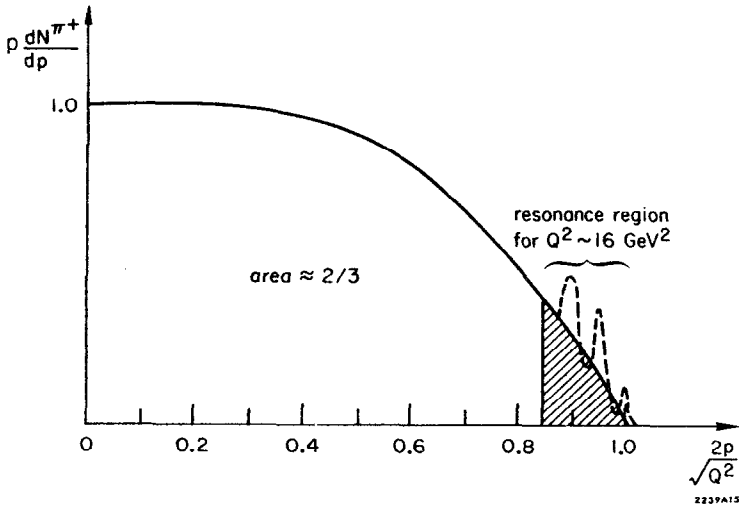

Fig. 8a

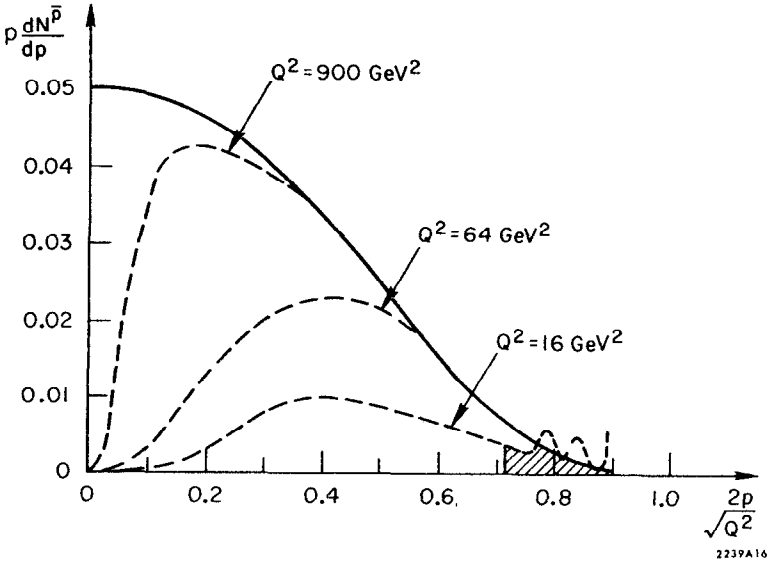

Fig. 8b

Estimated inclusive distribution functions for e^+e^- annihilation using correspondence arguments.

to obtain the electromagnetic form factor of the pion for timelike Q^2. The $(1-x)$ endpoint behavior once again turns out to imply $F_\pi \sim (Q^2)^{-1}$; $(1-x)^3$ implies $F_N \sim (Q^2)^{-2}$. I find this a very satisfying state of affairs.

II. Production Models

A. Heresies

What if everything does change with Q^2? Needless to say, there are models which suggest this, and I shall briefly describe them before moving on to the parton, Mueller-Regge, light-cone, etc. ideas which are consistent with the picture laid out in the first lecture.

If there is systematic change in electroproduction or neutrinoproduction final states, we expect this to happen predominantly in the photon-fragmentation region, because at fixed W the photon is what changes in the initial state as Q^2 changes. Thus, it is natural to look first at the kinematically simpler e^+e^- annihilation process, use vector-dominance to infer the properties of electroproduction at large ω, and then continue down to small ω. In the colliding-beam case, the highest possibility for the multiplicity is $\bar{n} \sim 2.5\sqrt{Q^2}$ (Q^2 measured in GeV^2, corresponding to a mean momentum per particle (presumed to be pions) of 400 MeV, and a mean $\langle p_\perp \rangle \sim 330$ MeV. Brodsky and I entertained that possibility[14] and arrived at Poisson distributions for the prong cross-sections. Also the inclusive distribution of pions falls exponentially with increasing p, a feature difficult to join smoothly onto the exclusive channels. In order to make a smooth joining, one needs the pion electromagnetic form factors to fall faster than any power. Recently Engels, Schilling and Satz[15] have revived and improved that model, arguing that it is correct if (and only if) one has a Hagedorn-Frautschi statistical bootstrap mechanism. The whole scheme may be in trouble experimentally; the CEA data on the charged multiplicity at $Q^2 = 16\ GeV^2$ ($\bar{n}_{ch} \sim 4$) implies already (if $\bar{n}_{\pi^0} \sim \frac{1}{2}\bar{n}_{ch}$) a mean momentum per particle of $\sim$ 650 MeV, quite a bit larger than the Hagedorn temperature.

The Landau hydrodynamical model,[16] as revived by Carruthers and Minh Duong-van,[17] leads to a similarly large $\bar{n}$, this time growing as $Q^{3/8}$. This comes about from the following assumptions: In the beginning the photon materializes into a hot fluid of many degrees of freedom (partons?) which expands adiabatically (the entropy is conserved). Provided this hot gas is scale invariant (pressure = $\frac{1}{3}$ energy density, like a gas of massless particles), the entropy density is proportional to T^3 and the energy density to T^4 (just like black-body radiation), where T is of course temperature. This follows just from dimensional analysis with $k = \hbar = c = 1$. Landau then assumes that when, in any region of space-time, the entropy-density becomes low, hadrons are materialized. The number of hadrons is proportional to the entropy. This can be motivated as follows: The density of partons in the hot gas is proportional to the entropy-density (again by dimensional analysis!). Then when the parton density (in the local rest frame of the gas) is $\sim$ 2 to 3 per cubic fermi, they materialize into a hadron or two. For the total entropy S in a volume V, one then has

$$S \sim V T^3 \tag{2.1}$$

and for the total energy Q

$$Q \sim V T^4 \tag{2.2}$$

Eliminating temperature T gives

$$S \sim Q^{3/4} V^{1/4} \tag{2.3}$$

In ordinary collisions, V is assumed to be proportional to Q^{-1} because of longitudinal Lorentz contraction, giving

$$\bar{n} \sim S \sim Q^{\frac{1}{2}} \sim E_{lab}^{\frac{1}{4}} \tag{2.4}$$

For e^+e^- annihilation, however, Carruthers and Minh Duong-van argue (in my opinion rather feebly) that $V \sim 1\ f.^3$ because there is no preferred direction and therefore, no Lorentz contraction. This gives

$$\bar{n}_{e^+e^-} \sim Q^{3/4} = (Q^2)^{3/8} \tag{2.5}$$

For the case of electroproduction, their argument is that $V \sim \gamma_{cm}^{-1}$ where γ_{cm} is the factor for a Lorentz boost from the laboratory frame to the photon-proton center-of-mass frame. That factor is

$$\gamma_{cm} = \frac{\nu + M_p}{W} = \frac{W^2 + M_p^2 + Q^2}{2M_p W} \tag{2.6}$$

leading to

$$\bar{n} \approx W^{3/4} \left(\frac{2M_p W}{W^2 + M_p^2 + Q^2} \right)^{\frac{1}{4}} \tag{2.7}$$

In the scale limit

$$\bar{n} \approx W^{\frac{1}{2}} \left(\frac{\omega' - 1}{\omega' + \frac{M^2}{W^2}} \right)^{\frac{1}{4}} \tag{2.8}$$

For any ω' other than ≈ 1, there is little difference from the hadronic situation. However, for W fixed and $Q^2 \to \infty$, $\bar{n} \sim W/Q^{\frac{1}{2}} \to 0$! The Lorentz contraction continues to increase without limit for increasing spacelike Q at fixed W. Also, all connections with vector dominance at large ω are utterly lost. This comes as little surprise inasmuch as the most glaring weakness of the hydrodynamic approach lies in its lack of explanation of the leading-particle effect in particular the retention of quantum numbers by the leading particles in hadron collisions. We shall return to the Landau model in the third lecture.

At the other extreme is the hypothesis of finite multiplicity as $Q^2 \to \infty$. This comes out of Drell and Yan's parton model,[18] early light-cone studies,[19] and other occasional models. It is the easiest result to get from diagrammatic models, but scarcely credible physically. Were it to be true, we could say that partons have been produced. For if $\bar{n} < \infty$ as $Q^2 \to \infty$, then there exists at least one exclusive channel which, as $Q^2 \to \infty$, is a finite fraction of the total. [Proof: Let $m(Q^2)$ be the median of the multiplicity distribution; i. e.

$$\sum_{n=0}^{m(Q^2)} \sigma_n = \tfrac{1}{2} \sigma_{tot} \tag{2.9}$$

If $m(Q^2) < \infty$ as $Q^2 \to \infty$, evidently $\sigma_n / \sigma_{tot} > 0$ as $Q^2 \to \infty$ for some $n < m$ because the sum is over a finite number of terms. However, if $m \to \infty$ as $Q^2 \to \infty$, we reach a contradiction

$$\bar{n}\, \sigma_{tot} > \sum_{m(Q^2)}^{\infty} n \sigma_n \geq m \sum_{m}^{\infty} \sigma_n = \frac{m}{2} \sigma_{tot} \to \infty \tag{2.10}$$

Q. E. D.] This comment also applies to the closely related situation in electroproduction for which the analogous statement is that the photon-fragmentation region contains a finite number of particles, even as $Q^2 \to \infty$.

One last heresy, already touched upon in the first lecture, is the possibility of high $p_\perp$ in the photon fragmentation region. That occured for the second option, discussed below Equ. (1.37). We can actually try to calculate the effect. Given in colliding beams

$$p \frac{dN}{dp d\Omega} \approx \left(1 - \frac{2p}{\sqrt{Q^2}} \right) \tag{2.11}$$

then

$$\langle p^2 \rangle = 3/2 \langle p_\perp^2 \rangle = \frac{\int_0^{\frac{1}{2}\sqrt{Q^2}} p\, dp \left(1 - \frac{2p}{\sqrt{Q^2}} \right)}{\int_0^{\frac{1}{2}\sqrt{Q^2}} \frac{dp}{p} \left(1 - \frac{2p}{\sqrt{Q^2}} \right)} \tag{2.12}$$

This gives $\langle p_\perp^2 \rangle \approx \frac{Q^2}{18} \frac{1}{\left[\log \frac{Q^2}{4p_{min}^2} - 2 \right]}$ (2.13)

For $p_{min}^2 \sim 0.1\ GeV^2$ and $Q^2 \sim 10\ GeV^2$, we get

$$\sqrt{\langle p_\perp^2 \rangle} \sim 650\ MeV$$

Were this to carry over to electroproduction, some broadening in $p_\perp$ should be discerned at these large Q^2. For $Q^2 \sim 50\ GeV^2$ the $\langle p_\perp \rangle$ is about 1 GeV. Experimentally, this option is perhaps still open, but it should be easy to close out (or verify) at NAL. It also should not be difficult to calculate this better. One should compute $d\sigma / dy\, dp_\perp^2$ by putting in a "reasonable" mass spectrum $\rho(m^2)$ of vector states and doing properly

the folds over angle, momentum, and mass.

B. Orthodox Models

What we call orthodox models are those which build upon various combinations of parton, light-cone, Mueller-Regge, and short-range-correlation-in-rapidity concepts. We start with the parton ideas, and shall assume some familiarity with the basic concepts and results[20]: Central is the hypothesis that, for purposes of calculation of deep-inelastic processes, an energetic hadron may be considered a beam of non-interacting, pointlike constituents, the partons, whose momentum spectrum looks like a hadronic inclusive spectrum:

$$\frac{dN_i}{dx} = \frac{1}{x}\, d_i(x) \qquad x = \frac{P_\mu^{(\text{parton})}}{P_\mu^{(\text{hadron})}} \tag{2.14}$$

Then in the scale limit

$$(1-x)\,\sigma_T = \frac{4\pi^2\alpha^2}{Q^2} \sum_i e_i^2\, d_i(x) \tag{2.15}$$

or $$\nu W_2 = F(x) = \sum_i e_i^2\, d_i(x)$$

Now we want to watch the evolution of the struck parton, which is to be considered as a quantum of some H_0: $H = H_0 + V$. In phase space (using the laboratory frame) the parton configurations just before and after the collision look something like the pictures in Fig. 9a and 9b. Now let us conjecture that sometime later (what happens in the interim is the subject matter of the third lecture), the struck parton has multiplied into many by a succession of soft, low-$p_\perp$ actions of V (which as time goes on operates in creating partons out of the vacuum). Then later on, the picture changes into what is shown in Fig. 9c. The new partons must lie approximately on a line extending from the origin, in order that the relative $p_\perp$ of the various created partons remain small. Once some kind of equilibrium has been established, the parton distribution may be expected to be quite similar to the parton distributions used in hadron collisions.[21]

To go further requires additional hypothesies. The main ones are

a) The momentum distribution of hadrons emerging in the direction of the struck

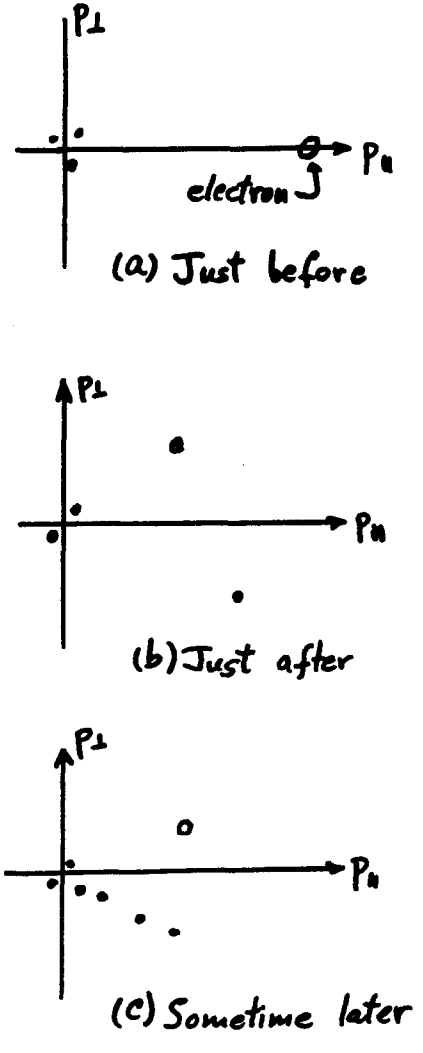

Deep inelastic electroproduction as seen in parton phase space (laboratory frame)

(a) Just before the collision

(b) Just after the collision

(c) Some time later

Fig. 9

parton scales in the Feynman sense:

$$\frac{dN}{dz}_{\text{hadron}} = D_q^h(z) \qquad z = \frac{P_\mu^{(\text{hadron})}}{P_\mu^{(\text{parton})}} \tag{2.16}$$

b) The distribution of hadrons with finite z depends only on the properties of the parent parton (already implied in Equ. (2.16).

Both these hypotheses are motivated by the expectation that the nontrivial action of V is confined to low - $p_\perp$, short-range-correlation-in-y processes. To apply these ideas, look first at e^+e^- annihilation. For the parent partons of spin $\frac{1}{2}$, folklore gives

$$R = \frac{\sigma(e^+e^- \to \text{hadrons})}{\sigma(e^+e^- \to \mu^+\mu^-)} = \sum_i e_i^2 = \begin{cases} \frac{4}{9} + \frac{1}{9} + \frac{1}{9} & \text{quarks} \\ 3 \times \frac{2}{3} & \text{red, white, blue quarks} \end{cases} \tag{2.17}$$

Thus, the probability of making first a $u\bar{u}$ quark pair is 67%, and $d\bar{d}$ or $s\bar{s}$ only 17%.

For inclusive pion distributions, say π^+, we get

$$\frac{dN\pi^+}{dz} = \frac{2}{3} D_u^{\pi^+}(z) + \frac{1}{6} D_d^{\pi^+}(z) + \frac{1}{6} D_s^{\pi^+}(z) \tag{2.18}$$

etc.

Also, from isospin selection rules

$$dN^{\pi^+} + dN^{\pi^-} = 2\,dN^{\pi^0}$$

This means for annihilation that

$$\frac{dN^{\pi^+}}{dz} = \frac{dN^{\pi^-}}{dz} = \frac{dN^{\pi^0}}{dz} \tag{2.19}$$

In electroproduction, we have a similar situation. For example, let $z = p_{\pi^+}/\nu$ and $x = Q^2/2M\nu = \omega^{-1}$. Then

$$\frac{dN\pi^+}{dz} = \frac{\sum_i e_i^2 d_i(x) D_i^{\pi^+}(z)}{\sum_i e_i^2 d_i(x)} \equiv \sum_i \epsilon_i(x) D_i^{\pi^+}(z) \tag{2.20}$$

where ϵ_i = probability parton of type i is struck by the incident electron. There are several D_i^h to determine, atop the problem of establishing all the $d_i(x)$ to begin with[22]. It therefore is of some value to survey what the composition of parton "beams" as produced in deep-inelastic processes is likely to be under various circumstances. We already saw that e^+e^- annihilation produces 67% $u + \bar{u}$, and we thus tend to measure $D_u^h + D_{\bar{u}}^h$ reasonably directly. [This also should hold for leading hadrons in electroproduction at very large ω.]

Neutrino-nucleon interactions at large x proceed via interaction with a q (not $\bar{q}$). [The evidence is the nearly $3/1$ experimental ratio of $\sigma_{\nu N}/\sigma_{\bar{\nu}N}$; the pointlike νq cross-section is 3 times the $\bar{\nu}q$ cross section.] Therefore νn or νp processes at large x produce a nearly pure beam of u-quarks, and $\bar{\nu}n$ or $\bar{\nu}p$ a pure beam of d-quarks. Likewise, at large x, ep scattering proceeds mainly from scattering of a u-quark; again antiquarks should be a small contamination:

$$\begin{aligned} \nu W_2^{ep} &\cong \frac{4}{9} d_u^{(p)}(x) + \frac{1}{9} d_d^{(p)}(x) \\ \nu W_2^{en} &\cong \frac{4}{9} d_u^{(n)}(x) + \frac{1}{9} d_d^{(n)}(x) \\ &= \frac{4}{9} d_d^{(p)}(x) + \frac{1}{9} d_u^{(p)}(x) \end{aligned} \tag{2.21}$$

Thus [hereafter using only the proton distributions $d_i^{(p)}$]

$$\frac{d_u}{d_d} = \frac{\epsilon_u}{\epsilon_d} = \frac{1 - \frac{1}{4}\left(\frac{N}{P}\right)}{\left(\frac{N}{P}\right) - \frac{1}{4}} \tag{2.22}$$

with $$\frac{N}{P} = \frac{\nu W_2^{en}}{\nu W_2^{ep}}$$

A rough estimate of this ratio, taken from the data, is shown in Fig. 10. Thus for ep scattering at large x, essentially only u-quarks emerge and fragment. The resulting spectrum of energetic hadrons should be the same as νp and νn in all respects. Only for en scattering is there ambiguity inasmuch as the above curve is then interpreted as the d/u ratio, and d's are coupled four times less strongly than u's ($e^2 = 1/9$, not $4/9$). Thus en scattering is especially sensitive to the nature of the distribution functions, and particle ratios should be strong functions of ω. All this is summarized in the following table:

PARTONS PRODUCED IN DEEP-INELASTIC PROCESSES

Process	Small ω	Medium ω (~ 5 - 10)	$\omega \to \infty$ (> 100 ?)
γp	Mostly u	Mostly u; some d and $\bar{u}$	$\frac{1}{3}$ u $\frac{1}{12}$ d $\lesssim \frac{1}{12}$ s
γn	Mixed u and d	Mostly u; some d and $\bar{u}$	$\frac{1}{3}\bar{u}$ $\frac{1}{12}\bar{d}$ $\lesssim \frac{1}{12}\bar{s}$
νp	Almost all u	Mostly u; some $\bar{d}$	$\frac{1}{2}$ u $\frac{1}{2}$ $\bar{d}$
νn	Almost all u	More u than νp Less d than νp	
$\bar{\nu} p$	Almost all d	Mostly d; some $\bar{u}$	$\frac{1}{2}$ d $\frac{1}{2}$ $\bar{u}$
$\bar{\nu} n$	Almost all d	Less d than $\bar{\nu} p$ More $\bar{u}$ than $\bar{\nu} p$	
e^+e^-			$\frac{1}{3}u$ $\frac{1}{3}\bar{u}$ $\frac{1}{12}d$ $\frac{1}{12}\bar{d}$ $\frac{1}{12}s$ $\frac{1}{12}\bar{s}$

The preferred parton fragmentations are listed below:[23]

$u \to \pi^+$ $\quad \bar{u} \to \pi^-$ $\quad s \to K^+; K^0$

$d \to \pi^-$ $\quad \bar{d} \to \pi^+$ $\quad \bar{s} \to K^-; \bar{K}^0$

C. Miscellaneous Questions

1. Is the parton charge retained in the parton fragmentation region?

Feynman[20] conjectured that the average charge found in the parton fragmentation region should equal that of the parent parton. This has been subsequently cast into some disrepute by Farrar and Rosner,[24] Feynman himself, and Cahn and Colglazier.[25] But it should still be checked: at large x the mean charge of the leading particles would equal $\frac{2}{3}$ for ep, νp, and νn, $\frac{1}{3}$ for $\bar{\nu} p$ and $\bar{\nu} n$, and variable for en (increasing from $\frac{1}{3}$ to $\frac{2}{3}$ as ω increases, then tending to zero as ω increases toward very large values). To see such effects, one should plot

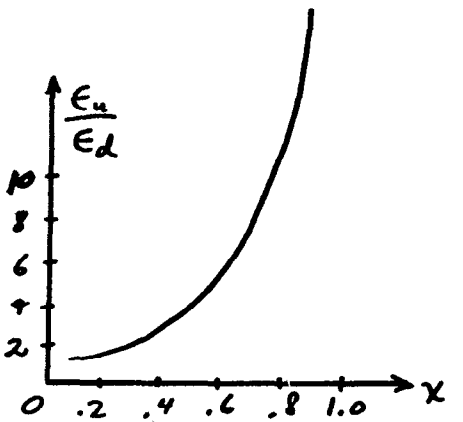

Ratio of u/d quarks in a proton as function of x.

Fig. 10

Charge found at rapidity greater than y versus y at $Q^2 = 0$.

Fig. 11

The same as Fig. 11 with Q^2 large and ω small.

Fig. 12

$$Q\,(>y) = \int_{y}^{y_{max}} \left(\frac{dN^{+}}{dy'} - \frac{dN^{-}}{dy'} \right) dy' \qquad (2.23)$$

versus y (Fig. 11). One probably needs extremely high energies ($\nu > 100$ GeV ?) to see this kind of thing.

2. What can be said about other regions in rapidity space?

a) Current plateau: As mentioned earlier, the simplest parton models tend to leave it empty. It is especially vexing in the covariant parton model of Landshoff and Polkinghorne. Their interpretation[26] is along the lines followed by advocates of the fragmentation model[27] in hadron physics: event by event one gets two isotropic fireballs in the hole and parton fragmentation regions (Fig. 13). By adjusting the probability of decay into various mass fireballs and the multiplicity distributions of the fireballs, any kind of inclusive hadron distribution can be generated, including fireballs with $\bar{n} \lesssim (Q^2)^{\frac{1}{4}}$. However, the question of how fractional charge manages to leak from one fireball to the other is not explicitly addressed. In any case, the crucial test comes in whether there exist strong positive 2-particle correlations in the current plateau region, just as for the hadronic analogue.

b) Hole fragmentation: This region is difficult. Some penetration has been attained by using Mueller-Regge analysis;[28] also, it has been discussed in the context of the Landshoff-Polkinghorne model.[29] The model of Coleman and Preparta,[30] discussed below, can provide a description, but not much has yet been done.

c) Hadron plateau and target region; large ω: Here everything should proceed as in ordinary hadron collisions.

d) Target fragmentation region at small ω: This region is characterized by difficult kinematics because t_{min} gets large. The particle distributions should depend nontrivially on ω. Existing attempts[31] to make sense of this region are complicated; a direct-channel (resonance) approach looks the most promising.[32]

3. What can be said about particle ratios?

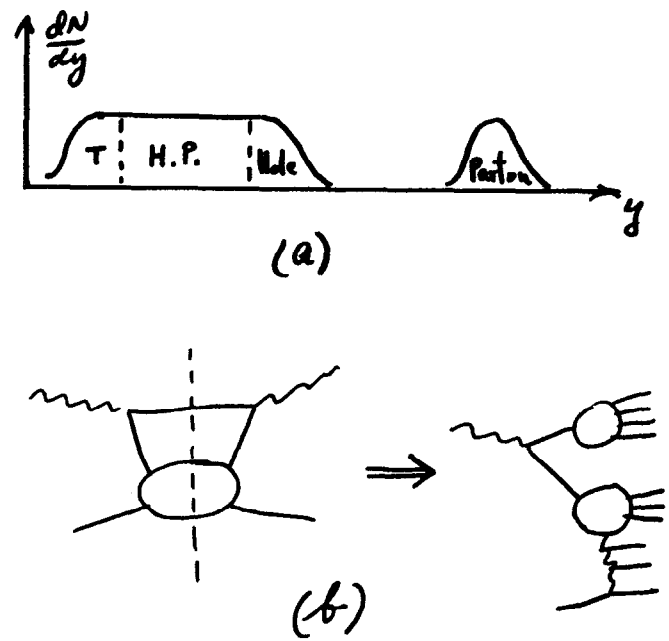

Fig. 13

Hadron production in the covariant parton model:

(a) Inclusive hadron distribution for a typical event.

(b) Nature of the diagrams which gives this.

To my knowledge there has been little progress in quantitative estimates of, say K^+/π^+ ratios. Feynman's conjecture applied to baryon number would imply in $\bar{e}p$ scattering at small ω and very high Q^2

$$\int_0^1 \frac{dz}{z} \left\{ \frac{dN^p}{dz} + \frac{dN^{\bar{n}}}{dz} - \frac{dN^{\bar{p}}}{dz} - \frac{dN^{\bar{n}}}{dz} \right\} \approx \frac{1}{3} \qquad (2.24)$$

That in turn implies lots of baryons of large z ($\lesssim 0.2$) produced. Isospin selection rules may be written down in the parton-fragmentation picture;[23] the most useful seems to be $dN_{\pi^0} = \frac{1}{2} (dN_{\pi^+} + dN_{\pi^-})$.

D. A Parton Model of Coleman and Preparata

In 1969, Coleman and Preparata[30] suggested a parton model which at first sounds totally crazy, but actually is in concordance with the "reasonable" picture put forth in the first lecture and the orthodoxy discussed above. It is quite similar to work of Loh-ping Yu,[33] who used dual n-point functions instead of Mueller-Regge amplitudes. The Coleman-Preparata version appears to provide a good basis for a phenomenology for deep-inelastic processes analogous to the very useful Mueller-Regge approach used in strong interaction phenomenology.

We start with e^+e^- annihilation, and draw the diagram shown in Fig. 14. Then write

a) γ_μ at the photon vertices

b) $\not{p}$ for the propagators. Put in no denominator because there is no support for the spectral function of a quark propagator. [The quarks have infinite mass].

c) For the vertices and reggeon $\gamma^\nu \gamma_\nu (Q^2)^{\alpha-1} F(p_1^2 \ldots p_4^2, t)$ where F vanishes rapidly if any of its variables becomes large.

Then, the vacuum polarization is

$$\pi_{\alpha\beta} \sim \int d\Omega_1 d\Omega_2 \, dp_1^2 \ldots dp_4^2 \, \mathrm{Tr}\, \gamma_\alpha \not{p}_1 \gamma_\nu \not{p}_2 \gamma_\beta \not{p}_3 \gamma^\nu \not{p}_4 (Q^2)^{\alpha-1} F$$

$$\sim (Q_\alpha Q_\beta - g_{\alpha\beta} Q^2)(Q^2)^{\alpha-1} \qquad (2.25)$$

which scales provided $\alpha = 1$ [Notice the angle integration $d\Omega_2$ provides a factor

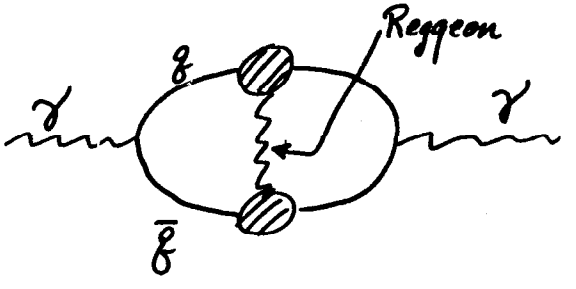

Fig. 14

Diagram for e^+e^- annihilation in the Coleman-Preparata model.

$\sim$ const/Q^2 because of the cutoff in t.] Furthermore, the generalization to electroproduction is again satisfactory. The details we leave as an exercise. The Mueller-Regge diagram for large ω is shown in Fig. 15. The vector-dominance paradox encountered in the first lecture is circumvented by the assumption that the $p_\perp$ of the $\bar{q}$ relative to the axis defined by the space momenta of the q and P (in some collinear frame of reference) is small. This is just the jet alignment discussed in the first lecture. Furthermore, the locations in rapidity-space, for given ω, of the q and $\bar{q}$ momenta are just the parton and hole fragmentation regions.

This model therefore is a concrete realization of the picture described in the first lecture. It has more power, because the approach to scaling of inclusive distributions (secondary Mueller-Regge trajectories) and correlation functions are easily attacked. For example, correlations of a particle in the parton region with one in the hole region is given in terms of a Mueller 10-point function, as shown in Fig. 16. It should be clear that nontrivial correlations will exist. Much of this has been worked out recently by Preparata.[34]

III. Space-Time Description of High Energy Processes

This lecture owes a great deal to many discussions with Moshe Kugler and Uzi Bar Gadda. It also draws much from the ideas of Leonard Susskind.[35]

A. Nonrelativistic Intuition

The need for understanding the evolution of deep inelastic processes in space-time, especially when studying the hadron final-state problem, can be illustrated already in my favorite nonrelativistic analogue. The analogue is the Coulomb scattering of an incident lepton by a point charge bound in a potential well.[36] There, the matrix element is

$$T_n(q) = \int d^3x\ \psi_n^*(x)\ e^{iq\cdot x}\ \psi_0(x) \tag{3.1}$$

and the structure function is

$$W(\nu, q^2) = \sum_n |T_n|^2\ \delta(E_n - E_0 - \nu) \tag{3.2}$$

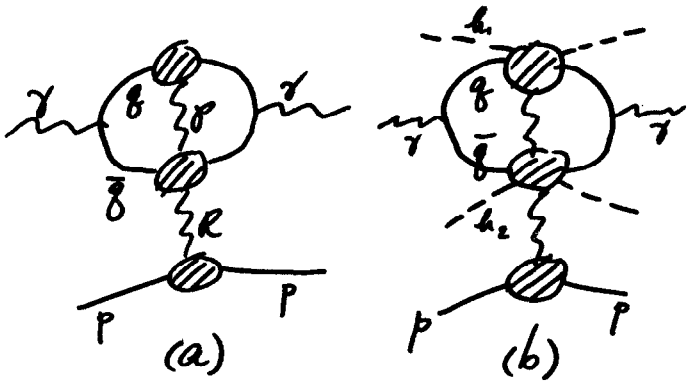

Fig. 15

Diagrams for electroproduction in the Coleman-Preparata model.

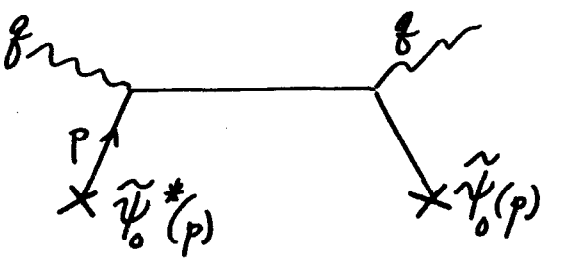

Fig. 16

"Handbag" diagram for non-relavistic analogue.

At high Q^2 the mean behavior of W is a peak centered about $\nu = q^2/2m$ (the classical value) doppler-broadened by the zero-point fluctuations in momentum. The area under the peak is normalized to unity. More specifically, there is

(i) an "Adler sum rule"

$$\int_0^\infty d\nu \; W(\nu, Q^2) = 1 \tag{3.3}$$

(ii) a scaling law

$$qW = F\left(\frac{\nu - q^2/2m}{q}\right) \equiv F(\omega) \tag{3.4}$$

(iii) a parton model

$$W \cong \int d^3p \left|\tilde{\psi}_o(p)\right|^2 \delta\left(\nu - \frac{(p+q)^2}{2m}\right) \tag{3.5}$$

where $\tilde{\psi}_o(p)$ is the momentum-space ground state wave function.

(iv) a bilocal operator

$$qW \to \int d^3p \left|\tilde{\psi}_o(p)\right|^2 \delta\left(\omega - \frac{p_z}{m}\right)$$
$$= \int d^2x\, dz\, dz'\, e^{i\omega(z-z')}\, \psi_o^*(x, z')\, \psi_o(x, z) \tag{3.6}$$

[Notice the scale variable is ground-state velocity.]

The simple "handbag diagram" (Fig. 16) suffices to determine the deep inelastic structure function. Yet if the oscillator well were harmonic, to use plane-wave eigenfunctions (the parton basis) would be, to say the least, inadequate to describe the nature of the final states as a set of discrete levels. And were an ionization potential reached, we would have the situation shown in Fig. 17.

Another way of seeing this is that the factor $e^{iq\cdot x}\psi_o(x)$ is a wave-packet of momentum $\sim q$. Provided that in the region near $x = 0$, where $\psi_o(x) \neq 0$, we have $\left|\nu(x) - \nu(0)\right| << q^2/2m$, we may then use a plane-wave basis <u>locally</u> for the excited states. But once the packet starts moving away, we no longer can. Then the interest turns to its classical motion: what is the orbit the packet follows??

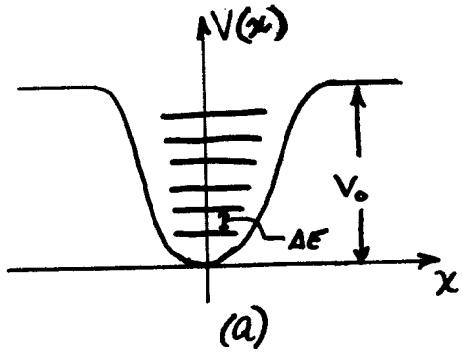

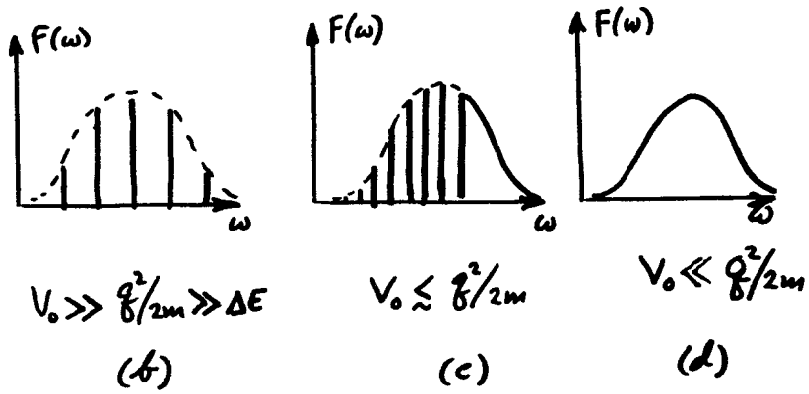

Fig. 17

Structure function in the analogue model for various q^2.

B. Hadron-hadron Collisions

The problem of interest is harder: we have relativity and we have many degrees of freedom. But there are similarities to the oscillator example: partons have quark quantum numbers, but nothing like that seems to exist in the spectrum of the full Hamiltonian H. (Better, if states of quark quantum numbers exist, they only do at energies so high they are irrelevant for this discussion.) Furthermore, the linear Regge trajectories and dual models suggest an oscillator-like potential. Thus there is no reason, intuitive or otherwise, to expect the partons to get out. However, it is clearly important to try to figure out how the entrapment occurs. The problem will certainly be no easier than understanding why quarks bind into hadrons.

Our strategy is first to look at the space-time development of ordinary collision processes. Then having become used to the pictures for them, we shall try to generalize to deep-inelastic processes. In passing, we will compare the short-range correlation, fragmentation, and Landau-hydrodynamic pictures of high energy collisions, with the emphasis on the first.

The most familiar pictures of these processes are shown below:

This is a proton at rest.

See the proton at rest.

This is an energetic proton.

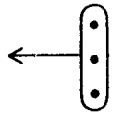

See the energetic proton.

This is the energetic proton after the collision.

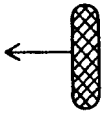

This is the excited proton after the collision.

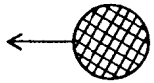

This is the diagram which motivates the model.

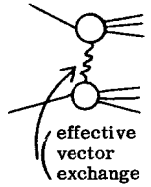

We shall return to this, but now turn to the short-range correlation picture. It is slightly more complicated, because of the presence of wee partons and/or hadrons, and what Kogut and Susskind [37] call "the long arm of the vacuum". As we boost the proton from rest, we "pull wee partons out of the vacuum".

Again, see the proton at rest (Fig. 18). It is composed of a few wee partons with excitation energies to resonances and other higher states of a few hundred MeV. Now see the proton in motion, with a Lorentz boost factor $\gamma \sim 3$ (Fig. 19). The moving proton couples nontrivially to wee vacuum fluctuations indicated by region II. These fluctuations are not Lorentz contracted.

Now boost yet another factor 3 (Fig. 20). We pull more wees from the vacuum, creating region III, and the old region II becomes Lorentz contracted. And so on. Notice now the following points characterizing the separate rapidity regions:

a) The internal momenta of the partons is of order e^{+y}.

b) The level density increases with y; $\Delta E \sim e^{-y}$ because

$$E_n = \sqrt{p_z^2 + p_\perp^2 + M_n^2} \cong P_z + \frac{P_\perp^2 + M_n^2}{2P_z} \tag{3.7}$$

and

$$\Delta E \sim \frac{\Delta M^2}{2p_z} \sim e^{-y} \tag{3.8}$$

c) The thickness of the configuration-space region housing the partons in a given rapidity bin (which we shall call the lag = Δz) decreases with increasing y because of Lorentz contraction:

$$y \approx -\log \text{lag} = -\log \Delta z \tag{3.9}$$

In configuration space rapidity can be determined by, or related to, the value of the lag.

d) The rate of interaction of the partons in a given rapidity bin decreases with increasing y like e^{-y}.

e) An implicit assumption is that the coupling between adjacent rapidity regions,

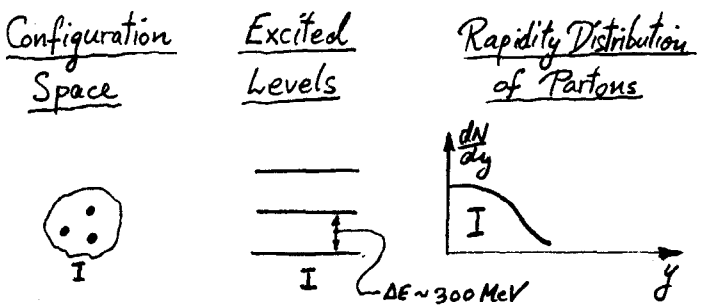

See the proton at rest.

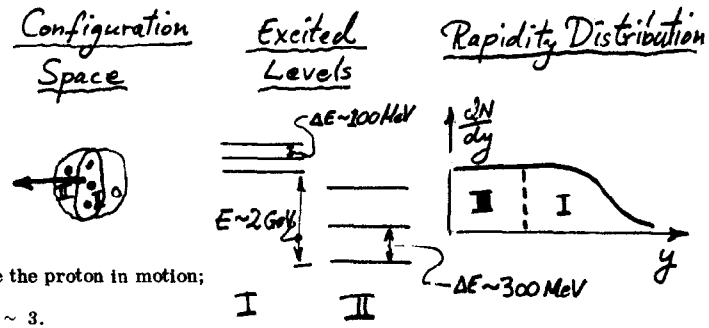

See the proton in motion;

$\gamma \sim 3$.

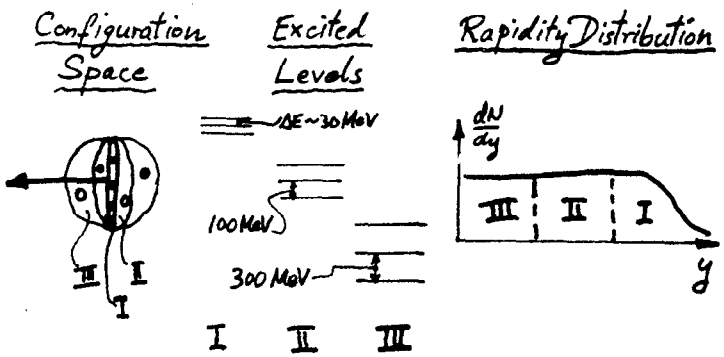

See the proton in motion;

$\gamma \sim 9$.

Figs. 18, 19, 20

while non-negligible, is still small enough that we can meaningfully discuss a spectrum of levels in the separate rapidity bins I, II, III, ... as a zeroth approximation.

f) Couplings between non-adjacent rapidity intervals are ignored.

If one boosts back to the rest frame and asks where regions II and III go, they evidently expand longitudinally into the vacuum surrounding the proton (Fig. 21) but with enormous excitation energies. Hence excitation of those regions are "frozen out" in collisions of moderate energies, and they remain in their ground state.

Now consider a collision process in the center-of mass frame (Fig. 22). The interaction is to occur, as Feynman suggested,[4] by interchange of partons: two gases (III and C) come into contact and exchange partons of comparable momenta (all wee), heating each other up. Just after this exchange, we have the situation shown in Fig. 23. Regions III and C are hot (i.e. excited states are populated); the other regions are cold (in the ground state). After a time ct ~ 1 f. these regions cool by two mechanisms. The first is emission of hadrons and the second is the heating up of the adjacent regions II and B, which is easily done because of the higher level density existing there. This state of affairs persists on a <u>longer</u> time-scale, because of the time-dilation of the dynamics, e.g. $ct_{II} \sim 3$ f. At such a time we have the pi cture illustrated in Fig. 24. At a time $ct_I \sim 9$ f., regions II and B have cooled, heating regions I and A, and emitting <u>non-wee</u> hadrons, as shown in Fig. 25. Evidently the total time duration of the process is ~the time required for regions I and A to cool, which in turn is proportional to the momenta of the partons in those regions, $\sim E_{cm}$. Furthermore, the wee hadrons emerge first from the interaction region (which is a cylindrical tube along the collision axis, of diameter ~1 f.), and the rapidity-plateau of the produced hadrons builds up from the center outwards as time increases. In a space-time diagram, the heating takes place on a proper-time shell, as shown in Fig. 26. To see this, notice that the time for any hadron to emerge from the interaction tube is proportional to its momentum (both from simple geometry, or from the time-dilatation argument). But then its lag (t - z) is $\sim P^{-1}$. Hence

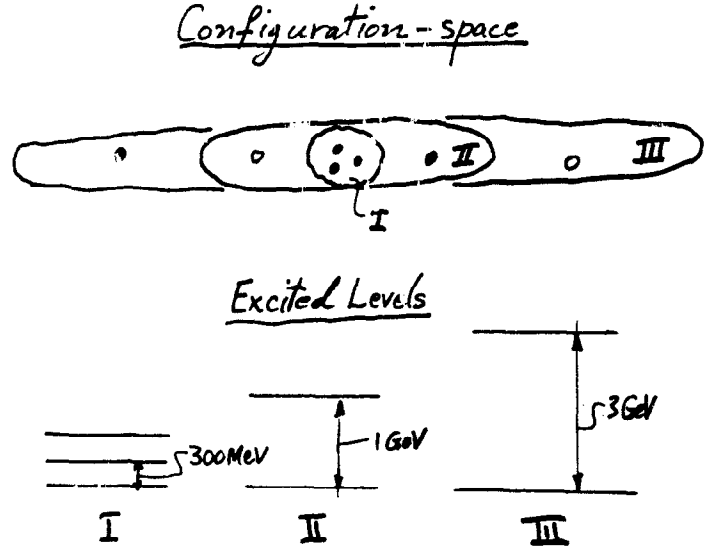

Fig. 21

See the proton at rest again. Where did the wee partons go? Into longitudinal configuration space.

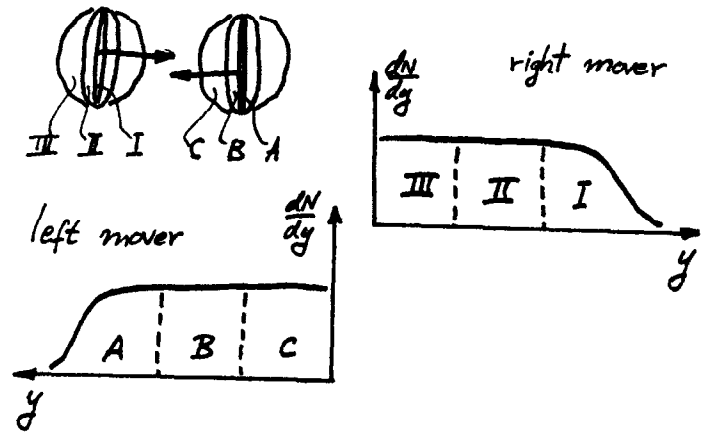

Fig. 22

See the proton-proton collision.

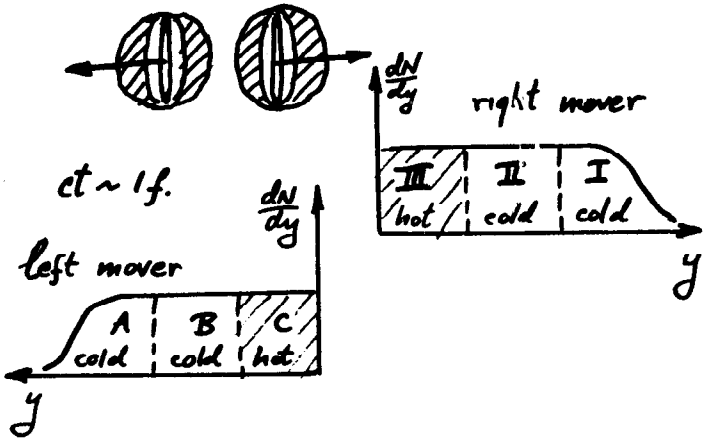

Fig. 23

See the protons at ct ~ 1f. after the collision. The wee regions are hot.

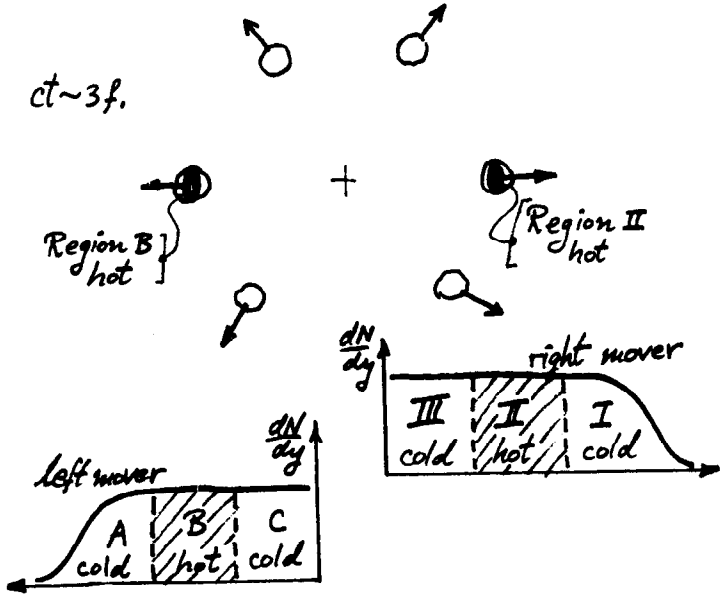

Fig. 24

See the products at ct ~ 3f. after the collision. The wee regions have cooled. Regions B and II are hot.

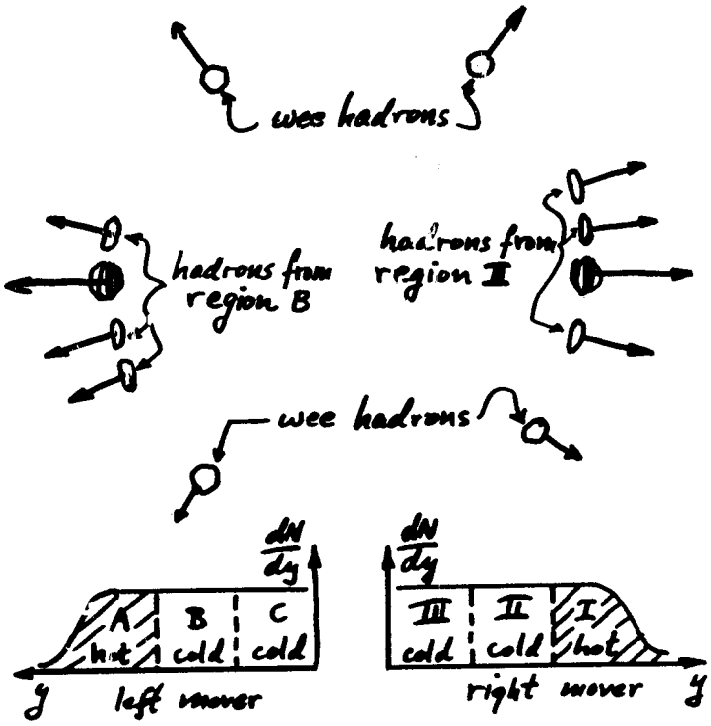

Fig. 25

See the products at ct ~ 9f. The leading partons are now hot.

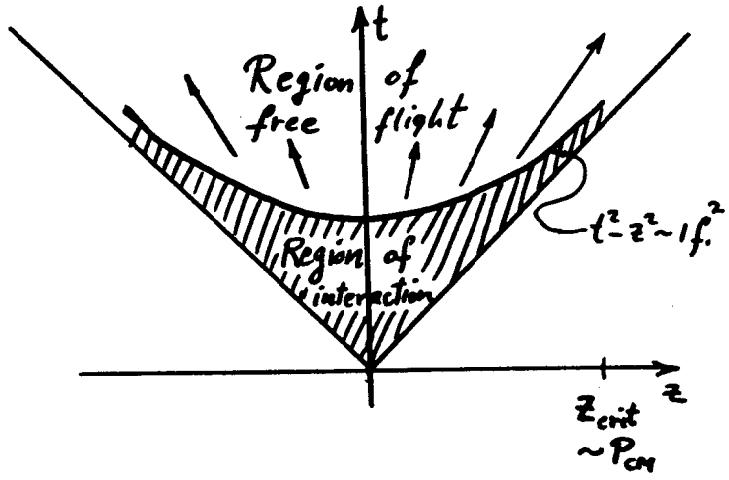

Fig. 26

Where the action is in space-time.

$$t^2 - z^2 = (t-z)(t+z) \sim P^{-1} P \sim 0 \ (1) \qquad (3.10)$$

and all the parton excitation is in the vicinity of the proper time surface (and of course the z - t plane).

It helps also to view the process in the FISR (Fool's Intersecting Storage Ring) configuration.[38] Take an ISR and inject both beams in the same direction (say, clockwise) and view the collision from the downstream side, as shown in Fig. 27. Then we see two uncontracted discs moving through each other at velocities $v/c \sim \theta$. Again we can divide the parton distributions into separate rapidity-cells, and expect interaction between cells of comparable rapidity. Take beam energies of 100 GeV and $\theta \sim 0.1$. The rapidity cells are shown in Fig. 28. Then we expect at best only I to interact with A, II with B, etc. But regions I and A cannot appreciably interact by parton interchange because the upward and downward movers have $p_\perp \sim +(5 \pm 0.3)$ GeV and $-(5 \pm 0.3)$ GeV respectively, and have little common transverse momentum. The situation is similar with regions II and B. Regions III and C have low $p_\perp$ and can excite each other by interchange of partons. This region of excitation is defined by the relation

$$p/p_{\max} \cong \frac{\langle p_\perp \rangle}{p_\perp^{\max}} \sim \frac{0.3 \text{ GeV}}{E_{cm}} \qquad (3.11)$$

Evidently regions III and C are analogous to the regions containing the wee partons at the wise-man's ISR, as discussed earlier, and the evolution with time can be worked out in a similar way.

What about the really wee regions at the FISR, e.g. IV, D and beyond? While the rapidities and $p_\perp$ of the partons again overlap, there is no excitation because the level density is so low. The energy needed to excite such regions is growing like E^{-1} as E decreases, while the momentum (and energy) exchanged doesn't grow; it is given by $\langle p_\perp \rangle$. There is a rough analogue with what happens in atom-atom scattering.[39]

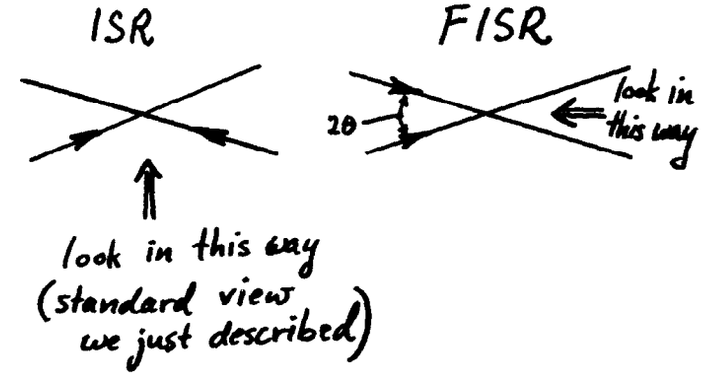

Fig. 27

The ISR and FISR.

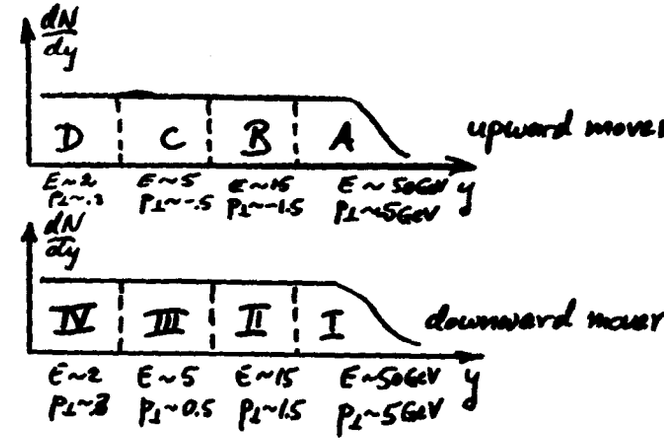

Fig. 28

Rapidity distributions of the upward and downward movers. (Or should they be inward and outward movers?)

Parton Model	Atomic Analogue
1. Leading right-moving partons don't interact strongly with leading left-moving partons.	1. Atom-atom collisions for $\bar{V}$ atom >> < V > electrons can be calculated using Born approximation for hard single-electron collisions.
2. Wee partons are interchanged between the two projectiles.	2. When $\bar{V}$ atom ~ < V > electrons, two Thomas-Fermi gases interpenetrate and heat each other.
3. Excitation of superwee partons is frozen out.	3. When $\bar{V}$ atom <<< $V >_{\text{valence electrons}}$, no inelastic scattering; adiabatic shift of levels during the collision.

So much for the short-range correlation picture. We return briefly to the fragmentation picture of the collision. There all the partons interact directly with each other. Perhaps we can say all rapidity cells are excited during the passage of the projectiles through each other ($ct \lesssim 1$ f.) and then de-excite on a time-scale proportional to the momentum in the cell. The time evolution would look the same as in Figs. 23 - 25 except that all cells with rapidities larger than the ones marked "hot" would also be hot.

However, this long-range correlation picture differs from the standard one discussed by Benecke, Chou, Yang, and Yen[27] and by Hwa[40] and others. There one envisages such strong coupling between the right-moving rapidity cells that one can only talk about a single right-moving fireball produced, which then decays. Event by event one gets a rapidity distribution as shown in Fig. 29. The fireballs occur at different y's depending on their mass, and this can generate a smooth inclusive

Fig. 29

Typical final configuration in the fragmentation model.

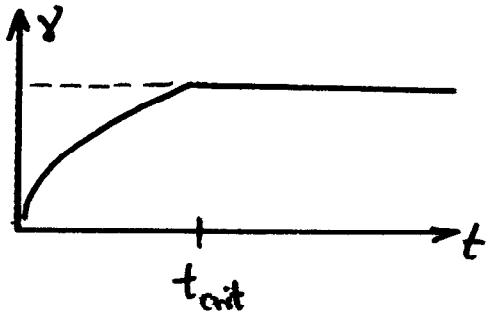

Fig. 30

Gas velocity at a given lag as function of time in Landau's model.

distribution. The central wee region becomes populated only by occasional big fireballs with $\bar{n} \sim E_{cM}$, providing an enormous positive two-particle correlation in that region. It is not seen experimentally. Notice that the volume from which that fireball emerges is not Lorentz contracted, because it decays roughly isotropically.

Even in the granddaddy of production models, Fermi's statistical model, the Lorentz contraction was put in. Landau elaborated this into a hydrodynamical model, which even today doesn't do badly when compared with experiment. In the Landau model, as described in the second lecture, the parton gas in the beginning is very hot, at rest in the center-of-mass frame, and in a very small Lorentz-contracted volume. The equation of state $E = \frac{1}{3} p$ and the hydrodynamic equation $\partial_\mu T^{\mu\nu} = 0$ is used to track the gas into the future. I will not describe the calculations but only the results:

i) In a given rapidity cell, defined in the configuration-space sense of $y \sim -\log lag$, the gas velocity increases with time; the boost factor γ grows like $\sqrt{t}$:

$$\gamma \sim \sqrt{\frac{t}{t-z}} \tag{3.12}$$

ii) The entropy in a given rapidity bin (computed in the local rest frame) decreases with time, according to the formula

$$\frac{dS}{dy} \sim \exp -\tfrac{1}{2}\left(\sqrt{\log t\, E_{cm}} - \sqrt{(y_{max} - y)}\right)^2 \approx t^{-\frac{1}{2}} \tag{3.13}$$

iii) For any given rapidity bin there is a critical time (the "time of conical flight") after which the transverse expansion of the gas cannot be neglected. At that point, the gas velocity has increased to the value it would have in the short-range correlation picture. [Remember that in that case, it is essentially a constant in time; nothing drastic happens to a parton in an ordinary collision process.] Thus the critical value is

$$\gamma_{crit} \sim \frac{E\ parton}{0.3\ GeV} \approx e^{y} \tag{3.14}$$

γ versus time is shown in Fig. 30. After the critical time, the gas in a given element of solid angle $d(\log \tan \theta/2) = dy$ expands radially, i. e. remains in that solid angle. As the gas expands, the entropy-density rapidly drops. As discussed before, entropy conservation implies that the number of hadrons emerging is still proportional to the entropy at the onset of conical flight. This critical time is $t \sim E \sim e^{y}$ (the same as for the short-range correlation picture). Hence

$$\log\ t\ E_{cm} \approx y_{max} + y \tag{3.15}$$

and at the critical point in time t_{crit}, from Equ. (3.13)

$$\frac{dN}{dy} \sim \frac{dS}{dy} \approx \exp -\tfrac{1}{2}\left(\sqrt{y_{max}+y} - \sqrt{y_{max}-y}\right)^2 \approx s^{-\frac{1}{4}} \exp -\tfrac{1}{2}\sqrt{y^2_{max} - y^2} \tag{3.16}$$

The general picture in space-time looks quite like the short-range correlation picture; the wee partons cool off fastest and the wee hadrons are emitted first; etc. However, the degree of excitation (entropy-density) is initially high everywhere in phase space. As time goes on, the entropy moves toward the central rapidity region until the critical point of conical flight is reached; then it is "frozen". This is opposite to the short-range-correlation model where the entropy originates in the central region and moves toward the leading partons as time increases. Also, in the short-range correlation picture the particles leaving the interaction cylinder are generally very little excited; in the hydrodynamical model they are still excited but rapidly cool off.

C. Deep Inelastic Phonomena

Now that we have gotten accustomed to this way of thinking, let us consider deep-inelastic phenomena in the same light. The central problem is to understand the current fragmentation regions in electroproduction, and the entire process in e^+e^- annihilation. We have seen that, in all the pictures of elementary collision processes at high energy, very large distances ($\sim \left(E/M_p\right)$ x 1 f.) are involved before the asymptotic state of all the produced hadrons is reached. Thus there is hope that, just as in the nonrelativistic oscillator example, it pays to try to follow the motion of the system in space-time trying to determine classically or semi-classically its motion. We must also keep in mind that the important distances in electroproduction are large. For example, in the "handbag diagram" analogous to

Fig. 16, we need quasi-free parton propagation (in the laboratory frame) over a distance $\sim \omega/M \approx 0.2\,\omega$ fermis.[41] In considering e^+e^- annihilation, assumed to begin by materialization of a parton-antiparton pair, it therefore does not seem appropriate to instantly destroy the propagation of the pair before they travel some distance away from the point of creation. In fact, the simplest analogue from the short-range-correlation picture for ordinary collisions is that it takes a time $t \approx Q$ for such an energetic parton to do something. According to this viewpoint, if there is a time scale τ for a 1 GeV parton to "fragment", the time-scale is 2τ for a 2 GeV parton, 10τ for a 10 GeV parton, etc. Then at sufficiently high energies the parton-antiparton pair is separated in space a large distance before it does anything (see Fig. 31). But at that time the groups can no longer communicate.[42] If the partons have fractional charge, so do the two groups of hadrons. Can this be evaded somehow? For example, let the parton radiate all its momentum, come to rest, and then start falling back into the center, as in Fig. 32. This doesn't work all that well, because a force field must be established to pull the q and $\bar{q}$ back together, and that must be done in a causal way. Either the field was established on the way out (by the $q\bar{q}$ pair itself; that means they really were interacting with quanta on the way out, contrary to what was assumed), or else it has to be somehow established after the quarks stop. In space-time, the activity would go on in a region as shown in Fig. 33. That picture is too far out in left field; it is awkward. I once advocated it,[43] but I want to make it clear that I now consider it inoperative.

Another somewhat disturbing feature is that the evolution of the final state is very different than for an ordinary collision. If, on the basis of the first lecture, we accept the expectation that nothing very striking differentiates hadron final states in deep-inelastic processes from those in ordinary processes, it might be hard to accommodate that result with a radically different early history of the final configuration. And, in any case, there seems no way of avoiding the conclusion that in e^+e^- annihilation something happens to the parton right away, within a region of diameter, say

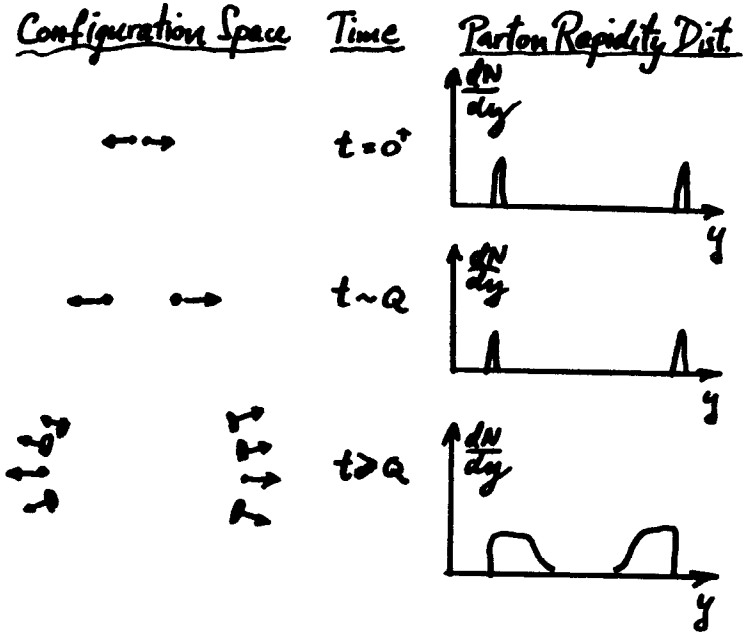

Fig. 31

Evolution of partons and hadrons in an "outside-inside" cascade process (e^+e^- annihilation).

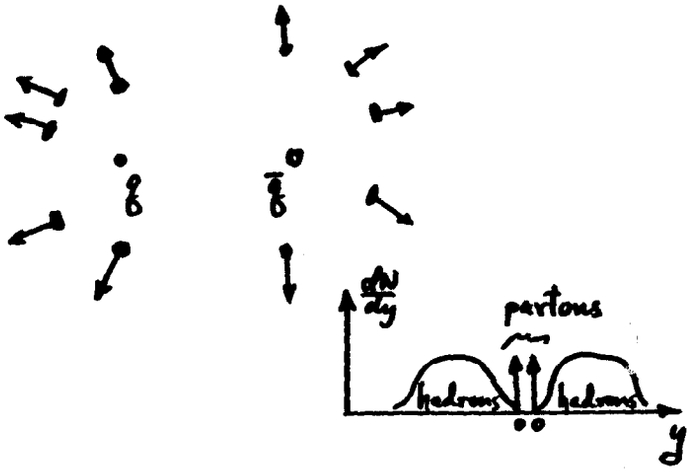

Fig. 32

Later on; the quarks are stranded.

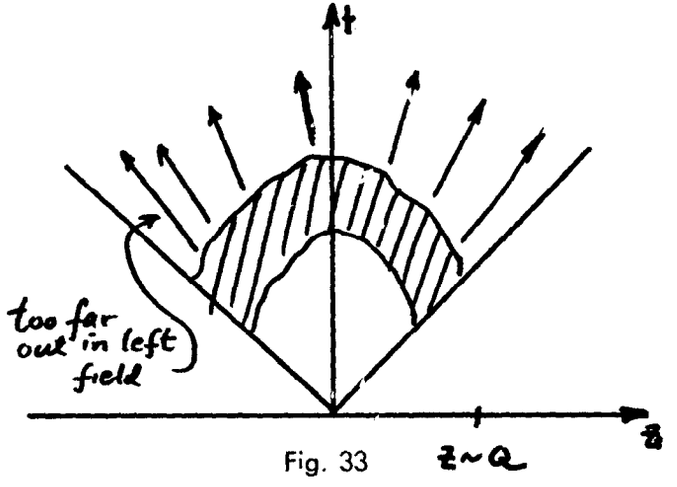

Fig. 33 $z \sim Q$

Where the action is in space-time for such a model.

$\lesssim 10^{-13}$ cm., independent of the parton momentum, before the parton separates from its antiparton. If the evolution of the final hadrons is at least similar to their evolution in ordinary processes, we need only go back to the previous case and ask whether the same evolutionary scheme can be applied. If so, the history will be as shown in Fig. 34, which should by now be self-explanatory. We see that a polarization charge develops behind the leading partons; this charge chases the original partons (with ever smaller lag) out until the plateau region is filled up with emitted hadrons. At about the time the plateau has filled up, the polarization charge has rapidity comparable to that of the leading parton and they can annihilate and neutralize each other. Evidently the plateau of hadrons is being built in a qualitatively similar way and at the same rate as for ordinary collisions. Thus the time-scale for capture of the leading parton is $t \sim Q$.

What is the price that has been paid to obtain this picture? It is clear: long-range correlations in rapidity when the dynamics involves spatial separation of fractional charge. The most natural way of paying that price is by introducing a coupling of the partons to $J = 1$ gluons, presumably via a gauge theory. Coupling of the parton to wee $J = 1$ gluons, in addition to providing the necessary long-range correlations in rapidity, also have the property of just putting an eikonal "Coulomb" phase on the leading parton wave-function. The effect of such an eikonal phase is to decelerate the leading partons, in compensation for the energy being pumped into hadron production in the central plateau. That energy becomes comparable to the parton energy only when the plateau has grown so as to fill up the phase space, i. e. at capture time $t \sim Q$. However, the effect on the parton wave function is slight for the important distance and time scales in deep inelastic processes: $t^2 - z^2 \sim 1/Q^2$ in e^+e^- annihilation, and $z \lesssim \nu/Q^2$ in electroproduction (laboratory frame kinematics), as compared with $t^2 - z^2 \sim m_\rho^{-2}$ and $z \sim \nu/m_\rho^2$ for the times required for parton capture.

Can a field-theory model actually reproduce this behavior?? An important step in the right direction was taken by Casher, Kogut, and Susskind,[44] who showed

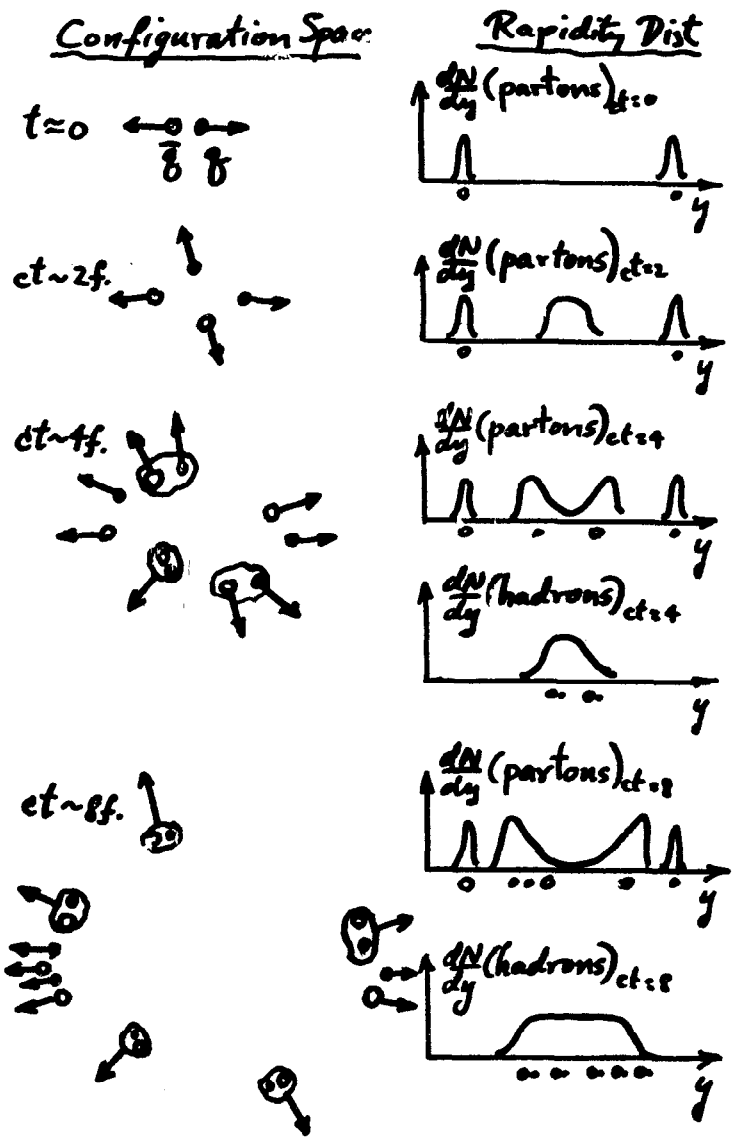

Fig. 34

Evolution of the final state for an "inside-outside" cascade (e^+e^- annihilation). The circles and dots are antipartons and partons; when joined by a line, they indicate a hadron.

that the soluble model of two-dimensional massless spinor electrodynamics[45] exhibits many of these features. In that model, the vacuum polarization is so strong that the Coulomb field is completely screened and becomes a Yukawa field $\sim e^{-\mu x}$ with $\mu^2 = e^2/\pi$. Casher, Kogut, and Susskind show:

1) Given an external source consisting of point charges created at t = 0 and moving in opposite directions at the speed of light, an induced current provided by a coherent state of the massive Yukawa gluons screens the charge, with a space-time development (lag $\sim t^{-1}$) just like we described.

2) If an external lepton ℓ scatters via a scalar coupling $\bar{\ell}\ell\ \bar{\psi}\psi$ with the charged fermionic "parton" in the theory (the vector coupling turns out to be too trivial; completely gluon-dominated), then the total annihilation cross-section $\bar{\ell}\ell \to$ anything at high Q^2 becomes the point cross-section for producing the parton pair. However, the final state consists only of gluons.

3) Deep-inelastic scattering of ℓ from the gluon likewise exhibits scaling. The inclusive momentum distribution is pure dx/x. Only gluons appear in the final states.

4) Because the lag $|t - z|$ is small compared to the natural transverse dimensions ($x_\perp \sim 1$ f.), there is cause for optimism that the two -dimensional problem may be similar to what goes on in four dimensions. (Fig. 35) It is the same geometrical situation as what exists in Landau's hydrodynamical model, and which allowed him to reduce the problem to a two-dimensional calculation.

There are still serious questions of whether the two-dimensional model is too trivial to teach us genuine truths about the real problem. But there is at the least a very strong suggestion that gauge theories of strong interactions, which by the Higgs mechanism or otherwise provide screening of the original long-range interactions and which screen the triality or other peculiar quantum numbers of the partons, are prime candidates for a theory of strong interactions which can give the preceding picture of final-state evolution.

A final encouraging point comes from the work of t' Hooft,[46] Politzer,[47] Gross

and Wilczek,[45] who show that the short-distance behavior of such theories is that of free fields (although the approach is only logarithmic in energy). Thus these theories also seem to be the best candidates around for understanding electroproduction scaling as well, using honest field theory as a starting point.

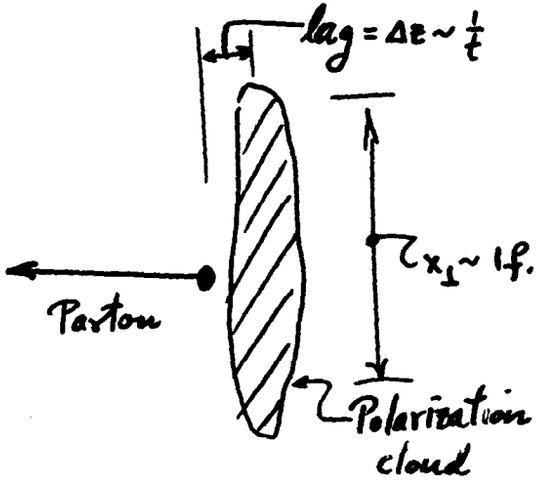

Fig. 35

Polarization cloud which chases the leading parton. The field of the cloud should be uniform in the neighborhood of the leading parton and the problem two-dimensional (one space, one time).

REFERENCES

1. S. Drell and T. Yan, Phys. Rev. Letters 24, 181 (1970).
2. G. West, Phys. Rev. Letters 24, 1206 (1970).
3. E. Bloom and F. Gilman, Phys. Rev. Letters 25, 1140 (1970).
4. R. Feynman, Phys. Rev. Letters 23, 1415 (1969).
5. J. Bjorken and J. Kogut, preprint SLAC-PUB-1213.
6. J. J. Sakurai and D. Schildknecht, Physics Letters 41B, 409; 42B, 216 (1972).
7. We follow a method due originally to T. D. Lee and C. N. Yang, Phys. Rev. 126, 2239 (1962). Our notation follows that of J. Bjorken and E. Paschos Phys. Rev. D1, 3151 (1970).
8. For example, N. Dombey, Rev. Mod. Phys. 41, 236 (1969).
9. For example, B. Dieterle, Nuovo Cimento 11A, 525 (1972).
10. A recent review is given by M. Jacob, CERN preprint CERN-TH 1683.
11. This is entertained in Ref. 6; also see M. Greco preprint CERN-TH-1617 and references cited therein.
12. D. Yennie, Cornell preprint (1973).
13. V. Gribov, Fourth Winter Seminar on the Theory of the Nucleus and the Physics of High Energies, 1969, Ioffe Institute of Engineering Physics, Acad. Science USSR.
14. J. Bjorken and S. Brodsky, Phys. Rev. D1, 1416 (1970).
15. J. Engels, H. Satz, and K. Schilling, CERN preprint CERN-TH-1674.
16. L. Landau, Izv. Acad. Nauk SSSR 17, 31 (1953); reprinted in Collected Papers of L. D. Landau, ed. D. TerHaar (Gordon and Breach, New York, 1965).
17. P. Carruthers and Minh Duong-Van, Physics Letters 44B, 507 (1973).
18. S. Drell and T. Yan, Phys. Rev. Letters 24, 855 (1970).
19. C. Callan and D. Gross, IAS preprint.
20. R. P. Feynman, Photon-Hadron Interactions, W. A. Benjamin, New York, 1972.
21. S. Berman, J. Bjorken and J. Kogut, Phys. Rev. D4, 3388 (1971).
22. Efforts to determine the Di have been made by J. Cleymens and R. Rodenburg (preprint) and by J. Dakin and G. Feldman, preprint SLAC-PUB-1273.
23. There is a large literature on this subject. For further references, see E. Colglazier's report; also R. Cahn and J. Ellis, SLAC preprint (in preparation).
24. G. Farrar and J. Rosner, Phys. Rev. D7, 2747 (1973).
25. R. Cahn and E. W. Colglazier, preprint SLAC-PUB-1267.
26. R. Kingsley, P. Landshoff, C. Nash and J. Polkinghorne, preprint DAMPT 73/19.
27. J. Benecke, T. Chou, C. N. Yang, and E. Yen, Phys. Rev. 188, 2159 (1969).
28. R. Cahn, J. Cleymens and E. Colglazier, Phys. Lett. 43B, 323 (1973); A. Schwimmer, Phys. Rev. D8, 974 (1973).
29. C. Pantin, Nuclear Physics B53, 473 (1973).
30. S. Coleman and G. Preparata, as reported by Preparata in Subnuclear Phenomena, ed. A. Zichichi (Academic Press, New York, 1970).
31. See e. g. P. Roy, Phys. Rev. D5, 227 (1972).
32. G. Domokos, S. Kovesi-Domokos and E. Schonberg, Phys. Rev. D3, 1184 (1971). See also J. Kogut, (as preprint) c00-2220-12.
33. L. P. Yu, Phys. Rev. D4, 2785 (1971).
34. G. Preparata, Phys. Rev. D7, 2973 (1973); R. Gatto and G. Preparata, preprint.
35. See for example A. Casher and L. Susskind, Tel Aviv. Univ. preprint TA UP 343-73 and references quoted therein.
36. I learned most of this from Helen Quinn, who worked much of it out while a graduate student.
37. J. Kogut and L. Susskind, Physics Reports 8, 75 (1973).
38. This reference frame was introduced by S. Drell and T. Yan, Annals of Physics (N. Y.) 66, 578 (1971), and has been exploited extensively by R. Blankenbecler, S. Brodsky and J. Gunion; e.g. Phys. Rev. D8, 187 (1973).
39.

40. R. Hwa, Phys. Rev. Letters 26, 1143 (1971).

41. B. Ioffe, Phys. Letters 30B, 123 (1969).

42. J. Kogut, D. Sinclair and L. Susskind, Phys. Rev. D7, 3637 (1973).

43. J. Bjorken, Proceedings of the International Conference on Duality and Symmetry in Hadron Physics, ed. E. Gotsman, Weizmann Science Press, Jerusalem, 1971.

44. A. Casher, J. Kogut, and L. Susskind, Phys. Rev. Letters 31, 792 (1973).

45. J. Schwinger, Phys. Rev. 128, 2425 (1962).

46. G. t' Hooft, unpublished.

47. H. Politzer, Phys. Rev. Letters 30, 1346 (1972).

48. D. Gross and F. Wilczek, Phys. Rev. Letters 30, 1343 (1972).

HADRON PRODUCTION IN THE COLLISION OF VIRTUAL PHOTONS WITH NUCLEONS - AN EXPERIMENTAL REVIEW

Martin L. Perl

Stanford Linear Accelerator Center

Stanford University

Stanford, California 94305

Table of Contents

1. Spacelike Virtual Photon Kinematics - Cross Sections and Photon Polarization
2. Theoretical Orientation
3. The Two-Body Channel: $\gamma^* + p \rightarrow \rho^0 + p$
4. Other Two-Body Channels.
5. Spacelike Virtual Photon Kinematics - Inclusive Reactions
6. Multiplicities and Feynman Scaling
7. The Search for Virtual Photon Effects - Transverse Momentum Distributions
8. The Search for Virtual Photon Effects - Forward Charge Ratios
9. Unanswered Questions

1. Spacelike Virtual Photon Kinematics - Cross Sections and Photon Polarization.

Although I am sure that many of you are well acquainted with the kinematics of charged lepton-nucleon inelastic scattering, I shall write out the details here. First it will establish the conventions I use. Second I will not have to take the time to talk about these kinematical considerations; and we will avoid the necessity of you having to copy many equations.

The basic one-photon exchange diagram for the reaction

$$(\text{e or u}) + N \rightarrow (\text{e or u}) + 2 \text{ or more hadrons} \tag{1-1}$$

is presented in Fig. 1-1b (Fig. 1-1a presents for comparison the elastic scattering diagram.)

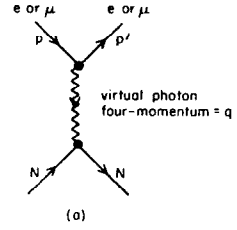

Fig. 1-1a Elastic Scattering

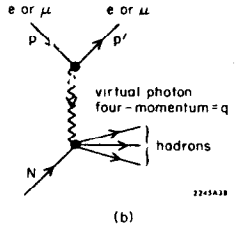

Fig. 1-1b Inelastic Scattering

We use

p = four-momentum of incident lepton (1-2)

p' = four-momentum of final lepton

P = four-momentum of incident nucleon N of mass M

P' = total four-momentum of all final hadrons

$q = p - p'$ = four-momentum of virtual photon γ^*

$\nu = q^0 = p^0_{lab} - p'^0_{lab}$ in laboratory frame

In our metric, a particle of mass m and four-momentum $p = (p^0, p^1, p^2, p^3)$ $= (E, \underset{\sim}{p}) = (E, p_x, p_y, p_z)$ has

$$p^2 = E^2 - \underset{\sim}{p}^2 = m^2 \tag{1-3}$$

Hence for our spacelike virtual photon

$$q^2 \leq 0 \quad ; \tag{1-4a}$$

And we define for convenience

$$Q^2 = -q^2 \geq 0 \tag{1-4b}$$

The invariant mass of the hadronic system is $W = \sqrt{s}$ where

$$s = W^2 = (q + P)^2 = q^2 + 2q \cdot P + M^2 \tag{1-5a}$$

$$= 2M\nu + M^2 - Q^2 \tag{1-5b}$$

$$= 2KM + M^2 \tag{1-5c}$$

Here K is the H and parameter

$$K = \nu - Q^2/2M \tag{1-5d}$$

We shall always take the lepton mass to be zero.

The study of the polarization state of the virtual photon always involves some messy algebra. There are various routes to the answer; I shall proceed through the hadronic Breit frame. But first let us consider the laboratory frame. We define in the laboratory frame, Fig. 1-2

E = energy of incident lepton

E' = energy of final lepton

Θ = scattering angle of lepton

α = angle between incident lepton and virtual photon

$\nu = q^0$

note that

$$\left|\underset{\sim}{q}\right|^2 = \nu^2 + Q^2 \tag{1-7}$$

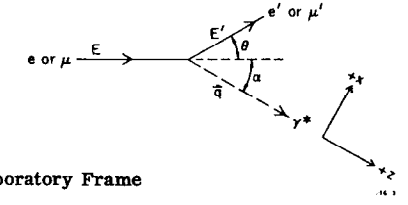

Fig. 1-2 Laboratory Frame

Then

$$\cos\ \alpha\ =\ \frac{2E\nu + Q^2}{2E\left|\underset{\sim}{q}\right|}\quad ,\qquad \sin\ \alpha\ =\ \frac{Q(4EE' - Q^2)^{1/2}}{2E\left|\underset{\sim}{q}\right|} \tag{1-8}$$

EXERCISE 1-1. Derive Eq. 1-8.

The hadronic Breit frame is the frame in which

$$P^0 = P'^0 \tag{1-9}$$

It is obtained from the laboratory frame by a Lorentz transformation along the $\underset{\sim}{q}$ axis but opposite to the direction of $\underset{\sim}{q}$, Fig. 1-2. This boost has the parameters

$$\beta\ =\ \frac{\nu}{\left|\underset{\sim}{q}\right|}\ ,\quad \gamma\ =\frac{\left|\underset{\sim}{q}\right|}{Q} \tag{1-10}$$

Then in the hadronic Breit frame, Fig. 1-3.

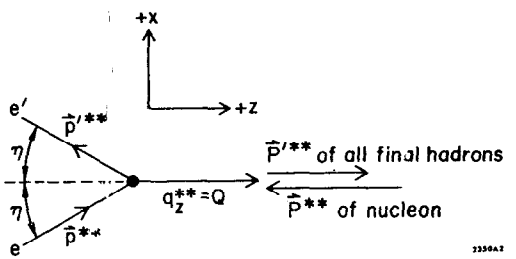

Fig. 1-3 Hadronic Breit Frame

$$E^{**}\ =\ \frac{(E + E')Q}{2\left|\underset{\sim}{q}_{lab}\right|}\ ,\ p_x^{**}\ =\ \frac{Q(4EE' - Q^2)^{1/2}}{2\left|\underset{\sim}{q}_{lab}\right|}\ ,\ p_y^{**}\ =\ 0\ ,\ p_z^{**}\ =\ \frac{Q}{2} \tag{1-11a}$$

$$q^{0**}\ =\ 0\ ,\ q_x^{**}\ =\ 0\ ,\ q_y^{**}\ =\ 0\ ,\ q_z^{**}\ =\ Q \tag{1-11b}$$

Here the ** indicates the hadronic Breit frame.

EXERCISE 1-2. Derive Eqs. 1-10 and 1-11.

We define the lepton electromagnetic four-current

$$j^{(\lambda',\lambda)}\ =\ \bar{u}^{\lambda'}\ (p')\gamma\ u^{\lambda}\ (p) \tag{1-12}$$

where j and γ are four-vectors; and $\lambda\ ,\lambda'\ = \pm\ 1/2$ abbreviated to $\pm$. In calculating j we use the Bjorken-Drell conventions[1] except that we use for the density of states $1/2E$, rather than m/E, for fermions as well as bosons.[2] Using, in the hadronic Breit frame,

$$u^{+}\ =\ \sqrt{E^{**}}\begin{pmatrix}\cos\ (\eta/2)\\ \sin\ (\eta/2)\\ \cos\ (\eta/2)\\ \sin\ (\eta/2)\end{pmatrix}\qquad u^{-}\ =\ \sqrt{E^{**}}\begin{pmatrix}-\sin(\eta/2)\\ \cos(\eta/2)\\ \sin(\eta/2)\\ -\cos(\eta/2)\end{pmatrix} \tag{1-13}$$

we obtain the beautifully simple result.

$$j^{(\pm\,\pm)}\ =\ 2E^{**}\ (\sin\ \eta\ ,\ 1\ ,\ \pm\ i\ \cos\ \eta\ ,\ 0\ ) \tag{1-14a}$$

$$j^{(\pm\,\mp)}\ =\ 0 \tag{1-14b}$$

EXERCISE 1-3. Show that Eq. 1-14b is a result of exact helicity conservation when the lepton mass is 0.

We think of $j^{(\lambda'\ ,\lambda\ )}$ as proportional to the virtual photon spin four-vector $\underset{\sim}{\epsilon}^{\pm} = (\epsilon^{0\pm}, \underset{\sim}{\epsilon}^{\pm})$. It is conventional to define the transverse virtual photon polarization

$$\epsilon\ =\ \frac{\left|\epsilon_x\right|^2 - \left|\epsilon_y\right|^2}{\left|\epsilon_x\right|^2 + \left|\epsilon_y\right|^2} \tag{1-15a}$$

Then

$$\epsilon\ =\ \frac{1 - \cos^2\eta}{1 + \cos^2\eta}\ ,\quad 0\ \leq\ \epsilon\ \leq\ 1 \tag{1-15b}$$

$$\epsilon\ =\ \frac{4EE' - Q^2}{2E^2 + 2E'^2 + Q^2} \tag{1-15c}$$

Conventionally we normalize ϵ^{+} so that $\left|\epsilon_x\right|^2 + \left|\epsilon_y\right|^2\ =\ 1$. Then

$$j^{++}\ =\ 2E^{**}\sqrt{\frac{2}{1+\epsilon}}\ \epsilon \tag{1-16a}$$

and explicitly

$$\not{\beta}^{\pm}_{\text{Breit}} = \left[\sqrt{\epsilon} \ , \ \sqrt{(1+\epsilon)/2} \ , \ \pm i\sqrt{(1-\epsilon)/2}, 0 \right] \tag{1-16b}$$

$\not{\beta}_x$ and $\not{\beta}_y$ are invariant to Lorentz velocity transformations along the $\underset{\sim}{q}$ axis; but $\not{\beta}^0$ and $\not{\beta}_z$ will change. Therefore, in general, the virtual photon spin vector has four nonzero components. Consider a boost along the $\underset{\sim}{q}$ axis from the Breit frame by a velocity β'. In this new frame $q = (q^0, \underset{\sim}{q})$.

$$\gamma' = \left|\underset{\sim}{q}\right|/Q \ , \quad \beta' = q^0/\left|\underset{\sim}{q}\right| \tag{1-17}$$

And

$$\not{\beta}^{\pm} = \left[\left(\left|\underset{\sim}{q}\right|/Q \right) \sqrt{\epsilon}, \sqrt{(1+\epsilon)/2}, \ \pm i\sqrt{(1-\epsilon)/2}, \ (q^0/Q)\sqrt{\epsilon} \right] \tag{1-18}$$

Of course for the laboratory frame $q^0 = \nu$.

Thus there are two spin states for the virtual photon which come from the two helicity states of the incident lepton. If the incident lepton is unpolarized, these states are incoherent. We shall from now on take the incident lepton to be unpolarized. We then define the spin density for the virtual photon

$$\rho^{\mu\nu} = \frac{1}{2} \left[(\not{\beta}^{+})^{\mu\dagger} (\not{\beta}^{+})^{\nu} + (\not{\beta}^{-})^{\mu\dagger} (\not{\beta}^{-})^{\nu} \right] \quad ; \tag{1-19a}$$

and for example in the laboratory frame

$$\rho_{\text{lab}} = \begin{pmatrix} \left(\frac{|\underset{\sim}{q}|}{Q}\right)^2 \epsilon & \left(\frac{|\underset{\sim}{q}|}{Q}\right)\sqrt{\frac{1+\epsilon}{2}} & 0 & \left(\frac{|\underset{\sim}{q}|}{Q^2}\right)\epsilon \\ \left(\frac{|\underset{\sim}{q}|}{Q}\right)\sqrt{\frac{1+\epsilon}{2}} & \frac{1+\epsilon}{2} & 0 & \frac{\nu}{Q}\sqrt{\frac{\epsilon(1+\epsilon)}{2}} \\ 0 & 0 & \frac{1-\epsilon}{2} & 0 \\ \left(\frac{|\underset{\sim}{q}|}{Q^2}\right)\epsilon & \frac{\nu}{Q}\sqrt{\frac{\epsilon(1+\epsilon)}{2}} & 0 & \left(\frac{\nu}{Q}\right)^2 \epsilon \end{pmatrix} \tag{1-19b}$$

EXERCISE 1-4. Derive Eqs. 1-15 through 1-19. For a discussion of the density matrix when the incident lepton is polarized. See Ref. 3 and 4. How should Eq. 1-18 be re-written so that it obeys the alternative normalization convention

$$\sum_{\mu=1}^{4} \phi^{\mu\dagger}\phi_{\mu} = -1$$

We can simplify ρ, but before doing this let us return to the general reaction

$$\ell + N \rightarrow \ell + (\mathcal{N} \text{hadrons in final state f}) \tag{1-20a}$$

Here ℓ is an e or μ, and the final state hadrons are denoted by n=1, 2, ..., $\mathcal{N}$. If only the scattered lepton is detected, the differential cross section for the production of the final hadronic state f in the laboratory frame is [2]

$$\frac{d\sigma_f}{d^3p'} = \frac{(2\pi)^4 e^4}{4EM\,(2\pi)^3 2E' Q^4} \sum_{\substack{\text{lepton} \\ \text{spins}}} \sum_{\substack{\text{hadron} \\ \text{spins}}} \int \left[\sum_{n=1}^{\mathcal{N}} \frac{d^3p_n}{(2\pi)^3 2E_n} \times \left| j \cdot J_f \right|^2 \delta^4(P' - P - q) \right] \tag{1-20b}$$

$\sum$ denotes an average over initial spin states and a sum over final spin scales. Here j is the lepton electromagnetic current, Eq. 1-12, and

$$J_f = \langle f \left| J \right| N \rangle \tag{1-21}$$

is the hadronic electromagnetic four-current. $e^2 = 4\pi\alpha$. If some of the hadrons in the state f are detected, then we can form the higher order differential cross sections

$$d\sigma_f / (d^3p' d^3p_1 d^3p_2 \ldots)$$

The virtual photon reaction

$$\gamma^* + N \rightarrow (\mathcal{N} \text{hadrons in final state f}) \tag{1-22a}$$

can be described by the virtual photon-nucleon cross sections

$$\sigma^{\mu\nu}_{\gamma^* f} = \frac{(2\pi)^4 e^2}{4KM} \sum_{\substack{\text{hadron} \\ \text{spins}}} \int \left[\sum_{n=1}^{\mathcal{N}} \frac{d^3p_n}{(2\pi)^3 2E_n} \times J_f^{\mu\dagger} J_f^{\nu} \, \delta^4(P' - P - q) \right] \tag{1-22b}$$

$\sigma^{\mu\nu}_{\gamma^* f}$ is a function only of the Lorentz scalars q^2 and $q \cdot P$. The superscripts $\mu\nu$ refer to a virtual photon whose spin state is described by $\rho^{\mu\nu}$. The use of K (Eq. 1-5d),

instead of $\left|\underset{\sim}{q}_{lab}\right| = \left[(P\cdot q)^2 - M^2q^2\right]^{1/2}$, in the incident flux factor is a convention.

Finally using Eqs. 1-20b, 1-22b, 1-16a and 1-19a, we obtain the general result

$$\frac{d\sigma_f}{d\Omega' dE'} = \Gamma_T \left[\sum_{\mu\nu} \rho_{\mu\nu} \sigma^{\mu\nu}_{\gamma^* f}\right] \tag{1-23a}$$

$$\Gamma_T = \frac{\alpha K E'}{4\pi^2 Q^2 E}\left(\frac{2}{1-\epsilon}\right) \tag{1-23b}$$

The significance Γ_T, a collection of kinematic factors, will be discussed below.

The conservation of the electromagnetic current

$$q\cdot j = 0 \ , \ q\cdot J = 0 \tag{1-24a}$$

leads to a very useful, but sometimes confusing, simplification of the quantity $\rho_{\mu\nu}\sigma^{\mu\nu}_{\gamma^* f}$. As long as the z axis is defined along $\underset{\sim}{q}$

$$q_z j_z = q^0 j^0 \ , \ q_z J_z = q^0 J^0 \tag{1-24b}$$

Then

$$j\cdot J = \left(\frac{Q}{q^0}\right)^2 j_z J_z - j_x J_x - j_y J_y \tag{1-24c}$$

There are various ways[3,4] to use Eq. 1-24c. We find it least confusing to absorb the entire $(Q/q^0)^2$ factor into the virtual photon spin vector. We define the spin *three-vector*

$$s^{\pm} = \left[\sqrt{(1+\epsilon)/2} \ , \ \ \pm i\sqrt{(1-\epsilon)/2} \ , \ -(Q/q^0)\sqrt{\epsilon}\right] \tag{1-25a}$$

to replace Eq. 1-18.

The corresponding 3x3 density matrix, in the laboratory frame, is

$$\rho'_{lab} = \begin{pmatrix} \frac{1+\epsilon}{2} & 0 & \frac{-Q}{\nu}\sqrt{\frac{\epsilon(1+\epsilon)}{2}} \\ 0 & \frac{1-\epsilon}{2} & 0 \\ \frac{-Q}{\nu}\sqrt{\frac{\epsilon(1+\epsilon)}{2}} & 0 & \left(\frac{Q}{\nu}\right)^2 \epsilon \end{pmatrix} \tag{1-25b}$$

Thus the virtual photon has two transverse components

$$\rho'_{lab,\,xx} = \frac{1+\epsilon}{2} \quad \text{in plane of lepton scatter}$$

$$\rho'_{lab,\,yy} = \frac{1-\epsilon}{2} \quad \text{perpendicular to plane of lepton scatter}$$

and a so-called longitudinal component

$$\rho'_{lab,\,zz} = \left(\frac{Q^2}{\nu}\right)^2 \epsilon$$

The x and z components are coherent so that there is also an interference term, $\rho'_{lab,\,xz}$. Eq. 1-23 then becomes

$$\frac{d\sigma_f}{d\Omega' dE'} = \Gamma_T\left[\frac{1}{2}\left(\sigma^{xx}_{\gamma^* f} + \sigma^{yy}_{\gamma^* f}\right) + \frac{\epsilon}{2}\left(\sigma^{xx}_{\gamma^* f} - \sigma^{yy}_{\gamma^* f}\right) + \left(\frac{Q}{\nu}\right)^2 \epsilon\, \sigma^{zz}_{\gamma^* f} - \left(\frac{Q}{\nu}\right)\sqrt{\frac{\epsilon(1+\epsilon)}{2}}\left(\sigma^{xz}_{\gamma^* f} + \sigma^{zx}_{\gamma^* f}\right)\right] \tag{1-26}$$

We remind the reader that Eq. 1-26 implicitly includes the higher order differential cross sections obtained by applying $(d/d^3p_1 d^3p_2 \ldots)$ to both sides. But if we integrate over the hadron three-momenta in the final state f, only two terms remain on the right hand side of Eq. 1-26

$$\sigma^{xx}_{\gamma^* f} = \sigma^{yy}_{\gamma^* f} = \sigma_{Tf} \tag{1-27a}$$

$$\epsilon\left(\frac{Q}{\nu}\right)^2 \sigma^{zz}_{\gamma^* f} = \epsilon\, \sigma_{Lf} \tag{1-27b}$$

and

$$\frac{d\sigma_f}{d\Omega' dE'} = \Gamma_T\left[\sigma_{Tf} + \epsilon\, \sigma_{Lf}\right] \tag{1-27c}$$

σ_{Tf} is the total cross section for the production of the final state f by a virtual photon with only transverse spin components: Γ_T is then the flux of transverse spin component virtual photons per unit energy and per unit solid angle of the scattered lepton. σ_{Lf} which by convention includes the (Q^2/ν^2) factor is the total cross section due to virtual photons with both $\mu = 3$ (longitudinal) and $\mu = 0$ (usually called scalar) spin components. The ratio of the longitudinal to the scalar component (ρ^{33}/ρ^{00}) depends on the Lorentz frame.

EXERCISE 1-5. Fill in the steps leading to Eqs. 1-26 and 1-27. Show that Γ_T and ϵ depend upon E, Q^2 and ν, but $\sigma^{ij}_{\gamma^* f}$, σ_{Tf} and σ_{Lf} depend only on Q^2 and ν. Of course, differential cross sections such as $d\sigma^{ij}_{\gamma^* f}/d^3p_n$ will also depend on the three-momentum of hadron n.

Finally, if we sum over all possible final hadronic states at fixed E, Q^2 and ν

$$\sigma_T = \sum_f \sigma_{Tf}, \quad \sigma_L = \sum_f \sigma_{Lf} \tag{1-28a}$$

we obtain the famous result

$$\frac{d\sigma}{d\Omega' dE'} = \Gamma_T \left[\sigma_T + \epsilon \sigma_L\right] \tag{1-28b}$$

This is basic equation for charged lepton-nucleon inelastic scattering experiments in which only the final lepton is detected. We will be discussing the more complicated situation in which some of the hadrons are detected. Therefore, we will be using the earlier and more complicated equations.

2. Theoretical Orientation

The production of hadrons in virtual photon-nucleon collisions is a vast subject. It includes two-body channels such as

$$\gamma^* + p \to \rho^0 + p \quad , \tag{2-1}$$

$$\gamma^* + p \to \pi^+ + n \quad , \tag{2-2}$$

$$\gamma^* + p \to \pi^+ + \Delta^0 \quad , \tag{2-3}$$

$$\gamma^* + p \to \pi^- + \Delta^{++} \quad , \tag{2-4}$$

$$\gamma^* + p \to K^+ + \Lambda^0 \ , \ K^+ + \Sigma^0 \quad , \tag{2-5}$$

few-body channels such as

$$\gamma^* + p \to p + \pi^+ + \pi^- \quad , \tag{2-6}$$

$$\gamma^* + p \to p + K^+ + K^- \quad ; \tag{2-7}$$

and many-body channels

$$\gamma^* + p \to 3 \text{ or more hadrons} \quad , \tag{2-8}$$

with their inclusive aspects

$$\gamma^* + p \to \text{hadron h} + \text{anything} \tag{2-9}$$

Obviously, in reviewing the experimental results in this subject, one must make choices as to what to emphasize. In this section I shall explain the theoretical *orientation which I have used to make these choices.*

Spacelike virtual photon physics introduces two new aspects into hadronic production compared to real photon-hadron physics or real hadron-hadron physics.

(1) The most important new aspect is that the incident particle has a known and variable *virtuality--its* Q^2 *value.*

(2) Compared to real photon physics, the virtual photon has a more complicated spin structure (Sec. 1). This is sometimes a blessing and sometimes a curse. For example, the measurement of the σ_L/σ_T ratio is of great value in parton model analyses of deep inelastic scattering. But, *as mentioned below, in two-body channels, the* longitudinal component can complicate an already complicated set of amplitudes. I am going to emphasize aspect (1), for it seems to me that the known and variable virtuality of the γ^* is the crucial new tool in virtual photon physics. Therefore, the reaction

$$\gamma^* + N \to 1 + 2 + 3 \ldots \tag{2-10a}$$

will usually be studied at <u>fixed</u> W (the total energy in the hadronic system) with Q^2 being <u>varied</u>. Of course, the reaction

$$\gamma + N \to 1 + 2 + 3 \ldots \tag{2-10b}$$

provides the $Q^2 = 0$ point. I will also emphasize data in which Q^2 effects can be studied in their simplest form. And this brings me to the subject of the two-body channels, Eqs. 2-1 to 2-7.

Consider real photon-hadron or hadron-hadron two-body reactions

$$a + b \to c + d \tag{2-11}$$

in which c and d are *stable hadrons or resonances. The problem is that we already* know too much for our own good--we know that there is no simple theory to explain all these reactions. We have only partial views from different vantage points of the correct theory. A t-channel exchange mechanism is needed to explain the dominance

in $d\sigma/dt$ of forward or backward peaks. A Regge type phenomenology is needed to explain the energy behavior. Some sort of absorption correction is needed. And some duality ideas are helpful. To make progress amid this riches of data and different theoretical insights some people have begun attempts to do a full analysis of all the helicity amplitudes involved in particular two-body channels. Others have emphasized the study of dips or breaks in $d\sigma/dt$, and zeros in the polarization. In either case, it is clear that when particle a in Eq. 2-11 is a virtual photon, we produce a more complex and richer situation. Therefore, at this time the general two-body channel

$$\gamma^* + N \rightarrow c + d \qquad (2\text{-}12)$$

is primarily a tool for studying individual two-body reaction mechanisms. I cannot even start upon this large topic. Therefore, I shall only discuss in detail the reactions

$$\gamma + p \rightarrow \rho^0 + n$$

$$\gamma + p \rightarrow \pi^+ + n$$

which have special uses in virtual photon physics.

Next a word about models and analogies. I shall tend to stay away from models, such as vector meson dominance[5] in which γ^* is taken to convert into a hadron a, all the virtuality effects being taken up in the $\gamma^* a$ coupling or the a propagator. Such a model is illustrated in Fig. 2-1 for a two-body channel

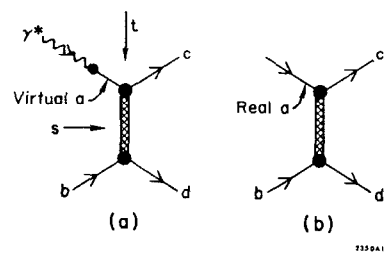

Fig. 2-1 a, b, c, d are hadrons

Here the cross hatched t-channel exchange mechanism is taken to be the same in Fig. 2-1a and in Fig. 2-1b. Such models may provide a good deal of insight; particularly in the small Q^2 region. But I want to search for significant Q^2 effects and to use models which emphasize those effects. Therefore, I emphasize models of the type in Fig. 2-2.

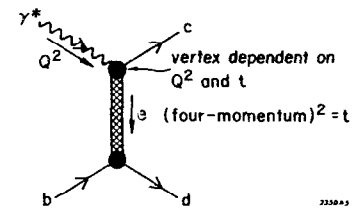

Fig. 2-2

Here the $\gamma^* c$ vertex is directly dependent on Q^2 as well as on t, where t is the four-momentum squared of e.

EXERCISE 2-1. In fig. 2-2, suppose that particles b, c and d have spin 0 and equal masses M. Suppose that the t-channel exchange mechanism is elementary one-particle exchange of a particle of mass m and spin 0. Let the vertex bed be a point interaction with coupling constant G. Let the coupling constant at the upper vertex be g, but also attach a form factor $F_{\gamma^* ec}$ to that vertex. Make some guesses as to the behavior of $F_{\gamma^* ec}$ as a function of Q^2 and t. Work out the cross sections $d\sigma_{\gamma^* b \rightarrow cd}(Q^2, W^2)/dt$ and $\sigma_{\gamma^* b \rightarrow cd}(Q^2, W^2)$.

EXERCISE 2-2. Repeat Ex. 2-1 if the t-channel exchange mechanism is a Regge pole with trajectory $\alpha(t)$. How can the effect of Q^2 be incorporated in the residue function, which is taken to be $\gamma(t) = A \exp(bt/2)$ when $Q^2 = 0$.

In discussing many-body channels, I shall use the parton model. The basic diagram, which will be discussed in detail during this week, is given in Fig. 2-3.

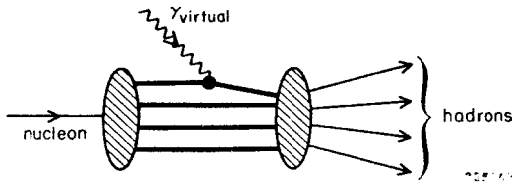

Fig. 2-3

For studies of σ_T and σ_L (or W_1 and W_2) we only care about the validity of the impulse approximation single parton interaction and the nature of the $x = Q^2/2M\nu$ distributions of the partons. But when we are interested in the details of the hadronic production, we must try to understand the mysterious cross hatched blob on the right hand side of the diagram.

Fig. 2-4 illustrates this problem in another way.

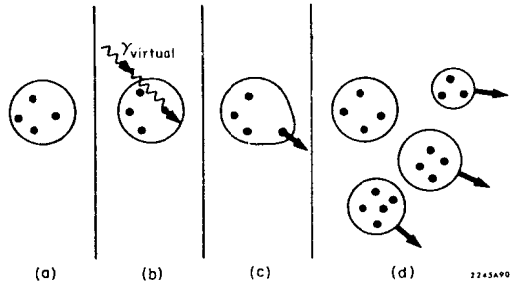

Fig. 2-4

We understand steps a, b, c in a fairly clear way. But how do we get from step c to step d? What is the mechanism whereby the parton which has absorbed q leads to the breakup of the nucleon into two or more hadrons?

Although we shall emphasize the Q^2 behavior, we shall look a little at the relative size of cross sections produced by longitudinal photons, σ_{Lf}, compared to those produced by transverse photons, σ_{Tf}. In doing this, we must remember that σ_L/σ_T has no direct physical meaning because of the arbitrariness in the definition of σ_L, Eq. 1-27b. Therefore, we must always consider the quantity

$$(\sigma_{Lf}/\sigma_{Tf}) \,/\, (\sigma_L/\sigma_T) \tag{2-13}$$

I remind you that where it has been measured

$$\sigma_L/\sigma_T \lesssim .2 \ , \quad Q^2 \neq 0 \tag{2-14a}$$

and

$$\sigma_L/\sigma_T = 0 \ , \quad Q^2 = 0 \tag{2-14b}$$

3. The Two-Body Channel: $\gamma^* + p \to \rho^0 + p$

In all its glory, the reaction

$$\gamma^* + p \to \rho^0 + p \tag{3-1}$$

has 18 independent helicity amplitudes, $T_{\lambda_\rho \lambda_{p'}\,;\,\lambda_\gamma \lambda_p}$! Why then do we think we can learn anything from such a reaction. First, inspired by the real photoproduction reaction

$$\gamma + p \to \rho^0 + p \tag{3-2}$$

we hope that the reaction in Eq. 3-1 will obey s-channel helicity conservation. Explicitly, we hope that

$$T_{\lambda_\rho \lambda_{p'}\,;\,\lambda_\gamma \lambda_p} = T_{\lambda_\rho \lambda_{p'}\,;\,\lambda_\gamma \lambda_p}\,\delta_{\lambda_\rho \lambda_\gamma}\,\delta_{\lambda_p \lambda_{p'}} \tag{3-3}$$

Second, this hope is validated by the fact that all existing electroproduction data[6,7] for $\gamma^* p \to \rho^0 p$ can be fit with this very restrictive assumption. Then there are only three independent helicity amplitudes.

$$\text{Independent T's} \equiv T_{1,\frac{1}{2};1,\frac{1}{2}} \ ; \ T_{0,\frac{1}{2};0,\frac{1}{2}} \ ; \ T_{-1,\frac{1}{2};-1,\frac{1}{2}} \tag{3-4}$$

and the diagram for the reaction is given in Fig. 3-1.

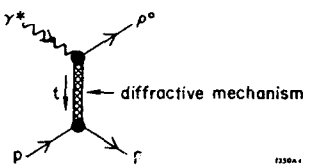

Fig. 3-1

Before using the restriction in Eq. 3-4, let us look at typical $d\sigma/dt$ plots, Fig. 3-2. We see that $d\sigma/dt$ has the typical forward peak (for $|t| \lesssim 0.5$ $(GeV/c)^2$)

$$d\sigma/dt \approx A\ e^{bt} \qquad (3\text{-}5)$$

As shown in Fig. 3-1, t is the square of the four-momentum carried from the $\gamma\rho^0$ vertex to the p vertex. The effect of Q^2 is clear

$$b \text{ decreases as } Q^2 \text{ increases} \qquad (3\text{-}6)$$

This effect is shown for the highest energies, $\langle s \rangle = 20\ GeV^2$, in Fig. 3-3. As $Q^2 \to 0$, b approaches the photoproduction value of about $8(GeV/c)^{-2}$. Now the photoproduction reaction, Eq. 3-2, in addition to conserving s-channel helicity, has been shown to be diffractive[8]. Its b is about the same as in elastic scattering, and its total cross section, $\sigma_{\gamma p \to \rho^0 p}$, decreases very slowly with increasing energy as does $\sigma_{elastic}$. Therefore, the general interpretation of Eq. 3-6 is that as Q^2 increases, $\gamma^* + p \to \rho^0 + p$ becomes less diffractive — the virtuality interfers with the diffractive process.

EXERCISE 3-1. Use the optical model of the diffractive process $a + b \to a' + b$ to write

$$b = (\bar{R}_a^2 + R_b^2)/2\ ,\quad \bar{R}_a^2 = (R_a^2 + R_{a'}^2)/2 \qquad (3\text{-}7)$$

where R is a Gaussian radius. If we maintain this model for $Q^2 \neq 0$, what does Fig. 3-3 say about $\bar{R}^2 = (R_{\gamma^*}^2 + R_\rho^2)/2$?

Another approach to understanding the momentum transfer distributions as a function of Q^2 and s has been proposed by Nieh[9]. He presents a physical picture in which the effective size of the photon is related to the amount of time, Δt, that an associated hadronic system can exist. Δt is calculated using the uncertainty principle. In the electroproduction of ρ^0 mesons,

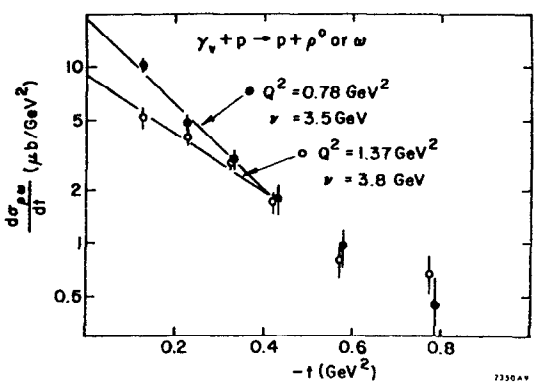

Fig. 3-2a. Ref. 6a

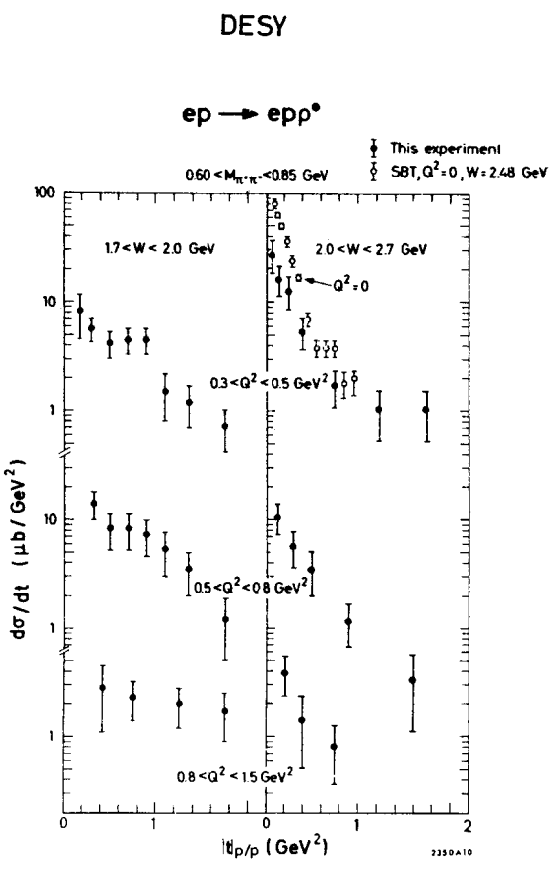

Fig. 3-2b. Ref. 6e

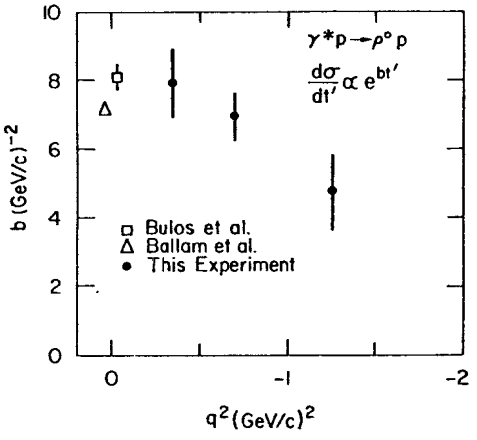

Fig. 3-3. Ref. 6c

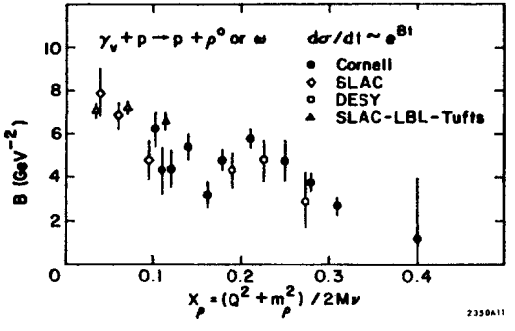

Fig. 3-4. Ref. 6a

$$\Delta t \approx \frac{2\nu}{m_\rho^2 + Q^2} \tag{3-8}$$

and the b parameter should be a function of Δt only. The data are in qualitative agreement with this approach. Fig. 3-4 shows b for a variety of Q^2 and s values plotted versus $X_\rho = (M\,\Delta t)^{-1}$.

EXERCISE 3-2. Derive and justify Eq. 3-8. The usual interpretation of Eq. 3-8 is the following. When Δt is long compared to the time duration, T, of a virtual photon-nucleon interaction, then it is the virtual hadrons associated with the virtual photon which interact with the nucleon. And it is then a hadron-hadron interaction, with the effective radius of the virtual photon being that of a hadron. Hence if R_h is the characteristic hadronic Gaussian radius (about 0.5 fermi), in Eq. 3-7 we have $b = R_h^2$. But if Δt is short compared to T, then the virtual photon interacts as a point particle. Then in Eq. 3-7, $R_a = 0$, where a is the virtual photon. This leads to a smaller b, namely $b = (3/4)R_h^2$. Often the entire $\bar{R}_a$ is set equal to 0 at large Q^2 and one writes $b\ (\text{large } Q^2) \approx b\ (Q^2 = 0)/2$. Discuss this interpretation.

If $\gamma^* + p \rightarrow \rho^0 + p$ becomes less diffractive as Q^2 increases we would expect that

$$\sigma_{\gamma^* p \rightarrow \rho^0 p} / \sigma_{tot} \text{ decreases as } Q^2 \text{ increases.} \tag{3-9}$$

$\sigma_{tot} = (\sigma_T + \epsilon\,\sigma_L)$ as defined in Eq. 1-28c. The truth of Eq. 3-9 is demonstrated in Fig. 3-5.

As Q^2 increases beyond 1 or 2 $(\text{GeV}/c)^2$, we do not know how to describe the basic mechanism for $\gamma^* + p \rightarrow \rho^0 + p$ beyond saying that the diffractive mechanism is no longer dominant. We do not have enough data in the larger Q^2 range.

For example, we cannot yet test Eq. 3-3 for $Q^2 > 1$ or 2 $(\text{GeV}/c)^2$. We only know it is a sufficient hypothesis for data averaged over the $Q^2 < 1$ or 2 $(\text{GeV}/c)^2$ range. In this range we can use Eq. 3-4 and Eq. 1-26 to separate the transverse and longitudinal cross sections, $\sigma_T(\rho^0 p)$ and $\sigma_L(\rho^0 p)$ respectively.

First, we rewrite the spin density matrix ρ'_{lab}, Eq. 1-25b, in terms of helicity states in the $\gamma^* + p \rightarrow \rho^0 + p$ production frame, Fig. 3-6. We obtain

$$\rho_{p\text{ p-plane}}(\gamma^*) = \begin{pmatrix} \frac{1}{2} & -\frac{1}{2}\sqrt{\epsilon_L(1+\epsilon)}\, e^{i\phi_e} & -\frac{\epsilon}{2} e^{2i\phi_e} \\ -\frac{1}{2}\sqrt{\epsilon_L(1+\epsilon)}\, e^{-i\phi_e} & \epsilon_L & \frac{1}{2}\sqrt{\epsilon_L(1+\epsilon)}\, e^{i\phi_e} \\ -\frac{\epsilon}{2} e^{-2i\phi_e} & \frac{1}{2}\sqrt{\epsilon_L(1+\epsilon)}\, e^{-i\phi_e} & \frac{1}{2} \end{pmatrix} \tag{3-10}$$

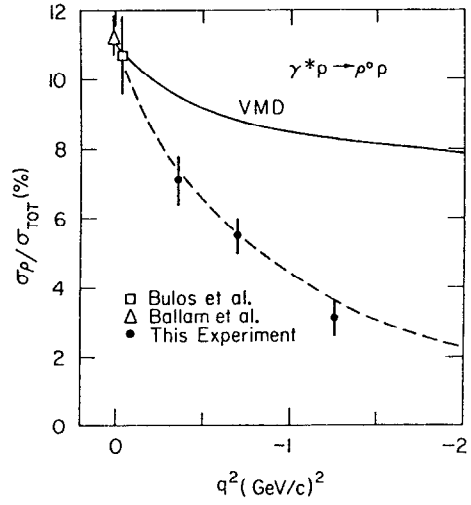

Fig. 3-5a. Ref. 6c

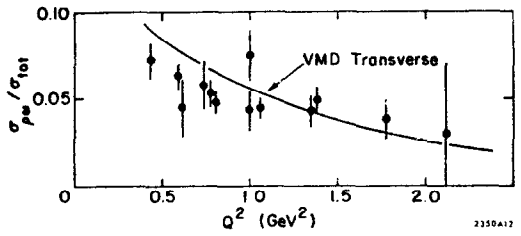

Fig. 3-5b. Ref. 6a

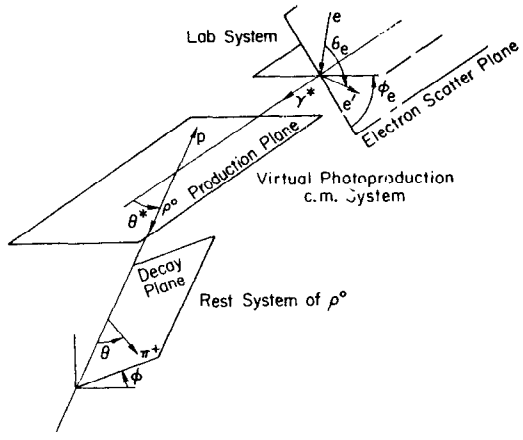

Fig. 3-6

where $\epsilon_L = (Q/\nu)^2 \epsilon$ and ϕ_e is defined in Fig. 3-6.

EXERCISE 3-3. Derive Eq. 3-10 and 3-12.

Now under the restriction of Eq. 3-3, we can immediately write down the ρ density matrix. By parity conservation, since we sum over the nucleon spins; $T_{1,\frac{1}{2};-1,\frac{1}{2}}$ and $T_{-1,\frac{1}{2};-1,\frac{1}{2}}$ are replaced by a single amplitude called T_1. And in analogy to Eq. 1-27b, we define

$$(Q/\nu)\ T_{0,\frac{1}{2};0,\frac{1}{2}} \equiv T_0 \tag{3-11}$$

Then

$$\rho_{\text{p-plane}}(\rho^0) = \begin{pmatrix} \frac{1}{2}|T_1|^2 & -\frac{1}{2}\sqrt{\epsilon(\epsilon+1)}\, e^{i\phi} T_1 T_0^* & -\frac{\epsilon}{2} e^{2i\phi}|T_1|^2 \\ -\frac{1}{2}\sqrt{\epsilon(1+\epsilon)}\, e^{-i\phi} T_1^* T_0 & \epsilon |T_0|^2 & \frac{1}{2}\sqrt{\epsilon(1+\epsilon)}\, e^{i\phi} T_1 T_0 \\ -\frac{\epsilon}{2}\epsilon^{-2i\phi}|T_1|^2 & -\frac{1}{2}\sqrt{\epsilon(1+\epsilon)}\, e^{-i\phi} T_1 T_0 & \frac{1}{2}|T_1|^2 \end{pmatrix} \tag{3-12}$$

Defining

$$R_\rho = |T_0|^2 / |T_1|^2 \tag{3-13}$$

$$\delta = \text{differences between phases of } T_0 \text{ and } T_1 \tag{3-14}$$

we obtain the angular distribution for the decay $\rho^0 \to \pi^+ + \pi^-$

$$W(\Theta, \Psi) = \frac{3}{8\pi^2(1+\epsilon R_\rho)} \left[\epsilon R_\rho \cos^2\Theta + \frac{1}{2}\sin^2\Theta(1+\epsilon\cos 2\Psi) - (\epsilon R_\rho (1+\epsilon)/2)^{1/2} \cos\delta \sin 2\Theta \cos\Psi\right] \tag{3-15}$$

Here $\Psi = \phi + \phi_e$, $W(\Theta, \Psi)$ is measured in the rest system of the ρ, and Θ is defined in Fig. 3-6.

EXERCISE 3-4. Derive Eqs. 3-12 through 3-15. For the very complicated general case, when Eq. 3-3 is not used, see Refs. 10 and 4.

By fitting Eq. 3-15, one can measure R_ρ and δ. It is best to do this analysis at high s to avoid interference effects between $\gamma^* + p \to \rho^0 + p$ and $\gamma^* + p \to \pi^- + \Delta^{++}$. The highest measurements, $\langle s \rangle \approx 20\ \text{GeV}^2$, are shown in Fig. 3-7. The values of R_ρ and cos δ are

$\langle q^2 \rangle$ (GeV/c)^2	-.36	-.70	-1.27
R_ρ	$.32^{+.24}_{-.18}$	$.63^{+.28}_{-.21}$	$.27^{+.52}_{-.25}$
cos δ	$.70^{+.24}_{-.26}$	$.75^{+.15}_{-.17}$	$.80^{+.20}_{-.48}$

Turning to the lower $\langle s \rangle$ measurements, Eckardt et al.[6e] report a value of $R_\rho = .30 \pm .14$ at $\langle q^2 \rangle = -.6\ (\text{GeV/c})^2$ and $\langle s \rangle = 5.3\ \text{GeV}^2$. Preliminary results for R_ρ from the SLAC hydrid bubble chamber experiment are in agreement with these measurements[1]; as are the results of Driver et al[6d] with some new analysis[12] Thus

$$\frac{\sigma_{L\rho^0 p}}{\sigma_{T\rho^0 p}} \sim 2\,\frac{\sigma_L}{\sigma_T} \qquad (3\text{-}16)$$

so that the longitudinal contribution to $\gamma^* + p \to \rho^0 + p$ is relatively larger than the longitudinal contribution to σ_{tot}. Incidently, this is a rough general argument against vector dominance models; for it shows that a substantial part of $\sigma_{\gamma^* p \to \rho^0 p}$ has little to do with σ_{tot}.

EXERCISE 3-5. Discuss more explicitly the significance of Eq. 3-16.

The measurements of cos δ plotted in Fig. 3-7b show almost maximal interference between transverse and longitudinal amplitudes. For a purely diffractive production process cos δ should be unity. Again the preliminary results of the SLAC hybrid bubble chamber experiment for cos δ are in excellent agreement with our measurements[11], but the DESY streamer chamber experiment reports no evidence for transverse-longitudinal interference[6e]. In conclusion

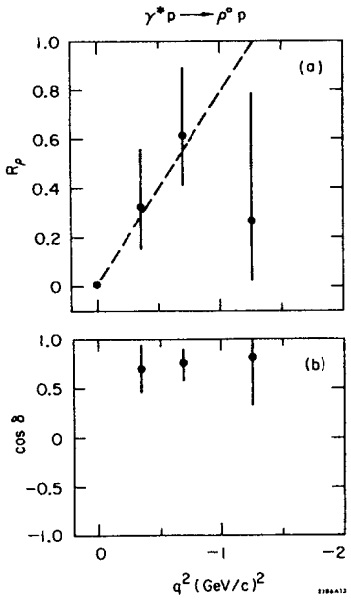

Fig. 3-7 Ref. 6c

A. The momentum transfer distribution broadens as Q^2 increases.

B. There is no evidence for s-channel helicity nonconservation. The production of longitudinally polarized ρ^0 mesons increases with Q^2 at a larger rate than can be easily accommodated by a vector meson dominance model interpretation of deep inelastic electron scattering. The interference between transverse and longitudinal amplitudes is almost maximal.

C. As a useful mnemonic device we note that the cross section decreases with Q^2 roughly as the ρ^0 propagator squared, $(1 + Q^2/m_\rho^2)^{-2}$.

D. It has also been observed that the cross sections for ω^0 and ϕ^0 production decrease with increasing Q^2.

Thus, we have some beautifully simple observations of the effect of Q^2 on $\gamma^* + p \to \rho^0 + p$; now we need a quantitative theory.

4. Other Two-Body Channels

A two-body channel for which we do have a quantitative theory is

$$\gamma^* + p \to \pi^+ + n \tag{4-1}$$

when t, the square of the four-momentum transfer to the nucleon, is small:

$$|t| \sim m_\pi^2 \tag{4-2}$$

For then we can use the models of Exs. 2-1 or 2-2. It does not matter which, because under the conditions of Eq. 4-2 both models have the same very small t behavior.

EXERCISE 4-1. Review the theoretical situation for real photoproduction, $\gamma + p \to \pi^+ + n$, at small t. Recall that one-pion exchange leads to $d\sigma/dt \to 0$ as $t \to t_{min}$. The sharp very forward peak (on top of the usual forward peak) at $t \to t_{min}$, Fig. 4-1, is caused by a drastic correction to the elementary one-pion exchange amplitude [13], which we prefer to interpret as an absorption correction.

In virtual photoproduction, we can avoid the problem discussed in Ex. 4-1 by

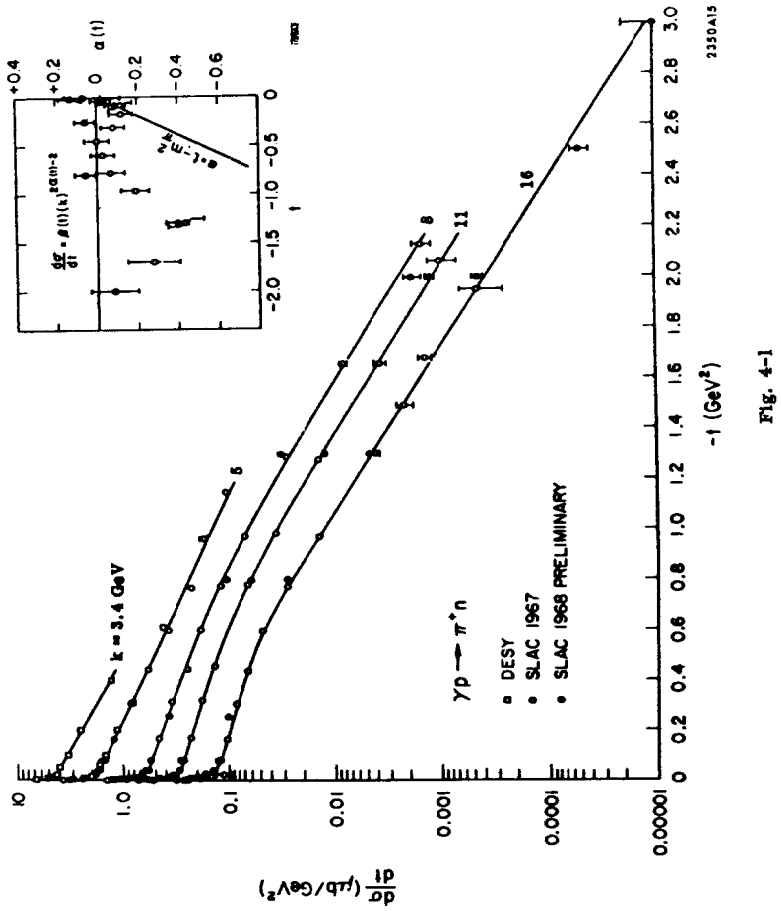

Fig. 4-1

considering the contribution of the longitudinal photons (helicity $_{\gamma^*} = 0$) to reaction 4-1. In the diagram of Fig. 4-2, the longitudinal photons do lead to a forward peak from the one-pion exchange amplitude, Ex. 4-2.

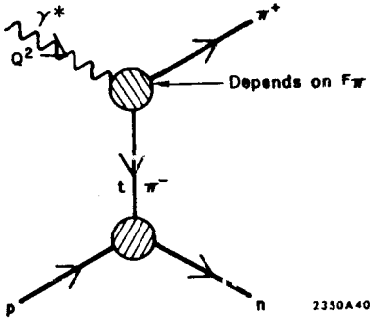

Fig. 4-2

EXERCISE 4-2. Work out the amplitudes for the diagram in Fig. 4-2 for the case in which the nucleon spin states are <u>not</u> observed. Show that as $t \to t_{min}$ the only unknown factor in the upper vertex is the pion form factor

$$F_\pi(Q^2) \approx F_\pi(Q^2, t = t_{min}) \tag{4-3}$$

Figure 4-3 shows typical $d\sigma_L/dt$'s for $\gamma^* + p \to \pi^+ + n$ as a function of Q^2. We note the forward peak again.

EXERCISE 4-3. How should $Q^2 >> m_\pi^2$ affect the sharp very forward peak seen in photoproduction? Compare Fig. 4-4.

Using a more sophisticated version of the theory discussed in Ex. 4-2 [15], the data from a number of groups, [14, 16, 17] leads to F_π in Fig. 4-5. Here

$$F_\rho = \left[\frac{1}{1 + Q^2/m_\rho^2}\right] \xrightarrow[Q^2 \to \infty]{} \frac{\text{constant}}{Q^2} \tag{4-4a}$$

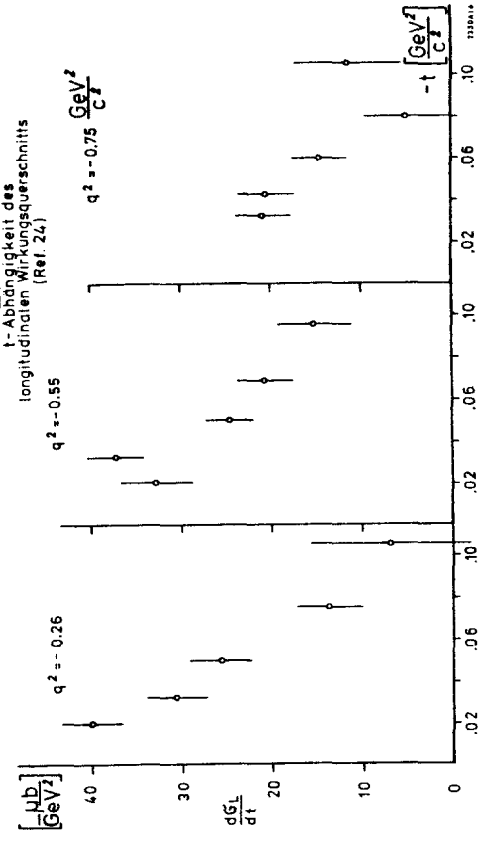

Fig. 4-3 Ref. 13

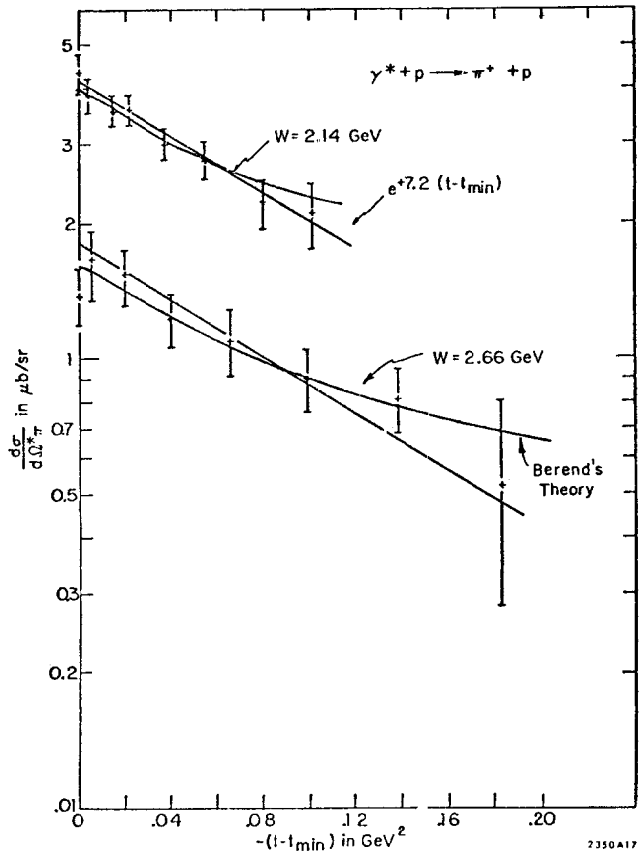

Fig. 4-4 Ref. 14. The W= 2.14 GeV data is at $Q^2 \sim 1.1$ (GeV/c)^2; the W= 2.66 GeV data is at $Q^2 \sim 2.0$ (GeV/c)^2.

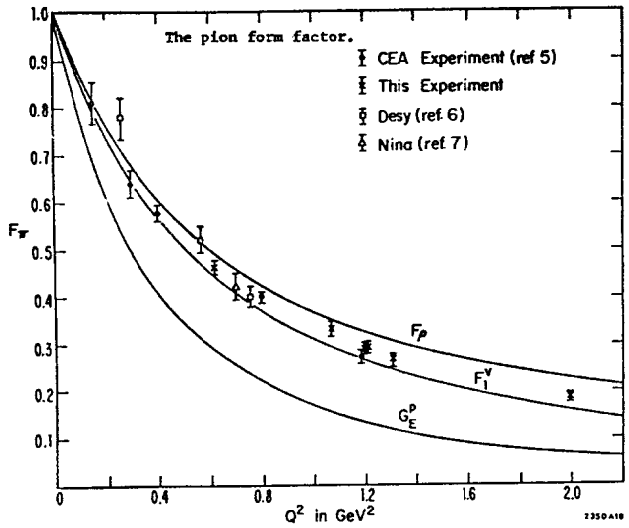

Fig. 4-5 Ref. 14

$$F_1^V = \left[1 + \frac{3.7Q^2}{4M^2 + Q^2}\right]\left[\frac{1}{(1 + Q^2/.71)^2}\right] \xrightarrow[Q^2 \to \infty]{} \frac{\text{constant}}{Q^4} \qquad (4\text{-}4b)$$

$$G_E^P = \left[\frac{1}{(1 + Q^2/.71)^2}\right] \xrightarrow[Q^2 \to \infty]{} \frac{\text{constant}}{Q^4} \qquad (4\text{-}4c)$$

Thus we cannot yet distinguish between Q^{-2} and Q^{-4} behavior as $Q^2 \to \infty$; but in this Q^2 range G_E^P definitely falls off much too fast. F_ρ falls off a little too slowly, but it is not a terrible fit.

EXERCISE 4-4. Discuss the reasons for the choice of form factors in Eq. 4-4.

EXERCISE 4-5. Although it is far from our subject, I cannot resist connecting this measurement of $F_\pi(q^2)$ in the spacelike, $q^2 \leq 0$, region with recent measurements of $\left|F_\pi(q^2)^\pi\right|$ in the timelike, $q^2 \geq 4m_\pi^2$, region. The latter is obtained from the electron positron colliding beam reaction

$$e^+ + e^- \to \pi^+ + \pi^- \qquad (4\text{-}5)$$

We use the dispersion relation

$$\text{Re } F_\pi(q^2) = \frac{1}{\pi} P \int_{4m_\pi^2}^{\infty} \frac{\text{Im } F_\pi(q'^2)}{q'^2 - q^2} \, d q'^2 \qquad (4\text{-}6)$$

with the singularities given in Fig. 4-6.

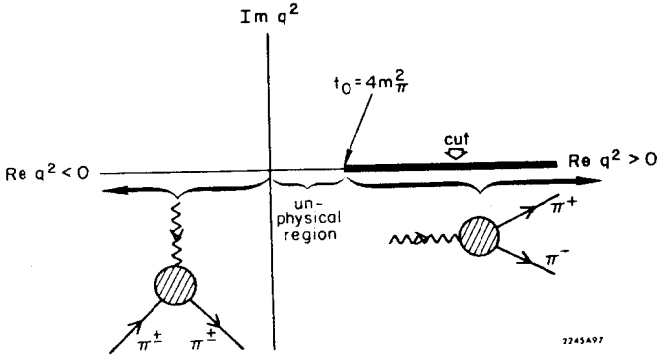

Fig. 4-6

In the region of the ρ^0, $q^2 = m_\rho^2$, the model

$$e^+ + e^- \to \rho^0 \to \pi^+ + \pi^- \qquad (4\text{-}7)$$

leads to the Breit-Wigner form for $F(\pi)$

$$\text{Re } F_\pi = \frac{-m_\rho^2 (q^2 - m_\rho^2)}{(q^2 - m_\rho^2)^2 + m_\rho^2 \Gamma^2} \qquad (4\text{-}8a)$$

$$\text{Im } F_\pi = \frac{m_\rho^3 \Gamma}{(q^2 - m_\rho^2)^2 + m_\rho^2 \Gamma^2} \qquad (4\text{-}8b)$$

This agrees quite well with experiment [18], although only $\left|F_\pi\right|^2$ is actually determined by experiment. For larger q^2 values, $\left|F_\pi\right|^2$ is shown in Fig. 4-7. In spite of the present experimental uncertainties we know that

$$\left|F_\pi(q^2)\right| \sim \frac{\text{constant}}{q^2}, \quad q^2 \gg 0 \qquad (4\text{-}9)$$

but the constant in Eq. 4-9 is too large to be given by the tail of the ρ contribution, Eq. 4-8. Using the dispersion relation, discuss what Im F_π, non-ρ we need in addition to Eq. 4-8b to fit all the measurements. Show that $F_\pi(q^2 \to \infty)$ will have the same $\left|q^2\right|$ behavior as $F_\pi(q^2 \to -\infty)$ if Im F_π is a reasonably well behaved function which goes to 0 reasonably rapidly as $q^2 \to \infty$.

To conclude this section, we take a momentary and non-analytic look at the two-body channel

$$\gamma^* + p \to \pi^- + \Delta^{++} \qquad (4\text{-}10)$$

which has been measured [19, 20] in the ranges $1.3 \lesssim W \lesssim 3.0$ GeV, $Q^2 \lesssim 1$ (GeV/c)^2. The cross section for the reaction, denoted by $\sigma_{\pi - \Delta^{++}}$ is shown in Fig. 4-8. The dot-dash line is

$$\left[\frac{\sigma_{\pi - \Delta^{++}}(Q^2 = 0, W)}{\sigma_{\text{tot}}(Q^2 = 0, W)}\right] \sigma_{\text{tot}}(Q^2, W) \qquad (4\text{-}11)$$

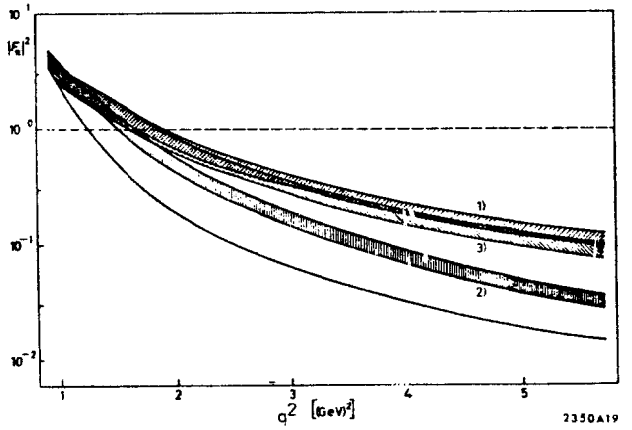

– Different fits of the experimental data on the pion form factor squared assuming different values of the ratio $\sigma_{KK}/\sigma_{\pi\pi}$ for $s > 2.25$ (GeV/c)^2: 1) $\sigma_{KK}/\sigma_{\pi\pi} = 0$; 2) $\sigma_{KK}/\sigma_{\pi\pi}$ as predicted by the VMD model; 3) $\sigma_{KK}/\sigma_{\pi\pi} = \frac{1}{4}(\beta_K/\beta_\pi)^3$. The bands correspond to one standard deviation. The full line is the Gounaris-Sakurai formula for the ρ^0 tail [9].

Fig. 4-7. Ref. 18b

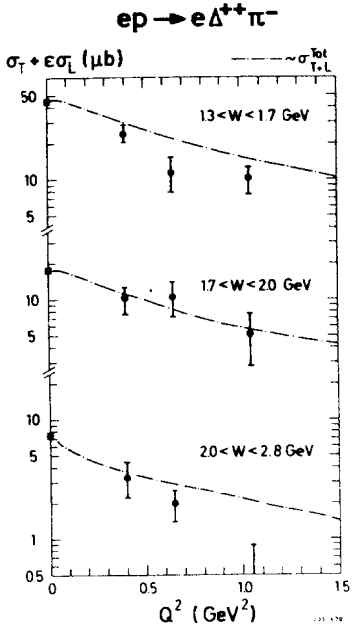

Fig. 4-8. Ref. 19

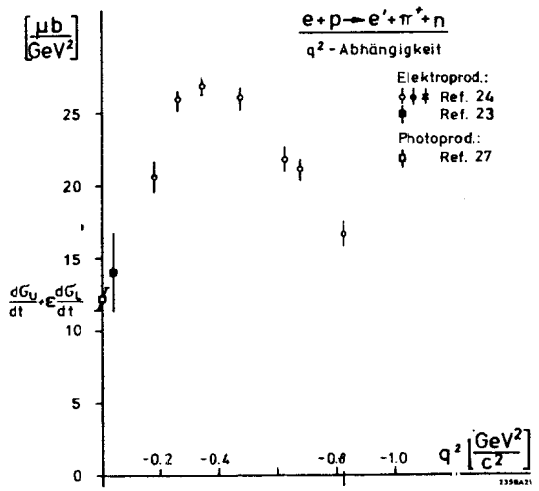

Fig. 4-9a. t is fixed at $-0.04\ (\mathrm{GeV/c})^2$. Ref. 7b

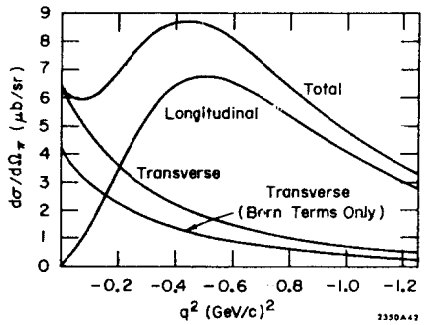

Fig. 4-9b. Ref. 7a

It is difficult to interpret the lower W data; but for $2.0 < W < 2.8$ GeV, we see that as Q^2 increases, the ratio

$$R_{\pi - \Delta^{++}}(Q^2, W) = \left(\frac{\sigma_{\pi - \Delta^{++}}(Q^2, W)}{\sigma_{tot}(Q^2, W)}\right) \Big/ \left(\frac{\sigma_{\pi - \Delta^{++}}(0, W)}{\sigma_{tot}(0, W)}\right) \qquad (4\text{-}12)$$

decreases below 1.

EXERCISE 4-6. Thus in this reaction, $\gamma^* + p \to \pi^- + \Delta^{++}$, and in the reactions $\gamma^* + p \to \rho^0 + p$ and $\gamma^* + p \to \pi^+ + n$ we see the same trend versus Q^2 at fixed and sufficiently high W. The ratio of this channel cross section to the total cross section decreases as Q^2 increases. Is this a general rule for all two-body channels

$$\gamma^* + p \to a + b \qquad ; \qquad (4\text{-}13)$$

σ_{ab}/σ_{tot} decreases as Q^2 increases at fixed W? What is the general explanation? Is it simply a form factor effect as in $\gamma^* + p \to \pi^+ + n$?

EXERCISE 4-7. For small values of Q^2, some two-body channels such as $\gamma^* + p \to \pi^+ + n$ have cross sections which increase with Q^2 due to the increase in the flux of longitudinal photons. This is illustrated experimentally in Fig. 4-9a, and the expected theoretical curves are shown in Fig. 4-9b. Discuss this effect.

5. Spacelike Virtual Photon Kinematics — Inclusive Reactions

The reaction is

$$\ell + N \to \ell + h + \text{anything} \qquad (5\text{-}1)$$

where h is a hadron of fixed type and charge. The fundamental measurement is the differential cross sections obtained from Eq. 1-26

$$\frac{d\sigma}{d\Omega'\, dE'\, d^3p_h} = \Gamma_T \sum_f \frac{d}{d^3p_h}\left[\left(\frac{\sigma^{xx}_{\gamma^* f} + \sigma^{yy}_{\gamma^* f}}{2}\right) + \epsilon\left(\frac{\sigma^{xx}_{\gamma^* f} - \sigma^{yy}_{\gamma^* f}}{2}\right) + \ldots\right] \qquad (5\text{-}2a)$$

where the hadron has four-momentum $p = (E_h, \underset{\sim}{p}_h)$. We define $\underset{\sim}{p}_h$ with reference to a coordinate system based on $\underset{\sim}{q}$ as shown in Fig. 5-1.

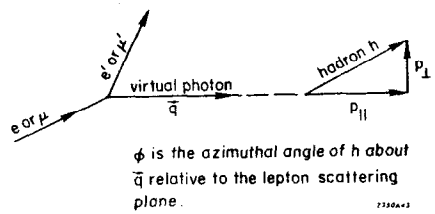

ϕ is the azimuthal angle of h about $\vec{q}$ relative to the lepton scattering plane.

Fig. 5-1

Then

$$\frac{d\sigma}{d\Omega' dE' d^3p_h} = \frac{d\sigma}{d\Omega dE' p_\perp dp_\perp dp_{||} d\phi} \qquad (5\text{-}3b)$$

where $p_\perp$ and $p_{||}$ are the hadron's momentum components perpendicular to and parallel to q. The differential cross section in Eqs. 5-2 could show a ϕ dependence, but experiments show that the ϕ dependence is less than 10 to 20%[11, 12]. Therefore, we average over ϕ; and the right hand side of Eq 5-2a simplifies to

$$\frac{d\sigma}{\pi\, d\Omega\, dE'\, dp_\perp^2\, dp_{||}} = \Gamma_T \frac{d}{\pi\, dp_\perp^2\, dp_{||}} \left[\sigma_T + \epsilon\, \sigma_L\right] \qquad (5\text{-}3)$$

Now in studying the inclusive properties, we want to ignore the dependence of Γ_T and of

$$\sigma_{tot} = \sigma_T + \epsilon\, \sigma_L \qquad (5\text{-}4)$$

on q^2 and ν. And to study Feynman scaling, we want to use Lorentz invariant momentum distribution. Therefore, we construct the quantity

$$F(q^2, \nu, p_\perp, p_{||}) = \frac{1}{\sigma_{tot}} \frac{E}{\pi} \frac{d\sigma_{tot}}{dp_\perp^2\, dp_{||}} \qquad (5\text{-}5)$$

Here we have dropped the subscript h on E.

Finally, we often work in the virtual photon-nucleon center of mass. We remind the reader that in that system, the total energy (Eq. 1-5) is

$$W = \left[2M\nu + M^2 - Q^2\right]^{\frac{1}{2}} \qquad (5\text{-}6a)$$

we often write

$$s = W^2 \qquad (5\text{-}6b)$$

Remember that to find the equivalent incident real photon energy, if Q^2 is small compared to s, just divide $s = W^2$ by $2M \sim 2$. In this system, denoted by a *, we define the Feynman x

$$x = p^*_{||} / p^*_{max}$$

Then

$$F(Q^2, s, p_\perp, x) = \frac{1}{\sigma_{tot}} \left(\frac{E^*}{\pi\, p^*_{max}}\right) \frac{d\sigma_{tot}}{dp_\perp^2\, dx} \qquad (5\text{-}7)$$

6. Multiplicities and Feynman Scaling

It is an interesting example of how poor is our intuition with respect to virtual photon physics that there is no obvious answer to the question, "At fixed s, how should the average charge multiplicity $\langle N_{ch} \rangle$ vary with Q^2?" Should we regard varying Q^2 as having the same effect as varying the mass of the incident particle? From that viewpoint, as long as Q^2 is less than 1 or 2 $(GeV/c)^2$, there should be little change. (π p and pp multiplicities are the same within one unit.) Or will varying Q^2 do something more drastic? For $Q^2 < 2(GeV/c)^2$ and $s \lesssim 16\ GeV^2$ the answer is given in Figs. 6-1 and 6-2. In this Q^2 range $\langle N_{ch} \rangle$ is only 5 or 10% smaller than its $Q^2 = 0$ value. And in Fig. 6-3, we see that the s dependence does not vary much with Q^2. Thus for this s and Q^2 range, there is no spectacular effect of Q^2 on $\langle N_{ch} \rangle$.

EXERCISE 6-1. As Q^2 increases at fixed s, t_{min} increases. Investigate this effect on $\langle N_{ch} \rangle$.

Next, we turn to the effect of Q^2 on $F(q^2, \nu, p_\perp, x)$ for the inclusive reaction

$$\gamma^* + p \rightarrow \pi^- + \text{anything} \qquad (6\text{-}1)$$

I remind you that Feynman scaling for the real photon reaction, namely for

$$\gamma + p \to \pi^- + \text{anything} \qquad (6\text{-}2)$$

$$\frac{E^* d\sigma}{\pi p^*_{max} dx dp_\perp^2} \equiv f(s, p_\perp, x) \xrightarrow[s \to \infty]{} f(p_\perp, x) \quad , \qquad (6\text{-}3)$$

is quite well obeyed. This is illustrated in Fig. 6-4. The peak near x = 1, which decreases rapidly as s increases, is due to the reaction

$$\gamma + p \to \pi^- + \Delta^{++} \quad , \qquad (6\text{-}4)$$

whose cross section varies as s^{-2}. We shall see the same effect in the virtual photon data.

To study the scaling behavior of $F(Q^2, s, p_\perp, x)$ we need only compare it with $F(Q^2 = 0, s, p_\perp, x) = \left[f(s, p_\perp, x)/\sigma\right]$. This is done for $\int_0^\infty F dp_\perp^2$ in Figs. 6-5 and 6-6. The comparisons are made with the $\gamma + p \to \rho^0 + p$ events excluded from the photoproduction data. This is an attempt to compensate for the effect (Sec. 3) that $(\sigma_{\gamma p \to \rho^0 p}/\sigma_{tot})$ decreases as Q^2 increases.

EXERCISE 6-2. Estimate the magnitude of this effect by calculating how the reaction $\gamma^* + p \to \rho^0 + p$, $\rho^0 \to \pi^+ + \pi^-$ populates the π^- inclusive spectrum.

From Figs. 6-5 and 6-6, we see that over this Q^2 range, there is no dramatic effect of Q^2 on $\int_0^\infty F dp_\perp^2$ after the contributions of the two-body channels are removed.

This is also true in the π^+ inclusive reaction

$$\gamma^* + p \to \pi^+ + \text{anything} \qquad (6\text{-}5)$$

illustrated in Fig. 6-7a. Here $p_\perp^2$ is fixed in the narrow band $p_\perp^2 < .02 (\text{GeV}/c)^2$. The two curves differ in both their Q^2 and the $W = \sqrt{s}$ values. But the F's are the same, except in the x close to 1 region where they differ due to the two-body channels $\gamma^* + p \to \pi^+ + n$ and $\gamma^* + p \to \pi^+ + \Delta^0$. This is shown very nicely in Fig. 6-7b where the same data is plotted versus the missing mass of the baryon system.

At this point, we shall turn to a more detailed examination of π^{+}_{-} inclusive

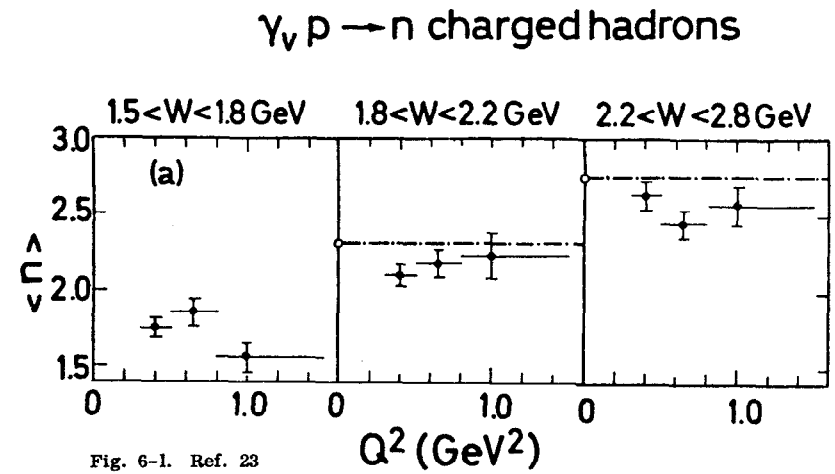

Fig. 6-1. Ref. 23

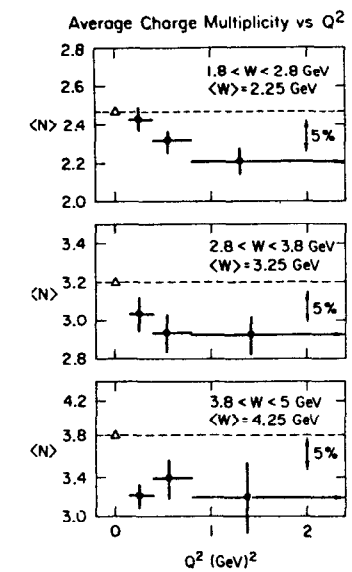

Fig. 6-2. The charged hadronic multiplicity as a function of Q^2 at fixed W. Ref. 24

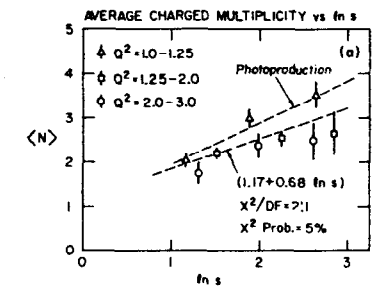

Fig. 6-3. Ref. 24

2350A22

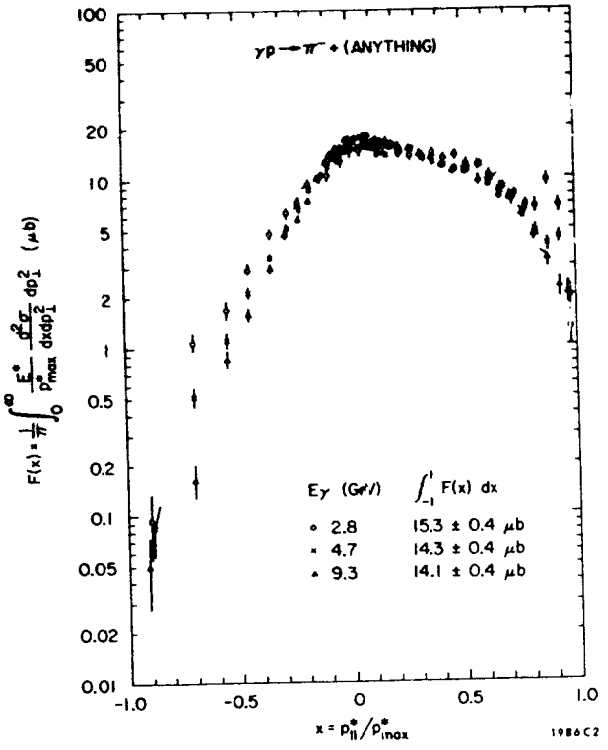

Fig. 6-4
Reaction $\gamma p \rightarrow \pi^- +$ (anything): Structure function F(x) for E_γ = 2.8, 4.7, and 9.3 GeV. Ref. 25

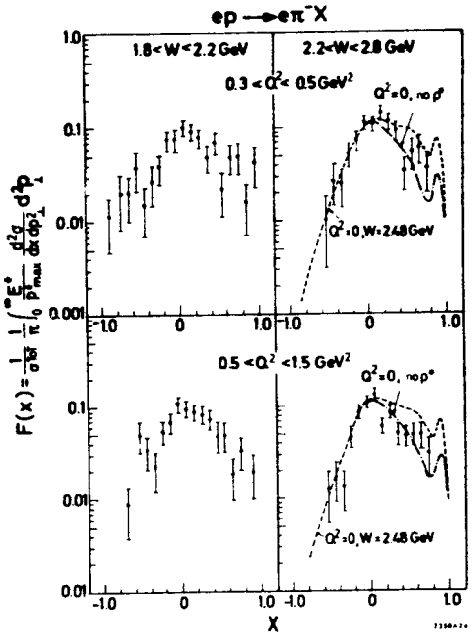

Fig. 6-5
Normalized structure function F(x) for inclusive π^- electroproduction for different W Q^2 intervals. The curves show the $Q^2 = 0$ results for all π^- tracks (dashed curves) and after the removal of the ρ^0 contribution (dashed-dotted curves) Ref. 23

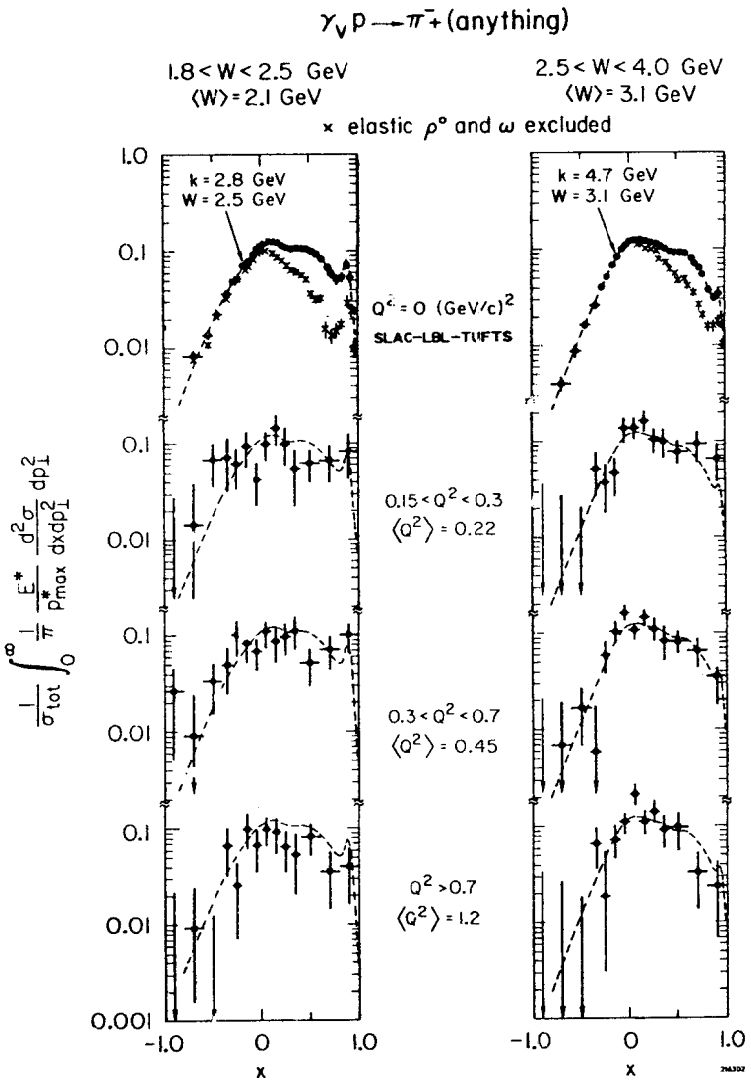

Fig. 6-6. Ref. 6b

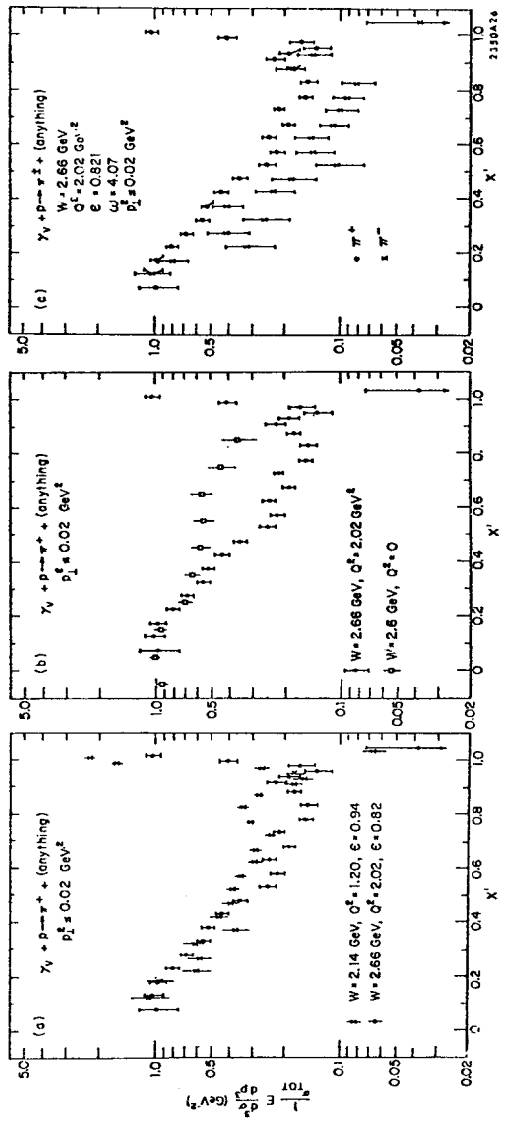

Fig. 6-7a. Ref. 14

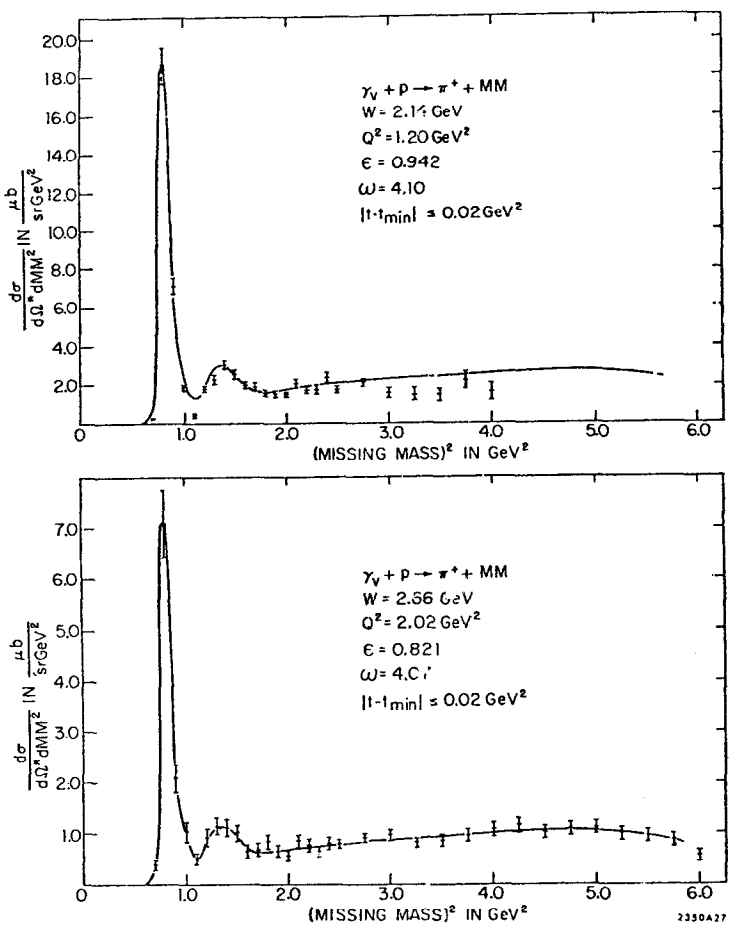

Fig. 6-7b. Ref. 14

electroproduction. We shall postpone to the end of this lecture, the discussion of K and p inclusive electroproduction for these K and p reactions introduce some puzzles and problems we wish to avoid for a while.

7. The Search for Virtual Photon Effects — Transverse Momentum Distributions

Since there are no gross and obvious effects of Q^2 on the x behavior of $F(Q^2, s, p_\perp, x)$, we must search with a little more care and judgement. Where might we expect to see Q^2 effects on inclusive spectra? From the fragmentation model we should expect some effects in the $x > .2$ or $.3$ region. For the particles in this region are supposed to come from the fragmentation of the virtual photon. And so their spectra might be different from that produced by real photon fragmentation.

The parton model, Fig. 2-4, leads to the same suggestion for a search region; although the parton model is very different from the fragmentation model. We look along the virtual photon three-momentum direction in the parton model because that is the direction in which particles will emerge which come most directly from the stopping of the struck parton in the nucleon. In other directions, we perhaps expect a less direct connection between the struck parton and the emerging hadron.

Let us therefore look at the distributions in $p_\perp$ for the forward x region, and see if these distributions vary with Q^2. Lower energy data is shown in Fig. 7-1 for $2.0 < W < 2.8$ GeV and in Fig. 7-2 for $2.5 < W < 2.8$ GeV. In both figures, the straight lines are fits of the form

$$\int_{x_1}^{x_2} \left[\frac{E^*}{\sigma_{tot}^{\pi} p^*_{max}} \frac{d^2\sigma}{dp_\perp^2 dx} \right] dx = A\, e^{-a p_\perp^2} \qquad (7\text{-}1)$$

The parameter for the π^+ data in Fig. 7-2 is plotted in Fig. 7-3. We see that for the electroproduction data a decreases slightly as Q^2 increases. (In all these comparisons, we are hesitant to use the photoproduction point because it always comes from a different experiment and may involve quite different fitting methods). The same effect

occurs in the $0.4 < x < 0.7$ π^- data in Fig. 7-2. But the effect is not seen in the $0.7 < x < 0.9$ data or in the highest Q^2 region in Fig. 7-1. However, new data from the same series of experiments that led to Fig. 7-1 — the DESY streamer chamber experiments — does show a decreasing as Q^2 increases[26].

The higher energy data, $\langle s \rangle \sim 20\ \text{GeV}^2$, does show a clear effect as illustrated in Fig. 7-4. Here the fit

$$\int_{x_1}^{x_2} \left[\frac{d\sigma}{\pi\ \sigma_{tot}\ dp_\perp^2\ dx} \right] dx = A\ e^{-bp_\perp^2} \qquad (7\text{-}2)$$

is used; the factor E^* in Eq. 7-1 being omitted. In this experiment h^- and h^+ refers to negative and positive hadrons of any type; but from other experiments, we know that these are predominantly pions.

It is sometimes claimed that this broadening of the transverse momentum distribution is related to the broadening of the forward peak in ρ^0 electroproduction. However, the connection is not straightforward. For example, if we use the concept of the lifetime of virtual-photon-associated-hadronic-systems, Eq. 3-8 and Ex. 3-2, then we have to make the following argument. When Q^2 is small, we see the usual transverse momentum distribution associated with hadron-hadron collisions. When Q^2 is large, we see the transverse momentum distribution associated with virtual photon-parton collisions. And the latter transverse momentum distribution is broader than the distribution associated with hadron-hadron collisions.

EXERCISE 7-1. Several explanations have been given for the broadness of the transverse momentum distribution from virtual-photon parton collisions [9]. One explanation is that the virtual photon contains transverse momentum components which are roughly measured by Q; and the emitted hadrons carry off this transverse momentum. Hence the width of the distribution increases as Q increases. Another explanation associ[illegible] the transverse momentum with the transverse momentum components of the

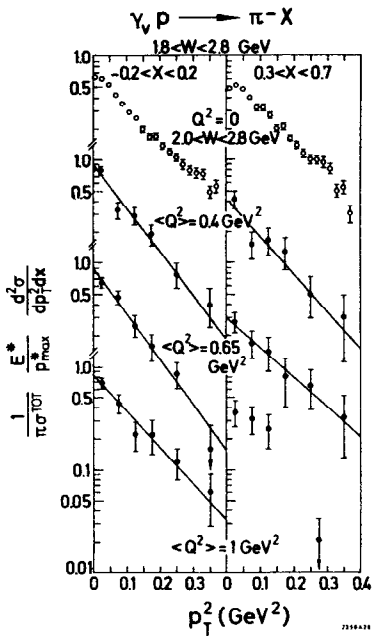

Fig. 7-1. Ref. 23

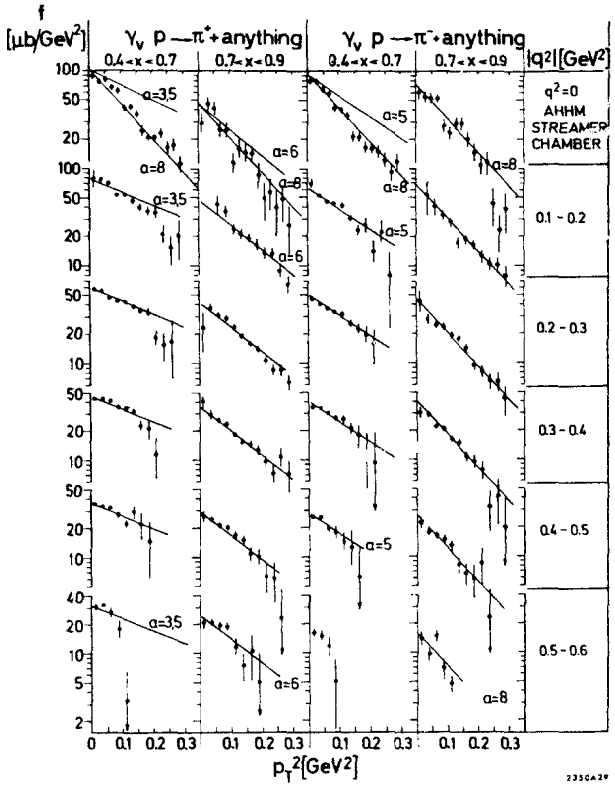

Fig. 7-2. Ref. 21

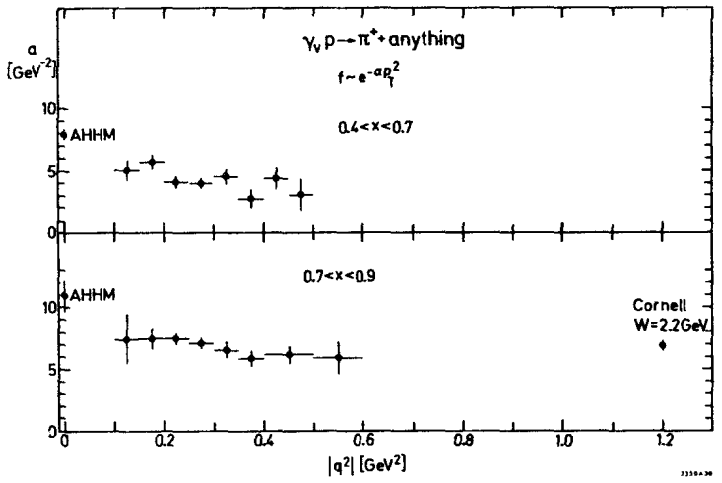

Fig. 7-3 Ref. 21

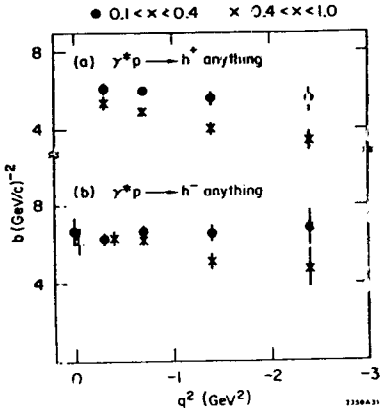

Fig. 7-4. Ref. 28

parton momentum distribution. Discuss these ideas.

8. The Search for Virtual Photon Effects -- Forward Charge Ratios

As happens so often in physics, we stumbled upon what we consider to be the most important Q^2 effect in inclusive electroproduction [22]. The first evidence for the effect of Q^2 on the ratio of positive to negative hadrons, N_h^+/N_h^-, produced in

$$\gamma^* + p \rightarrow h^{\pm} + \text{anything} \qquad (8\text{-}1)$$

is shown in Fig. 8-1. For $0 < x < .3$ there is a slight increase in N_h^+/N_h^- with Q^2, but for $0.3 < x < 1.0$ there is a clear increase. A beautiful example of this effect where the hadrons are identified as pions is shown in Fig. 8-2. Finally in Fig. 8-3 a composite of many experiments is given. Again, we note the difference between the forward x and central x regions.

What is the explanation of this effect. First, it is not due to the effect of Q^2 on two-body channels. This is demonstrated in Fig. 8-4, where at $Q^2 = 1.16$ $(\text{GeV}/c)^2$, $W = 2.63$ GeV, $p_\perp \sim 0.0$ the π^+ and π^- inclusive spectra versus the missing mass of the baryonic system are compared. We see that $(N_{\pi^+}/N_{\pi^-}) \sim 1.5$ to 2 in the continum region far above the nucleon and nucleon resonance region (which characterizes the two-body channels).

Next, what about the fragmentation model. In our view, the data contradicts any straightforward application of this model. For the fragmentation of the virtual photon, a neutral object, should give

$$N_h^+/N_h^- \approx 1 \qquad (8\text{-}2)$$

as occurs approximately in photoproduction. (The photoproduction ratio is about 1.2 or 1.3). Therefore, we regard the forward charge ratio data as evidence against the fragmentation model explanation of virtual photon-proton inclusive reactions in the forward x region. We should mention that one may attempt to save the fragmentation model in this regard by arguing that there is positive charge spillover from the proton fragmentation region; and arguing further that the spillover increases as Q^2 increases.

But there is evidence against this concept from the study of (N_h^+/N_h^-) in electroproduction on neutrons [28]

$$\gamma^* + n \rightarrow H^{\pm} + \text{anything} \tag{8-3}$$

This new data on neutron electroproduction will be discussed by Gary Feldman [29] at the Topical Conference on Deep Inelastic Scattering. I will only note here that while in photoproduction on neutrons

$$\frac{N_h^+}{N_h^-} \approx .8 \ , \ Q = 0 \ ; \tag{8-4a}$$

in electroproduction on neutrons

$$\frac{N_h^+}{N_h^-} \approx 1.4 \ , \ 0.3 < Q^2 < 3.0 \ (\text{GeV}/c)^2 \tag{8-4b}$$

for $0.4 \leq x \leq .85$. The spillover argument will of course not work with a neutron target.

As will be discussed in detail by Feldman[29,32] the simple quark-parton model does provide an explanation of the effect of Q^2 on the forward charge ratio. Using p, n to represent the standard quarks with the following properties

	B	I	Q	S
p	1/3	1/2	2/3	0
n	1/3	1/2	-1/3	0
λ	1/3	0	-1/3	-1

(8-5)

the nucleons consist of

$$\begin{aligned} &\text{Proton} = ppn + \text{quark-antiquark sea} \\ &\text{Neutron} = pnn + \text{quark-antiquark sea} \end{aligned} \tag{8-6}$$

If the quark which absorbs the virtual photon turns into a meson by picking up another quark, we have

$$\begin{aligned} &\text{p quark: } p\bar{n} \rightarrow \pi^+ \ , \ p\bar{p} \rightarrow \pi^0 \text{ or } \eta, \ p\bar{\lambda} \rightarrow K^+ \\ &\text{n quark: } n\bar{p} \rightarrow \pi^- \ , \ n\bar{n} = \pi^0 \text{ or } \eta, \ n\bar{\lambda} \rightarrow K^0 \end{aligned} \tag{8-7}$$

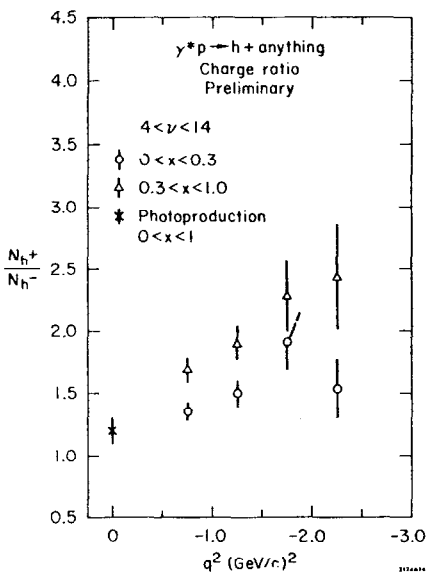

Fig. 8-1. Ref. 32

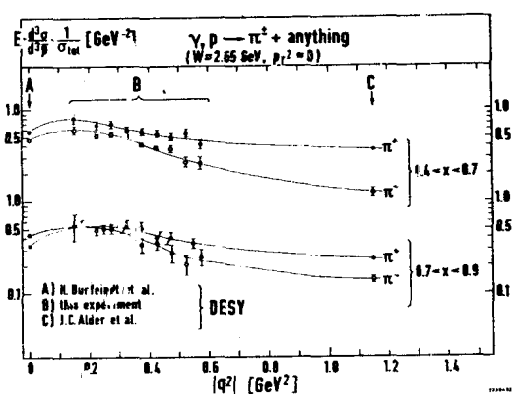

Fig. 8-2 Ref. 21

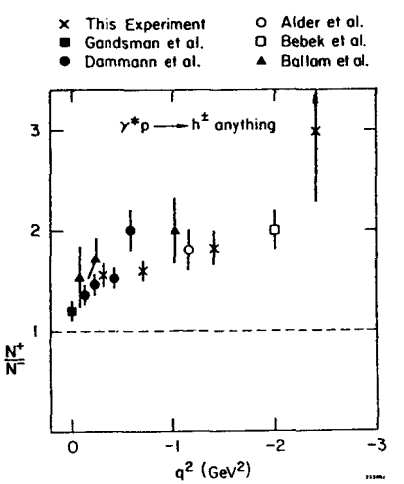

Fig. 8-3. Ref. 28

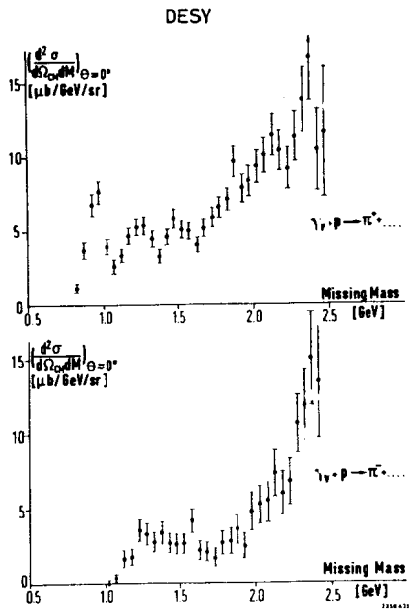

Fig. 8-4. Ref. 27

Then assuming that the virtual photon interacts only with the so-called valence quarks, and remembering that the absorption cross section is proportional to the square of the quark charge, the model predicts

$$\begin{aligned} &\text{Proton target} && 8\pi^+ : 4.5\,\pi^0 : 1\,\pi^- : 8K^+ : 1\,K^0 \\ &\text{Neutron target} && 2\pi^+ : 1.5\pi^0 : 1\,\pi^- : 2K^+ : 1\,K^0 \end{aligned} \qquad (8\text{-}8)$$

EXERCISE 8-1. Fill in steps leading to Eq. 8-8. Show that these ratios will approach 1 as the relative probability of the virtual photon interacting with the quark-antiquark sea is increased from 0. How will the K/π ratio change if the probability of picking up a $\bar{\lambda}$ is different from that for an $\bar{n}$ or $\bar{p}$?

Thus, this simple model predicts $N_h^+/N_h^- > 1$ when Q^2 is sufficiently large for the parton model to be used. Of course, we do not see the predicted 8:1 ratio. This may be explained by Q^2 not being sufficiently large or by the dilution effect of the quark-anti-quark (Ex. 8-1).

9. Unanswered Questions

In these lectures, we have come across many unanswered questions. But there are three questions, I want to discuss in closing.

First, we know very little about inclusive electroproduction of K mesons,

$$\gamma^* + p \rightarrow K^{\pm} + \text{anything} \; ; \qquad (9\text{-}1)$$

and what we know is puzzling. From the simple quark-parton model discussed at the end of the last section, we might expect the K^+/π^+ ratio to increase in the forward x region as Q^2 increases. The increase in Q^2 takes us from photoproduction where the K^+/π^+ ratio is small to the region of validity of the parton model. A first glance at the data, Fig. 9-1, seems to agree with this prediction. The K^+ invariant cross section is increasing with Q^2; whereas, we remember from Sec. 6 that the π invariant cross sections actually decrease with increasing Q^2, due to the dominance of two-body channels in this x region.

But if one looks at this and similar data in more detail, one finds that most of

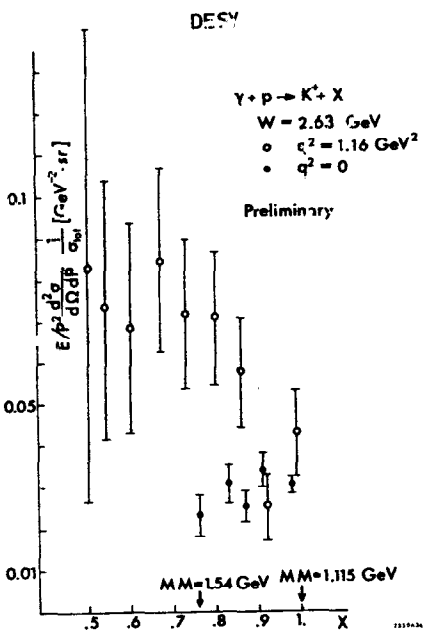

Fig. 9-1. Ref. 30

the K^+ are produced in two-body channels [7a, 14, 27, 30].

$$\gamma^* + p \rightarrow K^+ + \Sigma^0, \Lambda^0$$
$$\gamma^* + p \rightarrow K^+ + Y^{*0} \qquad (9\text{-}2)$$

The production of these channels is usually not explained through the parton model. Thus, we get the right prediction for the wrong reason. We do not know why these K^+ producing two-body channels are increasing with Q^2.

In studying the K spectrum, we are plagued by the lack of experimental data. K's have been studied in small solid angle two-arm spectrometer experiments, but they have not yet been studied in large solid angle or 4π solid angle experiments. We do know, however, that in the kinematic regions which have been studied[27]

$$K^+/\pi^+ \lesssim \frac{1}{4} \qquad (9\text{-}3)$$

Also, as illustrated in Fig. 9-2, the K^-/K^+ ratio is small. Thus one question, yet to be answered, is what is the general behavior of $(\gamma^* + p \rightarrow K^{\pm} + \text{anything})$ as a function of Q^2?

Our second question concerns the inclusive electroproduction of protons

$$\gamma^* + p \rightarrow p + \text{anything} \qquad (9\text{-}4)$$

In the backward x region, $x < -0.5$, we see a very pretty effect, Fig. 9-3. Looking at the $W > 2.5$ GeV data, the slow proton ($x \sim -.9$) peak in photoproduction disappears as Q^2 increases. Much of this is caused by the decrease with increasing Q^2 of

$$\gamma^* + p \rightarrow \rho^0 + p \qquad (9\text{-}5)$$

as discussed in Sec. 3. Some of the fall off is certainly also due to the decrease in

$$\gamma^* + p \rightarrow \omega^0 + p$$

and three-or-more-body diffractive processes

$$\gamma^* + p \rightarrow (\text{diffractive } 3\pi, 5\pi \ldots) + p \qquad (9\text{-}6)$$

It would be interesting to know something about the Q^2 dependence of the reaction in Eq. 9-6.

But of special interest to the parton model is the inclusive electroproduction

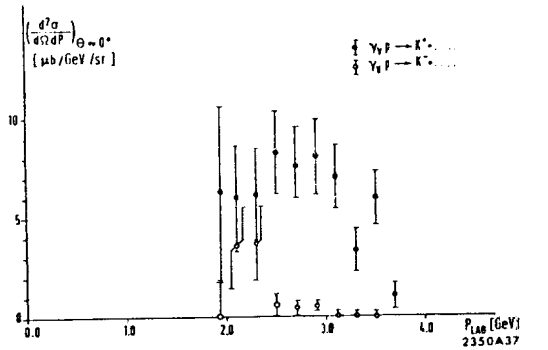

$d^2\sigma/d\Omega dP$ for inclusive electroproduction of K^+ and K^- in the direction of the virtual photon as a function of the lab momentum of the kaons above 1.9 GeV.

Fig. 9-2. Ref. 27

of protons [14, 31] in the forward x region, $0 < x < 1$. As shown in Fig. 9-4, for $p_\perp \sim 0$, $x \gtrsim 0$, $W = 2.89 - 2.70$ GeV

$$\frac{E}{\sigma_{tot}} \frac{d\sigma}{d^3p} \text{ increases as } Q^2 \text{ increases} \qquad (9\text{-}7)$$

(Unfortunately, as with K inclusive reactions, we have no data from the large solid angle or 4π experiments which would yield $p_\perp \neq 0$ information). If we accept Eq. 9-7 as characteristic of all the $x \gtrsim 0$ proton data, this is in agreement with a prediction of some quark-parton models. These models argue that absorption of the virtual photon by a quark pushes baryon number forward in the direction of q. And, they argue, as Q^2 increases more baryons should appear in the $x \gtrsim 0$ region. But as we used the parton model at the end of the previous section, [32] forward baryon production is a higher order process compared to meson production. The dominant way of dressing the struck quark is for it to pick up a single antiquark producing a meson. The relative probability for it to pick up two quarks, to make a baryon, seems to us to be small. My second question is then, at what Q^2 and with what abundance

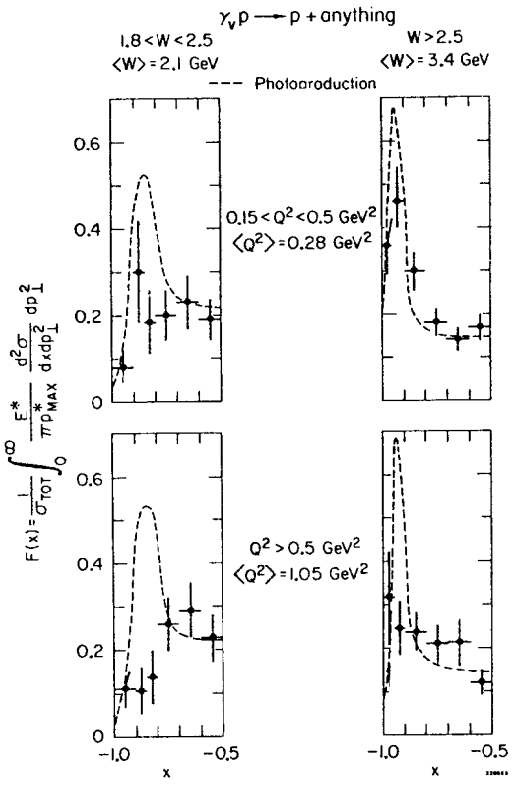

Fig. 9-3. Ref. 24

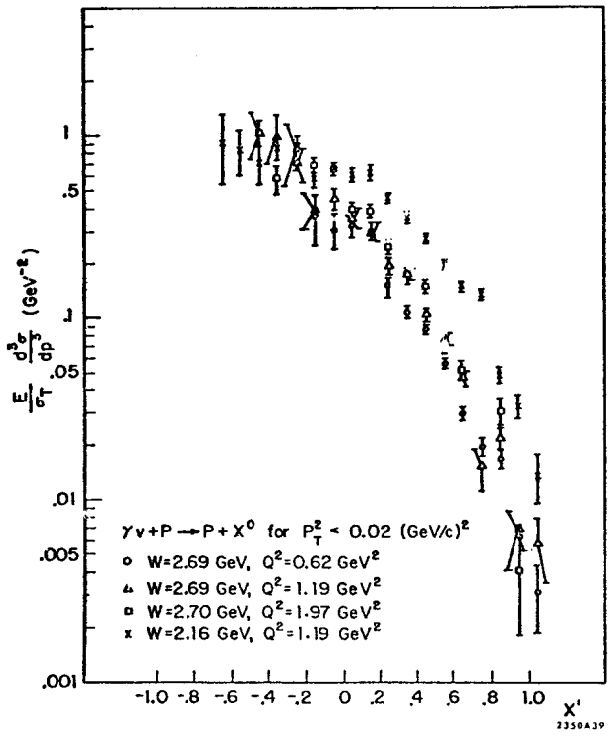

Fig. 9-4. Ref. 14

should we see an enchancement of forward proton production with increasing Q^2?

My third question has no experimental answer or even experimental hint at present. What will be the absolute and relative behaviors of

$$\gamma^* + p \rightarrow \pi^{\pm} + \text{anything}$$

$$\gamma^* + p \rightarrow K^{\pm} + \text{anything}$$

$$\gamma^* + p \rightarrow p, \bar{p} + \text{anything}$$

versus Q^2 for large transverse hadron momenta?

REFERENCES

1. J. D. Bjorken and S. D. Drell, Relativistic Quantum Mechanics, (McGraw-Hill, New York, 1964).
2. M. L. Perl, High Energy Hadron Physics (Wiley, New York, to be published).
3. N. Dombey, Rev. Mod. Phys. 41 236 (1969).
4. K. Schilling and G. Wolf, Deutsches Elektronen-Synchrotron Report No. DESY 73/13 (1973).
5. J. J. Sakurai and D. Schildknecht, Phys. Letters 40B, 121 (1972) and references contained therein.

6.a. L. Ahrens et al., Laboratory of Nuclear Studies (Cornell University) Report CLNS 227 (1973).

b. J. Ballam et al., in Proceedings of the 16th International Conference on High Energy Physics, 1972 (National Accelerator Laboratory, Batavia, Illinois, 1973), also see SLAC-PUB-1163 (1972) and SLAC-PUB-1242 (1973).

c. J. T. Dakin et al., Phys. Rev. D8, 687 (1973).

d. C. Driver et al., Nucl. Phys. B38, 1 (1972).

e. V. Eckardt et al., Phys. Letters B43, 240 (1973).

7. For a review of this subject and other electroproduction subjects see

a) K. Berkelman in Proceedings of the 16th International Conference on High Energy Physics, 1972 (National Accelerator Laboratory, Batavia, Illinois, 1973).

b) K. Heinloth, Deutsches Elektronen-Synchrotron Report No. DESY 72/61 (1972).

c) G. Wolf, Deutsches Elektronen-Synchrotron Report No. DESY 72/61 (1972).

8. D.W.G.S. Leith in Proceedings of the 16th International Conference on High Energy Physics, 1972 (National Accelerator Laboratory, Batavia, Illinois, 1973).
9. H. T. Nieh, Phys. Letters 38B 100 (1972). Also see H. Cheng and T. T. Wu, Phys. Rev. 183, 1324 (1969); J. D. Bjorken, J. B. Kogut, and D. E. Soper, Phys. Rev. D3, 1382 (1971); and J. B. Kogut, Phys. Rev. D5, 1152 (1972).
10. B. Dieterle, Nuovo Cimento 11A, 523 (1972).
11. K. C. Moffeit, private communication.
12. D. Schmidt, private communication.
13. C. Driver et al., Phys. Letters 35B, 77 (1971); Phys. Letters 35B, 81 (1971); Nucl. Phys. B30, 245 (1971).
14. C. Bebek et al., Cornell University and Harvard University preprint entitled Hadronic Final States in Electroproduction, (1973) (not numbered). Partially published in Phys. Rev. Letters 30, 624 (1973).
15. F. A. Berends and R. Gastmans, Phys. Rev. D5, 204 (1972); R. C. E. Devenish and D. H. Lyth, Phys. Rev. D5, 47 (1972); R. W. Manweiler and W. Schmidt, Phys. Rev. D3, 2752 (1971).
16. C. N. Brown et al., Phys. Rev. Lett. 26, 991 (1971).
17. P. S. Kummes, et al., Letters Nuovo Cimento 1, 1026 (1971).

18a. V. Silvestrini in Proceedings of the 16th International Conference on High Energy Physics, 1972 (National Accelerator Laboratory, Batavia, Illinois, 1973).

b. G. Barbiellini et al., Letters Nuovo Cimento 6, 557 (1973).

19. I. Dammann et al., Deutsches Elektronen-Sychrotron Report No. DESY 72/70 (1972).
20. V. Eckardt et al., Deutsches Elektronen-Synchrotron Report No. DESY 72/67 (1972).
21. I. Dammann et. al., Deutsches Elektronen-Synchrotron Report DESY 72/71 (1972).
22. J. T. Dakin et al., Phys. Rev. Letters 29, 746 (1972).
23. V. Eckardt et al., Nuc. Phys. B55, 45 (1973).
24. M. Della Negra, SLAC-PUB-1242 (1973).
25. K. C. Moffeit et al., Phys. Rev. D5, 1603 (1972).

26. H. Meyer, private communication.

27. J. C. Alder et al., Nucl. Phys. B46, 415 (1972).

28. J. T. Dakin et al., SLAC-PUB-1269 (1973).

29. G. J. Feldman, talk at SLAC Summer Institute on Particle Physics entitled Inclusive Electroproduction of Hadrons from Protons and Neutrons and Tests of the Quark Parton Model.

30. H. Burfeindt et al., Phys. Letters 43B, 345 (1973).

31. V. Korbel, Ph.D. thesis, Deutsches Elektronen-Synchrotron Report No. DESY F21-73/2 (1973).

32. J. T. Dakin and G. J. Feldman SLAC-PUB-1273 (1973).

PHENOMENOLOGICAL ANALYSIS

by

Frederick J. Gilman

LECTURE I - Inelastic Lepton Scattering with Polarized Beams and Targets

LECTURE II - Fixed Poles in Photoproduction and Electroproduction

INELASTIC LEPTON SCATTERING WITH POLARIZED BEAMS AND TARGETS*

Frederick J. Gilman

Stanford Linear Accelerator Center
Stanford University, Stanford, California 94305

I. Introduction

In the near future the possibility of performing experiments with both polarized lepton beams and polarized targets will become a reality. The muon beams at BNL, CERN, or NAL automatically possess a longitudinal polarization because of their origin in the weak decays of pions. At SLAC a polarized electron source is being installed. The planned experiment[1] on deep inelastic scattering will be a technological tour de force involving production of a polarized lithium atomic beam, an ultraviolet flash lamp operating at 180 pps to knock off the electrons, injection into the accelerator and acceleration without loss of polarization, magnetic bending of the beam into the end station at which point g-2 of the electron demands the energy be a multiple of 3.22 GeV so that the spin is rotated by a multiple of 180°, and finally the beam striking a longitudinally polarized proton target operating at 1°K in the field of a superconducting magnet.

With this exciting background of approaching experiments, in this lecture I would like to discuss some of the theory and phenomenology related to inelastic lepton scattering with polarized beams and targets. As we shall see, a number of interesting questions having to do with amplitude analysis, scaling, parton models or light cone algebra, sum rules, quark models for resonance excitation, and even exotic J-plane singularity structure are subject to direct experimental answer with polarized beams and targets.

*Work supported by the U. S. Atomic Energy Commission.

II. Polarized Beams

The scattering of a longitudinally polarized lepton beam on an unpolarized target should be independent of the lepton polarization if no hadrons are detected in the final state. This follows from parity conservation, and while this is well checked at small q^2 in the electromagnetic interactions of hadrons, an experiment[2] is planned at SLAC to verify this at large q^2 in deep inelastic scattering. Of course, if such a violation is found it is of enormous interest (due to weak interactions at an unexpected level?) and the theoretical questions discussed in the remainder of this talk become of secondary interest.

From this point on let us assume one photon exchange, together with the C, P and T invariance of electromagnetism. Let the initial (final) electron four-momentum be k_μ (k'_μ) with the virtual photon of four-momentum $q_\mu = k_\mu - k'_\mu$ interacting with a nucleon of four-momentum p_μ. We use the usual invariants[3,4] $\nu = -q\cdot p/M_n$ and q^2.

Suppose a final hadron (four-momentum p'_μ) is detected. Then $\vec{k}$ and $\vec{k}'$ define a plane (the lepton plane), as do $\vec{q}$ and $\vec{p}'$ (the hadron plane), with an angle ϕ between their normals.

Now recall for a moment the case of an unpolarized beam. There, to calculate a cross section[4] we must evaluate a lepton trace, $L_{\mu\nu}$, which is essentially the virtual photon density matrix. If we take the direction $\vec{q}$ as a z-axis, with x-axis in the lepton plane (so that the positive x direction is toward the leptons) then $L_{\mu\nu} = (1/2)(k_\mu k'_\nu + k'_\mu k_\nu + (q^2/2)\,\delta_{\mu\nu})$ can be written as

$$L_{\mu\nu} = \left(\frac{2}{1-\epsilon}\right)\left(\frac{q^2}{4}\right)\left\{\begin{pmatrix}\sqrt{\frac{1}{2}(1+\epsilon)}\\ 0\\ -\sqrt{q^2\epsilon/\nu^2}\\ 0\end{pmatrix}\overbrace{\begin{matrix}\sqrt{\frac{1}{2}(1+\epsilon)} & 0 & -\sqrt{q^2\epsilon/\nu^2} & 0\end{matrix}} + \begin{pmatrix}0\\ \sqrt{\frac{1}{2}(1-\epsilon)}\\ 0\\ 0\end{pmatrix}\overbrace{\begin{matrix}0 & \sqrt{\frac{1}{2}(1-\epsilon)} & 0 & 0\end{matrix}}\right\} \tag{1}$$

where

$$\epsilon = \frac{1}{1 + 2\left(1 + \frac{\nu^2}{q^2}\right)\tan^2\theta/2}\ , \tag{2}$$

with θ = the lepton scattering angle in the laboratory. We have subtracted multiples[5] of q_μ from the virtual photon polarization vector so as to make $L_{\mu\nu} = 0$ when μ or $\nu = 4$. As is seen from Eq. (1), the virtual photon is the incoherent sum of a piece with linear polarization in the x-z plane and a piece with linear polarization in the y-direction.

If $\epsilon^{(\gamma)}_\mu f_\mu$ is the amplitude for

$$\text{"}\gamma(q)\text{"} + N(p) \to \text{hadron}'(p') + \ldots\ , \tag{3}$$

with the property

$$q_\mu f_\mu = 0\ , \tag{4}$$

then from Eq. (1) we have that

$$\begin{aligned}\frac{d\sigma}{d^3p'} &\propto \left|\sqrt{\tfrac{1}{2}(1+\epsilon)}\, f_x - \sqrt{q^2\epsilon/\nu^2}\, f_z\right|^2 + \left|\sqrt{\tfrac{1}{2}(1-\epsilon)}\, f_y\right|^2 \\ &\propto \frac{1}{2}\left(|f_x|^2 + |f_y|^2\right) \\ &\quad + \frac{\epsilon}{2}\left(|f_x|^2 - |f_y|^2\right) \\ &\quad + \epsilon\left(q^2|f_z|^2/\nu^2\right) \\ &\quad - \sqrt{\tfrac{1}{2}\epsilon(1+\epsilon)}\ 2\,\mathrm{Re}\left(f_x\sqrt{q^2/\nu^2}\, f_z^*\right)\ .\end{aligned} \tag{5}$$

The four terms in Eq. (5) are in the form of the standard equation for, e.g., $\text{"}\gamma\text{"} + p \to \pi^+ + n$, where they are often labelled[6] $d\sigma_U/dt$, $d\sigma_P/dt$, $d\sigma_L/dt$, and $d\sigma_I/dt$ respectively, after their ϕ dependence is explicitly exhibited. This ϕ dependence is easily read off if f_x, f_y and f_z are rewritten in terms of helicity amplitudes (of the

virtual photon). The four terms behave respectively as constant, cos 2ϕ, constant, and cos ϕ.

With this background, consider a longitudinally polarized beam where the leptons have helicity $\pm 1/2$. The lepton trace now reads

$$L_{\mu\nu}^{(\pm)} = \frac{1}{2}\left(k_\mu k'_\nu + k'_\mu k_\nu + (q^2/2)\,\delta_{\mu\nu} \pm \epsilon_{\mu\nu\lambda\sigma} k_\lambda k'_\sigma\right) , \tag{6}$$

which can be rewritten with $\vec{q}$ as a z-axis, using the same manipulations as above, in the form[5]

$$L_{\mu\nu}^{(\pm)} = \left(\frac{2}{1-\epsilon}\right)\left(\frac{q^2}{4}\right)\left\{\begin{pmatrix} \sqrt{\frac{1}{2}(1+\epsilon)} \\ \mp i\sqrt{\frac{1}{2}(1-\epsilon)} \\ -\sqrt{q^2\,\epsilon/\nu^2} \\ 0 \end{pmatrix} \overbrace{\begin{matrix} \sqrt{\frac{1}{2}(1+\epsilon)} & \pm i\sqrt{\frac{1}{2}(1-\epsilon)} & -\sqrt{q^2\,\epsilon/\nu^2} & 0 \end{matrix}}\right\} . \tag{7}$$

The virtual photon now can be represented in terms of a single elliptical polarization state. For incident leptons with helicity $\pm 1/2$, the analogue of Eq. (5) for detection of a final hadron is (summed over the helicities of all hadrons):

$$\begin{aligned} \frac{d\sigma}{d^3p'} &\propto \left| \sqrt{\tfrac{1}{2}(1+\epsilon)}\, f_x \pm i\sqrt{\tfrac{1}{2}(1-\epsilon)}\, f_y - \sqrt{q^2\,\epsilon/\nu^2}\, f_z \right|^2 \\ &\propto \frac{1}{2}\left(|f_x|^2 + |f_y|^2\right) \\ &\quad + \frac{\epsilon}{2}\left(|f_x|^2 - |f_y|^2\right) \\ &\quad + \epsilon\left(q^2\,|f_z|^2/\nu^2\right) \\ &\quad - \sqrt{\tfrac{1}{2}\epsilon(1+\epsilon)}\; 2\,\mathrm{Re}\left(f_x \sqrt{q^2/\nu^2}\, f_z^*\right) \\ &\quad \pm \sqrt{\tfrac{1}{2}\epsilon(1-\epsilon)}\; 2\,\mathrm{Im}\left(f_y \sqrt{q^2/\nu^2}\, f_z^*\right) \quad , \end{aligned} \tag{8}$$

where we have gained the last term when compared with Eq. (5). An apparent term of the form $\sqrt{(1/4)(1-\epsilon^2)}\;\; 2\,\mathrm{Im}\,(f_x f_y^*)$ vanishes because of parity conservation, which becomes obvious when the amplitudes are rewritten in terms of (photon) helicity amplitudes.[7] In this form the ϕ dependence of the last term in Eq. (8) is also easily seen to be that of $\sin\phi$.

Since the (complex) amplitudes f_x, f_y, and f_z are characterized by six real quantities, with one overall phase, there are five real numbers which give all possible physical information on the amplitude f_μ. As there are five independent quantities in Eq. (8), we see that <u>all the physics contained in f_μ is obtainable with a polarized beam.</u>

Particular cases of interest in the literature are[8]

$$\text{"}\gamma\text{"} + N \to \pi + \text{anything} \quad , \tag{9}$$

and[9,10]

$$\text{"}\gamma\text{"} + N \to \rho^o + N \quad , \tag{10}$$

where one also has information on the ρ^o density matrix coming from its two pion decay mode. It has recently been shown[9] explicitly that all possible joint density matrix elements of the virtual photon and rho meson are determinable through use of a polarized lepton beam and examination of the rho decay angular distribution. In short, the use of a polarized lepton beam alone allows one to perform complete amplitude analyses of the photon segment of virtual photon induced processes.

III. Polarized Beam and Target Kinematics

As in the unpolarized case, there are two equivalent ways to proceed, each particularly useful for certain purposes. One method is to define virtual photon-nucleon total cross sections; the other is to define structure functions. We begin with the definition of total cross sections.

First we recall the unpolarized case,[4] where there are two independent photon-nucleon total cross sections, σ_T and σ_L. By the optical theorem they are proportional

to the imaginary part of the forward photon-nucleon scattering amplitude, $T_{\lambda'_\gamma\lambda'_N,\lambda_\gamma\lambda_N}(\nu, q^2, t=0)$:

$$\sigma_T(\nu,q^2) \propto \frac{1}{2}\left(\text{Im } T_{1\frac{1}{2},1\frac{1}{2}} + \text{Im } T_{1-\frac{1}{2},1-\frac{1}{2}}\right)$$
$$\sigma_L(\nu,q^2) \propto \text{Im } T_{0\frac{1}{2},0\frac{1}{2}} \quad . \tag{11}$$

In fact, the usual tensor, $W_{\mu\nu}$, is also proportional to Im $T_{\mu\nu}$, and the $\mu,\nu = 1,2,3$ (z axis along $\vec{q}$) components are[11]

$$W_{ij} = \frac{K}{4\pi^2\alpha}\begin{pmatrix}\sigma_T & 0 & 0\\ 0 & \sigma_T & 0\\ 0 & 0 & \nu^2\sigma_L/q^2\end{pmatrix} \quad , \tag{12}$$

where $K = \nu - q^2/2M_N$ is the real photon (laboratory) energy necessary to produce the same center-of-mass energy. The double differential cross section for detecting a final lepton of energy E' if the incident beam has energy E is given by[4]

$$\frac{d^2\sigma}{d\Omega' dE'} = \left(\frac{1}{2\pi}\right)^2\left(\frac{E'}{E}\right)\left(\frac{4\pi\alpha}{q^2}\right)^2 L_{\mu\nu}W_{\mu\nu} \quad , \tag{13}$$

so that using the lepton trace in Eq. (1) we have

$$\frac{d^2\sigma}{d\Omega' dE'} = \frac{\alpha}{4\pi^2}\frac{K}{2}\left(\frac{E'}{E}\right)\left(\frac{2}{1-\epsilon}\right)(\sigma_T + \epsilon\sigma_L)$$
$$= \Gamma(\sigma_T + \epsilon\sigma_L) \quad , \tag{14}$$

which is the standard result.

In the polarized beam and target case, one is able to measure separately the total cross sections $\sigma_{1/2}$ and $\sigma_{3/2}$ (net photon plus nucleon value of J_z equal to 1/2 and 3/2 respectively) and σ_{TL} defined by[12]

$$\sigma_{1/2}(\nu,q^2) \propto \text{Im } T_{1\frac{1}{2},1\frac{1}{2}}$$
$$\sigma_{3/2}(\nu,q^2) \propto \text{Im } T_{1-\frac{1}{2},1-\frac{1}{2}} \quad , \tag{15}$$
$$\sqrt{2}\sigma_{TL}(\nu,q^2) \propto \text{Im } T_{1\frac{1}{2},0-\frac{1}{2}} \quad ,$$

with the same proportionality constant as in Eq. (11), so that

$$\sigma_T = \frac{1}{2}(\sigma_{1/2} + \sigma_{3/2}) \quad . \tag{16}$$

Therefore, there are two new measurable quantities, which we take to be $(1/2)(\sigma_{1/2} - \sigma_{3/2})$ or the asymmetry,

$$A(\nu,q^2) = \frac{\sigma_{1/2}-\sigma_{3/2}}{\sigma_{1/2}+\sigma_{3/2}} = \frac{\frac{1}{2}(\sigma_{1/2}-\sigma_{3/2})}{\sigma_T} \quad , \tag{17}$$

and σ_{TL}. For these quantities we have the bounds[13]

$$\left|\frac{1}{2}(\sigma_{1/2}-\sigma_{3/2})\right| \le \sigma_T \quad \text{or} \quad |A| \le 1 \quad , \tag{18}$$

and

$$\sqrt{2}\,\sigma_{TL} \le \sqrt{\sigma_{1/2}\sigma_L} \quad \text{or} \quad \sigma_{TL} \le \sqrt{\sigma_T\sigma_L} = \sqrt{R}\,\sigma_T \quad . \tag{19}$$

It is not difficult to see from our definitions that if the nucleon target was polarized along $\pm\vec{q}$, only $\sigma_{1/2}-\sigma_{3/2}$ would contribute to the difference, while with polarization perpendicular to $\vec{q}$ (but still in the lepton plane), only σ_{TL} contributes to a difference between target spin orientations. However, in real life it is far easier to orient the target relative to the lepton beam, and not $\vec{q}$. For a nucleon target polarized antiparallel or parallel to the beam we find,[14]

$$\frac{d^2\sigma^{\uparrow\downarrow}}{d\Omega' dE'} - \frac{d^2\sigma^{\uparrow\uparrow}}{d\Omega' dE'} = 2\Gamma\left(\left(\frac{E-E'\epsilon}{E}\right)A\sigma_T + \frac{\sqrt{q^2}}{E}\epsilon\sigma_{TL}\right) \quad , \tag{20}$$

to be compared with the unpolarized result,

$$\frac{d^2\sigma^{\uparrow\downarrow}}{d\Omega' dE'} + \frac{d^2\sigma^{\uparrow\uparrow}}{d\Omega' dE'} = 2\Gamma(\sigma_T + \epsilon\sigma_L) \quad . \tag{21}$$

If we neglect σ_L and σ_{TL} as being small,[15] then we have that

$$\frac{\frac{d^2\sigma^{\uparrow\downarrow}}{d\Omega' dE'} - \frac{d^2\sigma^{\uparrow\uparrow}}{d\Omega' dE'}}{\frac{d^2\sigma^{\uparrow\downarrow}}{d\Omega' dE'} + \frac{d^2\sigma^{\uparrow\uparrow}}{d\Omega' dE'}} = \left(\frac{E-E'\epsilon}{E}\right) A(\nu, q^2) = \left(\frac{E-E'\epsilon}{E}\right) \frac{\sigma_{1/2} - \sigma_{3/2}}{\sigma_{1/2} + \sigma_{3/2}} \quad . \tag{22}$$

This simple result shows that the virtual photon-nucleon asymmetry is "degraded" by the factor $(E-E'\epsilon)/E$ in order to obtain the lepton beam-target asymmetry which is actually measured.

It is also possible to polarize the target perpendicular to the beam, but in the lepton plane. In this case we find[16]

$$\frac{d^2\sigma^{\uparrow\leftarrow}}{d\Omega' dE'} - \frac{d^2\sigma^{\uparrow\rightarrow}}{d\Omega' dE'} = 2\Gamma \left\{ \sqrt{\frac{1}{2}\epsilon(1+\epsilon)}\, \frac{\sqrt{q^2}}{E} A\sigma_T - \sqrt{\frac{2\epsilon}{1+\epsilon}}\, \frac{E-E'\epsilon}{E}\, \sigma_{TL} \right\} . \tag{23}$$

Under presently contemplated experimental conditions, the $A\sigma_T$ term has an order of magnitude greater weight than the σ_{TL} term in Eq. (20), while the situation is reversed in Eq. (23). Thus, while it is possible in principle to separate $A\sigma_T$ and σ_{TL} by only running with the target polarized parallel or antiparallel to the beam at different values of E, E', and θ (but the same ν and q^2), in practice this is very difficult. The use of perpendicular polarization (Eq. (23)) makes the task of separation much easier.[17,18]

Isolation of σ_{TL} may be of some importance in obtaining information on $R = \sigma_L/\sigma_T$. As R is known to be small in deep inelastic scattering, it is difficult to measure accurately. Equation (19), however, shows that measurement of σ_T and σ_{TL} will give a lower bound on R. For the particular case of elastic scattering, where $\sigma_{TL} \propto G_M G_E$, measurement of σ_{TL} may provide the only way to study G_E at large q^2.

Just as there were two new cross sections to define in the spin dependent case, there are two additional structure functions besides the familiar W_1 and W_2. We write,[19]

$$\begin{aligned} W_{\mu\nu} = {} & W_1(\nu, q^2)\left(\delta_{\mu\nu} - q_\mu q_\nu/q^2\right) \\ & + W_2(\nu, q^2)\left(p_\mu - p\cdot q\, q_\mu/q^2\right)\left(p_\nu - p\cdot q\, q_\nu/q^2\right)/M_N^2 \\ & - d(\nu, q^2)\, \epsilon_{\mu\nu\lambda\sigma} q_\lambda s_\sigma/4\pi M_N \\ & + g(\nu, q^2)\, s\cdot q\, \epsilon_{\mu\nu\lambda\sigma} q_\lambda p_\sigma/4\pi M_N \quad , \end{aligned} \tag{24}$$

where s_μ is a covariant spin four-vector associated with the nucleon target and possessing the properties

$$s\cdot p = 0 \quad , \qquad s\cdot s = +1 \quad . \tag{25}$$

In terms of the structure functions defined in Eq. (24), the measured difference between double differential cross sections with lepton and nucleon spins antiparallel and parallel is[14]

$$\frac{d^2\sigma^{\uparrow\downarrow}}{d\Omega' dE'} - \frac{d^2\sigma^{\uparrow\uparrow}}{d\Omega' dE'} = \frac{4\alpha^2 E'}{q^2 E}\left\{(E + E'\cos\theta)\, d(\nu, q^2) + (E - E'\cos\theta)(E+E')\, M_N g(\nu, q^2)\right\}/(4\pi M_N) \tag{26}$$

The catalogue is completed by giving the relationship of the structure functions to the previously defined total cross sections:

$$\frac{1}{4\pi M_N}\left[\nu\, d(\nu, q^2) + M_N(\nu^2 + q^2)\, g(\nu, q^2)\right] = \frac{K}{4\pi^2\alpha}\frac{\sigma_{1/2} - \sigma_{3/2}}{2} = \frac{K}{4\pi^2\alpha} A\sigma_T \quad , \tag{27a}$$

and

$$\frac{\sqrt{q^2}}{4\pi M_N}\, d(\nu, q^2) = \frac{K}{4\pi^2\alpha}\, \sigma_{TL} \quad . \tag{27b}$$

These allow one, for example, to go directly from Eq. (20) to (26).

The particular choice of structure functions given in Eq. (24) is of course not a unique one. In fact, each paper on this subject seems to define a new set, which can

only be linear combinations of the ones given here. As will be seen in the next section, $d(\nu, q^2)$ and $g(\nu, q^2)$ are slightly more convenient when one wishes to use the inequalities for total cross sections, Eqs. (18) and (19), to bound the integrands in certain sum rules.

IV. Scaling and Sum Rules

By now everyone is familiar with the scaling behavior[20] of the spin averaged structure functions: that as ν and q^2 become infinite, $W_1(\nu, q^2)$ and $\nu W_2(\nu, q^2)$ become nontrivial functions of $\omega = 2M_N\nu/q^2$. It comes as no surprise that a similar behavior is expected on the same basis for the spin-dependent structure functions. one expects[21,22] $\nu d(\nu, q^2)$ and $\nu^2 g(\nu, q^2)$ to scale. Neglecting q^2/ν^2 as ν and $q^2 \to \infty$ with ω fixed, $\nu d + M_N \nu^2 g \propto A(\nu, q^2) W_1$ from Eq. (27a), and we see that $A(\nu, q^2)$ should also scale.

What magnitude and sign might we expect for these new structure functions in the scaling domain? For purposes of a very rough orientation and guide to our intuition, let us consider the most naive parton model – something which can not possibly be completely correct and which I will consequently call "dumb" quarks. Namely, let the nucleon consist of three point quarks: the proton is ppn and the neutron is nnp, i.e., just the three "valence" quarks with no $q\bar{q}$ sea, gluons, etc. Then in the unpolarized case, the usual parton manipulations yield that νW_2 and W_1 scale with $\nu W_2 = (2M_N/\omega) W_1$ and $W_{1n}/W_{1p} = 2/3$. The same calculations show, as expected, that νd and $\nu^2 g$ scale with

$$\nu^2 g = 0 \quad , \tag{28}$$

for either the neutron or proton, and

$$\frac{\nu d + M_N \nu^2 g}{4\pi M_N} = \frac{5}{9} W_1 \quad \text{or} \quad A(\omega) = \frac{5}{9} \tag{29a}$$

for the proton and

$$\frac{\nu d + M_N \nu^2 g}{4\pi M_N} = 0 \quad \text{or} \quad A(\omega) = 0 \tag{29b}$$

for the neutron. Equation (28) is seen to follow in the detailed computation from the (assumed) Dirac point particle nature of the partons.

The positive, or at least nonnegative, values of A found in Eqs. (29) are to be expected on naive grounds. For A in a parton model is just a measure of the extent to which the parton and nucleon spins are aligned, weighted by the parton charges squared. Therefore, since we don't expect the parton spins on the average to tend to line up opposite to the nucleon's spin, we expect $A \geq 0$.

In general, the use of a polarized target and beam could be thought of as weighting the individual parton contributions to the scattering by an additional factor: their spin alignment.[23] For example, in the naive three quark model the p quark in the proton is weighted more heavily in $\sigma_{1/2}$ and less heavily in $\sigma_{3/2}$ than in the spin averaged cross section $\sigma_T = \frac{1}{2}(\sigma_{1/2} + \sigma_{3/2})$. If there is a connection of the parton charges to the excess[24] of positive hadrons projected forward in the hadronic final state at large q^2, then the excess should be different in $\sigma_{1/2}$ and $\sigma_{3/2}$.

Now let us turn from "dumb" quarks to what might be called "sophisticated" quarks. By this I mean the algebra of currents at equal time, and more generally the quark light cone algebra.[25] Here one abstracts certain algebraic properties from the free quark model; properties which might be exactly true in Nature. But one discards the quarks themselves. These algebraic relations can often be converted into sum rules. For example, the equal time commutator of two space components of the vector current as abstracted from the quark model,

$$\left[J_i^\alpha(\vec{x}, t),\ J_j^\beta(\vec{y}, t)\right] = -i\epsilon_{ijk}\, d^{\alpha\beta\gamma}\, J_{5k}^\gamma(\vec{x}, t)\, \delta^{(3)}(\vec{x} - \vec{y}) + \text{terms symmetric in i, j} \tag{30}$$

leads to the sum rule[26]

$$\lim_{q^2 \to -\infty} q^2 \int_0^\infty \frac{d\nu}{\nu} \left(\frac{\nu d + M_N \nu^2 g}{4\pi M_N} \right) = Z \quad . \tag{31}$$

Rewriting this in the scaling limit gives[27]

$$\int_1^\infty \frac{d\omega}{\omega} A(\omega) \left(\frac{2M}{\omega} W_1(\omega) \right) = Z \quad . \tag{32}$$

The quantity Z on the right-hand side of Eqs. (31) and (32) arises from the one nucleon matrix elements of the axial-vector current, J^γ_{5k}, on the right-hand side of Eq. (30). With the indices α and β chosen to correspond to the electromagnetic current, the index γ takes the values 3, 8, or 0, so that one has for protons and neutrons

$$\begin{aligned} Z_p &= Z^{(3)} + Z^{(8)} + Z^{(0)} \\ \text{and} \qquad & \qquad (33) \\ Z_n &= -Z^{(3)} + Z^{(8)} + Z^{(0)} \quad . \end{aligned}$$

$Z^{(3)} = g_A/6$ is directly measurable in weak interactions. Thus by taking the difference between Eq. (32) for protons and for neutrons, one obtains a sum rule with the known quantity $Z_p - Z_n = g_A/3$ on the right-hand side. $Z^{(8)}$, arising from the same octet of currents as $Z^{(3)}$ is calculable if we know the F/D ratio of the axial-vector currents. If $(F/D)_{axial} = 2/3$, then $Z^{(8)}/Z^{(3)} = 1/5$.

It is instructive to examine the sum rule, Eq. (32), in the naive quark parton model discussed previously. There $A = 5/9$ and $\int_1^\infty \frac{d\omega}{\omega} (2M_N/\omega) W_1(\omega) = 1$ for the proton, while in the same naive quark model $Z^{(3)} = 5/18$ (since $g_A = 5/3$), $Z^{(8)} = 1/18$, and $Z^{(0)} = 4/18$. Therefore $Z_p = (5 + 1 + 4)/18 = 5/9$ and the left- and right-hand sides of Eq. (32) are both 5/9 for the proton. Similarly, since $A = 0$ and $Z_n = (-5 + 1 + 4)/18 = 0$, both sides are zero for the neutron. Therefore we might regard Eq. (32) as being the correct "sophisticated" quark version of the "dumb" quark results in Eqs. (29).

Independent of any particular model recall that we expect $A \geq 0$. If this is to be correct for both proton and neutron,[28] $Z^{(8)} + Z^{(0)} > |Z^{(3)}|$. As a result $Z_p \geq 2Z^{(3)} = g_A/3 \simeq 0.41$, which, as we will see in a moment, demands large asymmetries over a considerable ω range for the proton.

A second sum rule for the spin dependent structure functions,[29]

$$\int_0^\infty d\nu \; g(\nu, q^2) = 0 \quad , \tag{34}$$

or[27,30]

$$\int_1^\infty d\omega \; \nu^2 g(\omega) = 0 \tag{35}$$

in the scaling limit, can be derived as a superconvergence relation or from the quark light cone algebra. Regge arguments indicate[29] that both Eqs. (31) and (34), where the amplitudes involved receive no contribution[31] from a Pomeranchuk pole, should converge on the basis of known Regge pole intercepts. In particular, one expects $A(\omega) \to 0$ as $\omega \to \infty$.

Can anything rigorous be said about the validity of these sum rules in the absence of actual data from polarized beam experiments? An examination of the left-hand side of Eq. (32) shows that if we replace $A(\omega)$ by its upper bound (of 1), then we have

$$Z \leq \int_1^\infty \frac{d\omega}{\omega} \left(\frac{2M_N}{\omega} W_1(\omega) \right) \quad . \tag{36}$$

However, $(2M_N/\omega) W_1(\omega) \to$ constant as $\omega \to \infty$ if the usual assumption of dominance of the high ω behavior by the Pomeranchuk singularity is made. The right-hand side of Eq. (36) is then logarithmically divergent, and we have no rigorous bound which is useful in this case.

We can use bounds on $A(\omega)$ and presently existing data though to answer a lesser question. For example, suppose $A_p \leq 0.5$ (remember that $A = 0.5$ is a large asymmetry — it is equivalent to $\sigma_{1/2}/\sigma_{3/2} = 3$). How far in ω do we have to carry the integration in Eq. (32) to get $Z = 5/9$, as in the naive parton model discussed above? Present data on $W_1(\omega)$ shows that the upper limit of integration must be $\gtrsim 50$. Even for $Z_p \geq g_A/3$, which we expect from the argument that A_p and A_n should be non-negative, the upper limit of integration must be $\gtrsim 25$. Thus if Z_p obeys our expectations, present data on deep inelastic scattering and the sum rule in Eq. (32) indicate that we must have large asymmetries over a very considerable range of ω values.[32] Put another way, if the sum rule in Eq. (32) is correct, it converges slowly and receives important contributions from the large ω region. In this regard it is similar to the Adler sum rule,[33] and the parton model sum rule[34]

$$\int_1^\infty \frac{d\omega}{\omega}\left[\nu W_{2p}(\omega) - \nu W_{2n}(\omega)\right] = 1/3 \quad . \tag{37}$$

One might ask in this regard if the coefficient of J^γ_{5k} in the commutation relation, Eq. (30), and consequently the Z on the right-hand side of Eq. (32), could be reduced by a factor K from the quark model value, making the sum rule easier to satisfy without large asymmetries. Here we are constrained by the Crewther relation[35]

$$3S = KR' \quad , \tag{38}$$

where K is defined as above ($K=1$ in the quark model), S is the coefficient of the Adler anomaly,[36] and R' is the ratio $\sigma(e^+e^- \to \gamma^{(3)} \to \text{hadrons})/\sigma(e^+e^- \to \mu^+\mu^-)$. Since $S = 1/6$ and $R' = 1/2$ for ordinary quarks, and $S = 1/2$ and $R' = 3/2$ for colored quarks, we see that the relation is satisfied in both these cases. Note that if S is fixed (say by PCAC and $\Gamma(\pi^0 \to \gamma\gamma)$) then large values of R' force K to be small and vice versa. One therefore has an interesting relation between the results of e^+e^- colliding beam experiments and those involving polarized lepton beams.

Finally, we note that if we subtract the second sum rule, Eq. (34), from the first, Eq. (31), and use Eqs. (19) and (27), we have

$$|Z| = \left| \lim_{q^2\to\infty} q^2 \int_0^\infty \frac{d\nu}{\nu} \frac{\nu d}{4\pi M_N} \right| \leq \lim_{q^2\to\infty} \int_0^\infty \frac{d\nu}{\nu} \sqrt{q^2 R}\, W_1$$

$$\leq \lim_{q^2\to\infty} \int_0^\infty \frac{d\omega}{\omega}\left[\frac{2M_N}{\omega} W_1(\omega)\right] \sqrt{\nu^2 R/q^2} \quad . \tag{39}$$

Therefore, if $Z \neq 0$, R must not vanish faster than $q^2/\nu^2 = \frac{2M}{\omega}\frac{1}{\nu}$ at fixed ω as $\nu, q^2 \to \infty$. Of course exactly the behavior[37] $R = (q^2/\nu^2)\, f(\omega)$ is what is expected from the quark light cone algebra from which both sum rules were derived, so that everything is consistent in this regard.

V. Duality and the Polarization Asymmetry in Deep Inelastic Scattering

By now it is rather well accepted that there is a substantial nondiffractive component of the structure functions, at least for $1 \leq \omega \leq 10$, and that the distinguishable s-channel nucleon resonances exhibit a behavior which is closely connected[38] with that of νW_2 near $\omega = 1$. Inasmuch as there is no Pomeranchuk pole contribution to the spin dependent structure functions, one might look here also for a connection of deep inelastic behavior with that of s-channel resonances. To examine this question further, it is useful to construct a sum of resonances, in the spirit of the Veneziano model, which duplicates parton model results, and in particular the results of the naive three quark model for the structure functions which we discussed earlier.

For this purpose, we consider the states generated by three quarks with harmonic potentials between them. We let the electromagnetic current interact with only one quark at a time, considering only interactions with the quark magnetic moments. This immediately leads to $R = \sigma_L/\sigma_T = 0$.

The ground and excited states of such a set of three quarks are classifiable in terms of SU(6) representations, with the nucleon itself being in the ground state, the

totally symmetric 56 representation. Since only one quark at a time is to be excited, only resonances in the totally symmetric 56 and mixed symmetry 70 representations can be produced. A little calculation[39] shows that summing over all possible excitations of resonances lying in a 56 at some given ν and q^2:

$$W_{1n}/W_{1p} = 12/17, \quad A_p = 5/17, \quad A_n = 0, \tag{40}$$

while for excitation of a 70,

$$W_{1n}/W_{1p} = 3/5, \quad A_p = 1, \quad A_n = 0. \tag{41}$$

In particular there exists a combination of 56 and 70 s-channel nucleon resonances excited in photon-nucleon collisions which yield

$$W_{1n}/W_{1p} = 2/3, \quad A_p = 5/9, \quad A_n = 0, \tag{42}$$

exactly the naive three quark parton model results. Therefore it is possible to construct[39] a sum of s-channel resonances which for some, or for that matter all, ν and q^2 duplicates the naive parton results. Varying the weights of different 56's and 70's with ν and q^2 then yields an infinity of models of the nondiffractive part of the structure functions in terms of an infinite sum of s-channel nucleon resonances.

Does this s-channel model make sense when compared to the behavior of the known individual resonances which have been classified in 56's or 70's of SU(6)? In particular, we have the well known $P_{33}(1236)$ in a 56 (with the nucleon), the $D_{13}(1520)$ in a 70, and the $F_{15}(1688)$ in another 56.

Now in photoproduction (on a proton target) all these resonances have $\sigma_{3/2}(\text{resonance}) \geq \sigma_{1/2}(\text{resonance})$, i.e., $A_p(\text{resonance}) < 0$. Quark models[40] with harmonic forces[41] provide a neat explanation of this for the D_{13} and F_{15}. Both magnetic and convection current terms enter $\sigma_{1/2}$, where they cancel, while $\sigma_{3/2}$ comes from the convection current alone. Thus $\sigma_{3/2} >> \sigma_{1/2}$ or $A \simeq -1$ for these two resonances. However, the same quark models also make a prediction. As $q^2 \to \infty$, the magnetic term dominates, just as we assumed in the model discussed above, and there is no longer any cancellation in $\sigma_{1/2}$ for these resonances. In fact $\sigma_{1/2} >> \sigma_{3/2}$ or $A \simeq +1$ is predicted for these resonances as $q^2 \to \infty$. Detailed calculations[39] show that this change from A(resonance) $\simeq -1$ to A(resonance) $\simeq +1$ should occur rapidly as q^2 goes from zero to a few tenths of a GeV^2. These resonances would then have the same sign (positive) of A at large q^2 as is expected for deep inelastic scattering.

Experimentally there are no results from using polarized beams and targets, but the relevant information on the D_{13} and F_{15} is obtainable from observation of the angular distribution of their πN decays.[40] Up to $q^2 \simeq 0.6$ GeV^2, where large effects are expected, no appropriate change is observed in the $\pi^0 p$ angular distributions.[42] It appears that the quark model with harmonic forces predicts the wrong result, as the D_{13} and F_{15} still seem to have the opposite sign of A at $q^2 \simeq 0.6$ GeV^2 from that expected in deep inelastic scattering and in the quark models of resonance excitation.

What then happens to duality for the spin dependent structure functions near $\omega = 1$? To discuss this one must first say what behavior the deep inelastic scattering will have. On the basis of the sum rules we have discussed here and the ratio $\nu W_{2n}/\nu W_{2p}$ observed near $\omega = 1$, I expect[39] that both A_p and A_n will be $\simeq +1$ at $\omega = 1$ with A_n dropping rapidly to zero with increasing ω, but A_p staying large and going to zero only at very large values of ω. There are then two possibilities for the resonances: (1) all resonances eventually have $A_p > 0$ for large q^2 and one has a kind of "local duality" as in the case of νW_2, with each resonance mimicking the deep inelastic behavior; or (2) only the nucleon (with $A = +1$), of the "prominent" resonances, has $A > 0$. A "global duality" situation holds, as in πN charge exchange at $t = 0$, and the average over many contributions of different sign must be taken to give the deep inelastic behavior.[43] Experimentally, a few sweeps through the region of prominent nucleon resonances with a polarized beam and target should answer this. Perhaps next year at this time we will know the answer to whether possibility (1) or (2) is realized in Nature.

VI. Summary

We have now seen some of the many and varied theoretical or phenomenological questions which are susceptible to experimental answer with a polarized lepton beam and target. Among the possibilities we have examined are that:

(1) A detailed, and in principle complete, amplitude analysis of virtual photon induced processes can be carried out;

(2) The scaling behavior of two new spin-dependent structure functions can be tested;

(3) The size of the asymmetry, A, which indicates in parton models the alignment of the charged constituent and nucleon spins can be measured. The various constituents are weighted in their contribution to the deep inelastic scattering in a different way from the spin averaged case;

(4) Rigorous sum rules exist which have right- and left-hand sides that both can be directly measured, providing a test of the quark light cone algebra;

(5) The asymmetries of individual resonances can be measured, providing a very restrictive check of quark models of resonance and their electromagnetic excitation, as well as of the validity and form duality takes in spin-dependent scattering near $\omega = 1$;

(6) The large ν or ω behavior of the structure functions is measurable, yielding additional information on Regge singularities which are essentially inaccessible in other processes, and in particular the position of the leading singularity of odd signature and even parity.

An interesting period of the beginning of experimental answers to these and other questions lies immediately ahead.

References

1. V. W. Hughes et al., Yale-SLAC proposal E-80 (1971).
2. C. Y. Prescott et al., SLAC Group A proposal E-95 (1972).
3. We use a metric where $p \cdot p = \vec{p}^2 - p_0^2$, so that $q^2 > 0$ for space-like four-vectors q_μ. The fine structure constant $\alpha = e^2/4\pi \simeq 1/137$.
4. See, for example, the review of the kinematics contained in F. J. Gilman, Physics Reports 4C, 98 (1972).
5. We may subtract multiples of q_μ since the virtual photon is coupled to a conserved electromagnetic current of the hadrons. A similar manipulation of the lepton trace and discussion of the photon polarization is presented by J. Kuti, MIT Center for Theoretical Physics publication No. 234 (1971) (unpublished).
6. See, for example, the talk of K. Berkelman in Proceedings of the XVI International Conference on High Energy Physics, edited by J. D. Jackson and A. Roberts (National Accelerator Laboratory, Batavia, Illinois, 1973), Vol. 4, p. 41 and references therein.
7. I thank Dr. R. Heimann for calling this to my attention. This term does not vanish if the helicities of all other particles are not summed over (e.g., with a polarized target).
8. T. P. Cheng and A. Zee, Phys. Rev. D 6, 885 (1972).
9. K. Schilling and G. Wolf, DESY preprint DESY 73/13 (1973) (unpublished).
10. The case of both a polarized beam and target has been considered by H. Fraas, University of Wurzburg preprint (1973) (unpublished).
11. We need only consider $\mu, \nu = 1, 2, 3$ since we have previously put $L_{\mu\nu}$ in a form where $L_{\mu 4} = L_{4\nu} = 0$.
12. While $\sigma_{1/2}$, $\sigma_{3/2}$, σ_L, and σ_T are all sums of squares of amplitudes, and hence nonnegative, σ_{TL} involves an interference between transverse and longitudinal amplitudes and has no positivity properties.

13. In this particular case, having assumed C, P, and T invariance, these inequalities follow simply from the positivity of $\sigma_{1/2}$ and $\sigma_{3/2}$ and the Schwartz inequality. The general case, which requires more powerful techniques, is discussed by M. G. Doncel and E. deRafael, Nuovo Cimento 4A, 363 (1971).

14. We use the notation $d^2\sigma^{\uparrow\downarrow}/d\Omega' dE'$ ($d^2\sigma^{\uparrow\uparrow}/d\Omega' dE'$) to denote the double differential cross section for scattering a helicity + 1/2 lepton on a nucleon target with spin direction antiparallel (parallel) to the beam. In all our equations we neglect the lepton mass.

15. Since σ_{TL} involves an interference between the transverse and longitudinal amplitudes, σ_{TL}/σ_T may not be small even though σ_L/σ_T is.

16. We denote by $d^2\sigma^{\uparrow\rightarrow}/d\Omega' dE'$ ($d^2\sigma^{\uparrow\leftarrow}/d\Omega' dE'$) the cross section for helicity + 1/2 leptons scattering on a nucleon target with spin direction perpendicular to the beam and toward (away from) the direction of the final lepton.

17. This was emphasized by C. E. Carlson and W. K. Tung, Phys. Rev. D 5, 721 (1972) and also in Ref. 18.

18. A. J. G. Hey and J. E. Mandula, Phys. Rev. D 5, 2610 (1972).

19. We use the structure functions defined by J. Kuti and V. F. Weisskopf, Phys. Rev. D 4, 3418 (1971).

20. J. D. Bjorken, Phys. Rev. 179, 1547 (1969).

21. L. Galfi et al., Phys. Letters 31B, 465 (1970);
C. E. Carlson and W. K. Tung, Ref. 17;
A. J. G. Hey and J. E. Mandula, Ref. 18;
C. Nash, Nucl. Phys. B31, 419 (1971);
M. Gourdin, Nucl. Phys. B38, 418 (1972).

22. The general scaling behavior of structure functions is treated by T. P. Cheng and A. Zee, Phys. Rev. D 6, 3182 (1972).

23. More detailed results of parton models can be found in J. Kuti and V. F. Weisskopf, Ref. 19; M. Gourdin, Ref. 21; and T. F. Walsh and P. Zerwas, DESY preprint DESY 72/36 (1972) (unpublished).

24. J. T. Dakin et al., Phys. Rev. Letters 29, 746 (1972) and J. T. Dakin et al., SLAC preprint SLAC-PUB-1269 (1973) (unpublished).

25. H. Fritzsch and M. Gell-Mann, in Scale Invariance and the Light Cone (Gordon and Breach, New York, 1971), Vol. 2, p. 1.

26. J. D. Bjorken, Phys. Rev. 148, 1467 (1966).

27. This sum rule has also been discussed in the scaling regime by C. E. Carlson and W. K. Tung, Ref. 17; A. J. G. Hey and J. E. Mandula, Ref. 18; C. Nash, Ref. 21; D. A. Dicus, R. Jackiw, and V. L. Teplitz, Phys. Rev. D 4, 1733 (1971). D. Wray, Nuovo Cimento 9A, 463 (1972) and B. Ward, Princeton preprint (1973) (unpublished) have also analyzed the sum rules for neutrinos.

28. J. Ellis and R. Jaffe (unpublished) have noted that the assumption that in a parton model of the nucleon the presence of λ and $\bar{\lambda}$ quarks is to be associated with the Pomeron, together with the absence of a Pomeron contribution to the spin dependent structure functions, allows one to relate $Z^{(0)}$ and $Z^{(8)}$. With an F/D value of 2/3 this implies $Z^{(3)} = Z^{(8)} + Z^{(0)}$, so that $Z_p = 2Z^{(3)}$ and $Z_n = 0$.

29. H. Burkhardt and W. N. Cottingham, Ann. Phys. (N.Y.) 56, 453 (1971).

30. The sensitivity of this sum rule to model dependent assumptions in the light cone approach has been emphasized by T. P. Cheng and A. Zee, Ref. 22.

31. A detailed Regge analysis of the spin dependent structure functions is presented in Refs. 5 and 29. The leading contributions correspond to an odd signature, positive parity (pole?) in one amplitude and an even signature, positive parity cut in the other.

32. Large asymmetries were previously argued on the basis of the sum rule in J. D. Bjorken, Phys. Rev. D 1, 1376 (1970).

33. For recent discussions of the saturation of the Adler sum rule see E. A. Paschos in Proceedings of the XVI International Conference on High Energy Physics, edited by J. D. Jackson and A. Roberts (National Accelerator Laboratory, Batavia, 1973), Vol. 2, p. 166; and S. F. Tuan, Phys. Rev. D 7, 2092 (1973) and references therein.

34. For a recent discussion of the saturation of Eq. (37), see E. D. Bloom, invited talk at the International Conference on New Results from Experiments on High Energy Particle Collisions, Vanderbilt University, Nashville, March 26-28, 1973 and Caltech preprint CALT-68-392 (1973) (unpublished).

35. R. Crewther, Phys. Rev. Letters 28, 1421 (1972).

36. S. Adler, Phys. Rev. 177, 2426 (1969).

37. This is spelled out explicitly in J. E. Mandula, Phys. Rev. D 8, 328 (1973).

38. See F. J. Gilman, Ref. 4, for a review of duality in electroproduction and further references.

39. F. E. Close, F. J. Gilman, and I. Karliner, Phys. Rev. D 6, 2533 (1972).

40. Photoproduction or electroproduction of the $P_{33}(1236)$ is predicted to be pure magnetic dipole in character by such quark models, which is equivalent to $\sigma_{3/2} = 3\sigma_{1/2}$ for this resonance. This agrees with the experimental data (see Ref. 42).

41. L. A. Copley, G. Karl and E. Obryk, Phys. Letters 29B, 117 (1969) and Nucl. Phys. B13, 303 (1969); D. Faiman and A. W. Hendry, Phys. Rev. 173, 1720 (1968); 180, 1572 (1969); R. P. Feynman, M. Kislinger, and F. Ravndal, Phys. Rev. D 3, 2706 (1971).

42. See F. E. Close and F. J. Gilman, Phys. Letters 38B, 541 (1972) and references to experiments therein. Very recent data at $q^2 = 0.45$ GeV^2 on $\pi^+ n$ electroproduction at forward angles, as presented by R. Meaburn et al., Daresbury Nuclear Physics Laboratory report DNPL/P163 (1973) (unpublished),

FIXED POLES IN PHOTOPRODUCTION AND ELECTROPRODUCTION*

Frederick J. Gilman

I. Introduction

The subject of fixed poles in the complex J-plane has received considerable attention in the past few years in theoretical discussions of the properties of the Compton amplitude for either real or virtual photons. In this lecture, I would like to review the subject of fixed poles, particularly in regards to their presence in two current amplitudes.

We shall begin with a short history of our knowledge of the presence of fixed poles in purely hadronic, one current, and two current amplitudes. The magnitude of fixed pole residues can be established through certain sum rules, which we derive in the case of a fixed pole at J = 0. For the forward Compton amplitude, these sum rules can be evaluated if certain additional phenomenological assumptions are made. We spell out these assumptions, indicating possible weak points, and describe the present state of these analyses concerning the magnitude of the residue of a possible J = 0 fixed pole.

With the assumption of polynomial residues, the J = 0 fixed pole in the Compton scattering amplitude for real photons is related to that in the amplitude for virtual photons. In particular, the fixed pole at J = 0 expected from the leading light cone singularity and from some parton model calculations is then tied to the fixed pole found at $q^2 = 0$. This and the phenomenological analysis of the real Compton amplitude leads to an interesting situation concerning the Regge behavior of deep inelastic scattering — a situation which is not yet resolved experimentally.

In the last year, both the general technique used in constructing meaningful sum rules for evaluation of fixed pole residues as well as many specific connections between different quantities which are all related to fixed pole residues, have been the subject of much research. The clarifications and connections between what appear to be unrelated subjects that results from this recent work are discussed in the final section.

*Work supported by the U. S. Atomic Energy Commission

33. For recent discussions of the saturation of the Adler sum rule see E. A. Paschos in Proceedings of the XVI International Conference on High Energy Physics, edited by J. D. Jackson and A. Roberts (National Accelerator Laboratory, Batavia, 1973), Vol. 2, p. 166; and S. F. Tuan, Phys. Rev. D 7, 2092 (1973) and references therein.

34. For a recent discussion of the saturation of Eq. (37), see E. D. Bloom, invited talk at the International Conference on New Results from Experiments on High Energy Particle Collisions, Vanderbilt University, Nashville, March 26-28, 1973 and Caltech preprint CALT-68-392 (1973) (unpublished).

35. R. Crewther, Phys. Rev. Letters 28, 1421 (1972).

36. S. Adler, Phys. Rev. 177, 2426 (1969).

37. This is spelled out explicitly in J. E. Mandula, Phys. Rev. D 8, 328 (1973).

38. See F. J. Gilman, Ref. 4, for a review of duality in electroproduction and further references.

39. F. E. Close, F. J. Gilman, and I. Karliner, Phys. Rev. D 6, 2533 (1972).

40. Photoproduction or electroproduction of the $P_{33}(1236)$ is predicted to be pure magnetic dipole in character by such quark models, which is equivalent to $\sigma_{3/2} = 3\sigma_{1/2}$ for this resonance. This agrees with the experimental data (see Ref. 42).

41. L. A. Copley, G. Karl and E. Obryk, Phys. Letters 29B, 117 (1969) and Nucl. Phys. B13, 303 (1969); D. Faiman and A. W. Hendry, Phys. Rev. 173, 1720 (1968); 180, 1572 (1969); R. P. Feynman, M. Kislinger, and F. Ravndal, Phys. Rev. D 3, 2706 (1971).

42. See F. E. Close and F. J. Gilman, Phys. Letters 38B, 541 (1972) and references to experiments therein. Very recent data at $q^2 = 0.45$ GeV^2 on $\pi^+ n$ electroproduction at forward angles, as presented by R. Meaburn et al., Daresbury Nuclear Physics Laboratory report DNPL/P163 (1973) (unpublished),

FIXED POLES IN PHOTOPRODUCTION AND ELECTROPRODUCTION*

Frederick J. Gilman

I. Introduction

The subject of fixed poles in the complex J-plane has received considerable attention in the past few years in theoretical discussions of the properties of the Compton amplitude for either real or virtual photons. In this lecture, I would like to review the subject of fixed poles, particularly in regards to their presence in two current amplitudes.

We shall begin with a short history of our knowledge of the presence of fixed poles in purely hadronic, one current, and two current amplitudes. The magnitude of fixed pole residues can be established through certain sum rules, which we derive in the case of a fixed pole at J = 0. For the forward Compton amplitude, these sum rules can be evaluated if certain additional phenomenological assumptions are made. We spell out these assumptions, indicating possible weak points, and describe the present state of these analyses concerning the magnitude of the residue of a possible J = 0 fixed pole.

With the assumption of polynomial residues, the J = 0 fixed pole in the Compton scattering amplitude for real photons is related to that in the amplitude for virtual photons. In particular, the fixed pole at J = 0 expected from the leading light cone singularity and from some parton model calculations is then tied to the fixed pole found at $q^2 = 0$. This and the phenomenological analysis of the real Compton amplitude leads to an interesting situation concerning the Regge behavior of deep inelastic scattering — a situation which is not yet resolved experimentally.

In the last year, both the general technique used in constructing meaningful sum rules for evaluation of fixed pole residues as well as many specific connections between different quantities which are all related to fixed pole residues, have been the subject of much research. The clarifications and connections between what appear to be unrelated subjects that results from this recent work are discussed in the final section.

*Work supported by the U. S. Atomic Energy Commission

II. A Brief History

We shall use the term fixed pole rather loosely in this lecture. While at certain times we should technically refer to the presence of Kronecker deltas in particular amplitudes, we shall consistently refer to complex J-plane singularities whose position is independent of t as fixed poles.

For purely hadronic amplitudes the presence of fixed poles at right signature points is generally not possible because the partial wave unitarity equation in the t-channel, extended to complex values of ℓ, is quadratic. The mismatch in powers of $1/(\ell - \alpha(t))$ if $\alpha(t)$ is fixed for all t between the two sides provides a contradiction which rules out fixed poles.[1] Although there are loopholes in this argument when sufficient spins enter the situation,[2] amplitudes containing fixed poles are either so contrived or the poles are relegated to such low values of J that they are not likely of physical importance.[3] Needless to say, compelling evidence of fixed poles in purely hadronic amplitudes at *right signature points has not been established.*[4]

For single current amplitudes, the situation is quite different in principle. Since the t-channel partial wave unitarity relation is now linear, rather than quadratic, there is no longer the same theoretical argument as before to rule out fixed poles on a fundamental basis.[5,6] On the other hand, as in the purely hadronic case, there is no *experimental evidence at this time which would definitely indicate their presence.* At various times in the past, the approximate $1/s^2$ behavior of $d\sigma/dt$ for certain photoproduction processes was advanced as an argument for fixed poles. In particular, this was the case for $\gamma p \to \pi^+ n$ and $\gamma n \to \pi^- p$. However, recent data[7] with linearly polarized photon beams clearly show a different energy dependence for the natural and unnatural parity exchange parts of $\gamma n \to \pi^- p$. Most interestingly, the "effective Regge trajectory" extracted for the unnatural parity exchange component of $d\sigma/dt$ is not independent of t, and is quite consistent with $\alpha(t) = (t - m_\pi^2)/\mathrm{GeV}^2$, i. e., a pion trajectory with a canonical slope.[8] Backward photoproduction processes, where baryon exchange dominates, have an energy dependence which rules out the presence of a possible fixed pole with the quantum numbers of the nucleon.[9]

For two current amplitudes, however, not only do we have no theoretical basis on which to exclude the presence of fixed poles, but we have good grounds on which to establish their existence. In fact, the standard sum rule which follows from local current algebra,[10]

$$\int_0^\infty d\nu \, \mathrm{Im} A^{(-)}(\nu, t, q_1^2, q_2^2) = F(t) \qquad (1)$$

is directly translatable[11] into a statement that the form factor F (t) is the residue of a J = 1, right signature fixed pole in the crossing odd amplitude, $A^{(-)}(\nu, t, q_1^2, q_2^2)$.

Soon after the realization that local current algebra demands the presence of fixed poles in certain two current amplitudes, an analysis[12] of the ordinary nucleon Compton amplitude revealed that the only way a Pomeranchuk pole could contribute to the forward amplitude, and hence to the total cross section, was either through the presence of a fixed pole at J = 1 or, what is essentially a reshuffling of the same phenomenon, through a singular residue function. In contrast to all our previous and future discussion, in this case the fixed pole is at a wrong signature point.

For several years the subject of fixed poles was relatively dormant. Then, an analysis[13] of the forward Compton amplitude employing finite energy sum rules indicated that there might be a term in the high energy behavior which would correspond to a right signature fixed pole at J = 0. This observation marks the beginning of research on the central topic of this lecture, to which we now turn.

III. Fixed Poles in Compton Scattering of Real Photons

To derive the sum rule[14] for the residue of a fixed pole at J = 0, let us consider an amplitude for some elastic scattering process, f (ν, t), which is even under crossing ($\nu \to -\nu$). Suppose at large laboratory energies, ν, that

$$f(\nu, t) \xrightarrow[\nu \to \infty]{} \sum_{\alpha_i > 0} \left(\frac{-1 - e^{-i\pi\alpha_i(t)}}{\sin \pi \alpha_i(t)} \right) \frac{c_i(t)}{4\pi} \nu^{\alpha_i(t)} + C(t) + (\text{terms which} \to 0 \text{ as } \nu \to \infty) . \quad (2)$$

C(t) is a purely real term corresponding to the residue of a fixed pole at J = 0. The discrete sum in Eq. (2) over Regge pole contributions can be generalized without difficulty to include integrals over $\alpha(t)$ which correspond to non-pole singularities, i.e., Regge cuts. Let us define the leading part of the high energy behavior as

$$f^R(\nu,t) \equiv \sum_{\alpha_i>0} \left(\frac{-1-e^{-i\pi\alpha_i(t)}}{\sin\pi\alpha_i(t)}\right) \frac{c_i(t)}{4\pi} \nu^{\alpha_i(t)} + C(t) . \qquad (3)$$

Both $f(\nu,t)$ and $f^R(\nu,t)$ should satisfy once subtracted dispersion relations. We choose the subtraction point at $\nu = 0$, so that[15]

$$f(\nu,t) = f(0,t) + \frac{\nu^2}{\pi} \int_0^\infty \frac{d\nu'^2}{\nu'^2(\nu'^2-\nu^2-i\epsilon)} \frac{\mathrm{Im}f(\nu',t)}{\nu'^2} , \qquad (4)$$

and

$$f^R(\nu,t) = C(t) + \frac{\nu^2}{\pi} \int_0^\infty \frac{d\nu'^2}{\nu'^2(\nu'^2-\nu^2-i\epsilon)} \frac{\mathrm{Im}f^R(\nu',t)}{\nu'^2} . \qquad (5)$$

Eq. (5) can be verified by explicitly substituting $\mathrm{Im}f^R(\nu,t)$ from Eq. (3) and performing the integration analytically.

Now we form the difference $f(\nu,t) - f^R(\nu,t)$ and let $\nu \to \infty$. By definition of $f^R(\nu,t)$, this difference vanishes as $\nu \to \infty$. Taking the corresponding difference of the dispersion representations, Eqs. (4) and (5), we find

$$\lim_{\nu\to\infty} [f(\nu,t) - f^R(\nu,t)] = 0 = f(0,t) - C(t) + \frac{1}{\pi} \int_0^\infty \frac{d\nu'^2}{\nu'^2} \mathrm{Im}[f^R(\nu',t) - f(\nu',t)] \qquad (6)$$

or

$$C(t) = f(0,t) - \frac{1}{\pi} \int_0^\infty \frac{d\nu'^2}{\nu'^2} \mathrm{Im}[f(\nu',t) - f^R(\nu',t)] . \qquad (7)$$

By definition of $f^R(\nu',t)$ the integral is convergent. This constitutes the anticipated sum rule for the fixed pole residue, C(t). In order to evaluate the sum rule one needs $f(0,t)$ and the large ν behavior of $\mathrm{Im}f(\nu,t)$, from which $\mathrm{Im}\, f^R(\nu,t)$ can be extracted.

Unfortunately, in many cases we have a lack of theoretical or experimental information either on $f(0,t)$ or on $\mathrm{Im}\, f(\nu,t)$ as $\nu \to \infty$. However, at $t = 0$ $\mathrm{Im}\, f(\nu,0)$ is related to a total cross section by the optical theorem. In the particular case of real Compton scattering on nucleons we also know theoretically the value of $f(0,0)$: it is just the Thomson limit. Denoting the non-flip forward amplitude by $f_1(\nu)$ we have

$$f_1(0) = -\alpha/M_N , \qquad (8)$$

and the optical theorem reads

$$\mathrm{Im}\, f_1(\nu) = \frac{\nu}{4\pi} \sigma_T(\nu) . \qquad (9)$$

We can therefore proceed to carry out a phenomenological analysis of the value of $C(0) = C$, as the sum rule in Eq. (7) becomes

$$C = -\alpha/M_N - \frac{1}{\pi} \int_0^\infty \frac{d\nu'^2}{\nu'^2} \mathrm{Im}[f_1(\nu') - f_1^R(\nu')] \qquad (10a)$$

or

$$C = -\alpha/M_N - \frac{1}{2\pi^2\alpha} \int_0^\infty d\nu' [\sigma_T(\nu') - \sigma_T^R(\nu')] \qquad (10b)$$

Any such phenomenological analysis immediately runs into the difference between things which are possible in principle, and those which are possible in practice. In principle, one can always go to sufficiently large ν with arbitrarily accurate data and determine $f^R(\nu)$. In practice, a finite amount of data at finite energies is not adequate to fix all the possible terms in the general high energy expansion of Eq. (2). Additional assumptions must be made. Usually these additional assumptions are that: (1) $f^R(\nu)$ can be adequately represented by a sum of powers of ν; (2) the leading J-plane singularity corresponds to the Pomeranchuk singularity with $\alpha_P(0) = 1$, and the remaining trajectories with $\alpha_i(0) > 0$ correspond to the ρ, ω, A_2, and f mesons, all with $\alpha_i(0) \simeq \frac{1}{2}$; and (3) data on $\mathrm{Im}\, f(\nu)$ can already be represented by just these leading powers of ν within the energy range of present accelerators.

With these additional assumptions one fits $\sigma_T(\nu)$ at "high" energies to an expression with a form like $c_1 + c_2/\sqrt{\nu}$. This determines $\mathrm{Im}\, f^{(R)}(\nu) \equiv (c_1\nu + c_2\sqrt{\nu})/4\pi$, and the sum rule in Eq. (10) then yields C once $f(0)$ is known.

For the forward proton Compton scattering amplitude the original result[16] of

such an analysis is $C_p \simeq -3\ \mu b - GeV = -\alpha/M_N$, i.e., consistent with the value of the Thomson limit. Later calculations with the same or slightly different assumptions, some based on newer data, confirm this result.[17] Such a value of C is an important component of the real part of $f_1(\nu)$ at moderate energies: for example, at $\nu = 4$ GeV, Re $f_1(\nu) \simeq -14\ \mu b - GeV$.

In the last year a similar analysis has been performed for the neutron.[18] Here one must carry out shadowing and smearing corrections to extract the neutron total photoproduction cross sections from deuterium data, in addition to making the assumptions on high energy data enumerated above. The result, $C_n \simeq 0$, is again consistent with the value of the Thomson limit for the neutron.

Without having to do shadowing or smearing corrections, the data on the photon-deuteron total cross section can be used directly to obtain C_d. The result, $C_d \simeq -3\ \mu b - GeV$ is not consistent with the Thomson limit for the deuteron, $-\alpha/M_D \simeq -\alpha/2M_N = -1.5\ \mu b - GeV$, but rather with the sum of the proton and neutron Thomson limits.

The size of the possible errors in these phenomenological analyses are hard to estimate, as they mostly lie in the assumptions made. Based on the errors in the data for the photon-proton total cross section, including those reflected in fitting its high energy behavior, it would appear that C_p is known to $\pm\ 1\ \mu b - GeV$.

More serious are possible errors in the assumptions. First of all, only total cross section data for $\nu \lesssim 30$ GeV has been used. If, for example, the total cross section rises at high energy, it implies a more complicated singularity structure near J = 1 than assumed above. This is probably not such a serious criticism since by definition of $f^R(\nu)$, in the sum rule, Eq. (7), we subtract off the high energy behavior of $f(\nu)$, whatever it may be. Thus the function $f^R(\nu)$ would correspondingly change if the behavior of the total cross section changed. Eq. (7) for the fixed pole residue is by construction dominated by its low energy part, and that is already known to us.

Second, and more serious, is the possible error induced through neglect of other Regge singularities with $0 \leq \alpha_i(0) \leq \frac{1}{2}$. It is in fact clear that a singularity with $\alpha_i(0)$ near zero can duplicate the behavior of a fixed pole arbitrarily closely. Although no known Regge pole trajectory with the correct quantum numbers is nearby, there is no way one can completely rule out such a singularity (cut?). If it is present, what is being "measured" in C is some unknown combination of a fixed pole residue and J-plane garbage.

Third, note that all the phenomenological work we have been discussing is at t = 0, where the optical theorem permits us to use total cross section data for $\mathrm{Im} f_1(\nu)$. One does not know that $\alpha(t) = 0$ for all t, as required for a true fixed pole. However, while we have no experimental or phenomenological reason, there is a theoretical basis for expecting a fixed pole, as we will see in the next section.

Finally, note that the phenomenological results suggest that both the neutron and proton Compton amplitudes have the values of their Thomson limits for the residues of their respective fixed poles. It has been suggested[13, 19] that this is generally the case: that the fixed pole is a sort of remnant of the Thomson limit amplitude which would exist if the strong interactions were "turned off". While tenable as at least a consistent hypothesis for real Compton scattering, we will see shortly that there is a conflict of this hypothesis with the quark light cone algebra plus polynomial fixed pole residues.

IV. Fixed Poles in Electroproduction

The same formalism which was developed in the last section can be straightforwardly applied in the case of electroproduction. Consider the amplitude $T_2(\nu, q^2)$, whose imaginary part is $W_2(\nu, q^2)$, one of the invariant amplitudes in the decomposition of the forward virtual photon-nucleon amplitude. We assume that as $\nu \to \infty$ we have the asymptotic behavior

$$\nu^2 T_2(\nu, q^2) \to \sum_{\alpha_i > 0} \beta_i(q^2) \left(\frac{-1 - e^{-i\pi\alpha_i(0)}}{\sin \pi \alpha_i(0)} \right) \nu^{\alpha_i(0)} - R(q^2) + (\text{terms which vanish as } \nu \to \infty), \quad (11)$$

with $R(q^2)$ the residue of the fixed pole. The manipulations discussed in the previous section can then be applied with the result:[20]

$$R(q^2) = \frac{1}{\pi} \int_0^\infty d\nu' \, [\, W_2(\nu', q^2) - W_2^R(\nu', q^2) \,], \quad (12a)$$

or

$$\frac{\pi M_N}{q^2} R(q^2) = \int_0^\infty d\left(\frac{2M_N \nu'}{q^2} \right) [\, \nu W_2(\nu', q^2) - \nu W_2^R(\nu', q^2) \,] \quad (12b)$$

At this point we make an important additional theoretical assumption:[21] the residue function, $R(q^2)$, is a polynomial in q^2. The strongest theoretical support for this assumption in my opinion, is that the leading light cone singularity, which results in the scaling behavior of deep inelastic scattering, also results in a $J = 0$ fixed pole being present in $T_2(\nu, q^2)$ with a polynomial residue.[22, 23] This fact is also reflected in calculations in the covariant parton model where the same result is found.[24, 25, 26] But, whether in a light cone or parton model framework, in order to show that the whole amplitude $T_2(\nu, q^2)$ has a fixed pole at $J = 0$ with a polynomial residue an assumption must be made either on the behavior of non-leading light cone singularities or on the neglect of certain diagrams, respectively. This assumption can be shown[27] to be equivalent to the absence of fixed poles in single current amplitudes where one of the photons is replaced by hadrons with the same total quantum numbers as the photon. Therefore, although the loss of polynomial residues in the virtual Compton amplitude implies the (unpalatable?) presence of fixed poles in single current amplitudes, the demand of polynomial residues must, in one way or another, be regarded as an assumption.

Given this assumption though, a number of powerful results follow. First note that $R(q^2)$ must be at least linear in q^2 near $q^2 = 0$, since otherwise the left hand side of Eq. (12b) is singular at $q^2 = 0$, while the right hand side is not. Second, as $q^2 \to \infty$ the right hand side of Eq. (12b) goes over into an integral which is finite in the scaling limit. Therefore the left hand side must be finite, i.e. $R(q^2)$ is at most linear in q^2 as $q^2 \to \infty$. These two conditions together imply that $R(q^2)$ is exactly linear, and we write

$$R(q^2) = \frac{q^2}{\pi M_N} R \, . \quad (13)$$

Then as $q^2 \to \infty$, we have from Eq. (12b):

$$R = \int_0^\infty d\omega \, [\, F_2(\omega) - F_2^R(\omega) \,] \, , \quad (14)$$

where $F_2(\omega)$ is the function $\nu W_2(\nu, q^2)$ in the scaling limit where $\nu, q^2 \to \infty$ with $\omega = 2M_N\nu/q^2$ fixed. As $q^2 \to 0$, we find from[28]

$$\nu W_2(\nu, q^2) \xrightarrow[q^2 \to 0]{} \frac{q^2}{4\pi^2\alpha} \sigma_T(\nu) \, , \quad (15)$$

that Eq. (12a) becomes[29]

$$R = 1 + \frac{M_N}{2\pi^2\alpha} \int_0^\infty d\nu' \, [\, \sigma_T(\nu') - \sigma_T^R(\nu') \,]$$
$$= -\frac{M_N}{\alpha} N \left[-\frac{\alpha}{M_N} - \frac{1}{\pi} \int_0^\infty \frac{d\nu'^2}{\nu'^2} \, \mathrm{Im} \, [\, f_1(\nu') - f_1^R(\nu') \,] \right] . \quad (16)$$

Equating these results for R we have[30, 31]

$$R = \int_0^\infty d\omega \, \tilde{F}_2(\omega) = 1 + \frac{M_N}{2\pi^2\alpha} \int_0^\infty d\nu \, \tilde{\sigma}_T(\nu) \, , \quad (17)$$

where we have introduced the notation $\tilde{T}$ to indicate $T\text{-}T^R$, i.e. that the leading Regge behavior of an amplitude (or cross section) has to be subtracted off down to terms corresponding to $\alpha = 0$.

Note that the quantity in brackets in Eq. (16) is just the quantity C discussed in the last section. If we accept the result of phenomenological analysis that $C_p \simeq -\alpha/M_N$, then it follows that $R_p \simeq +1$.

The phenomenological situation in electroproduction can be most easily understood by consideration of Figure 1. The sum rule for R, Eq. (14), involves the difference between the areas under the curves labelled $F_2(\omega)$ and $F_2^R(\omega)$, so that the net answer is the area indicated by (1) minus the area (2).

Is it possible to have $R_p \simeq +1$, i.e. area (1) − area (2) = +1? It is clear from the measured $F_2(\omega)$ in the region $1 \leq \omega \leq 10$, that if we assume $F_2(\omega) = C_1 + C_2/\sqrt{\omega}$

starting at, say, $\omega = 5$ then we have the situation[32] indicated in Figure 1a, with area ② > area ① and R negative! To make R positive, we must have a situation like that indicated in Figure 1b, which directly implies that there are large contributions of other (lower values of $\alpha(0)$)Regge singularities at $\omega = 5$ or 10. Said another way, dominance of $F_2(\omega)$ by the leading J-plane singularities only happens for $\omega >> 10$.

This situation has been analyzed in great detail[33] using various phenomenological fits to $\nu W_2(\nu, q^2)$, and imposing certain parton model sum rule constraints on νW_2 for both protons and neutrons. The result[33] is that it is possible to fit the present data on νW_2, satisfy the other sum rules, and still have polynomial residues and $R_p \simeq +1$. However, the "price" one pays, as discussed above, is that there are important contributions to $F_2(\omega)$ from terms[34] other than those arising from the leading Regge singularities at $\omega \simeq 10$. Consequently $F_2(\omega)$ must decrease considerably from its measured value at $\omega = 10$ as $\omega \to \infty$. The Pomeranchuk singularity in particular, contributes only a relatively small part ($\lesssim \frac{1}{2}$) to $F_2(\omega = 5)$.

This peculiar behavior of $F_2(\omega)$ is not as unlikely as it might first seem. Other indications of such a large non-diffractive part and the slow approach of $F_2(\omega)$ to its asymptotic behavior lie in (1) the slow approach[35] of $\nu W_{2n}/\nu W_{2p}$ to unity at large ω; (2) the corresponding slow convergence[35] of $\int_1^\infty \frac{d\omega}{\omega}(\nu W_{2p} - \nu W_{2n})$; (3) the necessity of important contributions[36] to the Adler sum rule from large values of ω if it is to be satisfied; and (4) the close connection between the behavior of nucleon resonances and νW_2 for $1 \lesssim \omega \lesssim 5$, implying a large non-diffractive component in this ω region.[37] This also bears on the question of finding a simple continuation[38] between real and virtual Compton scattering, or equivalently finding the ν value for real photons which corresponds to a given ω value for virtual photons in the scaling regime. If the situation discussed here is actually the case in Nature, then moderate ν values, like 5 GeV, correspond to very large values of ω (of order 100?).

Finally, let us note that the quark light cone algebra (or the quark parton model) plus the assumption of polynomial residues is not consistent with the conjecture that fixed pole residues in forward Compton scattering amplitudes for real photons are proportional to the values of their respective Thomson limits. This inconsistency becomes obvious if we observe that the quark light cone algebra yields non-zero structure functions and hence non-zero fixed poles for the virtual Compton amplitude only when there are non-exotic t-channel quantum numbers. On the other hand, the value of the Thomson limit for the fixed pole residue leads to exotic t-channel quantum numbers. The assumption of polynomial residues, which ties real and virtual Compton scattering fixed poles together, then yields a contradiction in t-channel quantum numbers.

Note that there is no contradiction of the quark light cone algebra or quark parton model results with the argument discussed previously on "turning off" the strong interactions and being left with a Compton amplitude which is equal to the Thomson limit. If the strong interactions are "turned off" in a quark model one no longer has a nucleon! One has three quarks and presumably a Compton amplitude which is the sum of the quark Compton amplitudes. Therefore each argument is self-consistent, and the question of which is correct must be settled on other (experimental?) grounds.

V. Connections to Other Quantities

The past year has seen the formulation and application of the general technique[39] of using amplitudes with their leading Regge behavior subtracted off in order to extract finite results from otherwise divergent, meaningless sum rules. For example, a meaningful version of the sum rule[40] for the Schwinger term is[39]

$$S = 4 \int_0^\infty \frac{d\omega}{\omega} \tilde{F}_L(\omega), \tag{18}$$

where

$$F_L(\omega) = \frac{\omega}{2M_N} F_2(\omega) - F_1(\omega). \tag{19}$$

Equation (18) holds in the absence of a non-polynomial fixed pole residue in the longitudinal amplitude. If such a term is present, Eq. (18) is modified by the subtraction of its residue function at $q^2 = \infty$, $C(\infty)$, from the right side.

The question of working with subtracted amplitudes enters the discussion of many other sum rules. For example, consider the structure functions W_4 and W_5. These amplitudes, which in principle are measurable, are the coefficients of $(q_\mu q_\nu / M_N^2)$ and $(q_\mu p_\nu + p_\mu q_\nu)/2M_N^2$, respectively, in the expansion of the hadronic tensor $W_{\mu\nu}$ for inelastic neutrino and antineutrino scattering. It has been established that[41] $\frac{\nu^2}{M_N} W_4(\nu, q^2)$ and $\frac{\nu^2}{M_N} W_5(\nu, q^2)$ *should scale in the quark gluon model* and we define these to be the functions $F_4(\omega)$ and $F_5(\omega)$ respectively. Then, within the quark gluon model[41,42] it may be shown that the so-called "σ-term" satisfies a sum rule which written in a meaningful way is of the form

$$\sigma_\pi = 2M_N \int_0^\infty \frac{d\omega}{\omega^2} \left[-\frac{\tilde{F}_5^{(+)}(\omega)}{4} + \frac{\tilde{F}_4^{(+)}(\omega)}{\omega} \right] , \tag{20}$$

assuming polynomial residues for $J = 0$ fixed poles.

Also the structure function

$$F_G(\nu, q^2) = \nu \left[\left(1 + \frac{\nu^2}{q^2}\right) W_2(\nu, q^2) - W_1(\nu, q^2) \right] , \tag{21}$$

which is proportional to the longitudinal total cross section, and should scale in the quark gluon model, satisfies the sum rule[43]

$$\int_0^\infty \frac{d\omega}{\omega^2} \tilde{F}_G^{(+)}(\omega) = -\frac{1}{2} \int_0^\infty \frac{d\omega}{\omega^2} \tilde{F}_5^{(+)}(\omega) + \int_0^\infty \frac{d\omega}{\omega^2} F_2^{(+)}(\omega). \tag{22}$$

Thus the longitudinal structure function F_G, the structure functions W_4 and W_5, and the σ-term are all related in the quark gluon model through sum rules involving subtracted amplitudes.

Further insight into these connections comes from the study of electromagnetic mass differences in the quark parton model. Recall[28] that with $x = 1/\omega$ and $f_i(x)$ the longitudinal momentum distribution of parton i that

$$F_2(x) = \sum_i Q_i^2 \, x \, f_i(x) , \tag{23}$$

where Q_i is the parton charge. Define[44]

$$\int_0^\infty \frac{\tilde{f}_i(x)}{x} dx = f_i , \tag{24}$$

where the tilde again indicates a subtraction of the leading Regge behavior as $x \to 0$ (which corresponds to $\omega = \frac{1}{x} \to \infty$). The integral appearing in the sum rule, Eq. (17), for the fixed pole residue in F_2 is

$$\int_0^\infty \tilde{F}_2(\omega) \, d\omega = -\int_\infty^0 \frac{dx}{x^2} \tilde{F}_2(x) = \sum_i Q_i^2 \int_0^\infty \frac{\tilde{f}_i(x)}{x} dx = \sum_i Q_i^2 f_i , \tag{25}$$

and the divergent part of the electromagnetic mass may be shown to be[44,45]

$$\delta M^2 = \sum_i \frac{3\alpha}{2\pi} \ln\Lambda^2 \, Q_i^2 \int_0^\infty \frac{\tilde{f}_i(x)}{x} dx$$

$$= \sum_i Q_i^2 \, f_i \left(\frac{3\alpha}{2\pi} \ln \Lambda^2\right) , \tag{26}$$

where Λ is a cut-off. The divergent part of the total electromagnetic mass is then a sum over the divergent part of the electromagnetic mass of the partons, weighted by the f_i.

The reason why all these quantities are related to the f_i is seen in the quark model with vector gluons where it is found that the matrix element of the scalar bilocal is[44]

$$\langle p | \bar{\psi}_i(0) \, \psi_i(0) | p \rangle = m_i \, f_i , \tag{27}$$

where m_i is the quark mass. In the same theory, the "σ-term" is[44]

$$\sigma_\pi = \frac{m^2}{M_N} (f_p + f_n) \tag{28}$$

where $m = m_p = m_n$ is the p or n quark mass. The connection of the quantities f_i to the scalar bilocal operator $\bar{\psi}_i(0) \, \psi_i(0)$ makes clearer the intimate connection of fixed poles, σ terms and electromagnetic masses, all of which are characterized by an operator with $J = 0$ and positive parity.

To return to the discussion at the beginning of this lecture, we have seen that while fixed poles generally are not allowed in strong interaction amplitudes at right signature points, they are suggested, if not demanded in some cases, in two current amplitudes. This provides an answer to the question that is sometimes asked of whether an on-mass-shell elastic hadronic amplitude can be exactly proportional to a two current amplitude. The answer is no, precisely because of the existence of fixed

poles in one case and not in the other. One might even postulate that in certain cases, say π N elastic scattering versus $(\partial_\mu A_\mu) + N \to (\partial_\mu A_\mu) + N$, that the real and imaginary parts of these amplitudes are proportional except for fixed poles. For the crossing odd amplitude for forward π N scattering this postulate applied to the $J = 1$ fixed pole leads directly to the Adler-Weisberger sum rule.[46] For the crossing even forward π N amplitude the postulate leads to an equation that states that the correction in going from the amplitude for $(\partial_\mu A_\mu) + N \to (\partial_\mu A_\mu) + N$ at $\nu = q^2 = 0$ to the $\pi + N \to \pi + N$ amplitude at the same point is given by a fixed pole. Thus the question of whether there is a small or large difference in these two amplitudes (essentially, whether "weak" or "strong" PCAC holds) is the same as the question of the magnitude of a fixed pole residue.[47]

We therefore see that what started a few years ago as a restricted question of the presence of an extra real constant term in the high energy behavior of the proton Compton amplitude, has spread far afield and has applications in many other areas. In particular, this phenomenological and theoretical work has now added an important component in our understanding of the special nature of two current amplitudes.

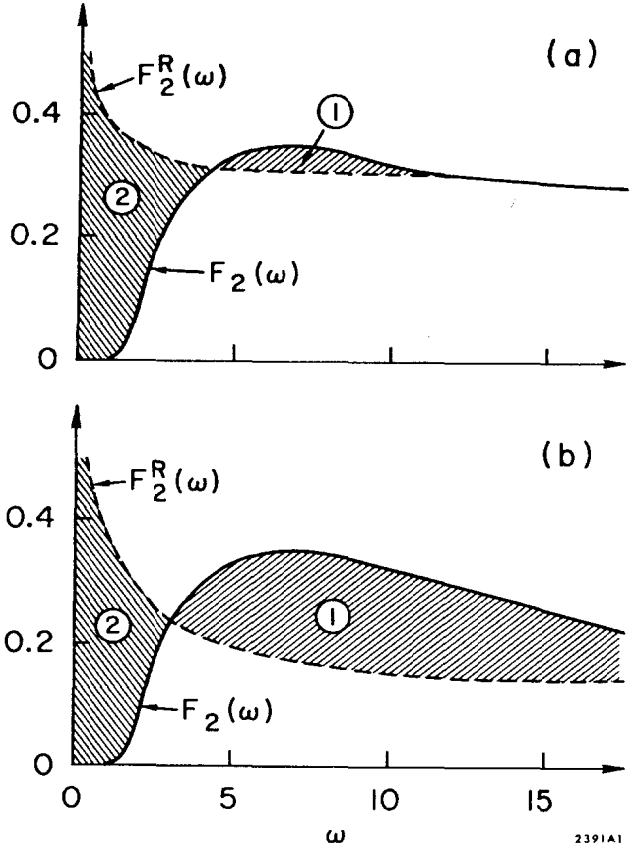

Fig. 1 – The phenomenological situation with regard to the sign of the $J = 0$ fixed pole residue in the forward virtual photon-proton amplitude. The value of the residue in the scaling regime is given by the area under $F_2(\omega) = \nu W_2(\omega)$ minus that under its leading Regge behavior, $F_2^R(\omega)$; i. e., area (1) minus area (2). The cases $R < 0$ and $R > 0$ are shown in Figures 1a and 1b respectively.

References

1. For a discussion see E. J. Squires, Complex Angular Momenta and Particle Physics (Benjamin, New York, 1963), p. 51. This argument against fixed poles holds at a right signature point only. At a wrong signature point it fails because of the presence of a cut due to the t-u double spectral function.
2. P. Finkler, Phys. Rev. D1, 1172 (1970) and D2, 173 (1970).
3. I thank J. Finkelstein for a discussion on this point and informing me of arguments due to Squires which eliminate such fixed poles at the highest values of J.
4. However, for the suggestion of the possibility of a fixed singularity near J = -1 in the $B^{(-)}$ amplitude of π N scattering see R. Aviv and D. Horn, Phys. Rev. Letters 21, 704 (1968). Also M. Dubovoy, Phys. Rev. D5, 193 (1972).
5. Theoretical arguments against such fixed poles when composite particles are involved have been presented by H. Rubinstein, G. Veneziano, and M. Virasoro, Phys. Rev. 167, 1441 (1968).
6. Theoretical arguments for such a fixed pole in rho photoproduction are given by R. A. Brandt et al, Lettere al Nuovo Cimento 2, 937 (1971).
7. D. J. Sherden et al, Phys. Rev. Letters 30, 1.30 (1973).
8. Recent analyses of data on $\pi^- p \to \rho^0 n$ seem to show the same result: P. Estabrooks and A. D. Martin, Phys. Letters 42B, 229 (1972).
9. R. F. Dashen and S. Y. Lee, Phys. Rev. Letters 22, 366 (1969).
10. S. L. Adler, Phys. Rev. 143, 1144 (1966);
    S. Fubini, Nuovo Cimento 43, 475 (1966);
    R. Dashen and M. Gell-Mann, Phys. Rev. Letters 17, 340 (1966).
11. J. Bronzan et al, Phys. Rev. Letters 18, 32 (1967) and Phys. Rev. 157, 1448 (1967).
12. H. D. I. Abarbanel and S. Nussinov, Phys. Rev. 158, 1462 (1967) and H. D. I. Abarbanel et al., Phys. Rev. 160, 1329 (1967) and references therein.
13. M. J. Creutz, S. D. Drell, and E. Paschos, Phys. Rev. 178, 2300 (1969).
14. We follow closely the derivation in M. Damashek and F. J. Gilman, Phys. Rev. D1, 1319 (1970).
15. By writing the limits of integration as 0 to ∞ in the integral over the imaginary part of the physical scattering amplitude we include the discrete Born pole as well as the continuum (starting at $\nu = \nu_0 > 0$) in the integral. Later, we will similarly write electroproduction sum rules with $\omega = 0$ as the lower limit of integration, even though the physical structure function νW_2 is zero for $\omega < 1$.
16. M. Damashek and F. J. Gilman, ref. 14; and C. A. Dominguez, C. Ferro Fontan, and R. Suaya, Phys. Letters 31B, 365 (1970).
17. F. J. Gilman, unpublished; F. E. Close and J. F. Gunion, private communication and ref. 33; C. A. Dominguez, J. F. Gunion, and R. Suaya, ref. 18; N. R. S. Tait and J. N. J. White, Nucl. Phys. B43, 27 (1972).
18. C. A. Dominguez, J. F. Gunion, and R. Suaya, Phys. Rev. D6, 1404 (1972).
19. M. J. Cruetz, S. D. Drell and E. Paschos, ref. 13, T. P. Cheng and W. K. Tung, ref. 19; H. Harari, invited talk in Proceedings of the 1971 International Symposium on Electron and Photon Interactions at High Energies, edited by N. B. Mistry (Laboratory of Nuclear Studies, Cornell University, 1972), p. 299.
20. Recall that $T_2(\nu, q^2)$, which behaves as $\nu \to \infty$ as $\nu^{\alpha(0)-2}$, would satisfy an unsubtracted dispersion relation in ν. Therefore there is no subtraction term in Eq. (12).
21. T. P. Cheng and W. K. Tung, Phys. Rev. Letters 24, 851 (1970).
22. J. Cornwall, D. Corrigan, and R. Norton, Phys. Rev. D3, 536 (1971);
    A. H. Mueller, Phys. Rev. D2, 2241 (1970); G. Mack, Phys. Letters 35B, 234 (1971); M. Bander, Phys. Rev. D5, 3274 (1972); R. Gatto and P. Menotti, Nuovo Cimento 7A, 118 (1972).
23. For discussions in the light cone framework see K. Wilson in Proceedings of the 1971 International Symposium on Electron and Photon Interactions at High Energies,

edited by N. B. Mistry (Laboratory of Nuclear Studies, Cornell University, 1972), p. 115; and Y. Frishman in Proceedings of the XVI International Conference on High Energy Physics, edited by J. D. Jackson and A. Roberts (National Accelerator Laboratory, Batavia, 1973), Volume 4, p. 119.

24. S. J. Brodsky, F. E. Close, and J. F. Gunion, Phys. Rev. D5, 1384 (1972), obtain fixed singularities in T_1 (a Kronecker delta) and T_2 (a fixed pole with polynomial residue) related by $T_1 = (\frac{\nu^2}{q^2}) T_2$ working in a general gauge invariant parton model framework.
25. Phenomenological implications of fixed singularities, as suggested in the parton model, are discussed by S. J. Brodsky, F. E. Close, and J. F. Gunion, Phys. Rev. D6, 177 (1972).
26. P. V. Landshoff and J. C. Polkinghorne, Phys. Rev. D5, 2056 (1972).
27. See Y. Frishman, ref. 23 for a discussion of this point.
28. See F. J. Gilman, Physics Reports 4C, 98 (1972) and references therein for a review of kinematics, scaling, the parton model, etc.
29. The 1 on the right hand side of Eq. (16) arises from explicitly separating out the Born term at $\nu = q^2/2M_N$. As $q^2 \to 0$, this pole is at $\nu = 0$, and is understood not to be included in the integral over total cross sections in Eq. (16).
30. J. Cornwall, D. Corrigan, and R. Norton, ref. 22.
31. R. Rajaraman and G. Rajasakaren, Phys. Rev. D3, 266 (1971); ibid., Erratum D4, 2940 (1971). See also H. Leutwyler and J. Stern, Phys. Letters 31B, 458 (1970).
32. M. Elitzur, Phys. Rev. D3, 2166 (1971).
33. F. E. Close and J. F. Gunion, Phys. Rev. D4, 742 (1971).
34. In the case of ref. 33 this is the $\omega^{-3/2}$ term in the expansion of $F_2(\omega)$.
35. The difference between neutron and proton structure functions and its implications is reviewed by E. D. Bloom, invited talk at the International Conference on New Results from Experiments on High Energy Particle Collisions, Vanderbilt University, Nashville, March 26-28, 1973 and Caltech preprint CALT-68-392, 1973 (unpublished).
36. For recent discussions of the saturation of the Adler sum rule see E. A. Paschos in Proceedings of the XVI International Conference on High Energy Physics, edited by J. D. Jackson and A. Roberts (National Accelerator Laboratory, Batavia, 1973), Volume 2, p. 166; and S. F. Tuan, Phys. Rev. D7, 2092 (1973) and references therein.
37. See the review of F. J. Gilman in Proceedings of the International Conference on Duality and Symmetry in Hadron Physics, edited by E. Gotsman (The Weizmann Science Press of Israel, Jerusalem, 1971), p. 116.
38. See, for example, V. Rittenberg and H. R. Rubinstein, Phys. Letters 35B, 50 (1971).
39. D. J. Broadhurst, J. F. Gunion, and R. L. Jaffe, SLAC preprint SLAC-PUB-1197, 1973 (unpublished), present a general discussion of finite scaling sum rules.
40. R. Jackiw, R. van Royen, and G. B. West, Phys. Rev. D2, 2473 (1970).
41. R. L. Jaffe and C. H. Llewellyn Smith, MIT report MIT-CTP-331 and Phys. Rev., in press, and references to previous work therein.
42. The superscript "(+)" denotes the isospin symmetric amplitude, i.e., the sum of the amplitudes for νp and $\bar{\nu} p$.
43. D. G. Broadhurst, J. F. Gunion, and R. L. Jaffe, MIT report MIT-CTP-339, 1973 (unpublished); also H. Fritzsch, M. Gell-Mann, and A. Schwimmer, to be published.
44. We follow here the work of J. F. Gunion, MIT report MIT-CTP-333, 1973 (unpublished).
45. See the earlier work of W. I. Weisberger, Phys. Rev. D5, 2600 (1972); R. Jackiw and H. Schnitzer, Phys. Rev. D5, 2008 (1972); S. J. Brodsky, F. E. Close, and J. F. Gunion, SLAC report SLAC-PUB-1243, 1973 (unpublished).
46. S. L. Adler, Phys. Rev. Letters 14, 1051 (1965); W. I. Weisberger, Phys. Rev. Letters 14, 1047 (1965).

47. M. Gell-Mann, Caltech lectures, 1973 (unpublished) and H. Fritzsch, M. Gell-Mann, and H. Leutwyler, to be published. The argument given here starts from a somewhat different origin, but arrives at the same equation for the connection in going from the $\partial_\mu A_\mu$ to pion amplitude as the above authors.

ASYMPTOTIC BEHAVIOUR AND SHORT DISTANCE SINGULARITIES

Y. Frishman*

Stanford Linear Accelerator Center,

Stanford, California 94305

Abstract

The behaviour of the structure functions for various short distance singularities is discussed.

I. Introduction

The subject discussed in this note was part of the lectures given by the author at the SLAC Summer Institute on Particle Physics (July, 1973), on "Formal theory - light cone and short distance methods". The latter included a review on the whole area of operator products at short and almost light like distances, and the applications to the region of deep inelastic lepton-hadron scattering for products of electromagnetic and weak current. Since reviews on these subjects by the present author exist already[1,2] it seems better to concentrate here on some aspects that were not discussed there in detail.

We shall discuss here the behaviour of electron-nucleon structure functions in the deep inelastic region for non-canonical short distance singularities. (The discussion is identical for the structure functions in neutrino scattering, and also for the spin dependent functions). In this case, Bjorken scaling[3] is not valid anymore. We argue that it is best to detect the effects of such violations at relatively small values of the ratio of energy to square momentum transfer.

In sec. II, we review briefly the kinematics and relate moments of the structure functions to the short distance singularities. In sec. III, we discuss the consequences for the behaviour of the structure functions.

---

* On leave from the Weizmann Institute, Rehovoth, Israel.

II. Short Distance Singularities and Moments of Structure Functions

The cross section for electron-nucleon scattering is

$$\frac{d^2\sigma}{d\Omega dE'} = \frac{\alpha^2 \cos^2 \Theta/2}{4E^2 M \sin^4 \Theta/2} \left[W_2(q^2,\nu) + 2\tan^2 \Theta/2 \; W_1(q^2,\nu) \right] \tag{1}$$

where E is the energy of the incident electron, E' the outgoing electron and $\Omega(\Theta)$ the scattering angle, all in the laboratory frame; M the mass of the nucleon and α the fine structure constant. Eq. (1) is derived assuming the one photon exchange approximation, with q the four momentum carried by the exchanged photon (the difference between the four momenta of the incoming and outgoing electrons), and ν the energy given to the nucleon, $M\nu = q\cdot p$. We also take an unpolarized nucleon, with structure functions W_1 and W_2 given by

$$W_{\mu\lambda}(qp) = \frac{1}{2} \sum_{s(\text{spin})} \int d^4x \, e^{iqx} \langle ps \left| [J_\mu(x), J_\lambda(0)] \right| ps \rangle = \left(-g_{\mu\lambda} + \frac{q_\mu q_\lambda}{q^2}\right) W_1(q^2,\nu) + \frac{1}{M^2}\left(p_\mu - \frac{M\nu}{q^2} q_\mu\right)\left(p_\lambda - \frac{M\nu}{q^2} q_\lambda\right) W_2(q^2,\nu) \tag{2}$$

$J_\mu(x)$ is the electromagnetic current. Bjorken scaling is[3]

$$W_1(q^2,\nu) \longrightarrow F_1(\omega)$$
$$\nu W_2(q^2,\nu) \equiv F_2(q^2,\nu) \longrightarrow F_2(\omega) \tag{3}$$

in the limit of $q^2 \to -\infty$, $\nu \to \infty$ with $\omega = \frac{2q\cdot p}{(-q^2)}$ fixed.

To discuss the behaviour of the structure functions we first write

$$[J_\mu(x), J_\nu(y)] = \left[\partial_\mu^{(y)} \partial_\nu^{(x)} - g_{\mu\nu} \partial_\alpha^{(x)} \partial^{\alpha(y)}\right] V_L(x,y) + \left[g_{\mu\alpha}\partial_\nu^{(x)} \partial_\beta^{(y)} + g_{\nu\beta} \partial_\alpha^{(x)} \partial_\mu^{(y)} - g_{\mu\alpha} g_{\nu\beta} \partial_\lambda^{(x)} \partial^{\lambda(y)} - g_{\mu\nu} \partial_\alpha^{(x)} \partial_\beta^{(y)} \right] \cdot V_2^{\alpha\beta}(x,y) + \ldots\ldots \tag{4}$$

where the other terms do not contribute to the spin averaged forward matrix elements. The form eq. (4) ensures conservation of the electromagnetic currents.[4] In momentum space, for the forward spin averaged matrix elements,

$$W_{\mu\nu}(q,p) = (q_\mu q_\nu - g_{\mu\nu}q^2)\ V_L(q^2,\ q\cdot p) + [g_{\mu\alpha}q_\nu q_\beta + g_{\nu\beta}q_\mu q_\alpha - g_{\mu\alpha}g_{\nu\beta}q^2 - g_{\mu\nu}q_\alpha q_\beta]\cdot\ V_2^{\alpha\beta}(q,p) \tag{5}$$

Since $W_{\mu\nu}$ is symmetric in $\mu \longleftrightarrow \nu$, it follows that $V_2^{\alpha\beta}(q,p)$ is symmetric in $\alpha \longleftrightarrow \beta$. Thus both V_L and $V_2^{\alpha\beta}$ are antisymmetric under $q \longrightarrow -q$. Writing,

$$V_2^{\alpha\beta}(q,p) = p^\alpha p^\beta V_2(q^2,\ q\cdot p) + \ldots\ldots \tag{6}$$

all terms except the first contribute like another V_L term. We have

$$\frac{\nu^2}{(-q^2)}\ W_2(q^2\nu) - W_1(q^2\nu) = (-q^2)\ V_L(q^2\nu);\ W_2(q^2\nu) = M^2(-q^2)\ V_2(q^2\nu) \tag{7}$$

V_L and V_2 have no kinematic zeros at $q^2 = 0$. We see that $(-q^2)\ V_L(q^2\nu)$ is proportional to the longitudinal combination, which is small experimentally.[5]

Let us now concentrate on the $V_2^{\alpha\beta}(x,0)$ part. In the short distance limit, $x \to 0$, we use Wilson's short distance expansion,[6]

$$V_2^{\alpha\beta}(x,0) \sim \sum_{mi} C_{mi}(x)\ x_{\alpha_1}\ldots\ x_{\alpha_m}\ T_i^{\alpha\beta\,\alpha_1\cdots\alpha_m}(0) \tag{8}$$

where $C_{mi}(x)$ are singular C-number functions and $T_i^{\alpha\beta\,\alpha_1\cdots\alpha_m}(0)$ local operators. Wilson argues that the notion of "asymptotic dimensionality" becomes exact at short distances. This implies power type singularities for the functions $C_{mi}(x)$. We now take, in eq. (8), the most singular term $C_{mi} \equiv C_m$ for each given m (assume there is only one such term and neglect the others). Since $C_m(x)$ is an invariant function, which is power behaved and vanishes for $x^2 < 0$, we have

$$c_m(x) = [\ (-x^2 + i\epsilon x_0)^{-d_m} - (-x^2 - i\epsilon x_0)^{-d_m}\ ]\ \Gamma(d_m) \tag{9}$$

The factor $\Gamma(d_m)$ ensures that $C_m(x)$ does not vanish for non-positive integer d_m,

$$c_m(x) \xrightarrow[d_m \to -m]{} \frac{2i\pi}{m!}\ \epsilon(x_0)\ \Theta(x^2)\ (x^2)^m \tag{10}$$

Thus,

$$V_2^{\alpha\beta}(x,0) \sim \sum_n C_n(x)\ x_{\alpha_1}\ldots x_{\alpha_{2n}}\ T^{\alpha\beta\,\alpha_1\cdots\alpha_{2n}}(0) \tag{11}$$

only even powers of x appear, since $C_n(x)$ is antisymmetric under $x \to -x$ and so is $V_2^{\alpha\beta}(x,0)$. Since the electromagnetic current has dimension 3 (in units of $\frac{1}{x}$),

$$2d_n = 4 + [2n - d(T^{\alpha\beta\,\alpha_1\cdots\alpha_{2n}})] \tag{12}$$

where $d(T^{\alpha\beta\,\alpha_1\cdots\alpha_{2n}})$ is the dimension of $T^{\alpha\beta\,\alpha_1\cdots\alpha_{2n}}$. Thus the singularity of C_n depends on the difference between spin and dimension of the respective local operator.[7]

Now, when taking the fourier transform as in eq. (2), any individual term in eq. (11) does not contribute to $W_{\mu\nu}$.[4] The reason is very simple. In the short distance limit one has $x_\alpha = \lambda\tilde{x}_\alpha$, $\tilde{x}_\alpha$ fixed and $\lambda \to 0$. This means in momentum space that $q_\alpha = \frac{1}{\lambda}\ \tilde{q}_\alpha$, with $\tilde{q}_\alpha$ fixed and $\lambda \to 0$. (Since we have q^2 space like, we take $\tilde{q}^2 < 0$.) But then $\omega \propto \lambda$, which means $\omega \to 0$ and we are below threshold.

The short distance expansion becomes very useful when discussing the full amplitude. We define

$$\begin{aligned} T_{\mu\lambda}(q,p) &= \frac{1}{2}\ \sum_s \int d^4x\ e^{iqx} \langle ps \left|\ T^*\ J_\mu(x)\ J_\lambda(0)\right|\ ps\rangle \\ &= \left(-g_{\mu\lambda} + \frac{q_\mu q_\lambda}{q^2}\right) T_1(q^2\nu) + \frac{1}{M^2}\left(p_\mu - \frac{M\nu}{q^2}q_\mu\right)\left(p_\lambda - \frac{M\nu}{q^2}q_\lambda\right)\ T_2(q^2\nu) \end{aligned} \tag{13}$$

where T^* denotes covariantized time ordering. We also define $t_L(x,y)$, $t_2^{\alpha\beta}(x,y)$ through an expansion of $T^*J_\mu(x)\ J_\nu(y)$ as in eq. (4). We then write a short distance expansion for $t_2^{\alpha\beta}(x,0)$, namely

$$t_2^{\alpha\beta}(x,0) \sim \sum_n t_n(x)\ x_{\alpha_1}\ldots x_{\alpha_{2n}}\ T^{\alpha\beta\,\alpha_1\cdots\alpha_{2n}}(0) \tag{14}$$

where the local operators are the same as $T^{\alpha\beta\,\alpha_1\cdots\alpha_{2n}}(0)$ for the commutator and

$$t_n(x) = (-x^2 + i\epsilon)^{-d_n}\ \Gamma(d_n) \tag{15}$$

as the singularity for a time ordered product. The expansion eq. (14) becomes relevant in the limit $q_\alpha = \frac{1}{\lambda}\ \tilde{q}_\alpha$, $\lambda \to 0$ and $\tilde{q}_\alpha$ fixed ($\tilde{q}^2 < 0$), in which case

$$t_2^{\alpha\beta}(q,p) \sim \sum_n a_n \langle p \left|\ T^{\alpha\beta\,\alpha_1\cdots\alpha_{2n}}(0)\right|\ p\rangle\ \ \frac{\partial}{\partial q_{\alpha_1}}\ldots\frac{\partial}{\partial q_{\alpha_{2n}}}(-q^2)^{d_n-2}$$

This is also the limit of $\omega \to 0$. If we now take $p_o \to \infty$, the leading contribution comes from the $(2n+2)$ spin part of $T^{\alpha\beta\,\alpha_1 \cdots \alpha_{2n}}(0)$, namely $\langle p \left| T^{\alpha\beta\,\alpha_1 \cdots \alpha_{2n}}(0) \right| p \rangle \sim p^{\alpha_1} \cdots p^{\alpha_{2n}}$ Thus,

$$(-q^2)\, T_2(q^2,\omega) \sim \sum_{n=0}^{\infty} b_n\, \omega^{2n}\, (-q^2)^{d_n} \tag{16}$$

In the above limit of $q_\alpha \to \infty$ in a space like direction and $p_o \to \infty$ with $\omega \to 0$.

We now write an unsubtracted dispersion relation for T_2,

$$T_2(q^2,\omega) = \frac{1}{\pi} \int_1^\infty \frac{W_2(\omega', q^2)\, d\omega'}{\omega'^2 - \omega^2} \tag{17}$$

For $\omega \to 0$,

$$\frac{(-q^2)}{4M}\, T_2(q^2,\omega) = \frac{1}{\pi} \sum_{n=0}^{\infty} \omega^{2n} \int_1^\infty \frac{F_2(\omega', q^2)\, d\omega'}{\omega'^{2n+2}} \tag{18}$$

Comparing with eq. (16), we get for $(-q^2) \to \infty$,

$$\int_1^\infty \frac{F_2(\omega', q^2)}{\omega'^{2n+2}}\, d\omega' \sim A_n\, (-q^2)^{d_n} \tag{19}$$

We will discuss properties and consequences for $F_2(\omega, q^2)$ in the next section. Bjorken scaling is achieved when $d_n = 0$ for all n.

Note that whenever d_n are non-integers, an expansion of T_2 in inverse powers of q_o for $q_o \to i\infty$ is not possible, as follows from eq. (16). Thus the Bjorken-Johnson-Low[8] method is not applicable in this case. When scaling holds, the p_o^{2n} part of the $\frac{1}{q_o^{2n+2}}$ term in T_2 exists and can be related to the p_o^{2n+2} part of the equal-time commutator $\langle p \left| [\, \partial_o^{2n+1} J_i(\vec{x}),\, J_j(\vec{0})\,] \right| p \rangle \propto p_o^{2n} p_i p_j\, \delta^{(3)}(\vec{x})$ ($\left|\vec{p}\right| \sim p_o$ for $p_o \to \infty$). For details, see ref. 2.

In the "asymptotically free" gauge theories[9], Bjorken scaling is violated by logarithmic terms only.[10] There

$$\int_1^\infty \frac{F_2(\omega', q^2)}{\omega'^{2n+2}}\, d\omega' \sim B_n\, [\ell n(-q^2)]^{\gamma_n} \tag{20}$$

Also, in these theories, the approach to the asymptotic limit is logarithmic too.

Present experiments indicate a faster approach (or, that we do not see the "asymptotic limit" yet).

III. *Consequences for the Behaviour of F_2*

Let us take

$$\int_1^\infty \frac{F_2(\omega', q^2)}{\omega'^{2n+2}}\, d\omega' \sim K_n\, [\, f(q^2)\,]^{\delta_n} \tag{21}$$

where $f(q^2)$ is monotonically increasing to infinity with $(-q^2)$ for large $(-q^2)$. This includes both cases eqs. (19) and (20). Obviously, from the positivity of F_2, it follows that the δ_n are a monotonically decreasing function of n. Moreover, one can show that δ_n is convex from above (This was first discussed by Nachtman[11]). This is easy to see by calculating $\frac{d^2}{dn^2}\,\delta_n$ and showing that it is positive (we consider the left hand side now as a function of the continuous variable n). For, differentiating both sides with respect to n,

$$\int_1^\infty \frac{F_2(\omega', q^2)\, \ell n(\omega'^2)}{\omega'^{2n+2}}\, d\omega' \sim K_n\, [\, f(q^2)\,]^{\delta_n}\, [\, \ell n\, f(q^2)\,] \left(-\frac{d\delta_n}{dn}\right)$$

where terms of order 1 where neglected compared with $\ell n(q^2)$. Hence

$$\left[\ell n(q^2)\right] \left(-\frac{d\delta_n}{dn}\right) \sim \left[\int_1^\infty \frac{F_2(\omega', q^2)\, \ell n(\omega'^2)}{\omega'^{2n+2}}\, d\omega'\right] \left[\int_1^\infty \frac{F_2(\omega', q^2)}{\omega'^{2n+2}}\, d\omega'\right]^{-1}$$

which shows that $\frac{d\delta_n}{dn} < 0$. Differentiating once again with respect to n,

$$\left[\ell n(q^2)\right] \left(-\frac{d^2\delta_n}{dn^2}\right) \sim \frac{\left[\int_1^\infty \frac{F_2(\omega', q^2)\, (\ell n \omega'^2)}{\omega'^{2n+2}}\, d\omega'\right]^2}{\left[\int_1^\infty \frac{F_2(\omega', q^2)}{\omega'^{2n+2}}\, d\omega'\right]^2} - \frac{\int_1^\infty \frac{F_2(\omega', q^2)}{\omega'^{2n+2}} \left(\ell n \omega'^2\right)^2 d\omega'}{\int_1^\infty \frac{F_2(\omega', q^2)}{\omega'^{2n+2}}\, d\omega'}$$

Defining

$$G_n(\omega q^2) = \frac{F_2(\omega, q^2)}{\omega^{2n+2}} \left[\int_1^\infty \frac{F_2(\omega', q^2)}{\omega'^{2n+2}}\, d\omega'\right]^{-1}$$

we get that

$$\int_1^\infty G_n(\omega' q^2)\ d\omega' = 1$$

which means that G_n is a probability distribution, and

$$\left[\ln f(q^2)\right]\left(-\frac{d^2\delta_n}{dn^2}\right) \sim \left[<(\ln \omega^2)>_n\right]^2 - <(\ln \omega^2)^2>_n < 0$$

where the averaging is with respect to G_n. Thus $\frac{d^2\delta_n}{dn^2} > 0$. Taking the n = 0 moment to be q^2 independent ($\delta_0 = 0$), we have for δ_n as a function of n,

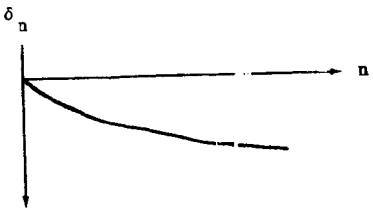

$\delta_0 = 0$ follows if $T^{\alpha\beta}$ in eq. (14) is proportional to $\Theta^{\alpha\beta}$, the energy momentum tensor, which must have dimension 4.[12] (For a more detailed discussion, see ref. 2). In case the n = 0 moment of the difference between proton and neutron is also q^2 independent, $T^{\alpha\beta}$ must include an isovector part of dimension 4. This is the situation at present experiments, with the value for the neutron integral about $\frac{2}{3}$ of the proton,[5] and the latter 0.16 ± 0.02 (the error includes extrapolition for $\omega \geq 20$). In the "asymplotically free" gauge theories[10] that difference decreases like a power of $\frac{1}{\ln(-q^2)}$.

Note that if $\frac{d\delta_n}{dn}$ vanishes at a point $n = n_1$, it has to vanish for all $n \geq n_1$, which means $\delta_n = \delta_{n_1}$ for $n \geq n_1$. In this case, we must have δ_n = (const.) for all n, otherwise T_2 would not satisfy an unsubtracted dispersion relation. This is so since now $t_n(x) = t_{n_1}(x)$ for $n \geq n_1$ in eq. (14) (now discussing integer n only), and thus only a finite number of terms, those with $n < n_1$, may have a different singularity. But, as we saw before, any finite number of terms does not contribute to the imaginary part, and due to their different (q^2) behaviour, they cannot be combined with the rest, the terms with $n \geq n_1$ (the latter having the same q^2 behaviour). Thus either all $\delta_n \equiv 0$, in which case we have Bjorken scaling, or they are all different. The strongest variation of δ_n with n is δ_n = (const.) n, corresponding to a vanishing second derivative. An example when such a behaviour is achieved is

$$F_2(\omega, q^2) \sim \omega^2 \delta\ (\omega - [f(q^2)]^\delta) \tag{22}$$

in which case $\delta_n = -(2\delta)n$. Another example,

$$F_2(\omega, q^2) \sim \Theta\ (\omega - [f(q^2)]^\delta) \tag{23}$$

Here $\delta_n = -(2n+1)\ \delta$, which means that the n = 0 integral does not scale. For fixed q^2, $F_2(\omega, q^2) \xrightarrow[\omega \to \infty]{} 1$ here.

A straightforward consequence of a behaviour like in eq. (21) is that, for any fixed interval $\omega_1 \leq \omega \leq \omega_2$, $F_2(\omega_1 q^2)$ has to decrease with q^2 at least as fast as $\left[f(q^2)\right]^{\delta_\infty}$. For assume $F_2(\omega, q^2) \geq G(q^2)$ for $\omega_1 \leq \omega \leq \omega_2$. Then $\int_1^\infty \frac{F_2(\omega', q^2)}{\omega'^{2n+2}}\, d\omega' \geq G(q^2) \int_{\omega_1}^{\omega_2} \frac{d\omega'}{\omega'^{2n+2}} = I_n\, G(q^2)$, which implies that $G(q^2)$ has to be smaller than $\left[f(q^2)\right]^{\delta_n}$ for any n. This also shows that for any given n, the contribution to the left hand side of any finite interval in ω is eventually negligible (when $(-q^2)$ becomes large enough).

We thus see that, starting from a certain $(-q^2) = K^2$, an increase in $(-q^2)$ implies a decrease of $F_2(\omega, q^2)$ for $\omega \leq \omega_m(K^2)$, and an increase for $\omega \geq \omega_m(K^2)$. This is so since $\int_1^\infty \frac{F_2(\omega', q^2)}{\omega'^2}\, d\omega'$ is q^2 independent. However, the point $\omega_m(K^2)$ has to increase for increasing K^2, since for each fixed ω the function $F_2(\omega, q^2)$ has eventually to decrease. Thus the above changes at low ω should be the place to check experimentally, since low ω means higher available $(-q^2)$ for a given incident beam energy, and the rate of decrease at low ω should be as strong as the increase at high ω.[13]

The rates of change with $(-q^2)$ for a certain ω are given by the strength of the function $f(q^2)$ and by the values of δ_n. As an example, let us consider

$$\delta_n = -a\left[1 - \frac{6}{(2n+2)(2n+3)}\right] \tag{24}$$

which has $\delta_0 = 0$, $\delta_\infty = -a$. Similar n dependence, with $f(q^2) = (-q^2)$, is obtained by summing ladders in a pseudoscalar Yukawa coupling field theory.[14] We get (see appendix),

$$F_2(\omega, q^2) \approx F_2(\omega, K^2) + 6a\left[\ln \frac{f(q^2)}{f(K^2)}\right]\left\{\frac{1}{\omega^2}\left[\int_1^\omega d\omega'\,(\omega - \omega')\,F_2(\omega' K^2)\right] - \frac{1}{6}\,F_2'(\omega, K^2)\right\} \tag{25}$$

for q^2 near enough to K^2 (the expansion is in powers of $\left[a \ln \frac{f(q^2)}{f(K^2)}\right]$).[15] For $F_2(\omega\, K^2) \xrightarrow[\omega \to \infty]{} C_\infty$, the term in the curly brackets in eq. (25) tends to $\frac{1}{3} C_\infty$. For $F_2(\omega\, K^2) \sim C_0\,(\omega - 1)^m$ as $\omega \to 1$, the curly brackets tend to $-\frac{1}{6} C_0\,(\omega - 1)^m$. We thus see the decrease with increasing $(-q^2)$ for low ω, and the increase for high ω.

Acknowledgement

It is a pleasure to acknowledge discussions with J. D. Bjorken.

APPENDIX

We consider

$$\int_1^\infty \frac{F_2(\omega' q^2)}{\omega'^{2n+2}}\,d\omega' \sim K_n\,[f(q^2)]^{\delta_n} \tag{A1}$$

with

$$\delta_n = -a\left[1 - \frac{6}{(2n+2)(2n+3)}\right] \tag{A2}$$

start from

$$\int_1^\infty \frac{F_2(\omega' q^2)}{\omega'^{2n+2}}\,d\omega' \sim K_n\,[f(q^2)]^{\delta_n} = K_n\,[f(K^2)]^{\delta_n}\left[\frac{f(q^2)}{f(K^2)}\right]^{\delta_n}$$

$$\approx K_n\,[f(K^2)]^{\delta_n}\left[1 + \delta_n \ln \frac{f(q^2)}{f(K^2)}\right]$$

for q^2 near enough to a certain fixed K^2. Write

$$F_2(\omega, q^2) = F_2(\omega, K^2) + f(\omega, q^2) \ln \frac{f(q^2)}{f(K^2)} \tag{A3}$$

Then

$$\int_1^\infty \frac{f(\omega' q^2)}{\omega'^{2n+2}}\,d\omega' \sim K_n \delta_n\,[f(K^2)]^{\delta_n}$$

Take now

$$f(\omega, q^2) = -a\,F_2(\omega, K^2) + g(\omega, q^2) \tag{A4}$$

Then

$$\int_1^\infty \frac{g(\omega, q^2)}{\omega'^{2n+2}}\,d\omega' \sim \frac{6a}{(2n+2)(2n+3)}\,K_n\,[f(K^2)]^{\delta_n}$$

$$\int_1^\infty \omega'^2 g(\omega' q^2)\left[\frac{d^2}{d\omega'^2}\,\omega'^{-(2n+2)}\right]d\omega' \sim (6a)\,K_n\,[f(K^2)]^{\delta_n}$$

Thus

$$\frac{d^2}{d\omega^2}\ [\ \omega^2\ g\ (\omega\ q^2)\ ]\ =\ (6a)\ \ F_2\ (\omega,\ K^2)$$

and

$$\omega^2\ g\ (\omega,\ q^2)\ =\ (6a)\ \int_1^{\omega} d\omega'\ \int_1^{\omega'} d\omega''\ \ F_2\ (\omega''\ K^2)\ =$$

$$=\ (6a)\ \int_1^{\omega} d\omega'\ \ (\omega - \omega')\ F_2\ (\omega'\ K^2)$$

Thus, finally

$$F_2\ (\omega, q^2)\ \approx\ F_2\ (\omega, K^2)\ +\ 6a\ \left[\ln \frac{f\ (q^2)}{f(K^2)}\right] *$$

$$* \left\{\frac{1}{\omega^2}\ \ \left[\int_1^{\omega} d\omega'\ (\omega - \omega')\ \ F_2\ (\omega'\ K^2)\right] -\ \frac{1}{6}\ \ F_2\ (\omega, K^2)\right\} \qquad (A5)$$

REFERENCES

1. Y. Frishman, Rapporteur talk at the XVI International Conference on High Energy Physics, Chicago - NAL, September, 1972, Vol. IV, p. 119.
2. Y. Frishman: "Light Cone and Short Distances", to appear as a Physics Reports.
3. J. D. Bjorken, Phys, Rev. 179 , 1547 (1969).
4. Y. Frishman, Annals of Physics 66 , 373 (1971).
5. For reviews of the experimental situation in electron-nucleon scattering see: H. Kendall, in Proceedings of the 1971 International on Electron and Photon Interactions at High Energies (Cornell); E. D. Bloom, Talk at the International Conference on High Energy Particle Collisions, Vanderbilt Univ. (1973). Calt - 68 - 392.
6. K. Wilson, Phys. Rev. 179, 1499 (1969).
7. D. J. Gross and S. B. Treiman, Phys. Rev. D4 , 1059 (1971).
8. J. D. Bjorken, Phys. Rev. 148 , 1467 (1966); K. Johnson and F. E. Low, Prog. Theor. Phys. (Kyoto) Suppl. 37 - 38 , 74 (1966).
9. D. J. Gross and F. Wilczek, Phys. Rev. Letters 30, 1343 (1973); H. D. Politzer, Phys. Rev. Letters 30, 1346 (1973).
10. D. J. Gross and F. Wilczek, NAL-PUB-73/49 - THY (1973).
11. O. Nachtman, Institute for Advanced Study, Princeton, Preprint (1973).
12. S. Cicciarello, R. Gatto, G. Sartori and M. Tonin, Phys. Letters 30B , 546 (1969).
13. R. Carlitz and W. K. Tung, University of Chicago preprint EFI 73/10, argue that high ω are the place to look, since $F_2(\omega, q^2) \propto (-q^2)^{-(\lambda_\alpha)}\ \omega^{\alpha-1}$ there. However, as we saw, such a behaviour cannot start from a fixed ω_o , since that would mean that all moments have the same q^2 behaviour. Thus that behaviour should start from $\omega \geq \omega_o\ (q^2)$, with $\omega_o\ (q^2)$ increasing with q^2. Thus, experimental checks would favor low ω with a higher $(-q^2)$ range.
14. S. J. Chang and P. M. Fishbane, Phys. Rev. D2 , 1084 (1972).

15. A similar formula, for the case $f(q^2) = (-q^2)$, was used by G. Parisi, Phys. Letters 43B, 207 (1973). He takes $d_n = -\left(\frac{1}{2} A\right) \left[1 - \frac{12}{(2n+3)(2n+4)}\right]$, and argues that $A \lesssim \frac{1}{2}$ from experiment $\left(|d_\infty| \lesssim \frac{1}{4}\right)$.

CLNS 227
May 1973

NOTE: **"Results on Electro-Rho Production at Cornell" was based on CLNS-227 (Phys. Rev. Letters 31, 131 (1973) and included material from both "Inclusive Proton Distributions in Electroproduction," Phys. Rev. Letters 29, 1409 (1972) and "Inclusive Pion Distributions in Electroproduction" Phys. Rev. Letters 29, 743 (1972). All three papers appear here in their entirety at the request of the lecturer, K. Berkelman.**

VECTOR MESON ELECTROPRODUCTION AT HIGH Q^2*

L. Ahrens, K. Berkelman, G.S. Brown, D.G. Cassel, W.R. Francis, P.H. Garbincius, D. Harding, D.L. Hartill, J.L. Hartmann, R.L. Loveless, R.C. Rohlfs, and D.H. White

Cornell University
Laboratory of Nuclear Studies
Ithaca, NY 14850

and

A.J. Sadoff

Ithaca College
Physics Department
Ithaca, NY 14850

ABSTRACT

We have measured ρ°, ω, and ϕ electroproduction over a range of virtual photon four-momentum Q^2 from 0.4 to 2.2 GeV^2 and for photon energies ν from 2.7 to 8.6 GeV. We find that the slope of the t (momentum transfer) dependence of the ρ° and ω forward peak decreases with increasing Q^2 to less than half of the photoproduction slope.

*Work supported by the National Science Foundation

The diffractive photoproduction of vector mesons has yielded valuable information on the hadronic interactions of photons at high energies.[1] In this experiment we extend the investigation to spacelike photons ($q^2 = -Q^2 < 0$) and explore the contribution of such diffractive channels to deep inelastic electron scattering.

The extracted beam of the Cornell electron synchrotron passed through a 1.3 cm liquid hydrogen target and into a Faraday cup monitor. Electrons scattered at 8.4° with momenta above about 3 GeV/c were observed with a 2 msterad spectrometer consisting of a bending magnet, wire spark chambers, scintillators, a threshold gas Cerenkov counter, and a lead-lucite shower hodoscope. Protons recoiling on the opposite side of the beam, between the angles 40° and 90°, were observed with a second spectrometer consisting of a wide-aperture bending magnet, wire spark chambers, and scintillation counters. The protons were identified by momentum and time of flight.

We made measurements with three beam energies: 8, 10, and 11.8 GeV. The data were grouped into Q^2 and ν bins (Table I) , and corrected for target wall background (<35%), random coincidences (<8%), pion contamination in each spectrometer (<50%), wire chamber inefficiencies (~10%), and geometric acceptance. From the ep coincidence cross sections we derive cross sections $d\sigma/dm_x^2 dt d\phi\ (Q^2, \nu, \varepsilon, m_x^2, t, \phi)$ for the reaction $\gamma_{virtual} + p \rightarrow p + x°$, dividing by the usual virtual photon flux factor.[2] Here t is the four-momentum-squared from $\gamma_{virtual}$ to the missing mass x°, and ϕ is the production azimuth around the virtual-photon axis.[3]

Fig. 1a shows $d\sigma(m_x^2)/dm_x^2 dt$ for a sample bin in Q^2, ν, and t. The experimental resolution in m_x^2 varied from typically 0.03 GeV² (r.m.s.) at low t to 0.1 GeV² at high t, not quite narrow enough to separate ρ° and ω contributions. The apparatus acceptance was generally uniform for $-t > 0.075$ GeV² and for m_x^2 up to a limit which exceeded 0.8 GeV² and increased with increasing ν.

For each bin in Q^2, ν, and t we fit the m_x^2 spectrum to a sum of four contributions: (1) a peak at $m_x^2 = 0$ with a width consistent with experimental resolution, corresponding to radiative ep scattering and a relatively small contribution from single π° electroproduction;[4] (2) a peak at $m_x^2 \sim 0.6$ GeV² from ρ° and ω electroproduction; (3) a φ peak at m_x^2 1.04 GeV²; and (4) a continuum[5] starting at $m_x^2 = 4\, m_\pi^2$. The shape of the ρ, ω peak used in the fitting is fixed by starting with a relativistic Breit-Wigner with a p-wave width,[7] multiplying by a generalized Ross-Stodolsky factor[8] $(m_\rho^2 + Q^2 - t)^2/(m_x^2 Q^2 - t)^2$, adding on an ω peak with an area fixed at 15% of the ρ peak,[9] and folding in the effect of the calculated experimental resolution and the radiative correction.[10]

Fig. 1b shows $d\sigma_{\rho\omega}(t)/dt$ plotted for two representative choices of Q^2 and ν. Each t distribution has been fitted to an exponential form, $d\sigma_{\rho\omega}/dt = (d\sigma_{\rho\omega}/dt)_{t=0} e^{Bt}$; the results are listed in Table I. In Fig. 2b we show the ρ° and ω cross section (the exponential fit integrated from t_{min} to t_{max}), divided by the total virtual photon absorption cross section,[11] plotted against Q^2 and compared with the transverse

vector dominance model,[12]

$$\sigma_{\rho\omega}(Q^2,s) = m_\rho^4(Q^2+m_\rho^2)^{-2}\exp(Bt_{min})\sigma_{\rho\omega}(0,s).$$

Although there is no compelling evidence in the data for any deviations from a simple exponential in t, it is clear from Table I that the t-slope B varies with Q^2 and ν. A decrease in the slope has been predicted[13] for diffractive photoproduction as the photon makes the transition from $Q^2 = 0$, where it has an effective hadronic "size" determined by its virtual vector meson components, to large spacelike Q^2, where the lifetime[14] $2\nu/(Q^2 + m_v^2)$ of the vector meson intermediate state (set by the uncertainty principle) becomes short and the photon-proton interaction becomes more nearly pointlike. In Fig. 2a we have plotted the measured slopes against the dimensionless inverse lifetime parameter $x_\rho = (Q^2+m_\rho^2)/2M\nu$ The data indicate that the slope decreases to less than half of its photoproduction value.

The ratio of the ϕ yield to the ρ° and ω yield, averaged over all our data above $s = 6$ GeV^2, is $2.3 \pm 0.5\%$, about half of the ratio observed in photoproduction at $s = 16$ GeV^2.[1]

We are indebted to F.M. Pipkin and collaborators for their generous loan of the electron spectrometer, and to D.R. Yennie for helpful suggestions on the analysis.

FOOTNOTES

1. For a recent review, see G. Wolf, Proceedings of the 1971 International Symposium on Electron and Photon Interactions at High Energies, edited by N.B. Mistry (Cornell University, Ithaca, NY, 1972)

2. For definitions of the virtual photon flux and polarization ε, see Ref. 1 page 264. We ignore the possible ε dependence of the virtual-photon cross section over the range of this experiment.

3. The experimental aperture covers photon azimuths ϕ within about 30° of the electron scattering plane on the side of the virtual-photon line opposite from the outgoing electron. In a separate experiment (to be described in detail elsewhere), using a scintillator hodoscope to detect recoil protons on both sides of the beam, we have established that the azimuthal asymmetry is zero within 15%. We will therefore integrate over ϕ assuming no ϕ dependence.

4. The zero-missing-mass yields are consistent with known radiative ep scattering cross sections and estimates of π° electroproduction. An estimate of the two-photon radiative tail of the one-photon peak is included in the fitting, but is generally too small to be significant.

5. The continuum is fitted to $a\sqrt{m_X^2-4m_\pi^2}$; higher order terms do not affect the vector meson results. The continuum yield (Fig. 1 is typical) has a generally smooth dependence on the kinematic variables and a flatter t dependence than ρ° and ω production. It is

similar to the proton missing mass continuum in photoproduction (Ref. 6), and is presumably a mixture of $\Delta\pi$ and nonresonant $p\pi\pi$ and $p\pi\pi\pi$ final states.

6. G.E. Gladding et al. (to be published). We are indebted to M.J. Tannenbaum for sending us the data before publication.

7. J.D. Jackson, Nuovo Cimento 34, 1644 (1964) we use m_ρ = 0.765 GeV and Γ_o = 0.143 GeV.

8. M. Ross and L. Stodolsky, Phys. Rev. 149, 1172 (1966). The Q^2 and t dependence used here was suggested by D.R. Yennie (private communication).

9. This is the ω/ρ^o ratio in photoproduction in the same energy range (see Refs. 1 and 6) and is consistent with the available ω electroproduction data: J. Ballam et al., contribution to the XVI International Conference on High Energy Physics, Chicago, 1972. Our fits are insensitive to this ratio.

10. A. Bartl and P. Urban, Acta Physica Austriaca 24, 139 (1966). Radiative effects lower the ρ,ω peak somewhat and add on a tail extending to higher masses.

11. Taken from the fit of F.W. Brasse et al., Nucl. Phys. B39, 421 (1972).

12. See, for example, H. Fraas and D. Schildknecht, Nucl. Phys. B14, 543 (1969). $s = 2M\nu + M^2 - Q^2$ is the square of the total hadron center-of-mass energy. We have included only the transverse contribution. According to Ref. 12, the longitudinal contribution is about 45% of the transverse at $Q^2 = m_\rho^2$. No longitudinal-transverse separation is made in the present experiment

13. H. Cheng and T.T. Wu, Phys. Rev. 183, 1324 (1969).

14. B.L. Ioffe, Soviet Physics - JETP Letters 9, 97 (1969) and Phys. Letters 30B, 123 (1969); H.T. Nieh, Phys. Letters 38B, 100 (1972).

15. J.T. Dakin et al., Phys. Rev. Letters 38B, 100 (1973).

16. V. Eckardt et al., Phys. Letters 43B, 240 (1973).

17. J. Ballam et al., Phys. Rev. D5, 545 (1972).

TABLE I

Cross sections and slopes for $\gamma_{virtual} + p \to p + \rho^\circ$ or ω.

Q^2 (GeV^2)	ν (GeV)	$d\sigma/dt$ at t=0 (μb/GeV^2)	B (GeV^{-2})
0.43	5.2	31±5	6.3±0.8
0.59	4.4	22±3	5.4±0.6
0.61	6.8	16±7	6.4±3.7
0.74	8.6	17±9	6.4±3.0
0.78	3.5	22±3	5.8±0.5
0.80	6.0	10±2	4.4±0.9
0.99	2.7	14±3	2.7±0.4
0.99	7.6	7.4±1.9	4.3±1.1
1.06	4.9	9.7±1.8	4.8±0.5
1.36	6.4	4.7±0.9	3.2±0.6
1.37	3.8	9.4±1.5	3.8±0.4
1.78	5.1	7.2±2.5	4.8±1.0
2.23	3.8	1.1±1.4	1.2±1.8

FIGURE CAPTIONS

Fig. 1 (a) Missing mass spectrum for one choice of Q^2, ν, and t. The curve shows the best fit to the γ, $\rho^\circ + \omega$, and ϕ peaks plus continuum, including the effects of radiation and experimental resolution. (b) Distribution in t for ρ° and ω production at two sample Q^2 ν values. Errors are statistical only.

Fig. 2 (a) Measured slope of the t distribution for ρ° and ω production plotted against x_ρ (see text). SLAC, DESY, and SLAC-LBL-Tufts (photoproduction) data are from Ref. 15-17. (b) Relative cross section versus Q^2 compared with a VMD prediction (see text).

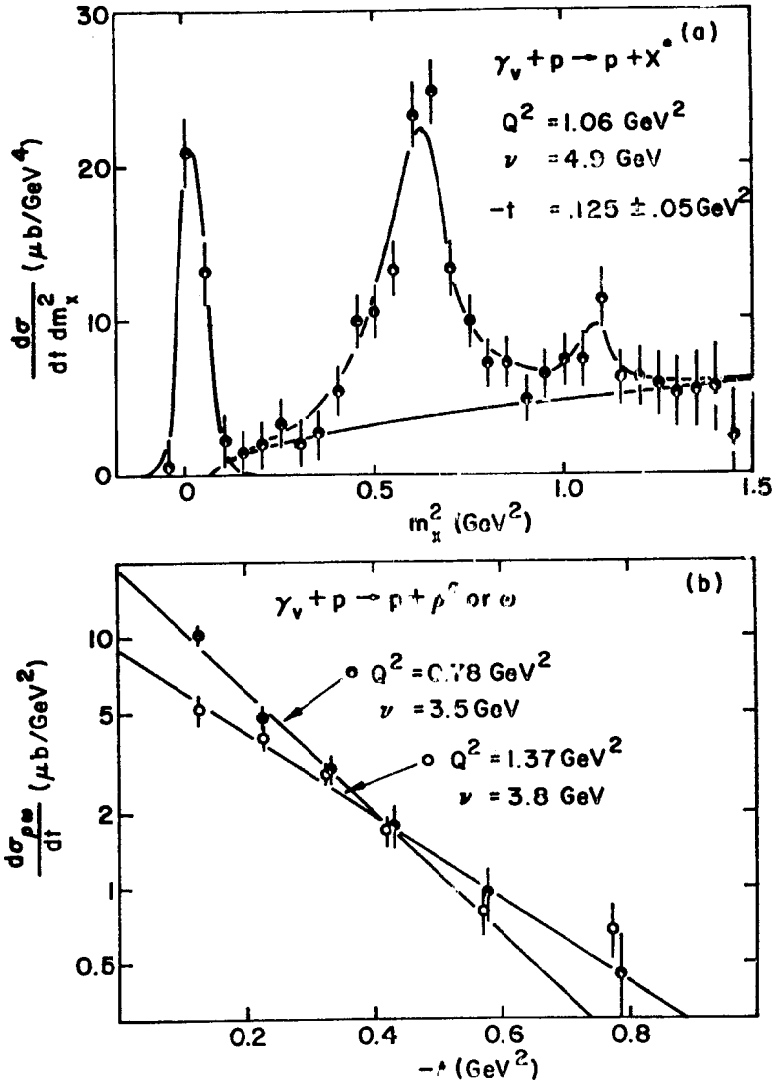

Figure 1

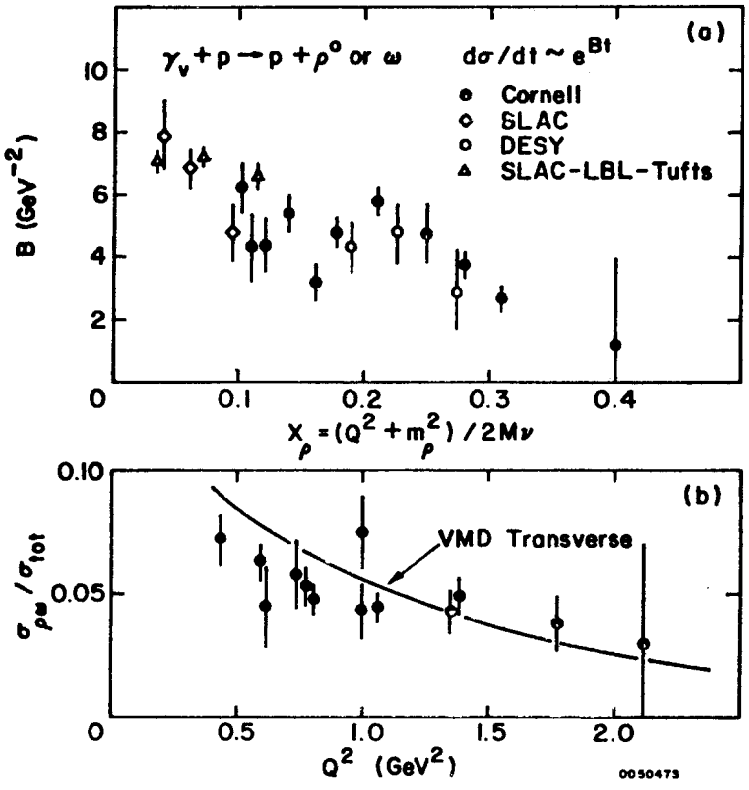

Figure 2

CLNS-191
August 1972

Inclusive Proton Distributions in Electroproduction*

E. Lazarus†, D. Andrews‡, K. Berkelman, G. Brown, D.C. Cassel,
W.R. Francis, D.L. Hartill, J.L.Hartmann, R.M. Littauer,
R.L. Loveless, R.C. Rohlfs, and D.H. White

Laboratory of Nuclear Studies
Cornell University
Ithaca, New York 14850

and

A.J. Sadoff
Physics Department
Ithaca College
Ithaca, New York 14850

ABSTRACT

Measurements are reported for the process $e+p \to e+p+$anything at $Q^2 = 0.3$, 0.6, and 1.2 GeV^2. Protons are produced predominantly backward in the center of mass frame, with average transverse momenta increasing with Q^2.

*Work supported by the National Science Foundation

†Present address: Brookhaven National Laboratory
Upton, Long Island, New York 11973

‡Present address: Department of Physics, University of Rochester
Rochester, New York 14627

To supplement the recent data on deep inelastic electron scattering[1] we have measured the distribution of recoil protons from the forward electroproduction of high-mass meson states. Electrons from the external beam of the Cornell synchrotron, inelastically scattered from protons at angles and energies corresponding to four-momentum transfer $Q^2 = 0.3$, 0.6, 1.2 GeV^2 and final-state hadron effective mass $W = 3.0$ GeV, were detected in a focussing magnetic spectrometer system[2]. In coincidence, protons emitted between about 45° and 80° laboratory angle were detected in a spark chamber array behind a large aperture bending magnet. Protons were identified by momentum and time-of-flight. Momenta above 230 MeV/c were detected. Data were corrected for detection efficiencies, geometric acceptance[3], random coincidences, and target wall background. Radiative effects have been estimated[4] and are small, but no correction has been made to the data.

For each electron-proton event we compute the missing mass m_x in the reaction $e + p \to e + p + x^\circ$, and the four-momentum transfer t (the square of the difference between the initial and final proton four-momenta). In terms of the virtual photon reaction, γ (virtual) $+ p \to p + x^\circ$, Q^2 is the spacelike photon mass squared, W (or $s^{1/2}$) is the total center-of-mass energy, m_x is the effective mass of the missing mesonic state, and t is the familiar momentum transfer variable.

The spectrum of missing masses below $m_x^2 = 0.8$ GeV^2 is dominated by the radiated photon peak at $m_x^2 = 0$, and by the ρ° and ω peak[5] at $m_x^2 \simeq 0.6$ GeV^2. The geometric aperture of the

detection system imposes an upper limit near $m_x^2 = 2.0$ GeV^2. Fig. 1 shows the Q^2, m_x^2, and t dependence of the virtual photon differential cross section[6] $d\sigma/dm_x^2 dt d\phi$ in the range $0.875 \leq m_x^2 \leq 1.875$ GeV^2. The spectrum is flat in m_x^2 over the range displayed, with no evidence (even with finer m_x^2 bins) for production of ϕ, A_1, etc. The t distributions are rather gradual, fitting a form e^{Bt} with B essentially independent of m_x^2 and decreasing somewhat with Q^2. B = 2.6±0.2, 2.2±0.2, and 1.8±0.2 GeV^{-2} at $Q^2 = 0.3$, 0.6, and 1.2 GeV^2 respectively (averaged over m_x^2). The Q^2 dependence is more striking when compared with the value B ≃ 4.0 GeV^{-2}, obtained at the same W and m_x^2 in photoproduction[7]. It has been suggested[8] that a decrease in B with increasing Q^2 would be evidence for "shrinking" of the photon as it makes the transition from a vector-meson-dominant real photon to a pointlike deep inelastic photon.

To study the Q^2 dependence of the cross section, we integrate over ϕ (assuming no ϕ variation), integrate over t (from the kinematic limit $t_{min} \approx -((Q^2+m_x^2)/2\nu)^2$, assuming the best exponential fit), and average over m_x^2 to get $d\sigma/dm_x^2$. We plot the integral in Fig. 2 as a function of Q^2. For comparison we have included data at $Q^2=0$ from photoproduction[7] at the same W and two values of m_x^2. Since there is an apparent m_x^2 dependence in the photoproduction cross section that is not seen in the electroproduction data, it is difficult to make general statements about the Q^2 dependence. However,

it seems clear that $d\sigma/dm_x^2$ is closer to the gradual Q^2 dependence of the total γ (virtual) + p cross section[1] (solid curve) than to the prediction of naive rho dominance (dashed curve).

The spectra in m_x^2 and t can be transformed into distributions in the proton momentum components in the center of mass, p_L (along the virtual photon direction) and p_T (transverse). The resulting invariant cross sections $2E d\sigma/dp_L dp_T^2 d\phi$ are flat in p_L and approximate the form a exp $(-b\ p_T^2)$, with a = 72±4, 41±2, and 20±2 μb/GeV^2 and b = 3.2±0.2, 2.7±0.2, and 2.4±0.2 GeV^{-2} for $Q^2 = 0.3$, 0.6, and 1.2 GeV^2, respectively. At $Q^2 = 1.15$ GeV^2, W = 2.63 GeV there are corresponding data for the forward hemisphere[9]. The $p_T = 0$ cross sections are plotted against $x = p_L/p_{max}$ and compared in Fig. 3. It is clear that protons are emitted predominantly in the backward hemisphere in the center-of-mass of the virtual-photon-proton collision, in contrast to some parton model predictions[10]. If the invariant cross section is actually flat throughout the backward hemisphere, as it appears to be in Fig. 3, then the corresponding m_x^2 distribution at $t = t_{min}$ is also flat out to the kinematic limit at $m_x^2 = (W-M_p)^2$. If we assume that B is also constant, it is then possible to extend our measured values of $d\sigma/dm_x^2$ (Fig. 2) and arrive at a rough estimate of the total cross section for γ(virtual) + p → p + x^0 for all $m_x^2 > 0.8$ GeV^2. The result is typically 40% of the total γ(virtual) + p cross section. The remaining 60% is presumably accounted for[11] by meson states below $m_x^2 = 0.8$ GeV^2 and by neutron final states.

FOOTNOTES

1. G. Miller, et al., Phys. Rev. D5, 528 (1972).
2. The apparatus is described in somewhat more detail by E. Lazarus, et al., Phys. Rev. Letters 29, 743 (1972).
3. At each of the three Q^2 values two runs were taken with different positions of the proton spark chambers, in order to extend the range in m_x^2. The data from the two geometries were combined after taking account of the geometric acceptances.
4. The soft photon (real and virtual) correction has been estimated using a modified form of the prescription given by A. Bartl and P. Urban, Acta Physica Austriaca 24, 139 (1966). The contribution of hard radiation events ($x^\circ = \pi^\circ+\gamma$) from the nucleon resonance region was estimated with a Monte Carlo technique using a reasonable model for resonance electroproduction. Soft radiation merely shifts the overall cross section normalization slightly; the hard radiation effect is completely negligible in our detection aperture.
5. A plot of the complete mass spectrum from a preliminary analysis of this experiment is given in the Proceedings of the 1971 International Symposium on Electron and Photon Interactions at High Energies, (Cornell University, Ithaca, New York, 1972), edited by N. B. Mistry, p. 273. The final results on the ρ° and ω contribution will be given in a separate report. Qualitatively, the conclusions of an earlier experiment, D. Andrews, et al., Phys. Rev. Letters 26, 864 (1971), are confirmed by the newer $\rho^\circ+\omega$ data.
6. The usual virtual photon flux factor Γ has been divided out of the measured electroproduction differential cross section. ϕ is the azimuthal angle of the state x° about the virtual photon line.
7. G.E. Gladding, J.J. Russell, M.J. Tannenbaum, J.M. Weiss, and G.B. Thomson, (unpublished). We are indebted to M.J. Tannenbaum for useful discussions and information on their results before publication.
8. H. Cheng and T.T. Wu, Phys. Rev. 183, 1324 (1969); R.W. Griffith, Phys. Rev. 188, 2112 (1969); J.D. Bjorken, J.B. Kogut, and D.E. Soper, Phys. Rev. D3, 1382 (1971).
9. F.W. Brasse, W. Fehrenbach, W. Flauger, K.H. Frank, J. Gayler, V. Korbel, J. May, P.D. Zimmerman, and E. Ganssauge, DESY preprint 71/19 (unpublished).
10. For example, see S.D. Drell, D.J. Levy, and Tung-Mow Yan, Phys. Rev. Letters 22, 744 (1969); and 24, 855 (1970).
11. The assumption has been made throughout this paper that there is no dependence of the cross sections on ϕ. The detection aperture in ϕ is not large enough to check this. In principle, since the virtual photon is polarized, it may be that the detected ϕ range is not representative of the average over ϕ.

FIGURE CAPTIONS

Fig. 1 Plots of $d\sigma/dm_x^2 dt d\phi$ for the reaction γ (virtual) + p→p + anything, as a function of m_x^2 and t for three values of Q^2. The units along the axes are the same for the three plots: m_x^2 and -t in GeV^2, cross sections in μb/GeV^4 (logarithmic scale).

Fig. 2 The average $d\sigma/dm_x^2$ over the range $0.875 \leq m_x^2 \leq 1.875$ GeV^2, as a function of Q^2. The points at $Q^2 = 0$ are taken from photoproduction (ref. 7). The curves are the total γ (virtual) + p cross section (solid) and the function $(Q^2+m_\rho^2)^{-2}\exp(Bt_{min})$ both renormalized to pass through the measured $d\sigma/dm_x^2$ at $Q^2 = 0.3$ GeV^2.

Fig. 3 The cross section $2Ed\sigma/dp_L dp_T^2$ at $p_T = 0$, $Q^2 = 1.2$ GeV^2, and W = 2.63 (DESY) or 3.0 (Cornell), plotted against $x = p_L/p_{max}$.

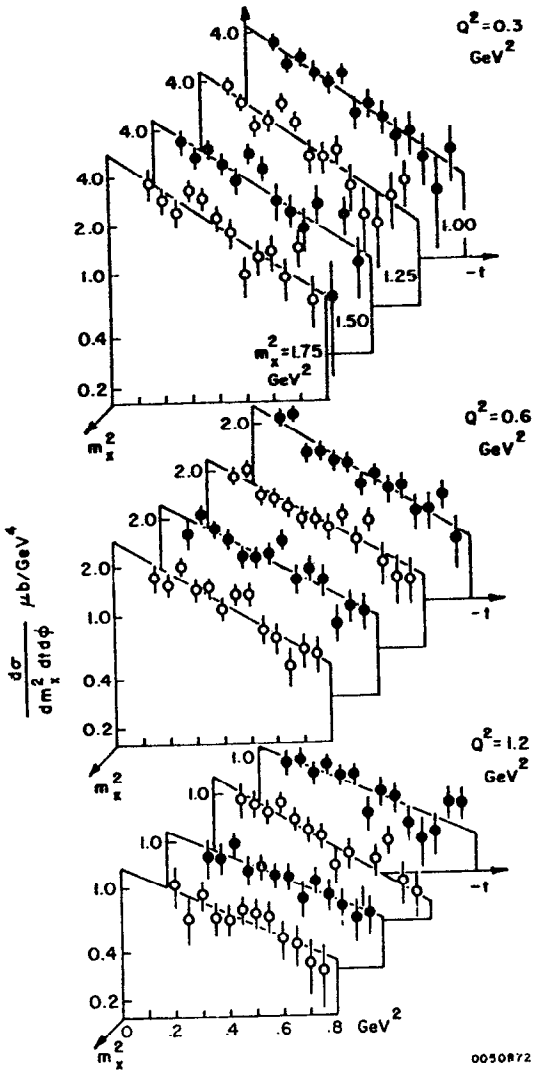

Fig. 1

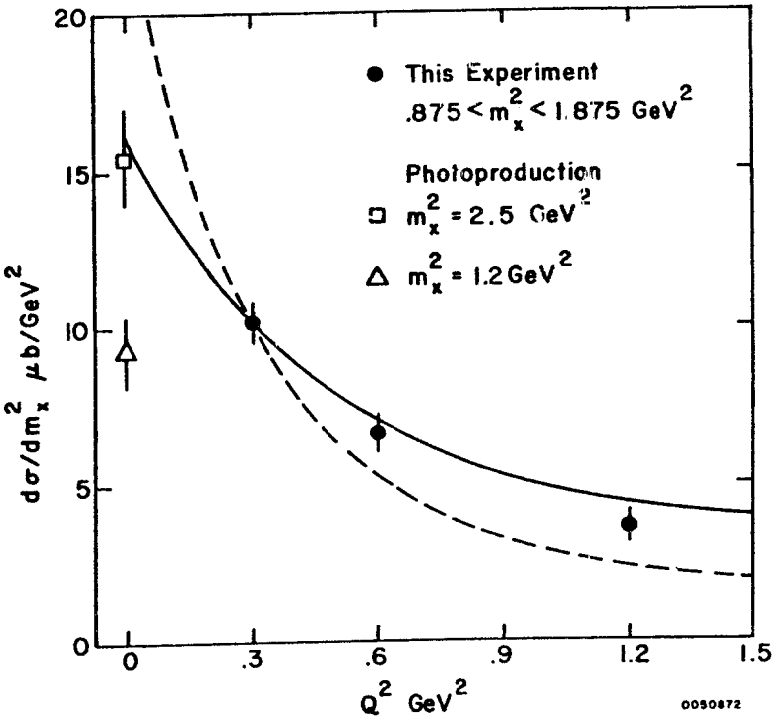
This Experiment
$.875 < m_x^2 < 1.875$ GeV^2
Photoproduction
$m_x^2 = 2.5$ GeV^2
$m_x^2 = 1.2$ GeV^2
$d\sigma/dm_x^2$ μb/GeV^2
Q^2 GeV^2
0050872

Fig. 2

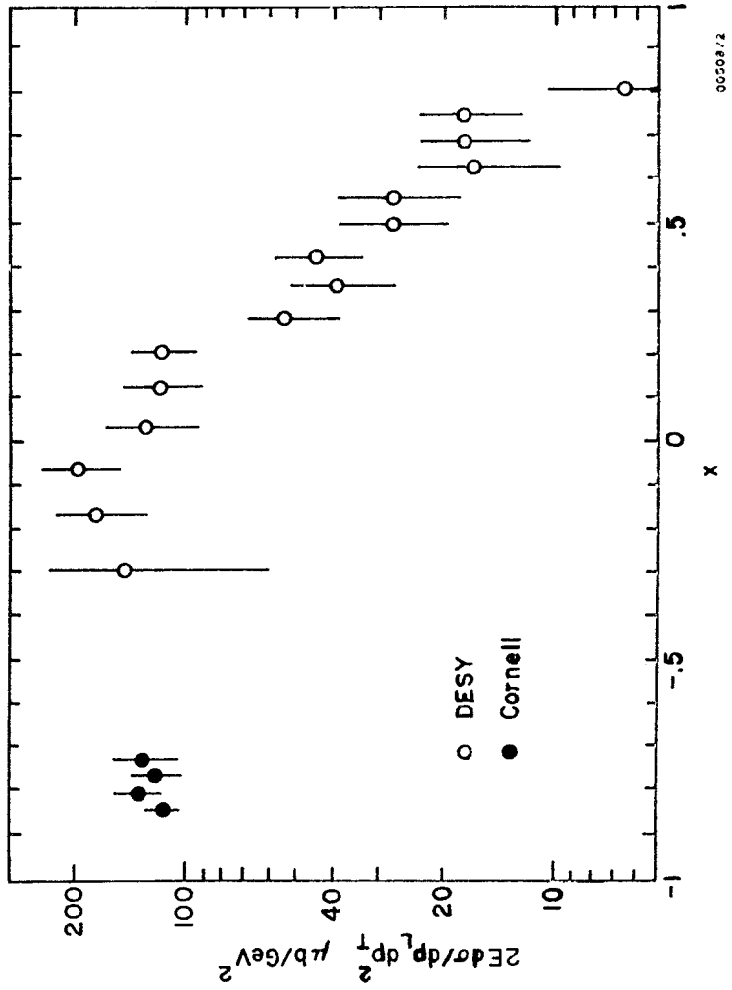
DESY
Cornell
$2E d\sigma/dp_L dp_T^2$ μb/GeV^2
x
005087.2

Fig. 3

CLNS - 190
July 1972

Inclusive Pion Distributions in Electroproduction*

E. Lazarus†, D. Andrews, K. Berkelman, G. Brown, D.G. Cassel,
W.R. Francis, D.L. Hartill, J. Hartmann, R.M. Littauer,
R.L. Loveless, R.C. Rohlfs, and D.H. White

Laboratory of Nuclear Studies,
Cornell University,
Ithaca, New York 14850
and
A.J Sadoff
Physics Department,
Ithaca College,
Ithaca, New York 14850

ABSTRACT

Measurements are reported for the process $e+p \to e+\pi^+ +$ anything.

*Work supported by the National Science Foundation

†Present address: Brookhaven National Laboratory
Upton, Long Island, New York 11473

The recent experimental data[1] on inelastic electron scattering at high energies have stimulated much theoretical speculation[2]. In the hope of learning more than can be obtained from electron data alone, we have measured the yield of positive pions in coincidence with the scattered electrons.

The external electron beam of the Cornell synchrotron struck a 2.7 cm liquid hydrogen target and was monitored in a Faraday cup. Inelastically scattered electrons passed through a spectrometer consisting of two quadrupoles and two bending magnets and were detected in eight proportional wire chamber planes, two scintillators, a freon gas Cerenkov counter, and a lead acetate shower Cerenkov counter.

Positive pions produced in the laboratory angle range between about 45° and 80° and at elevation angles within ± 10° passed through the aperture of a bending magnet, two wide-gap optical spark chambers, and a double bank of trigger scintillators. All momenta above 150 MeV/c were detectable. Pions were identified by comparing the measured time of flight with that calculated for the observed momentum and path length.

The electron four-momentum transfer Q^2 and the total center-of-mass energy W of the hadron final state are fixed by the incident and scattered electron energies and the scattering angle. These were chosen to correspond to Q^2 = 0.3, 0.6, and 1.2 GeV^2 with W centered on 3.0 GeV in each case. For each of the three Q^2 values, measurements were made with two positions of the pion spark chambers,

"forward" and "backward". Data were corrected for detection efficiencies, geometric acceptance, pion decays, random coincidences, and target-wall background. No radiative correction has been made.

For each event we compute p_L and p_T in the hadron final-state center-of-mass frame, with respect to the momentum transfer (virtual photon) direction. Fig. 1 shows the distribution of events in $x = p_L/P_{max}$ vs. p_T^2 for one of the six running conditions. The corresponding plots for the other five conditions look very similar, except that the detected region (defined by the pion chamber location) shifts to somewhat more positive x in the three "forward" measurements. The most striking feature of the data in each case is the rapid decrease in yield with increasing transverse momentum p_T.

This is seen more clearly in Fig. 2 where we plot the measured invariant cross sections[3] $2E\,d\sigma/dp_L dp_T^2 d\phi$ for the process γ (virtual) + p → π^+ + anything[4], versus the square of the transverse momentum[5], averaged over a band in x such as that indicated in Fig. 1. In each case the data are fit very well by the form $A \exp(-Bp_T^2)$; the best fit intercepts and slopes are given in Table I. Within statistical error (about 10%) all the data are consistent with $B = 9.5\ GeV^{-2}$. This corresponds to an r.m.s. transverse momentum of about 230 MeV/c for $Q^2 = 0.3$ to $1.2\ GeV^2$, $W = 3.0$ GeV, and small negative x. It has been suggested[6] that the photon-proton interaction may become more pointlike as the virtual photon becomes more

spacelike, resulting in an increase in the transverse momenta of the secondary products. No such increase is seen in the present data, although it is still possible that such an effect might be associated only with the virtual photon fragments in the forward hemisphere (x>o).

Since the present data were obtained at a fixed value of W ($=s^{1/2}$ for the γ (virtual) + p process), it is not possible to check for Feynman scaling[7]. To look at the Q^2 dependence we integrate the observed $2d\sigma/dx\,dp_T^2 d\phi$ over the appropriate x band, over all p_T^2 (assuming the best fit), and over ϕ (assuming no ϕ variation), then divide by the total γ (virtual) + p cross section for that Q^2 and W, obtained from the electron single-arm scattering data[1]. The result represents the average multiplicity of positive pions produced in the specified x range. This is shown in Fig. 3. It is interesting to note that although the yield shows the usual decrease with increasing |x|, there is little or no dependence[8] on Q^2. Apparently the increase in multiplicity suggested by some models[9] is not taking place at small negative x.

As a byproduct of this experiment, a limited amount of π^- data is available[10] centered on x = -0.3. Within the errors the p_T and Q^2 dependences are the same as in the π^+ case.

FOOTNOTES

1. G. Miller et al., Phys. Rev. D5, 528 (1972).
2. For several recent reviews of the abundant theoretical literature, see Proceedings of the 1971 International Symposium on Electron and Photon Interactions at High Energies (Cornell University, Ithaca, New York, 1972), edited by N.B. Mistry.
3. E is the pion energy in the center of mass of the γ (virtual) + p reaction; ϕ is the azimuth of the pion about the virtual photon direction. The factor 2 arises from the fact that the appropriate differential in transverse momentum is $1/2\ dp_T^2 = p_T\ dp_T$.
4. The usual virtual photon flux factor Γ has been divided out of the measured electroproduction differential cross section. For definition of Γ, see for example reference 2, page 264.
5. Although the pion detection system is sensitive beyond $p_T = .45$ GeV, such events are not included in the present analysis, since the separation between pions and other particles is less certain at the high momenta.
6. H. Cheng and T.T. Wu, Phys. Rev. 183, 1324 (1969); R.W. Griffith, Phys. Rev. 188, 2112 (1969); J.D. Bjorken, J.B. Kogut, and D.E. Soper, Phys. Rev. D3, 1382 (1971).
7. R.P. Feynman, Phys. Rev. Letters 23, 1415 (1969).

8. A preliminary analysis of the present data showed a possible increase with Q^2 (see reference 2, p. 276). This was based on a rather crude treatment of the geometric acceptance and is superseded by the analysis reported here.
9. See for example T.T. Chou and C.N. Yang, Phys. Rev. D4. 2005 (1971).
10. We are indebted to T. Killian for the analysis of the negative pion data.

TABLE I

Experimental results. $\Delta\sigma$ is the cross section for γ (virtual) + p → π^+ + anything, integrated over the specified x range. σ is the corresponding total cross section for γ (virtual) + p → anything, interpolated from data of reference 1. See text for other definitions.

Q^2 (GeV^2)	0.3	0.3	0.6	0.6	1.2	1.2
geometry	back	fwd	back	fwd	back	fwd
$E_{e,inc}$ (GeV)	7.5	7.5	9.5	9.5	10.0	10.0
$E_{e,scat}$ (GeV)	3.0	3.1	4.9	4.9	5.0	5.0
θ_e (degrees)	6.6	6.7	6.6	6.7	9.0	9.0
A (μb/GeV^2)	85±14	90±10	54±10	56±6	36±4	44±2
B (GeV^{-2})	8.4±1.8	9.9±1.1	9.4±1.9	9.3±.9	8.0±1.1	10.8±1.0
x_{min}	-0.15	-0.10	-0.15	-0.10	-0.15	-0.10
x_{max}	-0.10	-0.05	-0.10	-0.05	-0.10	-0.05
$\Delta\sigma$ (μb)	5.2±.5	5.6±.3	3.8±.3	3.8±.2	2.5±.1	2.7±.1
σ (μb)	77.3	76.4	52.7	52.0	33.4	33.0

FIGURE CAPTIONS

Fig. 1 Sample distribution of electroproduced π^+ in p_T^2 vs. x, in the virtual photon plus proton center-of-mass frame. The longitudinal axis is the virtual photon direction.

Fig. 2 Transverse momentum distributions for the three Q^2 values and two different ranges in x. W is fixed at 3 GeV.

Fig. 3 The number per virtual-photon-plus-proton event of π^+ produced into the specified x range, as a function of Q^2. This given by the ratio $\Delta\sigma/\sigma$ (Table I).

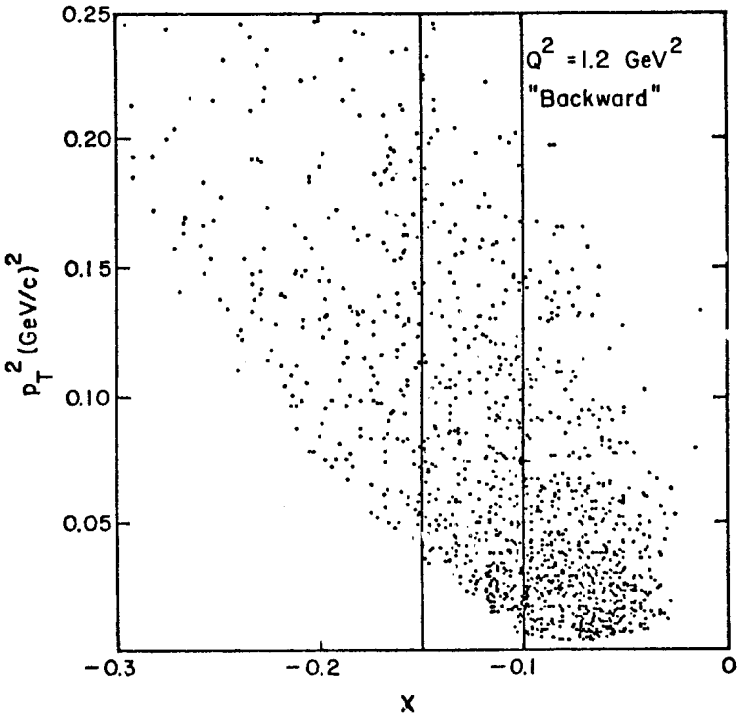
Q^2 = 1.2 GeV^2
"Backward"
p_T^2 (GeV/c)^2
X
0.25
0.20
0.15
0.10
0.05
−0.3
−0.2
−0.1
0

Fig 1

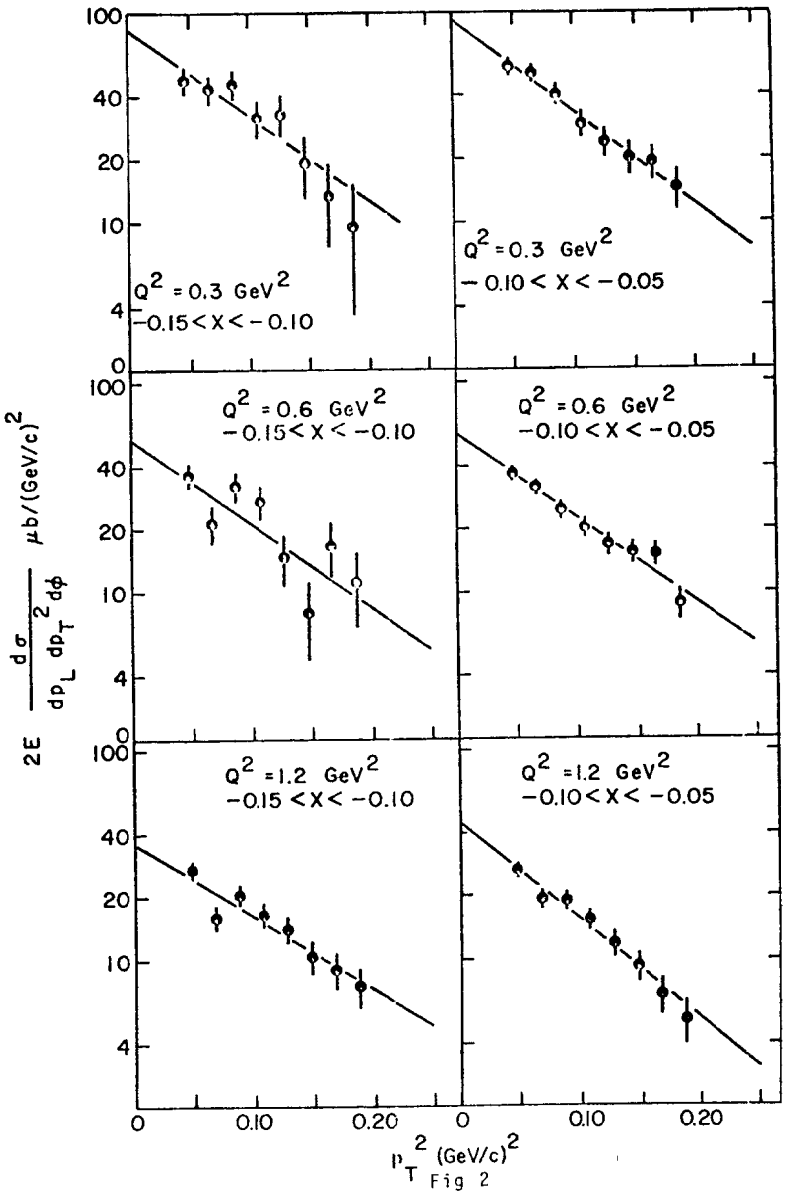
Q^2 = 0.3 GeV^2
−0.15 < X < −0.10
Q^2 = 0.3 GeV^2
−0.10 < X < −0.05
Q^2 = 0.6 GeV^2
−0.15 < X < −0.10
Q^2 = 0.6 GeV^2
−0.10 < X < −0.05
Q^2 = 1.2 GeV^2
−0.15 < X < −0.10
Q^2 = 1.2 GeV^2
−0.10 < X < −0.05
$2\varepsilon \frac{d\sigma}{dp_L\, dp_T^2 d\phi}$ μb/(GeV/c)^2
p_T^2 (GeV/c)^2
100
40
20
10
4
0
0.10
0.20

Fig 2

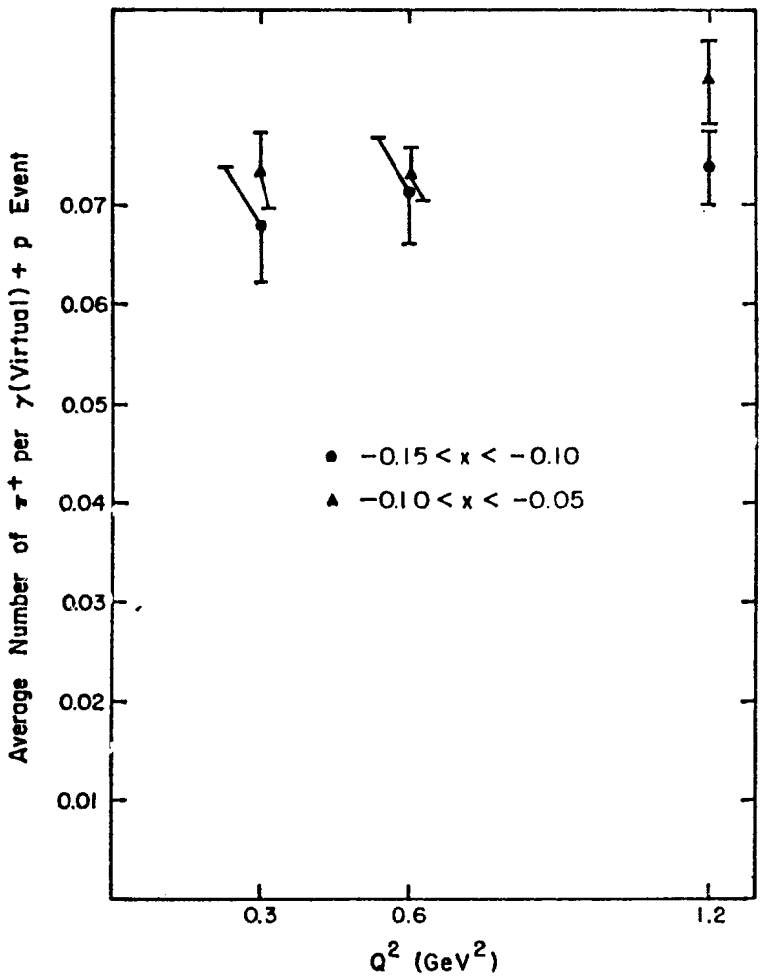
Average Number of π+ per γ(Virtual) + p Event
0.07
0.06
0.05
0.04
0.03
0.02
0.01
● −0.15 < x < −0.10
▲ −0.10 < x < −0.05
0.3
0.6
1.2
Q² (GeV²)

Fig 3

INCLUSIVE ELECTROPRODUCTION OF HADRONS FROM PROTONS AND NEUTRONS AND TESTS OF THE QUARK - PARTON MODEL*

G. J. Feldman

Stanford Linear Accelerator Center
Stanford University, Stanford, California 94305

Abstract

Data are presented on the inclusive electroproduction of hadrons from proton and neutron targets. The most striking behavior is the excess of positive to negative hadrons in the photon fragmentation region from both proton and neutron targets. It is shown that these charge ratios can be understood quantitatively in a reasonable quark-parton model. We investigate predictions of this model for charge ratios in electroproduction, neutrino production, and e^+e^- annihilation.

* Work supported by the U. S. Atomic Energy Commission

Introduction

As indicated by the title, I am going to talk today about two topics. First, I will describe some data on the inclusive electroproduction of hadrons from both hydrogen and deuterium targets.[1] This experiment was performed by Jim Dakin, Bill Lakin, Fred Martin, Martin Perl, Eric Petraske, Bill Toner and me. And second, I will describe some work I have been doing with Jim Dakin to investigate quantitatively the features that could be expected in a quark-parton model for various lepton-induced inclusive reactions.[2] As you might expect, work on the second topic was motivated by the results of the first.

Unfortunately, I will not have time to give a complete review of our experimental data. In particular, I will not be able to discuss our results on ρ^0 and φ meson electroproduction. This is unfortunate because our data nicely complement the data presented this morning by Karl Berkelman and the data which will be presented by the next two speakers, Heinrich Meyer and Terry Carrol. There is, however, a detailed description of this aspect of our experiment available as a SLAC-PUB and I refer you to that report.[3]

Without doubt, the kinematics of inclusive electroproduction are well known to everyone here, so we will review them very briefly. As shown in Fig. 1 we assume that the electron interacts with the nucleon by exchanging a single space-like virtual photon. This virtual photon can be characterized by three variables — q^2, the photon mass squared; s, the virtual photoproduction center of mass energy squared; and ϵ, a polarization parameter. We detect forward hadrons in coincidence with

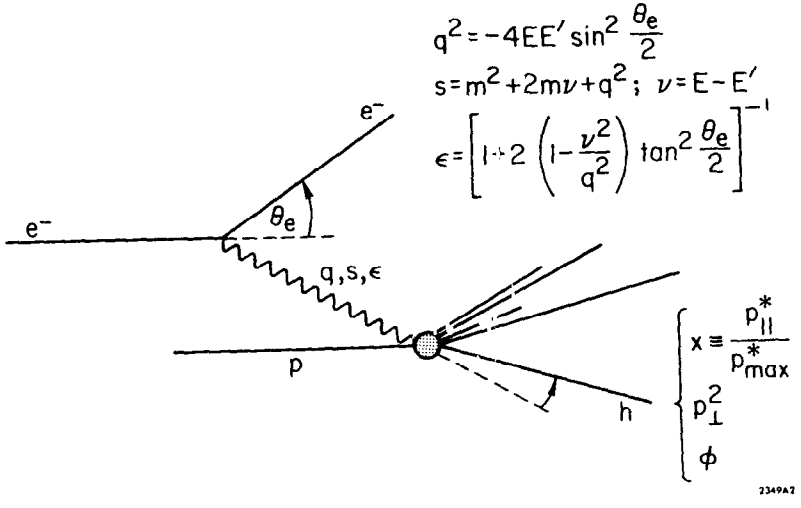

Fig. 1 Inclusive electroproduction kinematics

the scattered electron. In addition to its charge, each of these hadrons is characterized by three inclusive variables measured with respect to the virtual photon direction — x, the Feynman variable, which is the ratio of center of mass longitudinal momentum to the maximum possible; $p_\perp^2$, the transverse momentum squared; and Φ, the azimuthal angle between the electron scattering plane and the hadron production plane.

Experimental Apparatus and Procedure

The experimental set-up, shown in Fig. 2, consisted of a 19.5 GeV electron beam with 10^4 electrons per pulse incident on a 4 cm liquid hydrogen or liquid deuterium target. The scattered electron and produced hadrons were momentum analyzed by a large magnet and detected by two banks of optical spark chambers, two hodoscopes of scintillation counters and a bank of lead-lucite shower counters. The one technical innovation in the experiment was a superconducting beam pipe which allowed the unscattered electron beam including electrons with degraded energy to pass through the magnet in a field-free region.

The scattered electron was identified by giving a pulse height in a shower counter which corresponded to its measured momentum. We triggered the spark chambers on just the detection of a scattered electron. This allowed us to normalize the data internally to single arm electron scattering measurements.

Other in-time particles were assumed to be hadrons. There were no means of identifying whether the hadrons were π's, K's, or p's. For the purpose of kinematics, we assumed that they were all π's.

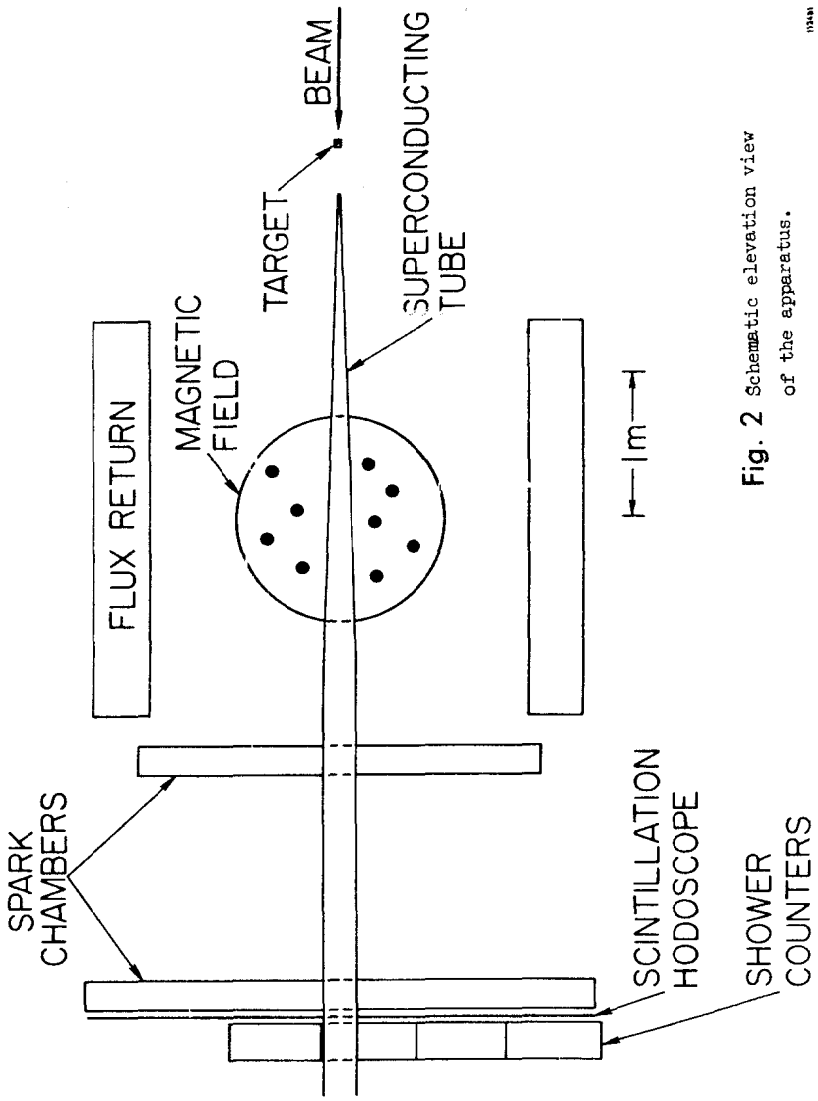

Fig. 2 Schematic elevation view of the apparatus.

Figure 3 shows a typical photograph of an event which happens to contain a candidate for an elastically produced ρ^o meson. We photographed 250,000 events with a H_2 target and 110,000 events with a D_2 target. All of the pictures were scanned and measured with a flying-spot digitizer and samples of the data were measured respectively by a conventional manual system to study biases and efficiencies. In the kinematic range $-.25 > q^2 > -3.0$ GeV^2, $12 < s < 30$ GeV^2, $p_\perp^2 < .7$ GeV^2 and $x > 0.1$, we obtained about 9000 inclusive events from a H_2 target and about 4500 inclusive events from a D_2 target.

Results

The azimuthal distributions we observe are consistent with being flat everywhere. In photoproduction from polarized photons, an 11% cos 2φ term is observed at high x after ρ^o mesons have been subtracted.[4] We cannot rule out that size effect occurring in our data also.

Figure 4 shows the dependence of the data on p^2 for positive and negative hadrons in two x regions for H_2 and D_2 targets. The values of b from fits to the form

$$\frac{d\sigma}{dp^2} \propto e^{-bp_\perp^2} \qquad (0)$$

are plotted as a function of q^2. Photoproduction results for h^- from a proton target are also shown.[4] There are no clear differences between data from H_2 and D_2 targets, although there is considerable scatter among the points. Concentrating on the higher statistics H_2 data, we see that for the low x region, $0.1 < x < 0.4$, there does not appear to be any significant change in the $p_\perp^2$ distribution as $|q^2|$ changes.

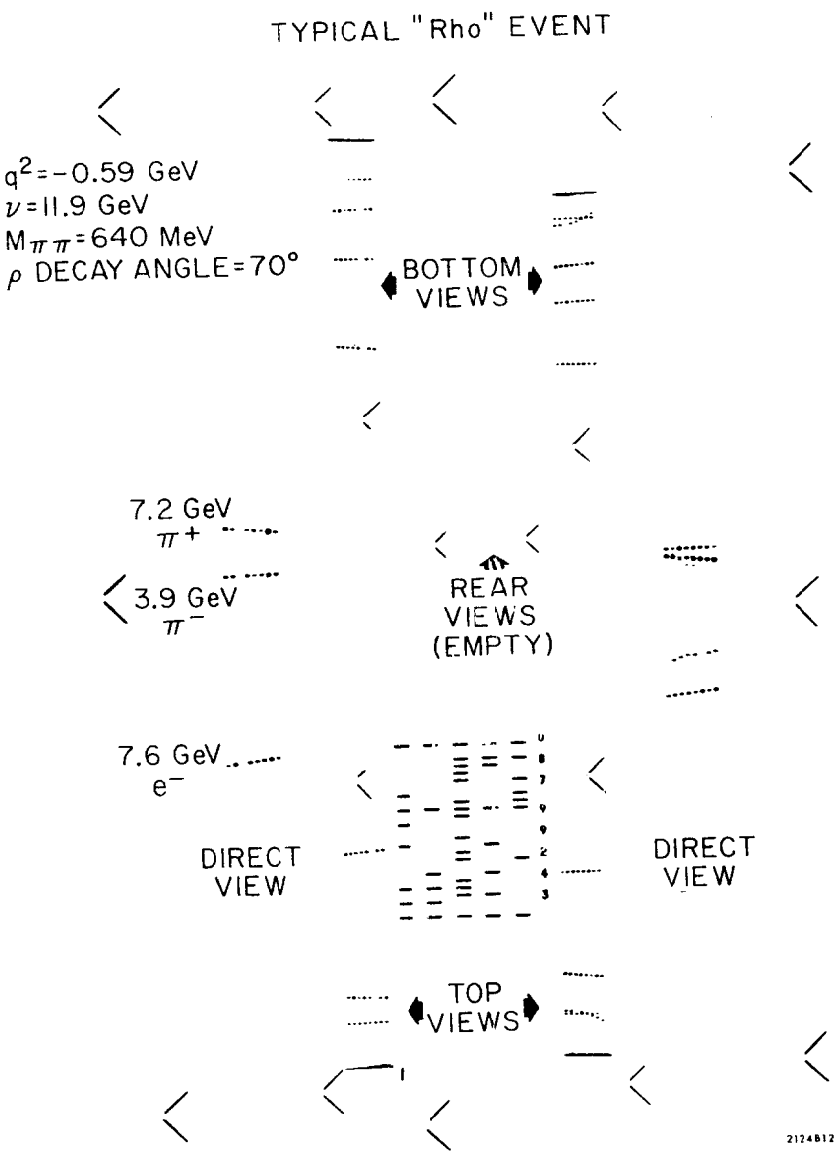

Fig. 3 Photograph of a typical event

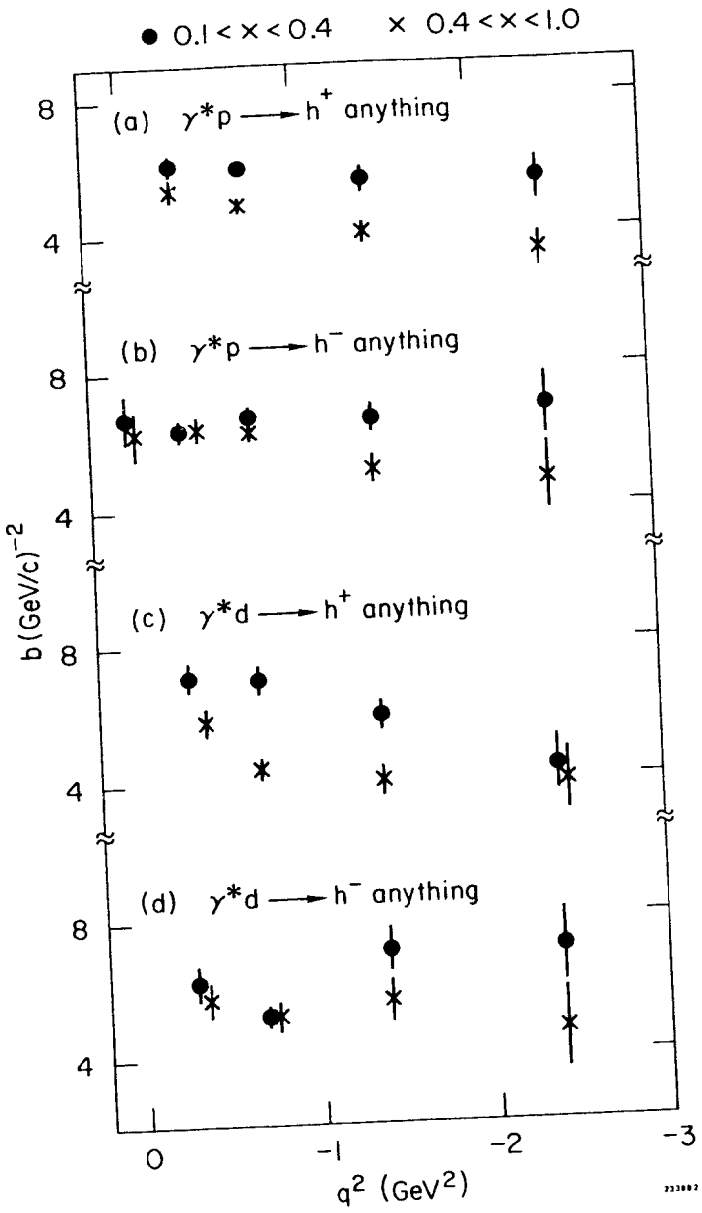

Fig. 4 Slope parameters describing the $p_\perp^2$ distributions for (a) h^+ from hydrogen, (b) h^- from hydrogen, (c) h^+ from deuterium, and (d) h^- from deuterium. The points at q^2=0 are from fits to photoproduction data at s=18.3 GeV^2 (Ref. 4).

However, in the high x region for both positive and negative particles, there is a clear tendency for the $p_\perp^2$ distribution to broaden as $|q^2|$ increases.

Figure 5 shows the dependence of the relative invariant cross section on x for a large kinematical region, $-0.5 > q^2 > -3.0$ GeV^2 and $6 < s < 30$ GeV^2. We also show the 9.3 GeV π^- photoproduction curve.[4] There is clearly a large difference in shape and normalization between the photoproduction and electroproduction data for negative hadrons. This is largely due to the decrease in the relative amount of eleastic ρ^o meson production, which we have measured.[3] Because this is a rather special channel, analogous to an elastic channel via the ideas of vector dominance, it is perhaps more informative to view the data with this channel excluded. This is done in Fig. 6 in which the ρ^o channel has been subtracted from both the differential and total cross sections for both the photoproduction and electroproduction data. The shapes are now similar, and the negative hadron electroproduction cross sections are somewhat smaller than the photoproduction cross sections. No radiative corrections have been applied to the inclusive cross sections, and these corrections would tend to increase the electroproduction cross sections in this region of x.

The most interesting aspect of Fig. 6 is the sizable difference between the positive and negative hadron cross sections. From a point of view which will appear very naive to this audience, this is a surprising result. If this were a hadronic reaction, we would refer to this region as the photon fragmentation region, and we would expect to see the fragments of the photon, which are, on the average, neutral.

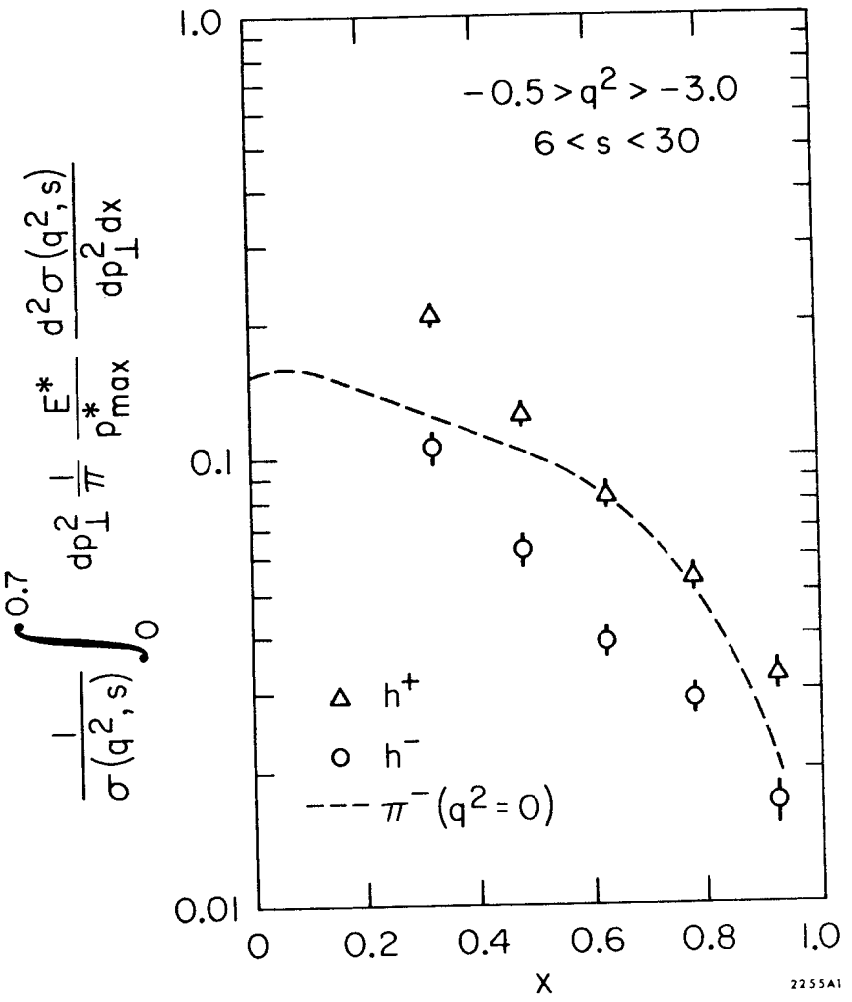

Fig. 5 The invariant cross section as a function of x

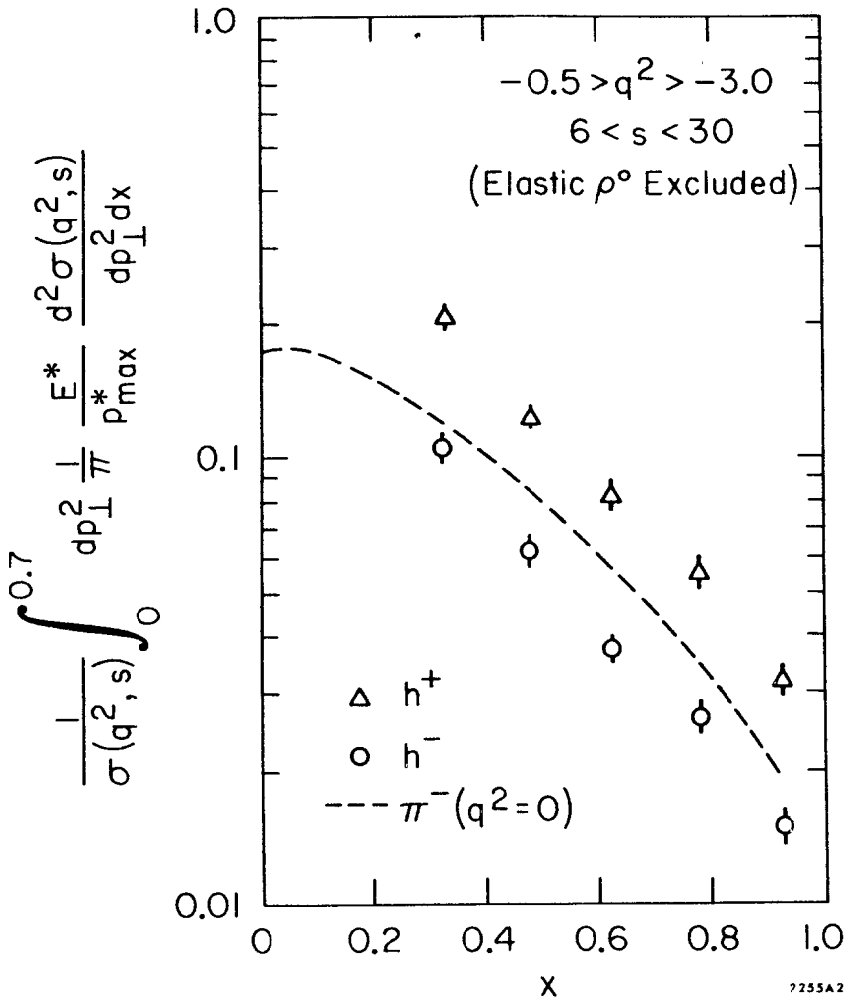

Fig. 6 The invariant cross section versus x with ρ^o meson production excluded

To a fair approximation, this is what happens in photoproduction, but it does not appear to be what is happening here.

In Fig. 7 we have plotted the ratio of positive to negative hadron production in the region $0.4 < x < .085$ for our experiment,[1] other electroproduction experiments,[5-8] and a photoproduction experiment.[9] There is a general rise in the ratio as $|q^2|$ increases. Our data from a neutron target for the same region are also shown. These data suffer from large statistical uncertainties. We obtained only half as much data from D_2 as from H_2 targets, which means only a quarter as much data from a neturon target as a proton target. And, of course, these data must be extracted by a subtraction. I should warn you that because of this subtraction, these two sets of data are not independent. A proton charge ratio which is too large due to a statistical fluctuation will yield a neutron charge ratio which is too small, and vice versa. In two cases in our data this may be happening. Also, based on our measurements of biases and efficiencies, we cannot rule out a systematic error of up to 20% in this ratio, although we know of no mechanism which could cause an error that large.

Now, having made all the proper disclaimers, I will say that I think these data are significant. On the average, the electroproduction data give a fair sized positive hadron excess while in photoproduction there appears to be about a 20% negative hadron excess.

Quark-Parton Model

How are we to understand these results? I am going to spend the remainder of this talk showing that these results can be accommodated quantitatively, and in a natural and reasonable way, in a quark-parton

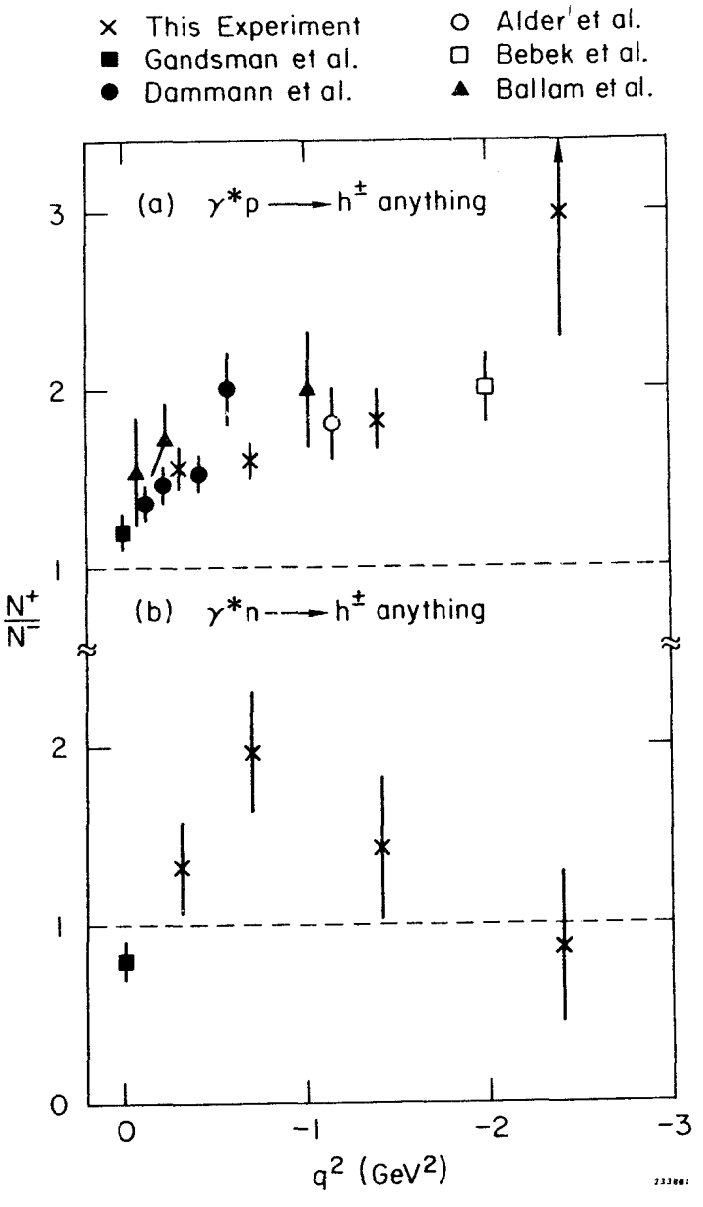

Fig. 7 Hadronic charge ratios in the range $0.4 < x < 0.85$. The data are from this experiment and Ref. 5-9.

model. Furthermore, such a model will yield numerical predictions for electroproduction, neutrino production, and e^+e^- annihilation, all of which will be susceptible to experimental tests in the next year or two.

Following Feynman[10] and coworkers,[11] the model is described in the current-parton Breit frame. As illustrated in Fig. 8(a), the nucleon, with (large) longitudinal momentum P, is regarded as a collection of independent point-like constituents. The lepton current, with momentum $-2xP$, interacts incoherently with a parton of momentum xP, reversing its momentum. The struck parton then fragments into hadrons, a typical one of which, h, will possess a fraction z of the parton's momentum. The remaining partons, with momentum $(1-x)P$, also fragment into hadrons, as shown in Fig. 8(b). It is assumed that the fragmentation processes are independent of x, since for finite **x** the struck parton is separated by a large momentum difference from the nucleon fragments.

(I have to apologize for the change in notation here. x is the scaling variable, $-2M\nu/q^2 = \omega^{-1}$ and, for the kinematical region we are considering, z is essentially the same as the Feynman x variable used earlier.)

The model requires the specification of two sets of functions, the parton distribution functions and the parton fragmentation functions. The former denote the average number of partons of a given type in a interval of x and are designated by the type of parton (e.g. $u(x)dx$, $\bar{s}(x)dx$, etc.). Similarly, the fragmentation functions specify the average number of hadrons of a given type in a interval of z arising from the fragmentation of a given type of parton. They are designated

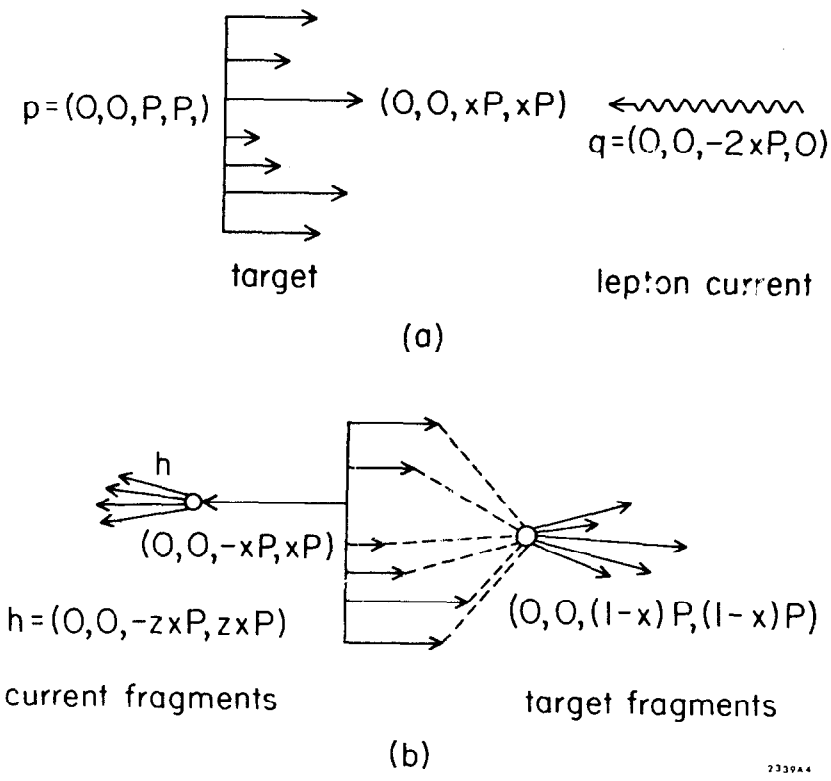

Fig. 8 Schematic diagram of inelastic lepton scattering in the parton model

in an obvious notation (e.g. $D_{\mu}^{\pi^+}(z)dz$, $D_{d}^{K^o}(z)dz$, etc.). From these the structure functions for various reactions can now be constructed. For example, for the case of inclusive π^- electroproduction from a proton target, we have

$$L_{2,\pi^-}^{ep}(x,z) = x\left\{\frac{4}{9}u(x)\,D_u^{\pi^-}(z) + \frac{4}{9}\bar{u}(x)\,D_{\bar{u}}^{\pi^-}(z) + \frac{1}{9}d(x)\,D_d^{\pi^-}(z) + \frac{1}{9}\bar{d}(x)\,D_{\bar{d}}^{\pi^-}(z) + \frac{1}{9}s(x)\,D_s^{\pi^-}(z) + \frac{1}{9}\bar{s}(x)\,D_{\bar{s}}^{\pi^-}(z)\right\} . \quad (1)$$

Nursery School Model

Just to set the stage and to illustrate clearly the nature of this model, let us work out results for the most naive set of assumptions. Bj has spoken about "kindergarden parton models";[12] to fit into that parlance, we will refer to this as the nursery school model. Assume that the proton is just 3 quarks, two u quarks and one d quark, and the neutron is two d quarks and a u quark, and that all quarks have the same momentum distribution. Further assume that a quark fragments only into a meson which contains that quark as part of its basic configuration. In other words, assume that a u quark fragments only into a π^+ and a d quark fragments only into a π^-.

Then we have

$$\langle n_{\pi^+}\rangle_{ep} \propto \frac{4}{9}u_p \propto 8, \quad (2a)$$

$$\langle n_{\pi^-}\rangle_{ep} \propto \frac{1}{9}d_p \propto 1, \quad (2b)$$

$$\langle n_{\pi^-}\rangle_{en} \propto \frac{4}{9}u_n \propto 4, \quad (2c)$$

and

$$\langle n_{\pi^-} \rangle_{en} \propto \frac{1}{9} d_n \propto 2. \tag{2d}$$

And thus we see that the charge ratio from a proton is 8:1 and from a neutron is 4:2. The neutron case illustrates the characteristic of the model which we wish to exploit — that one $\frac{2}{3}$ charge quark is twice as important as two $\frac{1}{3}$ charges quarks combined, because the interaction is proportional to the square of the charge.

The results bear no resemblance to the data and this is presumably because we have not picked reasonable distribution or fragmentation functions. We will attempt to do this shortly, but first we will take a minute for one important aside.

The GRZ Relation

There is one electroproduction quark-parton prediction which does not depend on the choice of distribution or fragmentation functions, but only requires that they satisfy the constraints of isospin and charge conjugation invariance. It was derived by Gronau, Ravndal, and Zarmi and is[11]

$$\frac{\int_1^\infty \left(\langle n_{\pi^+} \rangle_{en} - \langle n_{\pi^-} \rangle_{en} \right) F_1^n(\omega) \frac{d\omega}{\omega^2}}{\int_1^\infty \left(\langle n_{\pi^+} \rangle_{ep} - \langle n_{\pi^-} \rangle_{ep} \right) F_1^p(\omega) \frac{d\omega}{\omega^2}} = \frac{2}{7} \approx .29 \tag{3}$$

The factor of $\frac{2}{7}$ will be no surprise to those who have mastered the nursery school model. It is merely (4-2) divided by (8-1).

An experimental difficulty involved in testing this prediction is that it requires obtaining data from $\omega = 1$ to $\omega = \infty$, a formidable task. We have evaluated it for our data in the range $3 < \omega < 60$ and obtain a value of 0.24 ± 0.28. This is certainly the right ball park, but hardly a test of the relation.

The Distribution Functions

We now return to the task of constructing a reasonable quark-parton model.

The distributions functions are constrained by single arm inelastic scattering measurements since

$$F_2^{ep}(x) = x\left\{\frac{4}{9}\left[u(x) + \bar{u}(x)\right] + \frac{1}{9}\left[d(x) + \bar{d}(x)\right] + \frac{1}{9}\left[s(x) + \bar{s}(x)\right]\right\} \tag{4}$$

and

$$F_2^{en}(x) = x\left\{\frac{1}{9}\left[u(x) + \bar{u}(x)\right] + \frac{4}{9}\left[d(x) + \bar{d}(x)\right] + \frac{1}{9}\left[s(x) + \bar{s}(x)\right]\right\} \tag{5}$$

To reproduce the nucleon quantum numbers, they must also satisfy the following normalization conditions:

$$\int_0^1 [u(x) - \bar{u}(x)]dx = 2 \tag{6a}$$

$$\int_0^1 [d(x) - \bar{d}(x)]dx = 1 \tag{6b}$$

$$\int_0^1 [s(x) - \bar{s}(x)]dx = 0 \tag{6c}$$

These constraints and conditions are not sufficient to determine the functions uniquely, so one must make some reasonable physical assumptions. Two years ago, Kuti and Weisskopf constructed such a model.[13] In it the nucleon was assumed to consist of three valence quarks plus a core of quark anti-quark pairs. The sea of core quarks was assumed to be composed of equal numbers of each type, all with the same longitudinal momentum distribution,

$$u(x) = u_v(x) + c(x), \tag{7a}$$

$$d(x) = d_v(x) + c(x), \tag{7b}$$

$$s(x) = \bar{s}(x) = \bar{u}(x) = \bar{d}(x) = c(x) \ , \tag{7c}$$

where $u_v(x)$ and $d_v(x)$ represent the distribution functions for valence quarks.

The core quark momentum distribution was assumed to be given by phase space and the valence quark distributions by phase space and by Regge theory considerations at small x.

Since u_v and d_v are proportional in the Kuti-Weisskopf model, the model cannot accommodate a neutron-proton ratio, F^{en}/F^{ep}, of less than $\frac{2}{3}$, in contradiction to recent data.[14] McElhaney and Tuan have presented modified versions of the Kuti-Weisskopf distribution functions which remove this difficulty.[15] We will use one of their versions which is a four parameter fit to the data and is based on the addition of a low-lying daughter Regge trajectory:

$$u_v(x) = 1.74\ x^{-\frac{1}{2}}\ (1 - x)^3\ (1 + 2.3x) \tag{8a}$$

$$d_v(x) = 1.11\ x^{-\frac{1}{2}}\ (1 - x)^{3.1} \tag{8b}$$

$$c(x) = 0.10\ x^{-1}\ (1 - x)^{7/2} \ . \tag{8c}$$

These functions are certainly not unique, but they have the virtue of being an excellent fit to the data, and they should be quite adequate for our purposes. With the exception of the region around x = 1, I doubt that it is possible to construct a reasonable theory which both fits the data and differs numerically from these in any significant way. For example, the difference between the u and d functions, to which we are quite sensitive, is directly determined by the data,

$$F_2^{ep}(x) - F_2^{en}(x) = \frac{x}{3}\left[u(x) - d(x)\right] \ . \tag{9}$$

The Fragmentation Functions

Isospin and charge conjugation invariance reduces the number of independent D functions for pions to three:

$$D_u^{\pi^+} = D_{\bar{d}}^{\pi^-} = D_{\bar{u}}^{\pi^-} = D_d^{\pi^+} \tag{10a}$$

$$D_{\bar{d}}^{\pi^+} = D_{\bar{u}}^{\pi^-} = D_{\bar{d}}^{\pi^-} = D_u^{\pi^+} \tag{10b}$$

$$D_s^{\pi^+} = D_{\bar{s}}^{\pi^-} = D_{\bar{s}}^{\pi^+} = D_s^{\pi^-} \tag{10c}$$

We define the ratio

$$\eta(z) \equiv D_u^{\pi^+}(z)/D_{\bar{d}}^{\pi^+}(z) \tag{11}$$

We think of η as a favored to unfavored fragmentation ratio. It represents the ratio of the probability that a quark will fragment into a meson which can be formed by the addition of a single (anti-) quark to the probability that it will fragment into a quark which cannot be formed in this way. Based on this idea, we assume

$$D_{\bar{s}}^{\pi^+}(z) = D_{\bar{d}}^{\pi^+}(z) \tag{12}$$

because both of these functions are unfavored. The validity of this assumption will not be critical for our numerical results since even at quite large ω, say $\omega = 100$, strange quarks contribute only about 10% of the electron scattering cross section.

So that we can compare with data in a statistically significant way, we will consider the integrals of the D functions over the current fragmentation region. We take

$$D \to \int_{0.4}^{1} D(z)dz \qquad (13)$$

but we do not include the πN and the $\pi\Delta$ final states in the integral. These states arise primarily from π exchange and do not survive the Bjorken limit.[16]

Although our numerical results will be for an integral over the current fragmentation region, they will also be approximately valid for all $z > 0.4$, at least up to $z = 0.8$. This is because experimentally the π^+/π^- ratio in electroproduction from protons appears to be relatively constant in this region. The charge ratios from our experiment and the Harvard-Cornell[5] experiment are shown in Fig. 9. For $z > 0.4$ there is a tendency for the charge ratio to decrease.

ep Charge Ratios

We are now in a position to determine η from measurements of pion charge ratios in electroproduction from a proton target. Figure 10 shows data from four experiments for the pion charge ratio in the current fragmentation region as a function of ω.

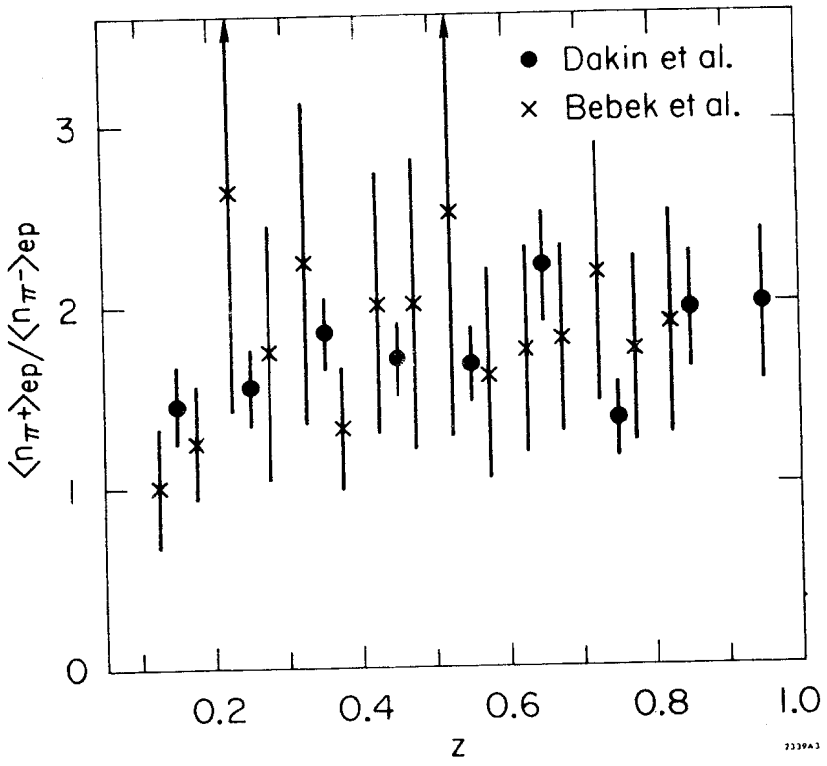

Fig. 9 Charge ratio in electroproduction from a proton target as a function of z. The data are from this experiment and Ref. 5.

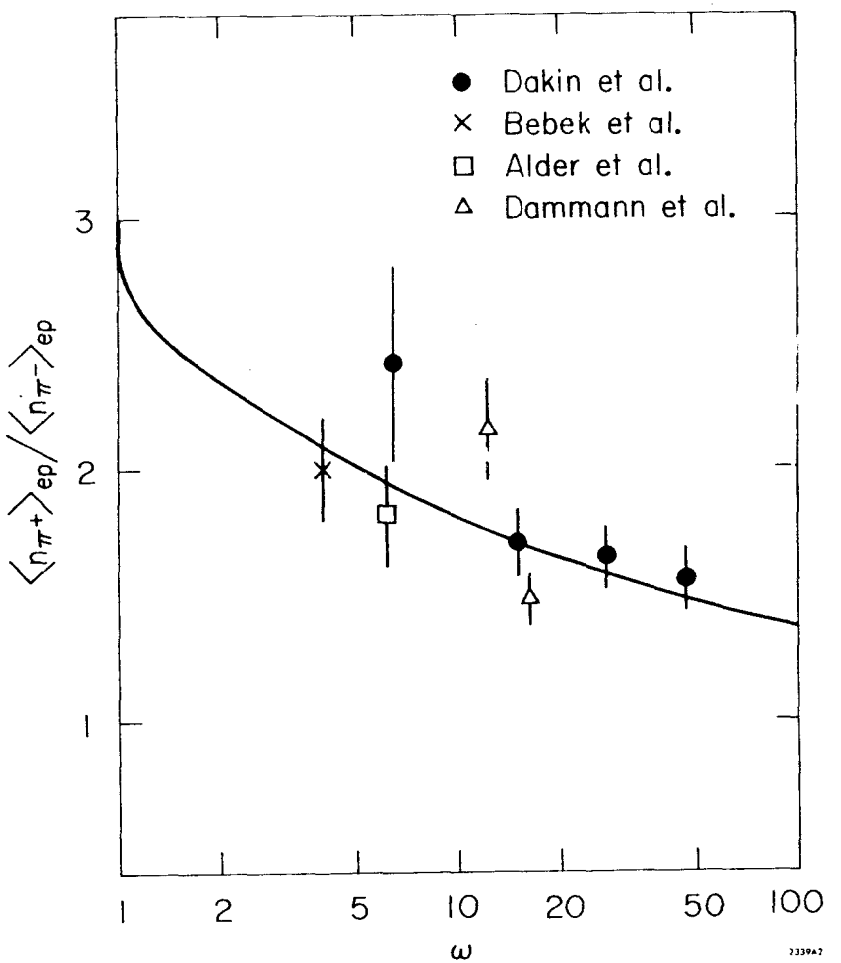

Fig. 10 Charge ratio in electroproduction from a proton target as a function of ω. The data are from this experiment and Ref. 5-7. The curve represents a one-parameter fit to the data, Eq. (14) with η = 3.0.

The curve on Fig. 10 is a fit to the quark parton model prediction,

$$\frac{\langle n_{\pi^+} \rangle_{ep}}{\langle n_{\pi^-} \rangle_{ep}} = \frac{4\eta\, u_v(x) + d_v(x) + (5\eta + 7)\, c(x)}{4u_v(x) + \eta\, d_v(x) + (5\eta + 7)\, c(x)} \qquad (14)$$

with η as a free parameter. It is a reasonable fit and the fit value of η is 3.0. Given the many uncertainties of this approach, we consider this value good to about 20%.

One obvious consequence of this model is that even as ω → 1, the charge ratio will not rise above η. I mention this because, by way of contrast, there are predictions in the literature for this region which are essentially the nursery school model values.[18]

en Charge Ratios

Having determined η from ep data, we can now predict the charge ratios for other reactions. For the electroproduction from a neutron target we expect

$$\frac{\langle n_{\pi^+} \rangle_{en}}{\langle n_{\pi^-} \rangle_{en}} = \frac{u_v(x) + 4\eta\, d_v(x) + (5\eta + 7)\, c(x)}{\eta\, u_v(x) + 4\, d_v(x) + (5\eta + 7)\, c(x)}\ , \qquad (15)$$

which is plotted in Fig. 11, with η = 3.0. This curve provides a rather unique test of the model. The charge ratio should rise to a broad maximum of between 1.2 and 1.3 around ω = 12, then fall to unity at ω = 1.7 and continue to fall below unity as ω → 1. The positions of the maximum and of the $\langle n_{\pi^+} \rangle_{en} = \langle n_{\pi^-} \rangle_{en}$ point do not depend on η. The predicted π^+/π^- ratio of between 1.2 and 1.3 at moderate ω is in sharp contrast to the π^+/π^- ratio of about 0.8 observed in photoproduction.[9]

Our data are also shown in Fig. 11. While not in disagreement with the predictions, they are clearly not of sufficient precision

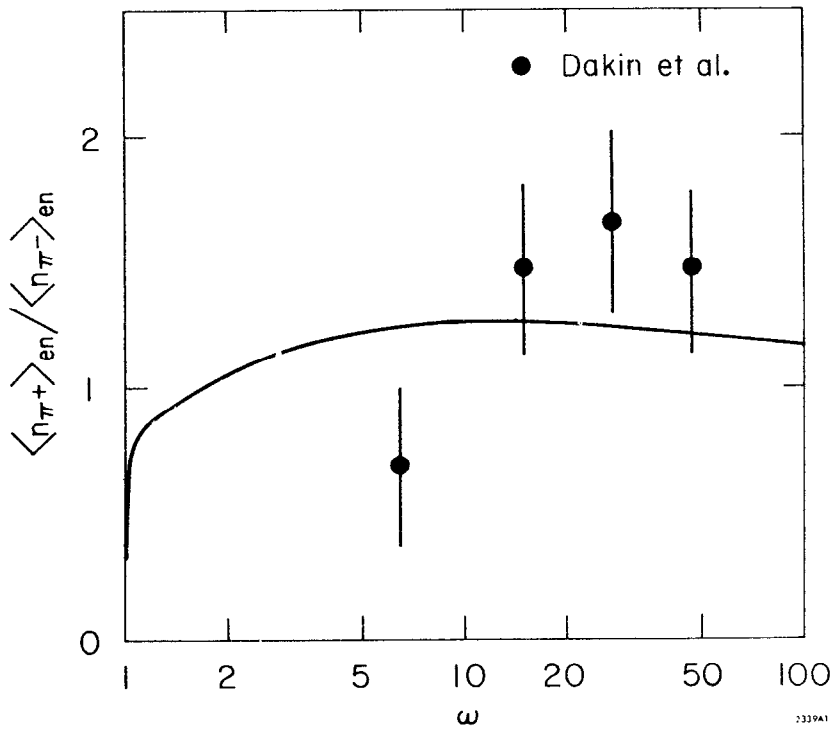

Fig. 11 Charge ratio in electroproduction from a neutron target as a function of ω. The curve is the prediction of the model, Eq. (15) with $\eta = 3.0$.

to test them. One of the main goals of our upcoming experiment, E-97, will be to provide high precision data on this ratio over all large range of ω. We also expect data from Cornell shortly and also possibly from the SLAC streamer chamber experiment.

Neutrino Experiments

The predictions for charge ratios from neutrino-induced reactions are rather simple. In the (very good) approximation that the square of the Cabbibo angle is zero, neutrinos interact only with d and $\bar{u}$ quarks, while anti-neutrinos interact only with u and $\bar{d}$ quarks. Therefore,

$$\frac{\langle n_{\pi^+} \rangle_{\nu p}}{\langle n_{\pi^-} \rangle_{\nu p}} = \frac{\langle n_{\pi^+} \rangle_{\nu n}}{\langle n_{\pi^-} \rangle_{\nu n}} = \frac{\langle n_{\pi^-} \rangle_{\bar{\nu} p}}{\langle n_{\pi^+} \rangle_{\bar{\nu} p}} = \frac{\langle n_{\pi^-} \rangle_{\bar{\nu} n}}{\langle n_{\pi^+} \rangle_{\bar{\nu} n}} = \eta = 3.0 \pm 0.6 \quad , \tag{16}$$

for the region $z > 0.4$. Neutrino bubble chamber experiments at CERN and NAL should be able to test this prediction in the near future.

e^+e^- Charge Ratios

Electron-positron annihilation into hadrons is conventionally described in this model as the pair production of a parton anti-parton pair, each of which subsequently fragments into hadrons. This is shown schematically in Fig. 12. The fragmentation process is assumed to be identical to that which occurs in lepton scattering. Thus,

$$\frac{d\sigma}{dz}(e^+e^- \to h + \text{anything})$$

$$= \frac{4\pi\alpha^2}{3q^2} \sum_i Q_i^2 \left[D_i^h(z) + D_{\bar{i}}^h(z) \right] \tag{17}$$

where the sum is over the type of parton and Q_i is the parton charge.

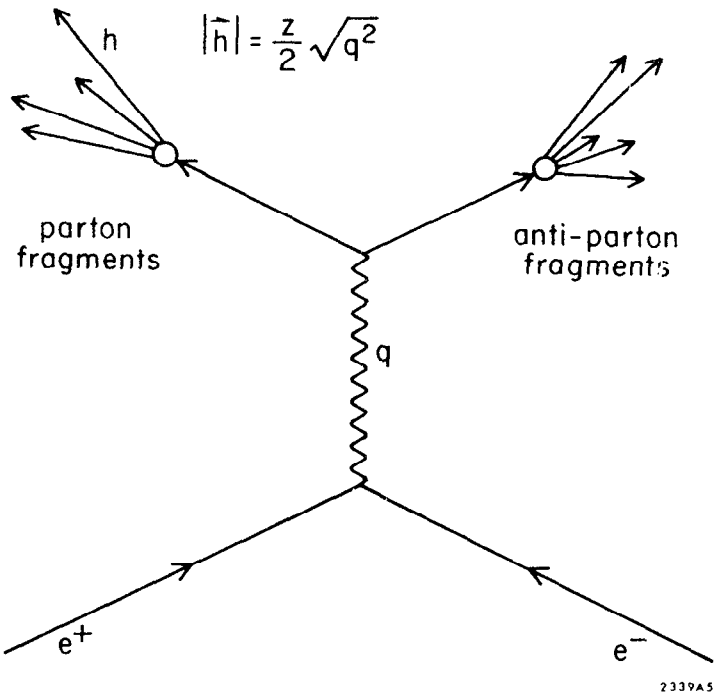

Fig. 12 Schematic diagram of e^+e^- annihilation in the parton model

Obviously charge conjugation invariance prohibits us from gaining any information on relative parton charges by observing pions. However, the kaon system offers hope of a successful test.

Isospin invariance yields

$$D_u^{K^+} = D_d^{K^0} , \tag{18a}$$

$$D_{\bar{s}}^{K^+} = D_{\bar{s}}^{K^0} , \tag{18b}$$

$$D_d^{K^+} = D_u^{K^0} , \tag{18c}$$

$$D_{\bar{d}}^{K^+} = D_{\bar{u}}^{K^0} , \tag{18d}$$

$$D_{\bar{u}}^{K^+} = D_{\bar{d}}^{K^0} , \tag{18e}$$

and

$$D_s^{K^+} = D_s^{K^0} . \tag{18f}$$

In addition, SU(3) invariance gives

$$D_u^{K^+} = D_{\bar{s}}^{K^+} = D_u^{\pi^+} , \tag{19a}$$

$$D_d^{K^+} = D_{\bar{d}}^{K^+} = D_s^{\pi^+} , \tag{19b}$$

and

$$D_{\bar{u}}^{K^+} = D_s^{K^+} = D_d^{\pi^+} . \tag{19c}$$

And thus for the ratio of charged to neutral kaon production, we obtain

$$\frac{\langle n_{K^+} \rangle_{e^+e^-}}{\langle n_{K^0} \rangle_{e^+e^-}} = \frac{5\eta + 7}{2\eta + 10} = 1.38 \pm 0.10 \tag{20}$$

again in the region $z > 0.4$.

Although SU(3) invariance is a sufficient condition for Eq. (20) to hold in this model, it is hardly necessary. One might imagine that SU(3) breaking occurs in such a way as to inhibit all kaon production relative to pion production by a constant factor. In such a case, the prediction will still be valid.

This prediction should be tested at SPEAR within the next year. It will, however, have to be measured by combining the results of two experiments. The magnetic detector experiment, SP-2, will measure K^o inclusive production, but will not be able to distinguish charged K's from charged π's in the necessary momentum range. The single arm spectrometer experiment, SP-8, on the other hand, will separate charged π's and K's, but should have a rather small solid angle for K^o's.

Conclusion

We have seen that a reasonable quark-parton model can accommodate the present electroproduction data, and to a certain extent explain these data in a natural way. However, there are a number of experimental tests that this model must face in the near future.

Postscript

All of the phenomena which we have been discussing have been at low transverse momentum. There are some little-known data[18,19] which indicates that in real inclusive photoproduction the pion charge ratio increases with $p_\perp^2$. This is shown in Fig. 13.

These data suggest a number of questions, the answers to which I certainly do not know, but which may be of interest to this audience:

1) Does this have anything to do with the electroproduction charge ratio which rises with q^2?

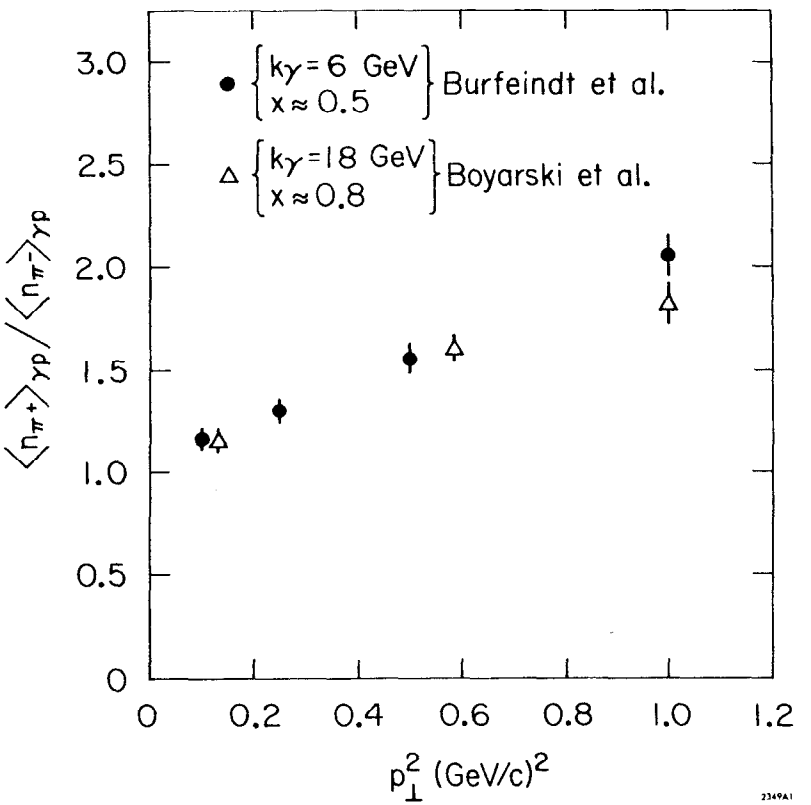

Fig. 13 Charge ratio in photoproduction as a function of $p_\perp^2$. The data are from Ref. 18 and 19.

2) Does this have anything to do with quarks or partons, or can it be understood more easily in terms of more conventional mechanisms?

3) In any case, what do you expect to happen from a neutron target?

References

1. J. T. Dakin, G. J. Feldman, W. L. Lakin, F. Martin, M. L. Perl, E. W. Petraske, and W. T. Toner, Phys. Rev. Lett. 29, 746 (1972), and J. T. Dakin, G. J. Feldman, F. Martin, M. L. Perl, and W. T. Toner, SLAC Report No. SLAC-PUB-1269 (1973), (to be published).
2. J. T. Dakin and G. J. Feldman, SLAC Report No. SLAC-PUB-1273 (1973), (to be published).
3. J. T. Dakin, G. J. Feldman, W. L. Lakin, F. Martin, M. L. Perl, E. W. Petraske, and W. T. Toner, SLAC Report No. 1211 (1973), [to be published in Phys. Rev. D8, No. 3 (1973)].
4. K. C. Moffeit, J. Ballam, G. B. Chadwick, M. Della-Negra, R. Gearhart, J. J. Murray, P. Seyboth, C. K. Sinclair, I. O. Skillicorn, H. Spitzer, G. Wolf, H. H. Bingham, W. B. Fretter, W. J. Podolsky, M. S. Rabin, A. H. Rosenfeld, R. Windmolders, G. P. Yost and R. H. Milburn, Phys. Rev. D5, 1603, (1972).
5. C. J. Bebek, C. N. Brown, C. A. Lichtenstein, M. Herzlinger, F. M. Pipkin, L. K. Sisterson, D. Andrews, K. Berkelman, D. G. Cassel, and D. L. Hartill, Phys. Rev. Let. 30, 624 (1973).
6. J. C. Adler, F. W. Brasse, E. C. Chazelas, W. Fehrenbach, W. Flauger, K. H. Frank, E. Ganbauge, J. Gayler, V. Korbel, W. Krechlok, J. May, M. Merkwitz and P. D. Zimmerman, Nucl. Phys. B46, 415 (1972).
7. I. Dammann, C. Driver, K. Heinloth, G. Hofmann, F. Janata, P. Karow, D. Luke, D. Schmidt, and G. Specht, Nucl. Phys. B54, 381 (1973).
8. J. Ballam, E. D. Bloom, J. T. Carroll, G. B. Chadwick, R. L. A. Cottrell, M. Della-Negra, H. DeStaebler, L. K. Gershwin, L. P. Keller, M. D. Mestayer, K. C. Moffeit, C. Y. Prescott, and S. Stein, SLAC Report No. SLAC-PUB-1163 (1972), (unpublished).
9. J. Gandsman, G. Alexander, S. Dagan, L. K. Jacobs, A. Levy, D. Lissauer, and L. M. Rosenstein, Department of Physcis and Astronomy, Tel-Aviv University Report No. TAUP-360-73 (1973).
10. R. P. Feynman, Photon-Hadron Interactions, (W. A. Benjamin, Reading, Massachusetts, 1972).
11. M. Gronau, F. Ravndal, and Y. Zarmi, Nucl. Phys. B51, 611 (1973).

12. J. D. Bjorken, SLAC Report No. SLAC-PUB-1017 (1972).
13. J. Kuti and V. Weisskopf, Phys, Rev. D4, 3418 (1971).
14. A. Bodek, M. Briedenbach, D. L. Dubin, J. E. Elias, J. I. Friedman, H. W. Kendall, J. S. Poucher, E. M. Riordan, M. R. Sogard, and D. H. Coward, Phys. Rev. Lett. 30, 1087 (1973).
15. R. McElhaney and S. F. Tuan, University of Hawaii Report UH-511-156-73, (1973), (to be published).
16. C. N. Brown, C.R. Canizares, W. E. Cooper, A. M. Eisner, G. J. Feldman, C. A. Lichtenstein, L. Litt, W. Lockeretz, V. B. Montana, and I. M. Pipkin, Phys. Rev. Lett. 26, 991 (1971), Phys, Rev. D8 (1973), (to be published).
17. C. F. A. Pantin, Nucl. Phys. B46, 205, (1972).
18. A. M. Boyarski, D. Coward, S. Ecklund, B. Richter, D. Sherden, R. Siemann, and C. Sinclair, Contribution to the International Symposium on Electron and Photon Interactions at High Energies, Ithaca, New York (1971), (unpublished).
19. H. Burfeindt, G. Buschhorn, H. Genzel, P. Heide, U. Kötz, K. H. Mess, P. Schmüser, B. Sonne, G. Vogel and B. H. Wiik, Contribution to the XVI International Conference on High Energy Physics, Batavia, Illinois (1972), (unpublished).

RESULTS ON ELECTROPRODUCTION EXPERIMENTS FROM DESY

Hinrich Meyer*

University of California

Santa Cruz, California 95064

Introduction

Recently, several experiments of hadron production in inelastic electron scattering have been performed at DESY. It is the aim of this talk to give a summary of the results of these experiments. After a very brief discussion of the experimental setups used, the kinematic region covered is discussed. It is seen that all data are from the transition region from photoproduction ($Q^2 = 0$ and $W < 3.5$ GeV) to the deep inelastic region, $Q^2 > 1\ GeV^2$ and $W > 1.8$ GeV (Ref. 1). This low boundary in Q^2 and W of the deep inelastic region, defined (experimentally) by scaling of the structure functions νW_2, W_1 is a real challenge for future experiments.

Because the scaling region may also be characterized by unusual properties of individual final states, it is very interesting to explore the transition region from photoproduction ($Q^2 = 0$) to the scaling region for specific final states, where rapid changes are to be expected, if one measures e.g. transverse momentum distributions in inclusive particle production, charge- and particle rations, or particle multiplicities.

The emphases in presenting the data will always be on the Q^2-dependence of these quantities at fixed W. Kinematically, it means to look at the data at decreasing $\omega' = 1 + \frac{W^2}{Q^2}$, the scaling variable.

---

*Permanent address: Deutsches Elektronen-Synchrotron (DESY), 2 Hamburg 52, Notkestieg 1, Germany.

Experimental Setups

There are four setups used recently at DESY in experiments to provide data on hadron production with photons ($Q^2 = 0$) and electrons ($Q^2 < 1.5\ GeV^2$). The kinematics of the process is defined in the usual manner

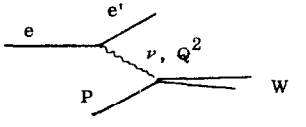

$(e - e')^2 = Q^2$	mass of the virtual photon
$E_e - E_{e'} = \nu$	energy of the virtual photon
$M_p^2 + 2 M_p \nu - Q^2 = W^2$	total mass of the hadronic system squared

In Figure 1, the range in Q^2 and ν covered by the DESY experiments is indicated. Two of the experiments measured the particle flux ($p\pi^+$, π^-, K^-, K^+) at $Q^2 = 0$ and $Q^2 = 1.15\ GeV^2$ for $W = 2.6$ GeV and at rather small transverse momentum of the hadrons, $p_\perp^2 < 0.02\ GeV^2$. (Ref. 2,3.)

As described in Ref. 2, scattered electrons are detected in an electron spectrometer at a scattering angle of $\sim 15^\circ$ and an energy of 2.64 GeV, for incident energy of 6.46 GeV (see Fig. 2). The hadrons are detected at a fixed angle of 10° with respect to the incident electron beam. Pions, Kaons and protons are separated by two cherenkov counters for lab momenta $p_{lab} > 1.9$ GeV. The average transverse momentum is small and given by the approximate relation $p_\perp = 0.047\ p_{lab}$.

A photoproduction experiment (Ref. 3) designed to complement the data of Ref. 2 used a focussing magnetic spectrometer to measure angle and momenta of the particles. Three cherenkov counters and time of flight measurements are used to identify the particles. The total energy of the hadronic system W is reasonably defined by taking data at two different end point energies for the bremsstrahlungs spectrum.

Another set of experiments, originally designed to look at specific two body final states $ep \rightarrow en\pi^+$, $ep \rightarrow e\pi\Delta$, (Ref. 4.5), also provided data on the inclusive channels $ep \rightarrow \pi^{\pm} e$ + any (Ref. 6). It uses two large aperture C-shaped magnets and optical spark chambers to measure the scattered electron in coincidence with one hadron. (Fig. 3) Electrons and hadrons are identified by two large acceptance cherenkov counters and two shower counters, in each spectrometer arm. Data are taken with incident electrons for the reactions $e^-p \rightarrow e^-\pi^+\Delta^\circ(1236)$ and $e^-p \rightarrow e^-\pi^+$ + anything and with incident positrons for the reactions $e^+p \rightarrow e^+\pi^-\Delta^{++}(1236)$ and $e^+p \rightarrow e^+\pi^-$ + anything. The incident energy varied between 4.0 and 5.4 GeV, and the kinematic region covered is indicated in Fig. 1. Δ production is studied at rather small values of the four momentum transfer from the virtual photon and the pion, $t - t_{min} < 0.07$ GeV^2. Inclusive $\pi^{\pm}$ production is measured in the forward half of the CMS, $X = \frac{P_L}{P_{max}} > 0.4$ and for rather small transverse momenta, $p_\perp^2 < 0.3$ GeV^2.

Furthermore, the streamer chamber setup (Fig 4) provided data on photo and electroproduction covering almost 4π in solid angle (Ref. 7, 8, 9, 10). In a photoproduction experiment data have been taken for incident photonenergies E_γ of 1.9 to 6.3 GeV (Ref. 7). Particles are identified by fitting the events to different hypotheses and using information on specific ionization loss. In a modified setup, electrons are scattered in a 9 cm. H_2 Target. Secondary electrons, for scattering angles $>4^\circ$ are identified by a shower counter and define the kinematic range covered as indicated in Fig. 1. Both experiments obtained data on multiplicities for charged hadrons, inclusive production of p, $\pi^{\pm}$, over the whole range in $X = P_L/P_{max}$ in the CMS and all transverse momenta $p_\perp$, as well as data on specific final states, like $\Delta^{++}\pi^-$ and vector meson (ρ°, ω°) production.

Q^2 Dependence of Specific Channels

The final state $p\pi^+\pi^-$ gives a prominent contribution to the total photoproduction cross-section. At low energy it is dominated by $\pi^-\Delta^{++}$, at higher energy by ρ°-production (Ref. 11, 12). The same tendency is found in electroproduction, as is apparent from Fig. 5 showing the $\pi^+\pi^-$ and $p\pi^+$ mass distributions for two W intervals.

The Q^2 dependence for the total cross sections of

$$ep \rightarrow ep\pi^+\pi^- \quad (1)$$

$$ep \rightarrow e\Delta^{++}\pi^- \quad (2)$$

$$ep \rightarrow ep\rho^\circ \quad (3)$$

are shown in Fig. 6, 7, 8, (Ref. 10). For comparison the Q^2-behavior given by the ρ° propagator, $\sigma(Q^2) \sim [M_\rho^2/(Q^2 + M_\rho^2)]^2$, is shown — also the Q^2-dependence of the total electroproduction cross-section, $\sigma_T + \varepsilon\sigma_L$ is indicated. It is apparent from the figures that the data for reaction 2 and 3 are consistent with the dependence given by the ρ° propagator, although for the reaction 1 (which contains 2 and 3) the Q^2-dependence might be weaker.

From Ref. 5 data on both reaction (2) and

$$ep \rightarrow e\Delta^\circ\pi^+ \quad (4)$$

are available.

The W dependence for reaction (2) is found to be of the form $(W^2 - M_p^2)^{-2}$ for $2.1 < W < 2.6$ GeV and $0.2 < Q^2 < 0.6$ GeV^2, at fixed $t - t_{min} = 0.05$ GeV^2 where t is the four momentum transfer from the virtual photon to the π-meson (Fig. 9). This agrees with photoproduction. The data at $W = 2.23$ GeV and $t - t_{min} = 0.04$ GeV^2 are shown in Fig. 10 as function of Q^2 for reactions (2) and (4), Fig. 10. Also here it is found that the form of the Q^2-dependence may be very well approximated by the ρ°-propagator.

From the same group a few data points are available for reaction (3) (Fig. 11,) again shown in comparison to the Q^2 dependence of the ρ°-propagator (Ref. 13).

We may conclude that reactions (1) and (4) show a Q^2-dependence given by the ρ°-propagator, as implied by vector meson dominance. Therefore, the reactions (1) and (4) are of lesser importance at higher Q^2.

Another reaction studied quite extensively is single π^+ production (Ref. 4).

$$ep \rightarrow en\pi^+ \quad (5)$$

At small t, it shows a large contribution from longitudinal photons, and is rather rapidly increasing with Q^2 (Fig. 12). But the dependence on W is given by $\sim (W^2 - M_p^2)^{-2}$, and therefore reaction (5) is of negligible importance at higher W.

ρ^o Production

We continue to discuss reaction (3) in more detail. It is of particular importance because very specific predictions from various models are available for reaction (3). From considerations about important distances in space time, when the mass of the virtual photon, Q^2, increases, Cheng and Wu predicted an increasing width for diffractive peaks in electroproduction (Ref. 14). ρ^o-production is the best known example of diffractive photoproduction and therefore very well suited for a study of this anti-shrinkage phenomenon. The data from Ref. 12 for $Q^2 = 0$ and Ref. 10 at three values of Q^2 are shown in Fig. 13. The effect predicted in Ref 14 is observed. This is more apparent from a fit to the t-distribution,

$$d\sigma/dt \ (ep \to ep\rho) = A \cdot e^{-bt} \qquad (6)$$

The values of b (GeV^{-2}) obtained are shown in Fig. 14. As is well known from photoproduction, the extraction of the ρ^o production cross section from the final state $p\pi^+\pi^-$ is rather model dependent. For the data shown in Fig. 14 the "phenomenological" representation has been chosen (see Ref. 12), for $Q^2 = 0$ and $Q^2 > 0$.

From the VDM no change in the slope b is expected and, in fact, the experimental observation just discussed might present a serious problem to the interpretation of ρ^o-electroproduction in terms of VDM. Within the framework of VDM it may be an indication of a breakdown of the diagonal approximation (Ref. 15).

Of great interest is also the question of contributions from longitudinal photons, σ_L, to ρ^o-electroproduction. Most data are only for the sum, $\sigma_T + \epsilon\sigma_L$, where the polarization parameter ϵ is defined as

$$\epsilon = \left[1 + 2\,\frac{Q^2 + \nu^2}{Q^2}\,\tan^2\theta/2\right]^{-1} \qquad (7)$$

and σ_T is the cross-section for transverse photons. A separation of σ_T and σ_L is possible by taking data at W, Q^2 fixed, but different scattering angle for the electron. No data are available, but the ratio $R = \sigma_L/\sigma_T$ can be obtained from the data by analyzing the decay angular distribution of the ρ^o-mesons, with the additional assumption of S-channel helicity conservation. This assumption is consistent with the data (Ref. 10). The values for R obtained* are shown in Fig. 15. They are consistent with a constant ratio R, as well as linear rise, as predicted by VDM, although the ratio is much larger than demanded by GVDM (Ref. 16).

Measurements of Inclusive Particle Production

Experimentally, inclusive measurements are the next step in sophistication over total cross-section measurements. If the deep inelastic region is characterized by some peculiar final states, this possibly may be detected already in inclusive experiments. The data available are given in terms of x, $p_\perp$, W^2, Q^2, where $x = P_L/P_{max}$, measured in the CMS, and P_L, $P_\perp$ are the longitudinal and transverse momentum of the hadron. In a fragmentation picture the produced particles are assumed to preserve some knowledge of which initial particle they come from. This is illustrated in Fig. 16. The fragments of the beam particle should be concentrated in the forward hemisphere, $x > 0.3$, the proton fragments in the backward hemisphere, $x < -0.3$, and particles from neither the beam nor the target particle are concentrated in the so-called central region around $x = 0$. It should be remarked here that at this low energy $1.8 < W < 3.5$ GeV, the inclusive language is only of rather limited value because particle multiplicities are small, masses of particles cannot always be neglected in comparison to energies involved, and conservation laws are of strong influence on the momentum distributions. But still, for parametrisation of Q^2-dependences it provides a convenient framework and we shall use it here (Ref. 17).

* We show more recent data from the streamer chamber group for R here, which is at slightly higher W.

Changes are to be expected for particles coming from the virtual photon. In fact, an increase of the average transverse momentum of particles $ep \rightarrow e\pi^{\pm}$ + anything is predicted on the same grounds as for the diffractive ρ^{o}-production (Ref. 14). In the framework of a model, where partons are identified with quarks, the charge ratio $\sigma(\pi^{+})/\sigma(\pi^{-})$ (or more general, $\sigma(h^{+})/\sigma(h^{-})$, with $h^{\pm}$ any hadron) is predicted to be more positive at higher Q^2 (Ref. 18). Other models predict for the photon fragmentation region an increase of proton production (Ref. 19), or an increase of K-meson production (Ref. 20). Unfortunately, for purely experimental reasons, (acceptance, particle identification, data rate) most of the data available is only for rather small transverse momenta of the hadrons.

Proton spectra

The data from three sources (Ref. 2, 3, 7) are plotted in Fig. 17. The transverse momenta of the protons are small, $p_{\perp}^2 < 0.02$ GeV^2. No change from $Q^2 = 0$ to $Q^2 \sim 1.2$ GeV^2 is apparent. In the backward direction a few points from Ref. 21 are included, (W = 3 GeV, $Q^2 = 1.2$ GeV^2), here a drop with Q^2 due to the decreasing ρ^{o}-production is seen. We want to add a remark on the W^2-dependence of the inclusive proton yield at $Q^2 = 0$. In the positive x-region the yield is dropping rather fast with W^2, as indicated in Fig. 18, (Ref. 7). In the negative x-region the inclusive yield is also falling with W^2, but not as fast as in the forward region.

Pion spectra

The π^{-} spectrum integrated over all transverse momenta is shown in Fig. 19 (Ref. 10). In the central region, as well as in the target fragmentation region, no change with Q^2 is detected so far. Taking the data in the central region, $-0.2 < x < 0.2$, and trying a parametrisation of the form

$$E^*/p^*_{max} \cdot d\sigma/dP_{\perp}^2\, dx = A \cdot e^{-bP_{\perp}^2} \qquad (8)$$

for not too large $P_{\perp}^2$ (< 0.3 GeV^2), both A and b, as shown in Fig. 20 are constant within $\sim \pm$ 10% with Q^2 up to 1 GeV^2. Also shown are data from Ref. 22 on inclusive π^{+} production, Fig. 21, and again no change is observed for both A and b with Q^2. This leaves also the ratio $R \equiv \sigma(\pi^{+})/\sigma(\pi^{-})$ unchanged, which is roughly 1.5.

On the other hand, the charge ratio, $\sigma(p + \pi^{+})/\sigma(\pi^{-})$ is ~ 2.5 in the central region at W = 2.6 GeV and $Q^2 = 0$. It is decreasing with rising W, due to the decreasing proton yield, and increasing π^{-} yield (Ref. 23).

Transverse momentum distributions for various Q^2 and two x-intervals are shown in Fig. 22. As stated before, the central region shows no variation with Q^2, whereas the photon fragmentation region shows some indication for a decreasing slope b, (~30%) in a parametrisation of the form (8).

In the same x-region, $0.3 < x < 0.7$, also the $P_{\perp}^2$ integrated x-distribution (Fig. 19) shows a decrease with Q^2. This may be explained by the decreasing ρ^{o}-contribution, reaction (3), and for the region $x > 0.8$ by the decreasing contribution from reaction (2), as indicated by the line, which represents the data at $Q^2 = 0$, but without the contribution from reaction (3).

Data on both π^{+} and π^{-}, but at rather small transverse momenta, $p_{\perp}^2 < 0.3$ GeV^2 (Ref. 6,) $p_{\perp}^2 < 0.02$ GeV^2, (Ref. 2, 3) are available at $x > 0.4$. From Ref. 6, the $p_{\perp}^2$ distribution at two values of Q^2 has been fitted to the form (8), values for the slope b are shown in Fig. 23 as function of x together with photoproduction data (Ref. 7). In the region of $x > 0.4$, where the π^{-} yield is decreasing, (Fig. 19) a rather flat $p_{\perp}^2$ distribution is found, for $p_{\perp}^2 < 0.2$ GeV^2. This is not necessarily inconsistent with the data in Fig. 22 from Ref. 10, which are averaged over $0.3 < x < 0.7$, and mostly from x near 0.3 because of the strong x-dependence of the inclusive π^{-} production. There is no data from Ref. 6 at $0.3 < x < 0.4$.

At $p_{\perp}^2$ close to zero, ($p_{\perp}^2 < 0.02$ GeV^2), the data taken at $Q^2 = 0$ (Ref. 3) $Q^2 = 0.4$ GeV (Ref. 6) and $Q^2 = 1.15$ GeV^2 (Ref. 2) are shown in Fig. 24 for π^{-} and π^{+}.

As can be seen, the π^{+} yield is decreasing only slightly, whereas the decrease of the π^{-} yield is more dramatic with Q^2. It follows that the π^{+}/π^{-} ratio is changing with Q^2. This is plotted in Fig. 25 which clearly shows a steady increase of $R = \pi^{+}/\pi^{-}$

with Q^2, most pronounced in the region $0.5 < x < 0.7$. The source of this effect in terms of specific channels is not yet known. It might be related to the dependence of prong cross-sections, $\sigma n/\sigma_{tot}$, on Q^2 where n is the charged particle multiplicity for hadrons (n = 1, 3, 5). The data from Ref. 10, shown in Fig. 26, are suggestive of an increasing n = 1 contribution which might produce the effect on the charge ratio observed above. But, one has to keep in mind that only a rather specific region in a range where photon fragments are to be expected is involved, which is only a rather small fraction of the total cross-section.

If this effect is related to the quark-parton model, (Ref. 18) is not at all clear, although it is consistent with some calculations in terms of this model (Ref. 24).

K^+ Production

The data from Ref. 3 at $Q^2 = 0$ and Ref. 2 at $Q^2 = 1.15$ GeV^2 for $p_\perp^2 < 0.02$ GeV^2 are compared in Fig. 27. In the region $x > 0.8$, where two body channels dominate, the fractional cross-section $\left(\frac{1}{\sigma} F(x)_1 \quad p_\perp^2 < 0.02 \text{ GeV}^2\right)$ at $Q^2 = 1.15$ GeV^2 is ~ 3 times as large than at $Q^2 = 0$. This is in contrast to the π^+ yield in the same region, which drops by approximately a factor of 2. Therefore, the π^+/K^+ ratio is roughly 3, at $Q^2 = 1.15$ GeV^2, a change by a factor of 6. The data from Ref. 25 qualitatively support the DESY data, which, if also true at higher Q^2 and W, is a distinctive difference to particle production by hadronic beams.

SUMMARY

1) The ρ°-propagator gives a reasonable description of the Q^2-dependence of ρ°-electroproduction.
2) A sizeable fraction of ρ°-electroproduction ($\sim 30\%$) is probably due to longitudinal photons.
3) There are indications for a broader t-distribution for ρ°-electroproduction at higher Q^2.
4) The photon fragmentation region shows several distinctive changes with Q^2.
   a. The π^+/π^- ratio is increasing, mainly because the π^- yield is decreasing faster than the π^+ yield.
   b. The average $P_\perp$ of both π^+ and π^- increases with Q^2.
   c. The ratio K^+/π^+ increases with Q^2.
5) The fractional cross section for production of one charged hadron σ_1/σ_{tot} is increasing with Q^2.

Figure captions

Fig. 1 The kinematic region covered by the DESY experiments in terms of Q^2 and ν. The data signed $\pi^{\pm}$, $\pi^{\pm}K^{\pm}p$, $\pi^{\pm}K^{+}p$, are from Ref. 6, Ref. 2, Ref. 3, respectively. The data from the electroproduction experiment in the streamer chamber come from the region enclosed by the dotted line, the photoproduction data are in the range $1.8 < E_\gamma < 6.3$ GeV (Ref. 7, 10). In addition, the lower boundary of the deep inelastic region in terms of Q^2 and W is indicated.

Fig. 2, 3, & 4 A sketch of the experimental setups for the data described in Ref. 2, Ref. 4, Ref. 10, respectively.

Fig. 5 The mass distributions for $p\pi^+$, $\pi^+\pi^-$, $p\pi^-$ from the reaction $ep \rightarrow ep\pi^+\pi^-$, in two W intervals, from Ref. 10. The shaded region in $M(\pi^+\pi^-)$ indicates events which are forward in the CMS, $\cos\theta^*(\pi^+\pi^-) > 0.75$.

Fig. 6, 7, & 8 The Q^2-dependence for the total cross-section of reactions $ep \rightarrow ep\pi^+\pi^-$, $ep \rightarrow e\Delta^{++}\pi^-$ and $ep \rightarrow e\Delta^{++}\pi^-$ and $ep \rightarrow ep\rho^\circ$ respectively. The $Q^2 = 0$ points are from Ref. 11, the electroproduction points from Ref. 10, the dotted line is a behavior of the form $\sigma(Q^2) \sim (M\rho^2/M\rho^2 + Q^2)^2$.

Fig. 9 The W- dependence for reaction $ep \rightarrow e\pi^-\Delta^{++}$ at fixed $|t-t_{min}| = 0.05$ GeV^2 for different Q^2 regions. The dotted line indicates a behavior $\sigma(W) \sim (W^2 - M_p^2)^{-2}$, where M_p is the proton mass, from Ref. 5.

Fig. 10 The Q^2-dependence of reactions $ep \rightarrow e\pi^-\Delta^{++}$ and $ep \rightarrow e\pi^+\Delta^\circ$. The momentum transfer is fixed and small, $|t-t_{min}| = 0.05$ GeV^2, the mass of the hadronic system W = 2.23 GeV. The photoproduction point for $\pi^+\Delta^\circ$ is scaled down from 16 GeV, using $\sigma(W) \sim (W^2 - M_p^2)^{-2}$. The dotted line indicates the Q^2-dependence according to the ρ° propagator. Ref. 5.

Fig. 11 The Q^2-dependence for $ep \rightarrow ep^\circ p$, for fixed $|t| = 0.08$ GeV^2 and W = 2.7 GeV from Ref. 13. Mainly transversely polarized ρ° mesons are detected in this experiment.

Fig. 12 The Q^2-dependence of reaction $ep \rightarrow e\pi^+n$ at small $|t| = 0.04$ GeV^2 and W = 2.2 GeV. The strong increase is attributed (at this small $|t|$) to contribution from σ_L, this statement is model dependent. (Ref. 4).

Fig. 13 The t-distribution for reaction $ep \rightarrow ep\rho^\circ$ at three Q^2 intervals. Also data at $Q^2 = 0$ are shown (Ref. 10).

Fig. 14 The slope, b, of the t-distribution for the reaction $ep \rightarrow ep\rho^\circ$, when a fit of the form $d\sigma/dt = A\, e^{-bt}$ is applied to the data, Ref. 10.

Fig. 15 The ratio R of the cross-section for longitudinally polarized ρ°-mesons σ_T. The extraction of the data points requires the assumption of S-channel helicity conservation, (SCHC). From Ref. 10 and footnote on page 6.

Fig. 16 Definition of the fragmentation regions in photoproduction. Also shown is the general behavior of inclusive proton π^+ and π^- production, for W = 3 GeV (Ref. 7, 17).

Fig. 17 Inclusive proton production, at small transverse momentum of the proton, $p_\perp^2 < 0.02$ GeV^2. The data , are from Ref. 21, Ref. 7, Ref. 3, Ref. 2 respectively.

Fig. 18 The S-dependence of inclusive photoproduction of protons at $x = -0.5$ and $x = 0.5$. The data are from Ref. 7.

Fig. 19 Inclusive photo- and electroproduction of $\pi^\pm$, $ep \rightarrow e\pi^- + \text{any}$, integrated over all $p_\perp^2$. The curve is photoproduction of π^-, $\gamma p \rightarrow \pi^- + \text{any}$, when the π^- from $\gamma p \rightarrow p\pi^+\pi^-$, with $M_{\pi^+\pi^-} < 1$ GeV, is left out. This eliminates the contribution from elastic ρ° production. (Ref. 10)

Fig. 20 Inclusive photo- and electroproduction data in the central region. The parametrisation $d\sigma/dP_\perp^2\, dx = A\, e^{-P_\perp^2 \cdot b}$ is chosen and A and b are plotted versus Q^2. The $\pi^\pm$ data are from Ref. 7 for $Q^2 = 0$, and Ref. 10 for $ep \rightarrow e\pi^- + \text{any}$, and Ref. 22 for $ep \rightarrow e\pi^+ + \text{any}$. The π^- data are at $1.8 < W < 2.8$ GeV, the π^+ data at W = 3 GeV.

Fig. 21 The reaction $ep \to e\pi^- +$ any in different x and Q^2 regions the data are from Ref. 12 and Ref. 10. Notice an indication of a flatter $p_\perp^2$-distribution in the photon fragmentation region.

Fig. 22 The slope, b, of the $p_\perp^2$-distribution for inclusive $\pi^\pm$ production as function of x. The data are from Ref. 7, Ref. 6, Ref. 22, Ref. 10. Note that the slope is fitted to only $p_\perp^2 < 0.3$ GeV^2. In the photoproduction data the well known "sea gull" effect is seen.

Fig. 23 Forward ($p_\perp^2 < 0.02$ GeV^2) production of $\pi^\pm$ for $x > 0.4$. The data at $Q^2 = 0$ are from Ref. 3, at $Q^2 \sim 0.4$ GeV^2 from Ref. 6 and at $Q^2 = 1.15$ GeV^2 from Ref. 2.

Fig. 24 The change with Q^2 in the charge ratio $R = \sigma(\pi^+)/\sigma(\pi^-)$ at $W \sim 2.6$ GeV and $p_\perp^2 < 0.02$ GeV^2. The dotted lines are smooth curves through the data from Ref. 2 and Ref. 6. Notice that pions are separated in these experiments from protons and kaons, in contrast to the data from Ref. 26.

Fig. 25 The fractional prong cross-section $\sigma n/\sigma_{tot}$, where n denotes the number of charged hadrons as function of W and Q^2. Data are from Ref. 10.

Fig. 26 The inclusive cross-section for K^+ production. The data are from Ref. 2 and Ref. 3.

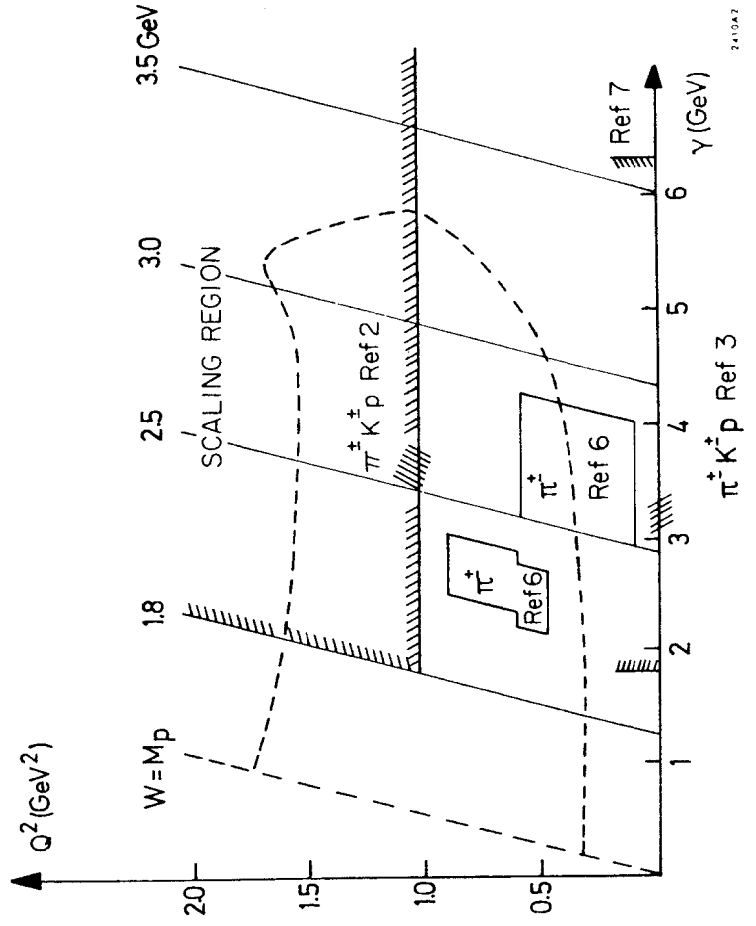

Fig. 1

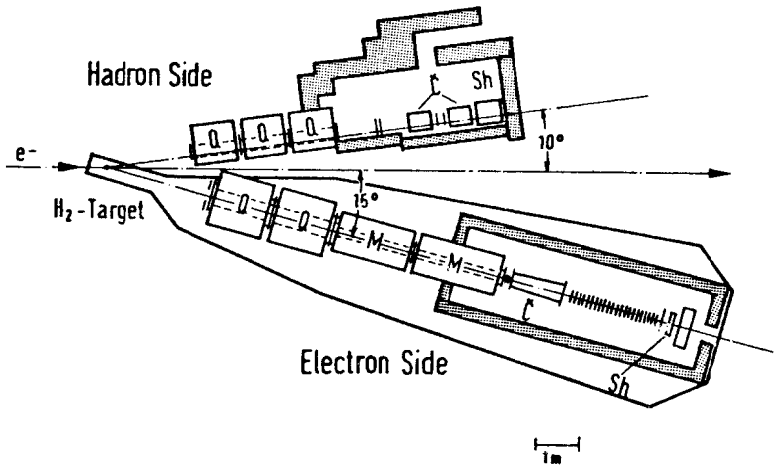

Figure 2

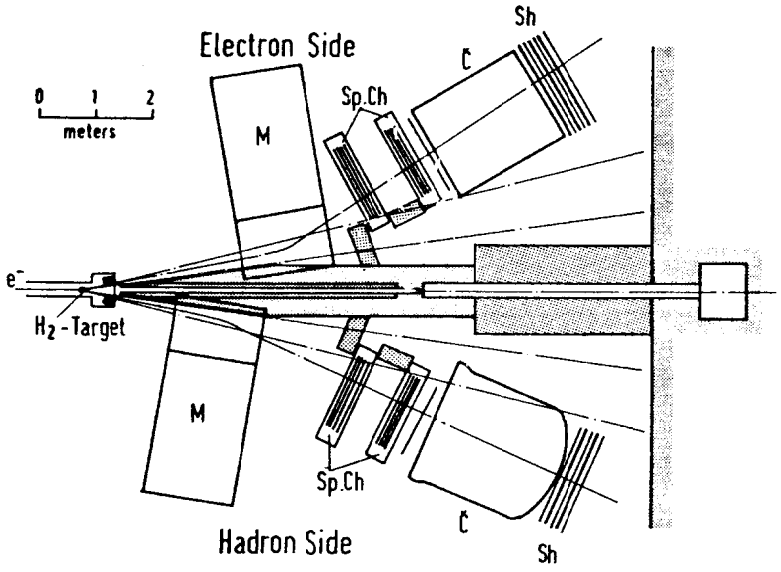

Figure 3

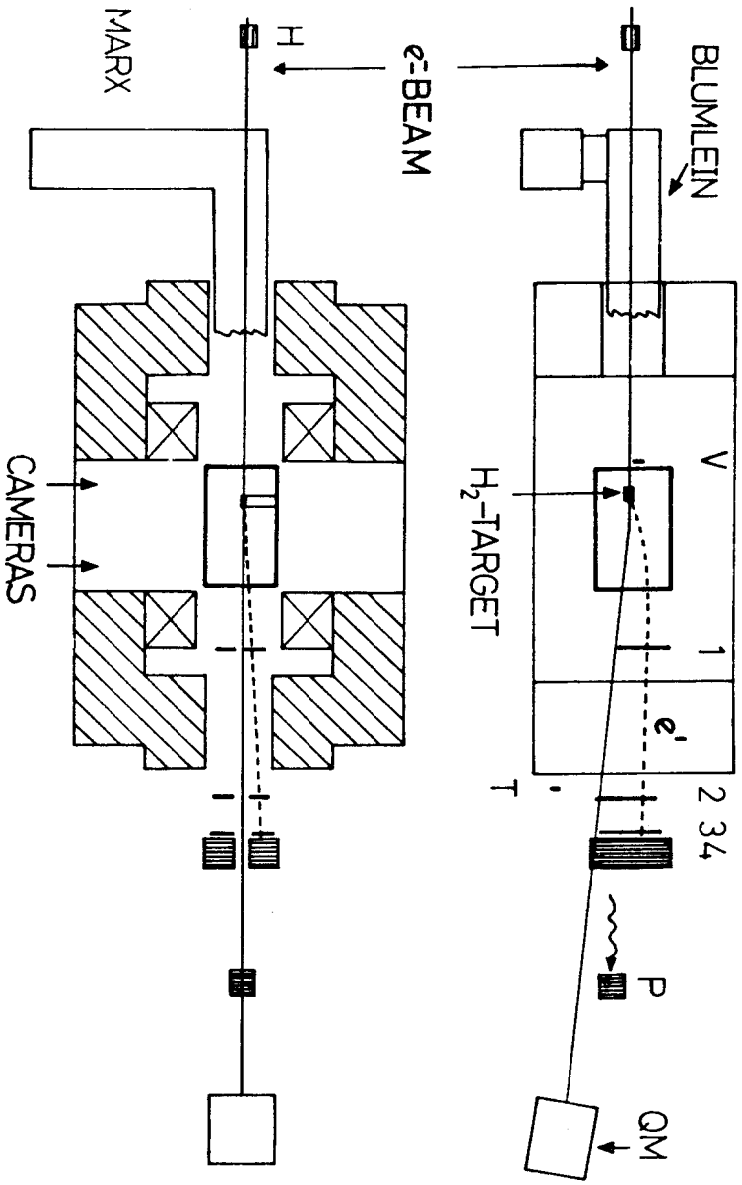

Figure 4

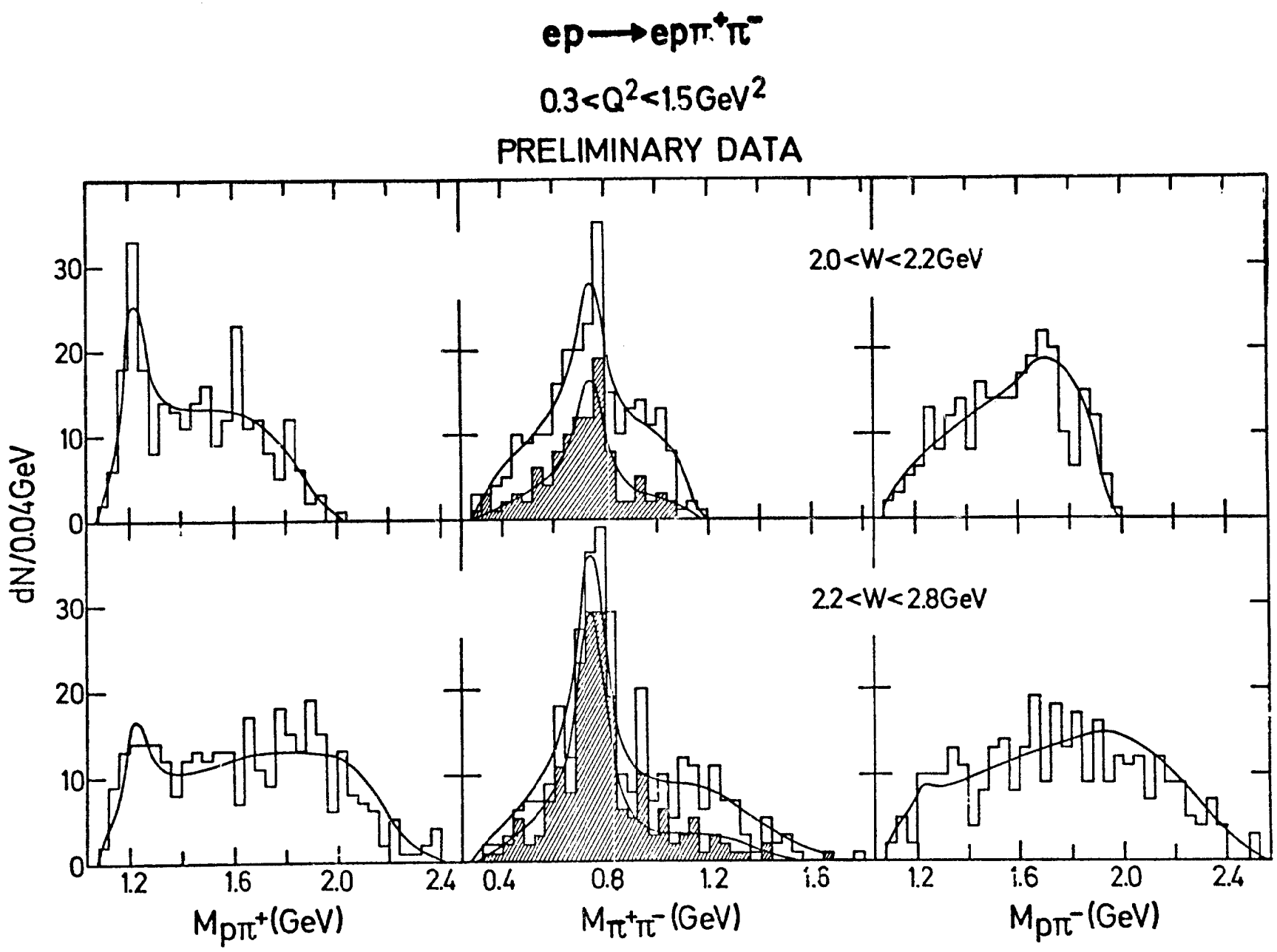
ep⟶epπ⁺π⁻
0.3<Q²<1.5GeV²
PRELIMINARY DATA
2.0<W<2.2GeV
2.2<W<2.8GeV
dN/0.04GeV
Mpπ⁺(GeV)
Mπ⁺π⁻(GeV)
Mpπ⁻(GeV)

Figure 5

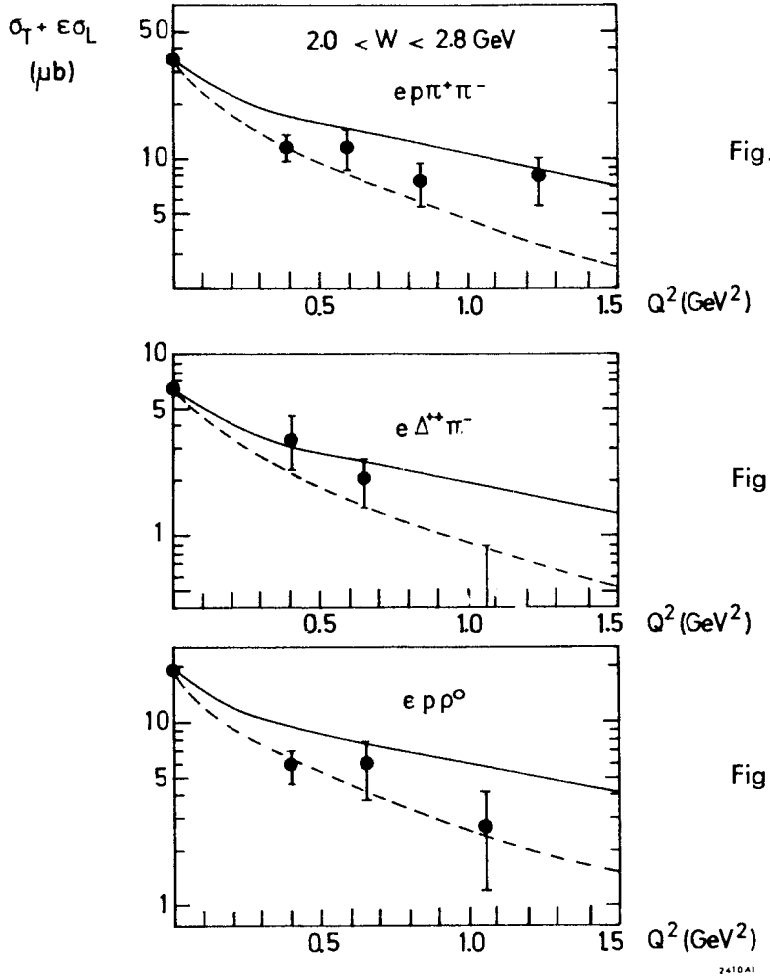

Fig. 6

Fig. 7

Fig. 8

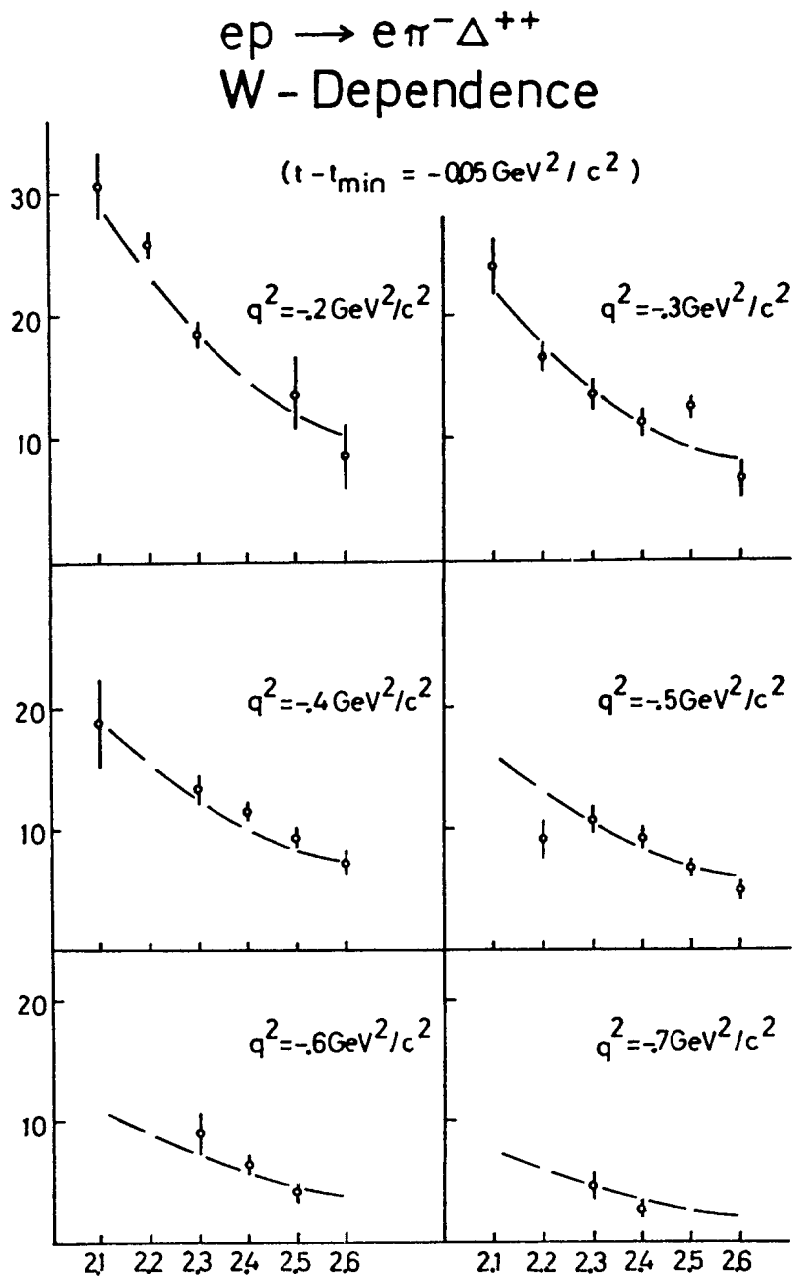

Fig. 9

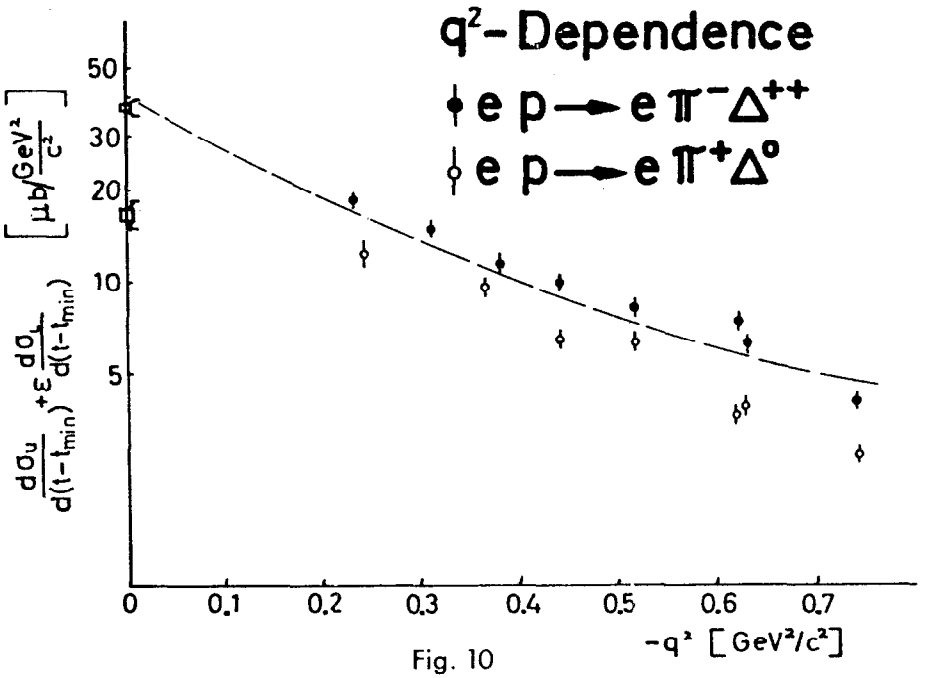

Fig. 10

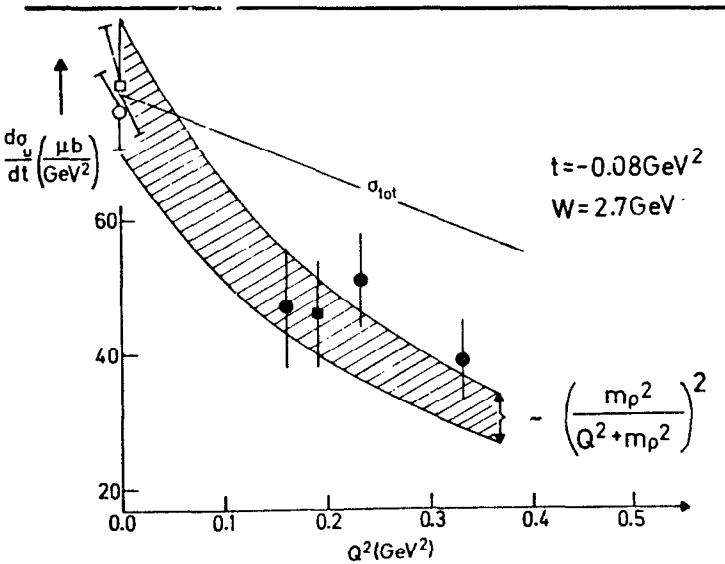

Fig. 11

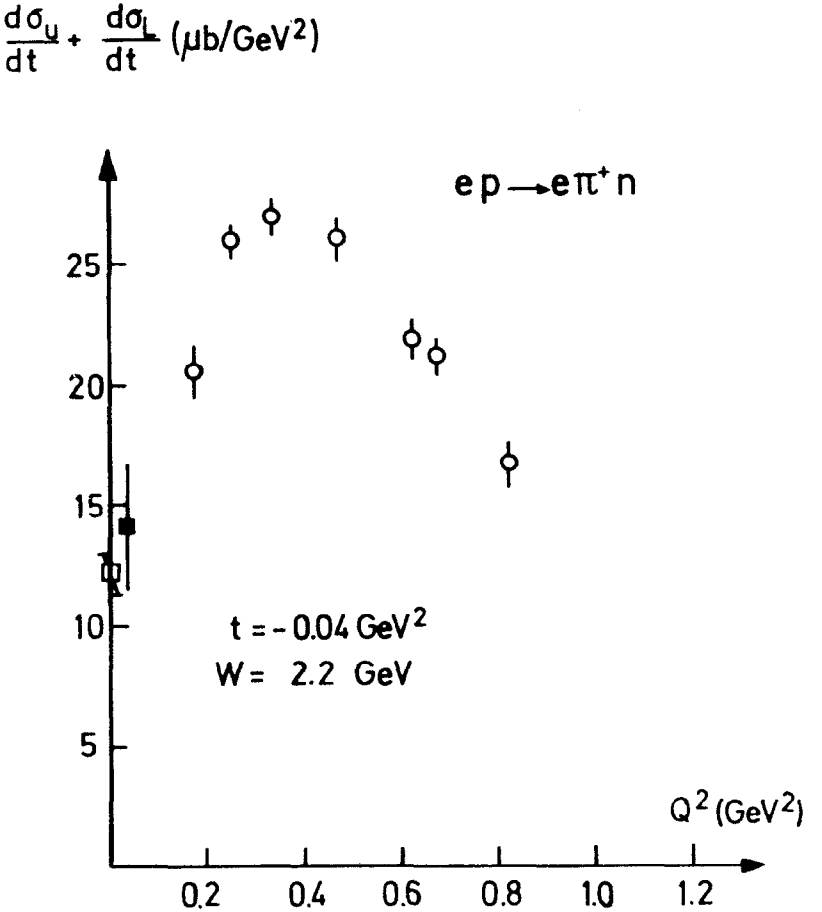

Fig. 12

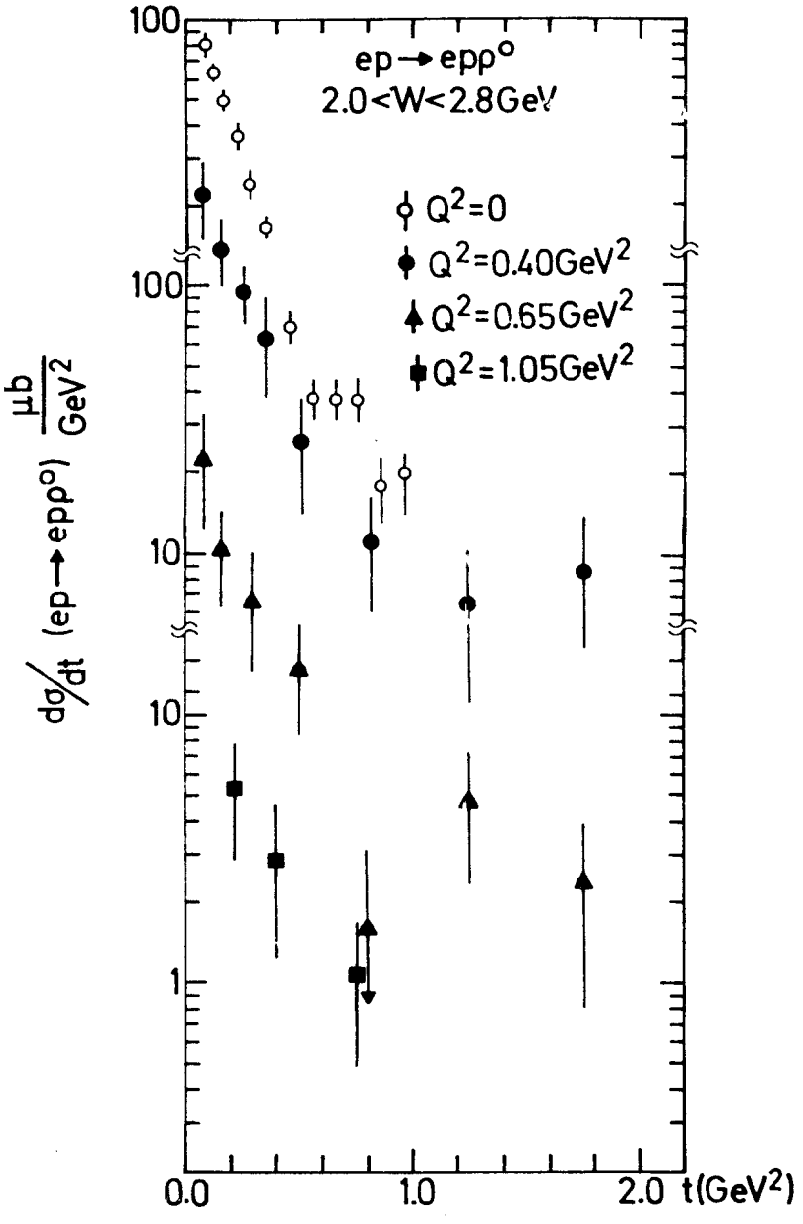
ep→epρ°
2.0<W<2.8GeV
Q²=0
Q²=0.40GeV²
Q²=0.65GeV²
Q²=1.05GeV²
dσ/dt (ep→epρ°) μb/GeV²
100
10
1
0.0
1.0
2.0
t(GeV²)

Fig. 13

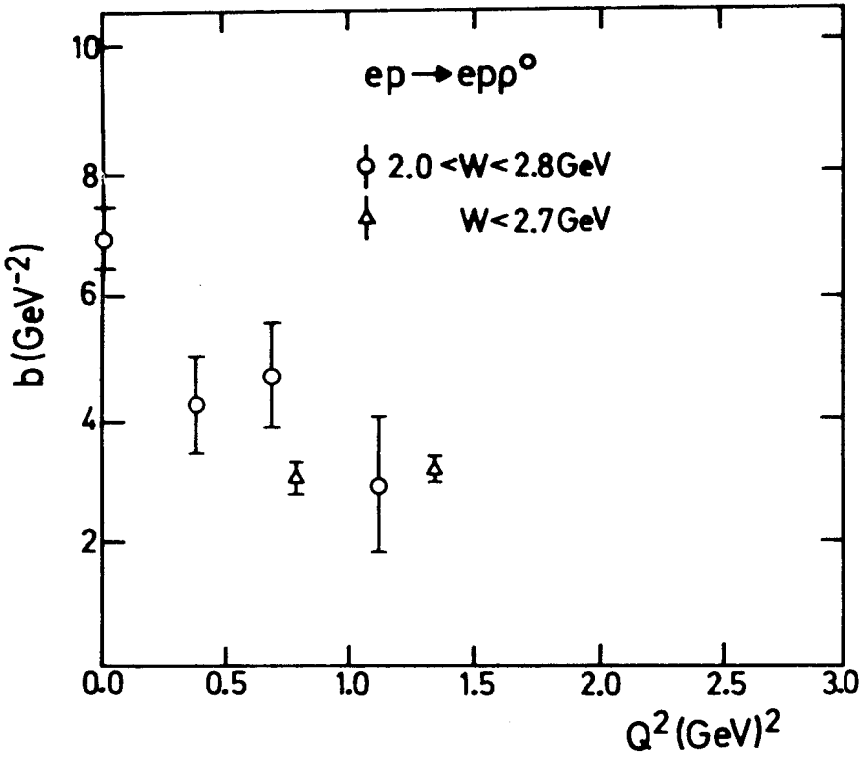
ep→epρ°
2.0<W<2.8GeV
W<2.7GeV
b(GeV⁻²)
10
8
6
4
2
0.0
0.5
1.0
1.5
2.0
2.5
3.0
Q²(GeV)²

Fig. 14

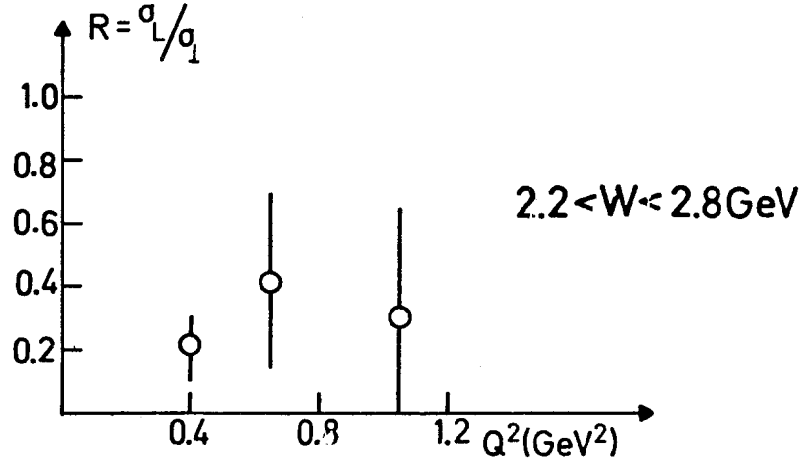
R = σL/σ1
1.0
0.8
0.6
0.4
0.2
0.4
0.8
1.2
Q²(GeV²)
2.2<W<2.8GeV

Fig. 15

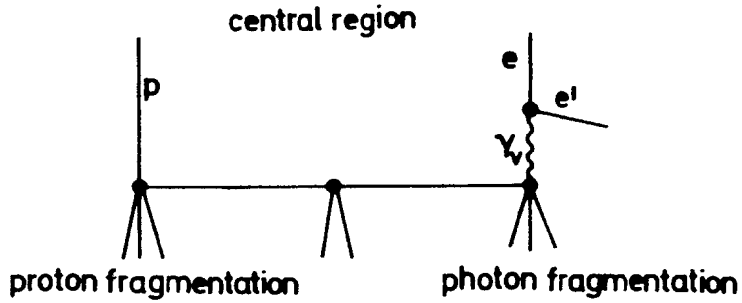
central region
p
e
e'
γv
proton fragmentation
photon fragmentation

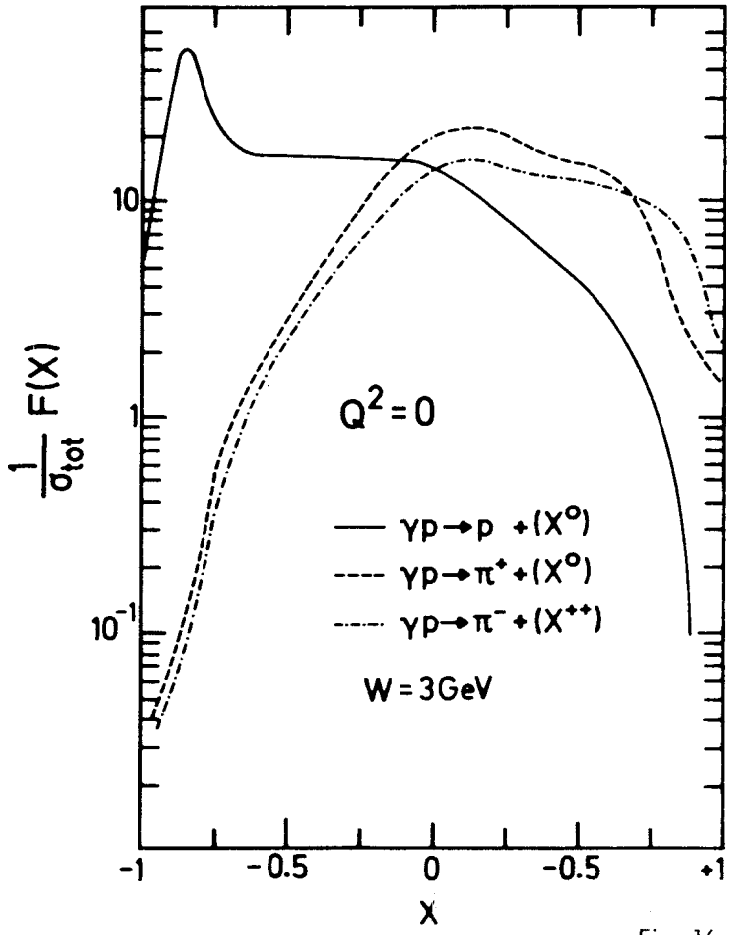
1/σtot F(X)
10
1
10⁻¹
Q² = 0
γp→p +(X°)
γp→π⁺+(X°)
γp→π⁻+(X⁺⁺)
W = 3GeV
-1
-0.5
0
-0.5
+1
X

Fig. 16

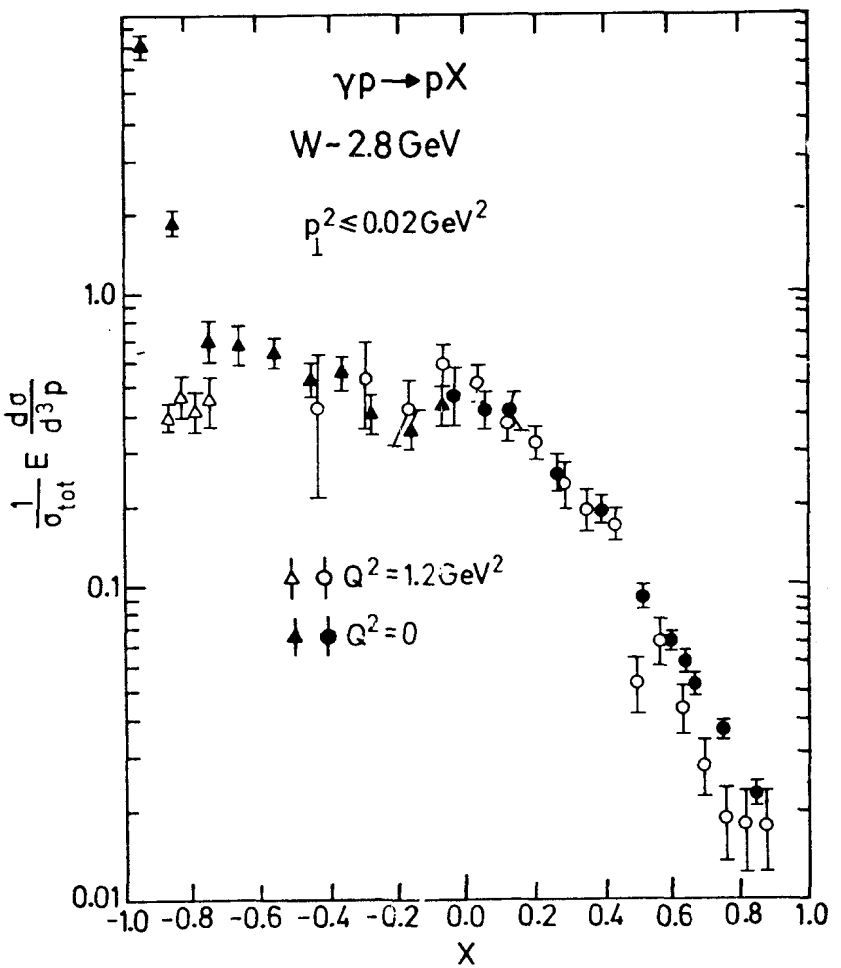
γp → pX
W~2.8GeV
$p_1^2 \leq 0.02 GeV^2$
$Q^2 = 1.2 GeV^2$
$Q^2 = 0$
$\frac{1}{\sigma_{tot}} E \frac{d\sigma}{d^3p}$
X
1.0
0.1
0.01
-1.0 -0.8 -0.6 -0.4 -0.2 0.0 0.2 0.4 0.6 0.8 1.0

Fig. 17

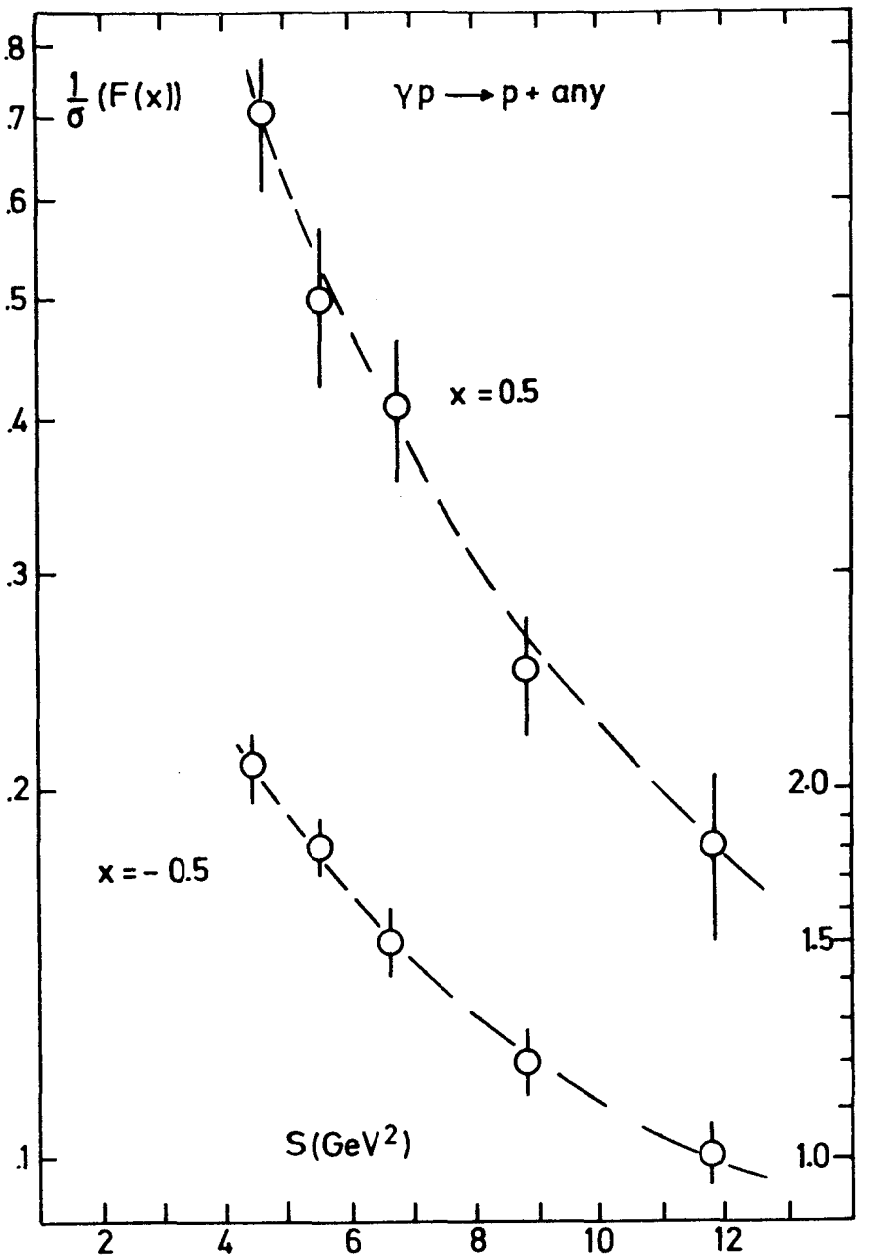
$\frac{1}{\sigma}$ (F(x))
γp → p + any
x = 0.5
x = - 0.5
S(GeV²)
.8
.7
.6
.5
.4
.3
.2
.1
2.0
1.5
1.0
2 4 6 8 10 12

Fig. 18

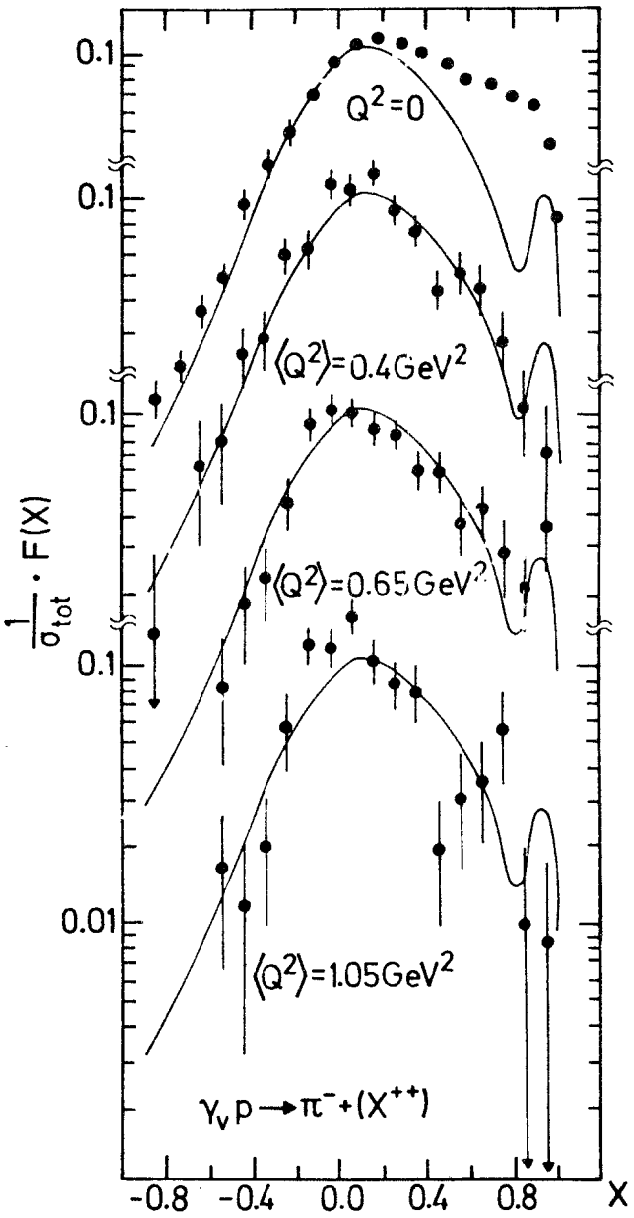

Fig. 19

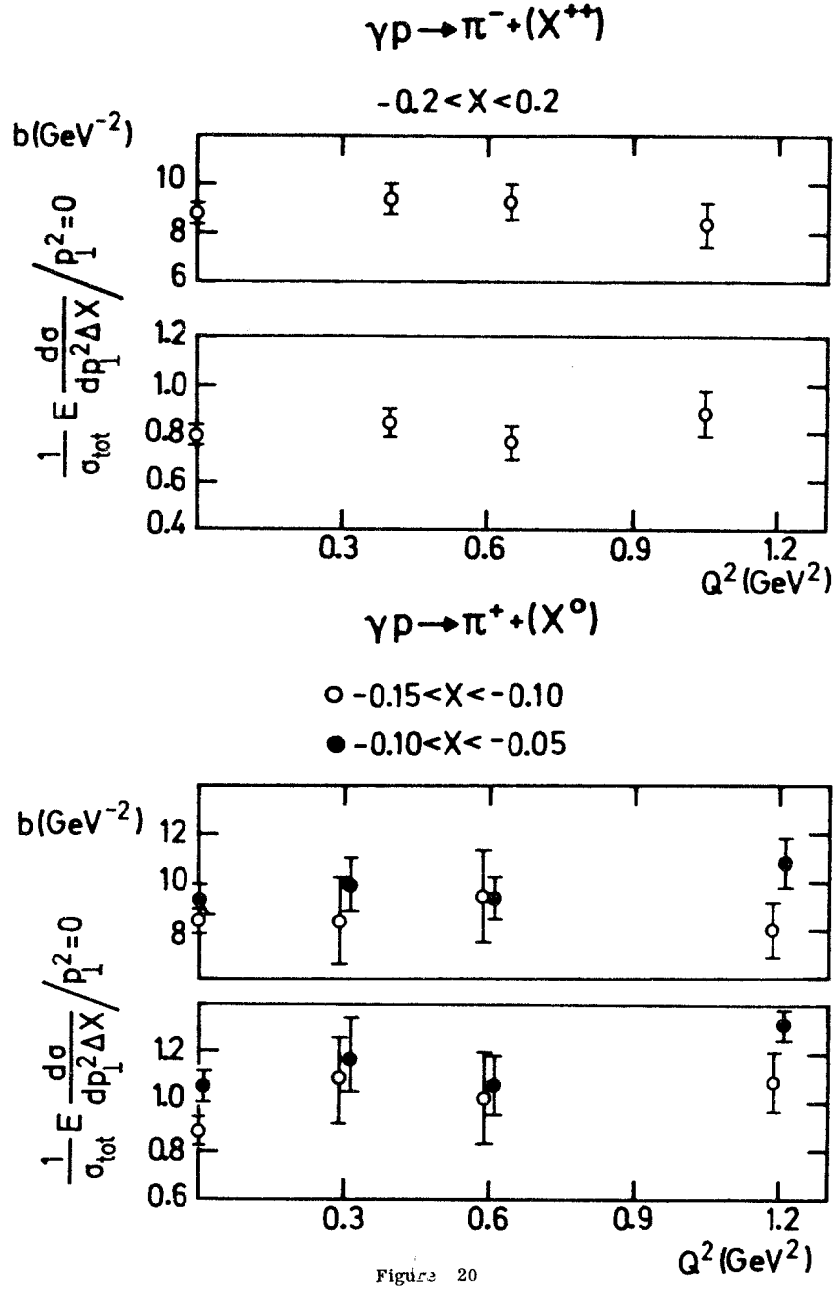

Figure 20

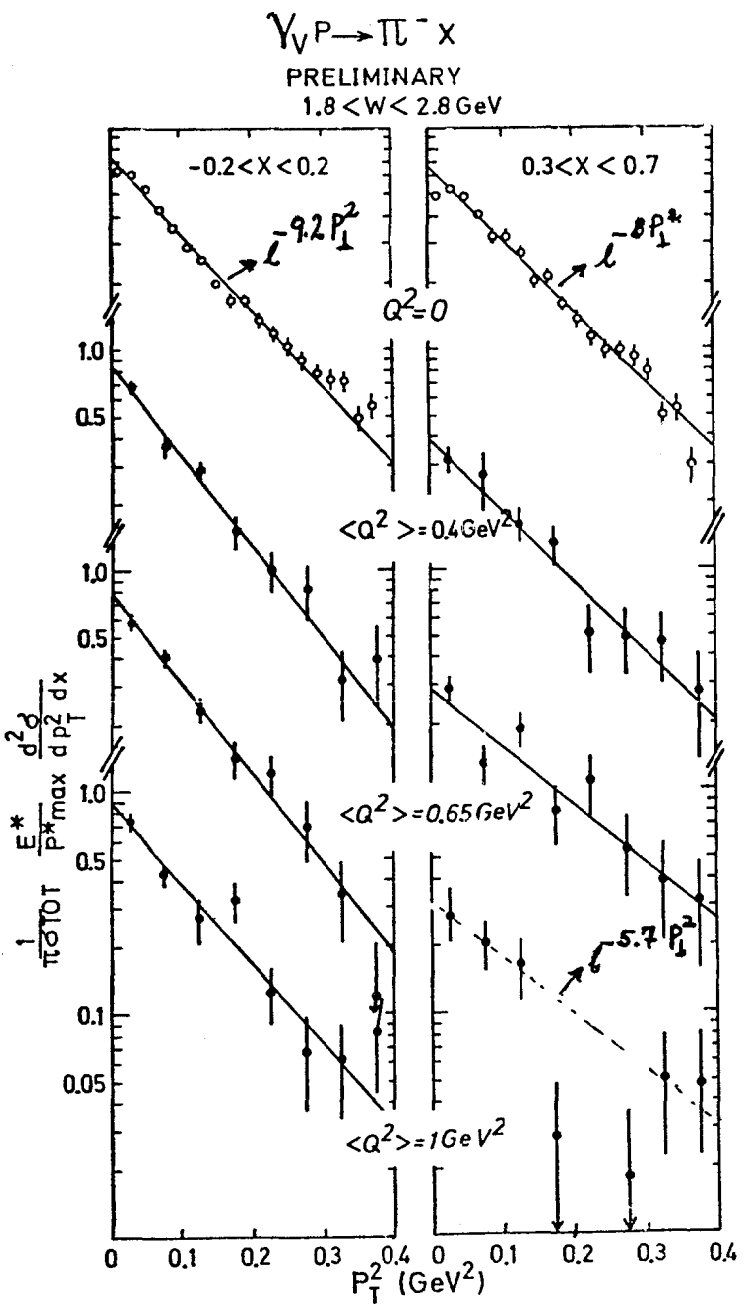

Figure 21

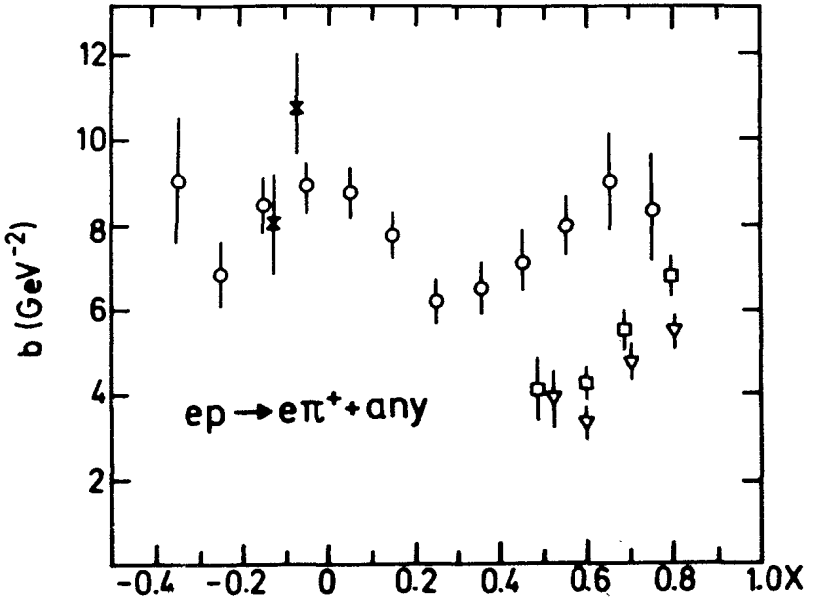

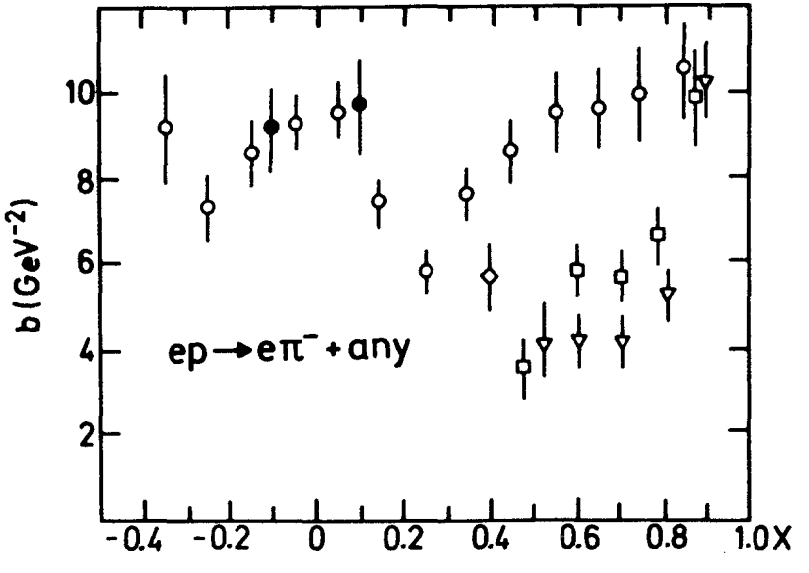

Fig. 22

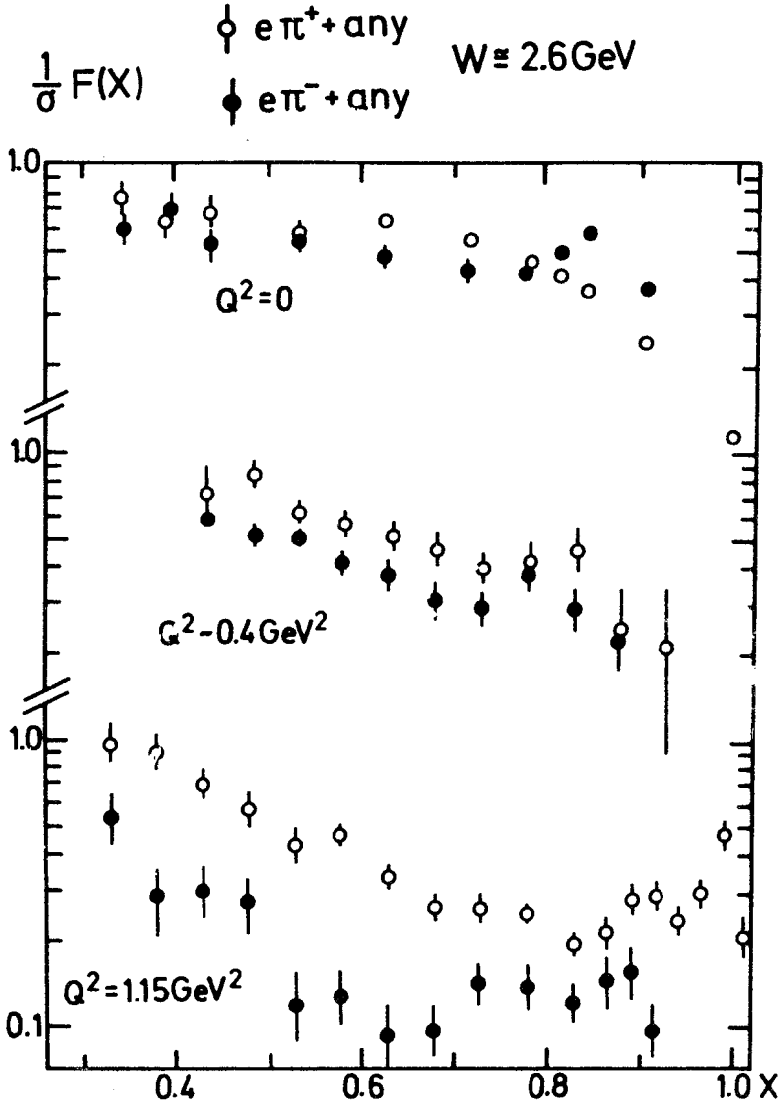
$\frac{1}{\sigma}$ F(X)
e π⁺ + any
e π⁻ + any
W ≅ 2.6GeV
1.0
1.0
1.0
0.1
Q²=0
Q²=0.4GeV²
Q²=1.15GeV²
0.4
0.6
0.8
1.0 X

Fig. 23

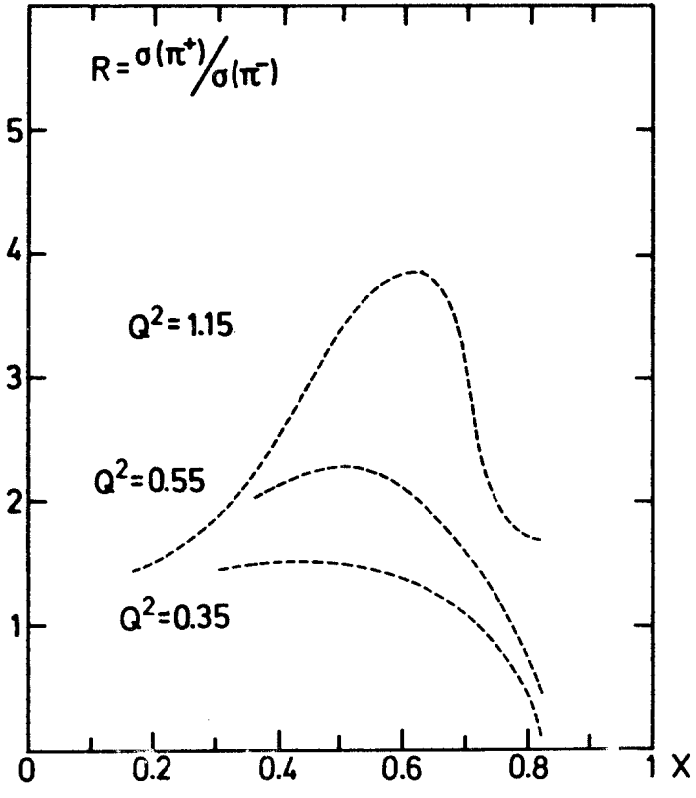
R = σ(π⁺)/σ(π⁻)
5
4
3
2
1
0
Q²=1.15
Q²=0.55
Q²=0.35
0.2
0.4
0.6
0.8
1 X

Fig. 24

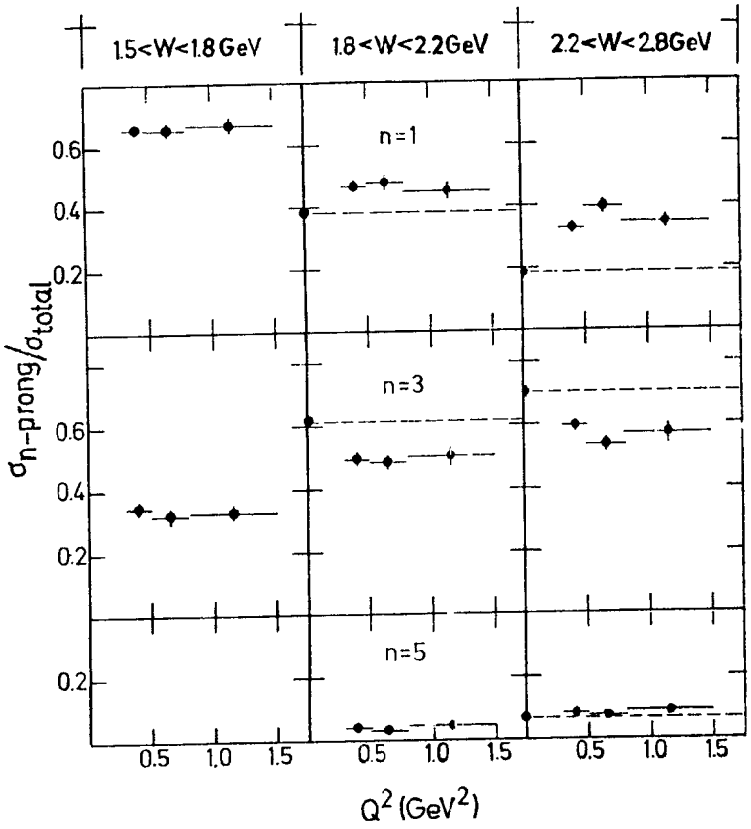
1.5<W<1.8 GeV
1.8<W<2.2GeV
2.2<W<2.8GeV
n=1
n=3
n=5
$\sigma_{n\text{-prong}}/\sigma_{total}$
Q^2 (GeV^2)

Fig. 25

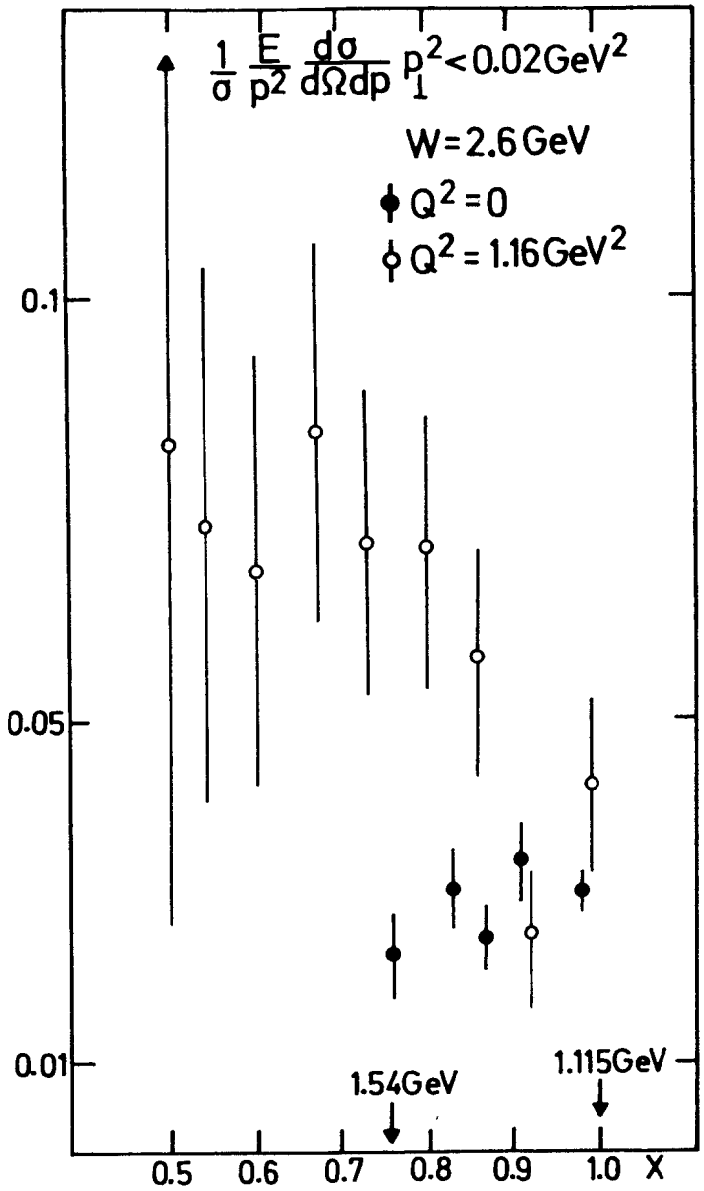
$\frac{1}{\sigma}\frac{E}{p^2}\frac{d\sigma}{d\Omega dp}$ p_1^2<0.02GeV^2
W=2.6 GeV
Q^2=0
Q^2 = 1.16GeV^2
1.54GeV
1.115GeV
X

Fig. 26

References

1. G. Miller et al., Phys. Rev. D5, 528 (1972).
2. J. C. Alder et al., Nucl. Phys. B46, 415 (1972).
3. H. Burfeindt et al., Phys. Letters B43, 345 (1973).
4. C. Driver et al., Nucl. Phys. B30, 245 (1971).
5. I. Dammann et al., Nucl. Phys. B54, 355 (1973).
6. I. Dammann et al., Nucl. Phys. B54, 381 (1973).
7. W. Struczinski et al. AHHM-Collaboration, Contribution to XVI International Conference on High Energy Physics, Chicago, 1972.
8. V. Eckardt et al., Nuovo Cimento Letters 6, 551 (1973).
9. V. Eckardt et al., Physics Letters 43B, Number 3, 240 (1973).
10. V. Eckardt et al., Nuclear Physics B55, 45 (1973).
11. ABBHHM Collaboration, Phys. Rev. 175, 1669 (1968).
12. SBT Collaboration, Phys. Rev. D5, 545 (1972).
13. C. Driver et al., Nuclear Physics B38, 1 (1972), and Erratum Nucl. Phys. B53, 643(1973).
14. H. Cheng, T. T. Wu, Phys. Rev. 183, 1324 (1969).
15. G. Cocho, M. Gregorio, J. Leon, and P. Rotelli, Internal report. Trieste June, 1973, IC/73/69.
16. J. J. Sakurai, P. Schildknecht, Physics Letters 40B, 121 (1972).
17. H. Meyer, "Experimental Results on Hadron Production in Inelastic Electron Scattering", DESY Internal Report F1-73/10 (1973).
18. M. Gronau, R. Ravndal, Y. Zarmi, Nucl. Phys. B51, 611 (1973).
19. S. D. Drell, D. J. Levy, T. M. Yan, Phys. Rev. 187, 2159 (1969).
20. K. Wilson, IC/71/47 Internal Report, Trieste, 1971.
21. E. Lazarus et al., Cornell preprint CLNS 191 (1972).
22. E. Lazarus et al., Phys. Rev. Letters 29, 743 (1972).
23. H. Meyer, W. Struczinski, DESY-Report 72/40, 1972.
24. J. T. Dakin, G. J. Feldman, SLAC-PUB 1273, July, 1973.
25. F. Pipkin, Talk given at this conference.
26. J. T. Dakin et al., Phys. Rev. Letters 29, 746 (1972).

HADRONIC FINAL STATES FROM INELASTIC MUON SCATTERING IN A HYBRID BUBBLE CHAMBER EXPERIMENT *

John T. Carroll
Stanford Linear Accelerator Center
Stanford University, Stanford, California 94305

I. Introduction

This experiment is a study of hadronic final states in inelastic muon scattering. The experiment was performed using the SLAC 40" hydrogen filled Bubble Chamber in a hybrid mode to selectively take pictures of inelastic muon-proton interactions. The experiment was a collaboration between Group A and Group BC at SLAC. Preliminary results from our data were presented at the "XVI International Conference on High Energy Physics." [1]

As shown in the top diagram in Fig. 1 the muon proton interaction

$$\mu^- p \to \mu^- + \text{hadrons}$$

is usually pictured as proceeding through the exchange of a single virtual photon. The incident lepton, ℓ, emits a photon of mass$^2 = -Q^2$ which interacts with the proton producing a final hadronic state at the lower vertex with center of mass energy W,

$$s = W^2 = M_p^2 + 2 M_p \nu - Q^2 \quad .$$

The detection of the scattered muons provides a virtual photon beam with variable mass. The lower diagram shows the photon mass relationship between electroproduction, photoproduction, and $e^+ e^-$ colliding beam experiments. This experiment, which studies the positive Q^2 region on this plot, was motivated by the MIT-SLAC single arm electroproduction experiments[2] which showed an inelastic cross section unusually large compared to the elastic cross section at $Q^2 >$ 1 GeV^2. These experiments also showed that the nucleon structure functions scale for $Q^2 > 1$ GeV^2 and $W > 2$ GeV. Most of our data falls in the transition region between photoproduction and the scaling region. Our experiment is basically a survey experiment designed to study the qualitative features of the hadronic final states in this transition region. We emphasize that in the comparison of our data with photoproduction data ($Q^2 = 0$) from the SLAC-LBL-Tufts collaboration[3], we were able to treat the raw data of both experiments in essentially identical ways.

* Work supported by the U. S. Atomic Energy Commission

II. Experiment

A. Muon Beam

This experiment used a muon beam whereas most previous studies have used electron beams. This choice avoided several problems associated with an electron beam in a bubble chamber (e.g. uncertainty in the beam and scattered e^- energy due to Bremsstrahlung, pair production of Brensstrahlung photons in the hydrogen, etc.). Using muons also minimizes but does not eliminate the problem of radiative corrections. Finally, measurements of μp scattering[4] have not shown significant differences between μp and e p scattering - cross sections differ by $\lesssim 10\%$.

The upper diagram in Fig. 2 shows a schematic representation of the muon beam. The muons were pair produced in a 2.5 radiation length (r.l.) target by a 20 GeV, 40 ma primary e^- beam. We used a high Z target to maximize the μ yield relative to the π yield. The muon beam consisted of four stages with three intermediate foci before the bubble chamber. The secondary beam momentum was defined by a 30 cm tungsten slit at focus 0. At this focus there was also a 3.7 m beryllium filter (~ 7.5 collision lengths) to reduce the π/μ ratio. The beryllium was placed close to the focus to minimize the effect of multiple scattering. It was important to minimize the π/μ ratio because the total μp cross section is ~ 1 μb for $Q^2 > .1$ GeV^2 compared to $\sigma_{\pi p} = 26$ mb. Even with our measured pion contamination of 5×10^{-5}, we still had roughly one pion interaction for each μp event in the bubble chamber. The secondary beam momentum after the Be filter was 16 GeV with a momentum spread of $\pm$ 3.7% (see Table I, next page).

The following stages in the beam were like a conventional π beam with considerable shielding at focus 1 and 2 to reduce beam halo (2 m of lead followed by 10 m of iron at each focus). There were also Proportional Wire Chambers at focus 1 and 2 and at the entrance to the Bubble Chamber, which were used to optimize the beam characteristics and reduce beam halo. Our optimized beam had a penetrating halo of 2%.

TABLE 1 - Beam Parameters and Event Rates

μ^- Beam		Event Rates
Momentum	16.0 GeV/c	30 million expansions at
Momentum spread	± 0.6 GeV/c (± 3.7%)	10 expansions per second
		100 μ's per pulse
Intensity	100 μ's/pulse	
Vertical size	11 cm FWHM	
Horizontal size	1.2 cm FWHM	94,000 triggered pictures
Vertical divergence	4 mrad FWHM	4922 useful good μ events
Horizontal divergence	3.5 mrad FWHM	1181 elastics (24%)
Penetrating halo	2%	3741 inelastics (76%)
Measured contamination	$\pi/\mu < 5 \times 10^{-5}$	

As noted in Table 1 the beam had a horizontal size of 1.2 cm. We needed this small width for 2 reasons: (1) the horizontal position in the bubble chamber was used to define the muon scattering angle, and (2) we wanted to veto the beam halo. The angular divergence of the beam in the bubble chamber was 4 mrad in the vertial and 3.5 mrad in the horizontal. This small divergence was possible, even after the 3.7 m Be filter, because the μ's were produced by pair production yielding an unusually small phase space at the target. Credit for the design and performance of our beam goes to Michel Della Negra, Lew Keller, and the LURCH beam transport program.

B. 40" Bubble Chamber

The lower diagram in Fig. 2 shows a cross section view of the 40" BC from the camera side of the chamber. The chamber is a 1 m diameter cylinder, 40 cm deep, with Scotchlite bright field illumination. The rectangular box around the chamber is the vacuum tank and the shaded region is an outline of the magnet yoke. The central field is 26 kG with half of the bending power outside of the visible region. Since we are using muons, our acceptance was not limited by the bubble chamber exit windows and in ~ 10% of our events the scattered μ passed through the magnet iron.

Because we are working with such a small cross section (~ 1 μb), a key part of this experiment was a program to improve the 40" pulse rate. The data we are presenting today required 30 million pulses of the 40" chamber. To put this in perspective, the 72" chamber took ~ 6 million pictures in the 10 year period before it came to SLAC. When this experiment was proposed the normal 40" pulse rate was 2/sec. Through the heroic efforts of Bob Watt and the 40" crew the chamber eventually ran at 10 pps and we took 90% of our data at this rate. In time the 40" ran as well at 10 pps as it had at 2 pps. The up-time was similar (50-60%) and we observed no degradation in the measuring accuracy.

Figure 3 shows a picture of a 4-prong event. The high beam flux which is 4 to 10 times that of a conventional BC experiment made the pictures obviously difficult to scan and measure. However, since we had a negative beam most events could be found by simply scanning for a positive track. The event shown in Fig. 3 has $Q^2 = .5$ GeV^2, W = 1.8 GeV, and fits $\mu^- p \to \mu^- p \pi^+ \pi^-$.

C. Muon Telescope

The μ dectector behind the bubble chamber, as shown in Fig. 2, provided the fast trigger that made the experiment feasible. Without a trigger our event density would have been 1 event/3000 pictures and we would have had to take ~ 15 million pictures. The detector consisted of 4 one foot blocks of iron sandwiched between eleven 1 m^2 magnetostrictive spark chambers (SC). The first SC was 3 m downstream of BC center. There were holes in the iron and dead areas in the spark chambers for the beam. The 4 blocks of iron which amount to 9.5 collision lengths (50 r.l.) were used to reject π triggers. From pictures taken with a π beam we estimated the π feed through in our final sample of events to be ~ 1/3%.

The trigger was defined by a coincidence between two planes of counters labeled S3 and S4 in Fig. 4. Each plane consisted of 8 counters. The inner counters in each plane were moveable and were adjusted to optimize the trigger rate and event acceptance. The trigger accepted muons scattered at an angle greater than approximately 1.4°. There were also 2 similar planes of veto counters upstream of the bubble chamber, which were used to reject beam halo. The veto rate was 5/pulse (2 were halo and the rest accidentals), and the veto dead time was about 12%. The overall dead time was 17% including 5% camera dead time.

The occurrence of a hardware trigger fired an interrupt to a PDP-8L computer. The computer read the trigger and veto counter status and checked the pattern of hits in the trigger counters to see if it was consistent with a track coming from the bubble chamber fiducial volume. This software check rejected 1/2 of the hardware triggers.

Table I summarizes our event rates. We obtained 1 accepted event, i.e. a good μp interaction, for every 16 computer triggers. With the bubble chamber running at 10 pps we took 120 pictures/hour from which we obtained 7.5 accepted events/hour. Our integrated μ flux for the entire experiment was ~ 2.5 billion muons. For comparison this is ~ 1/200 of one electron pulse in End Station A.

D. Data Reduction

Since this is a survey experiment and there was always at least a possibility that we would find something unexpected, like quarks, we scanned the film for all topologies. The film was scanned twice and a conflict scan was made to resolve discrepancies between the first two scans. Part of this scanning was done by the physicists. Finally we scanned the films a 3rd time looking at frames for which the pattern of sparks in the spark chamber trigger counters satisfied our criteria for a good μ^- track, but there was no corresponding event found by the first 2 scans. This scan yielded an additional 1.3% accepted events. Our final scanning efficiency was estimated to be 99%.

The film was measured on conventional film plane digitizers. We made at least 3 measurement passes on all rolls. Out of 5000 events in our final sample, 52 did not yield an acceptable measurement and 58 were unresolvable due to confusion. Despite the high beam flux of 100 μ's/pulse, this is a normal good bubble chamber pass rate.

The events were reconstructed using TVGP, the standard bubble chamber geometry program. The spark chamber tracks were reconstructed in a separate program. These 2 sets of data were input to the SQUAW kinematic fitting program. Here we identified the μ^- track in the bubble chamber by projecting the bubble chamber track to the muon telescope and requiring that it match the position and direction of a triggering spark chamber track. Having obtained a good match, we used the spark chamber measurements and the fringe field of the bubble chamber to improve the measurement of the μ^- direction and momentum in the bubble chamber.

In Fig. 5 we plot the error on the momentum vs the momentum for the scattered μ^- and observe a dramatic improvement in resolution by using the spark chamber data. The BC only plot does not quite do justice to the bubble chamber since we used an 84 cm fiducial volume in a 1 m chamber.* Of course, we used such a large fiducial volume because we knew we could improve the resolution using the spark chamber data. With only 12 cm of track in the bubble chamber we could measure the momentum of a 16 GeV track to ± 4%. The average error on the μ^- momentum (see Fig. 5) was 1.6%. The azimuth (φ) and dip angle (λ) errors were also improved.

After the reconstruction and kinematic fitting, all events were examined on the scan table by physicists. The physicist checked the μ^- match using a computer generated profile of the spark chambers as shown in Fig.6. Here we see a plane view of the μ^- projected from the bubble chamber, passing through the 11 spark chambers and the 4 blocks of iron. We checked that the track passed through the triggering counters, that there was a spark in one of the last two downstream chambers, and looked for multiple spark problems, etc. The physicist also selected the kinematic fits compatible with the observed bubble density. We identified protons with momentum up to 1.4 GeV.

III. Cross Sections and Multiplicities

Figure 7 shows the extent of our data in a plot of Q^2 vs W. There is a clear elastic peak at the left edge of the plot. Our data extends up to W = 5 GeV and to $Q^2 = 2.5$ GeV^2. With the exception of the high W region, we did not trigger on events with $Q^2 \lesssim .15$ GeV^2. In many of our plots we make a lower cut-off at $Q^2 \geq .2$ to eliminate the low Q^2 events which have an average W larger than the rest of the sample. The concentration at large W and small Q^2 came from events where the μ lost a lot of energy and was swept up into the trigger counters by the BC field. The contours of constant detection probability for the scattered μ^- were obtained from a Monte Carlo calculation. The detection probability is highest in the center of the plot, and is greater than 30% for most of the data.

The virtual photon cross section is related to the density of events in the Q^2 - W plane by:

*Using only the bubble chamber measurements, 75% of the events have $\Delta p/p < 0.1$ and $< \Delta p/p > = .037$ for the scattered μ^-.

$$\frac{d^2\sigma}{dQ^2 ds} = \left(\frac{\pi}{2MEE'}\right) \Gamma_t \left[\sigma_T (s, Q^2) + (\epsilon + \Delta)\, \sigma_S (s, Q^2)\right]$$

$$\sigma_T (s, Q^2) \xrightarrow[Q^2 \to 0]{} \sigma_{\gamma p} (s)$$

$$\Gamma_t = \frac{\alpha}{4\pi^2} \quad \frac{W^2 - M^2}{MQ^2} \quad \frac{E'}{E(1-\epsilon)}$$

$$\epsilon = \left[1 + \frac{2(Q^2 + \nu^2)\, \tan^2(\theta/2)}{Q^2 (1 - Q^2_{MIN}/Q^2)^2}\right]^{-1}$$

$$\Delta = \frac{2m_\mu^2}{Q^2} (1 - \epsilon)$$

$$Q^2_{MIN} = 2(EE' - |\vec{p}||\vec{p}'| - m_\mu^2)$$

This representation is more relevant to our presentation than the expression in terms of the structure functions since we emphasize the comparison with photoproduction. In our data, ϵ, the polarization parameter of the virtual photon varies from .8 to 1.0. Since we have only one beam energy we cannot separate σ_T and σ_S (by changing the beam energy one obtains the same Q^2 and W with different ϵ). The parameter Δ is an adjustment to the photon polarization which is negligible in our data. The virtual photon flux factor is $\Gamma_t \propto 1/Q^4$.

In the top part of Fig. 8(a) we plot the total cross section vs Q^2 in the W interval 1.8 - 2.8 GeV. The agreement with the single arm electroproduction data is satisfactory. We estimate our systematic error at ± 10% while the single arm measurements are good to ± 5%. We also plot the ratio of the topological cross section to the total cross section--the number of prongs is the number of charged hadrons. We have plotted cross section ratios because they should be less sensitive to systematic uncertainties than the cross section itself. At $Q^2 = 0$ we show the photoproduction topological cross section at the $< W >$ of the μp data. The fraction of 1 prongs is larger and the fraction of 3 prongs smaller than in photoproduction. Our data for $1.4 < W < 1.8$ show similar behavior. In Fig. 8(b) we plot the cross section for $2.8 < W < 3.8$ GeV. Again the 1-prong fraction increases, the 3-prong fraction decreases with Q^2, and there is no evident trend in the 5 and 7-prong data.

As I mentioned previously, we scanned the film for all topologies including strange particle events. In Fig. 9 we plot the ratio of the visible strange particle cross section to the total cross section. This cross section represents the number of observed neutral and charged decays. We observe no Q^2 dependence and find the ratio consistent with the photoproduction value in all 4 W bins shown. The ratio increases from 1% in the lowest W bin to 8% in the high W bin.

The only significant difference from photoproduction in these cross section plots is the increasing fraction of 1-prongs and the corresponding decrease in the 3-prongs. To further examine this feature of the data we plot $< N >$, the mean charged hadronic multiplicity; $< N > = \frac{\Sigma n\, \sigma_n}{\Sigma\ \sigma_n} = \frac{\Sigma n\, \sigma_n}{\sigma_{TOT}}$. In Fig. 10 we plot $< N >$ vs Q^2 in 3 W intervals. The triangles show the photoproduction multiplicity at the $< W >$ of the bin. In the lower W interval (1.8 - 2.8) the multiplicity is clearly falling over the Q^2 range of this experiment. In the central and high W intervals the multiplicity at high Q^2 is lower than in photoproduction.

The multiplicities shown here are corrected for radiated photons. These corrections are typically a few percent and are most significant for the lowest Q^2 point in each W interval. The largest correction was 16% for the lowest Q^2 point in the interval $3.8 < W < 5.3$ (for the lower W intervals we do not have data for $Q^2 < 0.15$ GeV^2). Without these corrections the data are roughly flat in Q^2 falling below the photoproduction point. If we were able to make these corrections to the topological cross section plots in Fig. 8 we might see a smoother transition near $Q^2 = 0$.

Another way of looking at the multiplicity is to plot the charge ratio defined as the ratio of positive to negative hadronic tracks. A SLAC Group E experiment[5] has shown that the charge ratio in the photon fragmentation region is larger than the photoproduction value. Here we plot the inclusive charge ratio vs Q^2 for events with $W > 2.5$ GeV in 3 x regions where x is the Feynman inclusive variable defined in the hadron C.M.S.

$$x = p^*_{\parallel} / p^*_{max} .$$

In the target region our low Q^2 point agrees well with photoproduction while by $Q^2 = 1$ GeV^2 the ratio is ~ 40% lower than in photoproduction. However, this high Q^2 point is within errors of the photoproduction point with elastic ρ events excluded (see solid triangle). In the central region the data show no Q^2 dependence. For $x > .3$ we also observe a charge ratio larger than the photoproduction value in agreement with the Group E data of Dakin et al.[5] The charge ratio is related to the multiplicity by charge conservation ($n_+ = n_- + 1$). Consequently our observation that the multiplicity decreases as Q^2 increases requires the charge ratio to increase when averaged over the entire x range.

IV. Inclusive Distributions

In Fig. 12 we plot F(x), the integrated structure function normalized to the total cross section.

$$F(x) = \frac{1}{\sigma_{TOT}} \int_0^{\infty} \frac{E^*}{\pi\, p^*_{max}} \frac{d^2\sigma}{dx\, dp_\perp^2}\, d\, p_\perp^2 \quad .$$

Here we show the π^- inclusive data for two Q^2 bins in two W intervals. In general the structure function can depend on both Q^2 and the center of mass energy squared $s = W^2$. The dashed line shows the corresponding structure function in photoproduction. These distributions include all events, including strange particle events. In the target fragmentation and central region of x we find good agreement with the photoproduction data. For $x \gtrsim 0.3$ the $Q^2 > 0$ points tend to be below the photoproduction values in all four Q^2 - W bins. We can obtain better agreement in this forward x region if we exclude the ρ^o events in the photoproduction data.

Figure 13 shows the integrated structure function for the inclusive π^+ reaction in the same Q^2 - w bins as used for the π^- data. We resolve pions from protons by ionization up to a laboratory momentum of ~ 1.4 GeV. Tracks that are ambiguous between the π^+ and p hypothesis are plotted in both π^+ and p distributions. Again we find good agreement with photoproduction for $x \lesssim 0$. There is a sharp forward peak which is more pronounced in all 4 bins than in the $Q^2 = 0$ data. In photoproduction this forward peak is associated with 2-body channels like πN and $\pi\Delta$.

Next we plot F(x) in Fig. 14 for slow laboratory protons ($x < -.5$). Again we have a low and high Q^2 bin in each of two W intervals. The strong backward peak in the photoproduction data (dashed line) comes mostly from diffractive ρ^o production. We see that particularly in the high Q^2 data, this backward peak has practically disappeared.

V. Resonance Production

A. ρ^o

We found 495 events which fit the 4-constraint reaction

$$\gamma_v\, p \to p\, \pi^+\, \pi^- \quad .$$

In Fig. 15 we plot $M(\pi^+\pi^-)$ vs W for these events and observe a distinct ρ^o signal with a background decreasing with increasing W. For our study of the ρ, we have used only events with $W \geq 2$ GeV. This cut eliminates most of the Δ^{++} signal while discarding few ρ^o events.

In Fig. 16 we plot $M(\pi^+\pi^-)$ in three Q^2 intervals and observe a strong ρ^o signal in all three bins. There is a small Δ^{++} signal for $.2 < Q^2 < .5$ GeV^2, but no evidence for Δ production in the other Q^2 bins. The $< W >$ = 3.17 GeV for the data with $Q^2 < .2$ while it is 2.8 and 2.83 GeV in the middle and high Q^2 intervals. As shown in Fig. 7 the larger $< W >$ at small Q^2 is a feature of the muon acceptance. Because of this larger $< W >$ we do not use the low Q^2 events in the cross section comparison to photoproduction.

In Fig. 17 we show the relative contribution of the $\pi^+\pi^-$ p channel to the total cross section. At this $< W >$ = 2.8 GeV the ratio is 21% in photoproduction. By $Q^2 = 1$ GeV^2 the ratio has decreased by ~ 40%. To determine the ρ cross section we made a maximum likelihood fit to the available Dalitz plot density allowing for ρ^o, Δ^{++}, and a phase space background. The resulting ρ and Δ^{++} cross sections are plotted vs Q^2 in Fig. 17. The ρ^o contribution to σ_{TOT} decreases from 15% in photoproduction to 8.5% by $Q^2 = 1$ GeV^2. Other experiments find similar results for the ρ cross section.[5,6] The smaller ρ signal at highe Q^2 accounts for much of the difference between the inclusive distributions in this experiment and in photoproduction.

In photoproduction the ρ mass distribution is skewed toward the low mass side of the peak. In the Ross-Stodolsky model this skewing comes from a factor $(M_\rho/M_{\pi\pi})^n = 4$. In electroproduction $M^2_{\pi\pi}$ is replaced by $M^2_{\pi\pi} + Q^2$, so at large Q^2 the change in $M_{\pi\pi}$ through the ρ peak region is not as significant as at $Q^2 = 0$ and the skewing should be less pronounced. To determine if the skewing changes with Q^2 we have fit the parameter n in the skewing factor for events with $|t| < 0.6$ GeV^2. The results as shown in Fig. 18 are consistent with n = 4, i.e. no change in the ρ mass shape as Q^2 increases.

In Fig. 18 we plot the ρ^o exponential slope parameter from fits to the t distributions. The photoproduction value is shown by the shaded band. While we observe a small decrease in the slope ($\sim 20\%$) by $Q^2 = 1$ GeV^2, the data is also consistent with no Q^2 variation.

Photoproduction of the ρ^o has been shown to conserve s-channel helicity. This is reflected in the ρ^o decay angular distribution which has a strong $\sin^2\theta$ dependence in the polar angle. However, in electroproduction the virtual photon has a longitudinal component which can give a longitudinal ρ with a $\cos^2\theta$ distribution.

In Fig. 19 we plot the ρ^o decay angular distribution in the helicity frame The $\cos\theta$ distribution is isotropic except for a slight enhancement near $\cos\theta = -1$ which results from a small Δ^{++} contamination. If we assume s-channel helicity conservation (SCHC), then this flat $\cos\theta$ distribution implies a contribution from longitudinal photons. The azimuthal angle distribution, ψ_H, also shows evidence of longitudinal ρ production. In photoproduction by linearly polarized photons the ψ_H distribution shows a clear $\cos^2\psi$ signal. Here this effect is still present on top of a flat ψ_H dependence from longitudinal ρ's.

In the scatter plot of $\cos\theta$ vs ψ the interference between longitudinal and transverse ρ production is seen as an increased density of events at ψ near 180° and $\cos\theta > 0$. For $\cos\theta < 0$ the interference gives a larger event density for ψ near 0° and 360°.

Assuming SCHC, the ρ decay angular distribution can be written in the form:

$$W(\theta, \psi) = \frac{3}{8\pi^2 (1 + \epsilon R)} \left[\epsilon R \cos^2\theta + \tfrac{1}{2} \sin^2\theta (1 + \epsilon \cos 2\psi) - \left(\frac{\epsilon R (1 + \epsilon)}{2}\right)^{\frac{1}{2}} \cos\delta \sin 2\theta \cos\psi \right]$$

ϵ = photon polarization parameter,

$R = \sigma_L(\rho) / \sigma_T(\rho)$,

δ = phase angle between longitudinal and transverse amplitudes .

There are only two free parameters, R and $\cos\delta$. From a maximum likelihood fit to the angular distribution we obtained values for R and $\cos\delta$ as plotted in Fig. 20. There is a tendency for R to increase with Q^2 as predicted in the vector dominance model of Sakurai and Schildknecht. However, the data do not exclude other behavior. Our results agree within errors with the data of Dakin et al.[5] The data show $\cos\delta$ near + 1.0 indicating maximal interference between the longitudinal and transverse components.

B. ω

In the upper half of Fig. 21 we plot $M(\pi^+\pi^-\pi^o)$ for events with a 1 C fit to the reaction

$$\gamma_v\, p \to p\, \pi^+\pi^-\pi^o \ .$$

We see a strong ω^o signal which persists when we demand $Q^2 > 0.5$ GeV^2 (shaded events). In the lower half of the figure we plot the ratio $\sigma(\gamma_v p \to p\,\omega)/\sigma_{TOT}$. Our data points agree well with the photoproduction cross section ratio of $\sim 3\%$, and show no evidence for a decrease in the ω cross section ratio at large Q^2. This difference in behavior from the ρ^o data which showed a decrease in the ρ^o cross section ratio may arise from a difference in production processes since the ω can be produced by both one-pion-exchange and diffractive scattering. The ω angular distributions in the helicity frame are consistent with isotropy.

C. ρ'

We have also looked for vector meson production in the 4π final state. In Fig. 22 we plot $M(4\pi)$ vs W for events which fit the 4-constraint reaction

$$\gamma_v\, p \to p\, \pi^+\pi^+\pi^-\pi^- \ .$$

Most of the events are near the kinematic boundary which is a diagonal line on this plot. In the ρ' mass region there are a few events at higher W. In photoproduction the ρ' was only resolvable at higher center of mass energies. We have attempted to place an upper limit on ρ' production by selecting events with $M(4\pi) < 2.0$ GeV and $W > 3$ GeV. As shown in Fig. 22, the resulting upper limit on the fraction $\sigma_{\rho'}/\sigma_{TOT}$ is consistent with photoproduction.

D. A_2^+

In Fig. 23 we plot $M(\pi^+\pi^+\pi^-)$ for events with a 1 C fit to

$$\gamma_v p \to \pi^+\pi^+\pi^- n \ .$$

The data show a clear A_2 signal. As shown by the shaded events, the A_2 signal persists when we cut at $|t| > 0.5$ GeV^2. This behavior is similar to A_2 production with hadronic beams. The data shown have $Q^2 > 0.2$ GeV^2. The data with $Q^2 > 0.5$ GeV^2 (82 events) show no clear evidence for A_2 production but the statistics are poor. For $Q^2 > 0.2$ GeV^2 and $W > 2.5$ GeV we estimate

$$\sigma(\gamma_v\, p \to A_2^+\, n) / \sigma_{TOT} = .012 \pm .004 \ .$$

The corresponding ratio in photoproduction is $.008 \pm {}^{+.005}_{-.003}$ (for $E_\gamma = 4.7$ GeV).

VI. Conclusions

1. The charged hadronic multiplicity decreases ~ 10% by $Q^2 = 1$ GeV^2.
2. The $\pi^\pm$ inclusive distributions normalized to σ_{TOT} show little W and Q^2 dependence except in the forward direction (x near 1.0).
3. The diffractive backward proton peak disappears as Q^2 increases.
4. The ρ^o contribution to σ_{TOT} is lower than in photoproduction by ~ 40% at $Q^2 = 1$ GeV^2.
5. The t distributions for ρ^o production have an exponential slope consistent with photoproduction, but ~ 20% smaller at $Q^2 = 1$ GeV^2.
6. The ρ^o angular distributions suggest a strong signal from longitudinal ρ production, assuming helicity flip terms are small.
7. We observe a strong ω signal with a fractional contribution to σ_{TOT} consistent with photoproduction.

ACKNOWLEDGEMENTS

We thank Bob Watt and the Bubble Chamber Operations crew for the operation of the 40" BC at 10 pps. Excellent technical assistance was provided by Gary Johnson and Warren Weeks. The careful scanning and accurate measuring by the scanners of the CDA group was essential for the success of this experiment. We thank Kenneth Eymann and Dennis Feick for their help in the data reduction and programming. The suggestions and help of Professor Yehuda Eisenberg, Dr. Jerry Friedman, Dr. William Johnson and Dr. Eliezer Kogan are gratefully acknowledged.

Figure Captions

1. Virtual photon exchange diagram for μp scattering and Q^2 range of e^+e^- colliding beams, photoproduction, and electroproduction.
2. Schematic representation of the experiment.
3. Picture of a 4-prong event.
4. Three dimensional view of the muon telescope showing trigger and veto counters.
5. Error on Momentum vs Momentum of scattered μ^-.
6. Geometric representation of μ-Detector in one projection, showing a typical event.
7. Data distribution in Q^2 - W plane.
8. (a) Total and topological cross sections vs Q^2 for $1.8 < W < 2.8$ GeV.
8. (b) Total and topological cross sections vs Q^2 for $2.8 < W < 3.8$ GeV.
9. Ratio of σ (strange particle) / σ_{Total} vs Q^2.
10. Charged hadronic multiplicity as a function of Q^2 at fixed W.
11. The charge ratio as a function of Q^2 for various x ranges.
12. The normalized structure function F(x) vs x for the reaction $\gamma_v p \to \pi^- +$ anything.
13. The normalized structure function F(x) vs x for the reaction $\gamma_v p \to \pi^+ +$ anything.
14. The normalized structure function F(x) vs x for the reaction $\gamma_v p \to p +$ anything.
15. $M(\pi^+\pi^-)$ vs W for $\gamma_v p \to \pi^+\pi^- p$.
16. $M(\pi^+\pi^-)$ for $\gamma_v p \to \pi^+\pi^- p$.
17. Fraction of σ_{TOT} vs Q^2 for $\pi^+\pi^- p$, $\Delta^{++}\pi^-$, and $\rho^o p$ final states.
18. Q^2-dependence of the skewing parameter n for events with $|t| < 0.6$ GeV^2. Q^2-dependence of the exponential slope A for $\gamma_v p \to p \rho^o$.
19. Decay angular distributions in the helicity frame for $\gamma_v p \to p \rho^o$.
20. Ratio of longitudinal to transverse ρ production and cosine of the longitudinal - transverse phase difference assuming SCHC.
21. $M(\pi^+\pi^-\pi^o)$ and σ_ω / σ_{TOT} for $\gamma_v p \to p \pi^+\pi^-\pi^o$.
22. $M(2\pi^+ 2\pi^-)$ vs W for $\gamma_v p \to p \pi^+\pi^+\pi^-\pi^-$, and $\sigma(M_{4\pi} < 2$ GeV) / σ_{TOT} vs Q^2 for $W > 3$ GeV.
23. $M(\pi^+\pi^+\pi^-)$ for $\gamma_v p \to \pi^+\pi^+\pi^- n$.

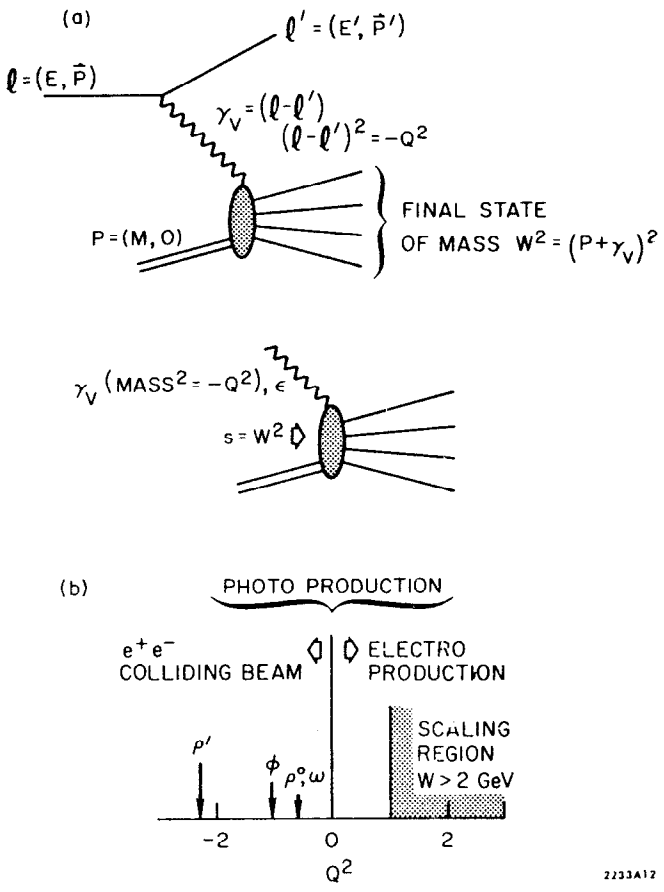
(a)
$\ell' = (E', \vec{P}')$
$\ell = (E, \vec{P})$
$\gamma_V = (\ell - \ell')$
$(\ell - \ell')^2 = -Q^2$
FINAL STATE
OF MASS $W^2 = (P + \gamma_V)^2$
$P = (M, 0)$
γ_V (MASS$^2 = -Q^2$), ϵ
$s = W^2$
(b)
PHOTO PRODUCTION
e^+e^-
COLLIDING BEAM
ELECTRO
PRODUCTION
SCALING
REGION
W > 2 GeV
ρ'
ϕ
ρ^0, ω
-2
0
2
Q^2
2233A12

Fig. 1

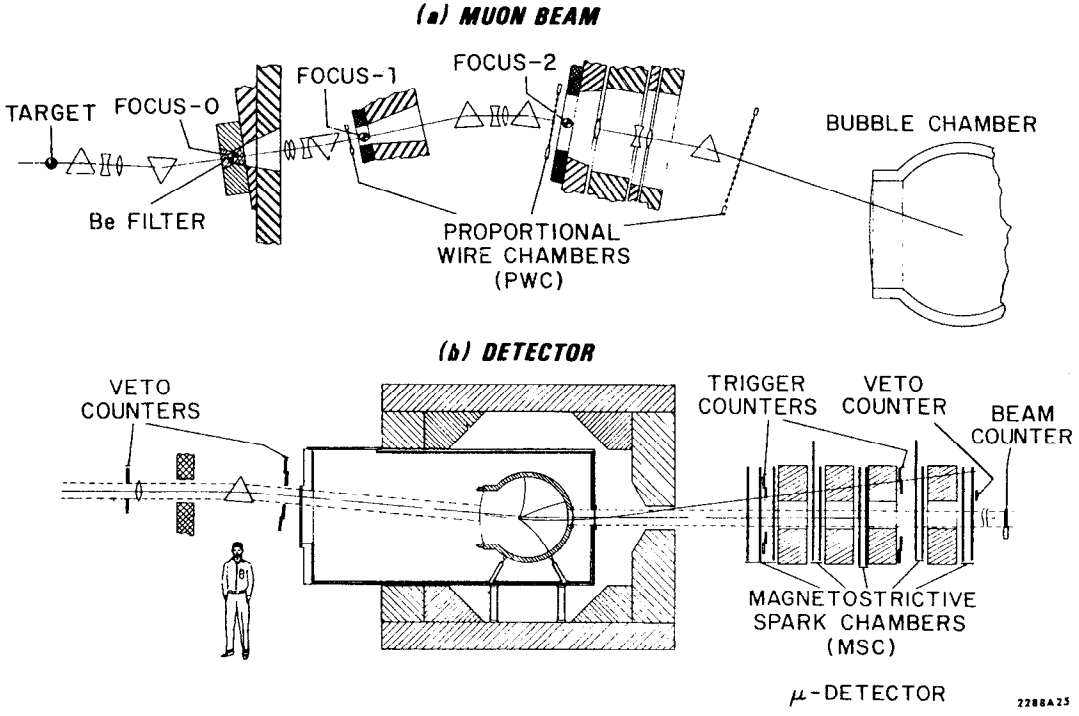
(a) MUON BEAM
TARGET
FOCUS-0
FOCUS-1
FOCUS-2
BUBBLE CHAMBER
Be FILTER
PROPORTIONAL
WIRE CHAMBERS
(PWC)
(b) DETECTOR
VETO
COUNTERS
TRIGGER
COUNTERS
VETO
COUNTER
BEAM
COUNTER
MAGNETOSTRICTIVE
SPARK CHAMBERS
(MSC)
μ-DETECTOR
2288A25

Fig. 2

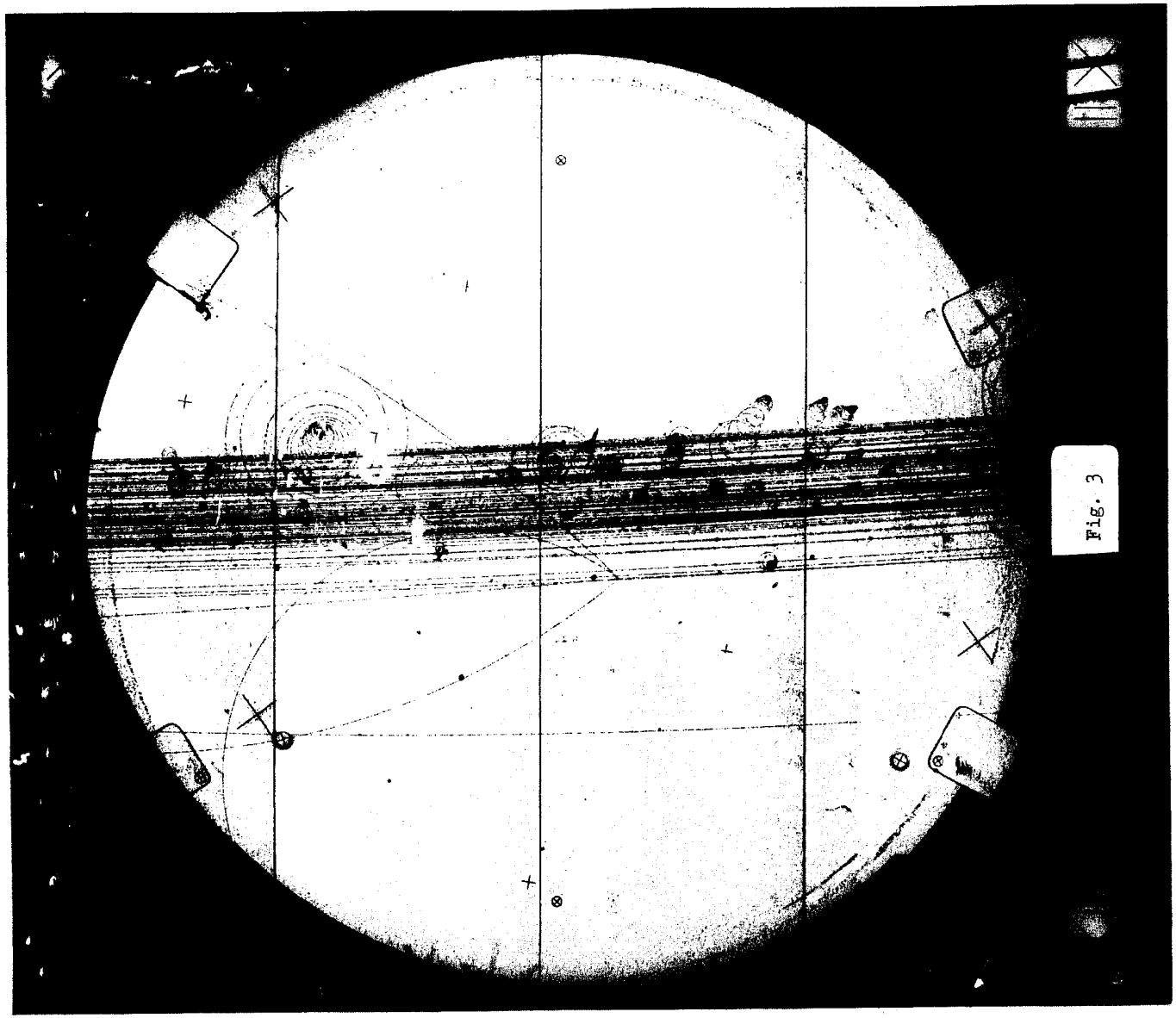

Fig. 3

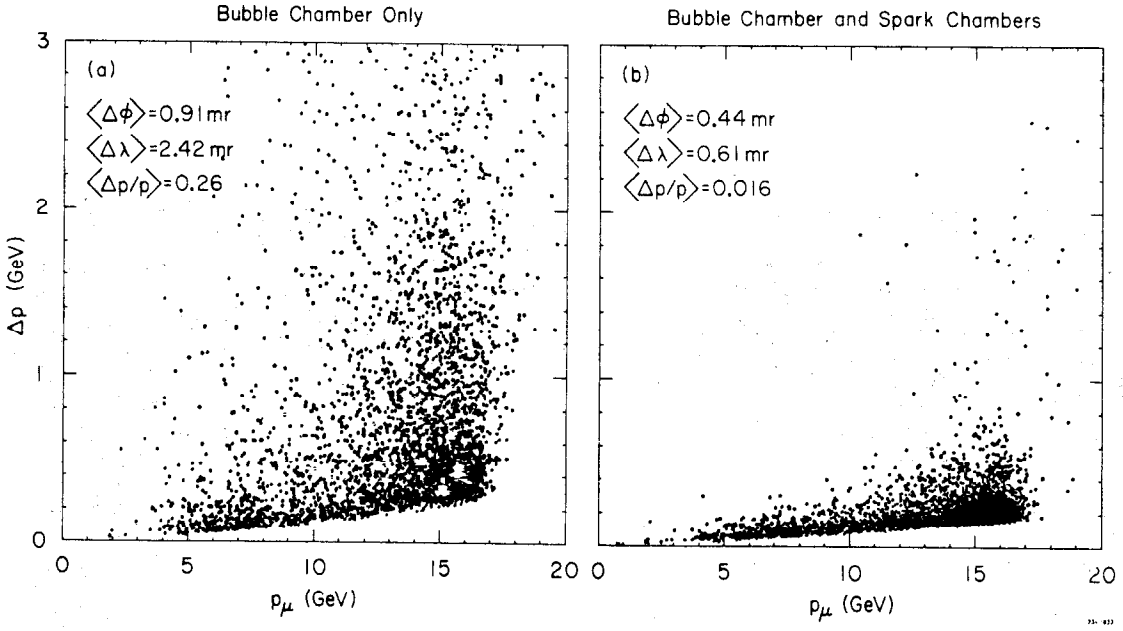
Bubble Chamber Only
Bubble Chamber and Spark Chambers
(a)
⟨Δφ⟩=0.91 mr
⟨Δλ⟩=2.42 mr
⟨Δp/p⟩=0.26
(b)
⟨Δφ⟩=0.44 mr
⟨Δλ⟩=0.61 mr
⟨Δp/p⟩=0.016
Δp (GeV)
pμ (GeV)
pμ (GeV)

Fig. 5

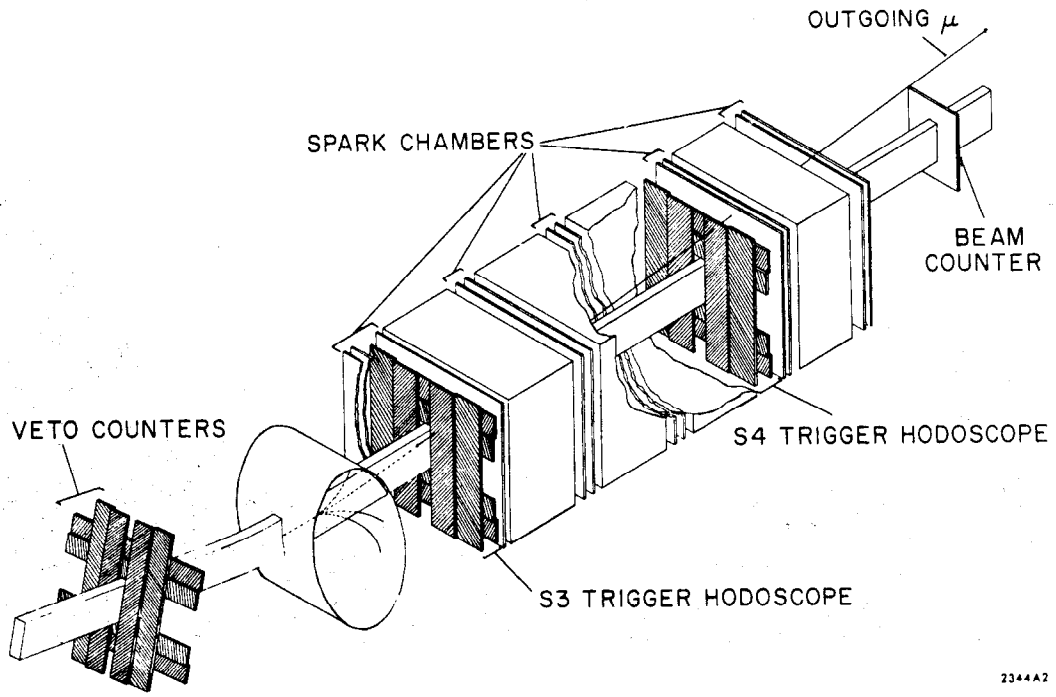
OUTGOING μ
SPARK CHAMBERS
BEAM COUNTER
VETO COUNTERS
S4 TRIGGER HODOSCOPE
S3 TRIGGER HODOSCOPE
2344A2

Fig. 4

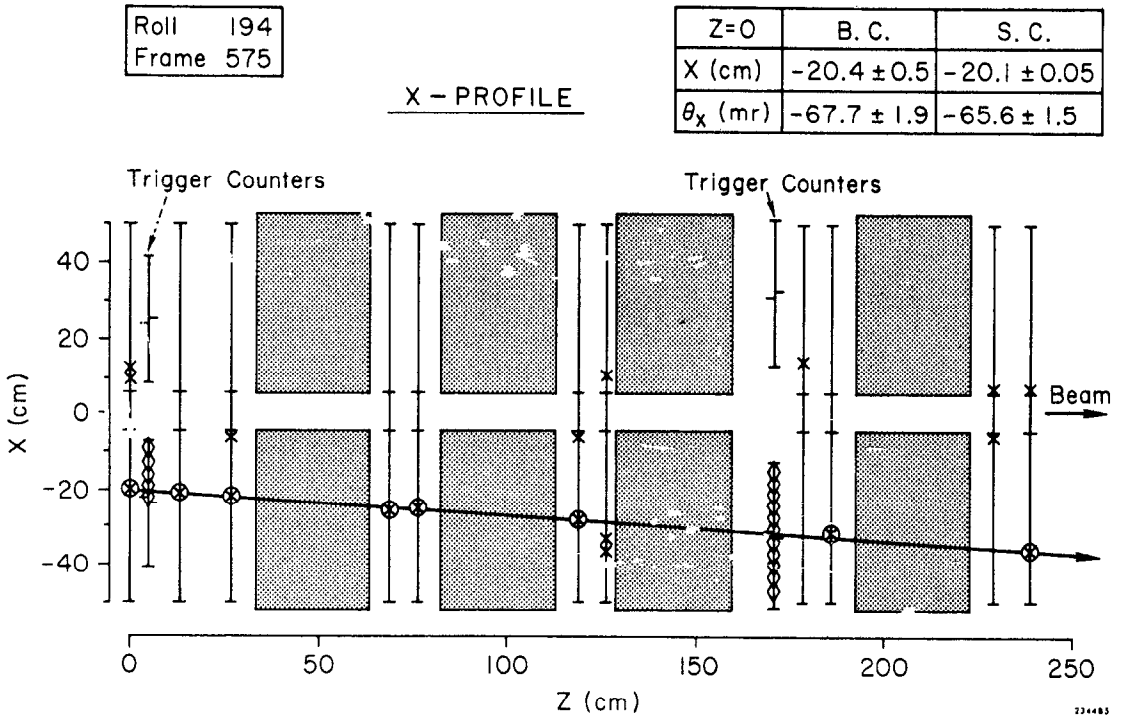
Roll 194
Frame 575
X – PROFILE
Z=0 | B. C. | S. C.
X (cm) | -20.4 ±0.5 | -20.1 ±0.05
θx (mr) | -67.7 ± 1.9 | -65.6 ± 1.5
Trigger Counters
Trigger Counters
Beam
X (cm)
Z (cm)

Fig. 6

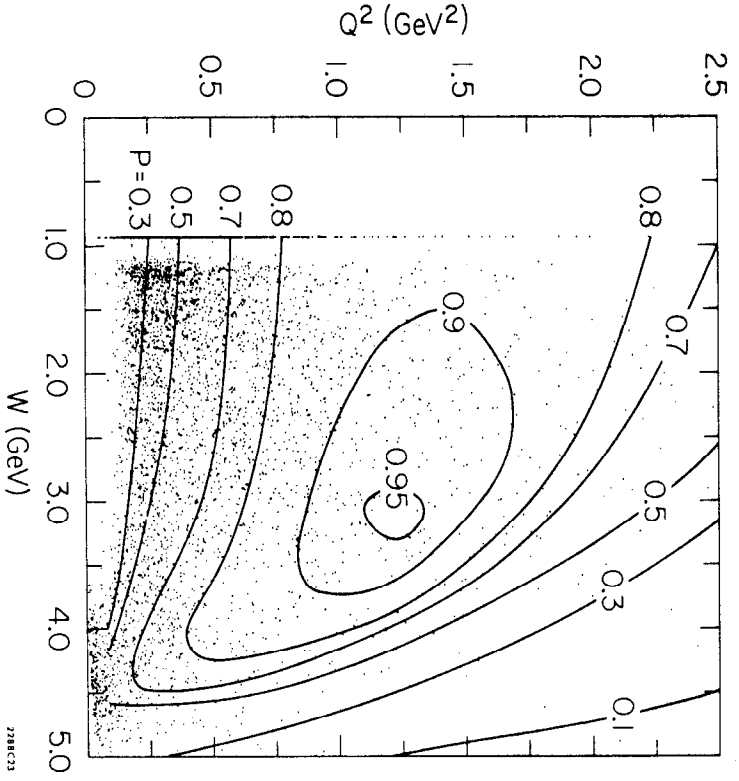
Q² (GeV²)
W (GeV)
P=0.3
0.5
0.7
0.8
0.9
0.95
0.8
0.7
0.5
0.3
0.1

Fig. 7

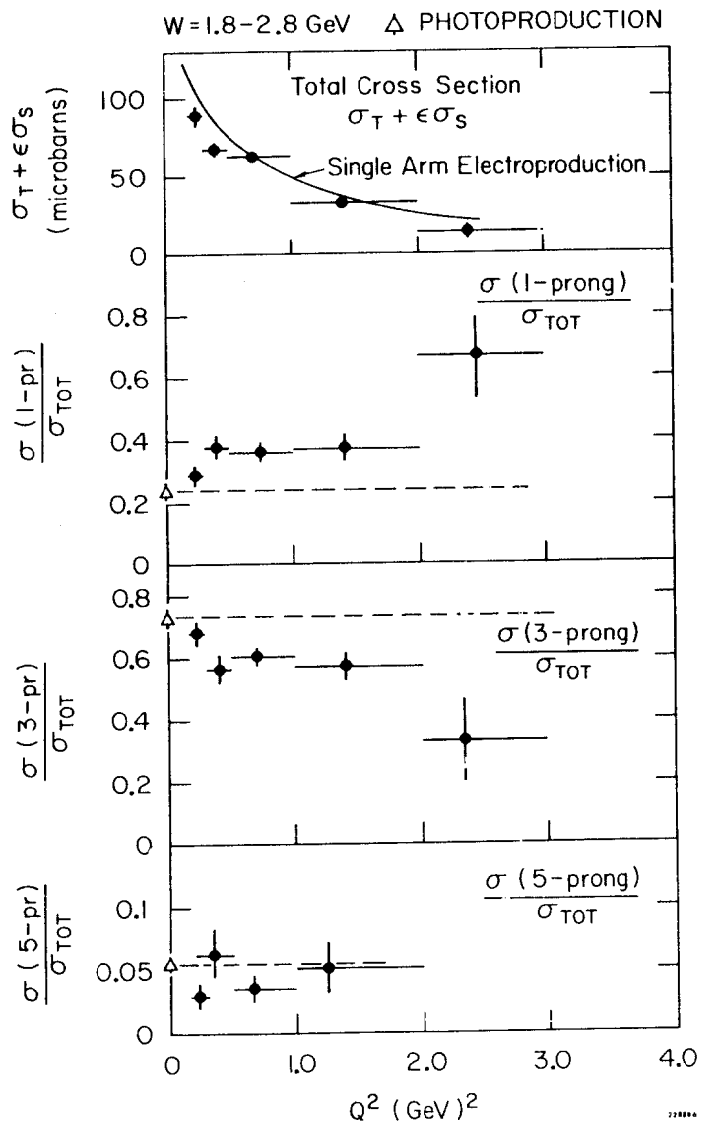
W = 1.8 – 2.8 GeV △ PHOTOPRODUCTION
Total Cross Section
$\sigma_T + \epsilon\sigma_S$
Single Arm Electroproduction
$\sigma_T + \epsilon\sigma_S$ (microbarns)
$\frac{\sigma\ (1\text{-prong})}{\sigma_{TOT}}$
$\frac{\sigma\ (1\text{-pr})}{\sigma_{TOT}}$
$\frac{\sigma\ (3\text{-prong})}{\sigma_{TOT}}$
$\frac{\sigma\ (3\text{-pr})}{\sigma_{TOT}}$
$\frac{\sigma\ (5\text{-prong})}{\sigma_{TOT}}$
$\frac{\sigma\ (5\text{-pr})}{\sigma_{TOT}}$
Q^2 (GeV)^2

Fig. 8 a

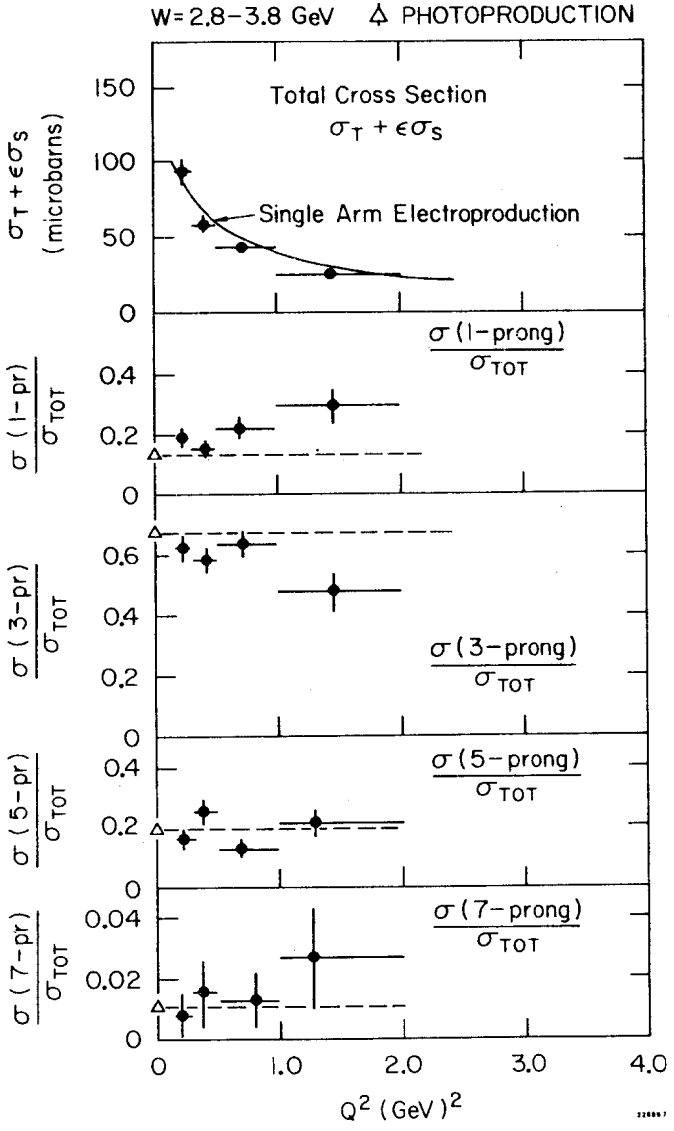
W = 2.8 – 3.8 GeV △ PHOTOPRODUCTION
Total Cross Section
$\sigma_T + \epsilon\sigma_S$
Single Arm Electroproduction
$\sigma_T + \epsilon\sigma_S$ (microbarns)
$\frac{\sigma\ (1\text{-prong})}{\sigma_{TOT}}$
$\frac{\sigma\ (1\text{-pr})}{\sigma_{TOT}}$
$\frac{\sigma\ (3\text{-prong})}{\sigma_{TOT}}$
$\frac{\sigma\ (3\text{-pr})}{\sigma_{TOT}}$
$\frac{\sigma\ (5\text{-prong})}{\sigma_{TOT}}$
$\frac{\sigma\ (5\text{-pr})}{\sigma_{TOT}}$
$\frac{\sigma\ (7\text{-prong})}{\sigma_{TOT}}$
$\frac{\sigma\ (7\text{-pr})}{\sigma_{TOT}}$
Q^2 (GeV)^2

Fig. 8 b

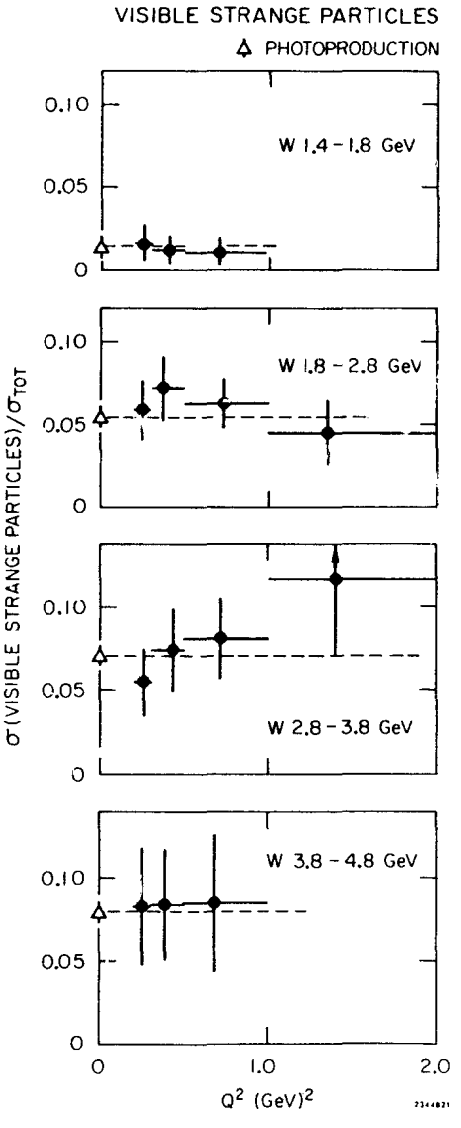
VISIBLE STRANGE PARTICLES
PHOTOPRODUCTION
W 1.4 - 1.8 GeV
W 1.8 - 2.8 GeV
W 2.8 - 3.8 GeV
W 3.8 - 4.8 GeV
σ(VISIBLE STRANGE PARTICLES)/σTOT
0.10
0.05
0
1.0
2.0
Q² (GeV)²

Fig. 9

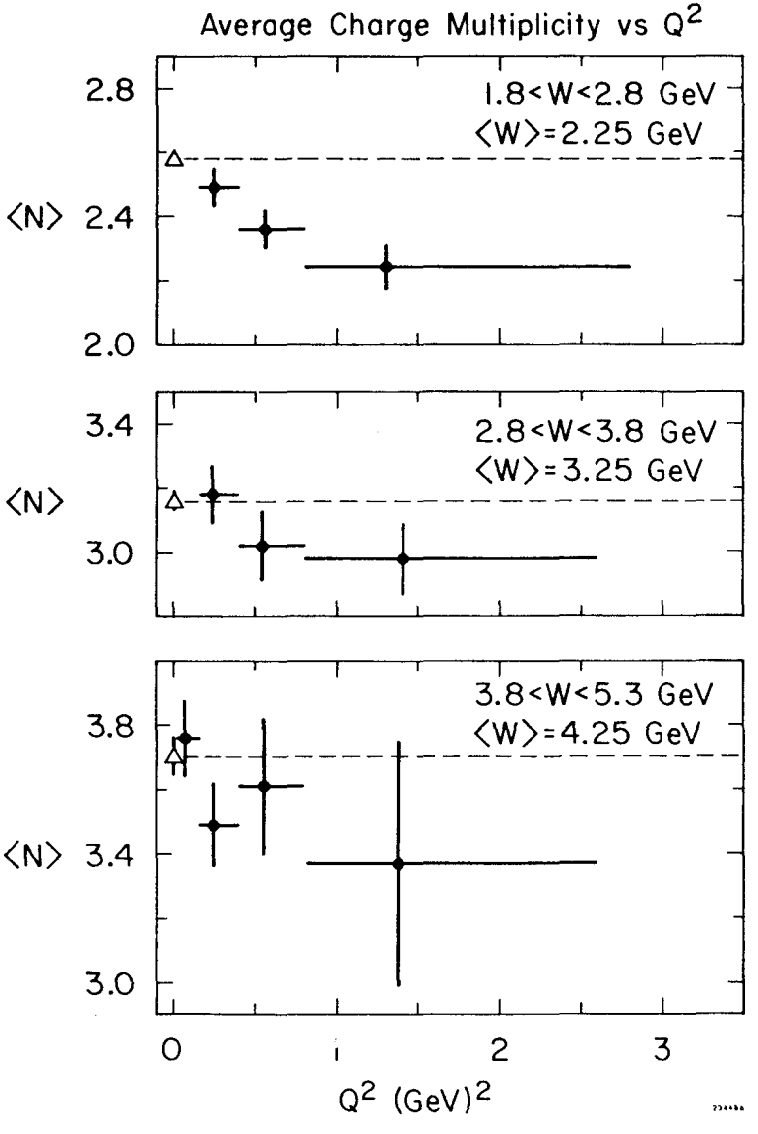
Average Charge Multiplicity vs Q²
1.8<W<2.8 GeV
<W>=2.25 GeV
2.8<W<3.8 GeV
<W>=3.25 GeV
3.8<W<5.3 GeV
<W>=4.25 GeV
<N>
2.8
2.4
2.0
3.4
3.0
3.8
3.4
3.0
0
1
2
3
Q² (GeV)²

Fig. 10

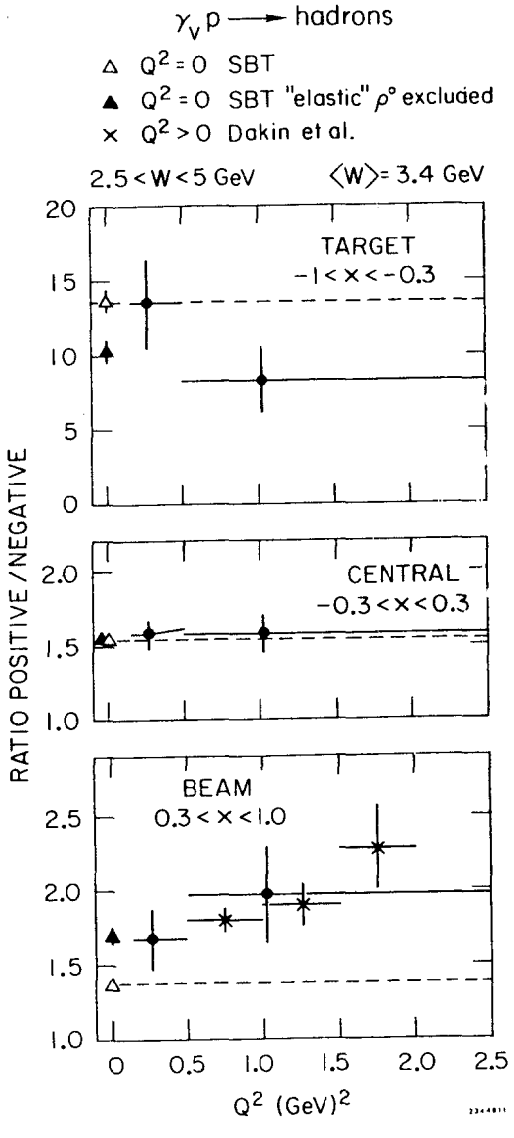
$\gamma_v p \longrightarrow$ hadrons
△ $Q^2 = 0$ SBT
▲ $Q^2 = 0$ SBT "elastic" ρ^0 excluded
× $Q^2 > 0$ Dakin et al.
2.5 < W < 5 GeV
⟨W⟩ = 3.4 GeV
TARGET
−1 < x < −0.3
CENTRAL
−0.3 < x < 0.3
BEAM
0.3 < x < 1.0
RATIO POSITIVE / NEGATIVE
Q^2 (GeV)^2

Fig. 11

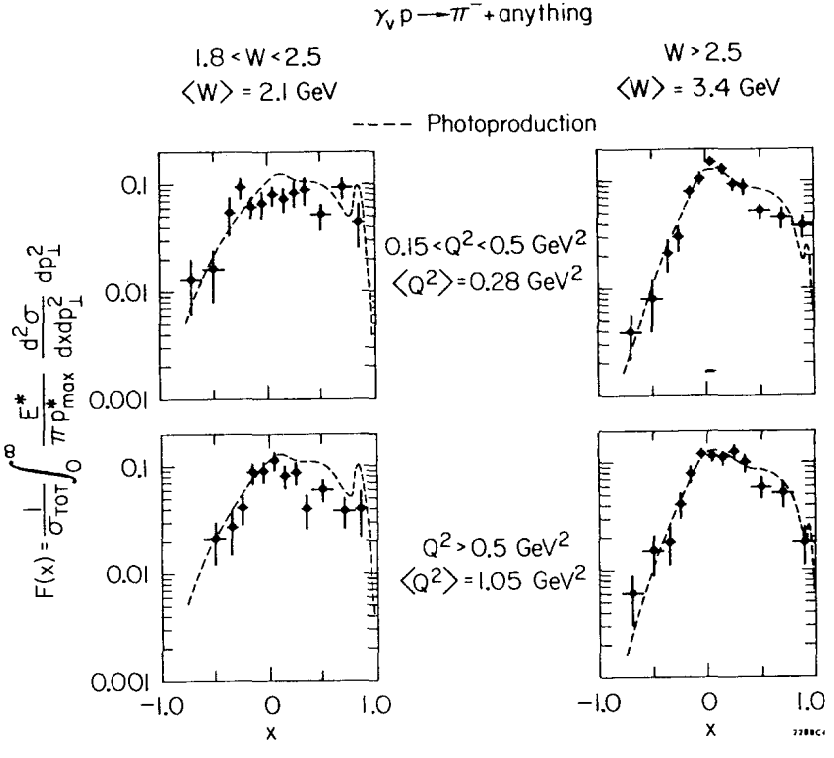
$\gamma_v p \longrightarrow \pi^- +$ anything
1.8 < W < 2.5
⟨W⟩ = 2.1 GeV
W > 2.5
⟨W⟩ = 3.4 GeV
---- Photoproduction
$0.15 < Q^2 < 0.5$ GeV^2
⟨Q^2⟩ = 0.28 GeV^2
$Q^2 > 0.5$ GeV^2
⟨Q^2⟩ = 1.05 GeV^2
$F(x) = \frac{1}{\sigma_{TOT}} \int_0^\infty \frac{E^*}{\pi p^*_{max}} \frac{d^2\sigma}{dx dp_\perp^2} dp_\perp^2$
x

Fig. 12

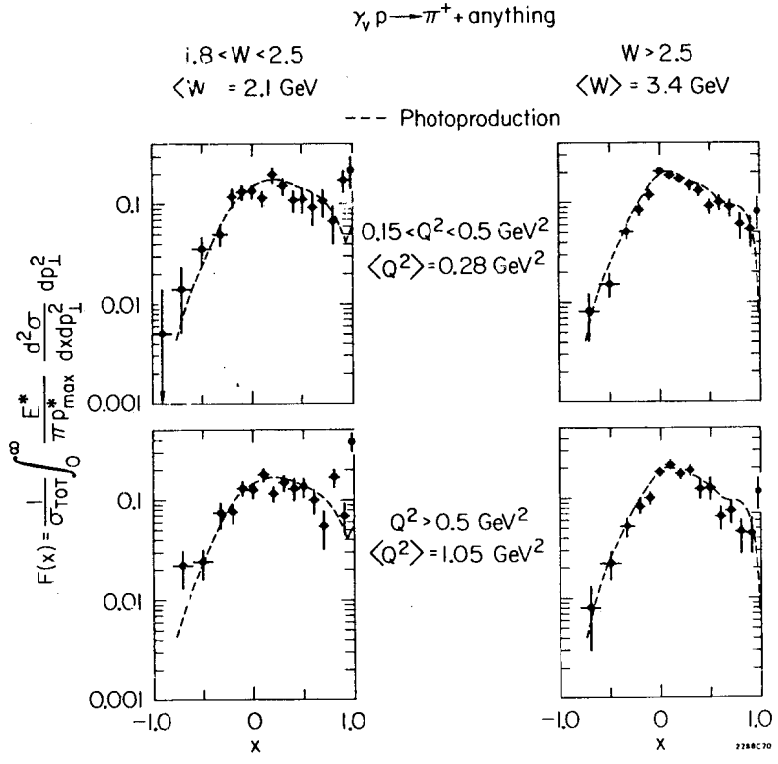
$\gamma_v p \rightarrow \pi^+ +$ anything
1.8 < W < 2.5
⟨W⟩ = 2.1 GeV
W > 2.5
⟨W⟩ = 3.4 GeV
--- Photoproduction
$0.15 < Q^2 < 0.5$ GeV^2
$\langle Q^2 \rangle = 0.28$ GeV^2
$Q^2 > 0.5$ GeV^2
$\langle Q^2 \rangle = 1.05$ GeV^2
$F(x) = \frac{1}{\sigma_{TOT}} \int_0^\infty \frac{E^*}{\pi p^*_{max}} \frac{d^2\sigma}{dx dp_\perp^2} dp_\perp^2$
0.1
0.01
0.001
-1.0
0
1.0
x

Fig. 13

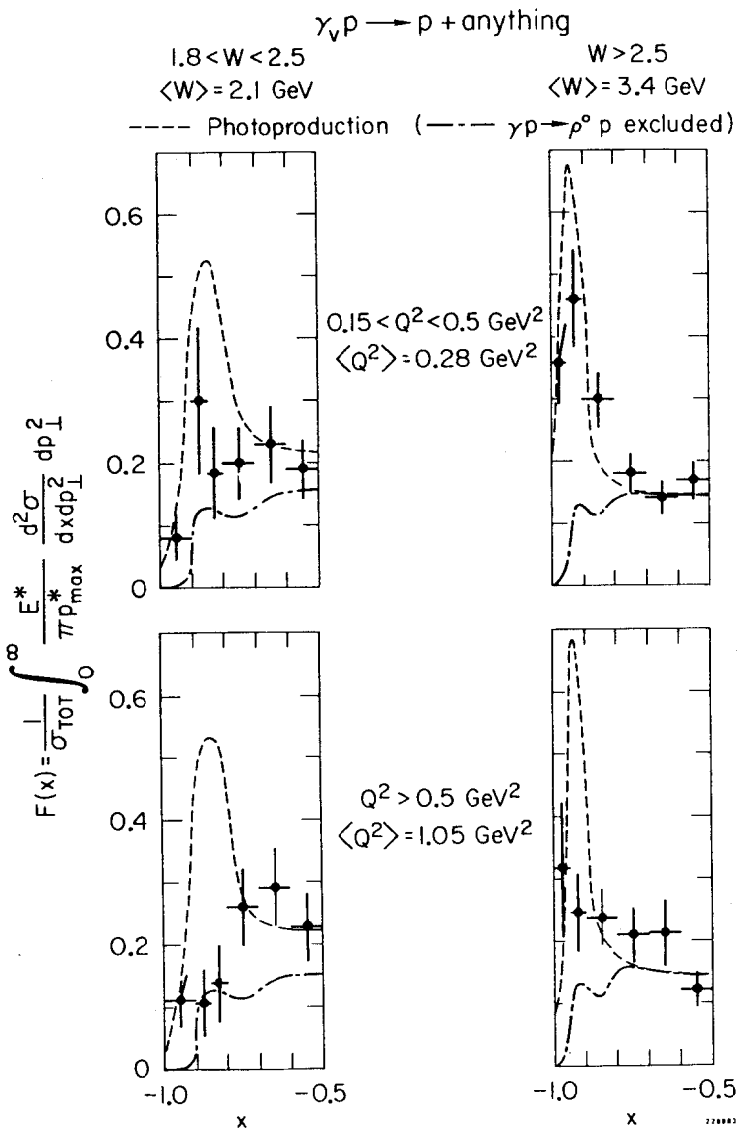
$\gamma_v p \rightarrow p +$ anything
1.8 < W < 2.5
⟨W⟩ = 2.1 GeV
W > 2.5
⟨W⟩ = 3.4 GeV
---- Photoproduction (—·— $\gamma p \rightarrow \rho^0 p$ excluded)
$0.15 < Q^2 < 0.5$ GeV^2
$\langle Q^2 \rangle = 0.28$ GeV^2
$Q^2 > 0.5$ GeV^2
$\langle Q^2 \rangle = 1.05$ GeV^2
$F(x) = \frac{1}{\sigma_{TOT}} \int_0^\infty \frac{E^*}{\pi p^*_{max}} \frac{d^2\sigma}{dx dp_\perp^2} dp_\perp^2$
0.6
0.4
0.2
0
-1.0
-0.5
x

Fig. 14

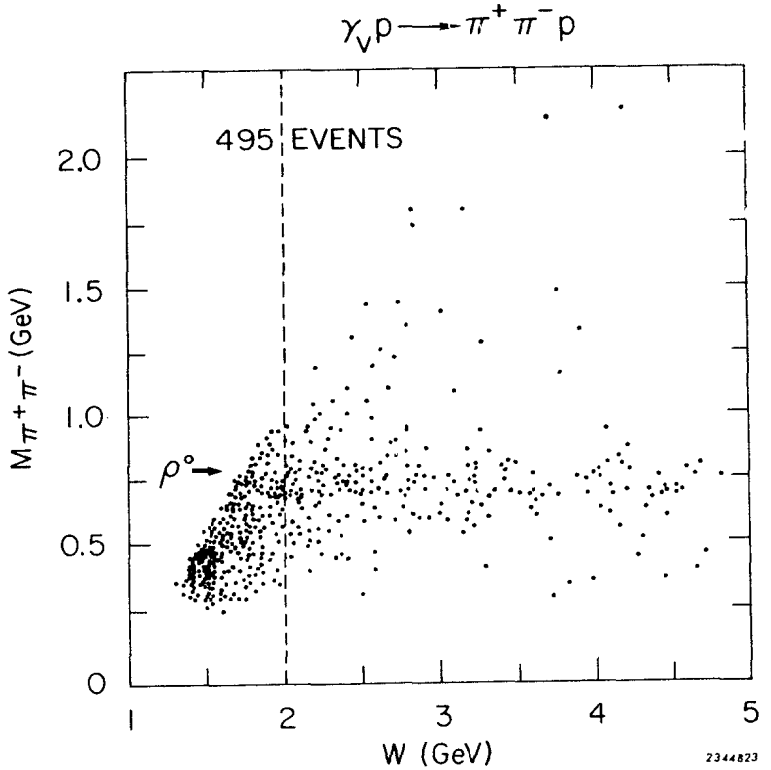
$\gamma_V p \rightarrow \pi^+ \pi^- p$
495 EVENTS
ρ°
$M_{\pi^+\pi^-}$ (GeV)
W (GeV)
2344823

Fig. 15

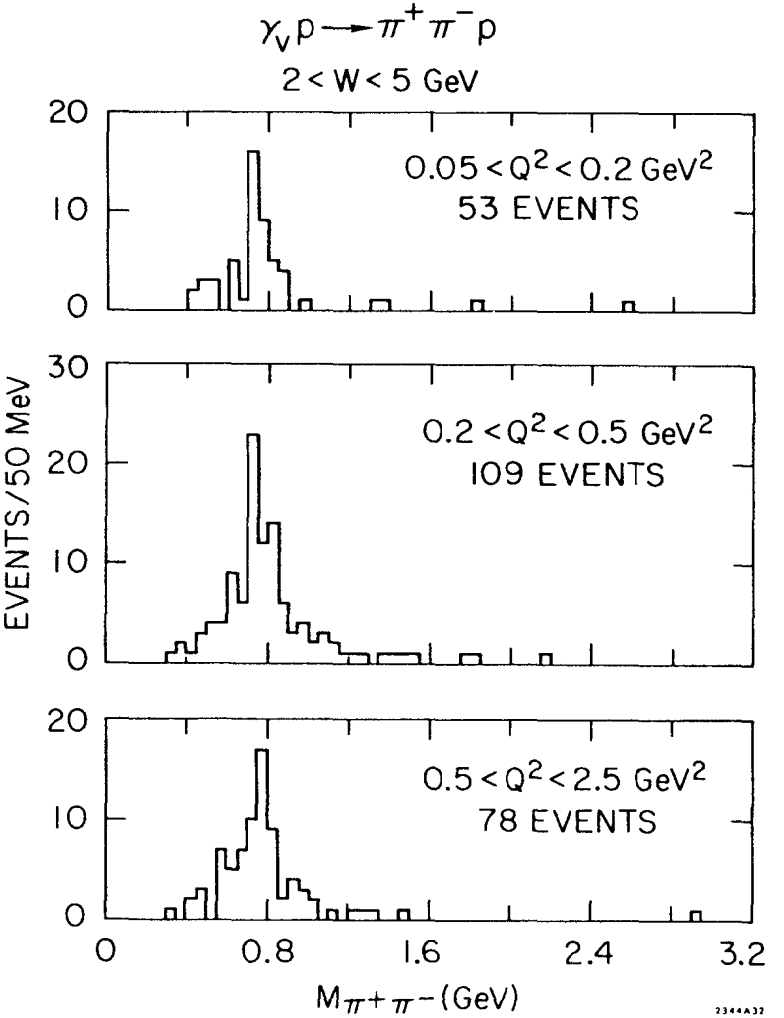
$\gamma_V p \rightarrow \pi^+ \pi^- p$
2 < W < 5 GeV
0.05 < Q² < 0.2 GeV²
53 EVENTS
0.2 < Q² < 0.5 GeV²
109 EVENTS
0.5 < Q² < 2.5 GeV²
78 EVENTS
EVENTS/50 MeV
$M_{\pi^+\pi^-}$ (GeV)
2344A32

Fig. 16

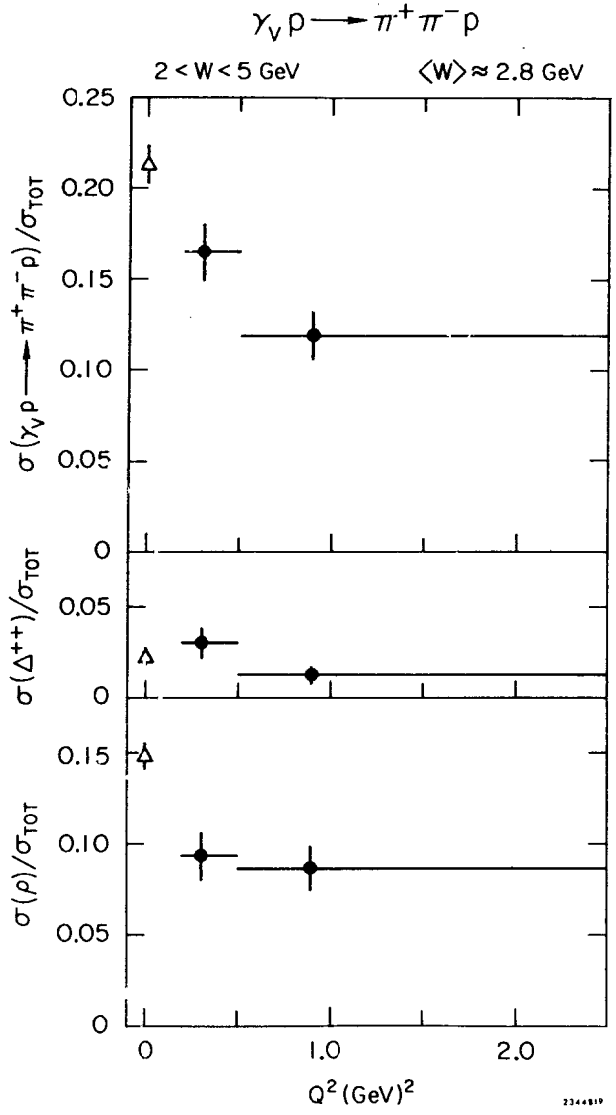
$\gamma_V p \longrightarrow \pi^+\pi^- p$
2 < W < 5 GeV
⟨W⟩ ≈ 2.8 GeV
$\sigma(\gamma_V p \longrightarrow \pi^+\pi^- p)/\sigma_{TOT}$
$\sigma(\Delta^{++})/\sigma_{TOT}$
$\sigma(\rho)/\sigma_{TOT}$
0.25
0.20
0.15
0.10
0.05
0
1.0
2.0
Q^2 (GeV)^2

Fig. 17

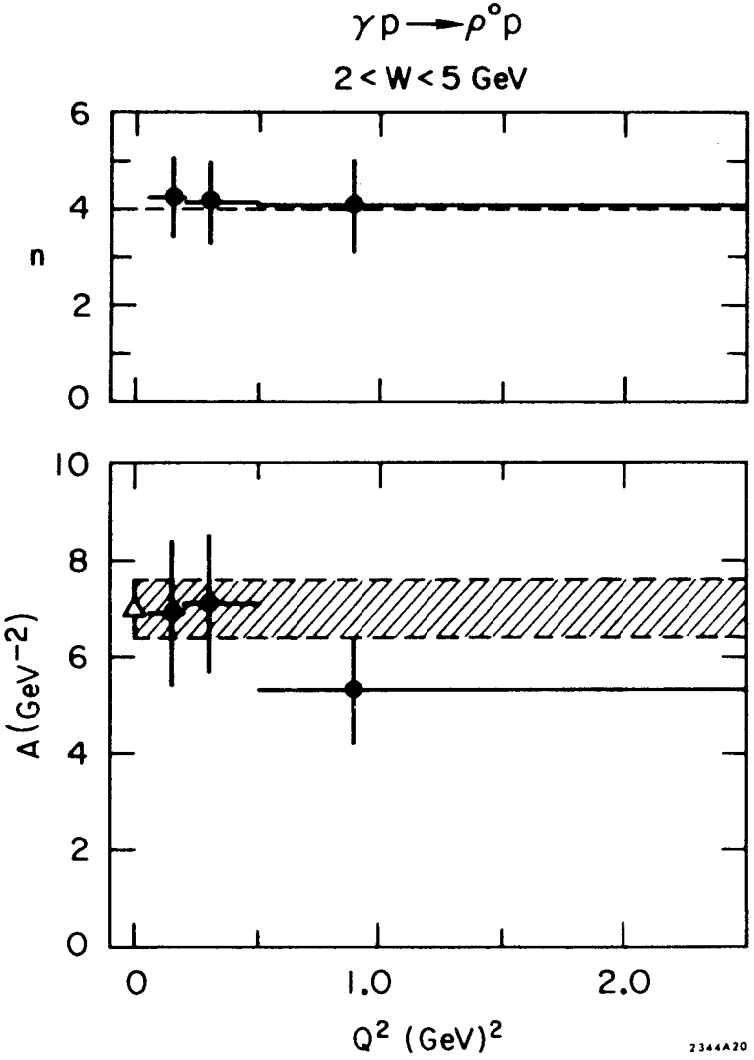
$\gamma p \longrightarrow \rho^0 p$
2 < W < 5 GeV
n
A (GeV^{-2})
0
1.0
2.0
Q^2 (GeV)^2

Fig. 18

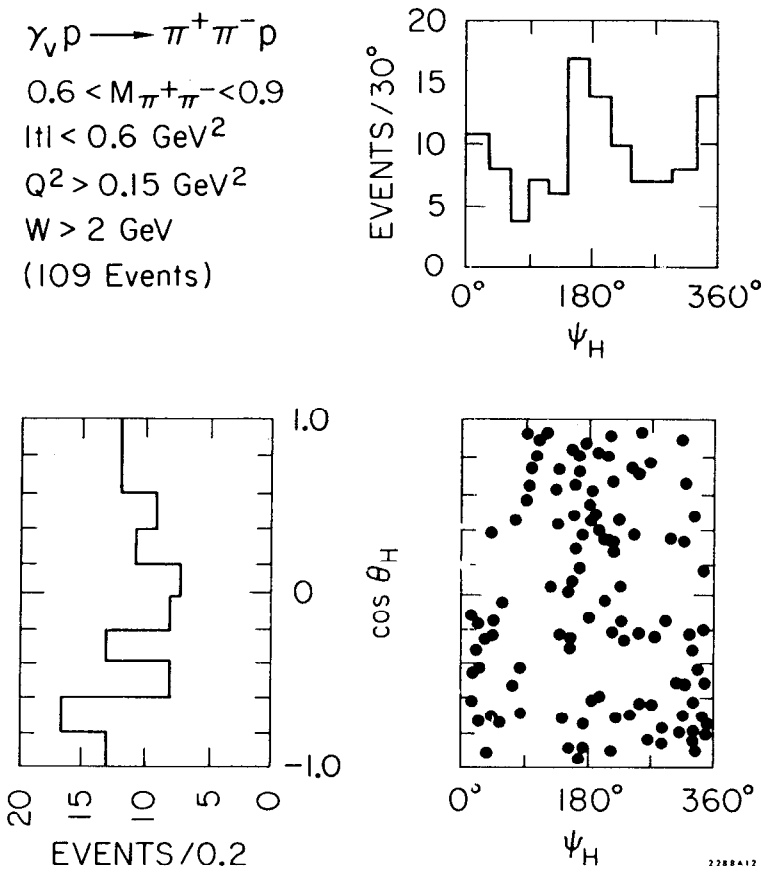
$\gamma_v p \longrightarrow \pi^+\pi^- p$
$0.6 < M_{\pi^+\pi^-} < 0.9$
$|t| < 0.6$ GeV^2
$Q^2 > 0.15$ GeV^2
$W > 2$ GeV
(109 Events)
EVENTS / 30°
20
15
10
5
0
0°
180°
360°
ψ_H
1.0
0
-1.0
20
15
10
5
0
EVENTS / 0.2
cos θ_H
0°
180°
360°
ψ_H

Fig. 19

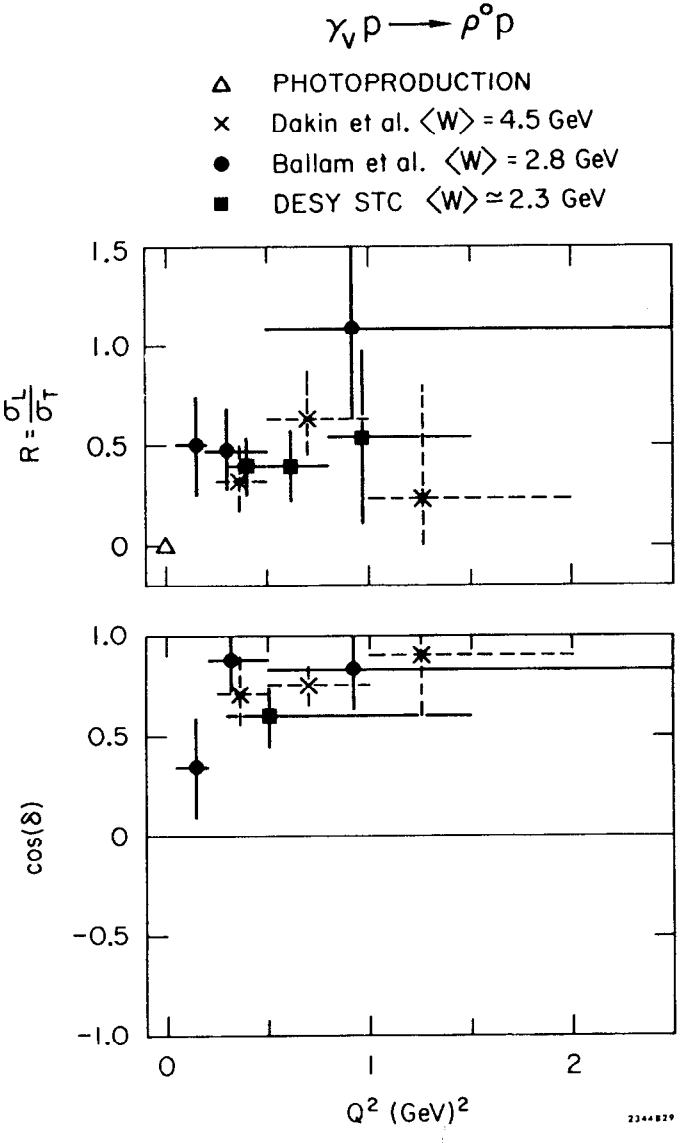
$\gamma_v p \longrightarrow \rho^0 p$
PHOTOPRODUCTION
Dakin et al. ⟨W⟩ = 4.5 GeV
Ballam et al. ⟨W⟩ = 2.8 GeV
DESY STC ⟨W⟩ ≃ 2.3 GeV
$R = \frac{\sigma_L}{\sigma_T}$
1.5
1.0
0.5
0
1.0
0.5
0
-0.5
-1.0
cos(δ)
0
1
2
Q^2 (GeV)^2

Fig. 20

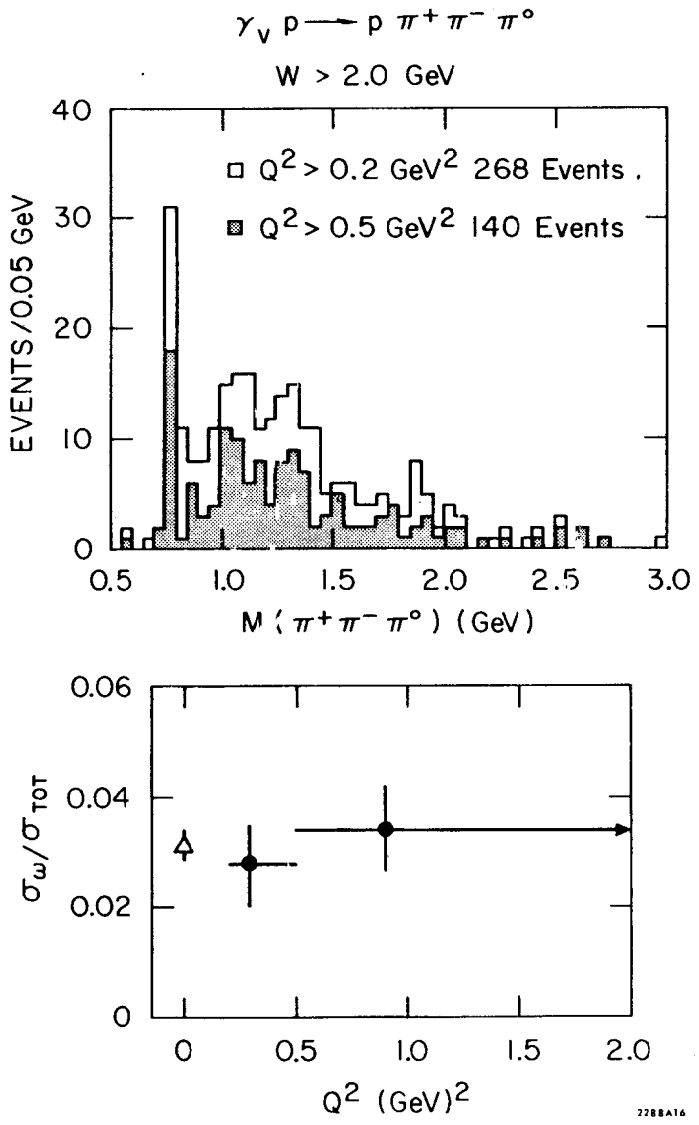
$\gamma_V p \longrightarrow p\,\pi^+\pi^-\pi^\circ$
W > 2.0 GeV
$Q^2 > 0.2$ GeV^2 268 Events
$Q^2 > 0.5$ GeV^2 140 Events
EVENTS/0.05 GeV
M ($\pi^+\pi^-\pi^\circ$) (GeV)
$\sigma_\omega/\sigma_{TOT}$
Q^2 (GeV)^2

Fig. 21

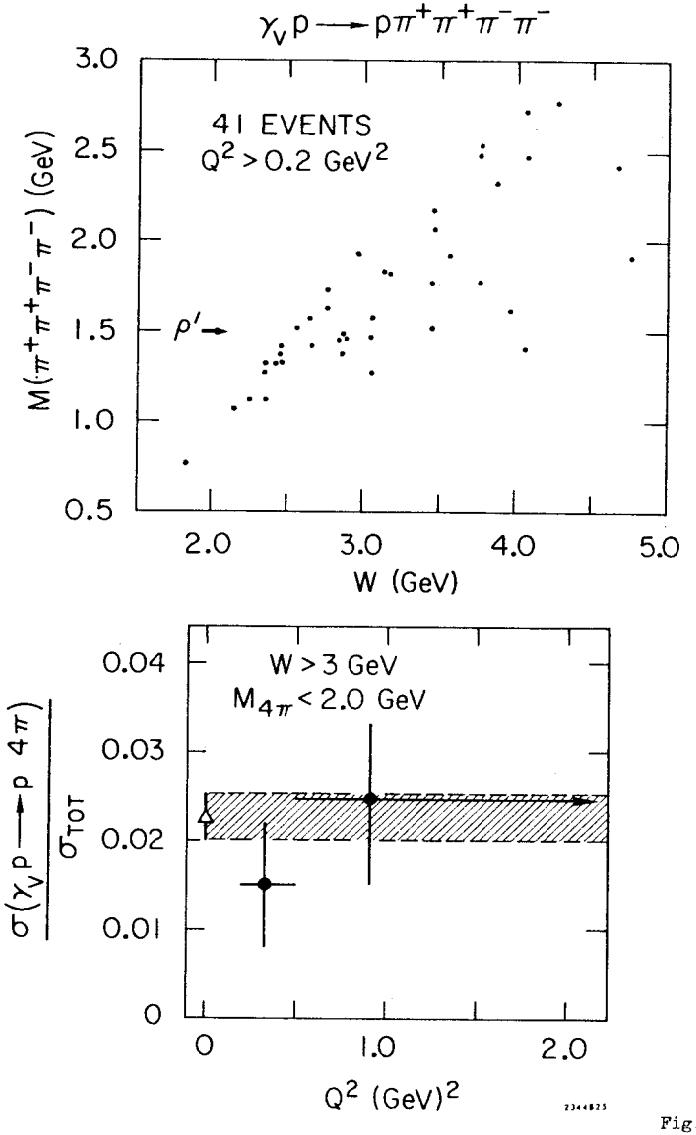
$\gamma_V p \longrightarrow p\pi^+\pi^+\pi^-\pi^-$
41 EVENTS
$Q^2 > 0.2$ GeV^2
ρ'
M($\pi^+\pi^+\pi^-\pi^-$) (GeV)
W (GeV)
W > 3 GeV
$M_{4\pi} < 2.0$ GeV
$\sigma(\gamma_V p \longrightarrow p\ 4\pi)/\sigma_{TOT}$
Q^2 (GeV)^2

Fig. 22

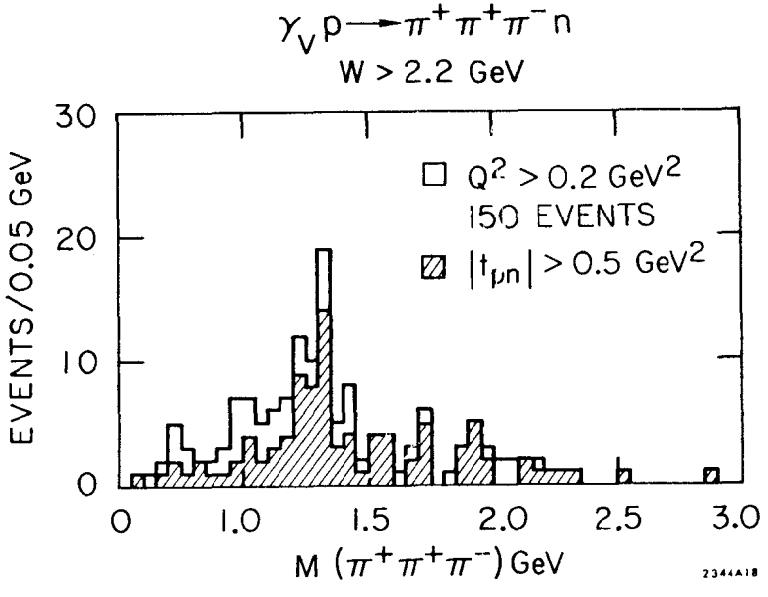

Fig. 23

References

1. J. Ballam, E. D. Bloom, J. T. Carroll, G. B. Chadwick, R.L.A. Cottrell, M. Della Negra, H. DeStaebler, L. K. Gershwin, L. P. Keller, M. D. Mestayer, K. C. Moffeit, C. Y. Prescott and S. Stein, SLAC-PUB-1163 (1972).
2. G. Miller et al., Rhys. Rev. D5, 528 (1972) and earlier references contained therein.
3. SLAC-LBL-TUFTS collaboration, J. Ballam et al., Phys. Rev. D5, 545 (1972); K. C. Moffeit et al., Phys. Rev. D5, 1603 (1972).
4. T. J. Braunstein et al., Phys. Rev. D6, 106 (1972).
5. J. T. Dakin et al., Phys. Rev. Lett. 29, 746 (1972); Phys. Rev. Lett. 30, 142 (1973).
6. V. Eckhardt et al., Nucl. Phys. B55, 45 (1973).

FORWARD ELECTROPRODUCTION EXPERIMENTS AT CORNELL

F. M. Pipkin

Cyclotron Laboratory

Harvard University

Cambridge, Mass.

The material presented in this talk was taken from four manuscripts that were submitted to the Bonn conference. The subjects treated were:

1. Single charged pion electroproduction
2. Measurements of inclusive pion electroproduction
3. Electroproduction of pions in the forward direction
4. Electroproduction of K^+ mesons in the forward direction

Copies of the complete manuscripts follow.

FURTHER MEASUREMENTS OF FORWARD CHARGED PION ELECTROPRODUCTION AT LARGE k^2*

C. J. Bebek, C. N. Brown, M. Herzlinger, S. Holmes, C. A. Lichtenstein, F. M. Pipkin and L. K. Sisterson

Cyclotron Laboratory

Harvard University

Cambridge, Massachusetts 02138

D. Andrews,+ K. Berkelman, D. G. Cassel and D. L. Hartill

Laboratory of Nuclear Studies

Cornell University

Ithaca, New York 14850

ABSTRACT

Measurements of the electroproduction reaction $e^- + p \rightarrow e^- + \pi^+ + n$ carried out at the Wilson Synchrotron Laboratory are reported. For fixed virtual photon-hadron center of mass energy, $W = 2.67$ GeV, data are presented with the mass of the virtual photon, $-k^2$, centered at 0.6, 1.2, and 2.0 $(GeV)^2$. At the central $-k^2 = 1.2$ $(GeV)^2$ point results are also given for $W = 2.15$ GeV. For the $W = 2.67$, $-k^2 = 1.2$ $(GeV)^2$ setting an angular scan is presented and the scalar transverse interference term is extracted. The data are compared with a dispersion theory calculation of Berends which has as its only free parameter the pion electromagnetic form factor. The theory is used to give a new determination of the pion form factor up to $-k^2 = 2.0$ GeV^2.

---

*Research supported in part by the U. S. Atomic Energy Commission and in part by the National Science Foundation.

+Present address: Physics Department, University of Rochester, Rochester, New York 14627.

FORWARD ELECTROPRODUCTION EXPERIMENTS AT CORNELL

F. M. Pipkin

Cyclotron Laboratory

Harvard University

Cambridge, Mass.

The material presented in this talk was taken from four manuscripts that were submitted to the Bonn conference. The subjects treated were:

1. Single charged pion electroproduction
2. Measurements of inclusive pion electroproduction
3. Electroproduction of pions in the forward direction
4. Electroproduction of K^+ mesons in the forward direction

Copies of the complete manuscripts follow.

FURTHER MEASUREMENTS OF FORWARD CHARGED PION ELECTROPRODUCTION AT LARGE k^2*

C. J. Bebek, C. N. Brown, M. Herzlinger, S. Holmes, C. A. Lichtenstein, F. M. Pipkin and L. K. Sisterson

Cyclotron Laboratory

Harvard University

Cambridge, Massachusetts 02138

D. Andrews,+ K. Berkelman, D. G. Cassel and D. L. Hartill

Laboratory of Nuclear Studies

Cornell University

Ithaca, New York 14850

ABSTRACT

Measurements of the electroproduction reaction $e^- + p \rightarrow e^- + \pi^+ + n$ carried out at the Wilson Synchrotron Laboratory are reported. For fixed virtual photon-hadron center of mass energy, $W = 2.67$ GeV, data are presented with the mass of the virtual photon, $-k^2$, centered at 0.6, 1.2, and 2.0 $(GeV)^2$. At the central $-k^2 = 1.2$ $(GeV)^2$ point results are also given for $W = 2.15$ GeV. For the $W = 2.67$, $-k^2 = 1.2$ $(GeV)^2$ setting an angular scan is presented and the scalar transverse interference term is extracted. The data are compared with a dispersion theory calculation of Berends which has as its only free parameter the pion electromagnetic form factor. The theory is used to give a new determination of the pion form factor up to $-k^2 = 2.0$ GeV^2.

---

*Research supported in part by the U. S. Atomic Energy Commission and in part by the National Science Foundation.

+Present address: Physics Department, University of Rochester, Rochester, New York 14627.

I. Introduction

In recent years, the pion electroproduction reaction

$$e^- + p \rightarrow e^- + \pi^+ + n \qquad (1)$$

has been studied intensively. This reaction has generated interest for two closely related reasons. First, it has been observed that for small momentum transfer, the electric Born model gives an adequate description of the equivalent photoproduction reaction

$$\gamma + p \rightarrow \pi^+ + n \qquad (2)$$

and of reaction 1. Second, if as suggested by the success of the electric Born model, there is a large contribution due to one pion exchange, reaction 1 can be used to determine the pion form factor.

In this paper, we present new measurements of pion electroproduction at higher values of $-k^2$ (the square of the mass of the virtual photon) and of W (the total center of mass energy of the virtual photon-proton system). Measurements were also made at the same k^2 and different W so as to study the dependence on the minimum momentum transfer. The measurements are compared with the predictions of the electric Born model and found to be in good agreement for small momentum transfer. A fit to the theory is used to determine the pion form factor for $-k^2$ up to 2 GeV^2.

These measurements represent a continuation of similar measurements at lower energies by some members of the group. Hence, we will rely on the previous report (ref 5) to supply the background for the kinematics, phenomenology and theoretical ideas needed in applying the electric Born model to our results.

II. Experiment

This experiment was performed at the Wilson Electron Synchrotron. Figure 1 gives a schematic view of the apparatus. A beam of 9.6 GeV electrons was incident on a 12.7 cm long liquid hydrogen target. An inelastically scattered electron was detected in the Cornell 10 GeV spectrometer. A freon gas Cerenkov counter and a heavy liquid shower counter were used to identify the scattered electron and a freon gas Cerenkov counter identified the scattered pion.

The electron spectrometer had a momentum acceptance of ± 20% and an angular acceptance of $\pm 1/2^\circ$ horizontally and $\pm 1^\circ$ vertically. The large momentum acceptance led to a spectrum of virtual photons with a high correlation in angle, W, ϵ (the polarization parameter) and to a lesser extent $-k^2$.

The hadron spectrometer had a momentum acceptance of ± 50% and an angular aperature of $\pm 1^\circ$ horizontally and -2° to $+5^\circ$ vertically. By studying the spectrum of events which did not fire the Cerenkov counter the efficiency of this counter for pions from reaction 1 was determined to be greater than 99%. The relative timing of the coincident pion and electron was measured with a resolution of 400 psec leading to a final correction due to arm-to-arm randoms of less than 5%.

Setting the electron spectrometer at a certain angle and energy determined the nominal value of the mass ($-k^2$) of the virtual photon and the total energy (W) of the final state. Figure 2 indicates the nominal values of these variables for which data were taken. For data points 1, 3, 6, and 7 the hadron spectrometer was set exactly along the nominal virtual photon direction. Data point 2 had the hadron arm 3° toward the beam ($\phi = 0^\circ$) from the virtual photon direction and data points 4 and 5 had the hadron arm 3° and 7° respectively outside the virtual photon direction ($\phi = 180^\circ$). We thus obtained data for varying $-k^2$ at fixed W = 2.67 GeV and also data at varying W for fixed $-k^2 = 1.2$ GeV^2.

By combining the known beam momentum with the measured momenta of the detected electron and pion the mass of the missing particles was calculated. Figure 3 shows a missing mass squared plot of the events obtained with the electron arm nominal settings W = 2.15 GeV and $-k^2 = 1.20$ GeV^2. A large signal from reaction 1 is evident. All events within the cuts shown were then constrained by adjusting the scattered electron and pion momenta equally to give the known neutron mass. These events were then binned in the variables θ, the polar angle of the emitted pion in the

center-of-mass of the virtual photoproduction reaction and ϕ, the angle between the plane determined by the virtual photoproduction reaction and the electron scattering plane.

The virtual photoproduction cross section has the form

$$\frac{d\sigma}{d\Omega}_{\pi} = A + \epsilon B \cos 2\phi + \epsilon C + \left[\frac{\epsilon (1+\epsilon)}{2}\right]^{1/2} D \cos\phi \quad . \qquad (3)$$

ϵ is the virtual photon polarization parameter. A, B, C, and D are functions of k^2, W, and θ and refer respectively to the unpolarized transverse production, interference between the two transverse helicity states, purely scalar production, and scalar-transverse interference.

A Monte Carlo calculation was made assuming unit center of mass cross section and incorporating all multiple scattering and detector resolution effects. This enabled us to correct the number of events in each bin for the acceptance of the apparatus and hence calculate the observed cross section for each bin. The normalization of the experiment was checked by independently observing elastically scattered electrons in both spectrometers and comparing the observed cross sections with the accepted elastic scattering cross sections.

The measured cross sections were corrected for nuclear absorption, dead-time effects, target wall background, and pion decay. The sum of all these corrections was less than 15% at all data points.

The cross sections were also corrected for losses due to the radiation of soft photons. The prescription for the radiative correction was taken from the work of Bartl and Urban.[6] It was checked by an independent calculation based on the work of Meister and Yennie.[7] The two calculations agreed to better than 0.5% for the data presented here. The full radiative correction was roughly 30% for all the data points.

The errors on the cross sections presented in this paper are statistical only. There is an additional systematic uncertainty which is estimated to be less than 7%. This systematic uncertainty is based on the normalization check with the electron scattering measurements and the uncertainty in the corrections to the data.

III. Results

The results are shown graphically in Figs. 4 through 8 as a function of the polar angle θ of the emitted pion for the virtual photoproduction plane parallel to the electron scattering plane ($\phi = 0^\circ$ or 180°) and for the virtual photoproduction plane perpendicular to the electron scattering plane ($\phi = -90^\circ$ or 90°). The values of W, $-k^2$ and ϵ listed for each curve are the average values for the central bin. The values of W, $-k^2$ and ϵ change considerably as θ changes and this change must be taken into account if the data are compared with theory or used to separate out the interference terms B and D.

We shall now compare the measured cross sections with the electric Born model with dispersion theory corrections as developed by Berends.[8] Before we can calculate the predicted angular distributions, we must arrive at a value for the pion form factor, the only free parameter in the theory. At zero degrees, the interference terms B and D vanish and the theory predicts that the pion exchange diagram dominates the cross section. For these reasons, we chose a value for the pion form factor by fitting the data in the five central bins ($\theta = 3^\circ$) at each data point. Table I summarizes the values of $F_\pi (-k^2)$ determined using this procedure. Figure 9 shows graphically the values of the pion form factor determined from this experiment and earlier experiments at the CEA[1], DESY[2] and NINA[4].

A functional parametrization of the pion form factor was then obtained by making a fit to these measurements together with the previous measurements made at the CEA[5]. A simple polynomial gave a satisfactory fit to the eleven data points. The form obtained was

$$F_\pi (-k^2) = 1 - 1.577\,(-k^2) + 1.635\,(-k^2)^2 - 0.909\,(-k^2)^3 + 0.192\,(-k^2)^4 \quad .$$

The prediction of the theory assuming the polynomial form for $F_\pi (-k^2)$ was then calculated for each bin using the average value of the kinematic parameters for that bin.

The smooth curves shown in Figs. 4 through 8 give the theoretical predictions. The actual value calculated for each bin deviated by a very small amount from the smooth curve due to the statistical nature of the average bin parameters. The theory does not fit the data at large angles and does not describe correctly the scalar-transverse interference term. The agreement between theory and experiment does not deteriate as $-k^2$ increases at fixed W.

Due to the high degree of correlation between the kinematic parameters, it is possible to interpolate the cross sections from data points 2, 3, 4 and 5 and obtain $\phi = 0^\circ$ and $\phi = 180^\circ$ cross sections at fixed W and $-k^2$. Table II summarizes the interpolated cross sections for 3 non-overlapping sets of virtual photon parameters. A linear interpolation between adjacent points was used to determine the interpolated cross sections. Figure 10 shows the interpolated cross sections together with the predictions of the theory.

The interpolated $\phi = 0$ and $\phi = 180^\circ$ cross sections at $W = 2.66$, $-k^2 = 1.20$, $\epsilon = 0.86$ can be combined with the $\phi = -90^\circ$ and $\phi = 90^\circ$ data which have the same value for these parameters. This makes possible a determination of the individual contributions $A + \epsilon C$, B and D. Table III summarizes the results of this analysis. Figure 11 shows these same results graphically together with the predictions of the theory. This analysis shows that the theory does not describe correctly the scalar-transverse interference term.

IV. Conclusion

For small momentum transfers and all values of the virtual photon mass $-k^2$, single pion electroproduction can be adequately described by the electric Born model with dispersion theory corrections. For fixed $-k^2$ the value of the pion form factor required to fit the data is independent of W and does not depend upon the minimum momentum transfer in the virtual photoproduction reaction. For the data points in this experiment with $-k^2 = 1.2\ \mathrm{GeV}^2$, the minimum momentum transfer and hence the minimum distance to the pion pole differs by almost a factor of two. The close agreement between the values of the pion form factor obtained at these two points indicates that the electric Born model gives a good representation of the data near the forward direction and given credence to the value of the pion form factor obtained at higher $-k^2$.

The theory does not give an adequate representation of the scalar-transverse interference or of the data at large momentum transfer. The precision of the data warrants renewed theoretical attempts to fully understand this simplest of virtual photon reactions.

V. Acknowledgements

We would like to thank Professor Boyce McDaniel and the staff of the Wilson Synchrotron for their gracious help during the course of this experiment. The program used for the electric Born model predictions was obtained from Professor F. Berends. Mr. P. Bucksbaum contributed clerical assistance in the production of this publication.

Table I. Values of the pion form factor $F_\pi(-k^2)$ determined from this experiment using the data for $\theta \leq 3^\circ$.

Data Point	$-k^2$ (GeV^2)	$F_\pi(-k^2)$
1	0.620	0.465 ± 0.015
2	1.069	0.332 ± 0.017
3	1.204	0.291 ± 0.010
4	1.314	0.266 ± 0.013
6	1.200	0.288 ± 0.012
7	2.015	0.185 ± 0.011

Table II. The interpolated cross sections determined from data points 2, 3, 4 and 5.

Bin		$\frac{d\sigma}{d\Omega_\pi}\left(\frac{\mu b}{sr}\right)$		
ϕ (deg)	θ (deg)	W=2.55 $-k^2$=1.26 ϵ=0.88	W=2.66 $-k^2$=1.20 ϵ=0.86	W=2.75 $-k^2$=1.16 ϵ=0.84
-45 to 45	15.75	$1.41 \pm .15$		
	14.25	$1.55 \pm .18$		
	12.75	$1.76 \pm .20$		
	11.25	$2.19 \pm .22$	$2.31 \pm .21$	
	9.75	$2.63 \pm .24$	$2.28 \pm .22$	
	8.25	$2.75 \pm .25$	$2.32 \pm .23$	$2.05 \pm .22$
	6.75	$3.23 \pm .30$	$3.38 \pm .32$	$3.52 \pm .33$
	5.25	$3.08 \pm .30$	$3.12 \pm .32$	$3.15 \pm .34$
	3.75	$4.25 \pm .49$	$4.08 \pm .44$	$3.78 \pm .43$
	2.25	$3.73 \pm .64$	$3.87 \pm .56$	$4.20 \pm .62$
all ϕ	0.0	$3.95 \pm .53$	$4.32 \pm .50$	$3.94 \pm .52$
135 to 225	2.25	$2.92 \pm .52$	$2.98 \pm .48$	$3.00 \pm .46$
	3.75	$2.99 \pm .40$	$2.76 \pm .37$	$2.59 \pm .34$
	5.25	$2.51 \pm .30$	$2.81 \pm .31$	$3.11 \pm .32$
	6.75		$2.59 \pm .28$	$2.60 \pm .27$
	8.25		$2.20 \pm .23$	$2.05 \pm .22$
	9.75		$1.58 \pm .18$	$1.46 \pm .17$
	11.25		$1.70 \pm .18$	$1.59 \pm .18$
	12.75		$1.19 \pm .16$	$1.12 \pm .15$
	14.25		$1.10 \pm .15$	$1.12 \pm .14$
	15.75		$.82 \pm .12$	$.78 \pm .11$
	17.25		$.61 \pm .10$	
	18.75		$.69 \pm .10$	
	20.25		$.58 \pm .09$	
	21.75		$.44 \pm .08$	
	23.25		$.33 \pm .07$	
	24.75		$.36 \pm .07$	
	26.25		$.29 \pm .07$	

Table III. The components of the cross section for W = 2.66 GeV, $-k^2 = 1.2\ \text{GeV}^2$ and $\epsilon = 0.86$.

θ (deg)	A+ ϵC (μb/sr)	B (μb/sr)	D (μb/sr)
2.25	3.41 $\pm$ .26	.02 $\pm$ .47	.52 $\pm$ .45
3.75	3.60 $\pm$ .21	-.33 $\pm$ .38	.81 $\pm$ .36
5.25	3.14 $\pm$ .17	-.33 $\pm$ .31	.20 $\pm$ .27
6.75	3.24 $\pm$ .15	-.47 $\pm$ .27	.49 $\pm$ .23
8.25	2.35 $\pm$ .13	-.16 $\pm$ .24	.07 $\pm$ .20
9.75	2.15 $\pm$ .12	-.20 $\pm$ .22	.43 $\pm$ .16
11.25	2.22 $\pm$ .12	-.20 $\pm$ .22	.37 $\pm$ .16

FIGURE CAPTIONS

Fig. 1. A schematic diagram of the apparatus: A, 20D84 bending magnet; B, wire spark chamber planes; C, gas Cerenkov counter; D, shower counter; E. 8Q48 half quadrupole magnets; F, 18D36 bending magnets; G, proportional wire chambers; H, Freon Cerenkov counter; I, lead acetate shower counter.

Fig. 2. A diagram showing the nominal values of $-k^2$ and W at which data were taken.

Fig. 3. A missing mass-squared plot for the data point with nominal setting W = 2.15 GeV and $-k^2 = 1.20\ \text{GeV}^2$.

Fig. 4. A plot of the virtual photoproduction cross sections versus θ for data points 1, 3 and 7.

a. W = 2.67, $-k^2 = 0.62$, $\phi = 0^\circ$, 180°

b. W = 2.67, $-k^2 = 0.62$, $\phi = 90^\circ$, 270°

c. W = 2.66, $-k^2 = 1.2$, $\phi = 0^\circ$, 180°

d. W = 2.66, $-k^2 = 1.2$, $\phi = 90^\circ$, 270°

e. W = 2.66, $-k^2 = 2.0$, $\phi = 0^\circ$, 180°

f. W = 2.66, $-k^2 = 2.0$, $\phi = 90^\circ$, 270°

Fig. 5. A plot of the virtual photoproduction cross section versus θ for data point 6.

a. W = 2.15, $-k^2 = 1.19$, $\phi = 0^\circ$, 180°

b. W = 2.15, $-k^2 = 1.19$, $\phi = 90^\circ$, 270°

Fig. 6. A plot of the virtual photoproduction cross section versus θ for data point 2.

a. W = 2.90, $-k^2 = 1.07$, $\phi = 0^\circ$

b. W = 2.90, $-k^2 = 1.07$, $\phi = 90^\circ$

Fig. 7. A plot of the virtual photoproduction cross section versus θ for data point 4.

a. W = 2.46, $-k^2 = 1.31$, $\phi = 0^\circ$, 180°

b. W = 2.46, $-k^2 = 1.31$, $\phi = 90^\circ$, 270°

Fig. 8. A plot of the virtual photoproduction cross section versus θ for data point 5.

Fig. 9. A plot versus $-k^2$ of the pion form factor as determined from this experiment and earlier experiments at the CEA, DESY and NINA.

Fig. 10. A plot of the interpolated cross section determined from data points 2, 3, 4 and 5.

Fig. 11. A plot shows the separated components of the cross section $A + \epsilon B$, C and D for W = 2.66 GeV, $-k^2 = 1.2$ GeV^2 and $\epsilon = 0.86$. The curves show the predictions of Berends' theory.

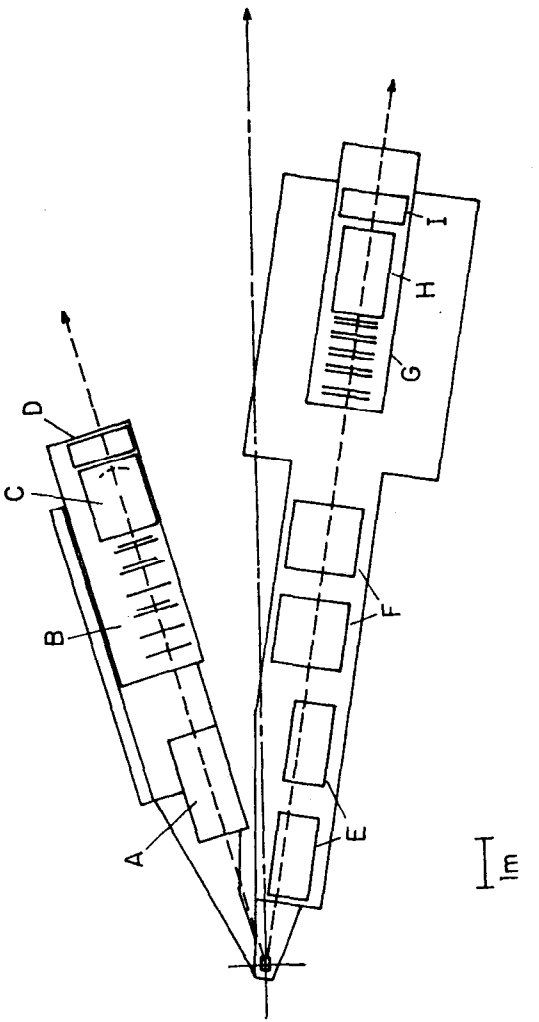

Figure 1

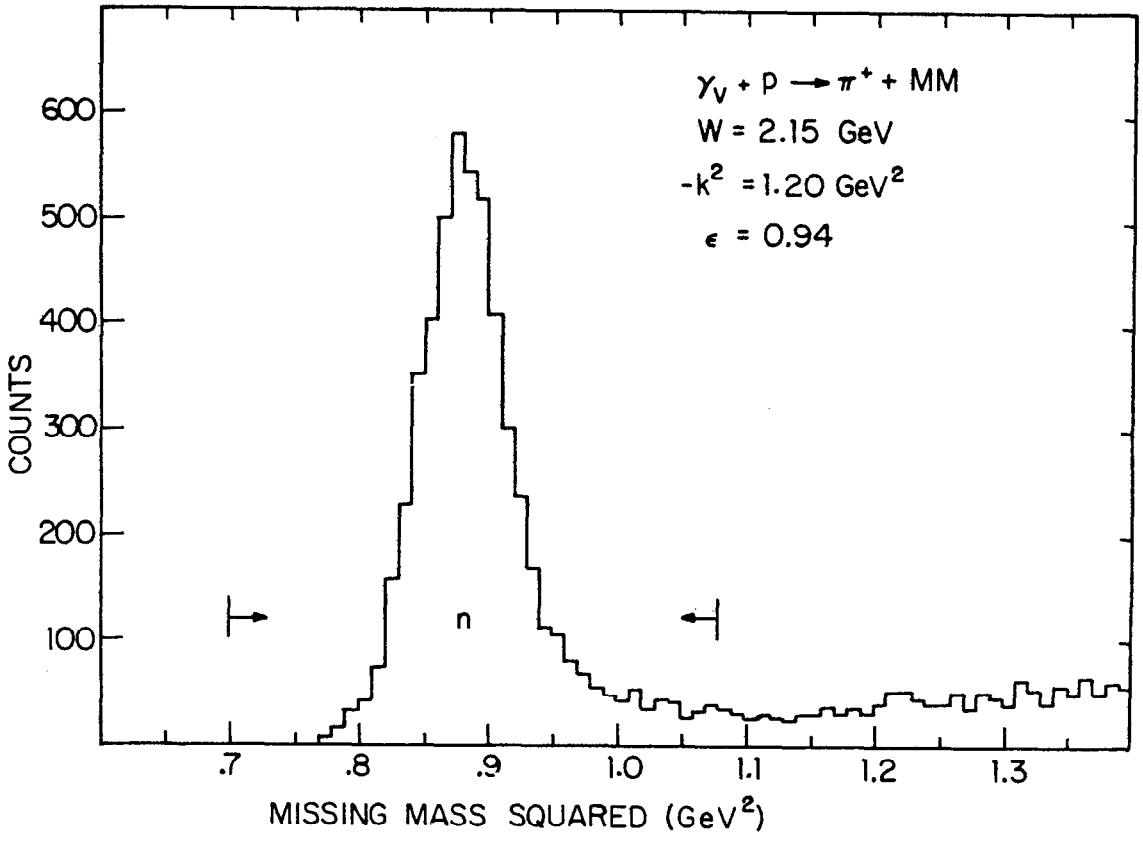

Figure 3

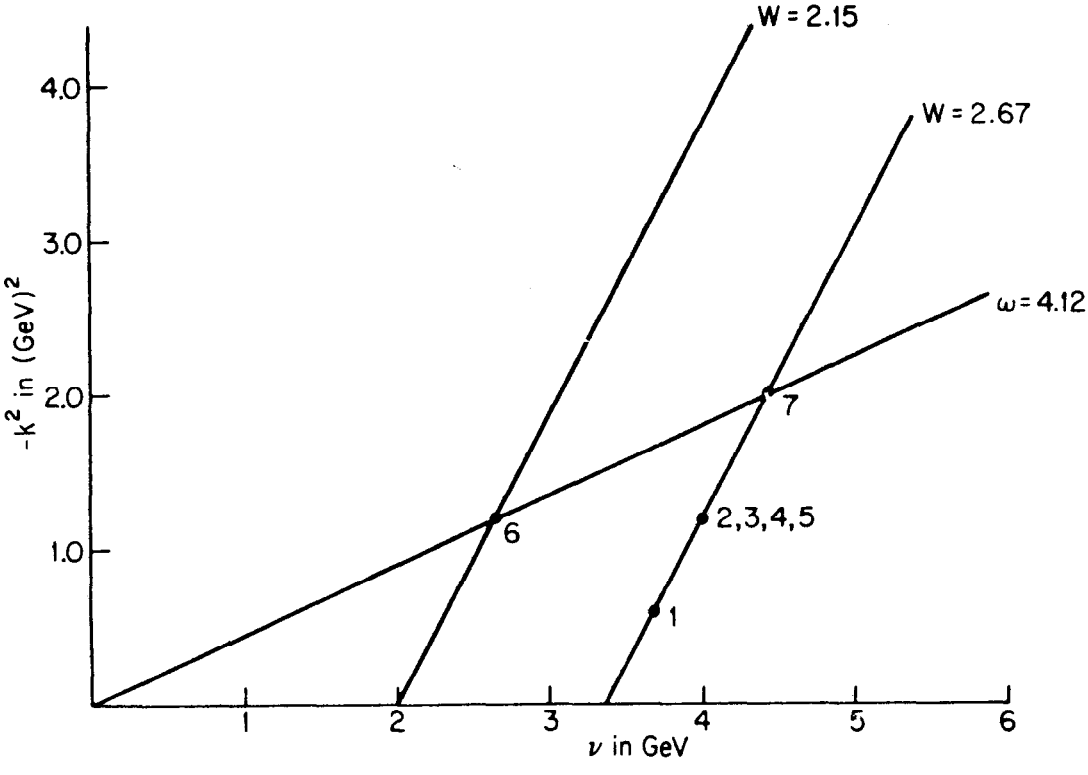

Figure 2

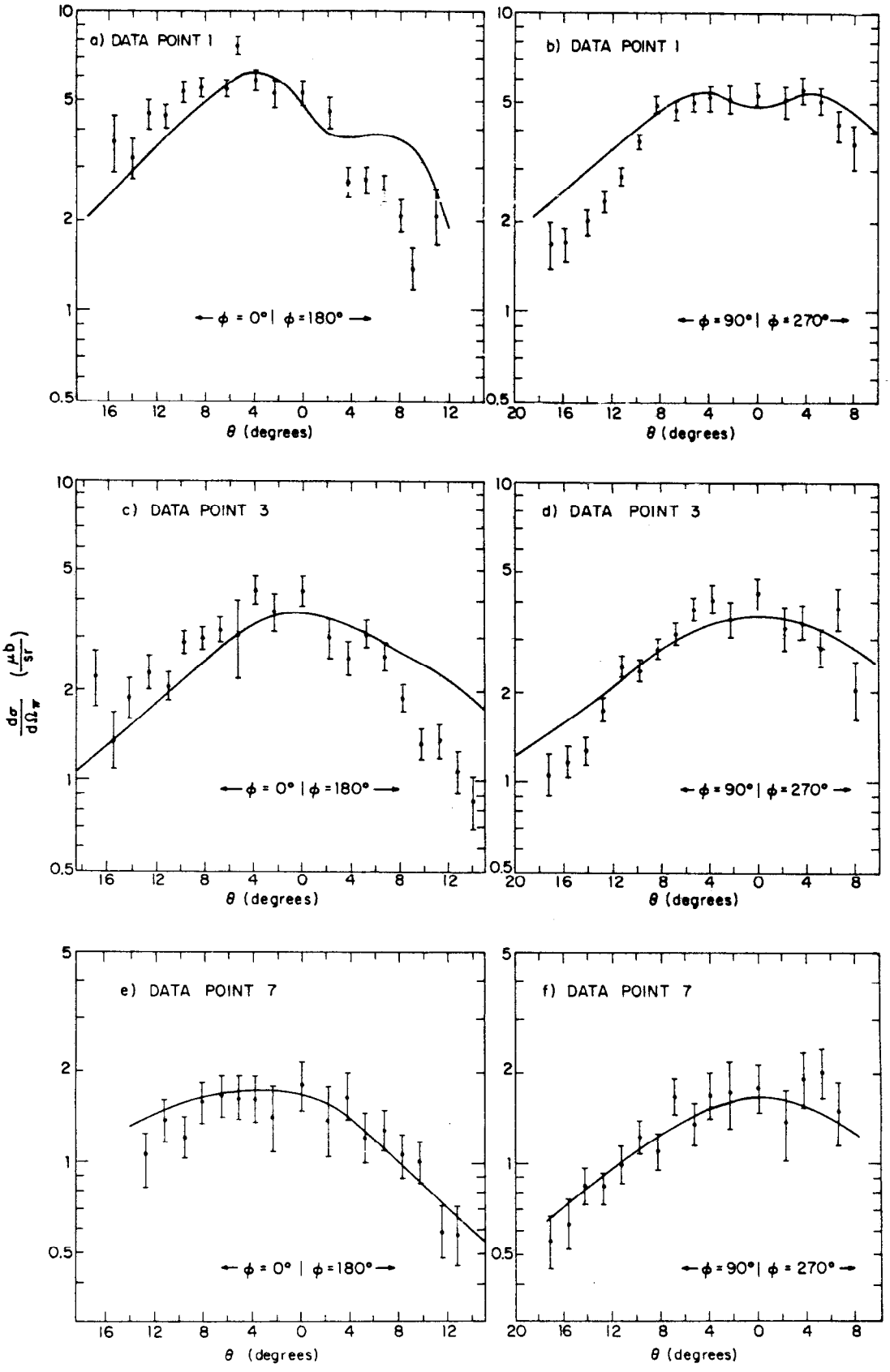
a) DATA POINT 1
b) DATA POINT 1
c) DATA POINT 3
d) DATA POINT 3
e) DATA POINT 7
f) DATA POINT 7
← φ = 0° | φ = 180° →
← φ = 90° | φ = 270° →
θ (degrees)
dσ/dΩ (μb/sr)

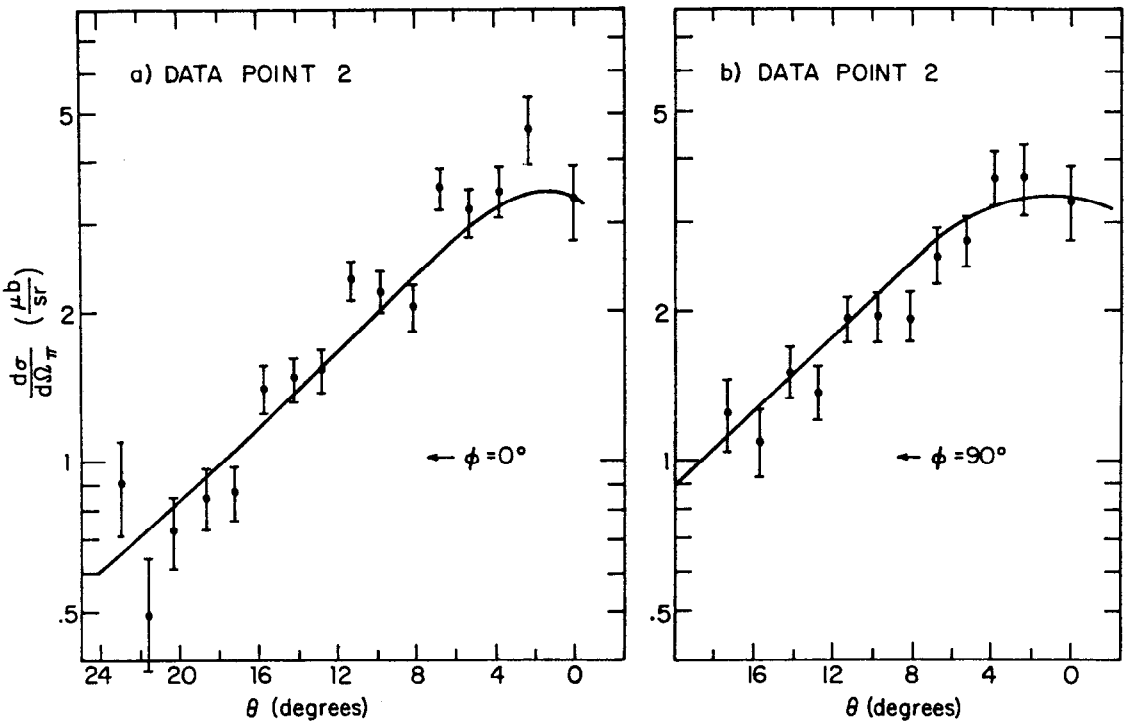

Figure 6

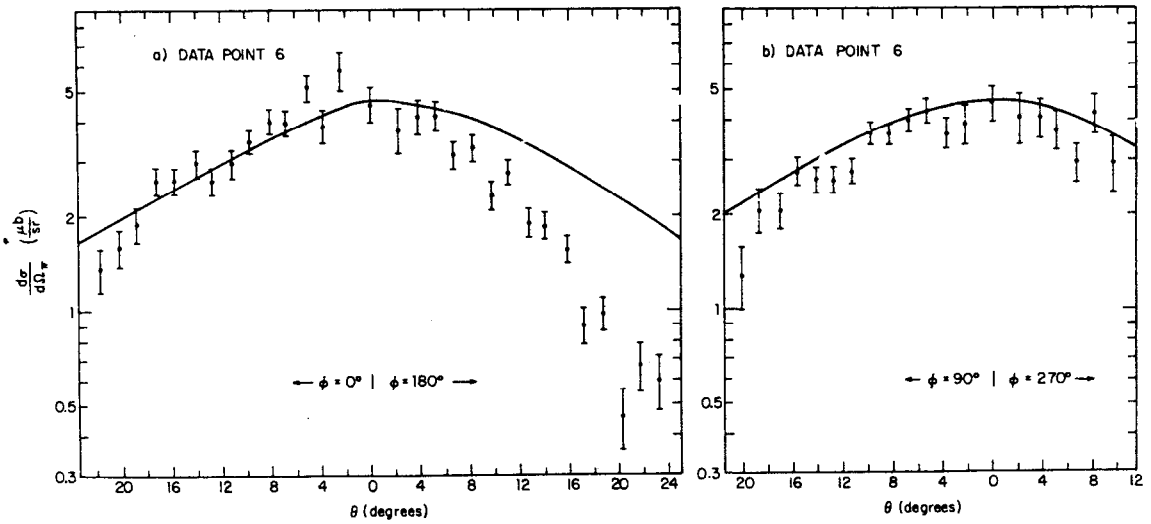

Figure 5

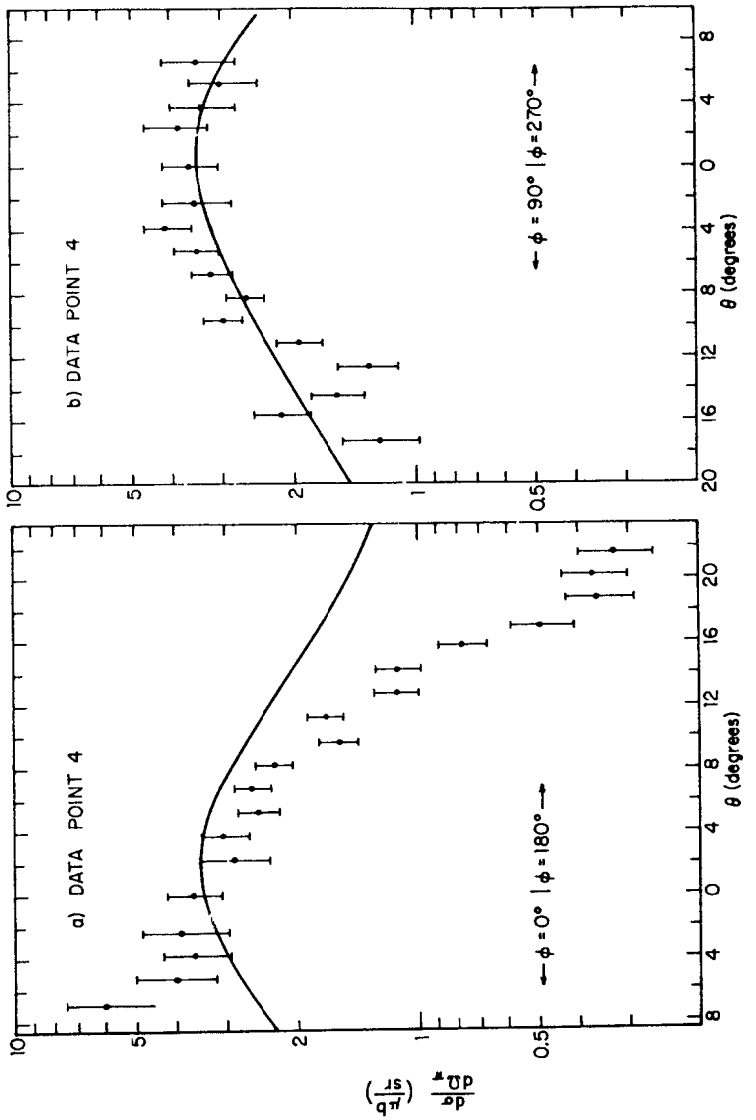

Figure 7

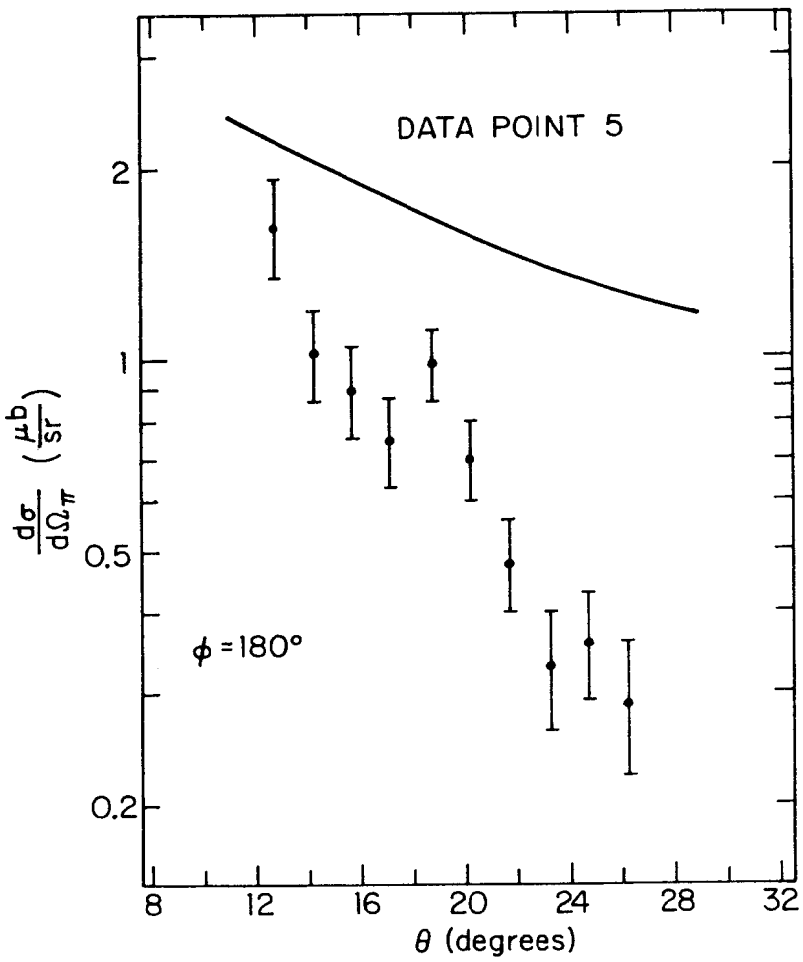

Figure 8

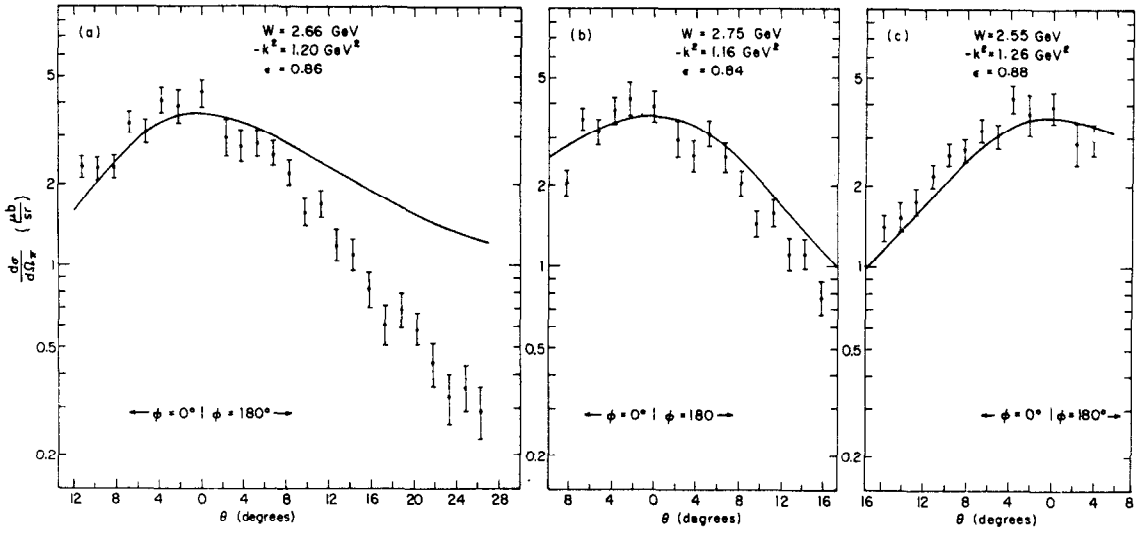

Figure 10

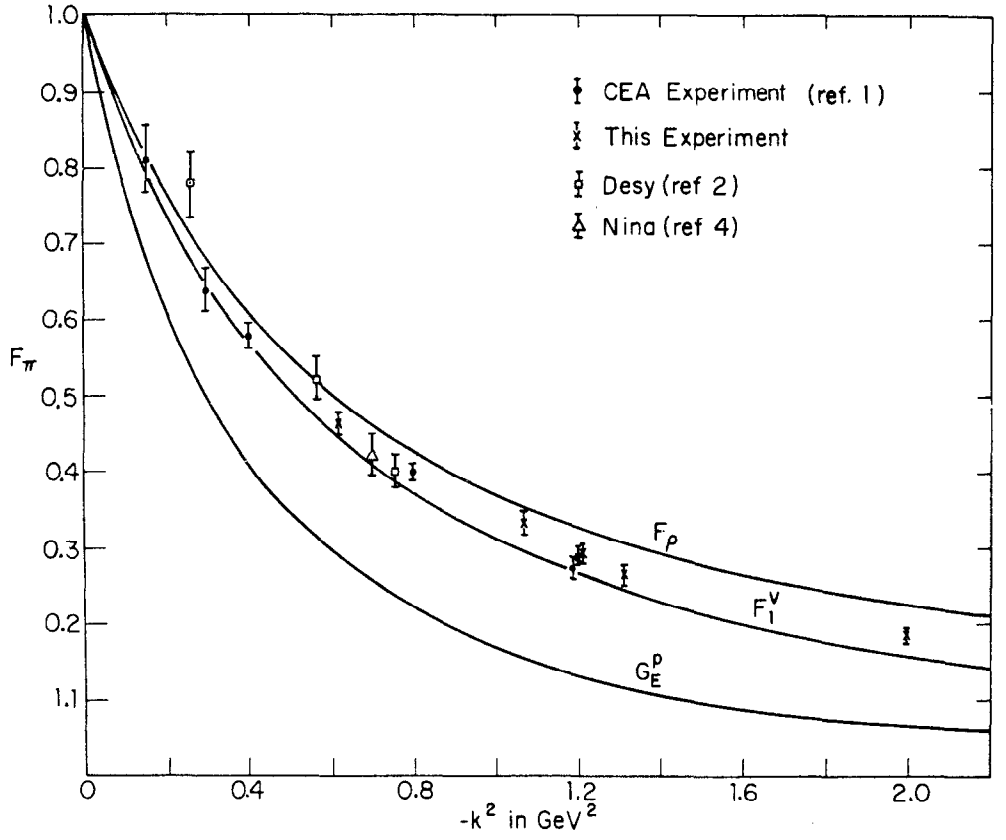

Figure 9

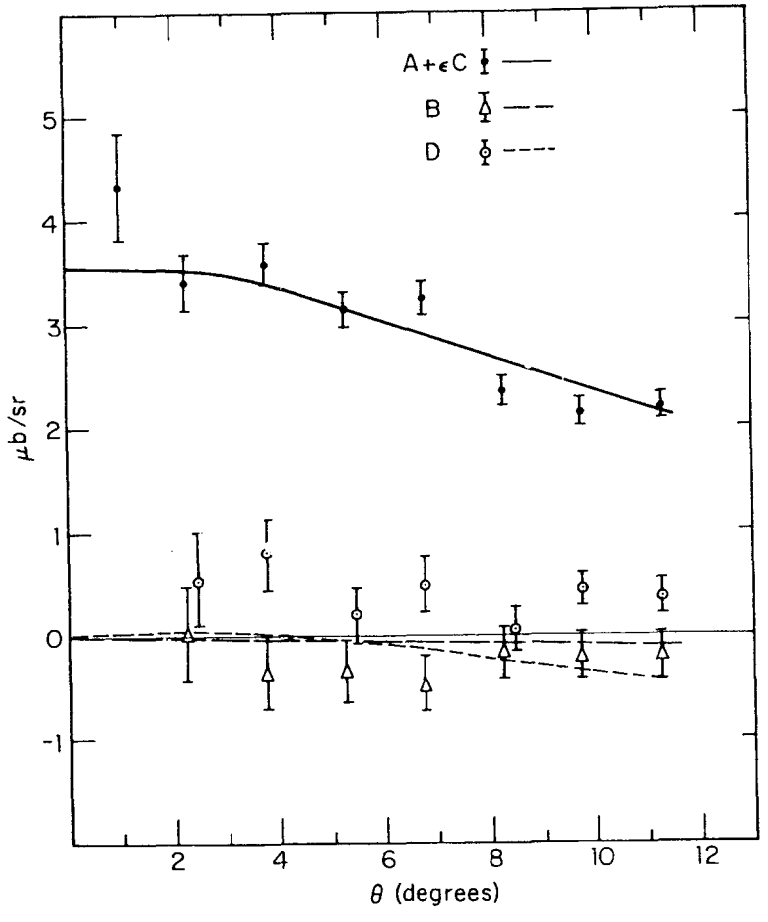

Figure 11

REFERENCES

1. C. N. Brown, C. R. Canizares, W. E. Cooper, A. M. Eisner, G. J. Feldman, C. A. Lichtenstein, L. Litt, W. Lockeretz, V. B. Montana, and F. M. Pipkin, Phys. Rev. Lett. 26, 987 (1971); 26, 991 (1971).
2. C. Driver, K. Heinloth, K. Hohne, G. Hofmann, P. Karow, D. Schmidt, G. Specht, and J. Rathje, Phys. Rev. Lett. 35B, 77 (1971).
3. P. S. Kummer, A. B. Clegg, F. Foster, G. Hughes, R. Siddle, J. Allison, B. Dickinson, E. Evangelides, M. Ibbotson, R. Lawson, R. S. Meaburn, H. E. Montgomery, W. J. Shuttleworth, and A. Sofair, Nuovo Cimento Lett. 1, 1026 (1971).
4. A. Sofair, J. Allison, B. Dickinson, E. Evangelides, M. Ibbotson, R. Lawson, R. S. Meaburn, H. E. Montgomery, W. J. Shuttleworth, A. B. Clegg, F. Foster, G. Hughes, P. Kummer, and R. Siddle, Nucl. Phys. B42, 369 (1973).
5. C. N. Brown, C. R. Canizares, W. E. Cooper, A. M. Eisner, G. J. Feldman, C. A. Lichtenstein, L. Litt, W. Lockeretz, V. B. Montana, and F. M. Pipkin, Phys. Rev. D8, 92 (1973).
6. A. Bartl and P. Urban, Acta. Phys. Austriaca 24, 139 (1966).
7. N. Meister and D. R. Yennie, Phys. Rev. 130, 1210 (1963).
8. F. A. Berends, Phys. Rev. D1, 2590 (1970).

MEASUREMENTS OF INCLUSIVE PION ELECTROPRODUCTION*

C. J. Bebek, C. N. Brown, M. Herzlinger, C. A. Lichtenstein,

F. M. Pipkin and L. K. Sisterson

Cyclotron Laboratory

Harvard University

Cambridge, Massachusetts 02138

D. Andrews,+ K. Berkelman, D. G. Cassel and D. L. Hartill

Laboratory of Nuclear Studies

Cornell University

Ithaca, New York 14850

ABSTRACT

Measurements of the inclusive pion electroproduction reaction $e^- + p \rightarrow e^- + \pi^\pm + X$ made at the Wilson Synchrotron Laboratory are reported. Data were taken at points with nominal (Q^2, W) values of (0.6, 2.67), (1.2, 2.67), (2.0, 2.67) and (1.2, 2.15) in (GeV^2, GeV). A more complete angular distribution was taken at (1.2, 2.67). The virtual photoproduction cross section for π^+ + Missing Mass is studied as a function of missing mass, Feynman scaling variables, Q^2 and W. The invariant cross section shows a simple behavior as a function of Q^2 and W. Its dependence on W, p_T^2, x' and ϕ is determined.

*Research supported in part by the U. S. Atomic Energy Commission and in part by the National Science Foundation.

+Present address: Physics Department, University of Rochester, Rochester, New York 14627.

I. INTRODUCTION

The large cross section for deep inelastic electron nucleon scattering, which shows scaling as a function of $\omega = 2M\nu/Q^2$, has aroused considerable theoretical and experimental interest in the processes which are responsible for it. Thus a number of experiments have been done and are being done to examine the details of the final hadronic state. In general there are only qualitative theoretical predictions concerning the nature and behavior of the final state hadrons and these are expected to be valid at higher energies than are currently available to the experimenter. This paper reports an experiment at center of mass energies just above the resonance region (the 2-3 GeV range) in which a charged pion moving in approximately the same direction as the virtual photon is detected.

In what is now standard notation,[1] electroproduction can be treated as photoproduction by a virtual photon, where the photon's mass squared $-Q^2$, energy ν, direction, and polarization parameter ϵ are tagged by the scattered electron. The cross section for the reaction

$$e^- + p \rightarrow e^- + \pi^\pm + \text{missing mass} \qquad (1)$$

is written

$$\frac{d\sigma}{d\Omega_e\, dE_e\, d\Omega^*_H\, dMM^2} = \Gamma\left(\frac{d\sigma_U}{d\Omega^*_H\, dMM^2} + \epsilon\,\frac{d\sigma_L}{d\Omega^*_H\, dMM^2} + \epsilon\,\frac{d\sigma_P}{d\Omega^*_H\, dMM^2}\cos 2\phi + \sqrt{\epsilon(\epsilon+1)/2}\,\frac{d\sigma_I}{d\Omega^*_H\, dMM^2}\cos\phi\right)$$

where Γ is the "flux" of virtual photons.

The first two terms are the main contributions arising from the transverse and longitudinal polarization states of the virtual photon; the other two terms are functions of the azimuthal angle ϕ and correspond to interference between the two transverse polarization amplitudes and between transverse and longitudinal amplitudes. If the cross section is integrated over ϕ, the interference terms do not contribute.

The hadronic cross section is a function of the virtual photon variables Q^2, ν (or W, the mass of the virtual photon-target proton system) and ϵ, and the variables describing the detected hadron in the virtual photon-target proton center of mass system θ^*, ϕ, MM^2. Another way to present the virtual photon-proton cross section is in terms of the Feynman scaling variables[2] x and P_T^2, where P_T is the momentum of the hadron transverse to the virtual photon direction and x is defined in terms of the center of mass momentum by

$$x = P_L^*/P^*_{max} \quad .$$

Here P^*_L is the component of momentum along the virtual photon direction and P^*_{max} is the maximum momentum for the hadron.

For experiments at the comparatively low energies which are presently possible, the variable x has the disadvantage that for x near 1 the range in P_T^2 is a function of x and W. To avoid this dependence, we have chosen instead to use x' where

$$x' = P_L^*/[(P^*_{max})^2 - P_T^2]^{1/2} \quad .$$

For $P_T \ll P^*_{max}$, x and x' are identical.

An additional variable that is useful for describing continuum final states is rapidity y defined by

$$y = 0.5 \log \frac{E + P_L}{E - P_L} \quad ,$$

where E is the energy and P_L the component of momentum of the hadron along the virtual photon direction. Since a Lorentz transformation simply shifts the origin of y, it may be evaluated in any frame. We have used the definition

$$y = 0.5 \log \left(\frac{E^*_{max} + (P^{*2}_{max} - P_T^2)^{1/2}}{E^*_{max} - (P^{*2}_{max} - P_T^2)^{1/2}} \Big/ \frac{E^* + P^*_L}{E^* - P^*_L} \right) \quad ,$$

that is, we have measured the rapidity in the hadronic center of mass with respect to the maximum rapidity for the hadron.

We have analyzed the data in terms of the differential cross section in missing mass squared and the invariant structure function,

$$F = \frac{E}{\sigma_{Tot}} \frac{d^3\sigma}{dp^3} = \frac{1}{\sigma_{Tot}} \frac{1}{\pi} \frac{E^*}{\left(P^{*2}_{max} - P_T^2\right)^{1/2}} \frac{d\sigma}{dx' \, dp_T^2} = \frac{1}{\pi\sigma_{Tot}} \frac{d\sigma}{dy \, dp_T^2} \quad ,$$

where σ_{Tot} is the total virtual photoproduction cross section for the total energy W and Q^2 of the reaction. The value of σ_{Tot} was taken from a fit to the SLAC-MIT measurements of νW_2 with the assumption that $\sigma_S/\sigma_T = 0.18$[3].

II. EXPERIMENTAL DETAILS

The two spectrometers shown in Fig. 1 were used to detect the scattered electron and the electroproduced hadron. The combination of a Cerenkov counter and a lead acetate shower counter identified the electrons. Pions were identified by a threshold gas Cerenkov counter when their momentum was greater than 1.8 GeV/c and by their time-of-flight when their momentum was less than that.

The spectrometers were set up to take data at the points in the (Q^2, ν) plane shown in Fig. 2. Points 1, 3 and 7 comprise a Q^2 scan at fixed W; points 6 and 7 lie on the same ω line and thus can be used to test scaling; points 3 and 6 give a W scan at fixed Q^2; points 2, 3, 4, 5 comprise an angular scan with the hadron arm which extends the aperture in P_T and allows an estimate of the interference terms in the cross section to be made. The acceptance of the apparatus is such that the W distribution is approximately 0.6 GeV wide and Q^2 about 0.3 GeV^2 wide at each data point.

The data have been corrected for random coincidences ($\sim$5%), for counter and spark chamber dead time ($\sim$2%), for absorption in the counters ($\sim$2%), for target wall background ($\sim$5%), and for decay losses, about 30% at the lowest momenta and 2% at the highest. No radiative corrections have been applied to the data shown in the graphs. The errors quoted are statistical; there is an additional overall normalization uncertainty of 7%.

III. MISSING MASS SQUARED AND LONGITUDINAL DISTRIBUTIONS

The missing mass squared distributions at data points 6 and 7 are shown in Fig. 3 for π^+ mesons which are moving forward in the hadronic center of mass with $t' = t - t_{min} < 0.02$ GeV^2. It is immediately clear that the overall shape has not changed significantly, though the scale has changed by more than a factor of two (roughly $1/(Q^2)^2$). The neutron peak stands out clearly; a detailed analysis of this channel, $\gamma_v p \to \pi^+ n$, appears in another[4] report.

The invariant structure function, F, for $P_T^2 < 0.02$ GeV^2 is plotted against x' in Fig. 4 and against y in Fig. 5, for all the data points. For $x' < 0.5$, the data appear to lie on a single curve. This is even true for the photoproduction data of Struczinski et al.[5]. Above $x' = 0.5$ there is a dramatic change as Q^2 increases which can be directly attributed to vector meson production which falls rapidly with increasing Q^2. Thus, apart from vector meson production, which is a diffractive type of process, the invariant structure function for π^+ mesons is consistent with a universal curve independent of both W and Q^2; the data show the same type of scaling as is found in hadron reactions. In Fig. 5 (b) and (c) we show also the invariant structure function for π^- at data points 3 and 7. In both cases, the values of F for π^- mesons are approximately a factor of 2 below the corresponding values of F for π^+ mesons over most of the range of y. However, for $y > 1.6$ (equivalent to $x' \sim 0.2$) at data point 7 (Fig. 5 (c)) the values of F for π^+ and π^- become equal. Assuming that the P_T^2 distributions are identical for π^+ and π^- this implies that, for $x' > 0.2$, the average multiplicity for π^+ is twice that for π^-.

IV. TRANSVERSE DISTRIBUTIONS AND INTERFERENCE TERMS

In order to obtain good estimates of the shape of the P_T^2 distributions, and to examine different regions of ϕ separately in order to look for the presence of the interference terms in the cross section, we took data at several different positions of the hadron spectrometer arm with the electron spectrometer arm fixed to give W=2.69 GeV, $Q^2 = 1.2$ GeV; these are data points 2, 3, 4 and 5.

We took the values of F and the kinematic averages for the data for the ϕ bins $-135^\circ < \phi < -45^\circ$, $-45^\circ < \phi < 45^\circ$, $45^\circ < \phi < 135^\circ$, $135^\circ < \phi < 225^\circ$ and for x' bins $0.2 < x' < 0.5$ and $0.5 < x' < 0.7$. For each x' bin separately, we fitted the data to the form,

$$N \exp(-AP_T^2) \exp(-Bx') ,$$

to determine the parameters A and B and normalization N. This expression is entirely empirical and clearly contains strong assumptions about the nature of the cross section. It also implicitly assumes that F does not depend on W and Q^2. However, since we fit to regions of data in which the x' variations are not too large, we expect that these functions are tolerable approximations to reality. A number of different fitting procedures were tried, and after observing that the P_T^2 slope was determined best by the bin $135^\circ < |\phi| < 225^\circ$, all the data in this ϕ bin were fitted simultaneously. The values of the fitted parameters are shown in Table I. The results of this fit were used to project the data from all ϕ bins onto fixed x' planes in order to display a pure P_T^2 distribution; the results are shown in Fig. 6. These plots are entirely synthetic in as much as the data points shown depend upon the fitted x' function, though the effect of this is small; the error bars have not been increased to allow for the fitting and projection errors. The description of the data is really quite good. It is immediately clear that any interference effects must be comparatively small compared to the errors. To verify this we fitted each P_T^2 bin for which there were measurements in all 4 ϕ regions to the form

$$\sigma_{uL} + \epsilon \sigma_P \cos 2\phi + \sqrt{\epsilon(\epsilon+1)/2}\, \sigma_I \cos\phi \quad \text{where } \sigma_{uL} = \sigma_u + \epsilon \sigma_L$$

and determined σ_{uL}, σ_P and σ_I; the results of these fits are shown in Table II. The values of σ_P and σ_I are generally consistent with zero. Fitting σ_{uL} alone (the results for this are also in Table II) gives good fits to the data. Thus, we have no evidence for any significant contribution to the cross section from the interference terms for $0.2 < x' < 0.7$, a continuum region which should not be dominated by any single channel.

The P_T^2 slopes for points 1, 6 and 7 were obtained in a similar manner, except that the data were not binned in ϕ. We also fitted the P_T^2 slope for $0.7 < x' < 0.9$ from point 3 in this manner. This region corresponds primarily to Δ^0 production which will be analyzed thoroughly in a separate paper. The fitted P_T^2 slopes are summarized in Table III. In general, the P_T^2 slope gets smaller as x' gets smaller. The W and Q^2 dependences of the slope are not clear, different x' regions show different trends and the errors are such as to preclude any definitive statement.

V. CONCLUSIONS

The data reported here show that, with the exception of two specific channels, the structure function for forward pions is independent of both W and Q^2. Thus, even at these low energies scaling of the type found in hadron reactions has set in. The only clear Q^2 dependences that are observed are that due to vector meson production which causes the pion structure function in the range $0.5 < x' < 0.8$ to fall with Q^2 and the channel $\gamma_v p \rightarrow \pi^+ n$ which falls like the pion form factor squared[4].

The P_T^2 distributions show no clear trend with Q^2 or W but the slope does change as a function of x', getting larger as x' increases. At W = 2.67 GeV, $Q^2 = 1.2$ GeV^2 the P_T^2 slope changes by a factor at 2 in going from the region $0.2 < x' < 0.5$ to $0.7 < x' < 0.9$, and while the data at the other (W, Q^2) values are not so good, they do confirm this trend. A detailed examination of the angular distribution for $0.2 < x' < 0.5$ and $0.5 < x' < 0.7$ reveals no evidence for the presence of interference terms in the cross section. For $x' > 0.2$, the structure function for π^- is only about one half that for π^+ and becomes equal to it just below $x' = 0.2$.

VI. ACKNOWLEDGEMENTS

We wish to acknowledge the support of Professor Boyce McDaniel, the staff of the Wilson Synchrotron Laboratory and the staff of the Harvard Cyclotron Laboratory.

TABLE I. RESULTS OF FITTING P_T^2 DISTRIBUTIONS AT DATA POINTS 2, 3, 4 and 5, W = 2.67 GeV, $Q^2 = 1.2$ GeV

x' region	P_T^2 slope (GeV^{-2})	x' slope
$0.2 < x' < 0.5$	2.67 ± 0.51	3.73
$0.5 < x' < 0.7$	3.22 ± 0.25	1.52

TABLE II. RESULTS OF FITTING P_T^2 BINS TO DETERMINE THE INTERFERENCE TERMS IN THE CROSS SECTION AT DATA POINTS 2, 3, 4 and 5

P_T^2 (GeV)^2	$\sigma_u + \epsilon\sigma_L$ (GeV^{-2})	σ_P (GeV^{-2})	σ_I (GeV^{-2})	P(χ^2)	for $\sigma_P = \sigma_I = 0$ $\sigma_u + \epsilon\sigma_L$ (GeV^{-2})	P(χ^2)
	x' = 0.35					
0.005	0.556± 0.022	-0.008± 0.026	-0.016 ± 0.058	0.11	0.556± 0.020	0.19
0.015	0.535± 0.024	-0.009± 0.027	-0.048 ± 0.064	0.44	0.533± 0.021	0.57
0.025	0.496± 0.035	-0.031± 0.039	0.057 ± 0.086	0.48	0.524± 0.027	0.53
0.035	0.501± 0.111	-0.040± 0.106	-0.182 ± 0.263	0.02	0.481± 0.053	0.03
0.05	0.463± 0.057	0.061± 0.060	0.201 ± 0.137	0.76	0.472± 0.023	0.81
	x' = 0.6					
0.005	0.247± 0.009	-0.010± 0.011	0.0001± 0.022	0.13	0.247± 0.008	0.18
0.015	0.264± 0.010	-0.017± 0.013	0.010 ± 0.028	0.16	0.267± 0.010	0.13
0.025	0.229± 0.014	-0.012± 0.015	0.051 ± 0.037	0.05	0.239± 0.014	0.02
0.035	0.265± 0.016	-0.032± 0.014	-0.035± 0.040	0.46	0.272± 0.014	0.22
0.05	0.211± 0.020	-0.026± 0.018	0.099 ± 0.048	0.04	0.252± 0.019	0.00
0.07	0.227± 0.023	-0.040± 0.016	0.020 ± 0.055	0.43	0.265± 0.016	0.10
0.09	0.218± 0.053	0.030± 0.046	0.078 ±0.116	0.19	0.219± 0.014	0.33

TABLE III. RESULTS OF FITTING THE P_T^2 DISTRIBUTIONS

W (GeV)	Q^2 (GeV^2)	x'	P_T^2 slope (GeV^{-2})	x' slope
2.68	0.6	0.7<x'<0.9	5. 8± 1.0	0.
2.68	1.2	0.7<x'<0.9	6.24± 0.85	0.
2.68	2.0	0.7<x'<0.9	4.76± 0.61	0.
2.68	2.0	0.5<x'<0.7	4.58± 0.80	1.5
2.15	1.2	0.7<x'<0.9	6.34± 0.36	0.
2.15	1.2	0.5<x'<0.7	4.09± 0.46	2.33

FIGURE CAPTIONS

1. The Cornell and Harvard spectrometers.
2. The (Q^2, ν) plane with five points at which data were taken in this experiment indicated.
3. Missing mass squared distributions for π^+ with $t' < 0.02$ GeV^2 at data points 6 and 7.
4. The structure function plotted against x' for π^+ with $P_T^2 < 0.02$ GeV^2 for all the data points together with that from the photoproduction measurements of ref 5.
5. The structure function plotted against rapidity y for π^+ with $P_T^2 < 0.02$ GeV^2 for the data from
   (a) Point 1, W = 2.75 GeV, Q^2 = 0.60 GeV^2, ϵ = .86
   (b) Point 3, W = 2.70 GeV, Q^2 = 1.18 GeV^2, ϵ = .85
   (c) Point 7, W = 2.70 GeV, Q^2 = 1.97 GeV^2, ϵ = .81
   (d) Point 6, W = 2.20 GeV, Q^2 = 1.17 GeV^2, ϵ = .93

   In (b) and (c) the structure function for π^- under the same conditions as for π^+ is plotted also.
6. The structure function plotted against P_T^2 for π^+ from data points 2, 3, 4, 5 for four regions of ϕ and two regions of x'.
   (a) and (b) 0.1 <x' <0.5
   (c) and (d) 0.5 <x' <0.7

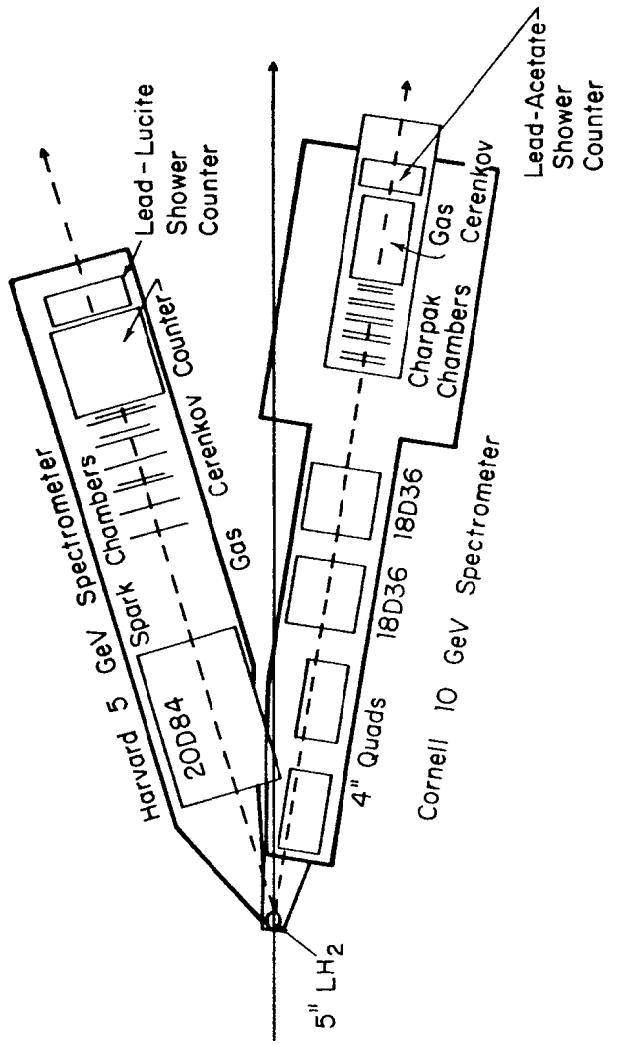

Figure 1

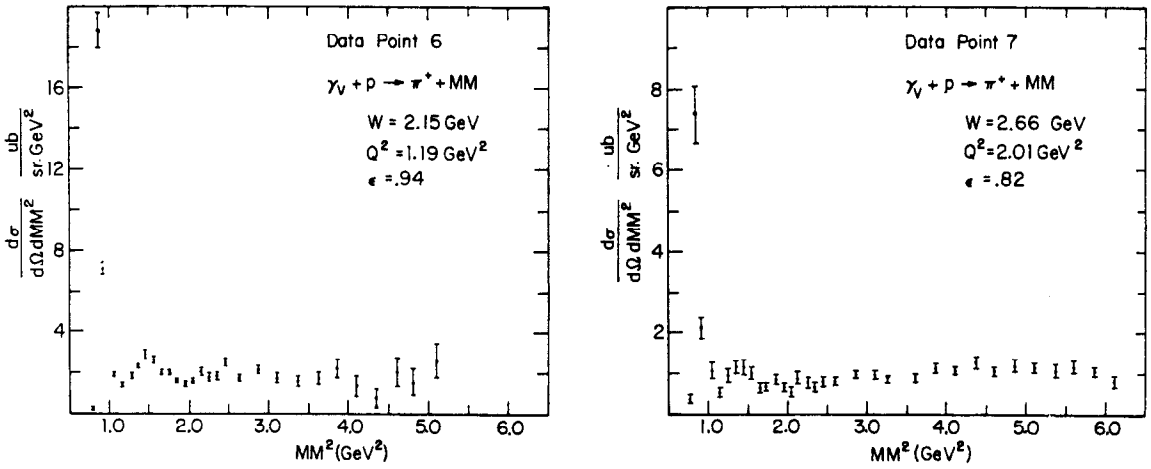

Figure 3

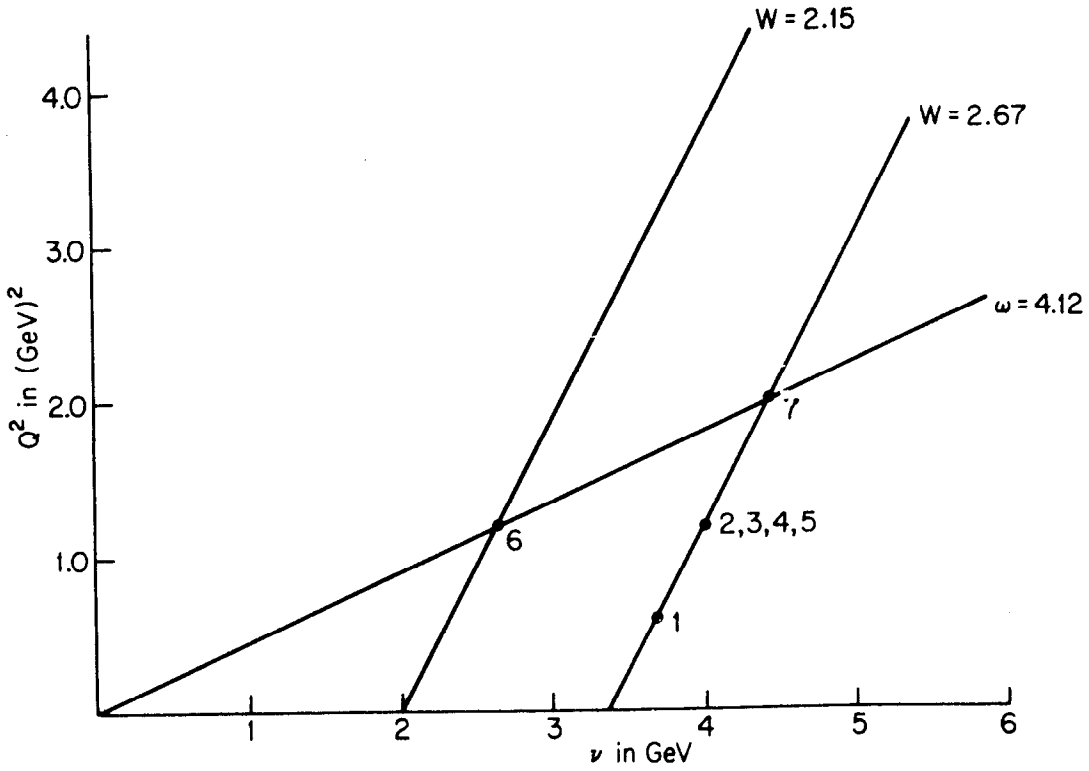

Figure 2

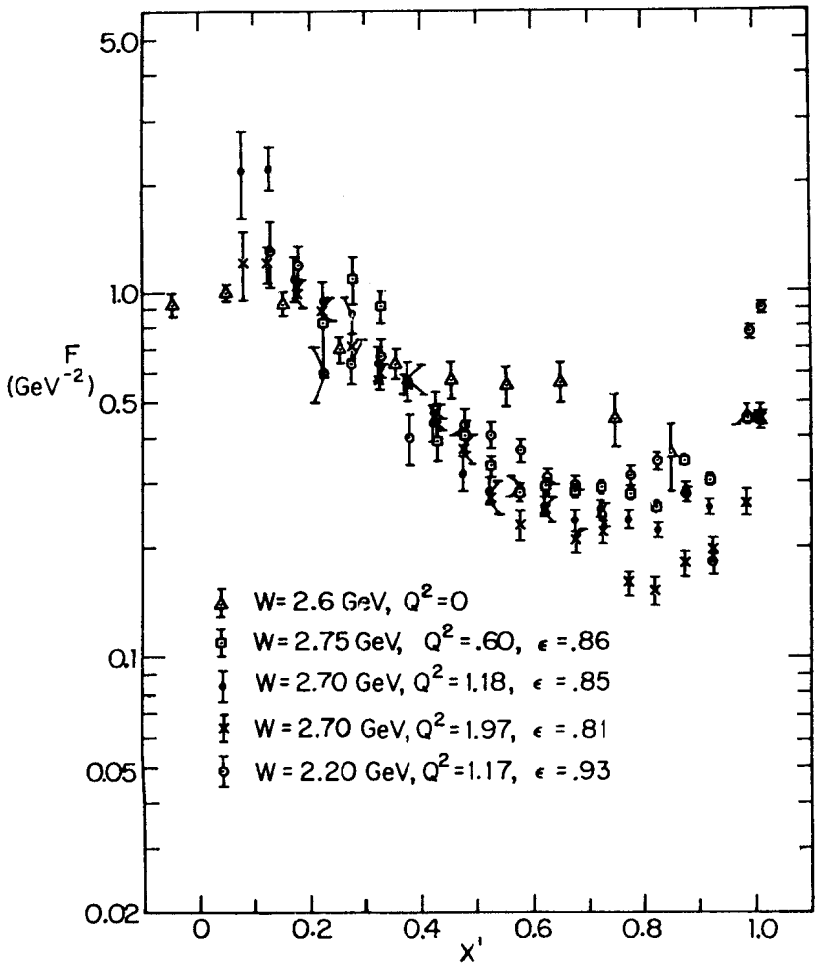

Figure 4

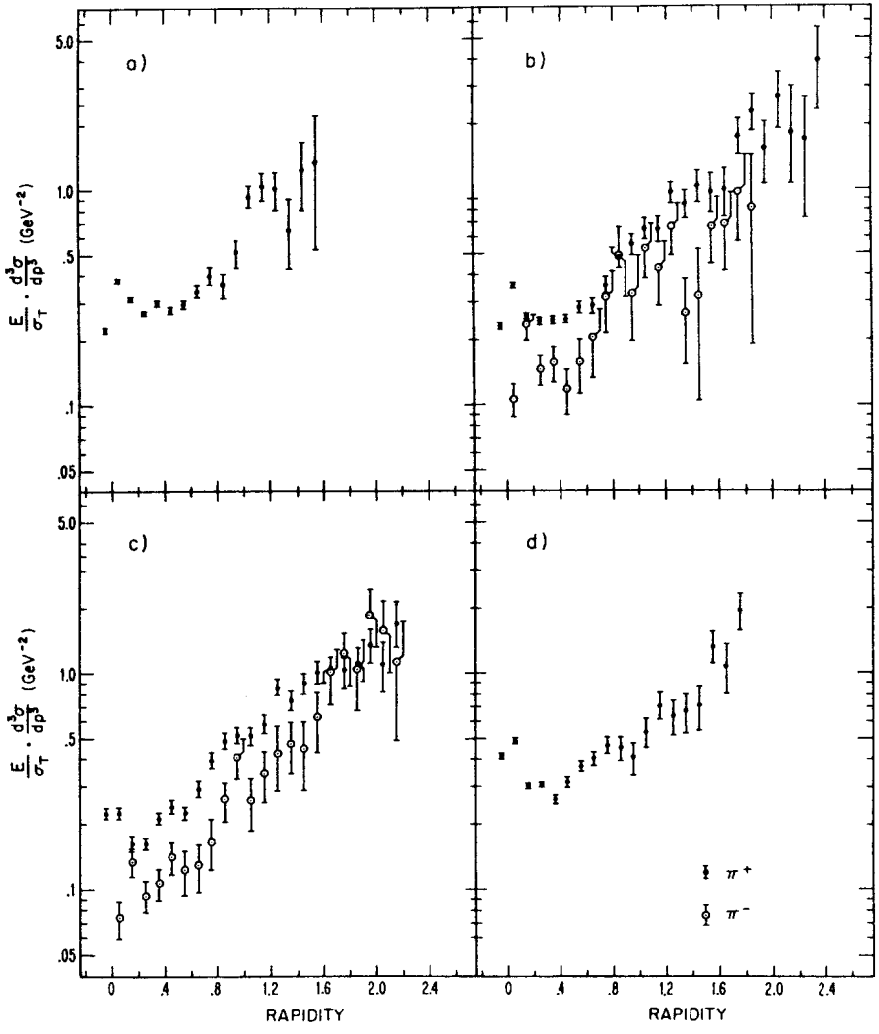

Figure 5

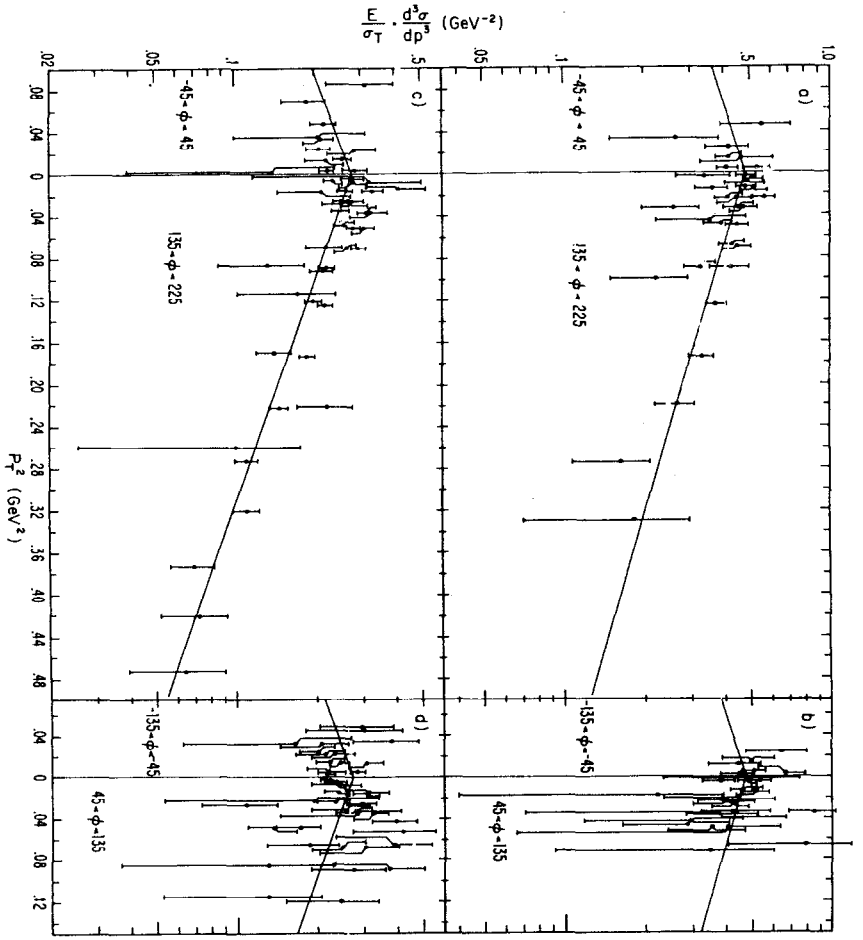

Figure 6

REFERENCES

1. K. Berkelman in Proceedings at the Sixteenth International Conference on High Energy Physics, National Accelerator Laboratory, Batavia, Illinois, 1972, edited by J. D. Jackson and A. Roberts (NAL, Batavia, Ill., 1973); L. N. Hand, Phys. Rev. 129, 1834 (1964).
2. R. P. Feynman, Phys. Rev. Let. 23, 1415 (1969).
3. W. B. Atwood, private communication.
4. C. J. Bebek, C. N. Brown, M. Herzlinger, S. Holmes, C. A. Lichtenstein, F. M. Pipkin, L. K. Sisterson, D. Andrews, K. Berkelman, D. G. Cassel and D. L. Hartill. Paper submitted to this conference.
5. W. Struczinski, et al., (DESY) paper contributed to the XVI International Conference on High Energy Physics, Batavia, Ill., 1972.

ELECTROPRODUCTION OF PROTONS IN THE FORWARD DIRECTION*

C. J. Bebek, C. N. Brown, M. Herzlinger, C. A.
Lichtenstein, F. M. Pipkin and L. K. Sisterson
Cyclotron Laboratory
Harvard University
Cambridge, Massachusetts 02138
D. Andrews,+ K. Berkelman, D. G. Cassel and D. L. Hartill
Laboratory of Nuclear Studies
Cornell University
Ithaca, New York 14850

ABSTRACT

We present data taken at the Wilson Synchrotron Laboratory on electroproduction off protons in which a proton moving in approximately the same direction as the virtual photon is detected. Measurements were made at data points with nominal (Q^2, W) values of (0.6, 2.67), (1.2, 2.67) (2.0, 2.67) and (1.2, 2.15) in (GeV^2, GeV). The virtual photoproduction cross section for p + Missing Mass is studied as a function of missing mass, Feynman scaling variables x and P_T^2, azimuthal angle ϕ, Q^2 and W. The invariant cross section shows a simple behavior as a function of Q^2 but not W. Its dependence on W, P_T^2, x' and ϕ is determined.

---

*Research supported in part by the U. S. Atomic Energy Commission and in part by the National Science Foundation.

+Present address: Physics Department, University of Rochester, Rochester New York 14727

I. INTRODUCTION

The large cross section for deep inelastic electron nucleon scattering, which shows scaling as a function of $\omega = 2M\nu/Q^2$, has aroused considerable theoretical and experimental interest in the processes which are responsible for it. Thus a number of experiments have been done and are being done to examine the details of the final hadronic state. In general there are only qualitative theoretical predictions concerning the nature and behavior of the final state hadrons, and these are expected to be valid at higher energies than are currently available to the experimenter. This paper reports an experiment at center of mass energies just above the resonance region (the 2-3 GeV range) in which a proton moving in approximately the same direction as the virtual photon is detected.

In what is now standard notation[1] electroproduction can be treated as photoproduction by a virtual photon, where the photon's mass squared $-Q^2$, energy ν, direction, and polarization parameter ϵ are tagged by the scattered electron. The cross section for reaction

$$e^- + p \rightarrow e^- + p + \text{missing mass} \qquad (1)$$

is written

$$\frac{d\sigma}{d\Omega_e dE_e d\Omega^*_h dMM^2} = \Gamma\left(\frac{d\sigma_u}{d\Omega^*_h dMM^2} + \epsilon \frac{d\sigma_L}{d\Omega^*_h dMM^2} + \epsilon \frac{d\sigma_P}{d\Omega^*_h dMM^2} \cos 2\phi + \sqrt{\epsilon(\epsilon+1)/2} \frac{d\sigma_I}{d\Omega^*_h dMM^2} \cos\phi\right)$$

with Γ the 'flux' of virtual protons.

The first two terms are the main contributions arising from the transverse and longitudinal polarization states of the virtual photon; the other two terms are functions of the azimuthal angle ϕ and correspond to interference between the two transverse polarization amplitudes and between transverse and scalar amplitudes. If the cross section is integrated over ϕ, the interference terms do not contribute.

The hadronic cross section is a function of the virtual photon variables Q^2, ν (or W, the mass of the virtual photon-target proton system) and ϵ, and the variables describing the detected hadron in the virtual photon-target proton center of mass system θ^*, ϕ, MM^2. Another way to present the virtual photon-proton cross section is in terms of the Feynman scaling variables[2] x and P_T^2 where P_T is the momentum of the hadron transverse to the virtual photon direction and x is defined in terms of the center of mass momentum by

$$x = P_L^* / P^*_{max}$$

Here P_L^* is the component of momentum along the virtual photon direction and P^*_{max} is the maximum momentum for the hadron.

For experiments at the comparatively low energies which are presently possible the variable x has the disadvantage that for x near 1 the range in P_T^2 is a function of x and the total center of mass energy. To avoid this dependence, we have chosen instead to use x' where

$$x' = P_L^* / [\,(P^*_{max})^2 - P_T^2\,]^{1/2}$$

For $P_T \ll P^*_{max}$, x and x' are identical.

An additional variable that is useful for describing continuum final states is rapidity y defined by

$$y = 0.5 \log\left(\frac{E + P_L}{E - P_L}\right)$$

where E is the energy and P_L the component of momentum of the hadron along the virtual photon direction. Since a Lorentz transformation simply shifts the origin of y, it may be evaluated in any frame. We have used the definition

$$y = 0.5 \log\left(\frac{E^*_{max} + \left(P^{*\,2}_{max} - P_T^2\right)^{1/2}}{E^*_{max} - \left(P^{*\,2}_{max} - P_T^2\right)^{1/2}} \Bigg/ \frac{E^* + P_L^*}{E^* - P_L^*}\right) ,$$

that is, we have measured the rapidity in the hadronic center of mass with respect to the maximum rapidity for the hadron.

We have analyzed the data in terms of the differential cross section in missing mass squared and the invariant structure function,

$$F = \frac{E}{\sigma_{Tot}} \frac{d^3\sigma}{dp^3} = \frac{1}{\sigma_{Tot}} \frac{1}{\pi} \frac{E^*}{\left(P^{*\,2}_{max} - P_T^2\right)^{1/2}} \frac{d\sigma}{dx'\,dp_T^2} = \frac{1}{\sigma_{Tot}} \frac{1}{\pi} \frac{d\sigma}{dy dp_T^2}$$

where σ_{Tot} is the total virtual photoproduction cross section for the total energy W and Q^2 of the reaction. The value of σ_{Tot} was taken from a fit to the SLAC-MIT measurements of νW_2 with the assumption that $\sigma_S / \sigma_T = 0.18$[3].

II. EXPERIMENTAL DETAILS

The two spectrometers shown in fig. 1 were used to detect the scattered electron and the electroproduced hadron. The combination of a Cerenkov counter and a lead acetate shower counter identified the electrons. Pions were identified by a threshold gas Cerenkov counter when their momentum was greater than 1.8 GeV/c and by their time-of-flight when their momentum was less than that. Neither protons nor kaons gave a signal in the Cerenkov counter, so they had to be separated from each other entirely by their time-of-flight. Figure 2 shows a typical time-of-flight spectrum for particles not detected by the Cerenkov counter; the peaks for K^+ and the proton are clearly seen. It is necessary to correct for the contamination of one peak by the tail of the other and for the loss of wanted events when we cut out the unwanted peak. This was done with timing cuts which varied in position according to the laboratory momentum of the particle in order to achieve optimum separation of the protons from K^+ mesons. For missing masses below 1 GeV there is no need for this since the smallest missing mass for a K^+ is that of the Λ. Indeed, only in the region of the mass of the Λ is the subtraction of the K^+ at all critical, elsewhere both subtractions and corrections are small for separating the protons from K^+ mesons. Misidentification of pions is also negligible except for the region of the missing neutron peak which occurs in the vector

meson region when the pion is misinterpreted as a proton.

The spectrometers were set up to take data at the points in the (Q^2, ν) plane shown in fig. 3. Points 1, 3 and 7 comprise a Q^2 scan at fixed W; points 6 and 7 lie on the same ω line and thus can be used to test scaling; points 3 and 6 give a W scan at fixed Q^2; points 2, 3, 4, 5 comprise an angular scan with the hadron arm which extends the aperture in P_T and allows an estimate of the interference terms in the cross section to be made. The acceptance of the apparatus is such that the W distribution is approximately 0.6 GeV wide and Q^2 about .3 GeV^2 wide at each data point.

The data have been corrected for random coincidences (~5%), for counter and spark chamber dead time (~2%), for absorption in the counters (~2%), and for target wall background (~5%). No radiative corrections have been applied to the data shown in the graphs. The errors quoted are statistical; there is an additional overall normalization uncertainty of 10%.

III. MISSING MASS SQUARED AND LONGITUDINAL DISTRIBUTIONS

The missing mass squared distributions are shown in Fig. 4 for protons which are moving forward in the hadronic center of mass with $u' = u - u_{min} < 0.02\ GeV^2$. The Q^2 scan at a fixed W = 2 62 GeV, Figs. 4(a), (b), (c), shows a small amount of π° and vector meson production and a substantial high mass continuum which all decrease with increasing Q^2. At W = 2.08 GeV, $Q^2 = 1.2\ GeV^2$, Fig. 4(d), the distribution is quite different; the two body channels $p\pi^\circ$, $p\rho^\circ/\omega^\circ$ are strong as is the continuum region. The cross section is clearly changing much more rapidly as a function of W than it is as a function of Q^2.

We have estimated the single channel cross sections $\gamma_v p \to p\pi^\circ$ and $\gamma_v p \to p\rho^\circ/\omega$ as follows. For $p\pi^\circ$ the missing mass squared plot was integrated between -0.15 and 0.05 GeV^2 and the result corrected for losses due to radiative processes. Since the ρ°/ω region lies in the continuum and misidentified pions from the channel $\gamma_v p \to \pi^+ + n$ give a missing mass peak in the vector meson region we fitted the data to the sum of several distributions representing these various effects. We fitted the missing mass squared distributions between 0.2 and 1.4 GeV^2 to the sum of

(a) background terms $(MM^2 - 4\ m_\pi^2)^{1/2}$, $(MM^2 - 4m_\pi^2)$,

(b) relativistic Breit-Wigner with mass dependent width corrected for resolution and radiative effects for ρ° using $m_\rho = .775$ GeV, $\Gamma_\rho = .124$ GeV ,

(c) fixed width relativistic Breit-Wigner corrected for resolution and radiative effects for the ω with $M_\omega = 0.784$ GeV, $\Gamma_\omega = .012$ GeV ,

(d) an experimentally determined estimate of the contamination by the $\pi^+ n$ channel (~1% of $\pi^+ n$, over 50% of the apparent vector meson peak in the worst case) .

The data were fitted three different ways: ρ only, ω only and ρ and ω together all with terms from (a) and (d) included. The results of these fits are shown in Table I. The Table shows only the sum of the ρ and ω contributions from the final fit since the individual ρ° and ω cross sections and errors are strongly correlated. It is evident that the "ω only" hypothesis is a marginally better description of the data than the other two though "ρ only" cannot be ruled out.

The backward π° cross section shows a rapid W variation comparable to that found in other experiments[4, 5]. The present data do not determine the Q^2 dependence at all well. The W dependence of the vector meson cross section is strong and roughly the same as that of the π°. The Q^2 dependence appears quite weak and the cross section could even be rising slowly with Q^2. Driver et al[6] also observe a comparatively small Q^2 dependence for the backward vector meson cross section, though their data is in a different region of the Q^2, ν plane and so cannot be compared directly with these results.

The difference in the behavior of the cross section as a function of W and Q^2 is clearly shown by the invariant structure function F, for $P_T^2 < 0.02\ GeV^2$, which we have plotted against x' and rapidity in Figs. 5 and 6 respectively. Here it is apparent that the forward proton cross section is changing in the same way as the total cross

section as a function of Q^2, but not as a function of W; the W dependence is much stronger than that of the total cross section. The relative independence of F with respect to Q^2 is confirmed by comparing these results with photoproduction data at a similar W; those of Burfeindt et al.[7] are also shown in Fig. 5. The photoproduction data are at a slightly lower W (2.63 GeV) and were taken at a fixed laboratory angle; this may be responsible for the small systematic shift between the photoproduction and electroproduction data. Our data agree well with those of Adler et al.[8] whose data are at W = 2.63 GeV, Q^2 = 1.2 GeV^2 and fixed laboratory angle. Thus from photoproduction to Q^2 = 2 GeV^2 the structure function for forward protons has not changed significantly. This appears inconsistent with the parton model of Drell, Levy and Yan[9] which predicts an increase in the forward proton cross section with increasing Q^2.

The shape of F for $x' > 0.2$ is close to $(1 - x)^n$, a distribution first suggested by Feynman[10]. Fitting the data to this form yields $n = 1.9 \pm 0.3$ at W = 2.69 GeV, $n = 1.3 \pm 0.1$ at W = 2.16 GeV. This is related[11] to the energy dependence of exclusive channels by $\alpha_o = (1 - n)/2$, where α_o is the intercept of the appropriate Regge trajectory. Our values of n lead to $\alpha_o = -0.45 \pm .15$ and $-0.15 \pm .05$ respectively, quite reasonable values in a region where baryon exchange is required. However, Bjorken and Kogut[11] also argue that the large Q^2 behavior of the form factor is related to the intercept of the dominant exchange in the exclusive electroproduction channel by

$$F_B(Q^2) = (Q^2)^{\alpha_o - 1} ,$$

where F_B is the exchanged baryon's form factor, probably that of the proton (ignoring the fact that the exchanged baryon is a long way off its mass shell). Thus we obtain

$$F_B(Q^2) = 1/(Q^2)^{1.45} \text{ and } 1/(Q^2)^{1.15}$$

which are more slowly varying than the proton form factor, which is more like $1/(Q^2)^{1.7}$. Unfortunately, such form factors as these imply cross sections which vary as $\sim 1/(Q^2)^{2.5}$ whereas the measured forward proton cross section is changing like the total cross section as $\sim 1/Q^2$. Thus although these arguments are not entirely consistent, which may not be surprising since we are at too low a center of mass energy for most theoretical arguments to be valid, the data do show certain interrelations when viewed in this manner.

The strong W dependence of the data is further illustrated in Fig. 7 where we have plotted F as a function of W for different regions of x', all for $P_T^2 < 0.02$ GeV^2. The W dependence clearly decreases as x' decreases; in the forward region, $x' > 0.6$ the data are close to W^{-6}, roughly the power law expected for Reggeized baryon exchange.

IV. TRANSVERSE DISTRIBUTIONS AND INTERFERENCE TERMS

It is difficult to extract a pure P_T^2 dependence from these forward proton data because the cross section is varying rapidly in three variables W, x' and P_T^2 which are correlated in the data by the shape of the acceptance. In addition we would like to treat different regions of ϕ separately so that we can look for the presence of the interference terms. To assist in this process, we took data at several different positions of the hadron spectrometer arm with the electron spectrometer arm fixed to give W = 2.69 GeV, Q^2 = 1.2 GeV^2; these are data points 2, 3, 4 and 5.

We took the values of F and the kinematic averages for the data for the ϕ bins $0^\circ < |\phi| < 45^\circ$, $45^\circ < |\phi| < 90^\circ$, $90^\circ < |\phi| < 135^\circ$, $135^\circ < |\phi| < 180^\circ$ and for x' bins $0.2 < x' < 0.6$ and $0.6 < x' < 1.0$. For each x' bin separately, we fitted the data to the form

$$N \exp(-AP_T^2) \exp(-Bx') W^{-C}$$

to determine the parameters A, B, C and normalization N. This expression is entirely empirical and clearly contains strong assumptions about the nature of the structure function. However, since we fit to regions of data in which x' and W variations are not too large, we expect that these functions are tolerable approximations to reality. We

were able to fit, not only the data from points 2, 3, 4 and 5 which were taken specifically for this purpose, but also that from point 6 where the total amount of data is substantial. Thus we determined the P_T^2 and W behavior for the two x' bins at a $Q^2 = 1.2$ GeV^2 for a W range from ~1.9 GeV to ~3.0 GeV. A number of different fitting procedures were tried, and after observing that, for the most part, the P_T^2 slope was the same for all ϕ bins, we finally fitted all ϕ bins simultaneously (this also clearly gives the best values for the parameters) omitting only the first two P_T^2 bins in each ϕ range (i.e. $P_T^2 < .04$ GeV^2). This was done because there is some slight evidence for interference effects in this region. The values of the fitted parameters are shown in Table II. The results of the fit were used to project the data onto fixed W, x' planes in order to display a pure P_T^2 distribution; the results are shown in Fig. 8. These plots are entirely synthetic in as much as the data points shown depend strongly upon the fitted W and x' functions; the error bars have not been increased to allow for the fitting and projection error. The description of the data is really quite good considering the complexity and strengths of the various kinematic dependences. It is immediately clear that any interference effects must be comparatively small compared to the errors. To verify this, we fitted each P_T^2 bin for which there were measurements in all 4 ϕ regions to the form

$$\sigma_{uL} + \epsilon\sigma_P \cos 2\phi + \sqrt{\epsilon(\epsilon+1)/2}\,\sigma_I \cos\phi \quad \text{where } \sigma_{uL} = \sigma_u + \epsilon\,\sigma_L$$

and determined σ_{uL}, σ_P and σ_I. The results of these fits are shown in Table III. The values of σ_P and σ_I are generally consistent with zero; for the P_T^2 bins where this is not the case, the χ^2 is extremely small, indicating that the problem is over parameterized. The results of a fit to σ_{uL} alone (also in Table III) give good fits to the data. Thus we have no evidence for any significant contribution to the cross section from the interference terms.

To evaluate the P_T^2 slopes for points 1 and 7 it is necessary to make some assumptions about the W dependence of the data in order to perform the projection of the P_T^2 bins to constant W. Unfortunately the data are inadequate to determine the W dependence by themselves (this was in fact tried, but resulted in error bars so large as to make the fit useless). We assume that the W dependence of points 1 and 7 is the same as that for points 2-5; they have the same nominal W but different Q^2. Since the x' distributions appear to be independent of Q^2 at fixed W, it would be a curious coincidence if the W dependence was a function of Q^2. The results of the fits to the P_T^2 distributions of points 1 and 7 averaged over all ϕ, are shown in Table IV.

V. MULTIPLICITY ESTIMATES

We can calculate the average multiplicity of any particle by using the following relation:

$$\langle n \rangle = \int \frac{E}{\sigma_T} \frac{d^3\sigma}{dp^3} \frac{dp^3}{E} = \pi \int F(y, P_T^2)\, dy\, dP_T^2$$

If we further assume that $F(y, P_T^2) = G(y)\,H(P_T^2)$, at least for sufficiently small regions of y, we can calculate <n> by integrating the rapidity distribution shown in Fig. IV and the P_T^2 distributions assuming them to be the measured exponentials right up to the kinematic boundary. Since we only have good data in the forward direction, we compute only the forward (x' >0) multiplicity; the results appear in Table V. They indicate that the forward multiplicity does not change significantly between W = 2.1 and W = 2.7 GeV. Although the longitudinal cross sections for $P_T^2 < 0.02$ GeV^2 are very different, the P_T^2 slope changes in such a way as to maintain constant multiplicity.

However, it should be noted that the bulk of the contribution to the multiplicity comes from data near x' = 0 where the W dependence is considerably weaker then near x' = 1. The multiplicity at point 1, $Q^2 = 0.6$ GeV^2, is some 2-3 standard deviations below that at the other data points and may be indicative of a gradual increase of forward proton multiplicity with Q^2. This of course supports the predictions of the parton model of ref. 7.

VI. CONCLUSIONS

The data from this experiment show that the structure function for protons in the forward direction is independent of Q^2 from photoproduction up to $Q^2 = 2\ GeV^2$. The structure function shows a strong W dependence which at large x' is typical of that expected from Reggeized baryon exchange. The shape of the structure function and the power law behavior in W and Q^2 show some interrelation though not entirely consistently. Estimates of the forward proton multiplicity indicate that it changes little with W and possibly rises slowly with Q^2. The angular distributions show no evidence for the presence of interference terms in the cross section.

VII. ACKNOWLEDGEMENTS

We wish to acknowledge the support of Professor Boyce McDaniel, the staff of the Wilson Synchrotron Laboratory and the staff of the Harvard Cyclotron Laboratory.

TABLE I

Backward π^0 and Vector Meson Cross Sections

Cross Sections for π^0 Production

W (GeV)	Q^2 (GeV)	ϵ	u' interval (GeV^2)	Cross Section ($\mu b/sr$)
2.60	0.60	0.88	$0<u'<.02$	0.0225 ± 0.0080
2.61	1.24	0.87	$0<u'<.02$	0.0225 ± 0.0080
2.60	2.00	0.83	$0<u'<.02$	no events (1 event = .0012 $\mu b/sr$)
2.10	1.21	0.95	$0<u'<.02$	0.0548 ± 0.0118

Cross Sections for Vector Meson Production

(a) ρ only

W (GeV)	Q^2 (GeV^2)	ϵ	u' interval (GeV^2)	Cross Section ($\mu b/sr$)	P (χ^2)
2.60	0.64	0.88	$0<u'<.04$	$0.050^{+}_{-} 0.032$	0.020
2.60	1.23	0.87	$0<u'<.04$	$0.048^{+}_{-} 0.027$	0.028
2.61	2.06	0.83	$0<u'<.04$	$0.071^{+}_{-} 0.016$	0.754
2.10	1.21	0.95	$0<u'<.02$	$0.247^{+}_{-} 0.088$	0.002
(b) ω only					
2.60	0.64	0.88	$0<u'<.04$	$0.031^{+}_{+} 0.014$	0.060
2.60	1.23	0.87	$0<u'<.04$	$0.025^{+}_{+} 0.012$	0.047
2.61	2.06	0.83	$0<u'<.04$	$0.032^{+}_{+} 0.009$	0.523
2.10	1.21	0.95	$0<u'<.02$	$0.146^{+}_{-} 0.027$	0.220
(c) ρ and ω together					
2.60	0.64	0.88	$0<u'<.04$	$0.019^{+}_{+} 0.038$	0.042
2.60	1.23	0.87	$0<u'<.04$	$0.028^{+}_{+} 0.035$	0.030
2.61	2.06	0.83	$0<u'<.04$	$0.065^{+}_{+} 0.020$	0.684
2.10	1.21	0.95	$0<u'<.02$	$0.119^{+}_{-} 0.073$	0.160

TABLE II

Results of Fitting the P_T^2 Distributions at $Q^2 = 1.2\ GeV^2$

$0.2 < x' < 0.6$

<W> GeV	P_T^2 slope $(GeV)^{-2}$	x' slope	Inverse power of W
2.15	3.78 ± 0.64	3.27 ± 0.27	3.99 ± 0.23
2.70	3.12 ± 0.34	4.12 ± 0.35	3.30 ± 0.49

$0.6 < x' < 1.0$

2.15	2.97 ± 0.63	5.00 ± 0.39	5.81 ± 0.24
2.70	2.27 ± 0.50	4.93 ± 0.71	4.99 ± 0.86

TABLE III

Results of Fitting P_T^2 Bins to Determine the Interference Terms in the Cross Section at $Q^2 = 1.2\ GeV^2$

P_T^2 (GeV^2)	$\sigma_u + \epsilon\sigma_L$ (GeV^{-2})	σ_P (GeV^2)	σ_I (GeV^{-2})	$P(\chi^2)$	for $\sigma_P = \sigma_I = 0$: $\sigma_u + \epsilon\sigma_L$ (GeV^{-2})	$P(\chi^2)$
W = 2.15 GeV, x' = 0.4						
0.01	$0.2913 \pm .0003$	$-.021 \pm .001$	$-.0129 \pm .0004$	.96	$0.287 \pm .009$	.18
0.03	$0.277 \pm .043$	$.071 \pm .064$	$.028 \pm .041$	.002	$0.303 \pm .029$	.000
0.05	$0.240 \pm .035$	$.065 \pm .048$	$.025 \pm .018$	.19	$0.273 \pm .020$	.032
W = 2.70 GeV x' = 0.4						
0.01	$0.133 \pm .003$	$.005 \pm .006$	$.0028 \pm .0056$	.42	$0.133 \pm .003$	.53
0.03	$0.119 \pm .004$	$.015 \pm .008$	$-.007 \pm .0057$	.63	$0.123 \pm .004$	.30
0.05	$0.116 \pm .009$	$-.004 \pm .014$	$-.014 \pm .0071$	.42	$0.118 \pm .006$	.26
0.07	$0.100 \pm .016$	$.034 \pm .023$	$-.010 \pm .0113$	.38	$0.123 \pm .008$	.29
0.09	$0.134 \pm .006$	$-.047 \pm .009$	$.003 \pm .0014$	.92	$0.100 \pm .002$	.95
W = 2.15 GeV x' = 0.8						
0.01	$0.0617 \pm .0002$	$.0004 \pm .0004$	$.007 \pm .0003$	.93	$0.0626 \pm .0029$	.23
0.03	$0.058 \pm .002$	$-.003 \pm .004$	$.004 \pm .003$	.49	$0.0584 \pm .0021$	.63
0.05	$0.053 \pm .005$	$-.005 \pm .008$	$.0001 \pm .006$	.17	$0.0507 \pm .0028$	.44
0.07	$0.0461 \pm .0003$	$-.0010 \pm .0005$	$.004 \pm .0003$	.94	$0.0462 \pm .0015$	.89
0.09	$0.45 \pm .015$	$-.005 \pm .025$	$.003 \pm .011$	.03	$0.0434 \pm .0050$	.17
W = 2.70 GeV x' = 0.8						
0.01	$0.0140 \pm .0014$	$.0004 \pm .0020$	$-.004 \pm .003$	.005	$0.0134 \pm .0015$	.001
0.03	$0.0174 \pm .0010$	$-.003 \pm .002$	$.001 \pm .001$	.41	$0.0168 \pm .0011$	.23
0.05	$0.0158 \pm .0016$	$.005 \pm .003$	$.001 \pm .003$	.21	$0.0166 \pm .0017$	.07
0.07	$0.0155 \pm .0018$	$-.003 \pm .003$	$.000 \pm .001$	.18	$0.0144 \pm .0013$	.27
0.09	$0.0138 \pm .0011$	$.001 \pm .002$	$-.001 \pm .001$	.77	$0.0143 \pm .00097$	.77

TABLE IV

Results of Fitting P_T^2 Distributions

After Correction to Fixed W and x'

Q^2 (GeV^2)	at W = 2.7 GeV x' region	P_T^2 slope (GeV^{-2})
0.6	$0.2 < x' < 0.6$	7.3 ± 3.3
	$0.6 < x' < 1.0$	3.3 ± 1.9
2.0	$0.2 < x' < 0.6$	4.2 ± 1.6
	$0.6 < x' < 1.0$	1.6 ± 1.2

TABLE V

Estimates of Forward Proton Multiplicity for $x' > 0$

W (GeV)	Q^2 (GeV^2)	Average forward proton multiplicity
2.70	0.6	0.078 ± 0.031
2.70	1.2	0.17 ± 0.02
2.70	2.0	0.15 ± 0.05
2.15	1.2	0.20 ± 0.03

FIGURE CAPTIONS

1. The Cornell and Harvard spectrometers.
2. Typical time-of-flight spectrum for hadrons not detected by the Cerenkov counter.
3. The Q^2, ν plane with the data points for this experiment indicated on it.
4. Missing mass squared distribution for protons with $u' < 0.02$ GeV^2 at
   (a) data point 1, W = 2.62 GeV $Q^2 = 0.64$ GeV^2, $\epsilon = 0.877$
   (b) data point 3, W = 2.62 GeV, $Q^2 = 1.22$ GeV^2, $\epsilon = 0.869$
   (c) data point 7, W = 2.62 GeV, $Q^2 = 2.04$ GeV^2, $\epsilon = 0.828$
   and (d) data point 6, W = 2.08 GeV, $Q^2 = 1.21$ GeV^2, $\epsilon = 0.946$
5. The structure function for protons with $P_T^2 < 0.02$ GeV^2 plotted against x' for (a) data points 3 and 6 together with photoproduction data from reference 7 (the points with the curve through them) and (b) data points 1 and 7 together with the curve for photoproduction as in (a).
6. The structure function for protons with $P_T^2 < 0.02$ GeV^2 plotted against rapidity for the data from
   (a) point 1, W = 2.69 GeV $Q^2 = 0.62$ GeV^2, $\epsilon = 0.86$
   (b) point 3, W = 2.68 GeV $Q^2 = 1.18$ GeV^2, $\epsilon = 0.85$
   (c) point 7, W = 2.70 GeV, $Q^2 = 1.97$ GeV^2, $\epsilon = 0.81$
   and (d) point 6, W = 2.16 GeV, $Q^2 = 1.18$ GeV^2, $\epsilon = 0.94$
7. The structure function for protons with $P_T^2 < 0.02$ GeV^2 plotted against W for
   (a) $-0.6 < x' < -0.2$
   (b) $-0.2 < x' < 0.2$
   (c) $0.2 < x' < 0.6$
   (d) $0.6 < x' < 1.0$
8. The structure function for protons plotted against P_T^2 for four ϕ bins for two x' regions at data points 2, 3, 4, 5 and at data point 6.

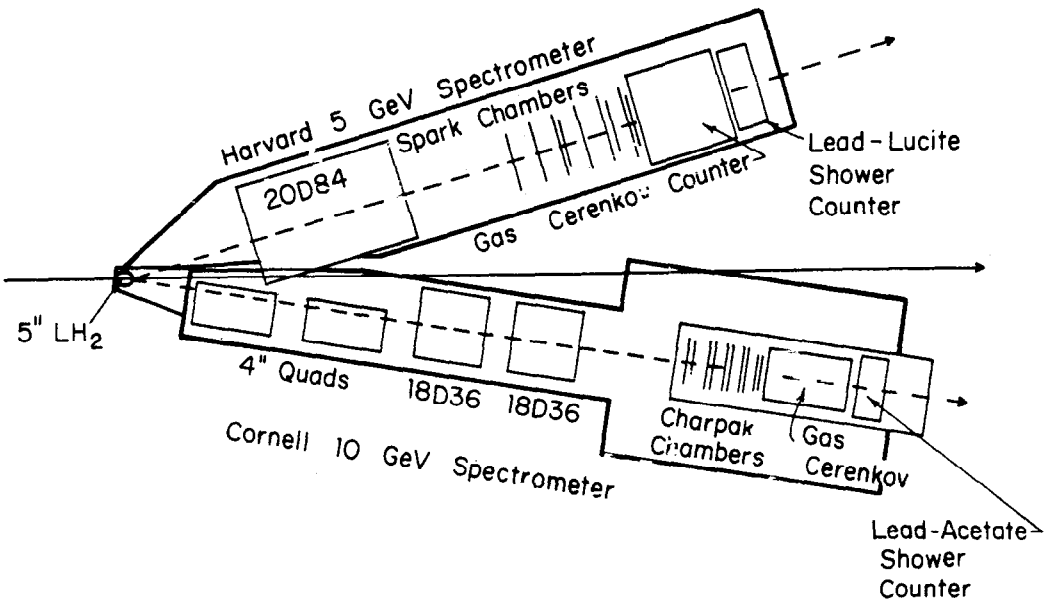

Figure 1

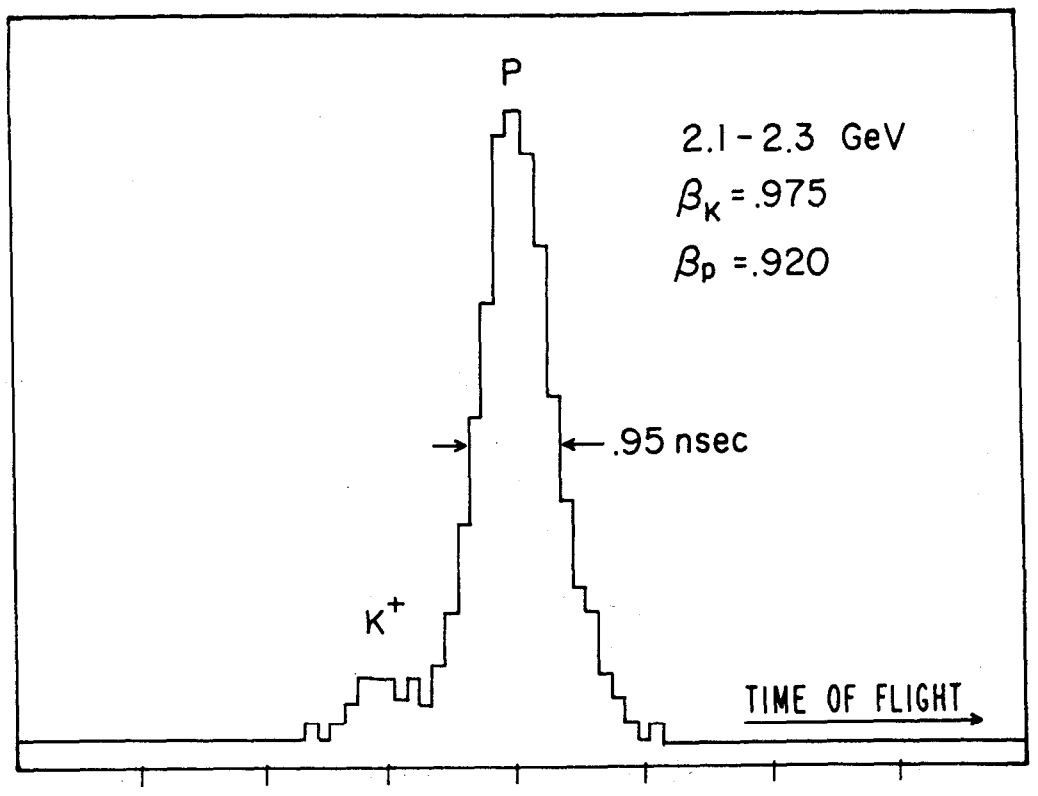

Figure 2

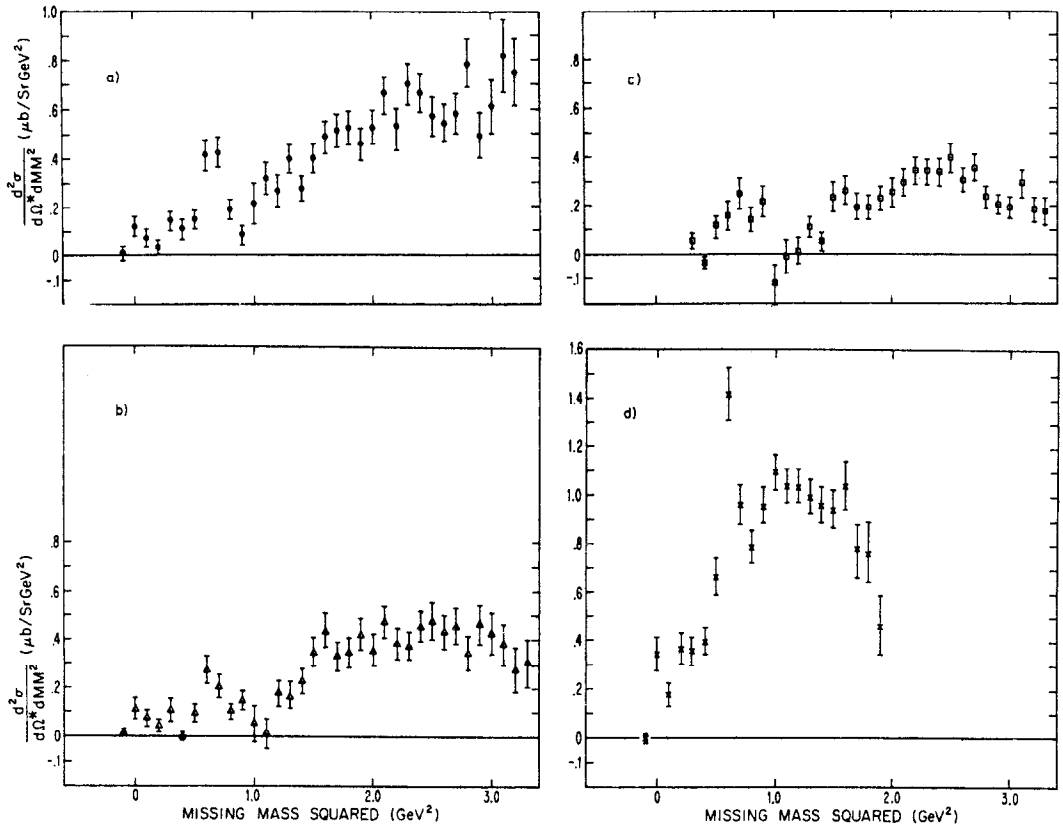

Figure 4

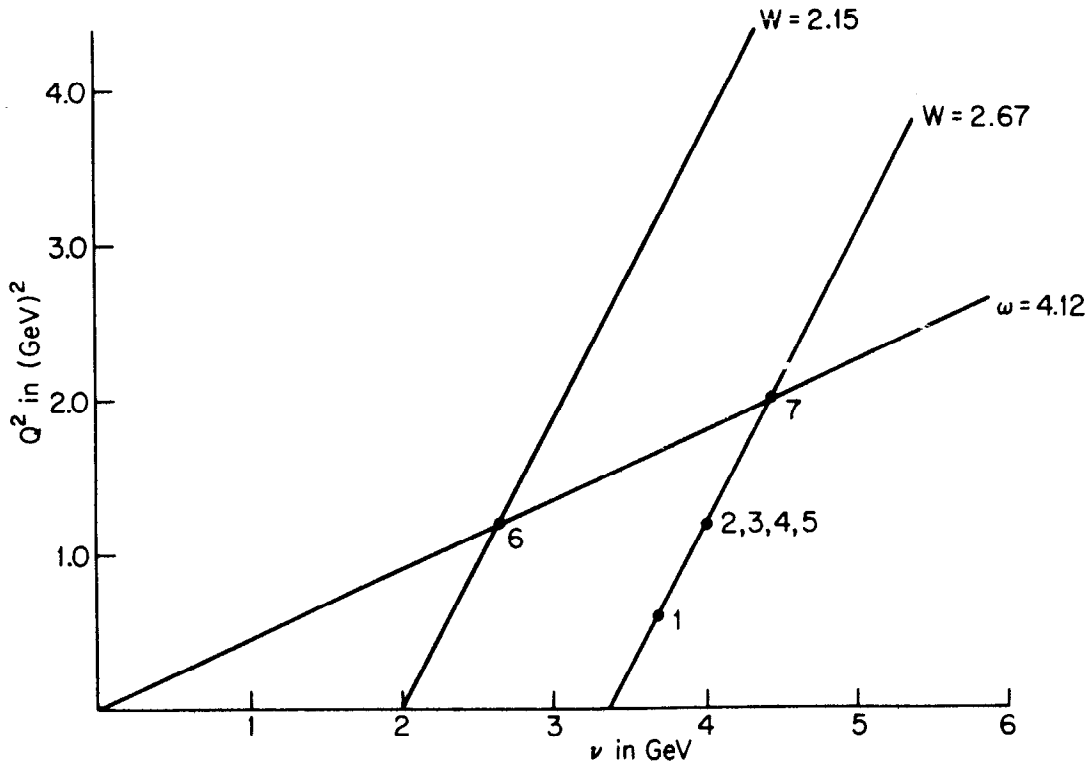

Figure 3

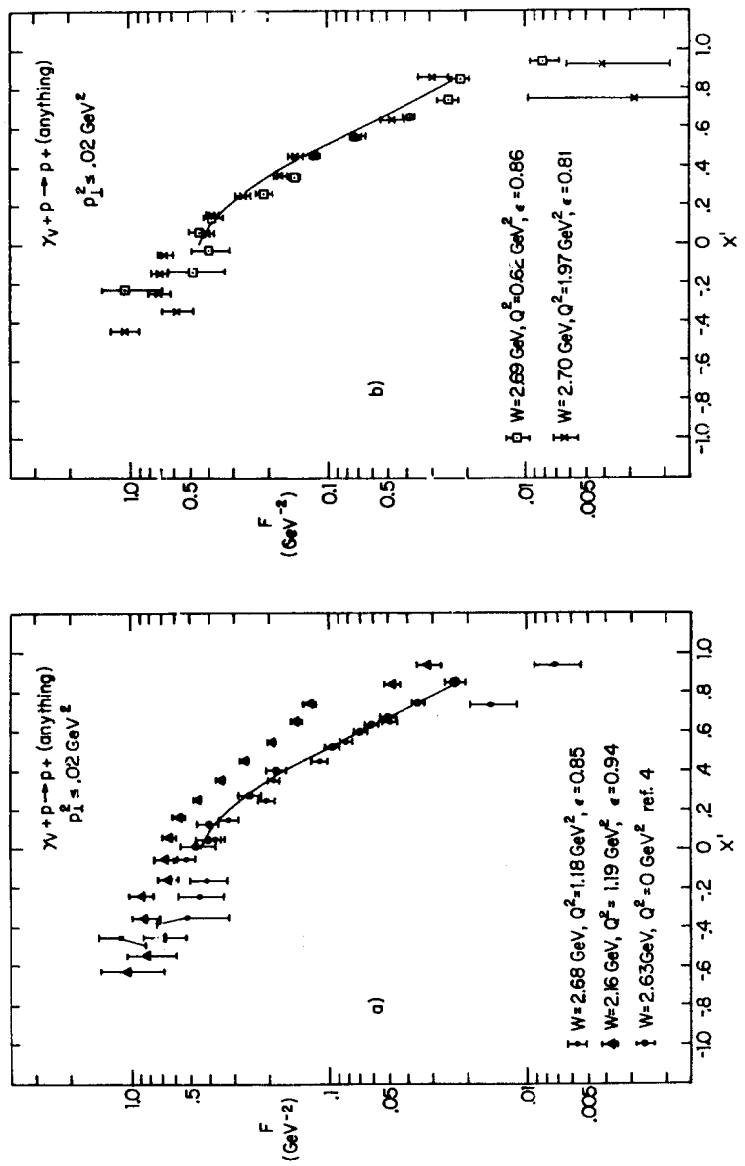

Figure 5

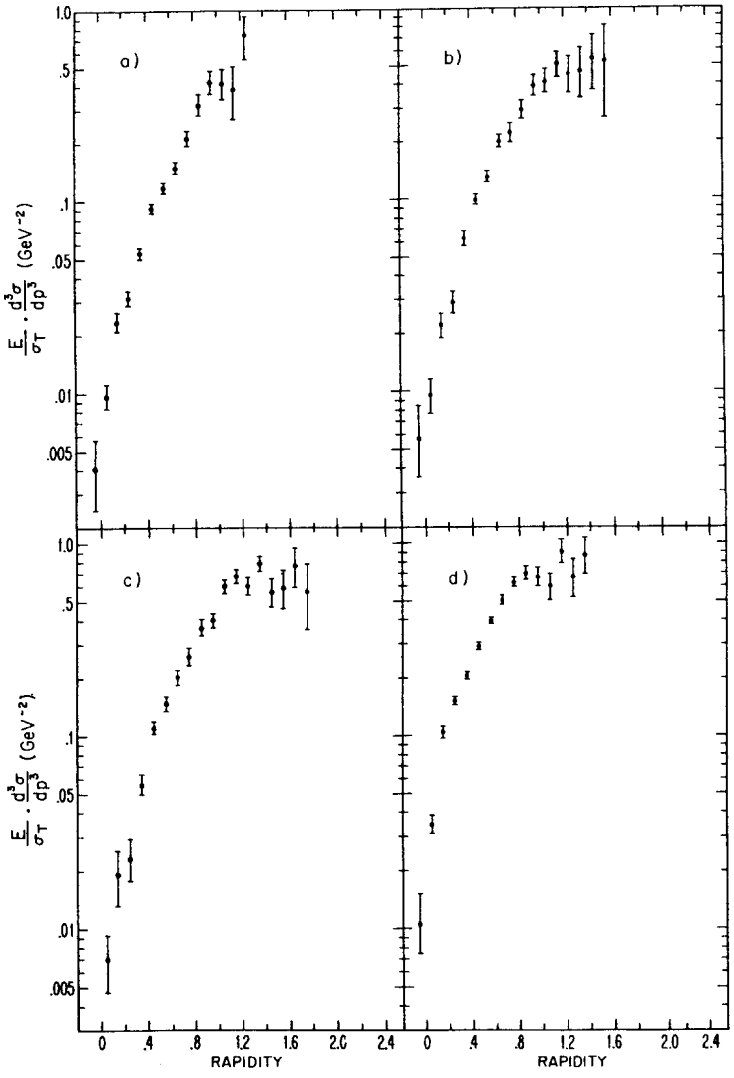

Figure 6

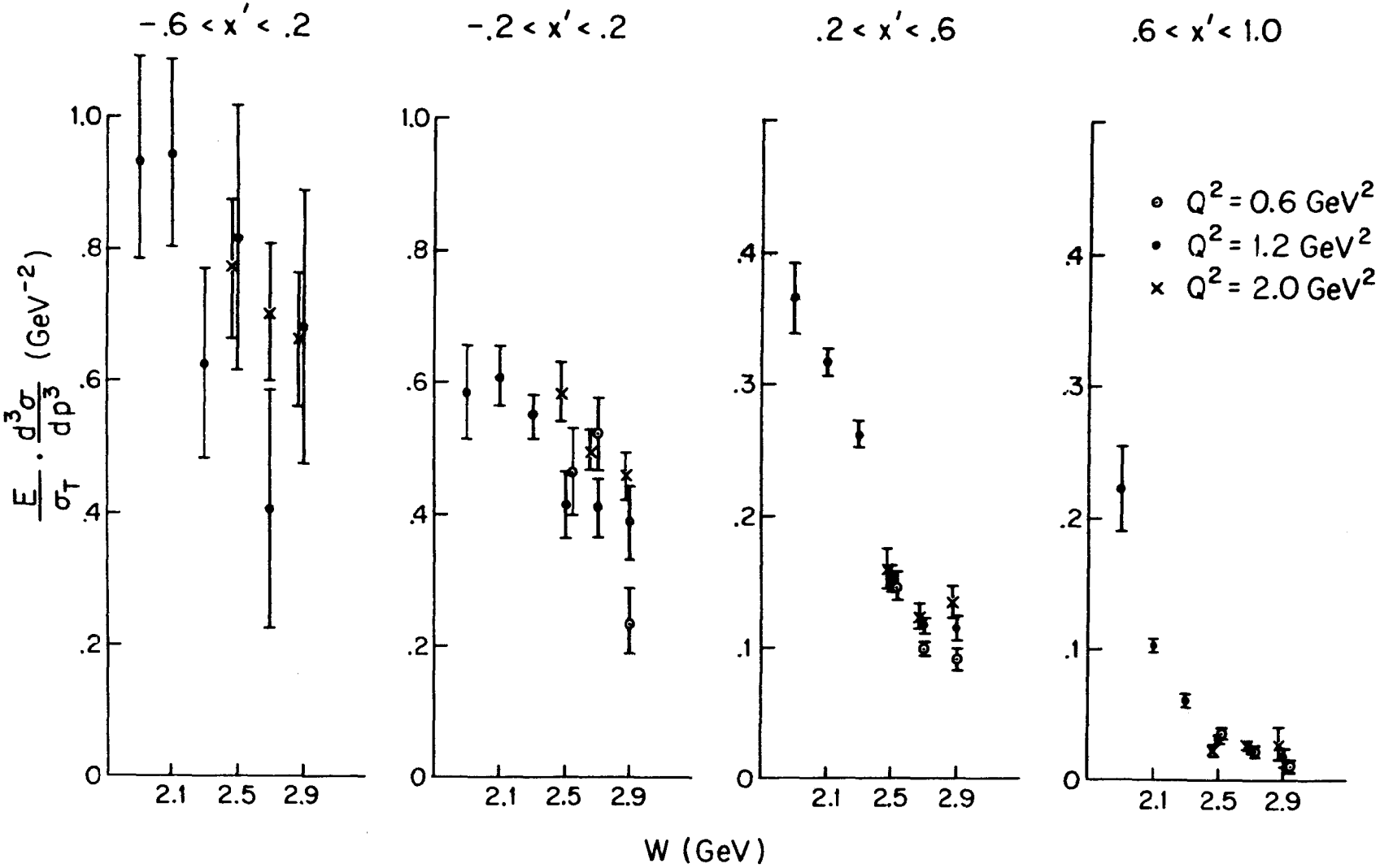
−.6 < x′ < .2
−.2 < x′ < .2
.2 < x′ < .6
.6 < x′ < 1.0
$\frac{E}{\sigma_T} \cdot \frac{d^3\sigma}{dp^3}$ (GeV^{-2})
Q^2 = 0.6 GeV^2
Q^2 = 1.2 GeV^2
Q^2 = 2.0 GeV^2
W (GeV)

Figure 7

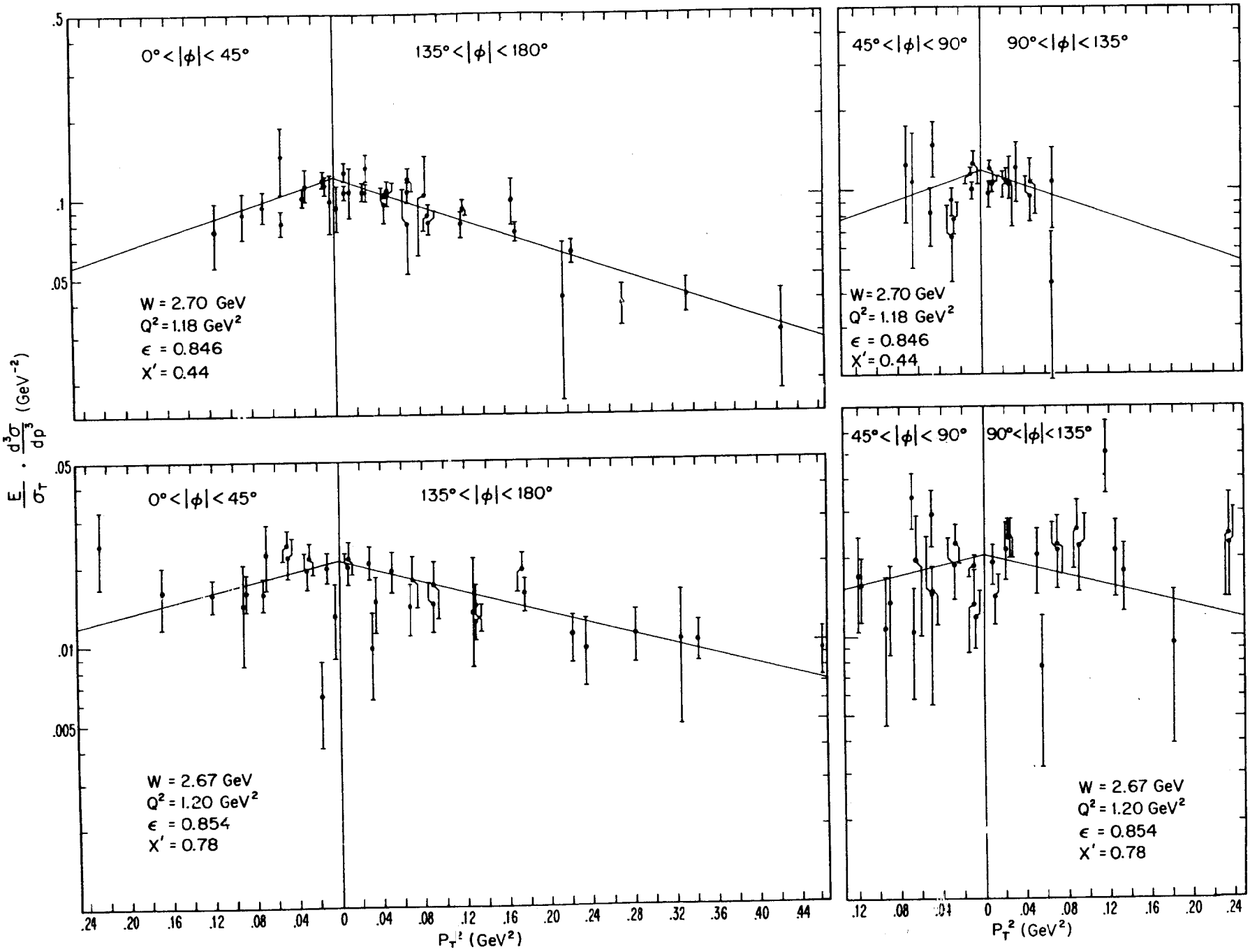
0° < |φ| < 45°
135° < |φ| < 180°
45° < |φ| < 90°
90° < |φ| < 135°
W = 2.70 GeV
Q² = 1.18 GeV²
ε = 0.846
X' = 0.44
W = 2.67 GeV
Q² = 1.20 GeV²
ε = 0.854
X' = 0.78
E/σT · d³σ/dp³ (GeV⁻²)
PT² (GeV²)

Figure 8a

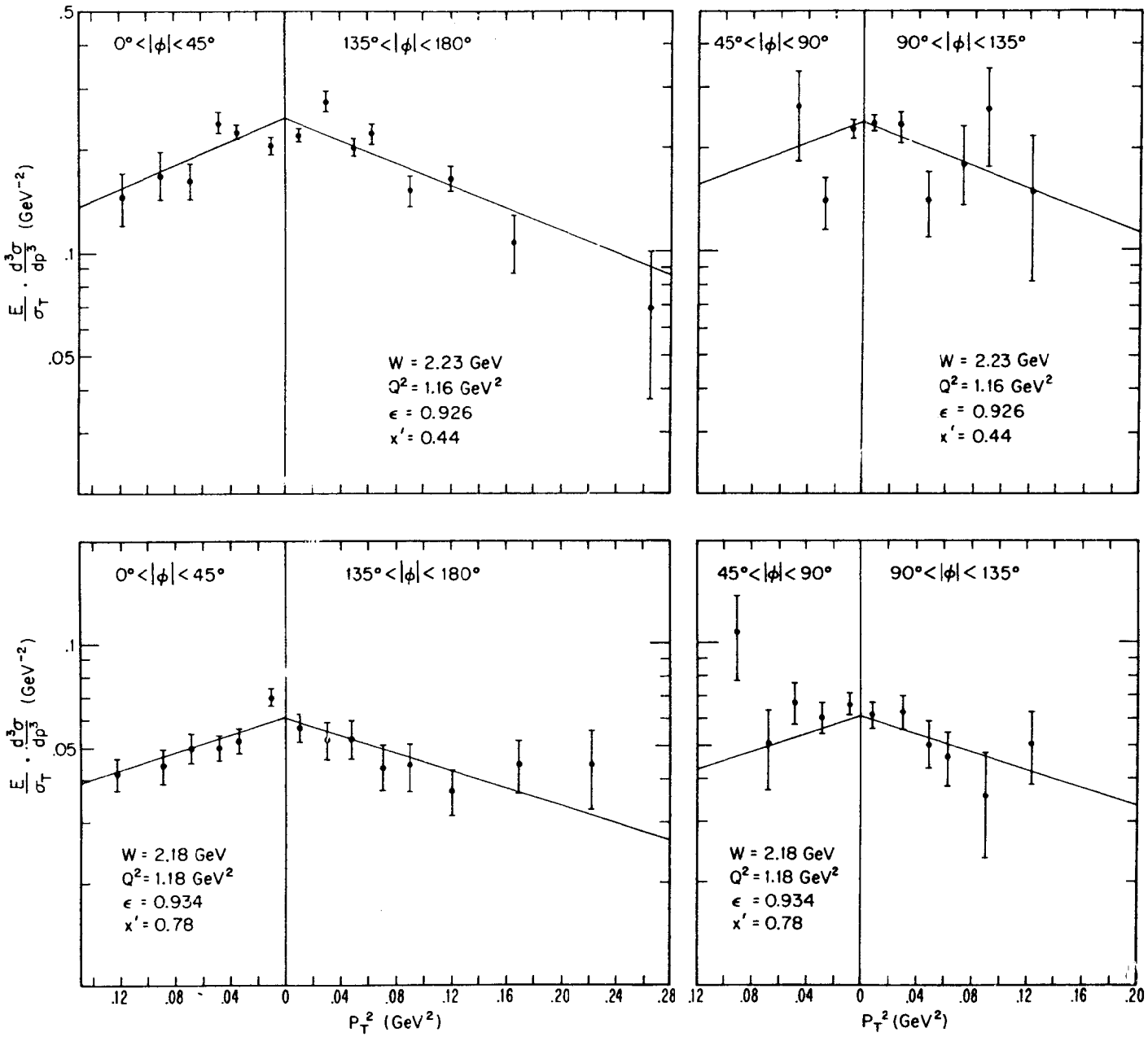
0°<|φ|<45°
135°<|φ|<180°
45°<|φ|<90°
90°<|φ|<135°
W = 2.23 GeV
Q² = 1.16 GeV²
ε = 0.926
x' = 0.44
W = 2.18 GeV
Q² = 1.18 GeV²
ε = 0.934
x' = 0.78
E/σT · d³σ/dp³ (GeV⁻²)
PT² (GeV²)

Figure 8b

REFERENCES

1. K. Berkelman in Proceedings of the Sixteenth International Conference on High Energy Physics, National Accelerator Laboratory, Batavia, Ill., 1972, edited by J. D. Jackson and A. Roberts (NAL, Batavia, Ill., 1973); L. N. Hand, Phys. Rev. 129, 1834 (1964).
2. R. P. Feynman, Phys. Rev. Lett. 23, 1415 (1969).
3. SLAC Group A, Private communication.
4. C. N. Brown, C. R. Canizares, W. E. Cooper, A. M. Eisner, G. J. Feldman, C. A. Lichtenstein, L. Litt, W. Lockeretz, V. B. Montana and F. M. Pipkin Phys. Rev. Lett 27, 1611 (1971).
5. C. Driver, K. Heinloth, K. Höhne, G. Hofmann, P. Karow, G. Pfeiffer, D. Schmidt, G. Specht and J. Rathje, Nucl. Phys. B33, 84, (1971).
6. C. Driver, K. Heinloth, K. Höhne, G. Hofmann, P. Karow, G. Pfeiffer, D. Schmidt, G. Specht and J. Rathje, Nucl. Phys. B39, 106 (1972).
7. H. Burfeindt, G. Buschhorn, H. Genzel, P. Heide, U. Kötz, K. H. Mess, P. Schmüser, B. Jonne, G. Vogeland, B. H. Wiik, Phys. Lett. 43B, 345 (1973).
8. J. C. Alder, F. W. Brasse, E. Chazelas, W. Fehrenbach, W. Flauger, K. H. Frank, E. Ganssauge, J. Gayler, V. Korhel, W. Krechlok, J. May, M. Merwite, and P. D. Zimmerman, Nucl. Phys. B46, 415 (1972).
9. S. D. Drell, D. J. Levy and T. M. Yan, Phys. Rev. Lett. 22 , 744 (1969) and 24 , 855, (1970).
10. R. P. Feynman, invited paper at the Third Topical Conference on High Energy Collisions of Hadrons, Stony Brook, New York, Sept. 1969.
11. J. D. Bjorken and J. Kogut, Phys, Rev. D8, 1341 (1973).

ELECTROPRODUCTION OF K^+ MESONS IN THE FORWARD DIRECTION*

C. J. Bebek, C. N. Brown, M. Herzlinger, N. Hicks, S. Holmes, C. A. Lichtenstein, F. M. Pipkin and L. K. Sisterson

Cyclotron Laboratory

Harvard University

Cambridge, Massachusetts 02138

D. Andrews,+ K. Berkelman, D. G. Cassel and D. L. Hartill

Laboratory of Nuclear Studies

Cornell University

Ithaca, New York 14850

ABSTRACT

We present data taken at the Wilson Synchrotron Laboratory on electroproduction off protons in which a K^+ meson moving in approximately the same direction as the virtual photon is detected. Measurements were made of data points with nominal (Q^2, W) values of (0.6, 2.67), (1.2, 2.67), (2.0, 2.67) and (1.2, 2.15) in (GeV^2, GeV). The virtual photoproduction cross section for K^+ + Missing Mass is studied as a function of missing mass, Feynman scaling variables, Q^2 and W. The data show that the $K^+\Sigma^0$ cross section falls more rapidly than the $K^+\Lambda^0$ cross section as Q^2 increases. There is evidence for hyperon resonance production. The variation with Q^2 of the K^+/π^+ ratio is determined.

*Research supported in part by the U. S. Atomic Energy Commission and in part by the National Science Foundation.

+Present address: Physics Department, University of Rochester, Rochester, New York 14627.

I. INTRODUCTION

The determination that the large cross section for deep inelastic electron-nucleon scattering could be expressed as a function of a single variable, $\omega = 2M\nu/Q^2$, has aroused considerable theoretical and experimental interest in the details of the processes which may account for this. Thus a number of experiments have been done or are being done to examine the details of the final hadronic state. In general, there are only qualitative theoretical predictions concerning the nature and behavior of the final state hadrons and these are expected to be valid at higher energies than are currently available to the experimenter. This paper reports an experiment in which we detect a kaon moving in approximately the same direction as the virtual photon. Center of mass energies, W, are just above the resonance region in the 2-3 GeV range.

In what is now standard procedure,[1] electroproduction is treated as photoproduction by a virtual photon whose mass squared, $-Q^2$, energy, ν, direction, and polarization, ϵ, are tagged by the scattered electron. The cross section for the reaction,

$$e^- + p \rightarrow e^- + K^+ + \text{missing mass} \qquad (1)$$

is written,

$$\frac{d\sigma}{dE\,d\Omega_e\,d\Omega_k^*\,dMM^2} = \Gamma \frac{d\sigma}{d\Omega_k^*\,dMM^2}$$

where Γ, the 'flux' of virtual photons, is given by

$$\Gamma = \frac{\alpha}{2\pi}\frac{E'}{E}\frac{W^2 - M^2}{2MQ^2}\frac{1}{1-\epsilon}$$

The hadronic cross section is a function of the virtual photon variables Q^2, W (or ν), and ϵ, and the variables describing the produced hadron in the virtual photon-proton center of mass system, θ^*, ϕ, and MM^2. An alternative to θ^* is the variable $t' = (t - t_{min})$. t' may be written in terms of the momenta of the virtual photon and the kaon, and the angle θ^* as,

$$t' = -2p_k p_\gamma (1-\cos\theta^*) .$$

The virtual photon-proton cross section may also be written in terms of the Feynman scaling variables[2] x and P_T^2, where P_T is the momentum of the hadron transverse to the virtual photon direction and x is defined in terms of the center of mass momentum by,

$$x = P_L^*/P^*_{max} .$$

Here P_L^* is the component of momentum along the virtual photon direction and P^*_{max} is the maximum momentum for the hadron.

For experiments at the comparatively low energies which are presently possible x has the disadvantage that for x near 1 the range in P_T^2 is a function of x and the total center of mass energy. To avoid this dependence, we have chosen instead to use x' where

$$x' = P_L^*/\left[(P^*_{max})^2 - P_T^2\right]^{1/2} .$$

For $P_T \ll P^*_{max}$, x and x' are identical.

We have analyzed the data in terms of the differential cross section in missing mass squared and the invariant structure function,

$$F = \frac{E}{\sigma_{Tot}} \frac{d^3\sigma}{dp^3} = \frac{1}{\sigma_{Tot}} \frac{1}{\pi} \frac{E^*}{\left[P^{*2}_{max} - P_T^2\right]^{1/2}} \frac{d\sigma}{dx'\, dP_T^2}$$

where σ_{Tot} is the total virtual photoproduction cross section for the total energy W and Q^2 of the reaction. The value of σ_{Tot} was taken from a fit to the SLAC-MIT measurements of νW_2 with the assumption that $\sigma_S/\sigma_T = 0.18$[3]. Also, the differential cross section $\frac{d\sigma}{d\Omega^*}$ is given for the channels,

$$e^- + p \rightarrow e^- + K^+ + \Lambda ,$$
$$e^- + p \rightarrow e^- + K^+ + \Sigma^0 ,$$
$$e^- + p \rightarrow e^- + K^+ + \Lambda(1520) .$$

II. EXPERIMENTAL DETAILS

The two spectrometers shown in Fig. 1 were used to detect the scattered electron and the electroproduced hadron. The combination of a Cerenkov counter and a lead acetate shower counter identified the electrons. Pions were identified by a threshold gas Cerenkov counter when their momentum was greater than 1.8 GeV/c and by their time-of-flight when their momentum was less than that. Neither protons nor kaons gave a signal in the Cerenkov counter, so they had to be separated from each other entirely by their time-of-flight. Fig. 2 shows a typical time-of-flight spectrum for particles not detected by the Cerenkov counter; the peaks for K^+ and proton are clearly seen. It is necessary to correct for the contamination of one peak by the tail of the other and for the loss of wanted events when we cut out the unwanted peak. This was done with timing cuts which varied in position according to the laboratory momentum of the particle in order to achieve optimum separation of the protons from the kaons.

The spectrometers were set up to take data at the points in the (Q^2, ν) plane shown in Fig. 3. Points 1, 3 and 7 comprise a Q^2 scan at fixed W; points 6 and 7 lie on the same ω line and thus can be used to test scaling; points 3 and 6 give a W scan at fixed Q^2; and points 2, 3, 4 and 5 comprise an angular scan with the hadron arm which extends the aperture in P_T. The acceptance of the apparatus is such that the W distribution is approximately 0.6 GeV wide and Q^2 about 0.3 GeV^2 wide at each data point.

The data have been corrected for random coincidences (≈ 5%), for counter and spark chamber dead time (≈ 2%), for absorption in the counters (≈ 2%), for target wall background (≈ 5%), and for decay in flight (20% to 100%). The errors quoted are statistical; there is an additional overall normalization uncertainty which is estimated to be 10%.

III. MISSING MASS SQUARED DISTRIBUTIONS

The data from points 1–4, 6 and 7 were analyzed with points 2, 3, and 4 combined

as one point. In this manner points 1, 3, 4, and 7 form a Q^2 scan at a W of approximately 2.65 GeV with the scan covering $0.6 \leq Q^2 \leq 2.0$. Points 2-4 and 6 both have a Q^2 value of about 1.2 GeV^2 while point 6 has a W of approximately 2.15 GeV.

The missing mass squared distributions for the K^+ are shown in Figs. 4. Figs. 4 (a), (b), (c) show the Q^2 scan at $W \approx 2.15$ GeV; Fig. 4 (d) shows the data for $W \approx 2.15$ GeV.

The peak around .8 GeV^2 is due to elastic pions which failed to fire the Cerenkov counter and passed through the timing cuts. As will be described later, the size of this peak was used to obtain an estimate of the pion contamination in the Λ-Σ° region. The Λ peak is very prominent on all the plots as is the peak at 2.3 GeV^2 corresponding to the Λ (1520). The Σ° is clearly present at point 1 and gradually disappears until it is absent at point 7. The hump at 1.9 GeV^2 is probably due to the Σ (1385) and/or the Λ (1405). It is seen from the plots that the cross sections fall with increasing Q^2 and W, although no quantitative statement can be made as to the rate of decrease other than that it seems to be slower than $1/Q^2$.

Fig. 5 shows the invariant structure function for $P_T^2 < .05$ GeV^2 plotted against x' for four values of W and Q^2. The data do not display a strong Q^2 dependence, and are inconclusive as to the extent of any W dependence. The values of the structure function are about 15% of those for the π^+ reaction[6] and the curves are similar in shape. The structure function does not appear to fall off nearly as sharply as the proton structure function[6] in the range $0.4 < x' < 1.0$.

Fig. 6 shows the ratio of the invariant structure functions for the K^+ and the π^+ at four values of W and Q^2. It is important to remember that the π^+ data was cut on $P_T^2 < .02$ GeV^2 while for the K^+ the cut was $P_T^2 < .05$ GeV^2. An interesting feature of the plot is that it shows the ratio of K^+ to π^+ to be independent of W and Q^2 for $x' < .6$. The ratio starts to increase for $x' > .7$ in the region of $Q^2 = 2$. This is due primarily to the decrease in the pion structure function in this region.

IV. TWO BODY CHANNELS

The two body channels analyzed were

$$\gamma^* + p \rightarrow K^+ + \Lambda ,$$

$$\gamma^* + p \rightarrow K^+ + \Sigma^\circ ,$$

$$\gamma^* + p \rightarrow K^+ + \Lambda(1520) .$$

The first two of these will be discussed together.

The Λ and Σ° cross sections were obtained through a fit of the missing mass squared distributions to a curve constructed by folding a Gaussian resolution function with a radiative tail.[4,5] The missing mass squared resolution for the apparatus was determined from a study of the reaction,

$$e^- + p \rightarrow e^- + \pi^+ + n . \qquad (2)$$

The rms width of this peak was found at each data point and this value was used to define the rms width of the Λ and Σ° peaks. The rms ranged from .030 GeV^2 to .043 GeV^2 over the data points. Using the appropriate curve, $\frac{d\sigma}{d\Omega^* dMM^2}$ was fit over the range $1.075\ GeV^2 < MM^2 < 1.575\ GeV^2$ (1.575 GeV^2 is the nominal beginning of the continuum). The cross section was assumed to be the sum of three contributions - one from the Λ, one from the Σ° and one from the feedthrough pions. The pion contribution was determined by dividing the peak for the $\pi^+ n$ reaction as seen on the missing mass squared distribution for the kaons by the peak obtained in the study of the reaction (2) and using this number to scale down the continuum region of the π^+ reaction. The background was assumed flat over the range $1.075\ GeV^2 < MM^2 < 1.575\ GeV^2$ and varied with the data point. A three parameter fit was then made to the data. The first parameter was a scale factor to fit the given curve to the Λ, the second was a similar factor for the Σ°, and the third was the location

of these curves on the missing mass squared scale. In the fit the distance between the Λ and Σ° missing masses squared was fixed at its known value. Fig. 7 shows a sample fit for the data from points 2-4, $\theta^* < 15^{\circ}$, with the three components and their sum labeled.

Table I summarizes the data obtained from the fits for $0 < \theta^* < 15^{\circ}$ and $0 < \theta^* < 30^{\circ}$ including the Σ°/Λ ratio. Data taken at the CEA[7] contains one point in common with our data -- that at point 6 for $\theta^* < 15^{\circ}$ where they obtained $\frac{d\sigma}{d\Omega^*}(\Lambda) = 0.277 \pm .045$ μb/sr and $\Sigma^{\circ}/\Lambda < .15$ in good agreement with the data presented here. The most striking feature of the data is the very low Σ°/Λ ratio which always remains less than .25 and is consistent with zero at a Q^2 of 2.0. In photoproduction[8] Σ°/Λ ratios are typically between .5 and 1 and so we may conclude that the Σ° cross section decreases much more rapidly with Q^2 than does the Λ cross section.

Fig. 8 shows the Λ cross section for $\theta^* < 15^{\circ}$, $W \approx 2.65$. Note that the cross section falls very slowly with Q^2, that is the fall is less than that for a $1/Q^2$ dependence. This is to be contrasted with the $\pi^+ n$ cross section which falls as $1/Q^4$ in this region. Fig. 9 is an identical plot for the Σ° cross section.

We have also investigated the t' dependence of the cross sections for the Λ and Σ° channels by fitting the $\frac{d\sigma}{d\Omega^* \, dMM^2}$ cross section for different regions of t' ; the results are summarized in Table II. The data for the Λ channel are also presented in Fig. 10 along with a least squares fit to the form

$$Ae^{Bt'} .$$

Table III summarizes the slopes obtained along with the chi square and degrees-of-freedom for each fit. The values of the slope are all around 7 $(GeV)^{-2}$. Similar fits for the $\pi^+ n$ channel[6] at points 6 and 7 give a slope of 7.2 $(GeV)^{-2}$.

The cross section for the $\Lambda(1520)$ was determined using a procedure similar to that used on the Λ and Σ°. The missing mass squared distribution was fitted to a Gaussian folded with the radiative correction for the resonance along with a linear background. The results of the fits are listed in Table IV.

V. CONCLUSIONS

The data for K^+ electroproduction show that the $K^+\Lambda$ cross section falls more slowly with Q^2 than the $K^+\Sigma^{\circ}$ cross section. The $K^+\Sigma^{\circ}$ cross section is essentially zero for $Q^2 = 2.0$ GeV^2 at a W of 2.65 GeV. The missing mass squared distributions provide considerable evidence for production of the $\Sigma(1385)$ and/or $\Lambda(1405)$, and $\Lambda(1520)$ resonances.

The rapid disappearance of the Σ° compared to the Λ as Q^2 increases could be explained by increasing domination of the scaler contribution to the cross section, which would suppress Σ° production because the coupling constants are known to satisfy

$$G_{KN\Sigma} \ll G_{KN\Lambda} .$$

The K^+/π^+ ratio is independent of W and Q^2 for values of x' less than .6 while its behavior for values of x' between .7 and .1 reflects the behavior of the resonances in this region.

VI. ACKNOWLEDGEMENTS

We wish to acknowledge the support of the Director, Professor Boyce McDaniel, and the staff of the Wilson Synchrotron Laboratory. We also wish to acknowledge the support of the Harvard Cyclotron Laboratory.

TABLE I

A summary of the fitted values of $\frac{d\sigma}{d\Omega^*}$ for Λ and Σ^0. W is in GeV, Q^2 in GeV^2, θ^* in degrees, and $\frac{d\sigma}{d\Omega^*}$ in $\mu b/sr$. Uncertainties include statistical and fitting errors.

Point	<W>	$<Q^2>$	$<\epsilon>$	$<\theta^*>$	$\frac{d\sigma}{d\Omega^*}(\Lambda)$	$\frac{d\sigma}{d\Omega^*}(\Sigma^0)$	Σ^0/Λ
$\theta^*<15^\circ$							
1	2.67	.62	.86	7.8	$.267 \pm .026$	$.035 \pm .015$	$.132 \pm .069$
2-4	2.66	1.20	.86	8.4	$.169 \pm .012$	$.038 \pm .008$	$.225 \pm .064$
7	2.66	2.00	.82	7.5	$.137 \pm .013$	$.006 \pm .006$	$.043 \pm .047$
6	2.20	1.18	.94	7.4	$.272 \pm .019$	$.035 \pm .012$	$.127 \pm .053$
$\theta^*<30^\circ$							
1	2.67	.62	.86	8.0	$.263 \pm .024$	$.027 \pm .014$	$.103 \pm .064$
2-4	2.67	1.20	.86	10.7	$.140 \pm .010$	$.032 \pm .008$	$.228 \pm .071$
7	2.66	2.00	.82	8.6	$.112 \pm .012$	$.001 \pm .006$	$.009 \pm .056$
6	2.28	1.15	.93	13.2	$.228 \pm .019$	$.030 \pm .011$	$.133 \pm .061$

TABLE II

The t' distribution for the $K^+\Lambda$ and $K^+\Sigma^0$ photoproduction cross sections. W is in GeV, Q^2 in GeV^2, t' in GeV^2 and $\frac{d\sigma}{d\Omega^*}$ in $\mu b/sr$. Uncertainties include statistical and fitting errors.

Point	<W>	$<Q^2>$	$<\epsilon>$	$-<t'>$	$\frac{d\sigma}{d\Omega^*}$
Λ:					
1	2.64	.62	.87	.010	$.287 \pm .024$
	2.63	.63	.87	.034	$.264 \pm .019$
	2.68	.61	.86	.068	$.153 \pm .046$
2-4	2.62	1.22	.87	.009	$.206 \pm .026$
	2.65	1.21	.86	.033	$.149 \pm .012$
	2.66	1.20	.86	.080	$.123 \pm .017$
	2.69	1.20	.85	.178	$.058 \pm .028$
7	2.63	2.03	.83	.009	$.155 \pm .037$
	2.65	2.00	.82	.035	$.132 \pm .017$
	2.67	1.99	.82	.080	$.085 \pm .022$
6	2.11	1.21	.94	.010	$.274 \pm .031$
	2.18	1.18	.94	.032	$.271 \pm .031$
	2.41	1.10	.91	.093	$.139 \pm .025$
	2.57	1.04	.89	.194	$.156 \pm .047$
Σ:					
1	2.70	.60	.86	.009	$.037 \pm .014$
	2.66	.63	.87	.031	$.080 \pm .014$
	2.97	.50	.79	.081	$.011 \pm .023$
2-4	2.65	1.20	.86	.010	$.055 \pm .017$
	2.67	1.21	.86	.032	$.023 \pm .007$
	2.69	1.18	.85	.088	$.021 \pm .013$
	2.88	1.09	.81	.183	$.000 \pm .030$
7	2.66	2.02	.82	.008	$.036 \pm .021$
	2.55	2.04	.84	.040	$.004 \pm .006$
6	2.17	1.21	.94	.010	$.029 \pm .018$
	2.32	1.12	.92	.032	$.024 \pm .017$
	2.45	1.08	.91	.093	$.050 \pm .020$
	2.59	1.02	.88	.236	$.025 \pm .019$

TABLE III

A summary of the slopes obtained from a fit of the t' distributions to the form $A_e^{Bt'}$ where B is the slope. B is in units of GeV^{-2}.

Point	<W>	$<Q^2>$	<ε>	Slope	FIT: DOF	CHI^2
1	2.65	.62	.87	6.5 ± 4.4	1	1.979
2-4	2.65	1.21	.86	6.8 ± 1.9	2	1.467
6	2.30	1.15	.92	6.2 ± 2.6	2	4.070 *
7	2.65	2.00	.82	8.6 ± 1.2	1	0.061

*Note: At point 6 there is a variation in <W> across the t' range of 460 MeV. At all other points this variation is less than 75 MeV.

TABLE IV

A summary of the fitted cross sections for $K^+\Lambda$ (1520) virtual photoproduction. W is in GeV, Q^2 in GeV^2, θ^* in degrees, and $\frac{d\sigma}{d\Omega^*}$ in $\mu b/sr$. Uncertainties are statistical and fitting errors.

Point	θ^*	<W>	$<Q^2>$	<ε>	$<\theta^*>$	$\frac{d\sigma}{d\Omega^*}$	FIT: DOF	CHI^2
1	$0<\theta^*<15^\circ$	2.71	.61	.86	6.65	$.127 \pm .016$	11	4.58
	$0<\theta^*<30^\circ$	2.71	.61	.86	6.84	$.128 \pm .016$	11	5.07
2-4	$0<\theta^*<15^\circ$	2.70	1.18	.85	7.96	$.081 \pm .013$	11	10.64
	$0<\theta^*<30^\circ$	2.73	1.17	.84	10.52	$.076 \pm .013$	11	16.00
6	$0<\theta^*<15^\circ$	2.32	1.14	.92	12.18	$.094 \pm .031$	8	6.51
	$0<\theta^*<30^\circ$	2.43	1.10	.91	17.65	$.074 \pm .016$	11	6.57
7	$0<\theta^*<15^\circ$	2.74	1.94	.80	8.76	$.067 \pm .018$	11	11.90
	$0<\theta^*<30^\circ$	2.76	1.92	.80	9.90	$.052 \pm .013$	11	8.65

FIGURE CAPTIONS

Fig. 1 Cornell and Harvard Spectrometers.

Fig. 2 A typical time-of-flight spectrum for hadrons not registering in the Cerenkov counter.

Fig. 3 The Q^2, ν plane with the points at which data have been taken indicated.

Fig. 4 Missing mass squared distributions for a detected K^+ at data points 1 (a), 2-4 (b), 7 (c), and 6 (d).

Fig. 5 The invariant structure function for kaons plotted against x' for data points 1, 2-4, 6 and 7.

Fig. 6 The ratio of the invariant structure functions for K^+ and π^+ plotted against x'. π^+ data came from ref. 6.

Fig. 7 A typical example of the fitting procedure used to extract the Λ and Σ° cross sections.

Fig. 8 The Q^2 dependence of the $K^+\Lambda$ cross section. The photoproduction point is from ref. 8.

Fig. 9 The Q^2 dependence of the $K^+\Sigma^\circ$ cross section.

Fig. 10 The t' dependence of the $K^+\Lambda$ cross section at data points 1 (a), 2-4 (b), 7 (c) and 6 (d).

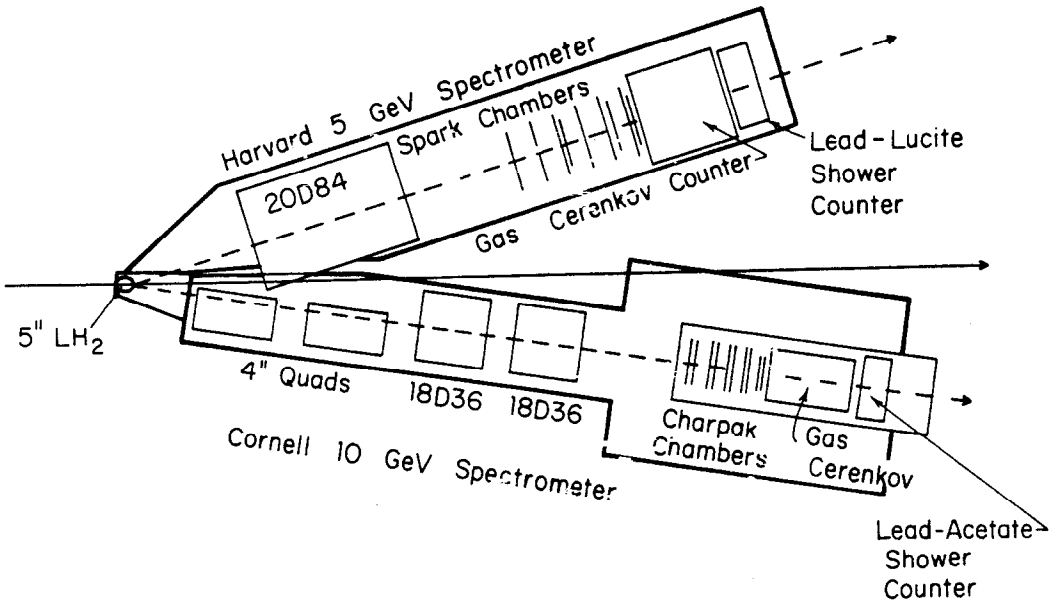

Figure 1

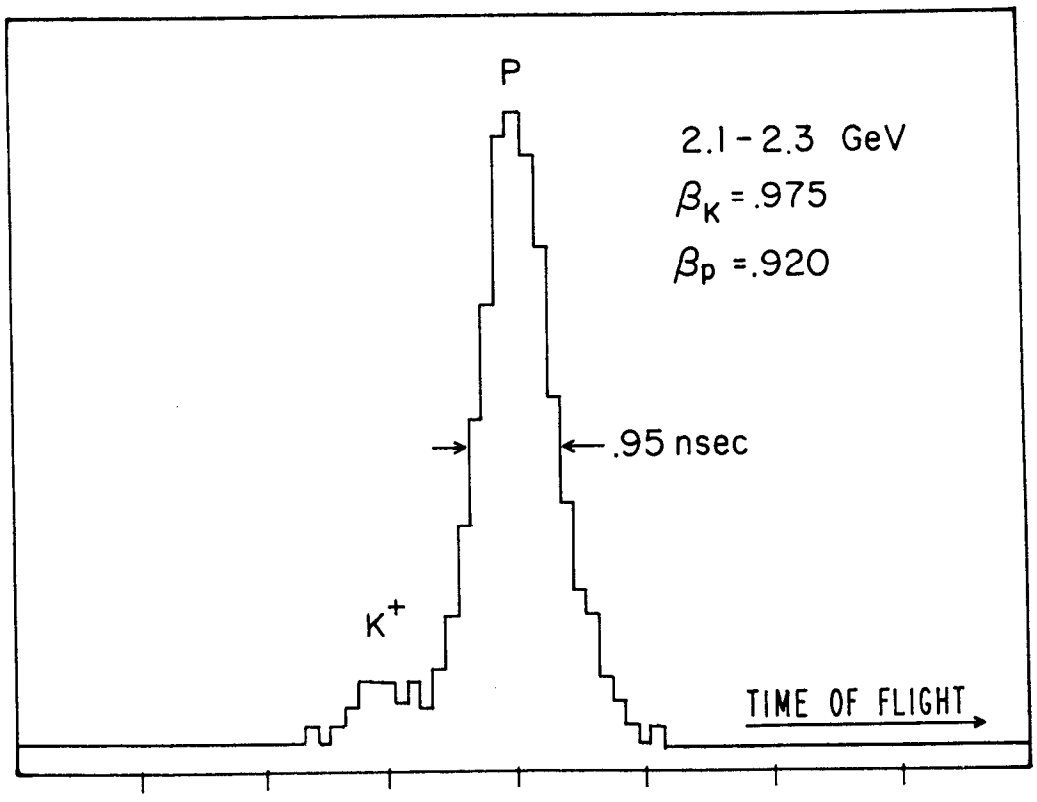

Figure 2

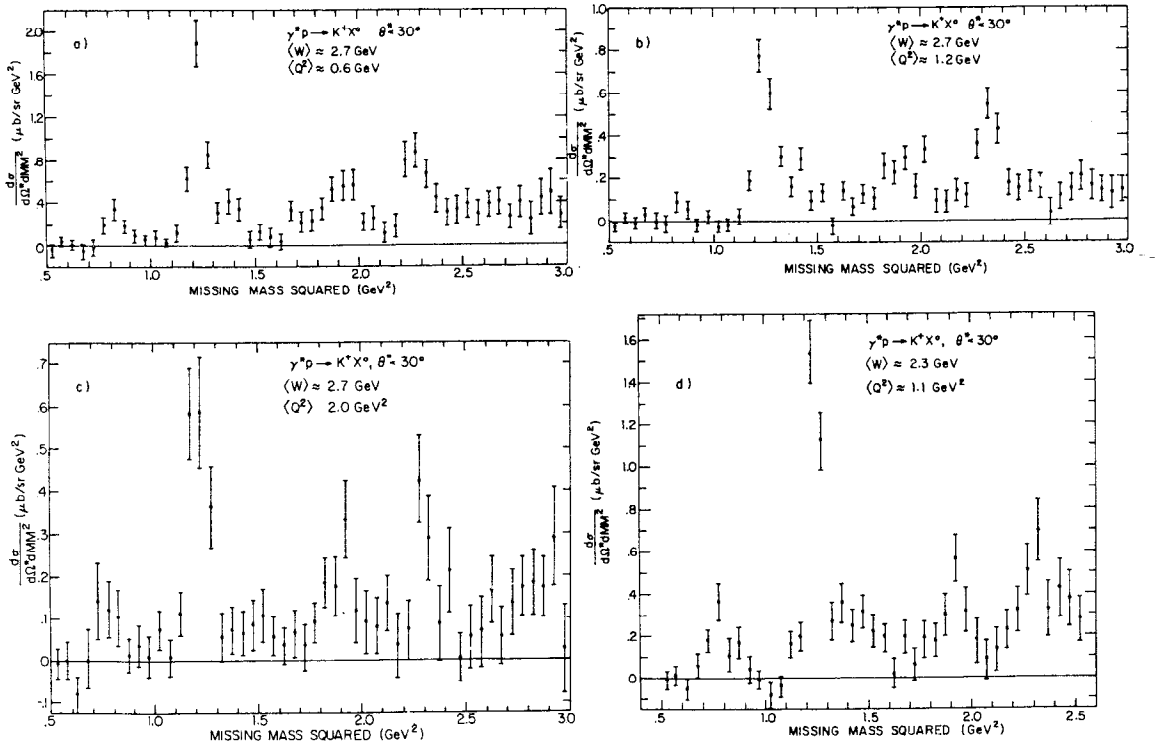

Figure 4

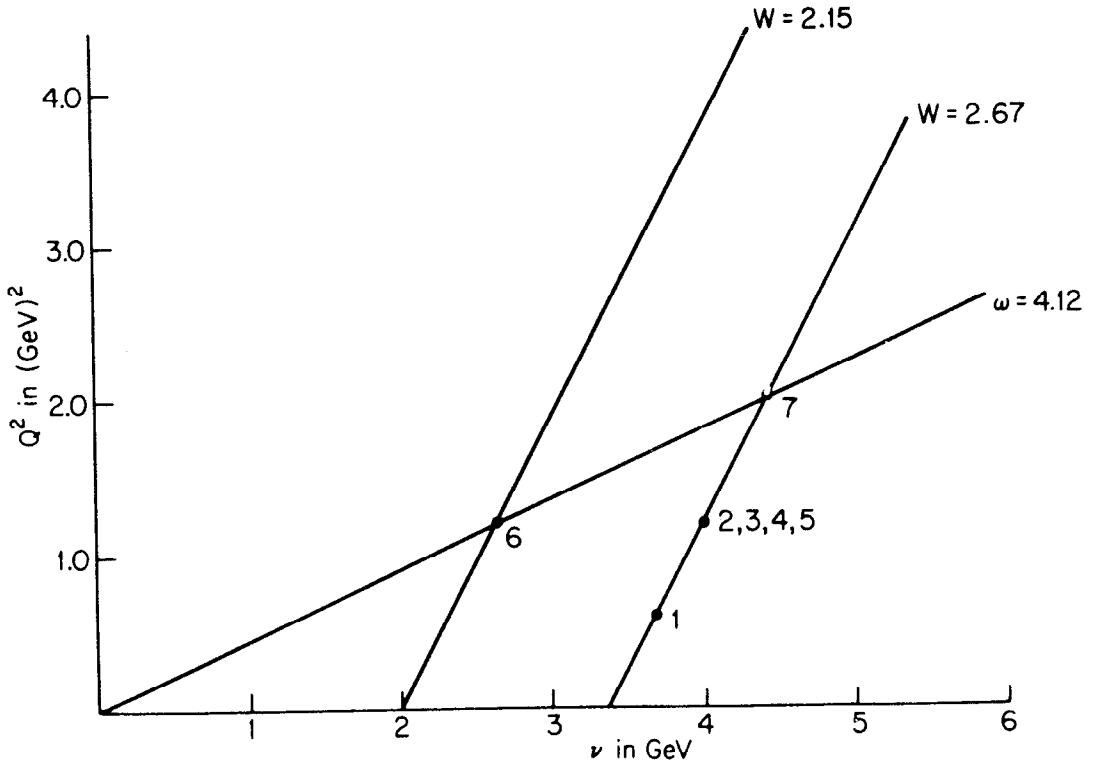

Figure 3

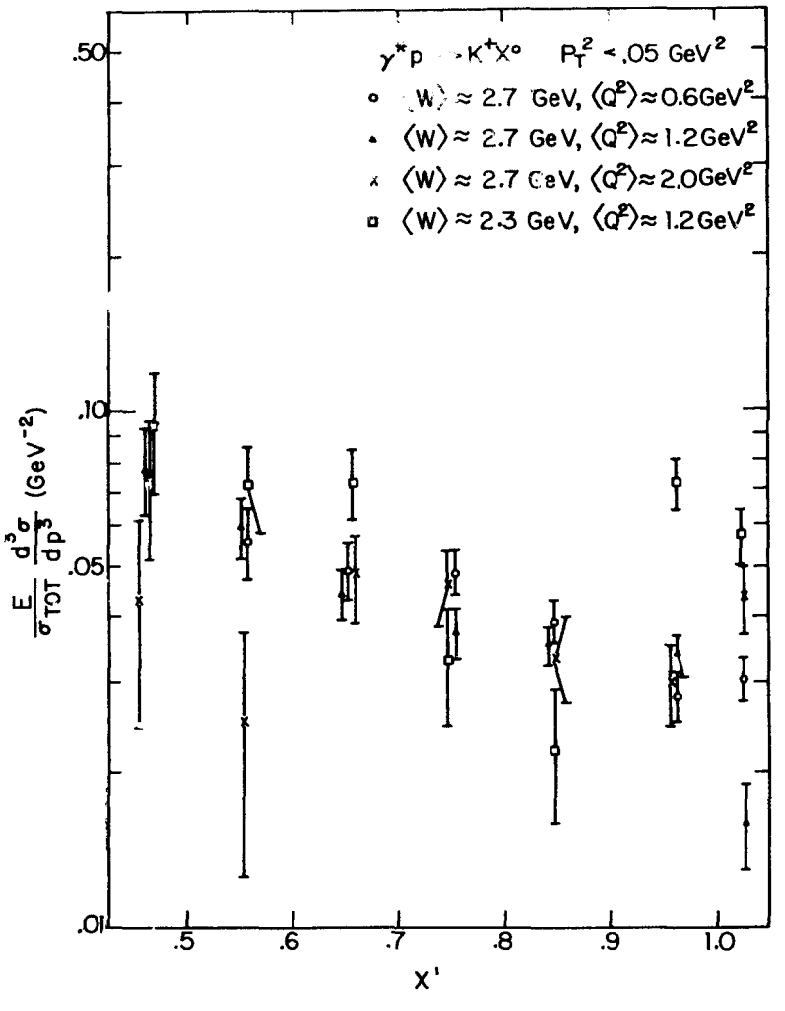

Figure 5

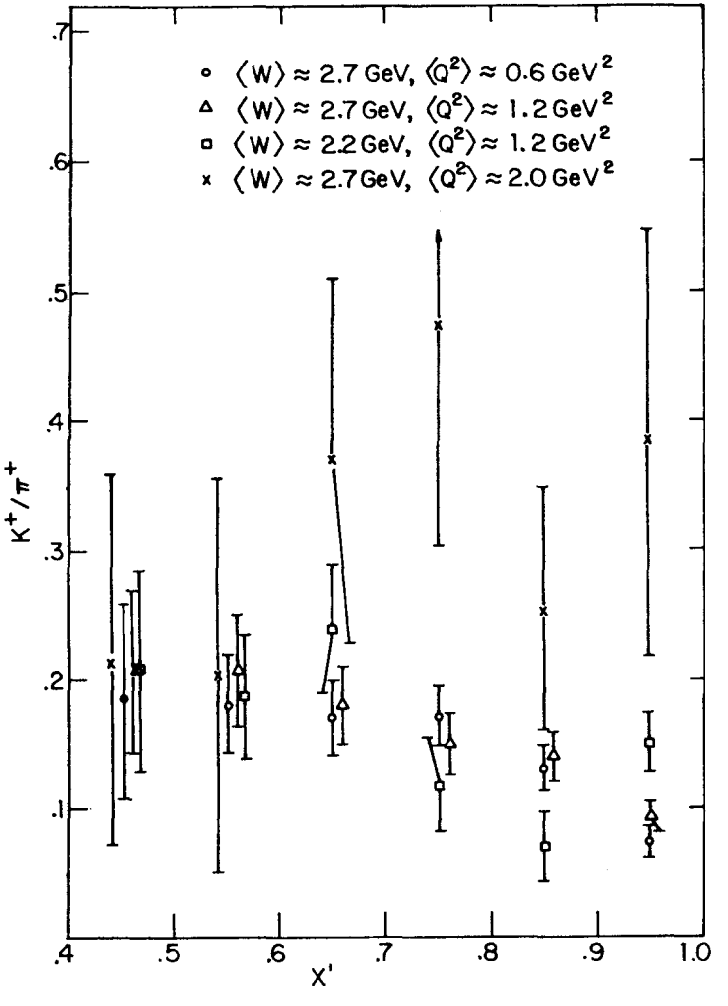

Figure 6

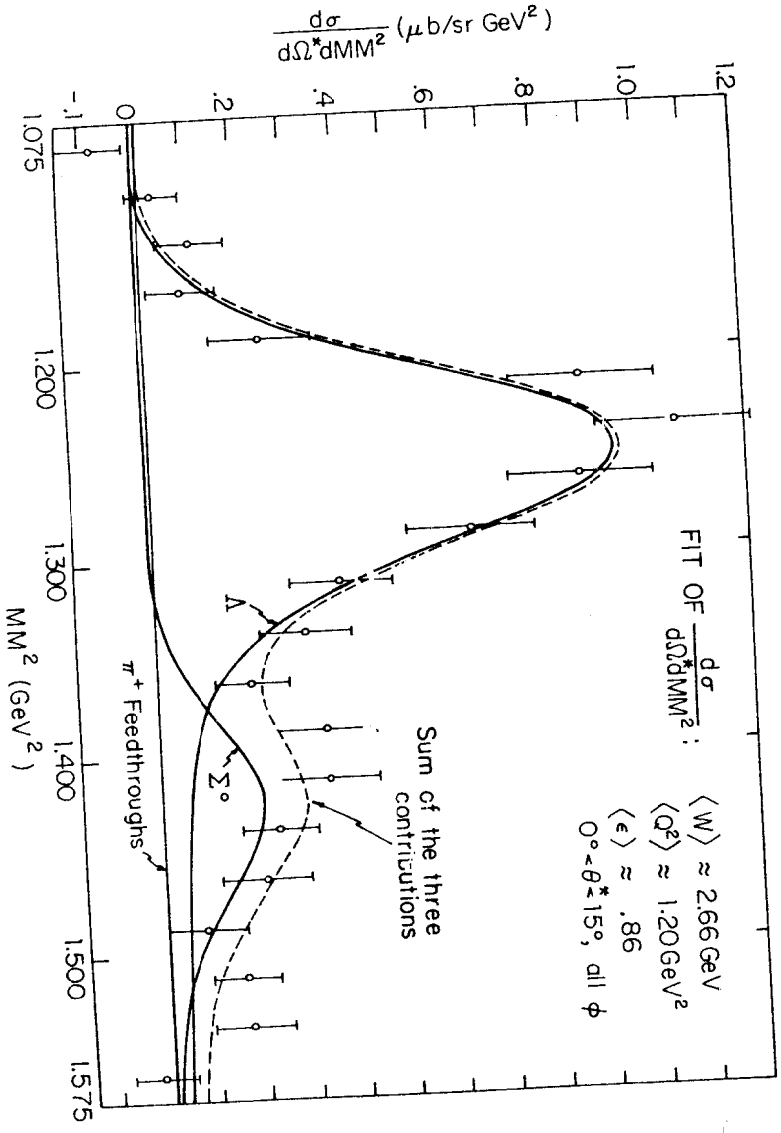

Figure 7

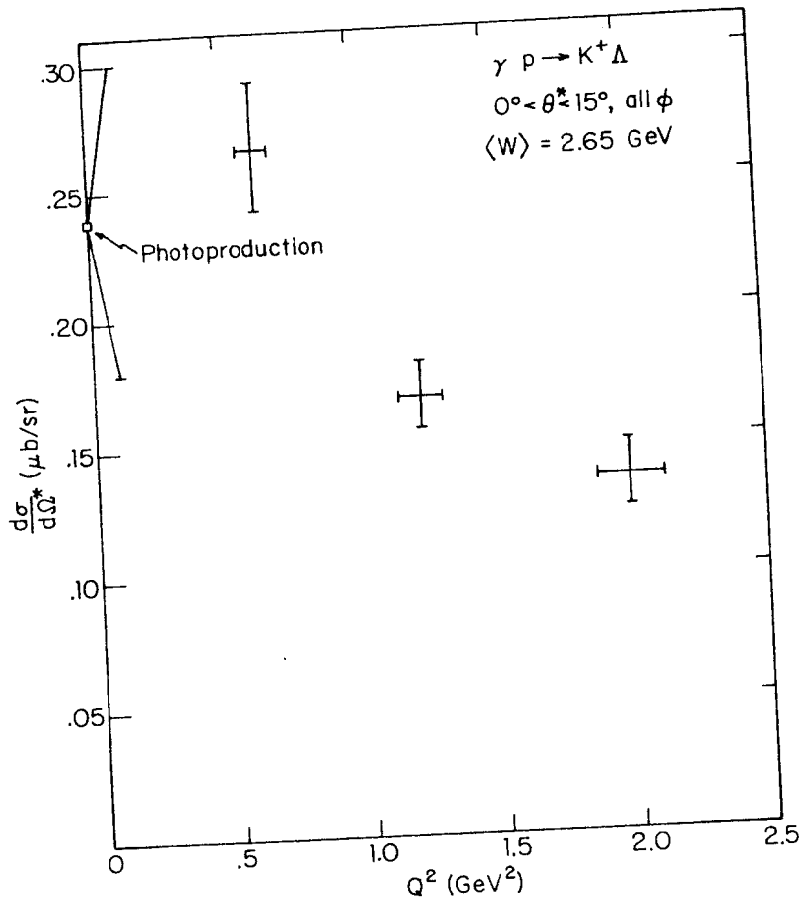

Figure 8

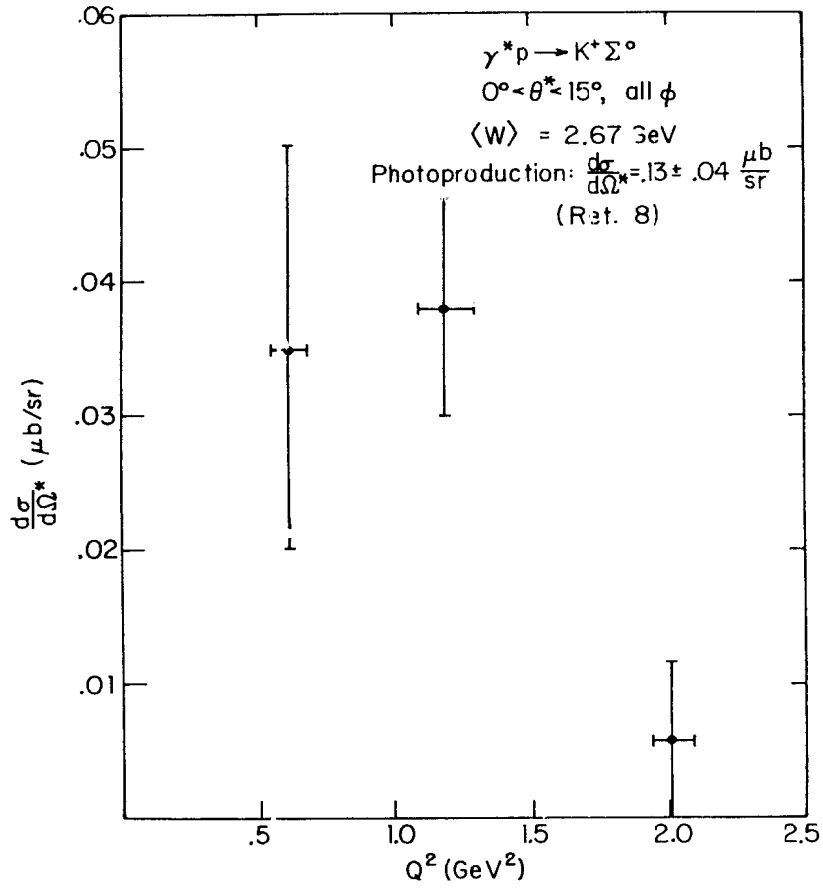

Figure 9

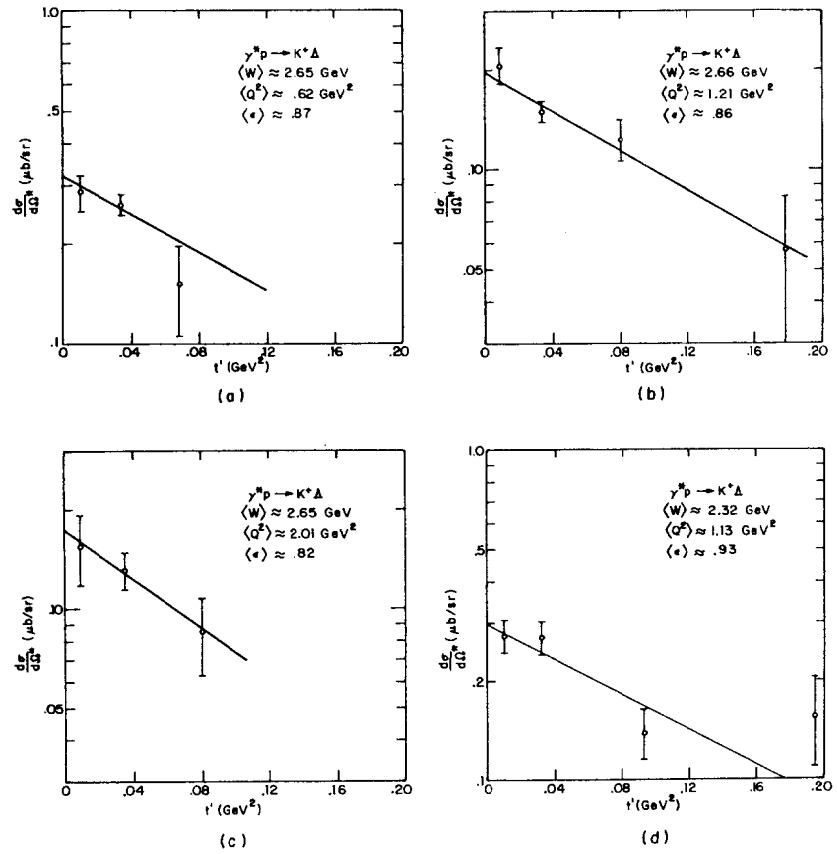

Figure 10

REFERENCES

1. K. Berkelman in Proceedings of the Sixteenth International Conference on High Energy Physics, National Accelerator Laboratory, Batavia, Ill., 1972, edited by J. D. Jackson and A. Roberts (NAL, Batavia, Ill., 1973); L. N. Hand, Phys. Rev. 129, 1834 (1964).
2. R. P. Feynman, Phys. Rev. Letts. 23, 1415 (1969).
3. W. B. Atwood, private communication.
4. A. Bartl and P. Urban, Acta Phys. Austr. 24, 139 (1966).
5. L. W. Mo and Y. S. Tsai, Rev. Mod. Phys. 41, 205 (1969).
6. C. J. Bebek et al., contributed to this conference.
7. C. N. Brown et al., Phys. Rev. Letts. 28, 1086 (1972).
8. R. Erbe et al., Phys. Rev. 188, 2060 (1969).

RESULTS ON HIGH ENERGY NEUTRINO SCATTERING AT NAL

D. Shields

California Institute of Technology

Pasadena, California

I. DEEP INELASTIC ν SCATTERING

Deep inelastic ν scattering is the weak interaction analog of inelastic ep scattering

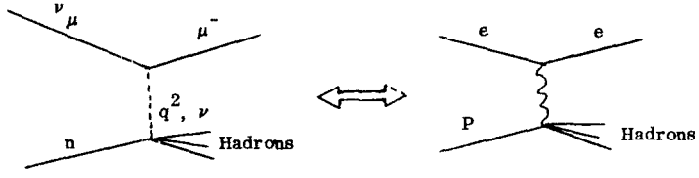

In the scaling limit, the doubly differential cross section may be written

$$\frac{d^2\sigma^{\nu,\bar\nu}}{dxdy} = \frac{G^2ME_\nu}{\pi}\left\{(1-y)\,F_2^{\nu,\bar\nu}(x) + \frac{y^2}{2}\,(2xF_1^{\nu,\bar\nu}(x) \mp y\,(1-\frac{y}{2})\,xF_3^{\nu,\bar\nu}(x)\right\} \quad (1)$$

for $E_\nu \to \infty$, q^2, $\nu \to \infty$, ν/q^2 finite and where the - (+) sign holds for $\nu(\bar\nu)$. The definitions are:

$$x = Q^2/2M\nu \qquad Q^2 = -q^2 = 4E_\nu E_\mu' \sin^2\frac{\theta}{2}$$

$$y = \nu/E_\nu = \frac{E_\nu - E_\mu'}{E_\nu}$$

The structure functions F(x) have been superscripted to indicate that in general they may be different for ν, $\bar\nu$.

One well known consequence of scaling of the structure functions is that $\sigma_{tot}^{\nu,\bar\nu}$ should rise linearly with lab ν energy E_ν. Integrating (1) over x, y

$$\sigma_{tot}^{\nu,\bar\nu} = \frac{G^2ME_\nu}{\pi}\int_0^1 dx\,\left\{\frac{F_2^{\nu,\bar\nu}(x)}{2} + \frac{x\,F_1^{\nu,\bar\nu}(x)}{3} \mp \frac{xF_3^{\nu,\bar\nu}(x)}{3}\right\} \quad (2)$$

The CERN Gargamelle data on $\sigma_{tot}^{\nu,\bar\nu}$ are shown in Fig. (1). In both instances, the data are consistent with a linear rise with E_ν.

One important point is whether the slopes observed are the values expected in the true scaling limit, since the data are not in the scaling region as defined by the SLAC-MIT ep experiments ($\frac{\nu}{M}$, $q^2/M^2 \geq 2$-3).

With some additional assumptions (other than scaling) we can predict the scaling limit slopes from the electron data (Ref. Perkins review talk at Batavia Conf.).

(a) $2xF_1(x) = F_2(x)$ The Callan-Gross relation

This is approximately valid in the SLAC-MIT experiments ($\sigma_S/\sigma_T \sim .14 \pm .10$) and in the CERN ν data.

(b) Isospin Symmetry

$$F_i^{\bar\nu p} = F_i^{\nu n} \qquad i = 1, 3$$

$$F_i^{\bar\nu n} = F_i^{\nu p}$$

Since in ν experiments done so far, we measure the isospin averaged cross section we have

$$F_i^{\bar\nu N} = \frac{1}{2}\,(F_i^{\bar\nu n} + F_i^{\bar\nu p}) = F_i^{\nu N}$$

where N refers to scattering on a nucleon.

(c) $\theta_c = 0$ Neglect $\Delta s = 1$ transitions

very roughly $\frac{\sigma(\Delta s = 1)}{\sigma(\Delta s = 0)} \sim \tan^2\theta_c = .06$

Using assumptions (a), (b), (c) in our expression (2), we have

$$\sigma_{tot}^{\nu,\bar\nu} = \frac{G^2ME_\nu}{\pi}\int_0^1 F_2^{\nu}(x)\,dx\,\left\{1 - \frac{1}{3}\,(1 \mp B)\right\} \quad (3)$$

where $B = -\int_0^1 x\,F_3^{\nu}(x)\,dx \Big/ \int_0^1 F_2^{\nu}(x)\,dx$

if we add $\sigma^{\nu} + \sigma^{\bar\nu}$ the B term drops out and

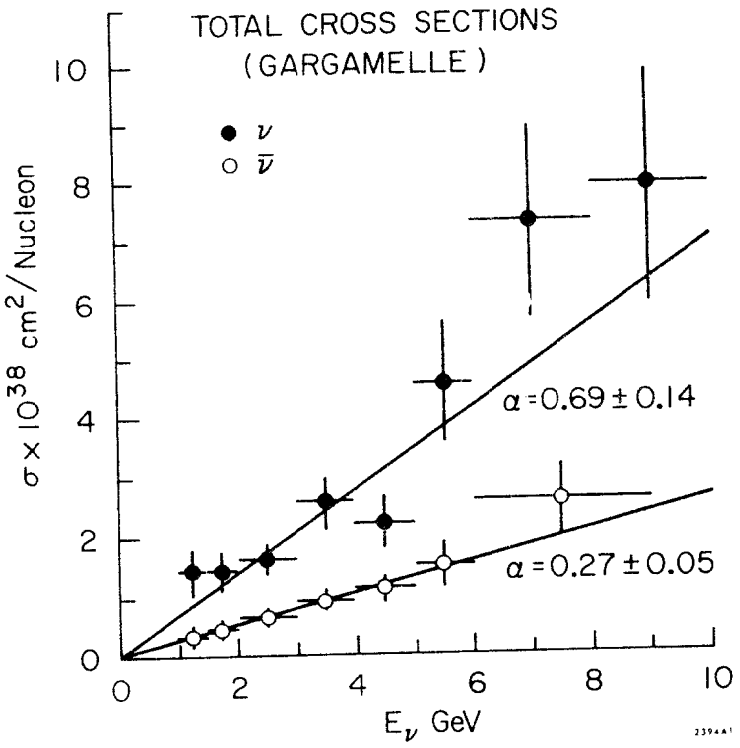

Fig. 1

$$\sigma^{\nu} + \sigma^{\bar{\nu}} = \frac{G^2 M E_{\nu}}{\pi} \quad \frac{4}{3} \quad \int_0^1 F_2^{\nu}(x)\, dx \tag{4}$$

using the CERN Gargamelle data, we find

$$\int_0^1 F_2^{\nu}(x)\, dx = .47 \pm .07 \tag{5}$$

In order to see what ep scattering predicts for this integral, we further assume

(d) Isoscalar Part of $F_2^{eN}(x) \leq 10\%$

where $F_2^{eN}(x) = \frac{1}{2}\,(F_2^{ep}(x) + F_2^{eN}(x)) = \frac{1}{2}\, F_2^{ed}(x)$

(e) Isotriplet Current Hypothesis

$$(F_2^{\nu N})_{\text{Vector}} = 2\,(F_2^{eN})_{\text{Isovector}}$$

(f) $|V| = |A|$ chiral symmetry

putting this together, we find

$$\int_0^1 F_2^{\nu N}(x)\, dx = 4 \int_0^1 F_2^{eN}(x)\, dx \tag{6}$$

using the SLAC-MIT data on ed scattering

$$\int_0^1 F_2^{ep}(x)\, dx = .18 \pm .01$$

$$\int_0^1 F_2^{eN}(x)\, dx = .13 \pm .01$$

$$\int_0^1 F_2^{eN}(x)\, dx = .15 \pm .01 \tag{7}$$

we find then

$$\int_0^1 F_2^{\nu N}(x)\,dx = .56 \pm .04 \quad \text{predicted from ed isoscalar subtracted (10\%)}$$

$$\int_0^1 F_2^{\nu N}(x)\,dx = .49 \pm .07 \quad \text{measured (corrected for } n \neq p \text{ and } \Delta s = 1) \qquad (8)$$

So the agreement is quite good!

Side comment on constituent models. (Quark-Parton)

$\int_0^1 F_2(x)\,dx$ = Fraction of momentum carried by quarks and anti-quarks in the nucleon. Hence, we find that ~ 50% carried by gluons.

in detail:

$u(x)$ = no. of isospin up partons in the proton with momentum fraction x

$d(x)$ = no. of isospin down partons in the proton with momentum fraction x

$\bar{u}(x)$ = no. of isospin up anti-partons in the proton with momentum fraction x

$\bar{d}(x)$ = no. of isospin down anti-partons in the proton with momentum fraction x

$s(x)$ = no. of strange partons in the proton with momentum fraction x

$\bar{s}(x)$ = no. of strange anti-partons in the proton with momentum fraction x

then we have

$$\int_0^1 F_2^{ep}(x) = \int x f_p(x) = \int_0^1 x \left\{ \frac{4}{9}(u + \bar{u}) + \frac{1}{9}(d + \bar{d}) + \frac{1}{9}(s + \bar{s}) \right\} dx \qquad (9)$$

$$\int_0^1 F_2^{en}(x) = \int x f_n(x) = \int_0^1 x \left\{ \frac{1}{9}(u + \bar{u}) + \frac{4}{9}(d + \bar{d}) + \frac{1}{9}(s + \bar{s}) \right\} dx \qquad (10)$$

so averaging (9) and (10)

$$\int_0^1 F_2^{eN}(x)\,dx = \int_0^1 \frac{1}{2}\,x\,dx \left\{ \frac{5}{9}(u + \bar{u} + d + \bar{d}) + \frac{2}{9}(s + \bar{s}) \right\} \qquad (11)$$

for ν scattering (ignoring the $\Delta s = 1$ contribution)

$$\int_0^1 F_2^{\nu N}(x)\,dx = \int_0^1 x\,dx \left\{ u + \bar{u} + d + \bar{d} \right\} \qquad (12)$$

finally, we have

$$g = 1 - \int_0^1 x\,(u + \bar{u} + d + \bar{d} + s + \bar{s})\,dx \qquad (13)$$

where g is the momentum not carried by isovector or strange quarks or anti-quarks. Using (11), (12), (13) and the measured values of $\int_0^1 F_2(x)\,dx$ for eN and νN scattering we can solve for g,

$$g = 1 + \frac{3}{2}\int_0^1 F_2^{\nu N}(x)\,dx - 9\int_0^1 F_2^{eN}(x)\,dx \qquad (14)$$

$$g \simeq .49 \pm .20$$

where the above analysis has assumed that the slopes measured at CERN ($\sigma_T^{\nu}, \bar{\nu}$ vs. E_ν) are the true scaling limits.

An interesting result is obtained if we assume that $g = 0$ (no gluons). Then the CERN result for $\int_0^1 F_2^{\nu N}(x)\,dx$ is not the scaling limit and we can place a limit on the value expected in the scaling region.

If $g = 0$, using (11), (13)

$$\int_0^1 (s + \bar{s})\,x\,dx = \frac{5}{3}\left(1 - \frac{18}{5}\int_0^1 F_2^{eN}(x)\,dx\right) \qquad (15)$$

$$\simeq .75$$

i.e. ~75% of the momentum is carried by strange quarks. Then using (12), we have

$$\int_0^1 F_2^{\nu N}(x)\,dx \simeq .25\ . \qquad (16)$$

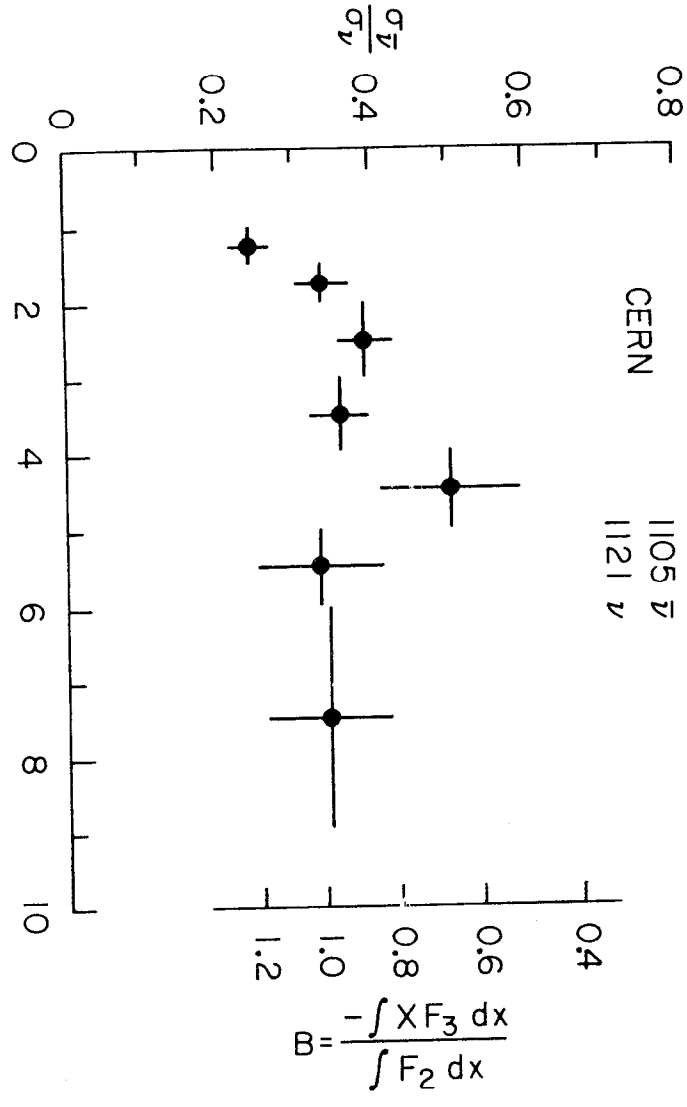

Fig. 2

This is about a factor of 2 different from the CERN measurements and should be readily checked at NAL once reliable flux determinations are made.

$F_3^{\nu N}$ STRUCTURE FUNCTION

This function has been extracted from the CERN data in two ways

① $\sigma_T(\bar{\nu}) / \sigma_T(\nu)$

② dn/dy for anti-neutrino events.

Using (3) for the cross sections and taking the ratio $\sigma(\bar{\nu})/\sigma(\nu)$, we have

$$\frac{\sigma_T(\bar{\nu})}{\sigma_T(\nu)} = \frac{2 - B}{2 + B} \implies \frac{1}{3} \leq \frac{\sigma(\bar{\nu})}{\sigma(\nu)} \leq 3 \qquad (17)$$

The CERN data for this ratio is shown in Fig. (2) with the result

$$\frac{\sigma_T(\bar{\nu})}{\sigma_T(\nu)} = .38 \pm .02$$

$$B = .9 \pm .04.$$

Using (1) and the Callan-Gross relation and integrating over x, we have

$$\frac{d\sigma^{\nu,\bar{\nu}}}{dy} \propto \left\{1 - (1 \mp B)\left(y - \frac{y^2}{2}\right)\right\} \qquad (18)$$

From this expression, we expect $\frac{d\sigma^{\nu}}{dy} \propto$ constant, $\frac{d\sigma^{\bar{\nu}}}{dy} \propto (1 - y)^2$ for B = 1. The CERN data are shown in Fig. (3). Again $B \simeq .9$. Thus, the V-A interference term F_3 is maximal. In a constituent model, this implies that spin 1/2 partons dominate and that the momentum fraction carried by partons is >> than that carried by anti-partons. Also, diffractive contributions to the cross section (which have F_3 small) are small or at least limited to very small x.

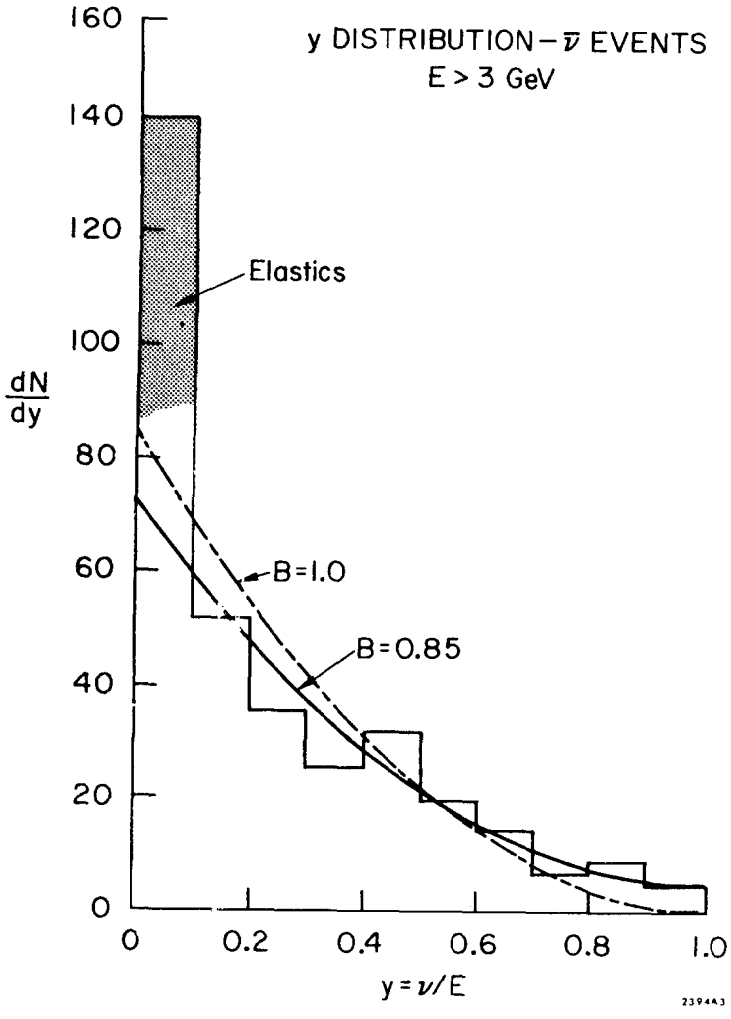

Fig. 3

II. THE CALTECH NEUTRINO EXP.

People

BARRY BARISH	FRANK MERRITT	DENNY SHIELDS
FRITZ BARTLETT	*YORI NAGASHIMA	* AL MASCHKE
DAVE BUCHHOLZ	FRANK SCIULLI	GEORGE KRAFCZYK
TOM HUMPHREY	HENRY SUTER	

*Departed

PURPOSE

Investigation of High Energy Neutrino Interactions using a Dichromatic ν Beam.

Fig. 4 shows a schematic layout of the neutrino area at NAL. Protons from the accelerator are targeted in the neutrino target hall (ν - hall) and a target tube containing magnets to form a beam of secondary hadrons (π, K, P) follows. Next in line is a decay region where the secondary π and K mesons may decay giving μ's and ν_μ's. Following the decay pipe is a dump to absorb secondary protons and π's and K's which did not decay. Following this is a shield (mostly dirt) ~500 meters long to range out μ's. The Caltech apparatus sits in a building placed in the ν beam line in a void in the shield.

In Fig. 5, we show the kinematics of our narrow band beam. We see that there should be two distinct bands of ν's. For a secondary beam energy of 160 GeV the ν's from K decay should be at ~150 GeV while those from π decay will be centered at ~45 GeV.

Some Features of the dichromatic beam.

① Sign selection of Hadrons implies that the beam selects ν_μ or $\bar{\nu}_\mu$. This is a valuable asset when looking for rare processes which result in "wrong" sign muons such as W boson production or heavy muon production.

② Simpler monitoring and normalization of fluxes which should make possible direct

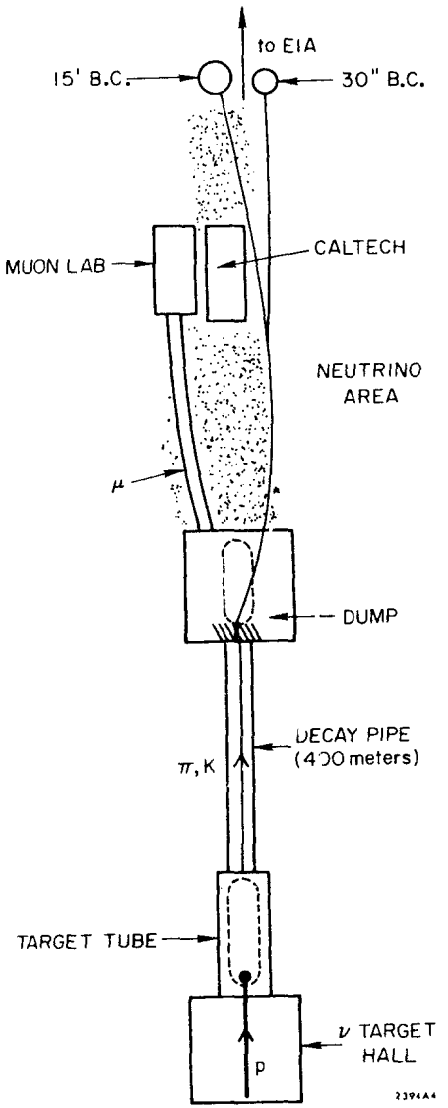
to EIA
15' B.C.
30" B.C.
MUON LAB
CALTECH
NEUTRINO
AREA
μ
DUMP
π, K
DECAY PIPE
(400 meters)
TARGET TUBE
ν TARGET
HALL
p

Fig. 4

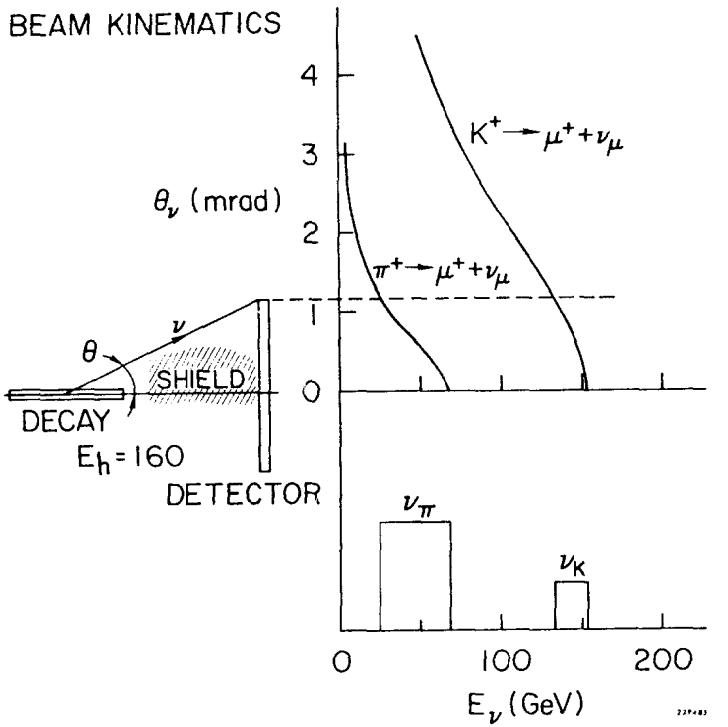
BEAM KINEMATICS
θ_ν (mrad)
4
3
2
1
0
$K^+ \to \mu^+ + \nu_\mu$
$\pi^+ \to \mu^+ + \nu_\mu$
ν
θ
SHIELD
DECAY
$E_h = 160$
DETECTOR
ν_π
ν_K
0
100
200
E_ν (GeV)

Fig. 5

measurements of $\sigma_T^{\nu,\bar{\nu}}$ vs E_ν. (By monitoring the total flux of secondary hadrons entering the decay region we can, with knowledge of the composition of the beam (π, K, P), calculate the ν_μ flux for σ_T normalization.)

③ The ν_μ energy spectrum is not steep and hence systematic errors in the energy measurements should be much less of a problem than with a broad band beam.

④ One <u>disadvantage</u> - the rate for such a beam will be considerably less than the horn focussed broad band beam.

<u>The Detector</u>

Fig. 6 displays schematically the Caltech detector. It consists of a massive target of 170 tons of steel, followed by an iron core toroidal magnet and spark chambers which make up the muon spectrometer.

The target itself doubles as a calorimeter to measure the energy deposited in hadrons in a ν_μ interaction. The steel is split into 4" sections and following each steel plate is a sampling scintillation counter. After every fourth scintillator, we have a spark chamber to measure the muon angle. All spark chambers in the detector have magnetostrictive readout. In addition to the calorimeter counters, we have a large veto array in front of the target and 3 trigger counters (T1, T2, T3) which signal the presence of a muon penetrating the spectrometer.

Measurements of muon energy ($\pm$ 20%) and hadron energy ($\sim\pm$ 20%) as well as muon angle are made in the detector. These measurements suffice to determine the kinematic quantities of interest (Q^2, ν) which describe ν interactions independent of any information about E_ν from the dichromatic beam.

<u>January Test Run</u>

The data to be described were recorded during a test run in January, 1973. The expressed purposes of this run were to shake down the apparatus and to look for big surprises in the physics of ν interactions at high energy.

For this run the proton energy was 300 GeV and the secondary hadron beam was

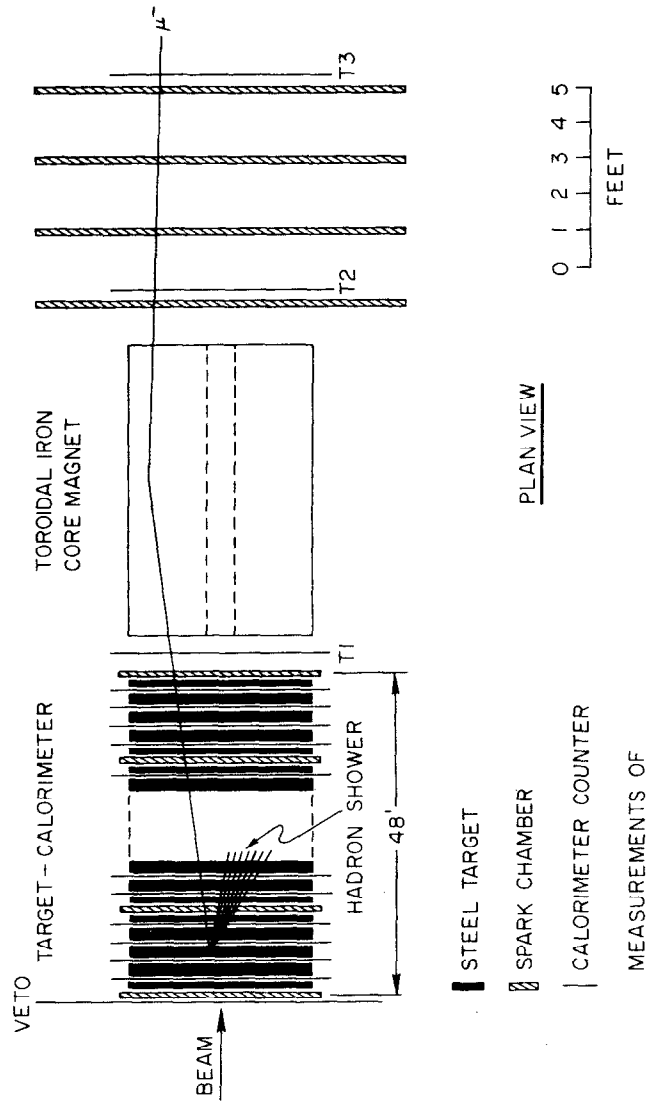

Fig. 6

tuned to 160 GeV. $\Delta p/p$ for the hadron beam was $\pm$ 11%. The duration of the run was 2.7×10^{16} protons on our target.

The detector is triggered in two ways:

a) Muon trigger ($\overline{\text{VETO}} \cdot T1 \cdot T2 \cdot T3$) signalling the presence of a muon penetrating the magnet from an interaction in the target - calorimeter.

b) Hadron trigger ($E_h \geq 8$ GeV) which implies a large hadron shower in the detector, again with no signal in the Veto bank. Here the muon need not go through the spectrometer.

For the data to be discussed we will use only type (a) triggers.

Results

From this run, we have isolated 167 ν_μ interactions in our target. Of these, 145 occur within a geometrically defined fiducial volume. 112 are analyzable in a complete sense with E_μ, E_h, Θ_μ measured. Any biases introduced by the sample reduction are insignificant at the statistical level of the present data.

A computer picture of a typical best event from this sample is shown in Fig. 7 which shows a side (vertical) and top (horizontal) view of the detector. In the box at the top of the figure are shown the pulse heights in the calorimeter counters. Near the interaction z position, we see large pulse heights corresponding to a large amount of hadron energy in the interaction. The parameters of this particular event are listed on the figure.

In Fig. 8 we display the ν energy spectrum derived by summing the hadron and secondary muon energies. The horizontal lines labeled ν_π, ν_K indicate the mean energy and width expected from the beam properties alone. We see that there are two groups of events of about the right mean energy and width. The additional width is undoubtedly due to apparatus resolution and some additional broad band background under the π peak. With this evidence that things are not working too badly, we begin to make some checks on the data.

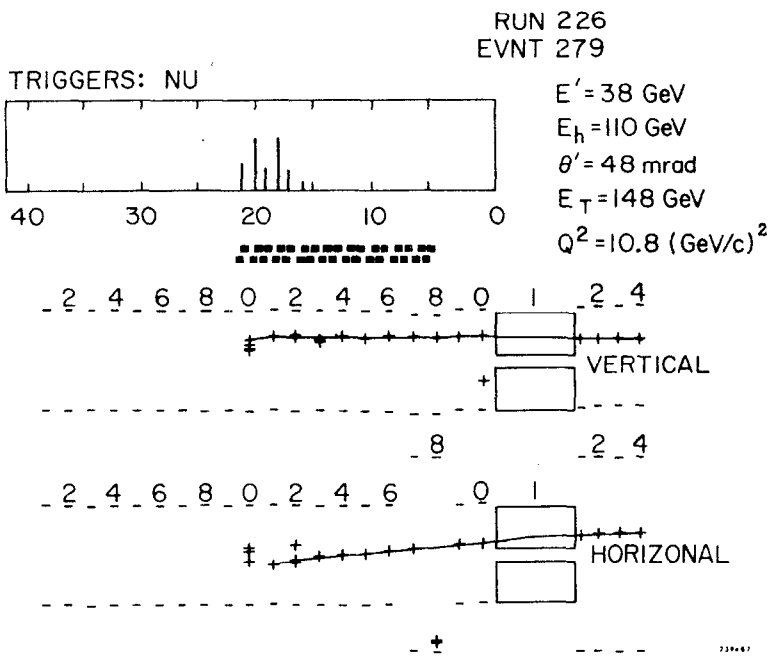

Fig. 7

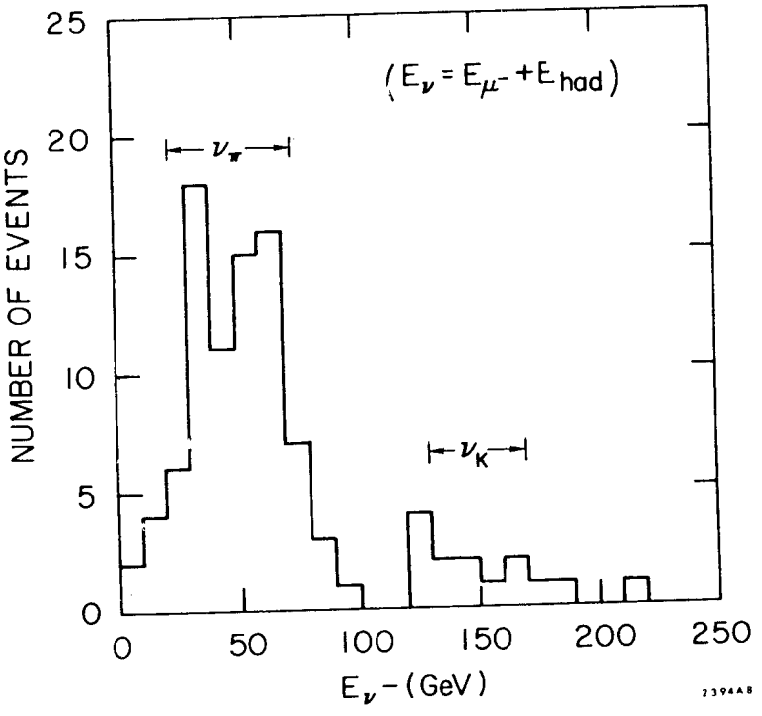

Fig. 8

Qualitative Results

Do the qualitative features of high energy ν_μ interactions look anything like "expected"?

The expected behavior is derived from the SLAC-MIT inelastic electron scattering results and the low energy CERN ν, $\bar{\nu}$ data. For simplicity, we assume:

(a) $2x\,F_1(x) = F_2(x)$ Callan-Gross

(b) $-x\,F_3(x) = F_2(x)$ pure V-A $\Longrightarrow$ (B = 1)

This is equivalent to assuming a quark parton model with no anti-quarks. The error introduced by assuming B = 1 (instead of B $\simeq$ .9 as measured) is negligible at the statistical level of our data.

Using (a), (b) we have from (1)

$$\frac{d^2\sigma^\nu}{dxdy} \simeq \frac{G^2 M E_\nu}{\pi} F_2^{\nu N}(x) \qquad (19)$$

$$F_2^{\nu N}(x) \sim F_2^{ed}(x) \quad .$$

Integrating, we find

$$\frac{d\sigma^\nu}{dy} \simeq \text{constant} \quad , \quad \frac{d\sigma^\nu}{dx} \sim F_2^{ed}(x) \quad .$$

We can now compare these predictions with our data using our more numerous ν_μ from π decay with $< E_\nu > \sim 50$ GeV.

In Figs. 9, 10 we show the x and y distributions for these data together with the above predictions. At the statistical level of the data there is very nice agreement. So qualitatively, the data agree with this simple picture.

Given this initial success, we push this foolishness one step further by looking at the energy dependence of our data. The obvious test is to measure σ_{tot} vs. E_ν. However, since we cannot normalize the present data, this is impossible. Instead as a first test of scaling we look at $< Q^2 >$ vs. E_ν. In terms of the variables x, y, we have

$$Q^2 = xy\,2M\,E_\nu$$

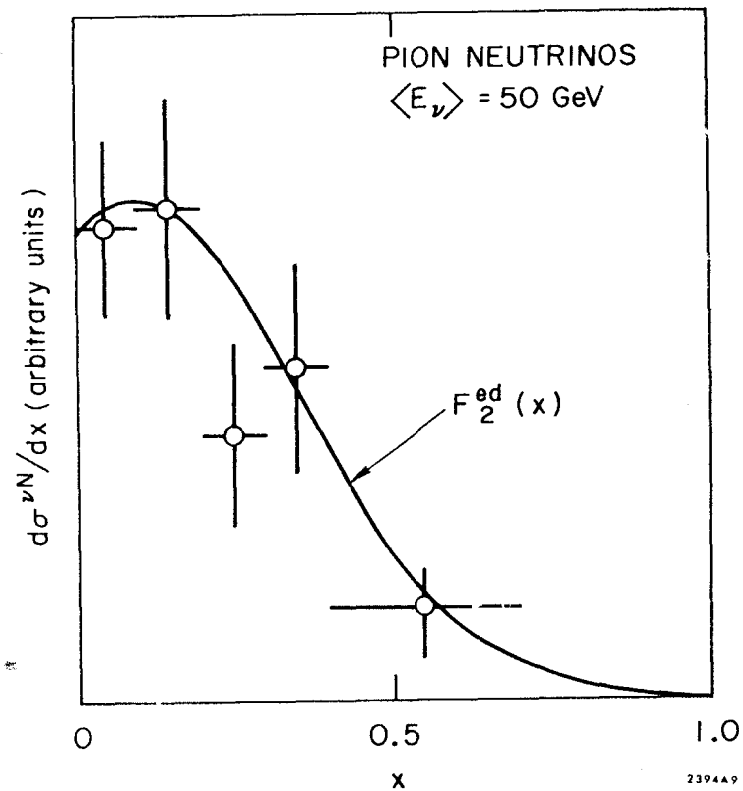
PION NEUTRINOS
⟨Eν⟩ = 50 GeV
dσνN/dx (arbitrary units)
F2ed (x)
0
0.5
1.0
x
2394A9

Fig. 9

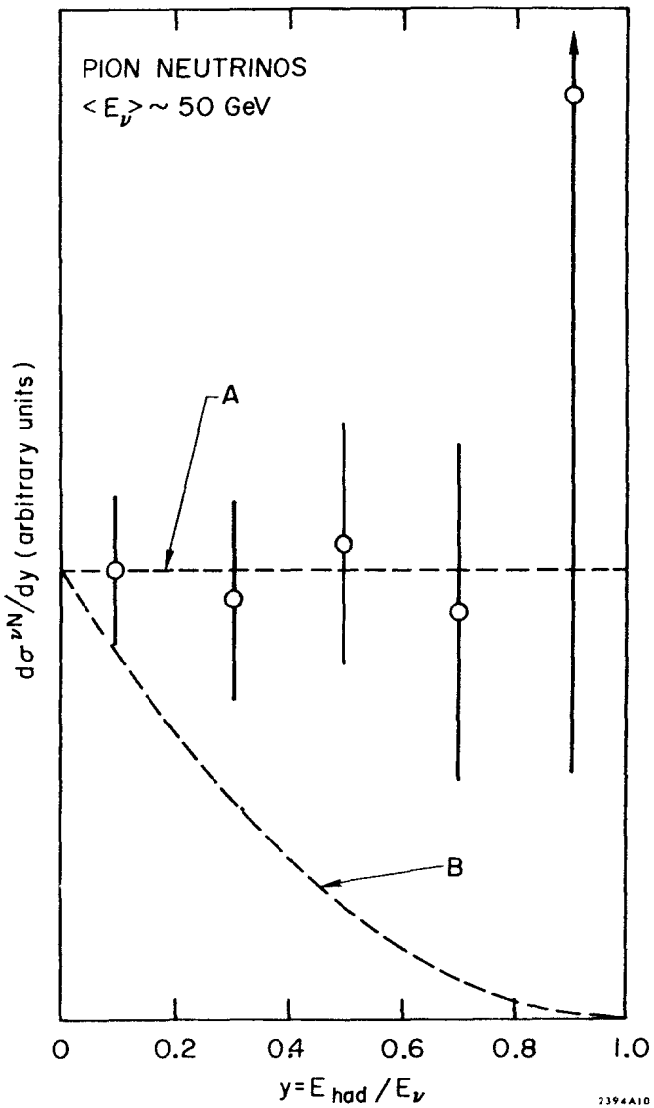
PION NEUTRINOS
<Eν> ~ 50 GeV
dσνN/dy (arbitrary units)
A
B
0
0.2
0.4
0.6
0.8
1.0
y=Ehad/Eν
2394A10

Fig. 10

assuming scaling

$$\frac{d^2\sigma}{dxdy} = \frac{G^2 M E_\nu}{\pi} \quad , \text{ where H (x, y) is separable}$$

and

$$< Q^2 > = 2ME_\nu \frac{\int_0^1 \int_0^1 xy\ H(x,y)}{\int_0^1 \int_0^1 H(x,y)} \tag{20}$$

hence $< Q^2 >$ should rise linearly with E_ν.

H (x, y) has the x, y dependence of the cross section in it and assuming scaling can be quite simply integrated. Upon doing this integration, we find that the slope of the expected line is insensitive to assumptions about the relative magnitudes of the structure functions. In particular assuming $F_1 = F_3 = 0$ gives only ~ 10% variation in the slope from our standard quark model assumptions. Thus this represents a nice test of scaling alone without complications due to not pure V-A etc.

To check whether our data are consistent with this hypothesis and to check our sensitivity to breakdowns of scaling, we again assume our simple quark model

$$\frac{d^2\sigma}{dxdy} = \frac{G^2 M E_\nu}{\pi} \frac{F_2^{ed}(x)}{\left(1 + \frac{Q^2}{\Lambda^2}\right)^2} \tag{21}$$

where the propagator term includes the possibility of a violation of scaling coming for instance from

(a) finite parton size Λ^{-1}

(b) W boson propagator $G \rightarrow \frac{G}{1 + Q^2/M_W^2}$.

In Fig. 11, we show our data split into 3 bins, two for the ν_μ from π decay and one for ν_μ from K decay.

The "expected" curve ($\Lambda^{-1} = 0$) does not rise precisely linearly because our

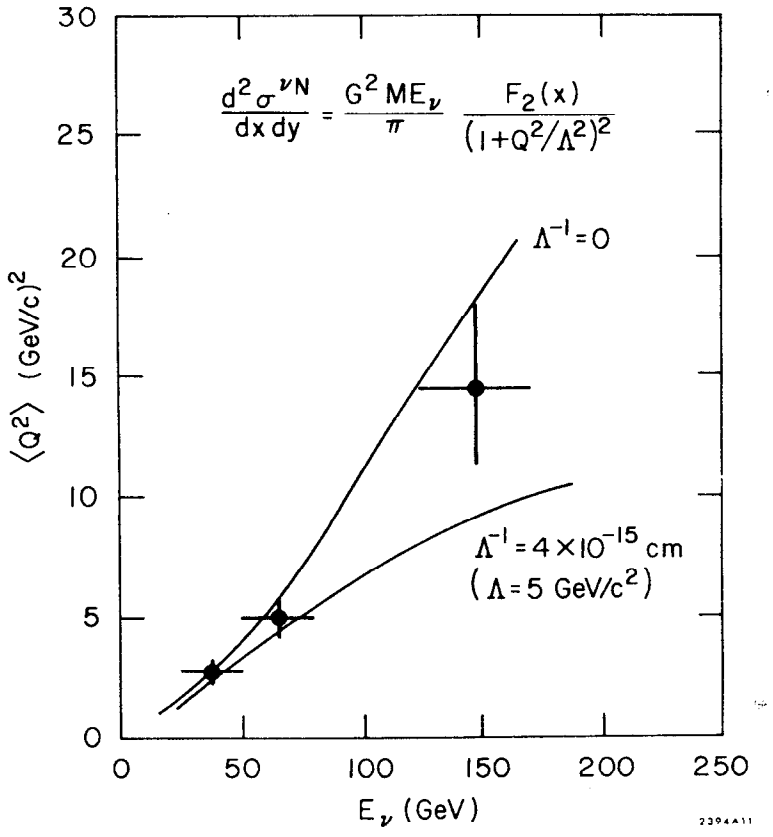

Fig. 11

apparatus does not accept the entire kinematic range with equal efficiency. Also shown is a curve corresponding to a breakdown with $\Lambda^{-1} = 4 \times 10^{-15}$cm.

Summary

The data at $E_\nu = 50$ GeV are qualitatively consistent with expected behavior (quark parton model - no anti-quarks).

The dependence of $< Q^2 >$ on E_ν agrees with scaling down to distances of 4×10^{-15} cm.

QUARKS, PARTONS, TRIALITY, EXOTICS AND COLORED GLUE[†]

Harry J. Lipkin[*]

National Accelerator Laboratory, Batavia, Illinois 60510

and

Argonne National Laboratory, Argonne, Illinois 60439

TOPICAL CONFERENCE ON DEEP INELASTIC SCATTERING
Stanford Linear Accelerator Center
July 16—18, 1973

[†] Work performed under the auspices of the U. S. Atomic Energy Commission.

[*] On leave from Weizmann Institute of Science, Rehovot, Israel.

TABLE OF CONTENTS

I. INTRODUCTION
- 1.1 Who Needs Quarks?
- 1.2 The Nuclear Physics Approach
- 1.3 The Slow-Motion-Strong-Binding Limit
- 1.4 Does the Quark Model Really Predict the Hadron Spectrum?
- 1.5 The Three Puzzles of the Quark Model

II. MODELS WITH EXTRA QUARKS
- 2.1 Color and Charm
- 2.2 The Deuteron World
- 2.3 The Ω^-, With and Without Color

III. THE COLORED GLUON MODEL
- 3.1 A Dynamical Model for the Deuteron World
- 3.2 The Colored Gluon Interaction for Hadrons
- 3.3 Answers to the Triality and Meson-Baryon Puzzles
- 3.4 The Exotics Puzzle—Spatial Properties of Wave Functions

IV. CONCLUSIONS

APPENDIX: Troubles with Parton Models for Inclusive Meson Production

QUARKS, PARTONS, TRIALITY, EXOTICS AND COLORED GLUE

Harry J. Lipkin

I. INTRODUCTION

1.1 Who Needs Quarks?

The quark was invented by Gell-Mann and Zweig to explain certain regularities found in the hadron spectrum and the interactions of hadrons. The spectrum of the observed hadron states was found to consist of multiplets which were described simply in the SU(3) symmetry scheme with indications for possible other higher symmetries such as SU(6) or SU(3) × SU(3). The quark model gave a very simple explanation for the underlying basis of the multiplet structure and symmetry schemes, but left many important questions unanswered, the principal one being why quarks have not yet been observed. For a number of years now the quark model has provided a very good description of many aspects of hadron structure. It continues to be more and more successful as new data are accumulated. However, the fundamental question of why quarks behave this way and yet elude all attempts to find them remains unanswered. There is no argument against saying that the quarks have a very high mass and therefore have not yet been found and that the interactions between them are so strong that they produce bound states whose masses are very much smaller than the quark rest mass. However, it is not satisfying to explain phenomena which we do not understand by postulating the existence of a model which cannot be checked directly by experiment even though this model may ultimately turn out to be correct.

A new impetus has been given to the quark model by the experimental discovery of scaling in deep inelastic lepton scattering. The fact that scattering cross sections in the so-called deep inelastic region depend only on dimensionaless combinations of kinematic variables and not on any parameter with the dimensions of mass which sets the scale has suggested the parton model in which hadrons are composed of point-like constituents that have no scale. It is tempting to identify these constituents of the parton model with quarks, but it soon becomes clear that they are not exactly the same. Today it is fashionable to talk about "constituent quarks" and "current quarks,"[1—3] and to avoid any commitment to either as real physical particles which may be discovered some day.

There is no difficulty in principle in postulating that hadrons are made of particles that have not yet been discovered. There is a difficulty in practice; namely keeping theorists honest. As long as quarks have not been observed, the theorists are free to endow them with any properties they wish without fear of being contradicted by experiment. But freedom to choose quark properties means effectively that any quark model has a large number of adjustable parameters. With enough adjustable parameters one can fit everything and predict nothing. So in this game you have to be careful and think about what you are doing. There is no substitute for using your head.

1.2 The Nuclear Physics Approach

We shall try to stay honest by using the approach of nuclear physics.[4] The nuclear physicists consider the nucleus ^{17}O as consisting of a valence neutron and a closed shell ^{16}O core. Electromagnetic transitions between low-lying states of ^{17}O are described in terms of transitions of the valence neutron between different orbits. From the experimental transition probabilities the properties of the valence neutron are calculated, and the neutron is found to have an "effective charge" between 0 and 1. Nobody believes that this is the charge of the free neutron. Clearly a complete description of the transition involves the ^{16}O core as well as the valence neutron. But the fact that these 17 particles "conspire" to make transitions behave as if they were produced by a single nucleon having an effective charge is a useful way to parametrize the data and

give physical insight. A more fundamental treatment is then given with an intuition borrowing concepts from field theory and quantum electrodynamics. The ^{16}O core is analogous to the vacuum, which can be "polarized" by the external particle to "renormalize" its charge. A useful concept is that of a "quasi-particle"[5] to describe excitations of complicated systems which appear to be single particle excitations, whereas in reality they are something much more complicated.

By analogy with valence nucleons in nuclei which have effective charges, interactions, form factors, scattering amplitudes, etc. which are very different from those of free nucleons, we can think of valence quarks in hadrons whose properties are very different from those of free quarks (if they exist). Many properties of the low-lying hadron spectrum can be interpreted in terms of these fictitious valence quarks, whose properties are determined to fit hadron data, and have no relation to properties of "real quarks." We can also think of free quarks, which may or may not be observable in nature, but which determine in some way the couplings of the electromagnetic and weak currents to hadrons. These free quarks can be used in current algebra, light cone algebra or parton model treatments of electromagnetic and weak processes under the assumption that the couplings of the currents to these quarks is well defined. These are the "current quarks." The wave function of the hadron in terms of these quarks is unknown and very complicated, like the exact nuclear wave function in terms of real nucleons. In the valence or "constituent" quark description, the hadron wave functions are simple and well known, but the nature of the quarks and their couplings, form factors, etc. are unknown phenomenological parameters which must be determined from the data. Their fundamental significance is very unclear, like that of the effective charge of the valence neutron in ^{17}O.

1.3 The Slow-Motion-Strong-Binding Limit

In our consideration of the old applications of the valence or constituent quark approach we use the slow-motion-strong-binding model of Amnon Katz[6] as a guide to the intuition. This model considers a two-body system in relativistic classical mechanics and shows that it is perfectly reasonable for it to be bound with a binding energy nearly equal to the rest mass of its constituents. The internal motion of the particles is described by nonrelativistic equations. The center-of-mass motion (and also the interaction with a weak gravitational field) is described by a mass parameter which is just what is expected from naive considerations, the difference between the sum of the rest masses of the constituents and the binding energy. This mass can be as low as one pleases without causing difficulties. However, the nonrelativistic internal motion is described by a mass parameter which depends upon the interactions. It is no longer the simple "reduced mass" of nonrelativistic two-body problems and can be anything from the order of the mass of the constituents to the mass of the bound state. Thus measurements on the bound system only can tell us this "effective reduced mass," and give no information on the mass of the free particle.

Similar conclusions are obtained from a quantum-mechanical treatment using the Dirac equation for a single particle in an external potential.[2] The relativistic two-body problem with strong-binding is outside the competence of theoretical physics at present. But since the slow-motion-strong-binding limit exists and has the same intuitively attractive features both in the classical relativistic two-body problem and in the quantum relativistic one-body problem with external fields, it seems reasonable to use it as a basis for intuition in our nuclear physics approach to valence quarks.

1.4 Does the Quark Model Really Predict the Hadron Spectrum?

In this talk we consider the unanswered puzzles posed by one of the outstanding "successes" of the quark model, the prediction of the hadron spectrum. The empirical rule that all observed hadron bound states and resonances have the quantum numbers found in the three-quark and quark-antiquark systems is in remarkable agreement with experiment. Since no alternative explanation or description has been given for this striking regularity in the hadron spectrum, this rule may constitute

evidence for taking quarks seriously. However, there has been no success in giving any explanation for this empirical rule. Why only 3q and $q\bar{q}$? Why not other configurations? I shall present an answer to this question in the framework of the simple minded nuclear physics approach to quarks. What exactly this answer means is not clear. But so far it provides the only answer to this question that has been proposed. That the question has an answer at all in any framework is interesting in itself, particularly since so far there are no other answers.

The quark model also predicts the energy level spectrum of the states constructed from the three-quark and quark-antiquark systems and observed experimentally as hadron resonances. These predictions also seem to be in reasonable agreement with experiment, but pose additional questions. To obtain agreement with the observed baryon spectrum, the symmetric quark model[7] must be used, which restricts the allowed states of the three-quark system to those being totally symmetric under permutations in the known degrees of freedom rather than totally antisymmetric, as one expects for fermions. This implicitly assumes that quarks obey peculiar statistics, or that there is a hidden degree of freedom sometimes called "color." The low-lying meson spectrum shows all the states "predicted by the quark model" without any supplementary conditions. All the states of the quark-antiquark system appear as meson resonances; there are no predicted states which are conspicuously absent.

In this talk we shall question the apparent success of the predictions of the spectrum. There is an inconsistency between the observation of bound states in all channels for $q\bar{q}$ scattering and the absence of bound states with quantum numbers of $2q\bar{q}$ and $3q\bar{q}$. If the quark-antiquark interaction is attractive in all possible channels, as indicated by the presence of bound states, an antiquark should be attracted by any composite state containing only quarks, like a diquark or a baryon, to make a bound state with quantum numbers which have not been observed. We suggest in this work that the only simple way to avoid this difficulty is to discard an apparent success of the quark model and to use the colored quark models which predict states for the $q\bar{q}$ system that are not observed as resonances.

In our discussion, we assume that quarks are very heavy, and we consider only effects on the mass scale of the quark mass. All observed particles have zero mass on this scale. The observed hadron spectrum is a "fine structure" which we are unable to resolve in this approximation. This is a reasonable approach, since as long as we are not treating spin in detail, we are unable to distinguish between a pion and a ρ meson, and are neglecting mass splittings of the order of the ρ-π mass difference. We therefore are only able to discuss whether a particle has "zero mass" and appears as an observed hadron, or whether it has a mass of the order of the quark mass and should not have been observed.

1.5 The Three Puzzles of the Quark Model

The question why only 3q and $q\bar{q}$ can be stated more precisely in terms of the following three puzzles:

1. The triality puzzle: With attractive interactions between quarks and antiquarks, why are three quarks and an antiquark not bound more strongly than a baryon or two quarks and an antiquark bound more strongly than a meson? Note that we are not asking about four quarks vs. three quarks. Symmetry restrictions, such as the Pauli principle with colored quarks can prevent the construction of a four quark state which is totally symmetric in space, spin and unitary spin. But there is no Pauli principle which prevents an antiquark from being added to a system of three quarks in all possible states. Thus if each quark in the baryon attracts the antiquark, some additional mechanism must be found to prevent it from being bound to the quark system.

2. The exotics puzzle: Even assuming some mysterious symmetry principle which prevents fractionally charged states from being seen, why are there no strongly bound states of zero triality, like those of two quarks and two antiquarks or four quarks and one antiquark? Note

that we are not discussing the Rosner exotics[9] which are baryon-antibaryon resonances decoupled from the two meson system. We are discussing states like an I = 2 dipion resonance or bound state with a mass near the mass of two pions. If the quarks and antiquarks in two pions attract one another, why is there no net attraction between two positive pions to produce a bound state or a resonance very near threshold?

3. The diquark or meson-baryon puzzle: Why is the quark-quark interaction just enough weaker than the quark-antiquark interaction so that diquarks near the meson mass are not observed, but three-quark systems have masses comparable to those of mesons? Vector gluons which are popular these days would bind the quark-antiquark system, but the force they provide between identical quarks is repulsive. Scalar or other gluons which are even under charge conjugation bind both the quark-antiquark and diquark systems equally. If the quark mass is very heavy, the single quark-antiquark interaction in a meson must cancel two quark masses, while the three quark-quark interactions in the baryon must cancel three quark masses. This suggests that the quark-quark interaction is exactly half the strength of the quark-antiquark interaction.[2] Such a result can be achieved by a suitable mixture of vector and scalar interactions, but it is not very satisfying to obtain such a simple fundamental property of hadrons by a model which fits it with an adjustable parameter.

In all of this discussion, we are considering one-particle states, with the assumption that multiparticle states exist which contain separated particles each having the properties we are trying to explain. Multiparticle states pose additional problems. The allowed spectrum for multiparticle states is not specified by a set of allowed quantum numbers, but by the condition that their constituent particles individually have allowed quantum numbers. Thus the puzzles cannot be answered by general symmetry principles which apply to all states. The triality puzzle is not answered by a symmetry principle forbidding all states which do not have zero triality, because multiparticle states of zero triality must also be forbidden if they are made of particles which individually have nonzero triality. Similarly, the exotics puzzle is not answered by a symmetry principle forbidding all states with exotic quantum numbers because multiparticle exotic states made from nonexotic particles are allowed. Thus any treatment which attempts to answer these puzzles must discuss both single-particle and multiparticle states, and must consider the space-time properties which distinguish between them. Algebraic arguments involving only internal symmetry groups cannot be sufficient.

II. MODELS WITH EXTRA QUARKS

Before considering these puzzles in detail, we review the modified quark models which consider the introduction of additional quark states.

2.1 Color and Charm

In the Gell-Mann-Zweig quark model hadrons are constructed from three quarks which form an SU(3) triplet. Other models with additional quarks have been proposed, primarily for theoretical reasons. Since the GMZ triplet is already sufficient to describe all the known conserved quantum numbers and gives an adequate description of the hadron spectrum (except for a possible difficulty with statistics in the baryons), any additional building block introduces new internal quantum numbers and new degrees of freedom which have not yet been observed, as well as new particle states. All such models require some excuse for throwing these extras away, either by postulating that they are simply not there, or by implying that extra states have a very high mass like the quarks themselves and may be observed at some time in the future.

The additional quarks introduced are of two types, which have been called "charmed" quarks and "colored" quarks. Charmed quarks are simply added to the GMZ triplet to make a total of n quarks and a symmetry SU(n) which includes SU(3) as a subgroup. All the new charmed quarks are singlets in the conventional SU(3). The number of charmed quarks defines a new conserved quantity called charm, analogous

to strangeness which is the number of strange quarks. Since no charmed hadrons or hadrons containing charmed quark-antiquark pairs have yet been observed, the charmed quarks are assumed to have a mass sufficiently higher than the conventional triplet so that bound states containing them have a high production threshold.

Colored quarks are sets of n SU(3) triplets, to give a total of 3n quarks. All the new quarks are SU(3) triplets, and the degree of freedom which distinguishes between the different triplets has been recently given the name of "color."

The three-triplet model, originally suggested to allow the three quarks in a baryon to have a symmetric wave function without violating Fermi statistics,[7] is now called a model with "red, white and blue" triplets. For those who find this American chauvinism distasteful, we recommend the "Equal Opportunity Quark Model" (EOQM) which has equal representation of black, white and yellow quarks.

A symmetry group SU(3n) can be defined which treats all quarks on an equal footing. This has a subgroup $SU(3) \times SU(n)_{color}$. There is no evidence for the rich hadron spectrum corresponding to the presence of states classified in nontrivial representations of $SU(n)_{color}$. The observed hadrons are assumed to belong to the trivial singlet representation of SU(n) and "color excitations" of higher representations are either postulated not to exist or are assumed to have a high mass. The color-excited states are sometimes also called charmed states, but there is a definite physical difference between these two types of nonobserved states. The charmed states discussed above contain charmed quarks which are different from those in the observed hadron states. The color-excited states contain exactly the same colored quarks as the observed hadrons, they differ only in having a different permutation symmetry in the space of the colors. Thus charmed states can be pushed up in mass by simply postulating a higher mass for charmed quarks. Color excitations can be pushed up only by having the interaction between quarks depend on the permutation symmetry in color-space since different colored quarks all have the same mass.

In colored quark models, the color may or may not be directly observable. In models where color is not observable, all quarks which differ only in color and otherwise have the same quantum numbers must have the same properties. In other models quarks of different colors have different observable properties, e.g., different electric charges. This possibility has been used to construct models with quarks of integral electric charges. Such integrally-charged colored quarks cannot satisfy the Gell-Mann-Nishijima relation and must have nonzero eigenvalues of a new additive quantum number which appears in the modified Gell-Mann-Nishijima formula. The electromagnetic current then has a component which is an SU(3) singlet and which is not a singlet in $SU(n)_{color}$.

The most recent theoretical models using charmed or colored quarks have been in gauge theories of electromagnetic and weak interactions.[10] These models use symmetries to provide selection rules against undesired weak transitions, such as those due to neutral currents in first or second order. These symmetries are incompatible with SU(3) and a higher symmetry is required to incorporate both SU(3) and the weak interaction symmetry. The higher symmetry requires extra quarks. The suppression of undesired second order transitions is achieved by a cancellation in which unobserved charmed or color-excited intermediate states play a crucial role. These cancellations can occur only if the dominant contribution comes from intermediate states having a much higher energy than the excitation energy of the unobserved states. Thus these models can place upper limits on the excitation energies of these states which can be tested by experiment.

In this talk, we are concerned primarily with the strong interactions which do not depend upon the couplings of quarks to the electromagnetic and weak currents. We therefore do not need to distinguish

between models with color-independent fractional charges and models with color-dependent integral charges (e.g., Han-Nambu[11]), since they can have identical strong interactions.

2.2 The Deuteron World

Some insight into the colored quark models is given by the analogy of a world in which all low-lying nuclear states are made of deuterons and have isospin zero; free nucleons have not yet been seen and experiment has not yet attained energies higher than the deuteron binding energy or the symmetry energy required to excite the first I = 1 states. In this isoscalar world where all observed states have isospin zero the isovector component of the electromagnetic current would not be observed since it has vanishing matrix elements between isoscalar states. The deuteron energy level spectrum (something like that of a diatomic molecule) would indicate that the deuteron was a two-body system, but there would be no way to distinguish between the neutron and the proton. The deuteron would thus appear to be composed of two identical objects which might be called nucleons. Since the deuteron has electric charge +1, the nucleon would be assumed to have electric charge +1/2. Furthermore, the nucleon would be observed to have spin 1/2 and be expected to satisfy Fermi statistics. However, the ground state of the deuteron and all other observed states would be found to be symmetric in space and spin. Thus, the nucleon would appear to be a spin 1/2 particle with fractional electric charge and peculiar statistics.

Some daring theorists might propose the existence of a hidden degree of freedom expressed by having nucleons of two different colors. There would be a hidden SU(2) symmetry (which might be called isospin) to transform between the two nucleon states of different colors. All the observed low-lying states would be singlets in this new color (or isospin) SU(2). Since the color singlet state of the two-particle system is antisymmetric in the color degree of freedom, the Pauli principle requires the wave function to be symmetric in space and spin, thus solving the statistics problem.

2.3 The Ω^-, With and Without Color

The direct analog of this deuteron problem in hadron quark models is the quark model for the Ω^-. In the conventional quark model, the Ω^- consists of three identical strange quarks (called λ-quarks by some people and s-quarks by others), with their spins of 1/2 coupled symmetrically to spin 3/2. Since the electric charge of the Ω^- is -1, the strange quark is required to have charge -1/3, and it is also required to have peculiar statistics because the system of three identical particles has a symmetric wave function in all known degrees of freedom. Some daring theorists have therefore proposed the existence of a hidden degree of freedom expressed by having strange quarks of three different colors,[7] and a hidden SU(3) symmetry to transform between the three strange quark states of different colors. All the observed low-lying states are singlets in this $SU(3)_{color}$ group. Since the color-singlet state of the three-particle system is antisymmetric in the color degree of freedom, the Pauli principle requires the wave function to be symmetric in the other degrees of freedom, in agreement with experiment and ordinary Fermi statistics. It is also possible to give these colored strange quarks different integral electric charges, one with charge -1 and two neutrals, by analog with the nucleons in the deuteron. However, as we are concerned primarily with strong interactions, we need not choose between models having different electric charges for colored quarks.

We have chosen the example of the Ω^- for this discussion to simplify the treatment of the conventional SU(3) degree of freedom by considering only strange quarks. When the full triplet of conventional SU(3) is considered, there are three colors for nonstrange as well as for strange quarks, and nine quarks altogether. There are two SU(3) groups, the conventional isospin and hypercharge SU(3) and the color SU(3), which are combined into the direct product $SU(3)_{I,Y} \times SU(3)_{color}$.

III. THE COLORED GLUON MODEL

We now return to the three puzzles. In the colored quark description of hadrons the restriction that only color singlet states are observed immediately solves the triality puzzle, since only states of zero triality can be color singlets. But requiring all low-lying states to be color singlets is thus equivalent to requiring all low-lying states to have zero triality; it merely replaces one ad hoc assumption with another. What is needed is some dynamical description in which the color singlets turn out to be the low-lying states in a natural way. To attack this problem we return to the fictitious deuteron world where all low-lying states are isoscalar and which is the analog of the colored quark description of hadrons. We follow the treatment of ref. 8.

3.1 A Dynamical Model for the Deuteron World

At first this isoscalar deuteron world seems very artificial. Why should all states with I = 0 be pushed down and all states with I ≠ 0 be pushed up out of sight? But there turns out to be a very natural nuclear interaction which creates exactly this isoscalar deuteron world; namely nuclear two-body forces dominated by a very strong Yukawa interaction provided by ρ exchange. This interaction is attractive for isoscalar states and repulsive for isovector states, in both nucleon-nucleon and nucleon-antinucleon systems. It thus binds only isoscalar states. The ρ-exchange interaction between particles i and j can be expressed in the form

$$v_{ij} = V \vec{t}_i \cdot \vec{t}_j, \tag{1a}$$

where $\vec{t}_i$ is the isospin of particle i and V contains the dependence on all other degrees of freedom except isospin. If we neglect these other degrees of freedom we can write for any n-particle system containing antinucleons and nucleons,

$$V(n) = \frac{1}{2}\sum_{i\neq j} v_{ij} = \frac{1}{2}\left[\sum_{\substack{\text{all}\\ij}} v\vec{t}_i \cdot \vec{t}_j - \sum_i V \vec{t}_i \cdot \vec{t}_i\right] = \frac{V}{2}[I(I+1) - nt(t+1)] \tag{1b}$$

where I is the total isospin of the system and t is the isospin of one particle; i.e., 1/2 for a nucleon.

The interaction (1b) is seen to be repulsive for the two-body system with I = 1 and attractive for all isoscalar states. A pair of particles bound in the I = 0 state is thus seen to behave like a neutral atom; it does not attract additional particles. Since the pair is "spherically symmetric" in isospace, a third particle brought near the pair sees each of the other particles with random isospin orientation, and its interaction with any member of the pair is described by the average of (1a) over a statistical mixture which is 3/4 isovector and 1/2 isoscalar. This average is exactly zero.

The neutral atom analogy is very appropriate for the description of the observed properties of hadrons. The forces between neutral atoms are not exactly zero, but are much weaker than the forces which bind the atom itself. These interatomic forces produce molecules which are much more weakly bound than atoms. Similarly the forces between hadrons do not vanish but are much weaker than the forces which bind the hadron itself. These interhadronic forces produce complex nuclei which are much more weakly bound than hadrons. In the approximation where we neglect energies much smaller than the quark mass these "molecular" effects are safely neglected.

3.2 The Colored Gluon Interaction for Hadrons

We now generalize this picture for the colored quark description of hadrons. If there are n colors, the interaction (1) must be generalized from SU(2) to SU(n). The quark-antiquark system then still saturates at one pair, but the multiquark system can be seen to saturate at n quarks. A quark-antiquark system which is a singlet in SU(n) exists for all values of n. However, the existence of a singlet in the two-quark system is an accident which occurs only in SU(2) and is not generalizable

to SU(n). However the I = 0 two-quark state is also characterized as antisymmetric under permutation of the two particles. This antisymmetry is generalized easily to SU(n) where totally antisymmetric states exist for a maximum of n particles, and the n particle antisymmetric state is a singlet in SU(n).

We now construct the analog of the interaction (1b) for a model with three triplets of different colors. Then the Yukawa interaction produced by the exchange of an octet of "colored gluons" has the form analogous to (1). For an n-particle system containing both quarks and antiquarks,

$$U(n) = \frac{1}{2} \sum_{i \neq j} u_{ij} \sum_{\sigma} g_{i\sigma} g_{j\sigma} \qquad (2)$$

where u_{ij} depends on all the noncolor variables of particles i and j and $g_{i\sigma}$ ($\sigma = 1, \ldots, 8$) denote the eight generators of $SU(3)_{color}$ acting on a single quark or antiquark i.

If the dependence of u_{ij} on the individual particles i and j is neglected, the interaction energy of an n-particle system can be calculated by the same trick used in eq. (1b) to give

$$V(n) = \frac{u}{2}(C - nc) \qquad (3a)$$

where u is the expectation value of u_{ij}, integrated over the noncolor variables, C is the eigenvalue of the Casimir operator for $SU(3)_{color}$ for the n-particle system and c = 4/3 is the eigenvalue for a single quark or antiquark. These eigenvalues are directly analogous to the SU(2) Casimir operator eigenvalues I(I + 1) and t(t + 1) in eq. (1b).

In the approximation where all energies small compared to the quark mass M_q are neglected, the interaction (3a) gives the mass formula

$$M(n) = nM_q + V(n) = n(M_q - \frac{cu}{2}) + Cu/2. \qquad (3b)$$

The interaction (2) and the mass formula (3b) were first proposed by Nambu,[13] and the saturation properties of the interaction were considered by Greenberg and Zwanziger.[14] However, the remarkable properties of this interaction as demonstrated above in the simplified example of the analogous deuteron world have received little attention.

3.3 *Answers* to the Triality and Meson-Baryon Puzzles

The formula (3b) can test the triality puzzle or the meson-baryon puzzle by showing whether observable "zero mass" hadron states exist for a given number of quarks and antiquarks. However, it cannot test the exotics puzzle, since it gives no information about the spatial properties of the states. It cannot distinguish between one-particle states and multiparticle scattering states and all zero-triality exotic states are allowed as multiparticle states.

Since C is positive definite and has the eigenvalue zero only for a singlet[8] in $SU(3)_{color}$, and $u \geq 0$ as is evident from the two-body system, the state of the n-particle system with the strongest attractive interaction is a color singlet. Since the interaction is a linear function of n all such singlet states have zero mass if $cu/2 = M_q$. For this case

$$M(n) = (C/c)M_q \quad \text{if } cu/2 = M_q. \qquad (3c)$$

The model thus gives observable hadron states for all quark and antiquark configurations for which C = 0 states exist. Since C = 0 states exist only for configurations of triality zero, this answers the triality puzzle.

The meson-baryon puzzle is also answered by this interaction, since zero mass is attained both in two-body and three-body systems. To obtain C = 0, the two-body system must be a quark-antiquark pair, while the three-body system must be a three quark state, totally antisymmetric in color space. The approximation of neglecting the dependence of u_{ij} on i and j is justified in these two cases since there is only one pair in the two-body system, and a totally antisymmetric function has the same wave function for all pairs. The values[8] of the interaction parameter C-nc and

the mass parameter C/c are listed in Table I for all states of the two-body system. These show that the quark-quark interaction in the baryon is exactly half of the quark-antiquark interaction in the meson, as required for the meson-baryon puzzle. The diquark mass is thus equal to one quark mass, since its interaction only cancels the mass of one of the two quarks.

TABLE I

Values of the Interaction and Mass Parameters C-nc and C/c

System	$SU(3)_{color}$ Representation		C	C-nc	C/c
quark-quark	triplet	(antisymmetric)	4/3	-4/3	1
quark-quark	sextet	(symmetric)	10/3	+2/3	5/2
quark-antiquark	singlet		0	-8/3	0
quark-antiquark	octet		3	+1/3	9/4

The interaction averaged over all quark-quark states is seen to be zero and similarly for all quark-antiquark states. An antiquark or quark added to a meson or baryon thus has a zero net interaction, as there can be no color correlations between particles in a singlet state and an external particle, and each pair f els the average interaction over all color states. This suggests that the exotics puzzle is also answered, and that the states of zero mass obtained fr in the interaction (2) for exotic quantum numbers are multiparticle continuum states rather than bound states or resonances.

3.4 The Exotics Puzzle—Spatial Properties of Wave Functions

To examine the exotics puzzle in more detail we consider the spatial dependence of the interaction (2) for the specific case of the two-quark-two-antiquark system, with an interaction u_{ij} depending only on the positions of the particles and not on momenta, spin and unitary spin. In the representation with the coordinates $\vec{r}_i$ of the four particles diagonal, the interactions u_{ij} are also diagonal and can be treated as c-numbers. In this representation the interaction (2) is a 2 × 2 matrix in color space as there are two independent couplings for four particles to a color singlet.

We diagonalize this 2 × 2 matrix to obtain two functions of the coordinates $\vec{r}_i$ which describe the spatial dependence of the interaction in its two color eigenstates.

It is convenient to choose a nonorthogonal basis, related by permutations, which displays quark-antiquark couplings to C = 0,

$$|\alpha\rangle \equiv |(13)_1(24)_1\rangle \tag{4a}$$

$$|\beta\rangle \equiv |(14)_1(23)_1\rangle \tag{4b}$$

where particles 1 and 2 are quarks, 3 and 4 are antiquarks and $(ij)_1$ denotes that particles i and j are coupled to C = 0. Several useful identities follow from the properties of the C = 0 two-particle state.

$$\langle\alpha|\beta\rangle = 1/3 \tag{5a}$$

$$\sum_\sigma g_{1\sigma}g_{3\sigma}|\alpha\rangle = \sum_\sigma g_{2\sigma}g_{4\sigma}|\alpha\rangle = -(8/3)|\alpha\rangle \tag{5b}$$

$$\sum_\sigma g_{1\sigma}g_{4\sigma}|\beta\rangle = \sum_\sigma g_{2\sigma}g_{3\sigma}|\beta\rangle = -(8/3)|\beta\rangle \tag{5c}$$

$$(g_{1\sigma}+g_{3\sigma})|\alpha\rangle = (g_{2\sigma}+g_{4\sigma})|\alpha\rangle = (g_{1\sigma}+g_{4\sigma})|\beta\rangle = (g_{2\sigma}+g_{3\sigma})|\beta\rangle = 0 \tag{5d}$$

$$\langle\alpha|g_{1\sigma}g_{4\sigma}|\alpha\rangle = \langle\beta|g_{1\sigma}g_{3\sigma}|\beta\rangle = 0 \tag{5e}$$

$$\langle\alpha|g_{1\sigma}g_{4\sigma}|\beta\rangle = \langle\beta|g_{1\sigma}g_{3\sigma}|\alpha\rangle = -(8/3)\langle\alpha|\beta\rangle = -8/9. \tag{5f}$$

By operating with the interaction (2) on the wave functions (4) and eliminating the color variables with the aid of the identities (5) we obtain

$$-3U|\alpha\rangle = (8u_\alpha - u_\beta + u_q)|\alpha\rangle + 3(u_\beta - u_q)|\beta\rangle \tag{6a}$$

and

$$-3U|\beta\rangle = 3(u_\alpha - u_q)|\alpha\rangle + (8u_\beta - u_\alpha + u_q)|\beta\rangle \tag{6b}$$

where

$$u_\alpha = u_{13} + u_{24};\quad u_\beta = u_{14} + u_{23};\quad u_q = u_{12} + u_{34}. \tag{7}$$

Solving the secular equation for eqs. (6) gives the eigenvalues for U,

$$U' = -(7/6)(u_\alpha + u_\beta) - (1/3)u_q \pm (1/2)\sqrt{8(u_\alpha - u_\beta)^2 + (u_\alpha + u_\beta - 2u_q)^2}. \quad (8)$$

If u_{ij} is a finite range potential which vanishes at large distances, the eigenvalues (8) reduce to those for two independent two-particle clusters for all values of the coordinates $\vec{r}_i$ which correspond to two pairs separated by a distance greater than the range of the potential. The case $u_\beta = u_q = 0$ describes such a separation between the pairs of particles (13) and (24). The corresponding eigenvalues from eq. (8) are $U' = -(8/3)u_\alpha$ and $U' = +(1/3)u_\alpha$ exactly those of Table I for two separated quark-antiquark pairs in the singlet and octet states. The case $u_\alpha = u_\beta = 0$ describes separated pairs of like particles (12) and (34) and has eigenvalues $U' = -(3/4)u_q$ and $U' = +(2/3)u_q$ exactly those of Table I for two separated quark-quark and antiquark-antiquark systems in the triplet and sextet states.

To test the exotics puzzle we look for coordinate configurations where four-particle correlations may give stronger binding than in two noninteracting clusters. Since u_α and u_β appear symmetrically in (8), we need only consider values of $u_\beta \leq u_\alpha$. For any value of u_α the value of $u_\beta \leq u_\alpha$ which minimizes the interaction (8) is $u_\beta = u_\alpha$ with the negative sign for the square root. This gives

$$U' = -(8/3)u_\alpha - (2/3)(u_\alpha - u_q). \quad (9)$$

This expression is minimized by choosing the minimum value of u_q consistent with a given value of u_α. For monotonically decreasing potentials this is achieved by placing the four particles at the corners of a square with the like particles at opposite diagonals.

For a square well potential the particles can be arranged in a square with the diagonal greater than the range of the forces and the sides less than the range. This configuration has $u_q = 0$ and forms a stable four-particle state with a binding 25% greater than that of two quark-antiquark pairs. However, the sharp edge of the square well is essential for this binding and does not seem reasonable physically. For smooth potentials without sharp edges such as Gaussian, Yukawa or harmonic oscillator potentials eq. (9) shows that such a four-particle cluster is less strongly bound than two noninteracting quark-antiquark pairs, and the system simply breaks up into two clusters. This leads to a description in which all states having exotic quantum numbers are just scattering states of particles which individually have nonexotic quantum numbers, and answers the exotics puzzle.

IV. CONCLUSIONS

An important conclusion from this discussion, irrespective of the validity of the colored gluon model, is that of the crucial role played by repulsive forces and the extra color degree of freedom in finding answers to the three puzzles. The conventional quark model has observed mesons in all states that can be constructed from a quark-antiquark pair. This has been hailed as a great success of the quark model. But perhaps this is not a success but a failure. With bound states in all channels the quark-antiquark force is required to be attractive in all channels and cannot prevent an antiquark from being bound to a baryon. With dominant two-body forces and no adhoc three-body forces, antiquark-baryon binding will occur unless the quark-antiquark interaction is repulsive in many states and repulsion dominates the antiquark-baryon interaction for all possible states of the antiquark. These many repulsive channels are provided in the three-triplet model which has 81 $q\bar{q}$ states where only nine are observed. The absence of the other 72 "charmed" states should not be held against the model, as repulsive quark-antiquark forces in all charmed channels not only explain this absence but also provide the necessary repulsion to explain the absence of all $3q\bar{q}$ bound states.

In the conventional quark model, vector gluons cannot bind both mesons and baryons, because the vector interaction between identical particles is repulsive and cannot bind states like the Ω^-, Δ^{++} and Δ^-

composed of three identical quarks. In the three-triplet model, the three quarks in each of these hadrons are no longer identical while all states containing three identical quarks are "charmed states" and should have a high mass. Thus repulsion between identical quarks is actually desired in the three-triplet model and there is no objection to vector gluons.

In the three-triplet model "color" correlations absent in the conventional quark model increase binding and help in saturation. The quantum numbers of individual bound quarks are not fixed; they change in a correlated way as a result of exchange forces. With Nambu's interaction[13] the two-body forces are attractive in certain color correlated states, while the interaction in an uncorrelated state (averaged over color) is zero, as repulsions and attractions cancel exactly. A color singlet state thus behaves like a neutral atom. There are no color correlations between an external particle and a quark in a color singlet and the interactions cancel.

The three-triplet model with colored vector gluon binding gives a good description of those dominant features of the hadron spectrum expected in zero order: namely that only the quark-antiquark and three-quark systems appear as bound states with a mass of approximately zero on the scale of the quark mass. This is in contrast with other models whose zero order results are in violent disagreement with experiment. These are unable to explain the three puzzles discussed in this paper, and can only hope that a better theory makes the puzzles go away. Further refinements in the description of the hadron spectrum can be expected in the framework of the three-triplet vector-gluon model by considering higher order effects, such as the additional phenomenological potentials commonly used[15] to calculate the hadron spectrum. These are entirely consistent with the three-triplet model since the symmetric quark model[7] is commonly used in all treatments for baryons. The three-triplet model should therefore be considered very seriously as an alternative to the single-quark model.

APPENDIX

Troubles with Parton Models for Inclusive Meson Production

This point was raised during the talk and is added here.

It is very tempting to make models for inclusive meson production in which a quark finds an antiquark partner and the two escape as a meson.[16] But the spins of the quarks cannot simply be ignored. If there are no spin correlations between the quark and antiquark, a quark-antiquark pair has a 75% probability of being in the triplet spin state and only a 25% probability of being in the singlet spin state. The triplet state is a meson resonance, which then decays to produce two or more pseudoscalar mesons. The singlet state can either be a pseudoscalar meson or a higher meson resonance. Thus at least three meson resonances are produced for every directly produced pseudoscalar meson and pseudoscalar meson production via resonance decay is at least six times greater than direct production. Kinematic factors may discriminate against resonance contributions because of the higher masses of resonances and because the resonance decay products individually have lower momenta than a directly produced meson. But it is clearly very risky to overlook resonance contributions. Any model which considers only direct production of pseudoscalar mesons must be viewed with suspicion.

As an example, consider the production of kaons and pions both directly and via decays of the vector nonet and the η. There is no obvious reason for leaving out tensor and higher mesons, but their presence can only make matters worse. Let $\hat{\sigma}(M)$ denote the cross section for the direct production of meson M and $\sigma(M)$ denote the total cross section which includes production via resonance decays. Then

$$\sigma(K^+) = \hat{\sigma}(K^+) + \frac{1}{3}\hat{\sigma}(K^{*+}) + \frac{2}{3}\hat{\sigma}(K^{*0}) + \frac{1}{2}\hat{\sigma}(\phi) \qquad \text{(A1a)}$$

$$\sigma(K^0) = \hat{\sigma}(K^0) + \frac{2}{3}\hat{\sigma}(K^{*+}) + \frac{1}{3}\hat{\sigma}(K^{*0}) + \frac{1}{2}\hat{\sigma}(\phi) \qquad \text{(A1b)}$$

$$\sigma(K^-) = \hat{\sigma}(K^-) + \frac{1}{3}\hat{\sigma}(K^{*-}) + \frac{2}{3}\sigma(\bar{K}^{*0}) + \frac{1}{2}\hat{\sigma}(\phi) \qquad \text{(A1c)}$$

$$\sigma(\bar{K}^0) = \hat{\sigma}(\bar{K}^0) + \frac{2}{3}\hat{\sigma}(K^{*-}) + \frac{1}{3}\sigma(\bar{K}^{*0}) + \frac{1}{2}\hat{\sigma}(\phi) \quad \text{(A1d)}$$

$$\sigma(\pi^+) = \hat{\sigma}(\pi^+) + \hat{\sigma}(\rho^+) + \hat{\sigma}(\rho^0) + \hat{\sigma}(\omega) + x\hat{\sigma}(\eta) + \frac{2}{3}\hat{\sigma}(K^{*+}) + \frac{2}{3}\hat{\sigma}(\bar{K}^{*0}) \quad \text{(A2a)}$$

$$\sigma(\pi^-) = \hat{\sigma}(\pi^-) + \hat{\sigma}(\rho^-) + \hat{\sigma}(\rho^0) + \hat{\sigma}(\omega) + x\hat{\sigma}(\eta) + \frac{2}{3}\hat{\sigma}(K^{*-}) + \frac{2}{3}\hat{\sigma}(K^0) \quad \text{(A2b)}$$

$$\sigma(\pi^0) = \hat{\sigma}(\pi^0) + \hat{\sigma}(\rho^+) + \hat{\sigma}(\rho^-) + \hat{\sigma}(\omega) + x\hat{\sigma}(\eta) + \frac{1}{3}\hat{\sigma}(K^{*+}) + \frac{1}{3}\hat{\sigma}(K^{*-}) + \frac{1}{3}\hat{\sigma}(K^{*0}) + \frac{1}{3}\hat{\sigma}(\bar{K}^{*0}) \quad \text{(A2c)}$$

where the factors 1/3, 2/3 and 1/2 are isospin Clebsch-Gordan coefficients which give branching ratios of different charged modes (isospin breaking is neglected) and x denotes the fraction of $\eta \to \pi^+\pi^-\pi^0$ decays. Other η decays producing pions are neglected.

Let us now assume that vector mesons are produced three times more frequently than pseudoscalars because of the statistical spin factor. Then

$$\hat{\sigma}(K^*) = 3\hat{\sigma}(K) \quad \text{(A3a)}$$

$$\hat{\sigma}(\rho) = 3\hat{\sigma}(\pi) \quad \text{(A3b)}$$

$$\hat{\sigma}(\omega) = 3\hat{\sigma}(\pi^0), \quad \text{(A3c)}$$

where eqs. (A3a) and (A3b) hold individually for any charge state. We also assume that η production is less than π^0 production by some factor and write

$$x\hat{\sigma}(\eta) = y\hat{\sigma}(\pi^0), \quad \text{(A3d)}$$

where $y < 1$.

Then from eqs. (A3), (A1) and (A2), we obtain

$$\sigma(K^+) = \sigma(K^0) = 2[\hat{\sigma}(K^+) + \hat{\sigma}(K^0)] + \frac{1}{2}\hat{\sigma}(\phi) \quad \text{(A4a)}$$

$$\sigma(K^-) = \sigma(\bar{K}^0) = 2[\hat{\sigma}(K^-) + \hat{\sigma}(\bar{K}^0)] + \frac{1}{2}\hat{\sigma}(\phi) \quad \text{(A4b)}$$

$$\sigma(\pi^+) = 4\hat{\sigma}(\pi^+) + (6+y)\hat{\sigma}(\pi^0) + 2\hat{\sigma}(K^+) + 2\hat{\sigma}(\bar{K}^0) \quad \text{(A5a)}$$

$$\sigma(\pi^-) = 4\hat{\sigma}(\pi^-) + (6+y)\hat{\sigma}(\pi^0) + 2\hat{\sigma}(K^-) + 2\hat{\sigma}(K^0) \quad \text{(A5b)}$$

$$\sigma(\pi^0) = (4+y)\hat{\sigma}(\pi^0) + 3\hat{\sigma}(\pi^+) + 3\hat{\sigma}(\pi^-) + \hat{\sigma}(K^+) + \hat{\sigma}(K^-) + \hat{\sigma}(K^0) + \hat{\sigma}(\bar{K}^0). \quad \text{(A5c)}$$

Equations (A4) give the surprising result that $\sigma(K)$ and $\sigma(\bar{K})$ production rates are independent of the charge of the kaon, even though the direct production rate may be charge dependent; e.g., $\sigma(K^+) = \sigma(K^0)$ even when $\hat{\sigma}(K^+) \neq \hat{\sigma}(K^0)$. This results because the contributions from K^* decays and direct production have opposite charge asymmetry. The pion has a higher isospin than a kaon; thus the charge asymmetry in the K^* distribution shows up in the decay pions, and the charge asymmetry in the decay kaons is the reverse. The exact cancellation of the charge asymmetries in direct and resonance productions results from the values of the Clebsch-Gordan coefficients.

Other quantities of interest which are obtained from eqs. (A4) and (A5) are the total pion and kaon production cross sections summed over all charge states. We denote these by $\sigma_{tot}(M)$.

$$\sigma_{tot}(K) = 4\hat{\sigma}_{tot}(K) + 2\hat{\sigma}(\phi) \quad \text{(A6a)}$$

$$\sigma_{tot}(\pi) = 7\hat{\sigma}_{tot}(\pi) + (9+3y)\hat{\sigma}(\pi^0) + 3\hat{\sigma}_{tot}(K) \quad \text{(A6b)}$$

$$= (10+y)\hat{\sigma}_{tot}(\pi) + (3+y)[2\hat{\sigma}(\pi^0) - \hat{\sigma}(\pi^+) - \hat{\sigma}(\pi^-)] + 3\hat{\sigma}_{tot}(K). \quad \text{(A6c)}$$

The ratio of pion to kaon production is seen to be considerably larger than predictions from direct production. For example, if we neglect the small η and ϕ contributions and assume equal direct production cross sections for all pion and kaon states, the π/K ratio is enhanced by a factor of 7/2 over the value predicted by direct production.

Another interesting relation is

$$\sigma(\pi^+) + \sigma(\pi^-) - 2\sigma(\pi^0) = -2[\hat{\sigma}(\pi^+) + \hat{\sigma}(\pi^-) - 2\hat{\sigma}(\pi^0)]. \quad \text{(A7)}$$

This particular linear combination of pion cross sections is predicted to vanish by the quark parton model. It also vanishes in any model which produces the pions via fragmentation[17] of an object with isospin 1/2. It is thus not surprising that the quantity (A7) vanishes for the total cross sections if it vanishes for the direct production cross sections, since the relevant resonance production and decay conserves isospin. ($\eta \to \pi^+\pi^-\pi^0$ decays do not contribute to this quantity.) However, it is amusing that any deviation from zero in the direct production has its sign reversed in the total production. If the direct production of neutral pions is less than half the direct production of charged pions, the total production of neutral pions will be greater than half the total production of charged pions.

REFERENCES

1. M. Gell-Mann, Acta Physica Austriaca, Suppl. IX, 733-761 (1972).
2. H. J. Lipkin, Quarks for Pedestrians, Weizmann Institute preprint WIS-73/8-Ph, to be published in Physics Reports.
3. F. J. Gilman and M. Kugler, Phys. Rev. Letters 30, 518 (1973); H. J. Melosh IV, Caltech Thesis (1973 unpublished. M. Kugler, these proceedings.
4. S. Yoshida and L. Zamick, Annual Review of Nuclear Science 22, 121 (1972). See in particular Tables 4 and 5 and section VIII.
5. G. E. Brown, Unified Theory of Nuclear Models, North-Holland Publishing Company, Amsterdam (1967), Chapter VIII.
6. A. Katz, Journ. of Math. Phys. 10, 2215 (1969).
7. O. W. Greenberg, Phys. Rev. Letters 13, 122 (1964); O. W. Greenberg and M. Resnikoff, Phys. Rev. 163, 1844 (1967).
8. H. J. Lipkin, Phys. Letters 45B, 267 (1973).
9. J. L. Rosner, Phys. Rev. Letters 21, 950 (1968); P. G. O. Freund, R. Waltz and J. Rosner, Nucl. Phys. B13, 237 (1969).
10. J. Primack, these proceedings. J. D. Bjorken, in Proceedings of the XVI International Conference on High Energy Physics, Edited by J. S. Jackson and A. Roberts, National Accelerator Laboratory (1972), Vol. 2, p. 299; H. J. Lipkin, Phys. Rev. D7, 1850 (1973).
11. M. Y. Han and Y. Nambu, Phys. Rev. 139, B1006 (1965).
12. H. J. Lipkin, Symmetries and Resonances (Theoretical), in Particle Physics (Irvine Conference, 1971), edited by M. Bander, G. L. Shaw and D. Y. Wong (American Institute of Physics, New York, 1972), p. 30.
13. Y. Nambu, in Preludes in Theoretical Physics, edited by A. de-Shalit, H. Feshbach and L. Van Hove (North-Holland Publishing Company, Amsterdam (1966), p. 133.
14. O. W. Greenberg and D. Zwanziger, Phys. Rev. 150, 1177 (1966).

15. R. H. Dalitz, in Quarks and Symmetries, Proceedings of International Conference on Symmetries and Quark Models, Detroit 1969, Edited by Ramesh Chand, Gordon & Breach, New York, 1970, p. 355, and in Methods and Problems of Theoretical Physics, Edited by J. E. Bowcock, North-Holland Publishing Co., Amsterdam (1970), p. 343.
16. G. Feldman, these proceedings.
17. H. J. Lipkin and M. Peshkin, Phys. Rev. Letters 28, 862 (1972).

SLAC SUMMER INSTITUTE ON PARTICLE PHYSICS
TOPICAL CONFERENCE ON DEEP INELASTIC SCATTERING

PREPRINT

RESULTS ON e^+e^- REACTIONS AT THE CEA (2.0 AND 2.5 GeV PER BEAM)

BY

HARVEY NEWMAN

MASSACHUSETTS INSTITUTE OF TECHNOLOGY
AND
CAMBRIDGE ELECTRON ACCELERATOR
CAMBRIDGE, MASSACHUSETTS

I. INTRODUCTION

The e^+e^- colliding beam facility at the Cambridge Electron Accelerator (C.E.A.) has been used to measure the cross-sections for the reactions:

a. $e^+e^- \rightarrow e^+e^-$

b. $e^+e^- \rightarrow \gamma\gamma$

c. $e^+e^- \rightarrow$ hadrons

at 4 and 5 GeV* center-of-mass energies.

The experimental program has been successfully carried out, thanks to many people from several institutions (Fig. 1), from early 1972 through the present.

II. The C.E.A. Bypass

Electron and positron beams collide in a straight section of the "Bypass" to the main synchrotron. These beams are strongly focused by a "low beta" section to increase the probability of collision. The main components of the Bypass are shown in Fig. 2. The non-magnetic Bypass On-Line Detector (BOLD), as well as the luminosity measuring counters, and the Bypass magnet assemblies are shown. "Tagging counters" are placed close to the beam orbit between the bending magnets to detect the scattered particles from two-photon processes.

* All results presented here at 5 GeV center-of-mass energy are preliminary.

III. LUMINOSITY MEASUREMENT

The measurement of luminosity is based on the event rate from the double bremsstrahlung reaction $e^+e^- \rightarrow e^+e^-\gamma\gamma$. This process is dominated by low momentum transfers, where the validity of quantum electrodynamics has been verified.

The bremsstrahlung γ rays in a small angular region around the incident electron and positron beams ($\theta = 0^\circ$ and 180°) are measured by ten radiation length lead scintillator sandwich counters placed outside the charged particle trajectories (Fig. 3). These counters were extensively tested, and calibrated, before, during, and after the BOLD experiments.

Random coincidences, chiefly from single bremsstrahlung, are subtracted continuously from true coincidences using the difference in arrival time for pulses from each counter. Charged particles are vetoed by an additional scintillator placed in front of each sandwich counter.

IV. BYPASS OPERATIONAL PARAMETERS

Several characteristics of the C.E.A. Bypass operation are indicated in Fig. 4. The high rf frequency and strong focusing lead to a short bunch length, as is evident in our Bhabha scattering data sample. Transverse beam sizes are inferred from measurements of the induced voltage on a 5 micron quartz fiber as it is flicked through the beam. The Bhabha scattering sample shows source dimensions transverse to the beam line larger than this due to the track reconstruction accuracy of the BOLD detector. Typical beam lifetimes, luminosities, and beam currents are also indicated.

V. THE BYPASS-ON-LINE-DETECTOR

Charged particles and gamma rays in the angular range $45^\circ < \theta < 135^\circ$ and in a range of ϕ covering approximately 70% of 2π (Fig. 5) are detected in BOLD. The main portion of the detector is a non-magnetic array of 20 scintillation counters and 48 magnetostrictive wire spark chambers comprising four quadrants. The remaining 30% in ϕ is covered by additional, "$\Delta\phi$", scintillation counters. Cosmic rays are rejected by measuring the time of flight between the outer scintillators.

Behind each horizontal quadrant is a large assembly of two double-gap wire spark chambers and iron plates, called a "hadron converter", to aid in the separation of hadrons from muons. Hadrons are expected to stop in the 1.8 collision lengths of iron, while the signature of a muon is of course a straight-through. Hadron converters were not installed above and below the top and bottom quadrants because of space limitations.

As a charged particle emerges from the interaction region into a BOLD quadrant (Fig. 6), it first passes through three double-gap, low mass wire spark chambers. These serve to define the particle trajectory. The particle then passes through a scintillation counter in which dE/dx is measured. The next three double-gap chambers are interleaved with iron-clad lead radiators and scintillation counters totaling 7 radiation lengths, in which electromagnetic showers may be both initiated, and observed through the

number and distribution of sparks. Scintillation counters in the shower region are used to trigger the apparatus as well as to measure the energy of a shower.

Photons will also be observed in the shower region of a quadrant, with no observable trajectory in the first three spark chambers. Hadrons may scatter through large angles in the radiators, and may sometimes end in nuclear stars, as observed through the spark configurations in the quadrants.

BOLD was used to detect both pure-Q.E.D. reactions and $e^+e^- \to$ hadrons. The results for the former processes will be presented first.

VI. Q.E.D. TESTS

Q.E.D. verification at high momentum transfers with the C.E.A. was achieved through observation of the following reactions:

$$e^+e^- \to e^+e^-$$

$$e^+e^- \to \gamma\gamma$$

$e^+e^- \to \mu^+\mu^-$ was also observed but analysis of the data has not been completed.

The lowest order Feynman diagrams are shown in Fig. 7. In Bhabha scattering the space-like one photon propagator diagram (the scattering amplitude) dominates, while $e^+e^- \to \gamma\gamma$ is dominated by the single fermion propagator diagrams. The $e^+e^- \to \mu^+\mu^-$ rate is given primarily by the one photon propagator time-like diagram (the annihilation channel) whose amplitude has a structure identical to that of the time-like diagram that contributes to the $e^+e^- \to e^+e^-$ process, in the approximation $m_\mu/E_{cm} \to 0$.

A. The Bhabha scattering cross-section is obtained, basically, by detecting charged colinear showering particles. One actually measures the quantity:

$$\frac{1}{2} \int_{\text{apparatus}} \left| \frac{d\sigma}{d\Omega}(\theta) + \frac{d\sigma}{d\Omega}(\pi-\theta) \right|$$

as the non-magnetic nature of the detector implies no charge determination.

The relevant triggers, and the requirements for identification of $e^+e^- \to e^+e^-$ events, are displayed in Table I. The restricted angular region, somewhat smaller than the geometric acceptance, was chosen to ensure > 99% detection efficiency for electrons and positrons.

The effectiveness of the identification criteria is demonstrated in Fig. 8 and Fig. 9. Fig. 8 compares the shower pulse height distribution for particles from a sample of $e^+e^- \to e^+e^-$ events from the interaction region at 2.5 GeV per beam to a sample of cosmic rays (minimum ionizing particles). Separation is excellent. Fig. 9 shows the acolinearity ($\Delta\theta$) distribution for the Bhabha scattering events at E_{cm} = 5 GeV, and Fig. 9a shows the acoplanarity ($\Delta\phi$) distribution. (No quantitative statement will be made on the breakdown of the peaking approximation at the present stage of analysis.)

A typical $e^+e^- \to e^+e^-$ event is shown in Fig. 10, as reconstructed by computer. The view is along the direction of motion of the e^- beam. The small circles are fiducial marks in the wire spark chambers. "+"-signs represent sparks, and the lines are computer-fitted trajectories.

The BOLD data analysis results for $e^+e^- \to e^+e^-$ are summarized in Table II.[1] All results in the table at E_{cm} = 5 GeV are preliminary. Results are consistent with Q.E.D. The cut-off parameters Λ_+ and Λ_- are included for completeness, and the form factor used in their calculation is specified.

Fig. 11 summarizes the comparison of theory to experiment for center-of-mass energies of 1.4 to 5.0 GeV for wide angle Bhabha scattering events. Frascati μπ Group[2] as well as C.E.A. data are shown. The C.E.A. data point at 5.0 GeV is a preliminary result.

B. Data on the reaction $e^+e^- \to \gamma\gamma$ was collected during the BOLD experiments, mainly through the trigger that required shower pulse heights in two opposite quadrants equivalent to ≥ 800 MeV deposited in each quadrant. Analysis of 34 events from the 2 GeV per beam run has been completed. These events are restricted to an angular range of $53^\circ \leq \theta \leq 127^\circ$, $\phi < 28^\circ$ from the normal to a quadrant to ensure > 99% shower detection efficiency. The events must also pass the requirement of being colinear to within 15°.

These results, consistent with Q.E.D., are summarized in Table III.[3] The ratio of experiment to theory for several experiments covering E_{cm} = 1 to 4 GeV is given in Fig. 12.[3,4,5,6] The average virtual lepton four-momentum for our data on $e^+e^- \to \gamma\gamma$ at E_{cm} = 4 GeV is $\sqrt{|\vec{q}|^2}$ = 2.35 GeV/c.

VII. HADRON PRODUCTION BY e^+e^- ANNIHILATION

A. The Data Sample

The BOLD Group has measured an unexpectedly large cross-section for electron-positron annihilation into three or more hadrons,[7] with at least two detected charged particles in the final state.

The lowest order, one photon annihilation Feynman diagrams for hadron production are shown in Fig. 13. The non-coplanarity requirement for our data excludes the hadronic pair production diagram from the events in our present analysis.

Table IV indicates the predominant triggers, as well as the precise identification criteria which lead to our multihadronic data samples. The angular requirements are necessary to isolate multibody production by e^+e^- annihilation from other processes (viz. $e^+e^-\gamma$, $e^+e^-\pi^+\pi^-$ final states, etc.). The "range cut" helps define a threshold energy for detected charged particles which eliminates delta-rays (and unfortunately, pions of < 20 MeV) from our data.

A 5-prong multihadronic event is presented in Fig. 14 that clearly shows a backward scatter, a large angle scatter, 2 gamma ray conversions and particles stopping in the iron absorber. Many of these characteristics help to demonstrate the hadronic nature of our data sample.

The BOLD I data (2 GeV per beam) has events with between 2 and 5 detected charged particles. The recent BOLD II data (2.5 GeV per beam), however, also contains 2 events with 6 prongs, 1 event with 7 prongs and 1 event with 8 prongs.

Fig. 15 shows a six prong event as reconstructed by computer, viewed along the beam line. The scattering, stopping, and formation of nuclear stars in the BOLD lead radiators or iron absorber are visible. Fig. 16 is the eight prong BOLD II event. In the upper quadrant there is a nuclear interaction. The shower pulse

height in this quadrant is quite low, and does not indicate an electromagnetic shower of an energy commensurate with the number of extra short "tracks" appearing between the radiators.

Concerning the hadronic nature of the events, the BOLD I data contained a total of 269 charged tracks. Of these 49 scattered by more than 8° in one of the BOLD radiators, 5 scattered by more than 90°, and 3 tracks ended inclearly visible nuclear stars. The BOLD II data sample of 354 prongs yielded 42 prongs that scattered by more than 8°, 8 prongs that scattered backward, and 5 prongs that ended in nuclear stars.

Simple calculations using the Mott cross-section set a conservative upper bound of 3 prongs scattered by more than 8° for either run if the resulting data sample were composed wholly of muons.

I will next consider the subtraction from the sample of "background" events, not originating from $e^{+}e^{-}$ reactions, and of "contamination" events, which do arise from $e^{+}e^{-}$ reactions, but not from the one photon annihilation into hadrons. In the following discussion I will concentrate on the BOLD II data where feasble, as the BOLD I data has already been published.

The subtraction process for BOLD II data is summarized in Table VI. The background events are due to beam-gas scattering and to cosmic rays.

For the beam-gas subtraction for BOLD II, increasing the acceptable z (along the beam line) by a factor of 2.2 leads to 11 additional events that satisfy all other identification criteria. Of these, 10 are two prong and 1 is a three prong event. This information is used as the basis for a statistical background subtraction from the data. A series of single beam runs in which the pressure in the interaction region was raised to 100 - 1000 times normal (torr × mA × sec equivalent to 17 BOLD II data-taking runs) was used to determine the distribution along the beam direction of the vertex-points of the beam-gas events. Knowledge of this distribution allowed us to extrapolate along z into the volume containing the data sample from the adjacent volumes. Hence 8 two-track events and 1 three-track event were subtracted.

The steel holder for the aforementioned quartz fiber, used in direct beam-size measurements, is a target from which hadronic final states are produced. A scatter plot of the vertex coordinates transverse to the beam line of all candidates prior to any interaction region cut clearly shows the outline of this target, as determined by direct surveying measurements. The BOLD I scatter plot appears in Fig. 17. These events are separable from the data sample and do not contribute to the backgrounds.

Sampling scatter plot regions away from the fiber holder and away from the main beam-gas background region, we find a very low density of additional background events. We expect these events to be due to cosmic ray showers and to be characterized by a uniform spatial distribution of vertex points. The small background subtraction attributed to cosmic rays in Table V is made on this basis.

The "contaminant" category is treated on an event by event basis. Radiative modifications to Bhabha scattering ($e^{+}e^{-} \rightarrow e^{+}e^{-}\gamma$) are identified by non-colinear high energy electrons ($\geq$ 1.5 GeV

deposited in the BOLD quadrant "shower" region) with or without the hard photon detected. At the present stage of analysis, some BOLD II events having two or more "electron-like" tracks, with shower pulse heights in the 500 MeV to 1 GeV range, must be separated out. These events do not appear to be the obvious result of low order one or two photon Q.E.D. processes. These events will be classified in future analysis after thorough examination. The "electron-like" nature of the tracks is not definite, and so further investigation is needed.

B. Two Photon Processes

The rates for the two-photon reactions:

$$e^+e^- \to e^+ + \gamma^* + e^- + \gamma^* \to e^+ + e^- + X$$

are known to increase as $(\ln(E/m_e))^2$ in the approximation $m_e/E \to 0$. Some of the lowest order Feynman diagrams for two-photon reactions ($X = e^+e^-$, $\mu^+\mu^-$, $\pi^+\pi^-$, multihadrons) are presented in Figs. 17a and 19. The rising behavior of the cross sections with E causes them to eventually rise over the corresponding processes:

$$e^+ + e^- \to \gamma^* \to X$$

which show a leading $\frac{1}{E^2}$ behavior (see Fig. 18).

At our energies, one might suspect that the two photon diagrams are a significant if not major contribution to our data. Detailed computations[9] for the BOLD I center-of-mass energy, however, which take into account the BOLD experimental conditions, show a low level of "contamination". These computations closely follow the equivalent-photon approximation methods of Brodsky, Kinoshita, and Terazawa.[8]

To deduce the experimentally relevant rates, one must modify the calculations used for Fig. 18. to conform with experimental conditions.

The relevant BOLD triggers for detection of these processes require that at least two of the final state particles have a relatively high kinetic energy (See Table IV.). This sets a rather high threshold center-of-mass energy for the two equivalent photons. The acoplanarity requirement for the case of two detected charged tracks sets a minimum transverse momentum for the equivalent-photons which leads to an even higher effective threshold in the center-of-mass. Beyond these energy constraints, we must consider the acceptance of the apparatus. Since BOLD covers only wide production angles in the LAB, most of the produced particles are not detected. These considerations sharply reduce the effective cross sections from the values given in Fig. 18. The curves in the figure correspond to a detector which can reliably detect charged particles down to zero kinetic energy over 4π steradians of solid angle.

I will use the recently completed BOLD I computations to demonstrate the above assertions. The results, summarized in Table V, show that two-photon processes contribute little to our data sample at $E_{cm} = 4$ GeV. The general behavior of the two-photon cross sections leads us to expect the same low level of contamination in the BOLD II data.

1. $\left.\begin{matrix} e^+e^- \to e^+e^-\mu^+\mu^- \\ e^+e^-\pi^+\pi^- \end{matrix}\right\}$:

We calculated these rates considering the minimum kinetic energy needed for a particle to trigger the detector to be 110 MeV for a muon and 120 MeV for a pion. The minimum kinetic energy needed increases as the angle of the particle with respect to the normal to a quadrant increases because of the greater effective depth of material that must be traversed. These threshold energies are averages over the relevant angular ranges for particles entering the detector. Using these thresholds we derived the following effective cross sections in the equivalent photon approximation, where the produced particles are strictly coplanar with the beam line:

$$\sigma_{e^+e^- \to e^+e^-\mu^+\mu^-} (T_\mu \geq 110 \text{ MeV}) = 0.97 \text{ nb}$$

$$\sigma_{e^+e^- \to e^+e^-\pi^+\pi^-} (T_\pi \geq 120 \text{ MeV}) = 0.16 \text{ nb}$$

The estimated number of events from these sources is then:

$$N_1 = \left\{ \begin{array}{l} \text{calculated number of } \mu \text{ and } \pi \\ \text{pairs in the BOLD solid angle,} \\ \text{arising from the two-photon} \\ \text{mechanism, and coplanar with} \\ \text{the beam line} \end{array} \right\} = 10.7 \pm 1 \text{ events}$$

(Note: the quoted error reflects the luminosity measurement error.)

From this calculation, we estimate the number of events that show the required acoplanarity: $|\Delta\phi| < 160^\circ$. Brodsky, et al.[8] show that the acoplanarity distributions of the produced pairs in $ee\mu\mu$ and $ee\pi\pi$ follow the form:

$$\frac{d\sigma_{ee \to ee\mu\mu, \text{ or } ee\pi\pi}}{d\psi} = \left\{ \begin{array}{ll} C, & \psi \leq \sqrt{m/E} \\ D/\psi, & \psi > \sqrt{m/E} \end{array} \right.$$

where C and D are constants depending on the identity of the particles produced and ψ is the coplanarity angle $\equiv 180^\circ - |\Delta\phi|$. One should note, though, that most of the non-coplanar events must arise from final state particles produced at or near threshold.

However, if one considers only those μ's and π's sufficiently energetic to trigger BOLD, then the above angular dependence leads to a gross overestimate of the number of events in our sample. This is due to the fact that the probability distribution for the emission of an equivalent photon at an angle $\theta_\gamma > \sqrt{m_e/E}$ falls rapidly with θ_γ.[11,12] Production of acoplanar pairs of μ's and π's of $\gtrsim$ 100 MeV per particle, and with $|\Delta\phi| < 160^\circ$, requires a total transverse momentum of the equivalent photons of $\geq$ 60 MeV. This requires that either the photon energy ω be quite high, or θ_γ be $\gg\sqrt{m_e/E}$. In either case the production is strongly suppressed. We therefore end up with:

$$N_2 \left\{ \begin{array}{l} \text{calculated number of } e^+e^- \to \\ \mu^+\mu^- \text{ and } e^+e^- \to e^+e^-\pi^+\pi^- \\ \text{events detected} \end{array} \right\} \ll 3.7$$

The BOLD I candidate events from the interaction region, with two detected tracks, with $\Delta\alpha < 160^\circ$ (α is the space angle) and $|\Delta\phi| \cong 180^\circ$, included 3 events identified as $ee \to ee\mu\mu$ or $ee\pi\pi$. Only the produced particle pair was detected. This is consistent with the expected number of events calculated without the $\Delta\alpha$ restriction and with approximate threshold conditions and BOLD geometry included.

2. $e^+e^- \to e^+e^-e^+e^-$

The contamination from the process $e^+e^- \to e^+e^-e^+e^-$ was also calculated, requiring only the produced e^+e^- pair to be detected

in BOLD. The trigger efficiency for each electron or positron was assumed to rise linearly from 0% to 100% as the particle kinetic energy increased from 100 - 600 MeV. This is a fair estimate, in view of the fact that each particle must fire the first three scintillators in a quadrant, and must therefore penetrate at least 4.1 radiation lengths of material. The result, without any angular cuts is:

$$\sigma_{ee \to e^+e^-e^+e^-}\ (\text{BOLD}) = 0.315\ \text{nb}$$

corresponding to 3.0 ± 0.3 events. 2 $e^+e^- \to e^+e^-e^+e^-$ events were identified, with $\Delta\alpha < 160^\circ$, $|\Delta\phi| \cong 180^\circ$. The acoplanarity condition $|\Delta\phi| < 160^\circ$ reduces the contamination to a negligible level.

3. $e^+e^- \to e^+e^-M^0$

The cross sections for $e^+e^- \to e^+e^-M^0$ were calculated assuming M^0 is a spin zero narrow width resonance. The η (with $\Gamma_{\eta \to 2\gamma} \approx 300$ eV[13]) does not contribute significantly to this rate. The η', on the other hand, has an estimated decay width into two photons of several keV (latest experimental upper bound in particle tables: $\Gamma_{\eta' \to 2\gamma} > 40$ keV). Therefore, detailed calculations were carried out for the η'(958 MeV), assuming $\Gamma_{\eta' \to 2\gamma} = 40$ keV.

Conservative upper limit estimates on the detection efficiency were made. This efficiency is strongly reduced by the low average kinetic energy and the center-of-mass motion of the decay products (e.g. $\eta' \to \pi^+\pi^-(\eta)$, $\pi^0\pi^0(\eta)$,$\gamma\gamma$, $\pi^+\pi^-\gamma$, etc.). As explained above, the acoplanarity cut leads to a further efficiency reduction. The overall result is an efficiency which is an order of magnitude less than the efficiency calculated for multihadronic states produced through the one photon annihilation channels. (Note: the efficiency calculations for the one photon processes will be discussed in detail later).

By these methods we calculate that although we could have produced as many as 28 ± 3 η''s during our experimental run at $E_{cm} = 4$ GeV, we estimate that $\lesssim 0.4$ such events contaminate our data sample.

4. $e^+e^- \to e^+e^-$ + multihadrons

Returning to Fig. 19, we see the lowest order Feynman diagram for two-photon production of a C+ state where the beam particles do not annihilate. The two virtual photons annihilate directly into a many-body system of at least three particles in this diagram, and it is this stage of the process whose rate is presently open to speculation. Brodsky et al.[8] assume a factorization of the cross section for $\gamma\gamma \to$ hadrons at high energies, and estimate $\sigma_{\gamma\gamma \to \text{hadrons}} \sim 0.3$ μb (See Figs. 18 and 19).

Using this value for $\sigma_{\gamma\gamma \to \text{hadrons}}$ leads to the fact that as many as 14 such hadronic events could have been produced during the BOLD expeimental run at $E_{cm} = 4$ GeV. However, the BOLD detector is found, once again, to be relatively insensitive to these final states. Consider $e^+e^- \to e^+e^-\pi^+\pi^-\pi^0$. Because the center-of-mass of the two virtual photons need not be stationary, and because final state particles are preferentially created near threshold, the average detection efficiency for the process $e^+e^- \to e^+e^-\pi^+\pi^-\pi^0$ is computed to be suppressed by a factor ∼ 10

with respect to $e^+e^- \to \gamma^* \to \pi^+\pi^-\pi^0$. We consider this reduction factor in the detector efficiency, that arises mainly because of the center-of-mass motion of the two virtual photons, as a typical correction factor to be applied to the efficiencies for the one photon annihilation processes (where the center-of-mass of the final state hadrons is always stationary in the LAB).

In this way we derive our best estimate for the contribution of $e^+e^- \to e^+e^-$ + multihadrons to the BOLD I data sample: < 0.5 events.

According to our present computations we therefore deduce that no corrections need be applied to the BOLD I data due to the processes $e^+e^- \to e^+e^-M^0$ and $e^+e^- \to e^+e^-$ + multihadrons. We expect this to hold for BOLD II as well, in that we expect future computations, quite similar to the above, to yield low contamination levels.

C. Data Results

The data samples, after subtractions, for e^+e^- annihilation into hadrons for BOLD I ($s = 16\ GeV^2$) and BOLD II ($s = 25\ GeV^2$) are displayed in Table VII. Based on the final count of 88 events for BOLD I, and a time-integrated luminosity of $9.45 \pm 0.86 \times 10^{33} cm^{-2}$, the model independent lower limit on the $e^+e^- \to$ multihadrons cross-section is 9.6 ± 1.4 nanobarns at 4 GeV center-of-mass energy. The BOLD II count of 109 events, and the time-integrated luminosity of $1.15 \pm 0.11 \times 10^{34} cm^{-2}$, yield a cross-section of 9.5 ± 1.4 nanobarns at 5 GeV in the center-of-mass.

D. Efficiency Calculations for $e^+e^- \to \gamma^* \to$ Multihadrons

In order to deduce the total cross section σ_{tot}, the model independent lower limits must be divided by the total detection efficiency ε_T:

$$\varepsilon_T = \frac{\sigma_{tot} \cdot L}{N_T} \qquad \begin{cases} N_T = \sum_p N_p \\ L = \int (\text{luminosity})\, dt. \end{cases}$$

The calculation of ε_T[10] is of course model dependent. We have assumed that all particles are pions produced according to a Lorentz-invariant phase space distribution. We also assume that for BOLD I, in which 2 through 5 charged tracks are detected, the contributing final states are $\pi^+\pi^-\pi^0$, $\pi^+\pi^-2\pi^0$, $\pi^+\pi^-\pi^+\pi^-$, and so on up to $4\pi^+4\pi^-$ (as specified in Table VIII.). For BOLD II, in which up to 8 charged tracks are detected, we will assume that states up to $8\pi^+8\pi^-$ contribute. Given the fact that the BOLD solid angle is approximately 2π steradians, it would seem that final state multiplicities of more than twice the maximum observed prong count would tend to contribute little to the observed prong count. This statement has been thoroughly checked for BOLD I, and initial indications are that it holds for BOLD II. These assumptions are summarized in Table VIII.

The first step in the calculation of ε_T is the determination of the efficiencies for detecting p charged tracks in BOLD, given that q charged pions are produced in the final state (i.e., from the reaction $e^+e^- \to q\pi^\pm + n\pi^0$). In what follows, these efficiencies will be called $\varepsilon(p, q)$. The values of $\varepsilon(p, q)$ are computed by a Monte Carlo program based on NVERTEX. The program simulates

the BOLD experimental conditions as far as possible. The program accounts for the geometric acceptance and trigger conditions for BOLD in detail. It also calculates the effects of nuclear absorption, including secondary pion regeneration, and considers ionization losses in the lead radiators. Of the events generated by the program, only those which pass the same criteria used for scanning the real data are considered "detected" as multihadronic events. The detection efficiencies for the assumed final states of BOLD I, including nuclear absorption, are shown in Table IX. The dependence on n, the number of π^0's, is weak so that an average over n is used. This result, different from the Frascati groups', is a consequence of the large BOLD solid angle and the short C.E.A. interaction region source length.

Given the observed number of events with prong count p, N_p, the unknown partial cross sections $\sigma(e^+e^- \to q\pi^\pm + \text{neutrals}) \equiv \sigma_q$ must satisfy the relationships:

$$N_p = L \times \sum_q \varepsilon(p, q)\, \sigma_q$$

where L is the time-integrated luminosity. The relevant values of p and q for the two experimental runs are specified in Figs. 20a and 20b, where the method of solution is outlined.

The method of least squares is applied to these equations. The physical requirement $\sigma_q \geq 0$ precludes exact solution of these equations, so that an optimal, or "best" solution must be found. This is done by letting the left hand side of each equation vary. If we call the new, varying, left hand side N_p', we can solve for a set of σ_q values by searching for a set of N_p' values which minimize χ^2 as defined in the figure:

$$\chi^2 \equiv \sum_p \frac{(N_p' - N_p)^2}{N_p}$$

What is the error in the efficiency due to possible statistical fluctuations in the observed number of prongs? This is determined by assuming that each observed prong count N_p could vary about its actual value according to a poisson distribution (with standard deviation = $\sqrt{N_p}$) in an uncorrelated way. This is equivalent to simulating, as best we can, the results of a "gedanken experiment" in which we repeat our actual experiment many times. We would expect to get, to the best of our present knowledge, the same mean prong count N_p for each p, and a standard deviation of each N_p about this mean governed by poisson statistics.

The remarkable outcome of our "gendanken experiment", as demonstrated by the BOLD I analysis, is that σ_{tot}, the <u>sum</u> of the partial cross sections σ_q, varies over a relatively narrow range, even though <u>each</u> σ_q is not well determined. (This is expressed as an error on the total efficiency ε_T in our analysis.) Even for sets of partial cross-sections which yield a set of prong counts very different from our observed counts for BOLD I, the total efficiency changes by a relatively small amount from a central average value of $\varepsilon_T = 38\%$.

To express how well a given set of "fluctuating" counts N_p^* match our observed set of N_p values we define another parameter:

$$\chi_0^2 \equiv \frac{(N_p^* - N_p)^2}{N_p} .$$

Larger χ_0^2 naturally occur relatively rarely as each count is allowed to vary independently. If for <u>each</u> set N_p^* we calculate the best set of σ_q's, and from that the total efficiency, we can observe the range of variation of efficiency as a function of χ_0^2. This is shown schematically in Fig. 20b. One observes that $\langle\varepsilon_T\rangle$ is independent of χ_0^2, $\frac{\partial\langle\varepsilon_T\rangle}{\partial\chi_0^2} = 0$.

In spite of the <u>wide</u> latitude in our choice of contributions from specific channels of different multiplicity we arrive at a well defined BOLD I total efficiency $\varepsilon_T = (38 \pm 8)\%$, and therefore $\sigma_{tot} = 234 \pm 52$. The average charged multiplicity $\langle n_{ch}\rangle = 4.2 \pm 0.6$.

The BOLD II calculations for the efficiency are now underway. Although more cumbersome due to the larger number of linear equations involved, the indication at this time is that the same sort of behavior holds. Our present best estimate of the BOLD II efficiency is $(48 \pm 2)\%$.

The effect of statistical fluctuations on the the efficiency is but one source of error. Another important source of error stems from our lack of knowledge of the dynamics of the hadronic production process. For example, had we assumed that the final states contributing to our data sample were dominated by a small number of resonance channels, the resulting angular and mass correlations could significantly change our calculations. Quasi-two-body resonance production, a mechanism of intrinsic physical interest through its relationship to all jet-like models (such as parton models) was studied in some detail.

Our Monte Carlo program was used to generate the following quasi two-body channels:

1. $e^+e^- \rightarrow \rho^+\rho^-$
2. $e^+e^- \rightarrow A_1^{\pm}\pi^{\mp} \rightarrow \pi^+\pi^-\pi^0\pi^0$
3. $e^+e^- \rightarrow A_1^{\pm}\pi^{\mp} \rightarrow \pi^+\pi^-\pi^+\pi^-$
4. $e^+e^- \rightarrow A_1^{+}A_1^{-} \rightarrow 6\pi$

For each simulated process, we carried through our efficiency calculations. We also "mixed" contributions from the above channels with contributions from the reactions shown in Table VIII. In each case we carefully noted the changes in $\varepsilon(p, q)$, and the resulting ε_T, that followed from different dynamical assumptions.

We found that the correlation between pions in these dynamical models always produces a "back-to back" tendency that causes a lower overall efficiency than phase-space production, primarily due to a lower efficiency for detecting two tracks. This low two-track efficiency is a direct result of the fact that when two tracks appear in BOLD, they tend to be close to back-to-back, and therefore fail the angular cuts that we apply to our data. Even when the angular distribution at the meson production vertex is assumed to be $\sin^2\alpha$ (α the space angle between the two intermediate particles), the mass correlations always lead to the same general result: the phase space total efficiency is higher than the two-resonance production total efficiency. Hence, although we do not know the detailed dynamics, we are confident that had we assumed that our data was dominated by two-body resonance production, we would have calculated lower

overall efficiencies, and therefore higher total cross sections.

In terms of angular correlations, we found that our assumed phase-space mechanism was consistent with our data at E_{cm} = 4 GeV. An example of our findings is shown in Fig. 21. Here we compare the normalized distribution of the cosines of the angles between two prongs in all BOLD I real events to this distribution for Monte Carlo events generated by two mechanisms:

1. 6π phase space
2. $e^+e^- \to A^+ A^- \to \pi^-\rho^0 \to \pi^-(\pi^+\pi^-)$ (strongly correlated pions)
   $\hookrightarrow \pi^+\rho^0 \to \pi^+(\pi^+\pi^-)$

The phase space mechanism seems to match. The strong forward-backward peaking for the A^+A^- mechanism is not evident in the data. The figure therefore suggests the appropriateness of the phase space production model for our event sample.

Another interesting comparison of the BOLD I data with the predictions of Monte Carlo phase space (no nuclear absorption) is shown in Fig. 22. The patterns of the real 4-prong events as they appear in BOLD (that is, how many charged tracks appear in each of the four quadrants), are compared with the assumption that the events are produced by $4\pi^+ + 4\pi^-$ states where the pions follow phase space. Agreement appears excellent. No "jet structure" of the type one might expect for quasi two-body resonance production is indicated.

Similar calculations for BOLD II are now underway.

E. Results for $e^+e^- \to$ Multihadrons

The results of the BOLD I analysis at $s = 16\ GeV^2$, and preliminary results of the BOLD II analysis at $s = 25\ GeV^2$ are presented in Table X. The number of events in each data sample, and the time-integrated luminosity, lead to the model independent lower limits on the cross section shown as σ_{min}. The best estimates of the total event detection efficiency are used to derive total cross section estimates. The ratio of the total cross section to the muon cross section is presented, and for BOLD I we show the average charged multiplicity.

Figure 23[7] shows a recent summary of world data on the ratio:

$$\frac{\sigma(e^+e^- \to \text{multihadrons})}{\sigma_{theory}(e^+e^- \to \mu^+\mu^-)}$$

as a function of ln(s), updated to include our new preliminary results. Predictions of the familiar quark model and the more recent "colored" quark model are presented for comparison.

TABLE CAPTIONS

I. Triggers, identification criteria, and geometric restrictions for the Bhabha scattering data samples.

II. Results: Bhabha scattering data at E_{cm} = 4 GeV and 5 GeV.

III. Results: $e^+e^- \to \gamma\gamma$ data at E_{cm} = 4 GeV.

IV. Triggers and identification criteria for the $e^+e^- \to$ multihadrons data sample.

V. Summary of BOLD I two-photon contamination.

VI. Preliminary summary of the BOLD II subtraction of backgrounds and contamination from the data.

VII. BOLD data samples after subtractions: $s = 16\ GeV^2$ and $25\ GeV^2$.

VIII. Basic assumptions for the BOLD efficiency calculations for $e^+e^- \to \gamma^* \to$ multihadrons.

IX. Computed average detection efficiencies for BOLD at E_{cm} = 4 GeV, for the assumed final states.

X. Results for $e^+e^- \to$ multihadrons at $s = 16\ GeV^2$; $s = 25\ GeV^2$. BOLD II results are preliminary.

TABLE I. $e^+e^- \to e^+e^-$ DATA SAMPLE

A. Triggers for $e^+e^- \to e^+e^-$ Events

1. 3 of First 4 Scintillators Fire in Opposite Quadrants. $(K.E.)_{MIN} \gtrsim$ 500 MeV per Quad.
2. Shower Pulse Heights in Opposite Quadrants Equivalent to $\gtrsim$ 800 MeV Deposited per Quad.

B. Identification Criteria

1. Particle Trajectories Intersect in the Interaction Region (9.5 cm Long, 2 cm High and Wide).
2. Each Particle Produces a Large Pulse in the Shower Counter System.
3. The Angle in Space Between the Two Tracks is Within 15^0 of Being Back-to-Back.

C. Geometric Restrictions

Events Accepted for Final Data Sample Only If:

1. Scattering Angle $50^0 < \theta < 130^0$.
2. Azimuthal Angle φ Within 30^0 of the Normal to a Quadrant.

TABLE II. RESULTS: $e^+e^- \rightarrow e^+e^-$

	BEAM ENERGY (GeV) 2.0	2.5 (PRELIM.)
1. NUMBER OF EVENTS	260	225
2. $\int L\,dt$ (cm^{-2})	$1.06 \pm .10 \times 10^{34}$	$1.25 \pm .15 \times 10^{34}$
3. $R = \frac{\sigma_{EXP}}{\sigma_{THEORY}}$	$0.88 \pm .10$	$1.0 \pm .12$ (1ST 60% OF DATA: $1.CS \pm 0.13$)
4. SPACE-LIKE q^2 $(\frac{GeV}{c})^2$:		
A) RANGE	$-13.1 < q^2 < -2.8$	$-20.4 < q^2 < -4.4$
B) $\langle q^2 \rangle$	5.3	-8.3
5. TIME-LIKE q^2	16	25
6. $\Lambda_\pm$ (GeV), FROM $F_\pm(q^2) = 1 \pm \frac{q^2}{q^2 - \Lambda_\pm^2}$	$\Lambda_+ > 12$; $\Lambda_- > 6$	$\Lambda_+ > 8.5$; $\Lambda_- > 8.5$

TABLE III. RESULTS: $e^+e^- \rightarrow \gamma\gamma$, $E_{CM} = 4$ GeV

NUMBER OF EVENTS	34
q^2 RANGE $(\frac{GeV}{c})^2$	$-12.8 < q^2 < -3.2$
$\langle q^2 \rangle$	-5.5
R	$1.04 + .22 - .21$
Λ_{e^*}, FROM $F(q^2) = 1 + 8\left(\frac{E}{\Lambda_{e^*}}\right)^4 \sin^2\theta$	3.9 GeV

TABLE IV. MULTIHADRON EVENT SAMPLE DEFINITION

A. Triggers

1. Charged Particles in Two or More Quadrants. $(K.E.)_{MIN} \approx$ 95 MeV for a Pion or Muon.
2. Showers in Two or More Quadrants. Shower Pulse Height Equivalent to $\geq$ 800 MeV Deposited per Quadrant.

B. Identification:

1. $\geq$ 2 Charged Tracks Detected.
2. Each Charged Particle Penetrated $\geq$ 10.7 gm/cm^2 Iron Equivalent.
3. If Two Prong Event:
   a) Angle in Space Between Tracks $< 160^0$.
   b) Azimuthal Angles Differ by $< 160^0$
4. Vertex Point for All Tracks Lies in a Volume about the Interaction Point as Determined by e^+e^- Elastic Scattering Events.

TABLE V. SUMMARY OF BOLD I TWO-PHOTON CONTAMINATION

Process	Calculated Events in Sample
$e^+e^- \to e^+e^-\mu^+\mu^-$ $e^+e^- \to e^+e^-\pi^+\pi^-$	$\ll 3.7$
$e^+e^- \to e^+e^-e^+e^-$	~ 0 $(3 \pm .3$ with $\lvert\Delta\phi\rvert \cong 180^0)$
$e^+e^- \to e^+e^-\eta'$	0.4
$e^+e^- \to e^+e^-$ + HADRONS	0.25 { 2 Energetic π's and Others near Threshold 0.50 { Prong Distribution as in $e^+e^- \to \gamma^* \to$ HADRONS

TABLE VI (prelim.)

BOLD II BACKGROUND AND CONTAMINATION SUBTRACTIONS

Charged Tracks	Before Subt. ①	Gas Subt. ②	Cosmic Ray Subt. ③	eeγ Subt. ④	Special "e-like" Subt. ⑤	Final Counts
2	50	-8	-1	-4	-3	34
3	39	-1	-0	-0	-4	34
4	28	-0	-0	-0	-0	28
5	9	-0	-0	-0	-0	9
6	2	-0	-0	-0	-0	2
7	1	-0	-0	-0	-0	1
8	1	-0	-0	-0	-0	1

BACKGROUND CONTAMINATION

TOTAL EVENT COUNT AFTER SUBTRACTIONS : 109

TABLE VII. DATA SAMPLES AFTER SUBTRACTIONS

Number of Prongs	BOLD I (s = 16 GeV^2)	BOLD II (PRELIM.) (s = 25 GeV^2)
2	31	34
3	29	34
4	20	28
5	8	9
6	0	2
7	0	1
8	0	1
Totals	88	109
$\int L\,dt$ (10^{33} cm^{-2})	9.45 ± 0.86	11.5 ± 1.1

TABLE VIII. ASSUMPTIONS FOR EFFICIENCY CALCULATIONS

1. All Particle Pions
2. Lorentz Invariant Phase Space Production
3. Contributing Final States
   A. BOLD I:

$$e^+e^- \rightarrow q\pi^{\pm} + n\pi^0$$

$q = 2, 4, 6, 8; n \leq 2; q+n \leq 8$

   B. BOLD II:

$$e^+e^- \rightarrow q\pi^{\pm} + n\pi^0$$

$q = 2, 4, 6, 8, 10, 12, 14, 16; q+n \leq 16$

TABLE IX

Average Detection Efficiency

Number of prongs	Number of observed events	Assumed final states			
		$\pi^+\pi^-\pi^0$ $\pi^+\pi^-2\pi^0$	$2\pi^+2\pi^-$ $2\pi^+2\pi^-\pi^0$ $2\pi^+2\pi^-2\pi^0$	$3\pi^+3\pi^-$ $3\pi^+3\pi^-\pi^0$ $3\pi^+3\pi^-2\pi^0$	$4\pi^+4\pi^-$
p	N_p	q = 2	q = 4	q = 6	q = 8
2	31 $\{\|\Delta\phi\|<160^\circ$ $\Delta\alpha<160^\circ$	0.116	0.193	0.146	0.094
3	29	0	0.178	0.253	0.217
4	20	0	0.049	0.163	0.244
5	8	0	0	0.049	0.141
6	0	0	0	0.007	0.056

TABLE X. RESULTS FOR $e^+e^- \longrightarrow$ MULTIHADRONS

	BOLD I $s = 16$ GeV^2	BOLD II (PRELIM) $s = 25$ GeV^2
N_T	88	109
$L_{(CM^{-2})}$	$9.45 \pm 0.86 \times 10^{33}$	$11.5 \pm 1.1 \times 10^{33}$
σ_{MIN}(nb)	9.6 ± 1.4	9.5 ± 1.4
ε_T	0.38 ± 0.08	0.48 ± 0.12
σ_{TOT}(nb)	26 ± 6	20 ± 7
$\frac{\sigma_{TOT}}{\sigma(e^+e^- \to \mu^+\mu^-)}$	4.7 ± 1.1	6.8 ± 2.0
$\langle n_{ch} \rangle$	4.2 ± 0.6	4.5 ± 1

FIGURE CAPTIONS

1. Authors and institutions contributing to the BOLD experiments.
2. Main components of the C.E.A. Bypass.
3. Schematic diagram of the double bremsstrahlung luminosity monitoring system.
4. Bypass operational parameters, and BOLD running conditions.
5. Bypass On-Line Detector (BOLD); overall layout, angular definitions.
6. View of one of the BOLD quadrants.
7. Lowest order Feynman diagrams for pure Q.E.D. e^+e^- colliding beam reactions.
8. Shower pulse height distributions for a sample of $e^+e^- \to e^+e^-$ events compared to a sample of cosmic rays detected in a BOLD quadrant.
9. Acolinearity ($\Delta\theta$) distribution of Bhabha scattering events at $E_{cm} = 5$ GeV.

9a. Acoplanarity ($\Delta\phi$) distribution of Bhabha scattering events at $E_{cm} = 5$GeV.

10. A typical Bhabha scattering event, reconstructed by computer, as viewed along the beam line. "+"-signs represent sparks; small circles are wire spark chamber fiducial marks; lines are computer-fitted trajectories.
11. Frascati $\mu\pi$ and C.E.A. data on Bhabha scattering: the ratio of experiment to theory as a function of center-of-mass energy.

C.E.A. data points include luminosity measurement errors; Frascati $\mu\pi$ data points do not ($\sim$ 5% systematic error). The C.E.A. 5 GeV point is preliminary.

12. Ratio of experiment to theory for $e^+e^- \to \gamma\gamma$, vs. E_{cm}, as measured by C.E.A. and other experiments.

13. Lowest order Feynman diagrams for the production of hadrons by one photon annihilation in e^+e^- colliding beam reactions.

14. A multihadronic event detected in BOLD at E_{cm} = 4 GeV with five detected charged tracks plus γ rays. View along the beam line.

15. An $e^+e^- \to$ multihadrons event in BOLD at E_{cm} = 5GeV. Six detected charged tracks and computer analysis and reconstruction are shown.

16. Another $e^+e^- \to$ multihadrons event at E_{cm} = 5 GeV with eight detected charged tracks.

17. Scatter plot of the vertex coordinates transverse to the beam line of $e^+e^- \to$ multihadrons candidates at E_{cm} = 4 GeV prior to any interaction region cut. The steel holder for the quartz fiber is outlined.

17a. Lowest order Feynman diagrams for the "two Photon" process

$e^+e^- \to e^+e^-e^+e^-$
$\to e^+e^-\mu\,\mu^-$
$\to e^+e^-\,A\,\bar{A}$

18. A plot of two-photon mechanism reaction cross sections versus center-of-mass energy. Narrow resonance, pion pair and multihadrons production are included. For unspecified threshold s-values, zero kinetic-energy final states are allowed in the calculated cross sections.

19. The dominant Feynman for two-photon production of a C = + state in a colliding-beam experiment where the beam particles do not annihilate.

20a. Outline of detection efficiency calculations for $e^+e^- \to$ (three or more hadrons). Assumptions and methods are outlined.

20b. Continuation of 20a; plot of distribution of calculated total efficiencies for all χ_0^2 allowed as the prong counts N_p fluctuate according to Poisson statistics (based on E_{cm} = 4 GeV data).

21. Normalized distribution of the cosines of the angles between two prongs in BOLD I real data, in Monte Carlo events generated by a 6π phase space mechanism, and in an $A\bar{A}$ quasi-two body mechanism.

22. Patterns of 4 prong real BOLD I events versus $4\pi^+4\pi^-$ Monte Carlo phase space predictions.

23. A recent summary of world data on the ratio:

$$\frac{\sigma(e^+e^- \to \text{multihadrons})}{\sigma_{\text{theory}}(e^+e^- \to \mu^+\mu^-)}$$

as a function of ln(s). The C.E.A. 5 GeV point is preliminary. Predictions of the "quark" and "colored quark" models are shown for comparison.

Fig. 1.

AUTHORS { C.E.A., M.I.T., HARVARD, S.M.U., TECHNION

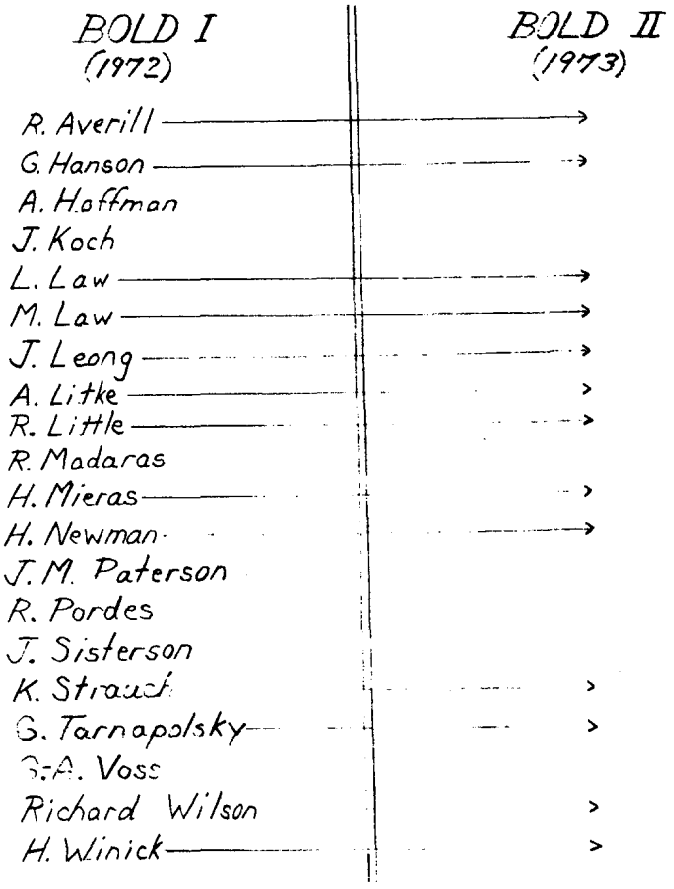

Fig. 1

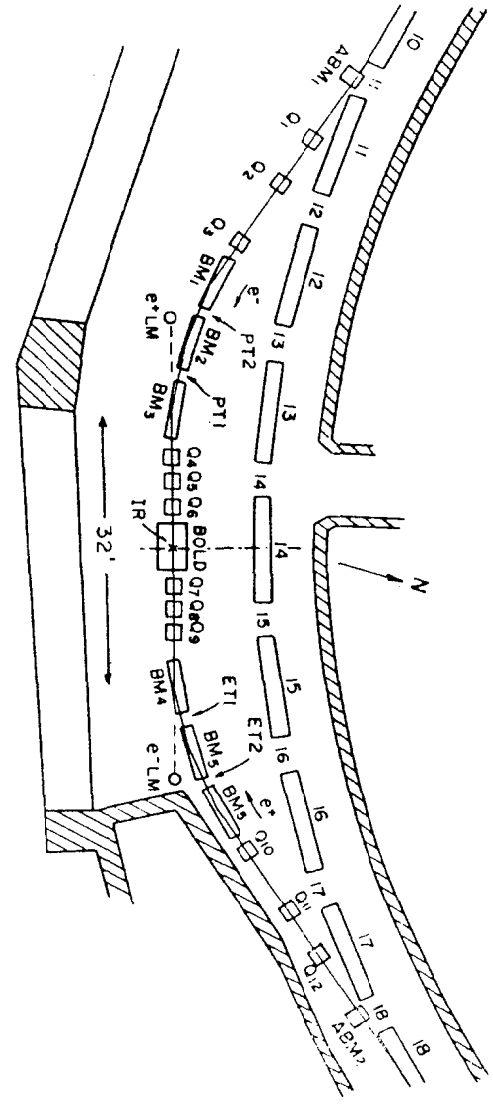

Fig. 2 Main Components of the CEA Bypass. The Symbols Q, BM, ABM, LM, and IR Stand for Quadrupole Magnet, Bending Magnet, Auxiliary Bending Magnet, Luminosity Monitor and Interaction Region

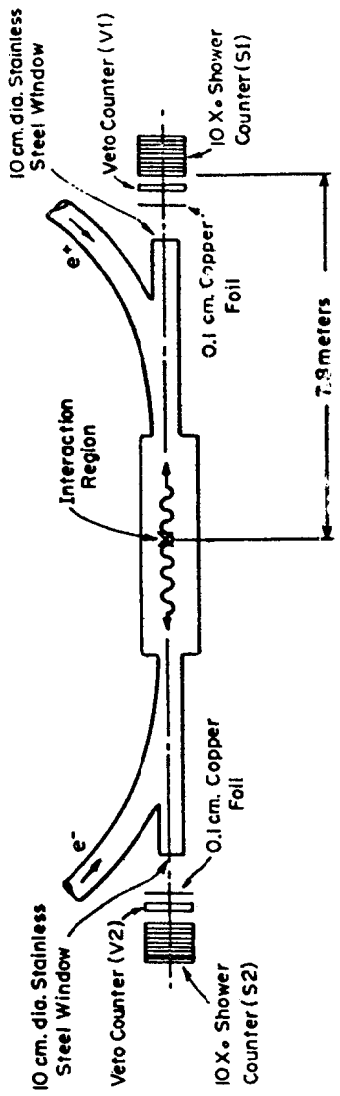

Fig. 3 Schematic Diagram of the Double Bremsstrahlung Luminosity Monitoring System.

FIG. 4. MACHINE PARAMETERS

BOLD I AND BOLD II:

1.	RF Frequency	475 MHz
	Circumferential Frequency	1.3 MHz
	Number Bunches each Beam	≈ 100
	Synchrotron Pressure	10^{-9} - 10^{-8} Torr
	IR Pressure	$\approx 3 \times 10^{-10}$ Torr
	Injection Time	$\approx$ 7 Minutes
	Storage Time	$\approx$ 20 Minutes
2.	Beam Lifetime	$\approx$ 3000 Seconds
	Beam Size (cm)	$\sigma_z \approx 1.5$
		$\sigma_H \approx 2.5 \times 10^{-3}$ } FIBER MEASUREMENT
		$\sigma_V \approx 2.5 \times 10^{-3}$ } FIBER MEASUREMENT

	BOLD I	BOLD II
Typical Currents (mA)	4 x 4	5 x 4
Peak Luminosity ($cm^{-2} sec^{-1}$)	$\approx 3 \times 10^{28}$	$\approx 4 \times 10^{28}$
Average Luminosity (24 hours)	3×10^{27}	4×10^{27}
	$\int \mathcal{L} dt \sim 10^{34}$	} OVER THE EXPERIMENTAL RUN

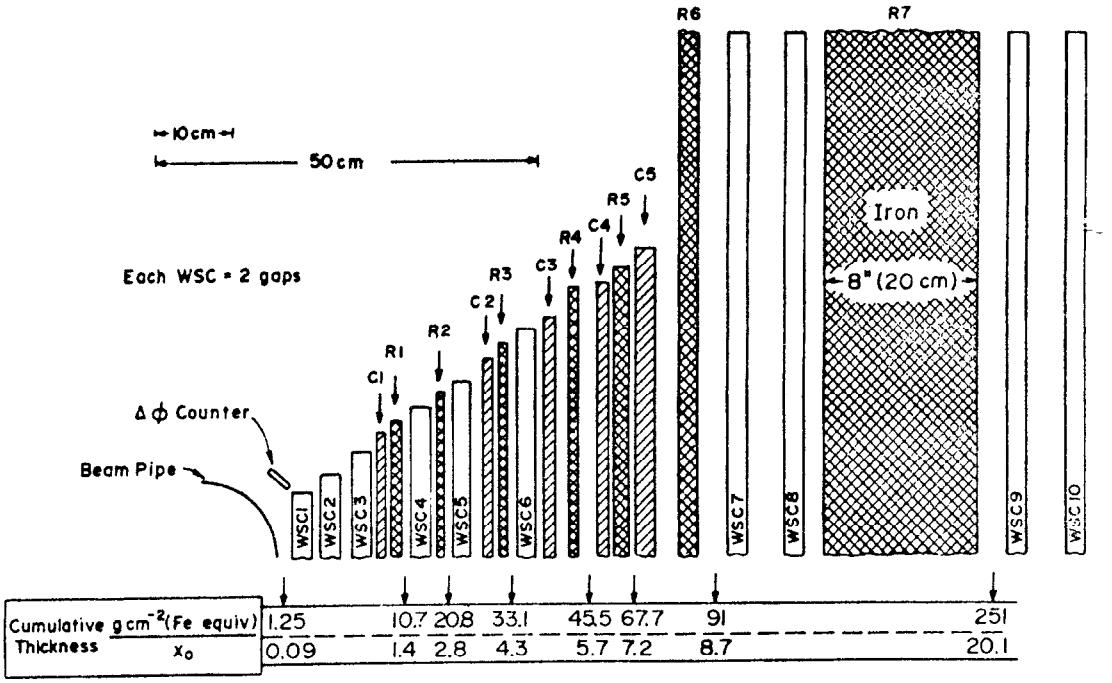

Fig. 6 VIEW OF OUTER BOLD QUADRANT

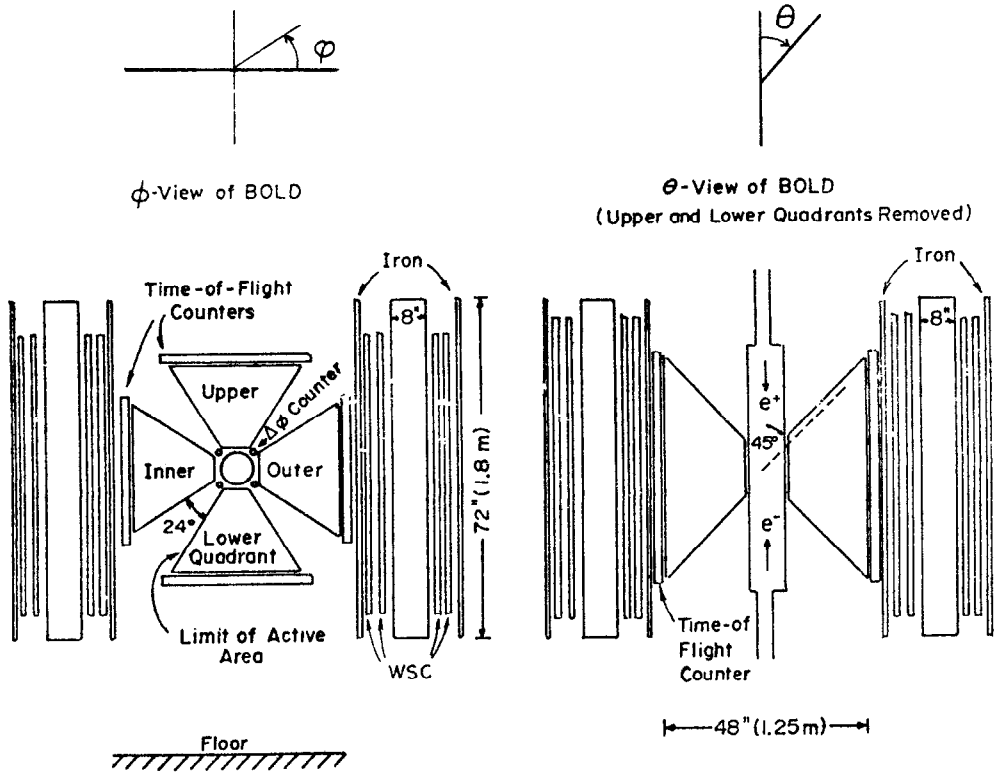

Fig. 5 THE BYPASS ON-LINE DETECTOR
(NON-MAGNETIC)

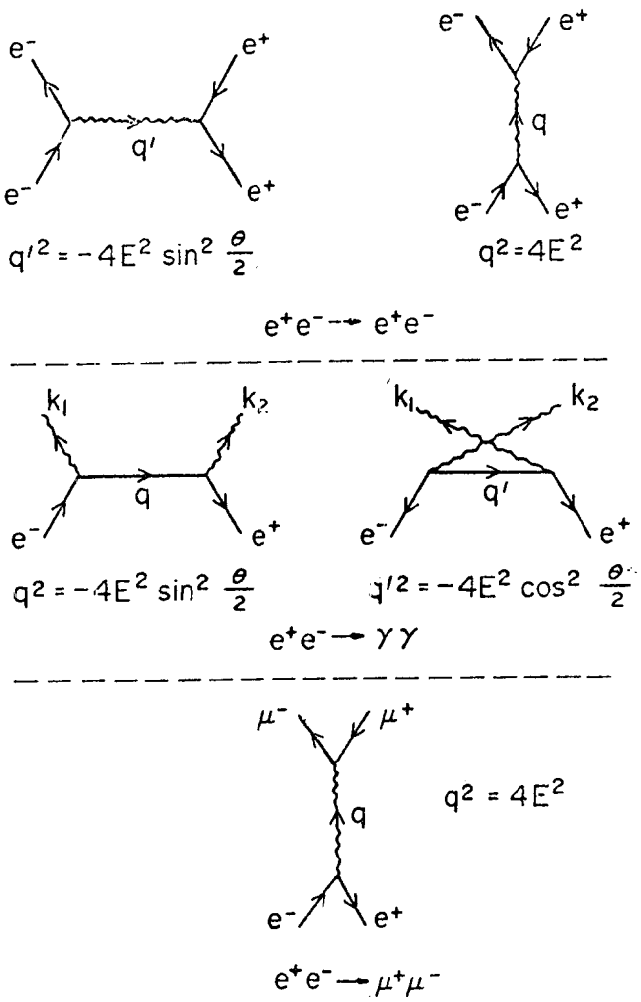

Fig. 7 FEYNMAN DIAGRAMS FOR e^+e^- COLLIDING BEAM REACTIONS TO LOWEST ORDER IN QED

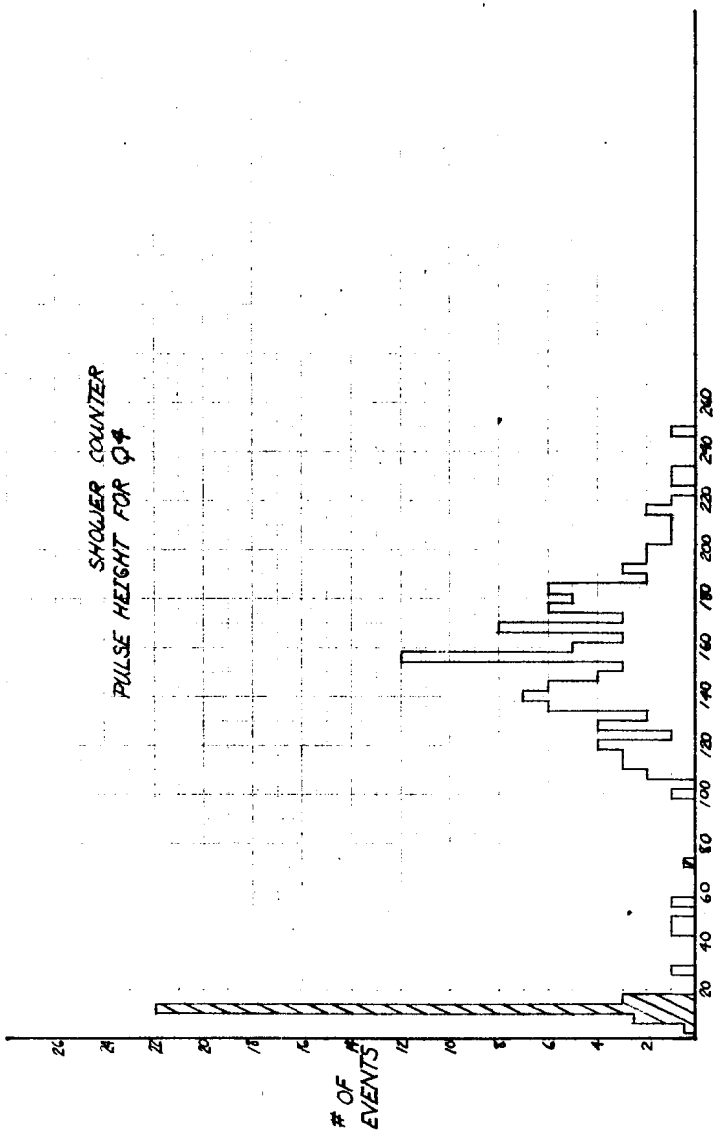

Fig. 8 QUADRANT-4 SHOWER COUNTER PULSE HEIGHT (ARB. UNITS)

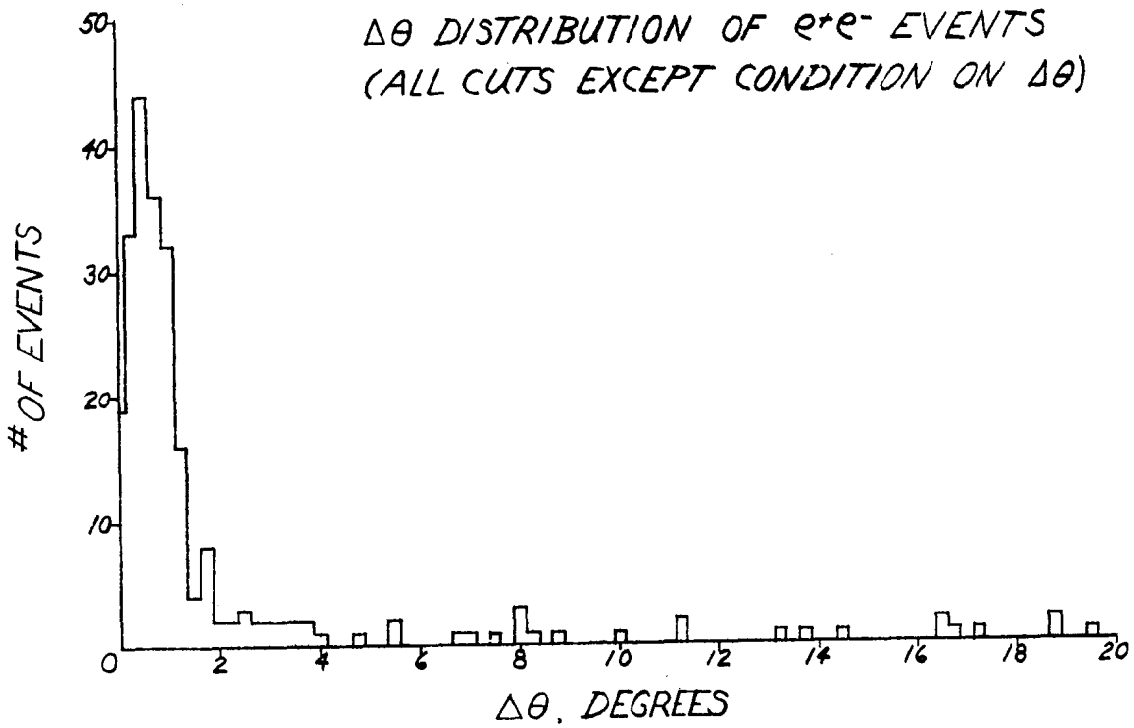
Δθ DISTRIBUTION OF e⁺e⁻ EVENTS
(ALL CUTS EXCEPT CONDITION ON Δθ)
OF EVENTS
50
40
30
20
10
0
2
4
6
8
10
12
14
16
18
20
Δθ, DEGREES

Fig. 9

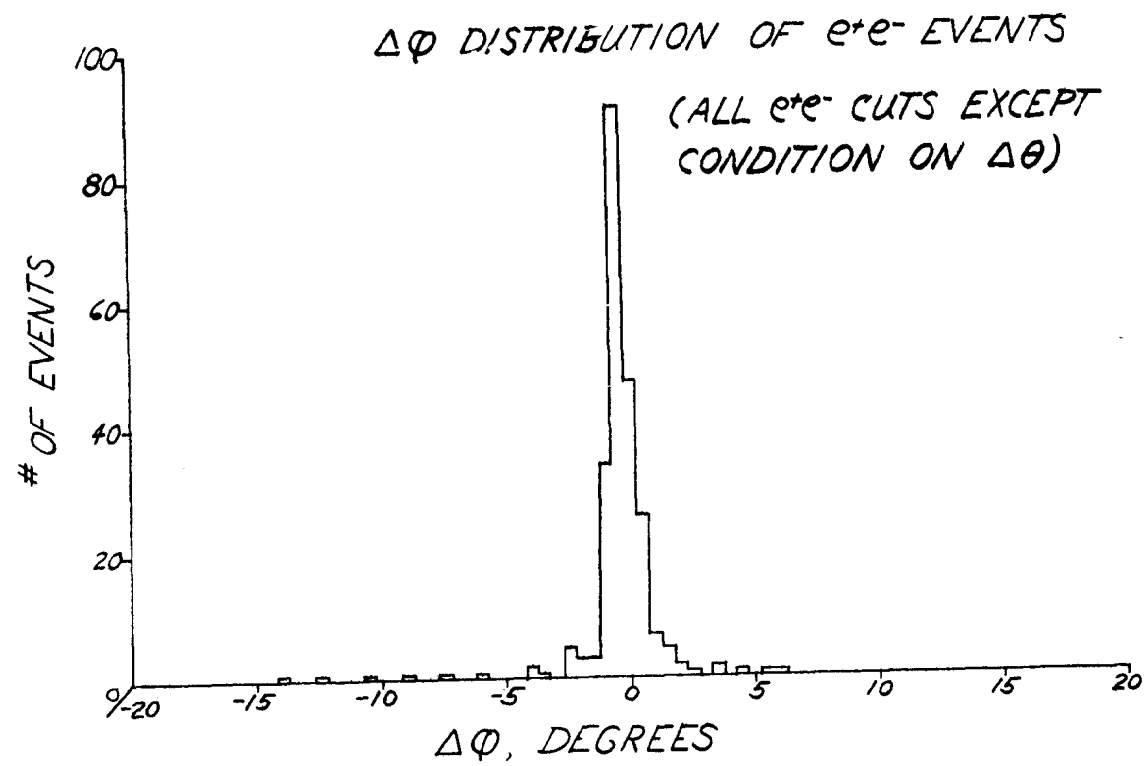
Δφ DISTRIBUTION OF e⁺e⁻ EVENTS
(ALL e⁺e⁻ CUTS EXCEPT
CONDITION ON Δθ)
OF EVENTS
100
80
60
40
20
0
-20
-15
-10
-5
0
5
10
15
20
Δφ, DEGREES

Fig. 9a

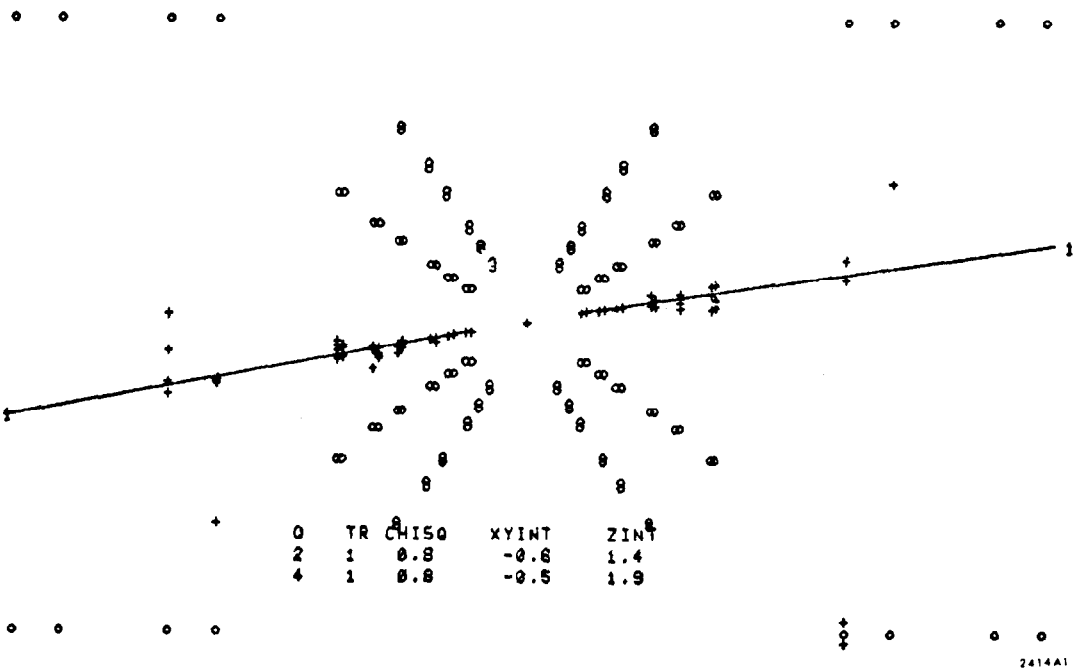
Q TR CHISQ XYINT ZINT
2 1 0.8 -0.6 1.4
4 1 0.8 -0.5 1.9
2414A1

Fig. 10

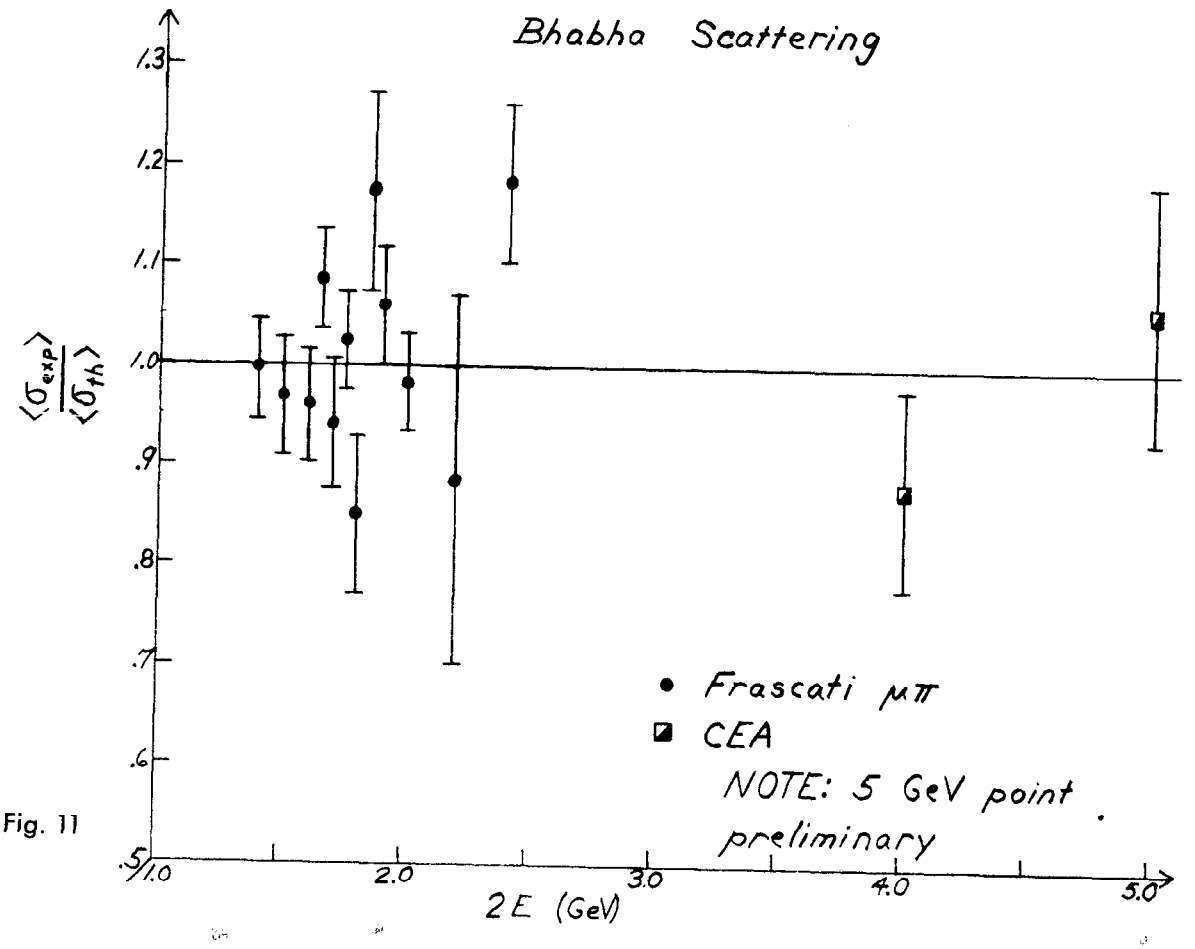
Bhabha Scattering
$\langle\sigma_{exp}\rangle / \langle\sigma_{th}\rangle$
1.3
1.2
1.1
1.0
.9
.8
.7
.6
.5
1.0
2.0
3.0
4.0
5.0
2E (GeV)
Frascati μπ
CEA
NOTE: 5 GeV point
preliminary

Fig. 11

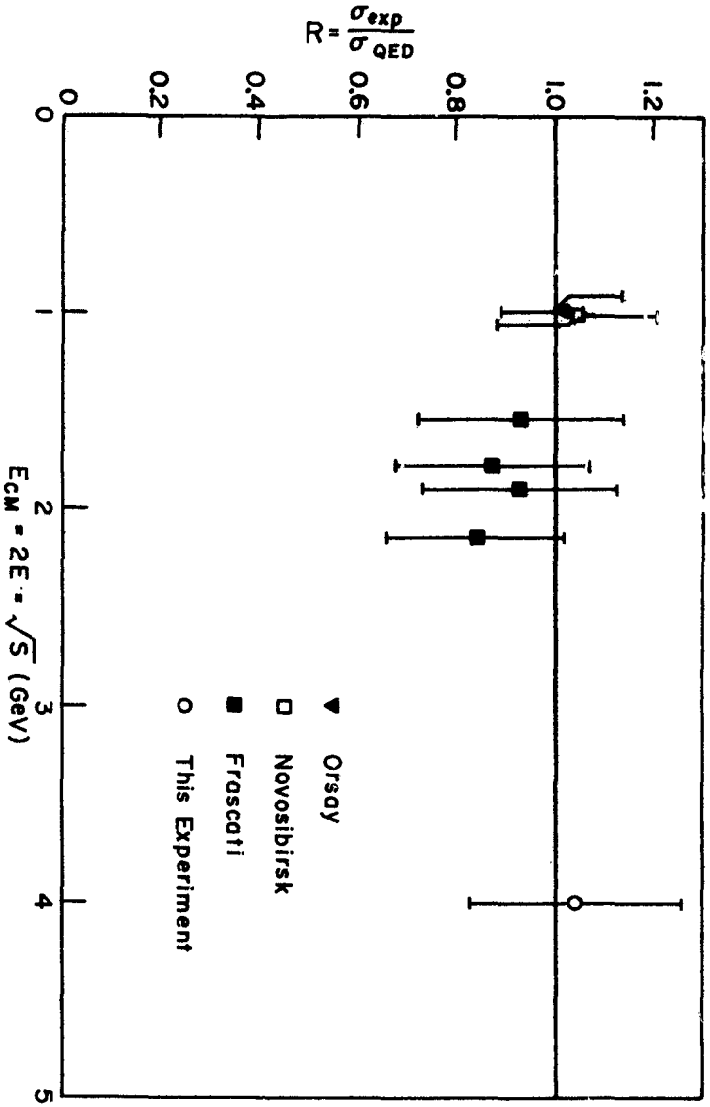

Fig. 12 RATIO OF EXPERIMENT TO THEORY FOR $e^+e^- \to \gamma\gamma$ AS MEASURED BY OTHER EXPERIMENTS

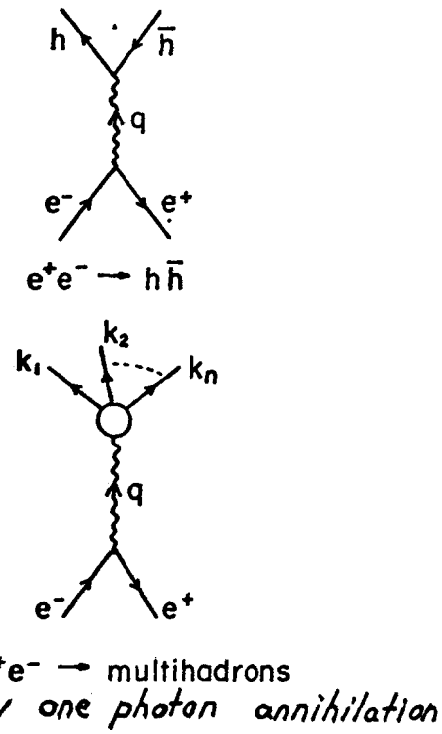

Fig. 13 FEYNMAN DIAGRAMS FOR THE PRODUCTION OF HADRONS IN e^+e^- COLLIDING BEAM REACTIONS

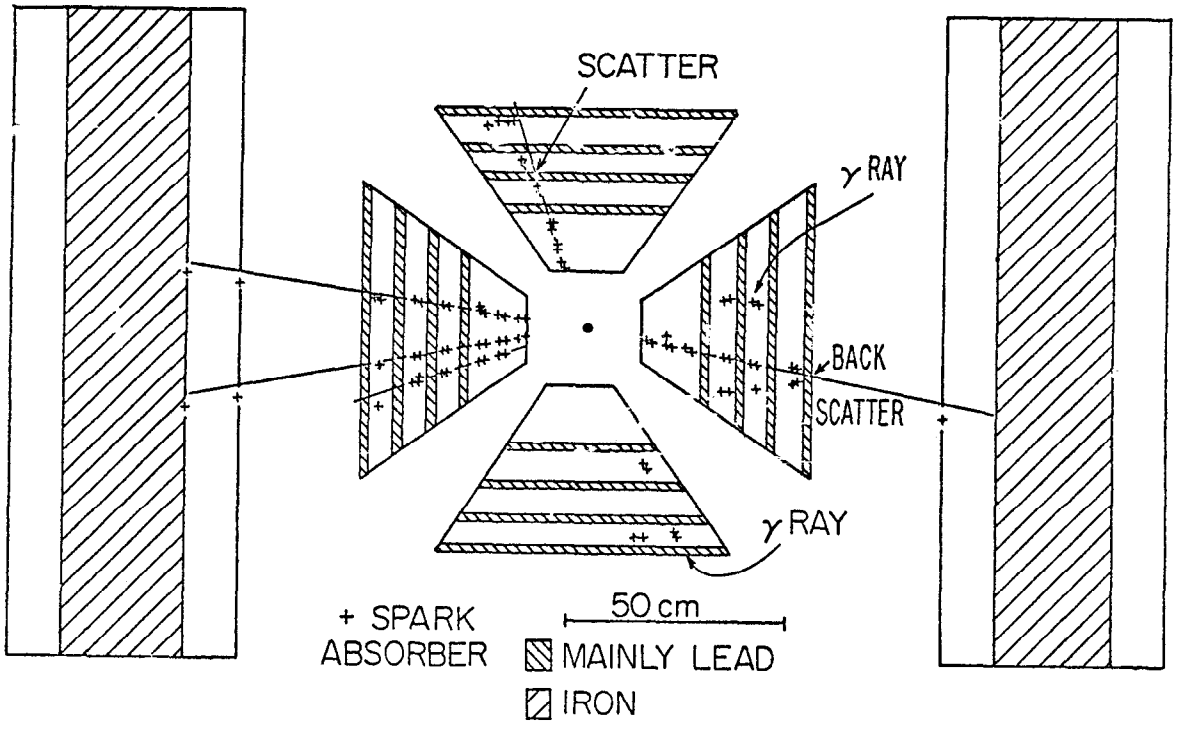
SCATTER
γ RAY
BACK
SCATTER
γ RAY
+ SPARK
ABSORBER
50 cm
MAINLY LEAD
IRON

Fig. 14

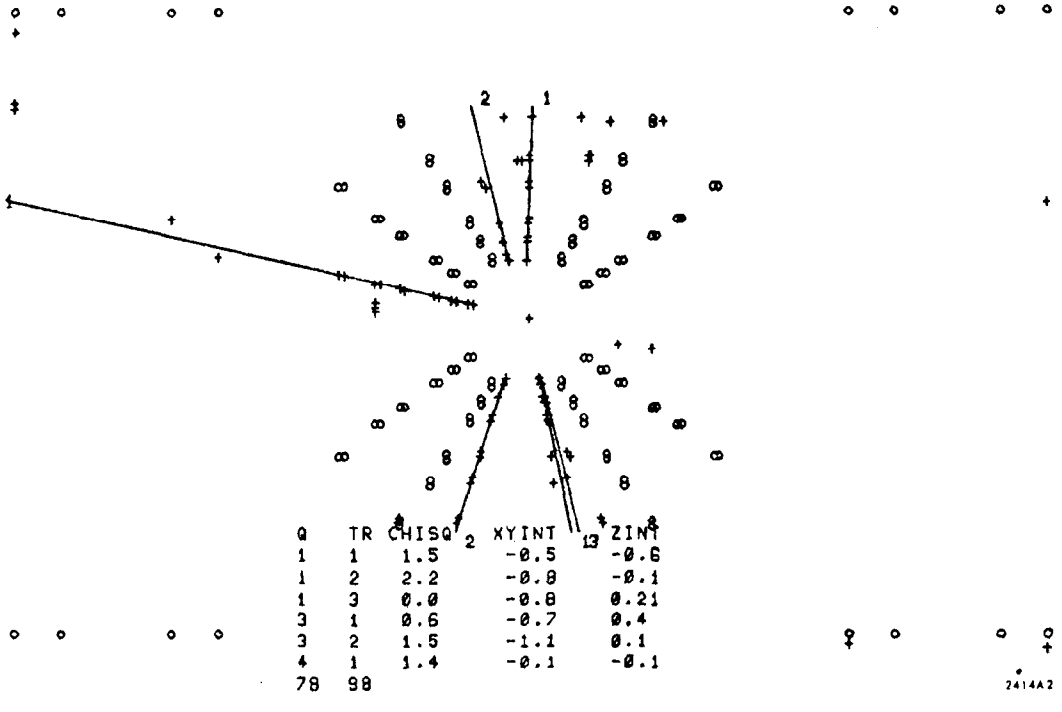
Q TR CHISQ XYINT ZINT
1 1 1.5 -0.5 -0.6
1 2 2.2 -0.8 -0.1
1 3 0.0 -0.8 0.21
3 1 0.6 -0.7 0.4
3 2 1.5 -1.1 0.1
4 1 1.4 -0.1 -0.1
78 98
2414A2

Fig 15

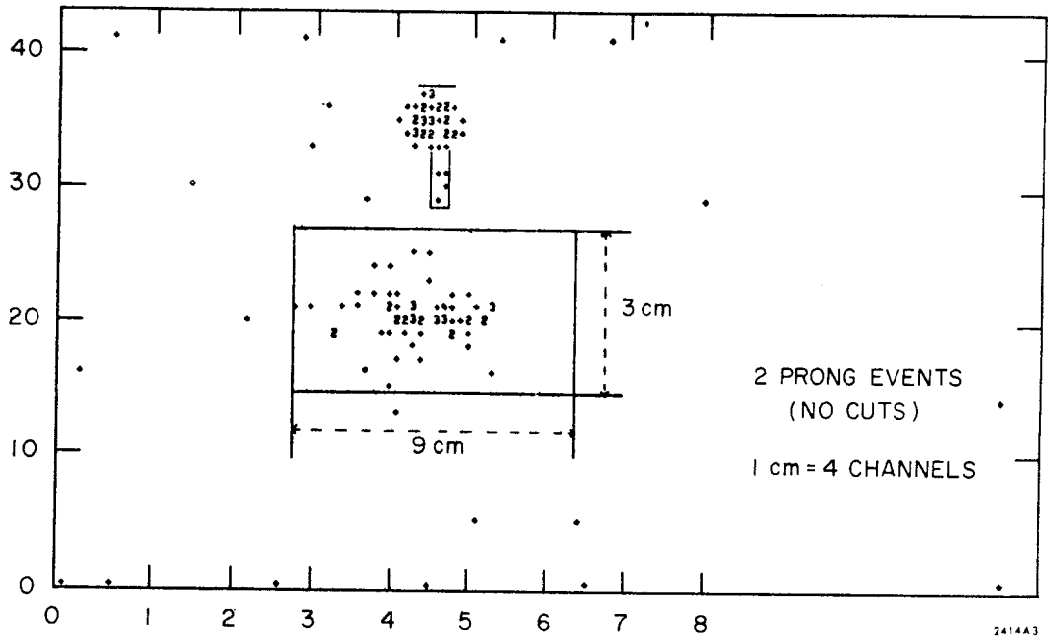
40
30
20
10
0
0
1
2
3
4
5
6
7
8
3 cm
9 cm
2 PRONG EVENTS
(NO CUTS)
1 cm = 4 CHANNELS
2414A3

Fig. 17

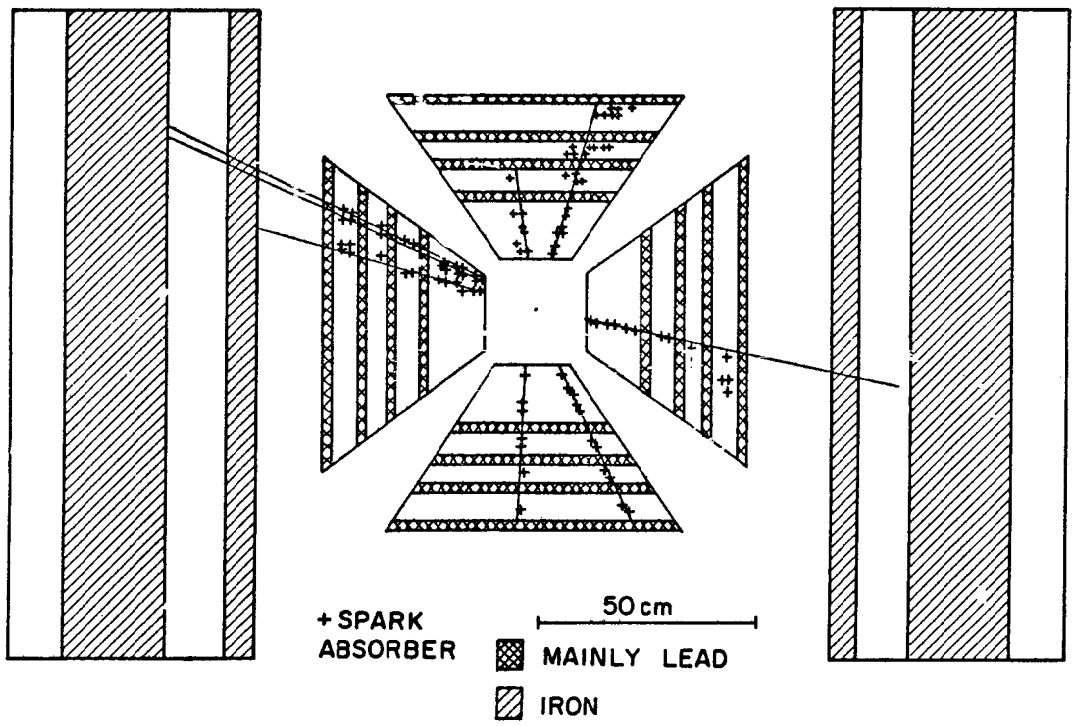
+ SPARK
ABSORBER
50 cm
MAINLY LEAD
IRON

Fig. 16

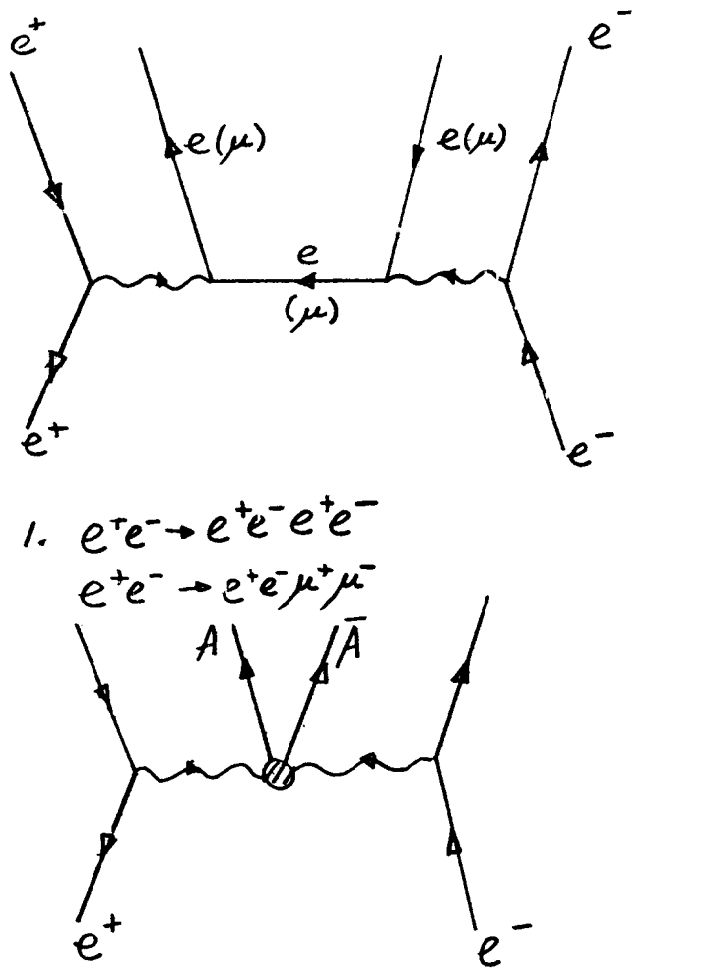

Fig. 17a

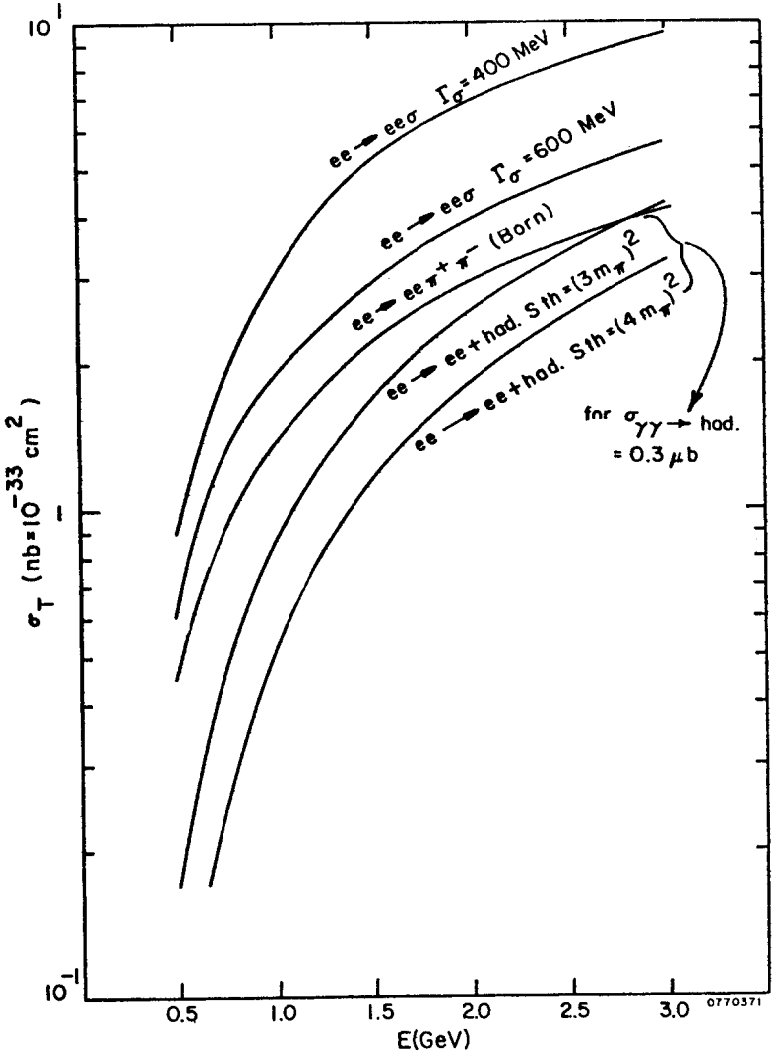

Fig. 18

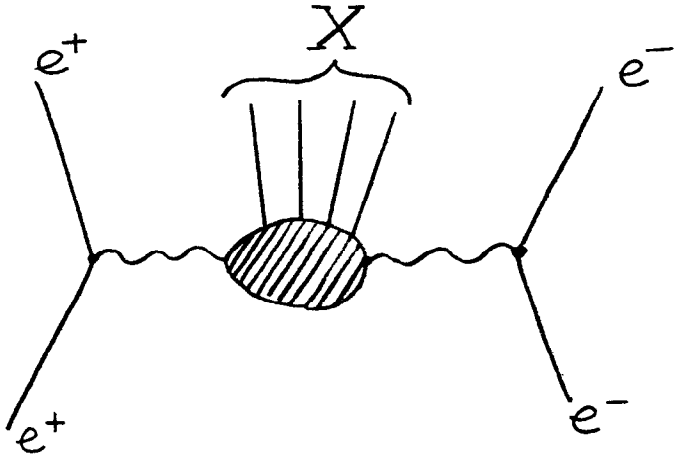

$$\sigma^{asympt}_{\gamma\gamma\to had} = \sigma_{\gamma\gamma\to had}(s'\to\infty) \overset{?}{\sim} \frac{\sigma_{\gamma p}(s'\to\infty)^2}{\sigma_{pp}(s'\to\infty)}$$

$$\sim 0.3\,\mu b$$

Fig. 19

$$N_p = L \times \sum_q \mathcal{E}(p,q)\,\sigma_q(e^+e^- \to q\pi^\pm + \text{neutrals})$$

BOLD I: $p = 2,3,4,5$ $\quad q = 2,4,6,8$

BOLD II: $p = 2,3,4,5,6,7,8$ $\quad q = 2,4,6,8,10,12,14,16$

Restriction : $\sigma_q \geq 0$

Method :1. Solve by least squares

2. Since exact solution not generally possible let each LHS vary.

3. If calculated LHS is N_p', then minimize:

$$\chi^2 \equiv \sum_p \frac{(N_p' - N_p)^2}{N_p}$$

4. Let the N_p vary according to Poisson statistics. $N_p \to N_p \pm \theta(\sqrt{N_p})$

Calculate solutions for each set of N_p counts.

Fig. 20a

Results of Calculations for σ_q

1. $\sum_q \sigma_q = \sigma_{TOT}$

2. $\mathcal{E}_T = \dfrac{\sigma_{TOT} L}{N_T}$; $N_T = \sum_P N_P$

   $L = \int (\text{luminosity})\, dt$

3. σ_q not well determined, but efficiency varies in narrow band for even "improbable" σ_q sets {i.e. large χ_0^2}

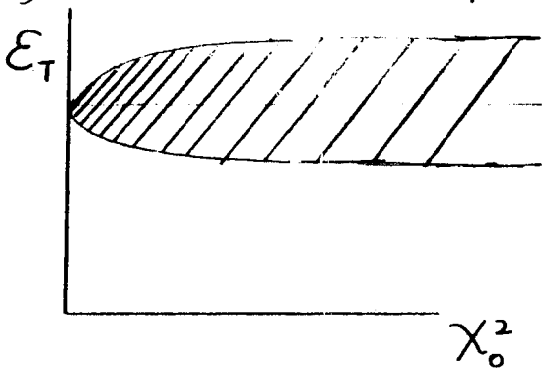

Fig. 20b

$$\chi_0^2 \equiv \sum_P \frac{(N_P^* - N_P)^2}{N_P}$$

Distributions of the cosine of the angle between two prongs (normalized to the number of prong pairs)

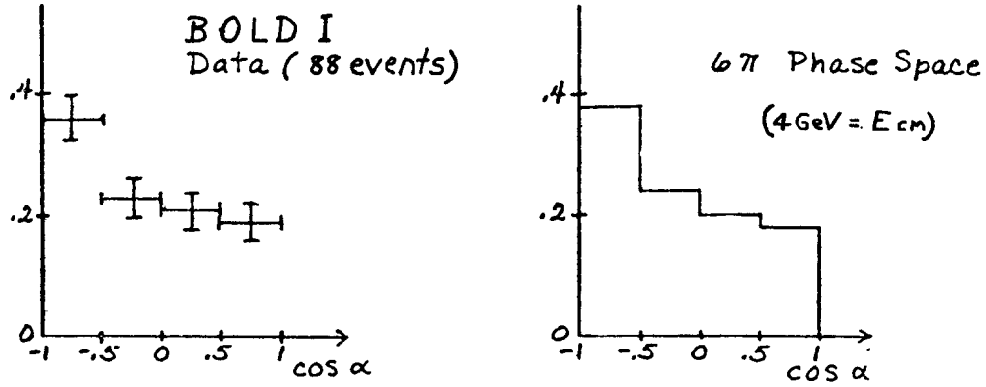

α = angle between any 2 prongs

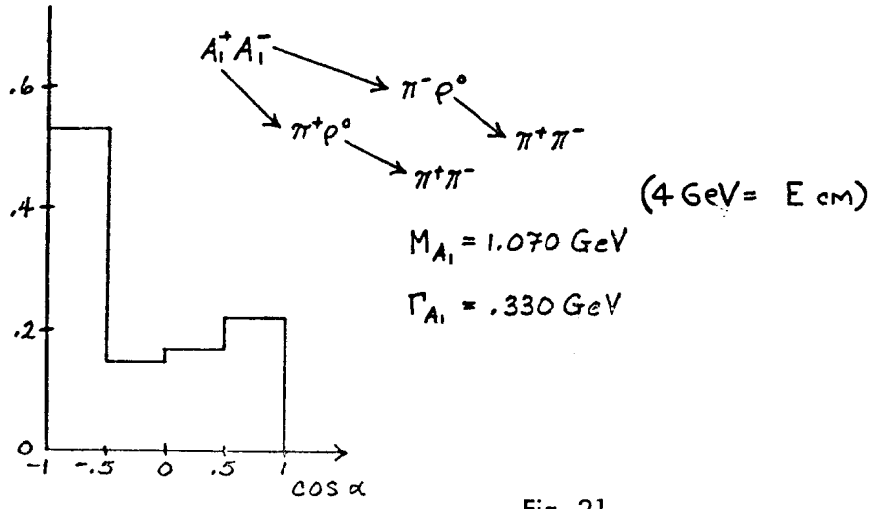

(4 GeV = E cm)

$M_{A_1} = 1.070$ GeV

$\Gamma_{A_1} = .330$ GeV

Fig. 21

Jet Structure ?

Configurations of 4-prong events in BOLD quadrants compared with Monte Carlo predictions for 8 $\pi^{\pm}$ invariant phase space:

Pattern	Monte Carlo	Observed
4000	0	0
3010	1.2	0
3100	0.6	1
2020	2.0	3
2200	0.5	1
2101	3.4	3
2110	9.3	10
1111	3.9	3

Fig. 22

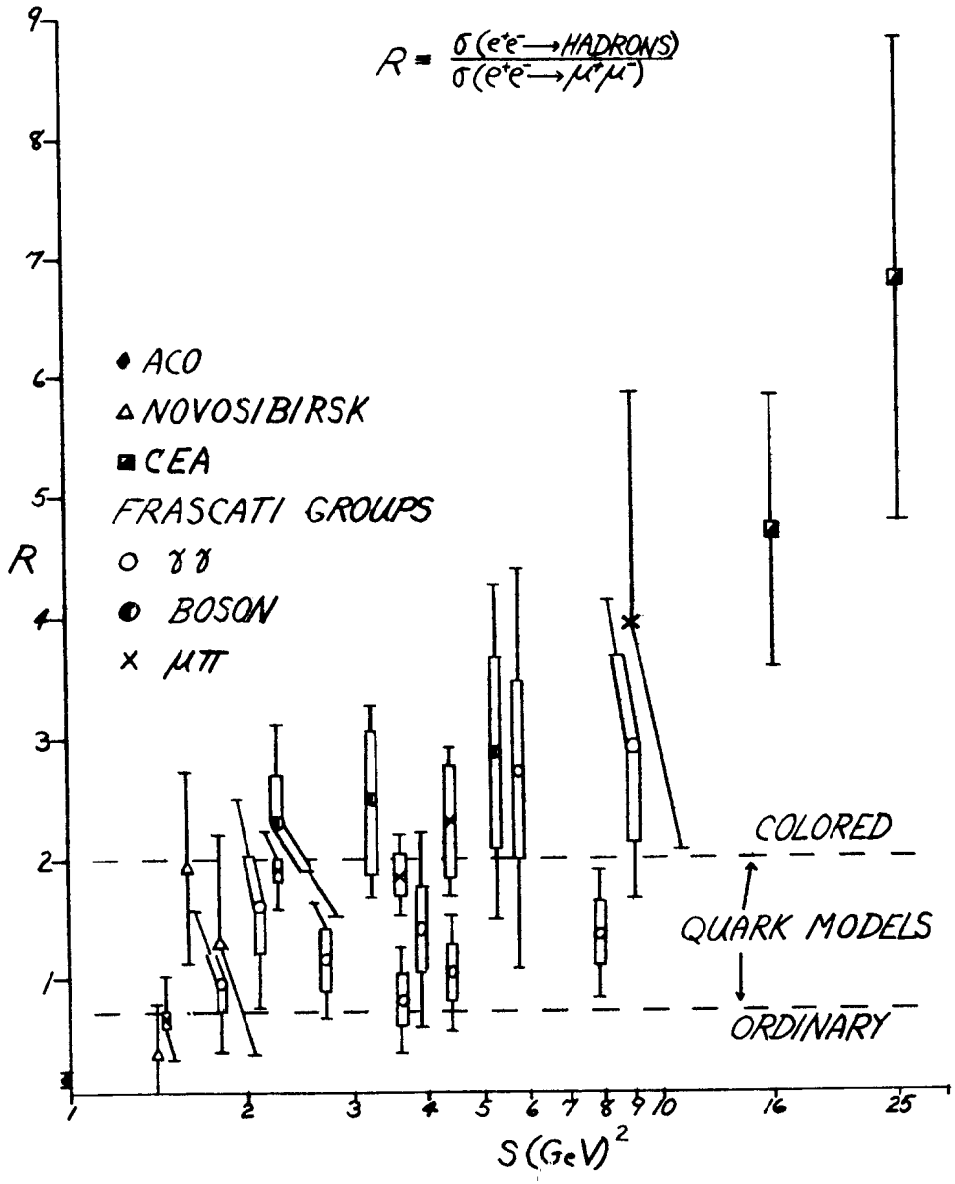

Fig. 23

REFERENCES

[1] R. Madaras, et al., Phys. Rev. Lett. 30, 507 (1973).

[2] C. Bernardini, "Results on e^+e^- Reactions at Adone", International Symposium on Electron and Photon Interactions at High Energies, Cornell, 1971; LNF 71/13, Frascati, 1971.

[3] G. Hanson, Lett. Nuovo Cimento, to be published.

[4] G. Szklarz, Thèse de Troisieme Cycle, University of Paris VII, 1972 (unpublished).

[5] V. E. Balakin, et al., Phys. Lett. 34B, 99 (1971).

[6] C. Bacci, et al., Lett. Nuovo Cimento 2, 73 (1971).

[7] A. Litke, et al., Phys. Rev. Lett. 30, 1189 (1973), and references therein.

[8] S. Brodsky, T. Kinoshita, H. Terazawa, Phys. Rev. D4, 1532 (1971).

[9] G. Tarnopolsky, D.Sc. Thesis, Technion, Haifa (unpublished).

[10] G. Tarnopolsky, Internal C.E.A. memos, 1972-73.

[11] P. Kessler, Nuovo Cimento 17, 809 (1960).

[12] N. Artega-Romero, A. Jaccarini, P. Kessler, and J. Parisi, Phys. Rev. D3, 1569 (1971).

[13] A. Browman et al., CLNS 224, Cornell, April 1973.

ILL-(TH)-73-11

ANALYTIC CONTINUATION FROM THE SCATTERING TO THE ANNIHILATION REGION*

by

J.D. SULLIVAN

Physics Department
University of Illinois at Urbana-Champaign
Urbana, Illinois 61801

Talk presented at the SLAC Topical Conference on Deep Inelastic Electroproduction, July 16-18, 1973.

*Work supported in part by the National Science Foundation under Grant No. NSF GP 35303.

I. INTRODUCTION

In this review we address the question, "What relation, if any, exists between the structure functions $F_{1,2}(\omega)$ of deep inelastic scattering and the corresponding structure functions $\bar{F}_{1,2}(\omega)$ of the deep inelastic annihilation region?" Previous review talks are listed in Refs. 1-4.

The above question can be broken down naturally into two parts: (i) Does scaling behavior for the scattering $e^-+p\to e^-+X$ imply scaling behavior for the annihilation $e^++e^-\to\bar{p}+X$? and (ii) "If so, can $\bar{F}_{1,2}(\omega)$ be obtained from $F_{1,2}(\omega)$ by analytic continuation? We will answer both of these questions in the affirmative after pointing out certain subtleties one must appreciate in carrying out the analytic continuation.

Before delving into all this it is perhaps useful to place analytic continuation in its proper perspective. Even though analytic continuation here and elsewhere touches upon questions of experimental importance it is essentially a theoretical tool. To put it bluntly one does not and cannot analytically continue data. For example although the process $\pi N\to\pi N$ and $\bar{N}N\to\pi\pi$ are related by analytic continuation, no one can take the data (alone) for $\pi N\to\pi N$ and predict the $\bar{N}N\to\pi\pi$ data. Only theoretical models, formulas, etc. can be analytically continued.

There is by now a considerable body of literature concerned with the question of analytic continuation from the scattering to the annihilation region. A casual scan of this literature leaves one with a confusing picture. Historically it was first suggested by Drell, Levy and Yan[10] on the basis of simple diagram calculations in cutoff field theory, that indeed scaling occurred in the annihilation region and analytic continuation held, namely

$$F_1(\omega) = -\bar{F}_1(\omega) \tag{1}$$

and

$$F_2(\omega) = F_2(\omega) \quad . \tag{2}$$

[See below and Appendix A for definitions.] (Pestieau and Roy[9] also suggested this on the basis of an incomplete argument involving current commutators.)

Next came a barrage of counterexamples[5,6,21] saying that the analytic continuation was not generally true. Most recently a number of authors[6,7,8] have looked at the question from a more general viewpoint and settled the issue. To put it briefly the conclusion is, yes F and $\bar{F}$ are related by analytic continuation, but you have to do it correctly.

II. GENERAL PROCEDURE

A. Kinematic Review

Let us begin by briefly reviewing the kinematics and at the same time fix our notation. It is useful to consider simultaneously three distinct physical processes which are, formally at least, related by the substitution law of field theory. The processes are:

inelastic scattering

$$e^-(\ell) + P(p) \to e^-(\ell') + X \tag{3a}$$

three-body annihilation

$$e^-(k^-) + e^+(k^+) + P(p) \to X \tag{3b}$$

and annihilation

$$e^-(\ell^-) + e^+(\ell^+) \to \bar{P}\ (P) + X \quad . \tag{3c}$$

The proton (antiproton) in Eq. (3a), (3b), (3c) can be replaced by any other hadron of interest. Fig. 1 illustrates the one-photon-exchange approximations to the corresponding amplitudes.

For these processes we pick variables as follows:

inelastic scattering

$$q^2 = (\ell-\ell')^2 < 0 \tag{4a}$$

$$\nu = p\cdot(\ell-\ell')/m > 0 \tag{5a}$$

$$\cos\theta_a = \hat{\ell}'\cdot\hat{\ell} \tag{6a}$$

three body annihilation

$$q^2 = (k^- + k^+)^2 > 0 \tag{4b}$$

$$\nu = p\cdot(k^- + k^+)/m > 0 \tag{5b}$$

$$\cos\theta_b = \hat{k}^- \cdot \hat{k}^+ \tag{6b}$$

and annihilation

$$q^2 = (\ell^- + \ell^+)^2 > 0 \tag{4c}$$

$$\nu = -P\cdot(\ell^- + \ell^+)/m < 0 \tag{5c}$$

$$\cos\theta_c = \hat{\ell}\cdot\hat{P} \ . \tag{6c}$$

Both $\cos\theta_a$ and $\cos\theta_b$ are measured in the proton rest frame ($\vec{p}=0$), while $\cos\theta_c$ is measured in the center-of-mass frame ($\vec{q}=0$). [Note that according to Eq. (5c) for the annihilation case ν is the negative of the virtual photon energy in the frame $\vec{P}=0$.] In Eqs. (5a)-(5c) m denotes the proton mass.

It is sometimes convenient to use the mass squared, s, of the unobserved system X in place of the variable ν. The relation is

$$s = (q+p)^2 = m^2 + q^2 + 2m\nu \geq m^2 \tag{7a,b}$$

for (3a) and (3b) and

$$s = (q-P)^2 = m^2 + q^2 + 2m\nu \geq m^2 \tag{7c}$$

for (3c).

The physical regions for the three processes are shown on Fig. 2. Note that if we had not neglected the electron mass the processes (3a) and (3b) would be separated by a gap $\Delta q^2 = 4m_e^2$.

We denote the structure functions for the three cases by (see Appendix A):

inelastic scattering

$$W_1(q^2,\nu),\ W_2(q^2,\nu) \tag{8a}$$

three body annihilation

$$\tilde{W}_1(q^2,\nu),\ \tilde{W}_2(q^2,\nu) \tag{8b}$$

and annihilation

$$\bar{W}_1(q^2,\nu),\ \bar{W}_2(q^2,\nu) \ . \tag{8c}$$

The Bjorken limit for all three processes is described by $|\nu| \to \infty$, $|q^2| \to \infty$ with

$$\omega \equiv \frac{2m\nu}{-q^2} = \frac{s-m^2}{-q^2} + 1 \tag{9}$$

fixed. In the three physical regions one has:

inelastic scattering

$$1 \leq \omega \tag{10a}$$

three body annihilation

$$\omega \leq 0 \tag{10b}$$

annihilation

$$0 \leq \omega \leq 1 \tag{10c}$$

as shown in Fig. 2.

B. Non-Forward Compton Amplitude

We now discuss in what way these three distinct physical processes are related. It turns out that the answer depends critically on the signs of certain $i\epsilon$'s so one needs to be precise. The secret is to consider the non-forward-virtual-Compton amplitude illustrated in Fig. 3. We denote it by

$$T^{\mu\nu}(s,t,q_1^2,q_2^2) \tag{11}$$

where $t = (q_1-q_2)^2$ and $s = (p_1+q_1)^2$. In place of s we sometimes use the more symmetric variable

$$\nu \equiv \frac{s-u}{4m} ,$$

$$u = (p_1-q_2)^2 . \tag{12}$$

It is well known that the structure functions for inelastic scattering are given by the discontinuity of the forward-virtual-Compton amplitude, Fig. 4(a)

$$W_{1,2}(q^2,\nu) \sim \{T^{\mu\nu}(s+i\epsilon,0,q^2,q^2) - T^{\mu\nu}(s-i\epsilon,0,q^2,q^2)\}$$

$$\equiv \text{disc}_s\, T^{\mu\nu}(s,0,q^2,q^2) . \tag{13a}$$

The $\pm$ in Fig. 4(a) refers to the sign of the $i\epsilon$ corresponding to the s variable. Since $q^2<0$ we are not in a region where $T^{\mu\nu}$ has cuts in q^2 and hence no $i\epsilon$ prescription is necessary for the q_1^2, q_2^2 variables.

Similarly the structure functions for annihilation are given by a discontinuity, Fig. 4(c),

$$\bar{W}_{1,2}(q^2,\nu) \sim \{T^{\mu\nu}(s+i\epsilon,0,q^2+i\epsilon',q^2-i\epsilon'') - T^{\mu\nu}(s-i\epsilon',0,q^2+i\epsilon',q^2-i\epsilon'')\}$$

$$= \text{disc}_s T^{\mu\nu}(s,0,q^2+i\epsilon',q^2-i\epsilon'') . \tag{13c}$$

Note that since in this case $q^2>0$, one is in the region of cuts in the q_1^2 and q_2^2 variables. As indicated in Fig. 4(c) one must take q_1^2 above its cut $(+i\epsilon')$ and q_2^2 below its cut $(-i\epsilon'')$ to insure that one selects the (real) annihilation structure functions. Fig. (4b) shows the analogous situation for process (3b).

In taking the discontinuities indicated in Fig. 4 one must beware of the overlapping cut structure which occurs for $q^2>0$, Fig. 5. Unlike the familiar situation of the scattering of stable mass particles, here when $q^2>0$ the normal threshold singularities in the s and u variables overlap. The structure functions correspond to the discontinuity across the s cut only; one must avoid crossing the u cut. Given a theoretical expression for $T^{\mu\nu}$ this is always possible.

For completeness let us mention three other related processes: $e^-+\bar{P} \to e^-+\bar{X}$, $e^-+e^+ \to \bar{P}+\bar{X}$, and $e^-+e^+ \to P+\bar{X}$. These are given by u channel discontinuities of the Compton amplitude. The corresponding physical regions are shown in Fig. 6. Given that the electromagnetic current has a definite (odd) property under charge conjugation it is easy to show that the structure functions for these three processes are equal to their counterparts (3a)-(3c).

C. Analytic Continuation

As we have already assumed, one expects on the basis of field theory that the virtual-Compton amplitude $T^{\mu\nu}$ has (for $t<0$) right and left-hand cuts in s and right-hand cuts in q_1^2 and q_2^2. [Actually one anticipates additional "anomalous" singularities. We illustrate an example of one of these in Appendix B.] Therefore $\text{disc}_s T^{\mu\nu}(s,0,q_1^2,q_2^2)$ while not expected to have any simple analyticity properties in s still has good analyticity properties in q_1^2 and q_2^2. Because lines of fixed $s(s \geq m^2)$ pass through the physical regions of inelastic scattering and annihilation (see Fig. 2) we may

nevertheless get from one to the other by continuing in q^2 at fixed s. All that is necessary is to distinguish q_1^2 and q_2^2 and to continue q_1^2 above its cut and q_2^2 below its cut.

It is obvious also what one must do in the Bjorken scaling limit. In place of the single scaling variable

$$\omega = \frac{s-m^2}{-q^2} + 1 \tag{9}$$

which is suitable for the strictly forward case one needs to introduce a pair of scaling variables

$$\omega_{1,2} = \frac{s-m^2}{-q_{1,2}^2} + 1 \tag{14}$$

and consider the generalized Bjorken limit $s \to \infty$, with t, ω_1, ω_2 fixed. All of the arguments, models, etc. which proport to explain the scaling behavior of the forward amplitude will also lead to scaling behavior of the non-forward amplitude. We may now write the correct statement of analytic continuation. It is:

$$-\overline{F}_1(\omega) = F_1(\omega+i\epsilon, \omega-i\epsilon) \tag{15}$$

and

$$\overline{F}_2(\omega) = F_2(\omega+i\epsilon, \omega-i\epsilon) \tag{16}$$

where

$$F_1(\omega_1,\omega_2) = \lim_{\substack{s\to\infty, \\ \omega_1,\omega_2 \text{ fixed}}} \left(mW_1(q_1^2, q_2^2, s, t=0)\right) \tag{17}$$

and

$$F_2(\omega_1,\omega_2) = \lim_{\substack{s\to\infty, \\ \omega_1,\omega_2 \text{ fixed}}} \left(\nu W_2(q_1^2, q_2^2, s, t=0)\right). \tag{18}$$

Clearly $F_1(\omega,\omega)$ $(F_2(\omega,\omega))$ is, for $\omega > 1$, the structure function usually denoted by $F_1(\omega)$ $(F_2(\omega))$.

For certain purposes, especially light cone expansions, the variables used by Mason[25] /

$$\omega_+ = \frac{s}{-\frac{1}{2}(q_1^2+q_2^2)} - 1 \tag{19}$$

and

$$\omega_- = \frac{(q_1^2-q_2^2)}{q_1^2+q_2^2} \tag{20}$$

are probably superior to ω_1, ω_2.

One might object that the deep inelastic scattering experiments measure only $F_{1,2}(\omega)$ and not $F_{1,2}(\omega_1,\omega_2)$ and hence Eqs. (15) and (16) are of no use. That is true but as we remarked earlier one cannot continue that data anyway so nothing is lost. Any complete theory will handle the non-forward as well as the forward case, and hence Eqs. (15) and (16) have real meaning. (See also the discussion below of the threshold region.)

III. EXAMPLES

With the general procedure of Sec. II in hand it is easy to look at various models and examples and to understand the results.

A. Ladder Models

In the original work of Drell, Levy and Yan[10] as well as in the work of others[16-19,24] diagrams of the type shown in Fig. 8 were considered for inelastic scattering 8(a) and annihilation 8(b). Since these are tree diagrams with bare propagators everywhere the amplitudes are obvious real. The corresponding virtual-Compton amplitude therefore has an s-channel discontinuity, Fig. 9(c) free of cuts in q_1^2 or q_2^2. Hence, in the continuation from scattering to annihilation no distinction need be made between ω_1 and ω_2. The naive continuation formulas Eqs. (1) and (2) will hold, as well of course as the general formulas Eqs. (15) and (16).

B. Resonance Production

One can consider more complicated ladder models[19] in which the produced particles are unstable as illustrated in Fig. 9(a). These amplitudes are no longer real. However, the s channel discontinuity of the corresponding virtual-Compton amplitude, Fig. 9(c) still has no cuts in q_1^2 or q_2^2. The naive continuation, Eqs. (1) and (2), thus holds.

C. Resonance Exchange

Next consider ladder models[6,21] with resonance exchange. A simple example is shown in Fig. 10. For $q^2<0$, Fig. 10(a), the amplitude is real whereas for $q^2>0$, Fig. 10(b), the amplitude is complex. The virtual-Compton amplitude, Fig. 10(c), will reflect this by having cuts in q_1^2 and q_2^2. Hence the naive continuation will fail and only the general prescription, Eqs. (15) and (16), will be true.

D. Landshoff-Polkinghorne-Short Model

In the non-perturbative covariant parton model of Landshoff, Polkinghorne and Short[20] $\text{disc}_s T^{\mu\nu}(s,t,q_1^2,q_2^2)$ is calculated from the "continguous vertex" or "handbag" diagram of Fig. 11. The lines carrying momenta k_1, k_1+q_1, and k_2 are point-like parton lines. The lower blob is a parton-proton scattering amplitude

$$M(s',t,k_1^2,k_2^2)$$

where

$$s' = (p_1-k_1)^2 .$$

One may expect this amplitude to have cuts in k_1^2 and k_2^2. Indeed the authors of this model suppose M goes to zero sufficiently fast as $|k_1^2|, |k_2|^2 \to \infty$ such that the integral

$$\text{disc}_s T^{\mu\nu} \propto \int d^4k \; \text{disc}_{s'} M(s',0,k^2+i\epsilon,k^2-i\epsilon)\,\delta((q+k)^2) \qquad (21)$$

converges rapidly, ensuring Bjorken scaling. The existence of the k_1^2, k_2^2 cuts in M will show up as q_1^2, q_2^2 cuts in $\text{disc}_s T^{\mu\nu}$. Hence the naive continuation is not possible, only the general prescription holds.

E. Bound State Model

In the bound state model of Drell and Lee[27] the proton is a composite of two (or more) elementary particles. Fig. 12(a) illustrates this in a ladder

approximation. In the Bjorken limit only contiguous vertex diagrams survive and one has the structure illustrated in Fig. 12(b). It differs from an elementary box diagram by the presence of vertex factors $\Gamma(k_a^2, m_b^2, m^2)$ at the two lower vertices. The vertex function Γ falls rapidly as $|k_a^2| \to \infty$, hence Bjorken scaling is achieved. Because of the Γ factors one has cuts in the k^2 variable and, just as in the Landshoff-Polkinghorne-Short model, this generates q_1^2 and q_2^2 cuts in $\text{disc}_s T^{\mu\nu}$. Again only the general continuation prescription is valid.

F. Neutral Vector Gluon Model

The neutral vector gluon model[22,23] is interesting because it is an example of a model in which the Bjorken limit is controlled by diagrams which are not all of the continguous vertex type.[30] An example is shown in Fig. 13.

It is clear immediately from the structure of the diagram that $\text{disc}_s T^{\mu\nu}$ has cuts in q_1^2 and q_2^2 coming from the vertex corrections at the top (current) vertices. Thus in this case too only the generalized continuation formula holds.

G. Current Commutators

As we have seen above, the annihilation region $q^2 > 0$ is technically more complicated than the inelastic region $q^2 < 0$. This added complication is closely related to the kinds of intermediate states which appear in the one-proton matrix element of the commutator of two electromagnetic currents.

It is well known that for $q^2 < 0$ the deep inelastic structure functions are expressible in terms of

$$W_{\mu\nu}(q,p) = \int d^4x \, e^{iq\cdot x} \langle p | [j_\mu(x), j_\nu(0)] | p \rangle \quad . \tag{22}$$

For a definite sign of q^0 (say $q^0 > 0$) only one of the two terms of the commutator is non-vanishing.

For $q^2 > 0$ there are four types of intermediate state contributions which occur as illustrated in Fig. 7. Only the Z diagrams, Fig. 7(b), are related to the annihilation structure functions. Thus the usual machinery of current commutators is not enough; one needs additional knowledge. For details see Refs. 9-15 and also the lectures at this school by Y. Frishman.

IV. THRESHOLD REGION

Gatto, Menotti and Vendramin have given a very important theorem pertaining to the threshold region $\omega \to 1$. [For the bound state model see Ref. 27.] The theorem is true under very general circumstances.

The theorem states:

If as $\omega \to 1+$

$$F_1(\omega) \to A(\omega-1)^{\alpha}+\dots \quad . \tag{23}$$

Then as $\omega \to 1-$

$$\bar{F}_1(\omega) \to A(1-\omega)^{\alpha}+\dots \quad . \tag{24}$$

Note that this theorem is compatible with the naive continuation, Eq. (1), only if α=odd integer (which need not be the case). For arbitrary α there is no contradiction with the general continuation, Eq. (15), since the latter is always true.

Let us sketch the proof. For all of the models discussed above, except the neutral vector gluon model, the Bjorken limit is controlled by the contiguous vertex diagram shown in Fig. 11. The corresponding F_1 structure function takes the form

$$F_1(\omega), \bar{F}_1(\omega) \sim \int ds'\, d^2k_\perp \, \mathrm{disc}_{s'} M(s', 0, k^2+i\epsilon, k^2-i\epsilon) \tag{25}$$

where

$$k^2 = \frac{s'+\omega k_\perp^2}{1-\omega} + \frac{m^2}{\omega} \quad . \tag{26}$$

Clearly as $\omega \to 1$ one is probing the large k^2 behavior of $\mathrm{disc}_{s'} M$. In particular for inelastic scattering where $1<\omega$ as $\omega \to 1+, k^2 \to -\infty$ whereas in the annihilation region $0<\omega<1$ as $\omega \to 1-, k^2 \to +\infty$. The rate at which $\mathrm{disc}_s M$ vanishes determines the rate at which $F, \bar{F}$ vanish at threshold.

Suppose for example

$$\mathrm{disc}_{s'} M(s', 0, k_1^2, k_2^2) \underset{\substack{|k_1^2| \to \infty \\ |k_2|^2 \to \infty}}{\propto} \frac{1}{(-k_1^2)^{\gamma}} \frac{1}{(-k_2^2)^{\gamma}} \tag{27}$$

where γ need not be integral. Then in the deep inelastic case where $k_1^2 \to -\infty$, $k_2^2 \to -\infty$ the integrand behaves as

$$\mathrm{disc}_{s'} M \propto \frac{1}{|k^2|^{2\gamma}} \quad . \tag{28}$$

In the deep annihilation limit $k_1^2 \to +\infty + i\epsilon$ and $k_2^2 \to +\infty - i\epsilon$

$$\mathrm{disc}_{s'} M \propto \frac{1}{(|k^2|^{\gamma} e^{i\pi\gamma})} \frac{1}{(|k^2|^{\gamma} e^{-i\pi\gamma})} = \frac{1}{|k^2|^{2\gamma}} \quad . \tag{29}$$

Thus in both cases the integrand is the same; hence the theorem. The proof of the theorem still goes through if $\mathrm{disc}_{s'} M$ has additional logarithmic structure, etc. in its asymptotic behavior.

This threshold theorem, unlike the more esoteric property of analytic continuation, has immediate experimental application. On the basis of inelastic scattering data we believe $\alpha \approx 3$. This can be checked by annihilation experiments.

One can do more. The same contiguous vertex structure of Fig. 11 which underlies the threshold theorem is also the key to the Drell-Yan-West relation[31,32] which relates the index α in Eq. (22) to the asymptotic behavior of the elastic form factor

$$F_p^{el}(q^2) \underset{q^2 \to -\infty}{\propto} \left[\frac{1}{(-q^2)^n}\right] \tag{30}$$

according to

$$\alpha = 2n-1 \quad . \tag{31}$$

Pions, and kaons too, will probably be copiously produced in the annihilation region. The threshold theorem coupled with the Drell-Yan-West relation will enable one to get at the asymptotic behavior of the pion form factor. This is a question of considerable interest in its own right and moreover enters prominently in a number of current theories.

The threshold theorem, based as it is on the contiguous vertex approximation could fail if this approximation is not valid. The only evidence on this score are leading logarithm calculations[22,23] in the (scale breaking) neutral vector gluon model. The threshold theorem continues to be true at the leading logarithmic level but may very well fail at the next-to-leading logarithm level.

V. RECIPROCAL RELATION

Gribov and Lipatov[22] have pointed out a remarkable reciprocal relation which holds in the γ_5 and γ_μ field theories to leading logarithmic accuracy. See also Refs. (18) and (23). This reciprocal relation is

$$\bar{F}_1(\omega, \ell n\, q^2) = \frac{1}{\omega} F_1\left(\frac{1}{\omega}, \ell n(-q^2)\right) \quad . \tag{32}$$

The presence of $\ell n\, q^2$ factors in the arguments of F_1 and $\bar{F}_1$ in Eq. (32) signifies the $\ell n\, q^2$ factors which cause Bjorken scaling to breakdown in renormalizable perturbation theories. (The reciprocal relation is not true in superrenormalizable field theories, like φ^3, which show Bjorken scaling behavior.) The reciprocal relation is interesting because unlike analytic continuation, it relates values of F_1 in its physical region to values of $\bar{F}_1$ in its physical region.

Recently Ferrara, Gatto and Parisi[28] and separately Etim[29] have shed additional light on the reciprocal relation. Ferrara, et al. consider the case where both the reciprocal relation and the naive analytic continuation relation hold. One then has a relation between $F_1(\omega, \ell n(-q^2))$ and $F_1(\frac{1}{\omega}, \ell n(-q^2))$. The authors call this a "twin symmetry" and show how to derive it using conformal group methods.

Etim considers the more general case in which only the reciprocal relation between F_1 and $\bar{F}_1$ holds. He also is able to derive the relation without explicit perturbation theory calculations by means of conformal group techniques. Of course none of these works has extended the range of validity of the reciprocal relation; it is still a leading-logarithm theorem.

Instead of discussing these recent developments let us ask if the reciprocal relation might somehow be true in the real world. For this to be the case one

would have to believe that the scaling breaking $\ell n\, q^2$ dependence is absent, say due to some transverse momentum damping beyond that of perturbation theory, but that the ω dependence is unaffected.

I believe that it is not possible that the reciprocal relation is true in the real world for pions, protons, etc. Let me illustrate with two arguments, the first uses the parton model and the second is an argument due to Bjorken.[1]

In the parton model the structure function $F_1^T(\omega)$ for deep inelastic scattering from a target T is determined by a function $f_T^q(x)$ $(x = \frac{1}{\omega})$ which is the probability of finding parton q with a fraction x of the target's linear momentum. The annihilation function $\overline{F}_1^T(\omega)$ is determined by a function $g_q^T(\omega)$ which gives the probability of finding the species T in the cascade of a parton q with fraction ω of the parton's momentum. For the reciprocal relation (32) to be true it is necessary that f_T^q and g_q^T be identically the same functions. There is obviously no need for this to be true in general.

In Bjorken's argument one considers the case of $T = U^{238}$. Deep inelastic scattering from U^{238} will have a large cross section, roughly

$$F_1^{U^{238}} \approx 238\, F_1^{p,n} \quad . \tag{33}$$

The reciprocal relation, if true, would say that $\overline{F}_1^{U^{238}}$ is large also

$$\overline{F}_1^{U^{238}} \approx 238\, \overline{F}_1^{p,n} \tag{34}$$

Eq. (34) is riduculous. No one believes U^{238} will be prolifically produced in e^+e^- annihilations.

Clearly one's feeling that U^{238} will not be copiously produced in annihilation is related to the fact that U^{238} is a composite, loosely bound system of protons and neutrons. But the proton, pion, etc. are also composite systems even though the true nature of the constituents is not entirely clear. Thus we do not expect the reciprocal relation to be true for protons, pions, etc.

VI. CONCLUDING REMARKS

We have seen that both the inelastic and annihilation structure functions are well defined discontinuities of the virtual Compton amplitude. It is necessary, however, to consider the non-forward Compton amplitude and then to go to the forward limit with the initial and final virtual photon masses on opposite sides of their cuts.

With this understood we saw that the analytic properties one may expect for the Compton amplitude insure that scaling will occur in the annihilation region if it occurs in the scattering region. Furthermore the annihilation structure functions can be reached by analytic continuation from the scattering channel.

We cautioned, however, that analytic continuation alone cannot enable one to make predictions about the annihilation region on the basis of the scattering data. It can happen that the departures from Bjorken scaling are small in the inelastic scattering region but when analytically continued lead to large corrections in the annihilation region.

The threshold theorem discussed in Sec. IV, which is different from analytic continuation, is an important and experimentally testable relation between the scattering and annihilation regions.

The reciprocal relation is another relation which is experimentally testable. In Sec. V we discussed reasons why we believe that it cannot apply to real world protons, pions, etc.

APPENDIX A

We gather here a few useful, standard formulas for deep inelastic scattering and annihilation.

For inelastic scattering, Fig. 1(a), the hadronic part of the cross section is given by

$$\frac{1}{\pi} W^{\mu\nu}(\nu,q^2) = \sum_n \langle P(p)|j^\mu(0)|n\rangle\langle n|j^\nu(0)|P(p)\rangle(2\pi)^3\delta^4(p+q-p_n)$$

$$= \frac{1}{m^2} W^2(\nu,q^2)\left(p^\mu - \frac{p\cdot q}{q^2} q^\mu\right)\left(p^\nu - \frac{p\cdot q}{q^2} q^\nu\right) + W_1(\nu,q^2)\left(-g^{\mu\nu} + \frac{q^\mu q^\nu}{q^2}\right) \qquad (A.1)$$

where an average over proton spins is implied. In Eq. (A.1) we use an invariant normalization for the proton states

$$\langle P(p')|P(p)\rangle = \frac{E}{m}\delta^3(\underline{p}'-\underline{p}) \qquad (A.2)$$

The actual $e^-+P\to e^-+X$ cross section is

$$\frac{d^2\sigma}{dE'\,d\Omega_{\ell'}} = \frac{4\alpha^2}{(q^2)^2}\ell'^2\left[W_2\cos^2(\tfrac{1}{2}\theta_a)+2W_1\sin^2(\tfrac{1}{2}\theta_a)\right]. \qquad (A.3)$$

In the Bjorken limit, $\nu\to\infty$, $-q^2\to\infty$, one defines

$$F_1(\omega) \equiv \lim_{B_j}\left(mW_1(\nu,q^2)\right) \qquad (A.4)$$

$$F_2(\omega) \equiv \lim_{B_j}\left(\nu W_2(\nu,q^2)\right) \qquad (A.5)$$

where

$$\omega = 2m\nu/(-q^2) \quad . \qquad (A.6)$$

In the physical region (only), $\omega \geq 1$, the following positivity conditions must hold:

$$F_1(\omega) \geq 0 \tag{A.7}$$

$$F(\omega) \equiv F_1(\omega) - \frac{1}{2}\omega F_2(\omega) \geq 0 . \tag{A.8}$$

For three-body annihilation, Fig. 1(b), one defines

$$\frac{1}{\pi}\tilde{W}^{\mu\nu}(\nu,q^2) = \sum_n \langle P(p)|j^\mu(0)|n\rangle_c \langle n|j^\nu(0)|P(p)\rangle_c (2\pi)^3 \delta^4(p+q-p_n)$$

$$= \frac{1}{m^2}\tilde{W}_2(\nu,q^2)\left(p^\mu - \frac{p\cdot q}{q^2}q^\mu\right)\left(p^\nu - \frac{p\cdot q}{q^2}q^\nu\right) + W_1(\nu,q^2)\left(-g^{\mu\nu} + \frac{q^\mu q^\nu}{q^2}\right) . \tag{A.9}$$

For annihilation $e^- + e^+ \to \bar{P} + X$, Fig. 1(c), one has

$$\frac{1}{\pi}\bar{W}^{\mu\nu}(\nu,q^2) = \sum_n \langle 0|j^\mu(0)|\bar{P}(P),n\rangle_c \langle P(P),n|j^\nu(0)|0\rangle_c (2\pi)^3 \delta^3(q-P-p_n)$$

$$= \frac{1}{m^2}\bar{W}_2(\nu,q^2)\left(P^\mu - \frac{P\cdot q}{q^2}q^\mu\right)\left(P^\nu - \frac{P\cdot q}{q^2}q^\nu\right) + \bar{W}_1\left(-g^{\mu\nu} + \frac{q^\mu q^\nu}{q^2}\right) . \tag{A.10}$$

In Eq. (A.10) we have <u>averaged</u> over the antiproton spin.

The colliding ring, center-of-mass cross section is

$$\frac{d^2\sigma}{dE\, d\Omega_{\hat{P}}} = \frac{2\alpha^2}{(q^2)^2} m^2 \left(\frac{\nu^2}{q^2} - 1\right)^{1/2} \left[2\bar{W}_1 + \left(\frac{\nu^2}{q^2} - 1\right)\bar{W}_2 \sin^2\theta_c\right] . \tag{A.11}$$

The Bjorken limit of annihilation is $q^2 \to \infty$, $-\nu \to \infty$ with

$$\bar{F}_1(\omega) \equiv \lim_{B_j}\left(m\bar{W}_1(\nu,q^2)\right) \tag{A.12}$$

$$\bar{F}_2(\omega) \equiv \lim_{B_j}\left(-\nu\bar{W}_2(\nu,q^2)\right) . \tag{A.13}$$

In the physical region $0 \leq \omega \leq 1$ (only) the inequalities

$$\bar{F}_1(\omega) \geq 0 \tag{A.14}$$

$$\bar{F}_L(\omega) \equiv \bar{F}_1(\omega) + \frac{1}{2}\omega\bar{F}_2(\omega) \geq 0 \tag{A.15}$$

must hold.

The correct analytic continuation statements are (fermions)

$$-\bar{F}_{1,L}(\omega) = F_{1,L}(\omega_1 = \omega + i\epsilon,\ \omega_2 = \omega - i\epsilon) \tag{A.16}$$

or equivalently

$$\bar{F}_2(\omega) = F_2(\omega_1 = \omega + i\epsilon,\ \omega_2 = \omega - i\epsilon) . \tag{A.17}$$

APPENDIX B

A number of authors[5,16,19,21,24] have done explicit perturbation theory calculations in scaling theories to study the singularities of the scaling functions in the complex ω plane. Let us illustrate with a simple case, the box diagram shown in Fig. 14(a).

One has normal thresholds at $s = (m_a+m_b)^2$ and at $q^2 = (m_1+m_a)^2$, $(m_1+m_b)^2$. In the Bjorken limit $s \to \infty$, $|q^2| \to \infty$ these are far away.

Contracting the line a (b) one has the triangle diagram 14(b) (14(c)) which still has a non-zero s channel discontinuity. Fig. 14(b), for example, has the well-known anomalous (triangle) singularities at (see Ref. 5 for details)

$$2m_2^2(m_1^2-m_a^2-q^2) = \{(m_2^2+m_a^2-q^2)(m_1^2+m_2^2-s) \pm [\Delta(m^2,m_2^2,m_a^2)\Delta(m_1^2,m_2^2,s)]^{1/2}\} . \qquad (B.1)$$

Where Δ is the triangle function

$$\Delta(x,y,z) = x^2+y^2-z^2-2xy-2xz-2yz . \qquad (B.2)$$

The discontinuity across the s cut carries both of these branch points.

In the Bjorken limit these singularities become fixed in ω at

$$\omega_{1\pm} = 1 - \frac{1}{2m_a^2}\{m_2^2+m_a^2-m^2 \pm \Delta^{1/2}(m_2^2,m_a^2,m^2)\} . \qquad (B.3)$$

(Note the locations of these singularities are independent of m_1^2 as befits the light cone dominance of this process.) As indicated these singularities are in the scaling variable ω_1. Diagram 14(c) will give a corresponding pair of singularities in ω_2 at points obtained by the substitution $m_a \to m_b$ in Eq. (B.3).

For the case of the box diagram with point vertices the above singularities at $\omega_1 = \omega_{1\pm}$ are simple poles. For more complicated cases they are branch points.

This appendix illustrates that the singularity structure of the scaling functions in ω is not something which is simple. The familiar normal threshold singularities have little to do with the matter. It is the less familiar anomalous singularities which come to the fore in the Bjorken limit. This is not too surprising since this limit probes the internal structure; anomalous singularities manifest this internal structure.

FIGURE CAPTIONS

Fig. 1 Three processes which are formally related by the substitution rule: (a) inelastic scattering, (b) three body annihilation, and (c) annihilation.

Fig. 2 The physical regions for the three processes shown in Fig. 1.

Fig. 3 The non-forward-virtual Compton amplitude.

Fig. 4 The discontinuities of the Compton amplitude which give the structure functions for the three processes shown in Fig. 1. The $\pm$ in the central sector refers to the sign of the $i\epsilon$ for the s variable. The $\pm$ in the smaller sectors refer to the signs of the $i\epsilon$ for the q_1^2 and q_2^2 variables. In (c) the line labeled $-P_1$ ($-P_2$) represents an outgoing (ingoing) anti-proton with physical four momentum P_1 (P_2).

Fig. 5 The cut structure in the complex ν plane for the three processes under discussion. The dotted line indicates the path one must follow to select the appropriate s-channel discontinuities.

Fig. 6 The physical region for the three processes which correspond to u channel discontinuities of the virtual-Compton amplitude.

Fig. 7 Contributions to the one-proton expectation value of the commutator of two currents: (a) fully disconnected piece, (b) Z diagrams, (c) direct diagrams, and (d1) and (d2) semidisconnected diagrams. For space-like q^2 only (c) contributes. For time-like q^2 all contribute but only (b) is related to the annihilation structure functions.

Fig. 8 Ladder diagrams for (a) inelastic scattering and (b) annihilation. The corresponding discontinuity of the Compton amplitude is shown in (c).

Fig. 9 Ladder diagrams as in Fig. 8 but with resonance production.

Fig. 10 Simple ladder diagrams with resonance exchange for (a) scattering and (b) annihilation. The corresponding virtual Compton discontinuity (c) must be evaluated with the complex self energy factors as indicated to obtain the correct structure functions when $q^2 > 0$.

Fig. 11 The contiguous vertex or handbag diagram of the non-perturbative parton model. Only diagrams of this structure contribute in the Bjorken limit.

Fig. 12
(a) The important diagram in the bound state model in the Bjorken limit.
(b) The correct $i\epsilon$ prescriptions for the vertex in the annihilation region, $q^2 > 0$.

Fig. 13 A diagram of the neutral-vector gluon model which contributes in the Bjorken limit. It is not of the contiguous vertex type and moreover has cuts in the $q_{1,2}^2$ variables.

Fig. 14
(a) Simple box diagram for the Compton amplitude.
(b) and (c) Contractions of (a) which have anomalous (triangle) singularities which are fixed in ω in the Bjorken limit.

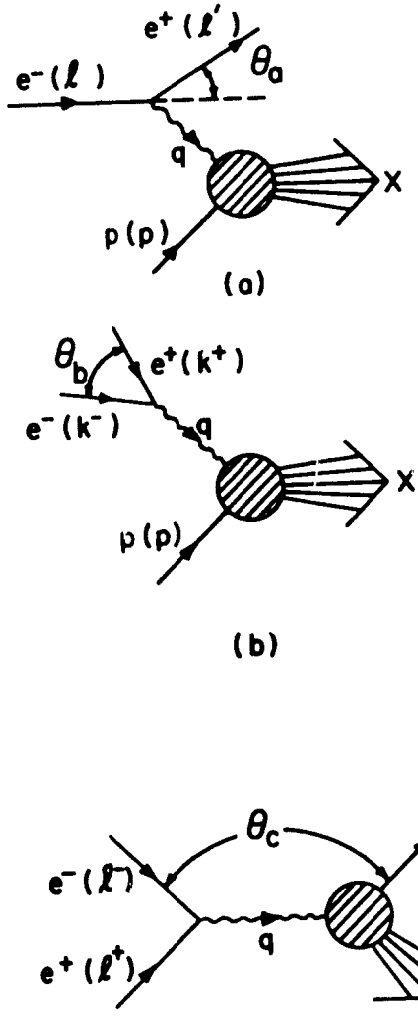
e⁺ (ℓ′)
θa
e⁻ (ℓ)
q
X
p (p)
(a)
θb
e⁺(k⁺)
e⁻ (k⁻)
q
X
p (p)
(b)
θc
p̄(P)
e⁻ (ℓ⁻)
q
e⁺ (ℓ⁺)
(c)

Fig. 1

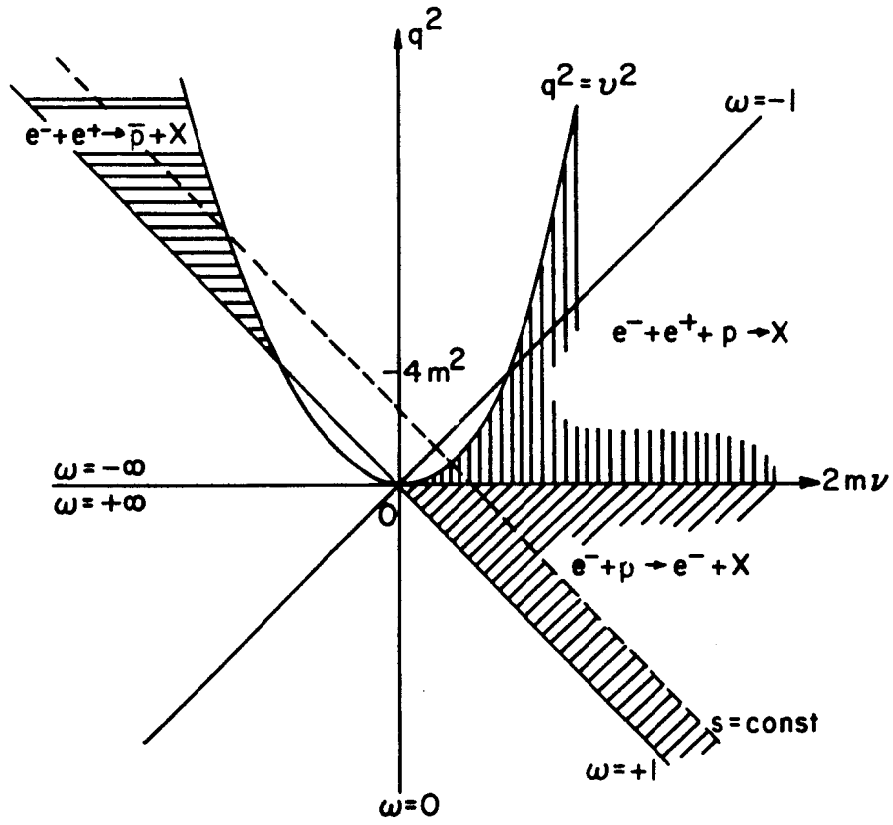
q²
q² = υ²
ω = −1
e⁻+e⁺→p̄+X
e⁻+e⁺+ p →X
−4 m²
ω = −∞
ω = +∞
0
2mν
e⁻+p → e⁻+X
s = const
ω = +1
ω = 0

Fig. 2

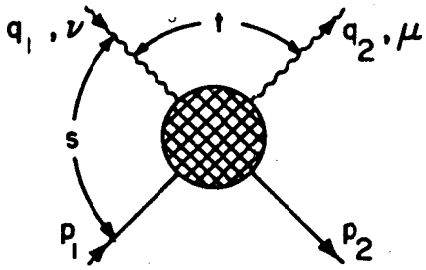

Fig. 3

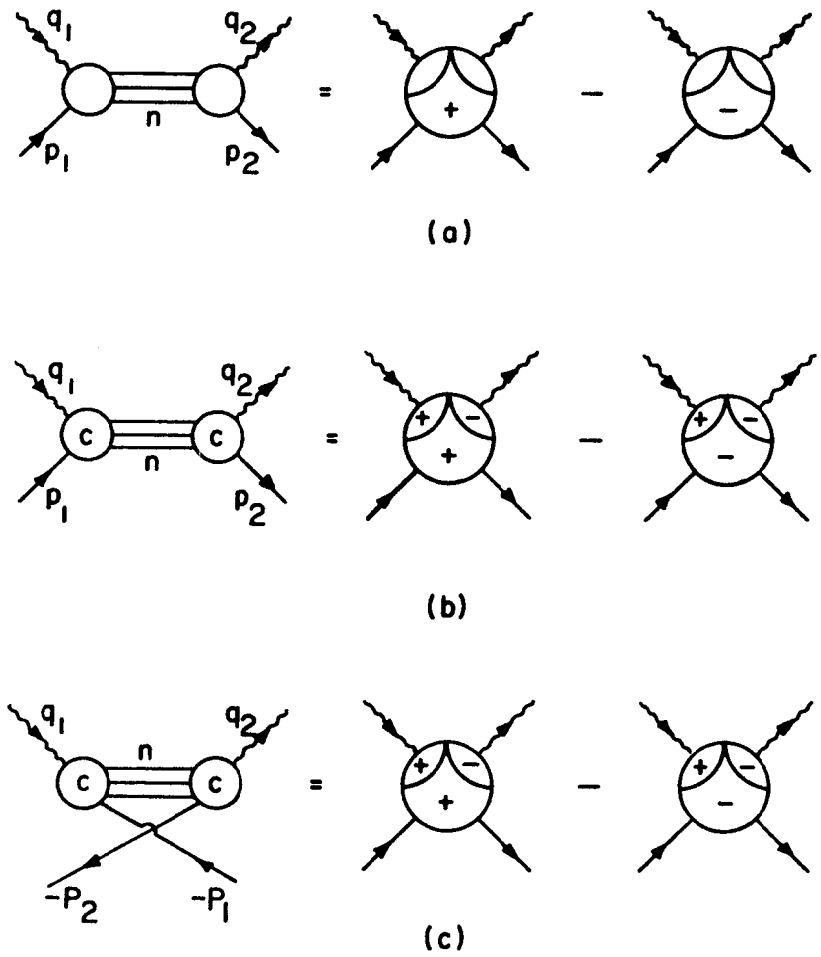

Fig. 4

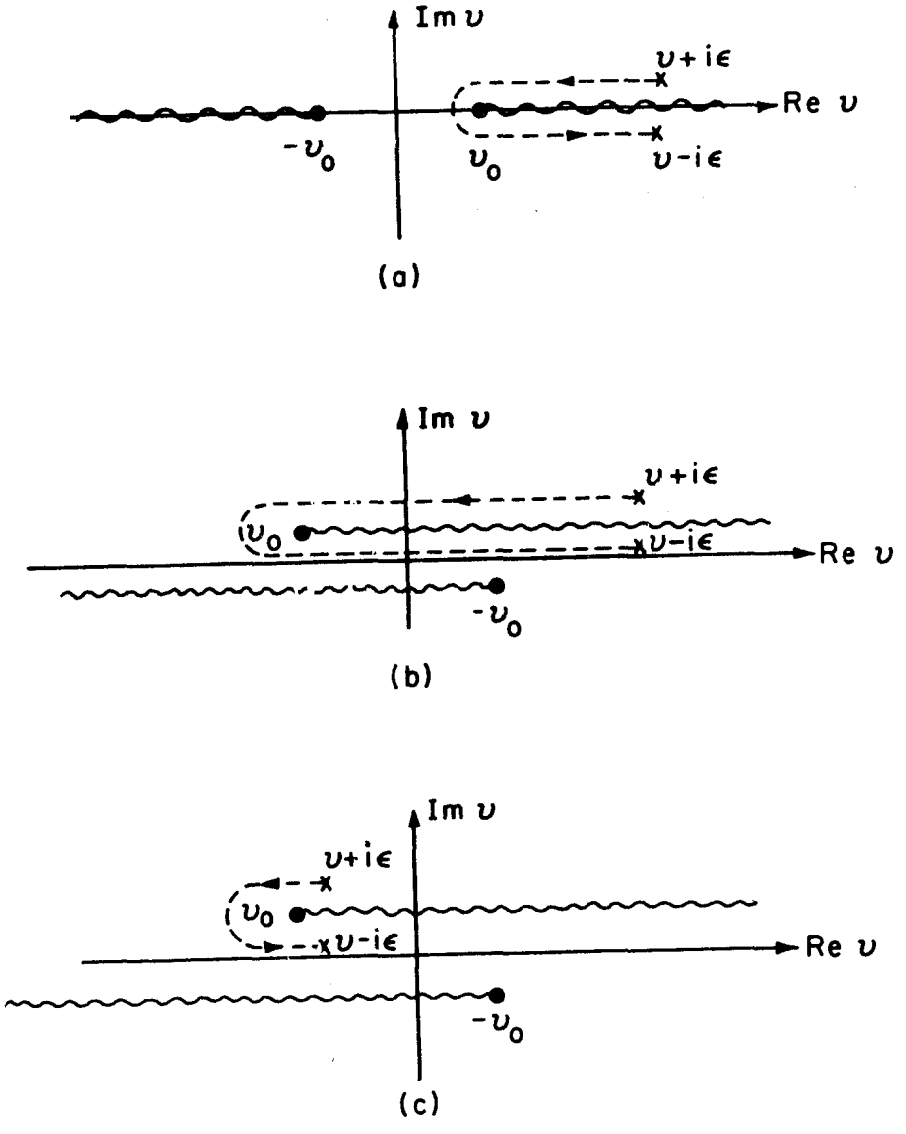
Im υ
υ+iϵ
Re υ
-υ0
υ0
υ-iϵ
(a)
Im υ
υ+iϵ
υ0
υ-iϵ
Re υ
-υ0
(b)
Im υ
υ+iϵ
υ0
υ-iϵ
Re υ
-υ0
(c)

Fig. 5

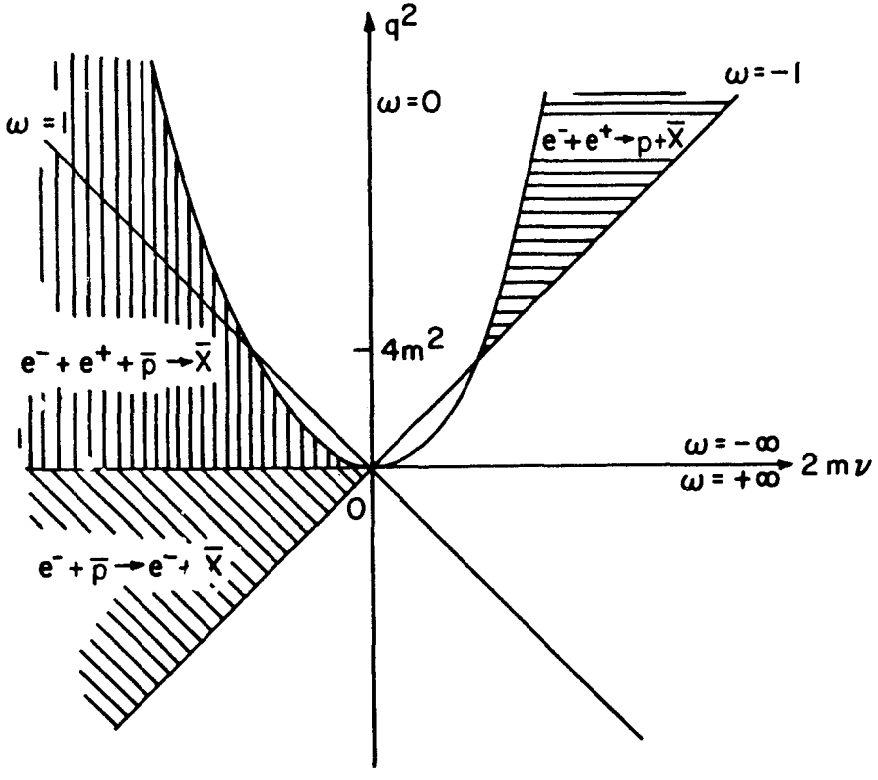
q2
ω=0
ω=-1
ω=1
e-+e+→p+X̄
e-+e+→X̄
-4m2
ω=-∞
ω=+∞
2mν
0
e-+p̄→e-+X̄

Fig. 6

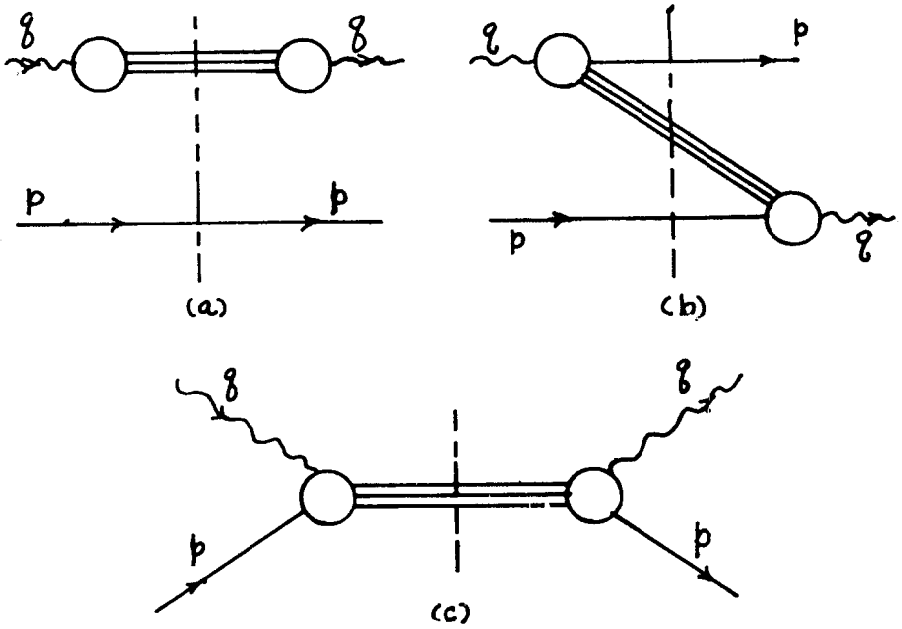

Fig. 7

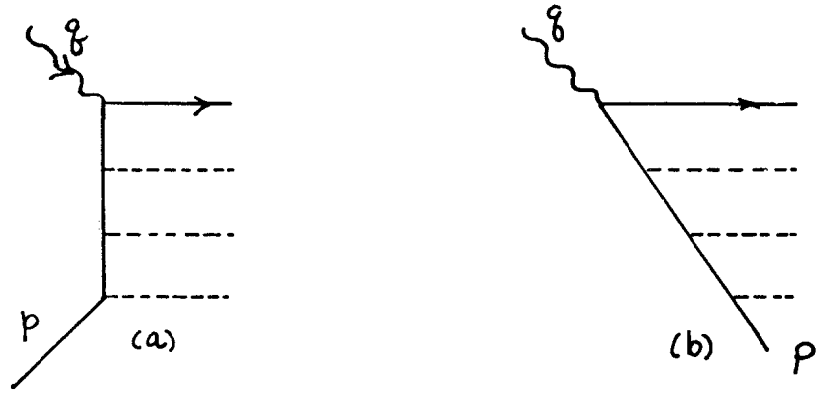

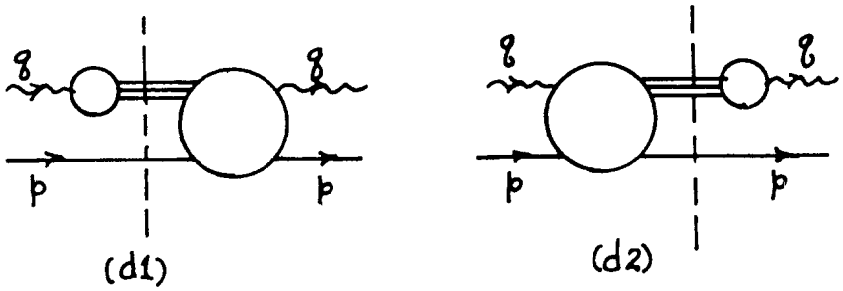

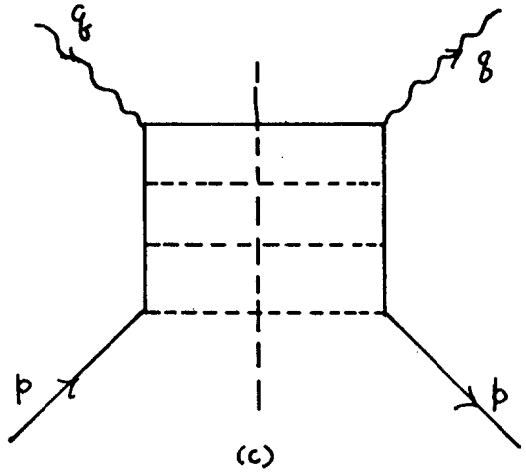

Fig. 8

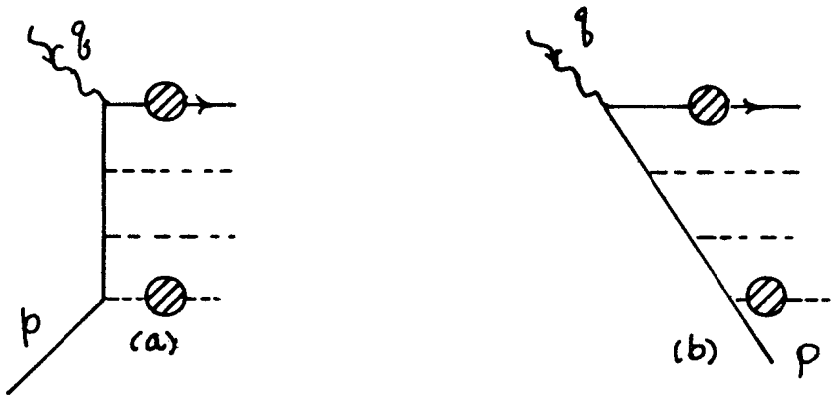

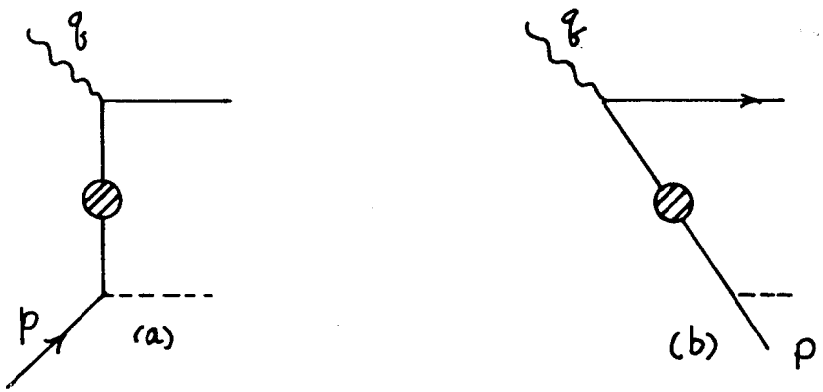

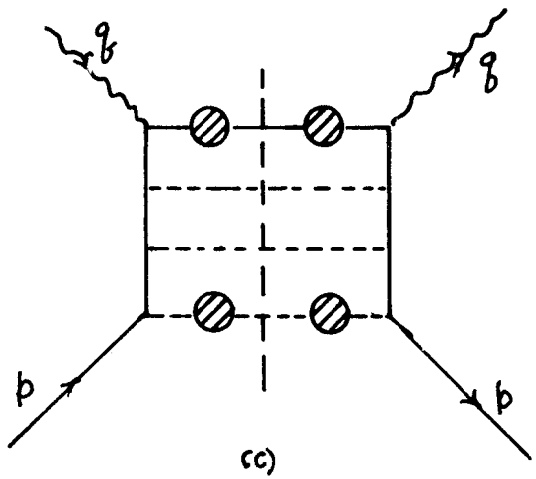

Fig. 9

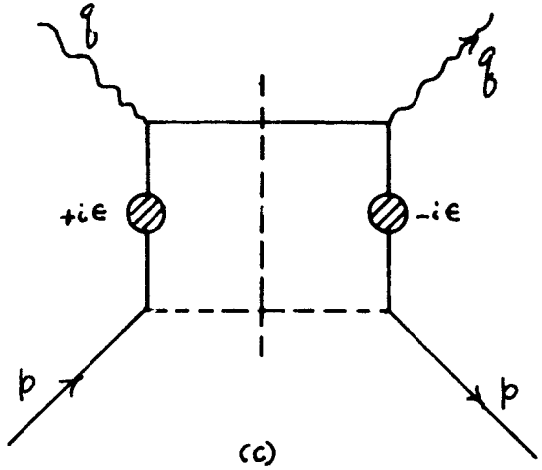

Fig. 10

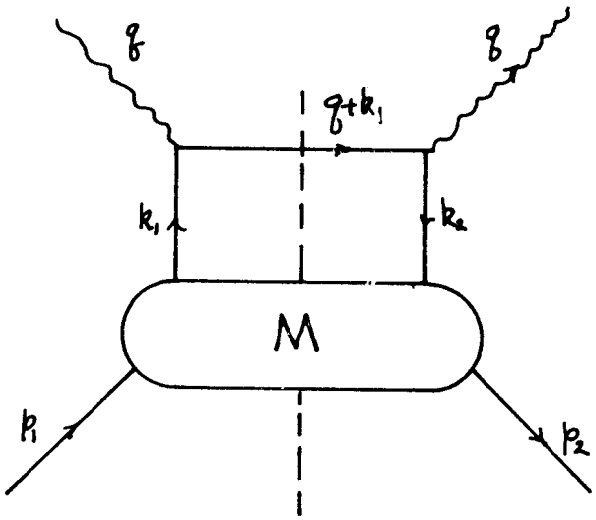

Fig. 11

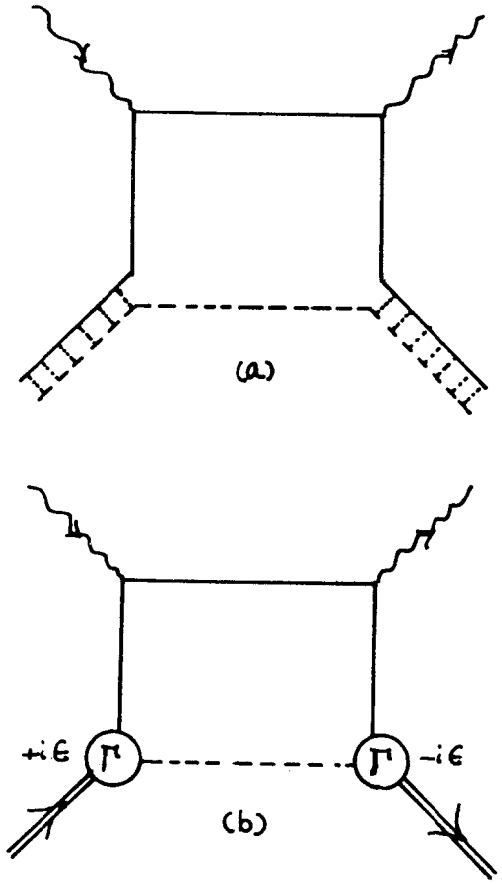

Fig. 12

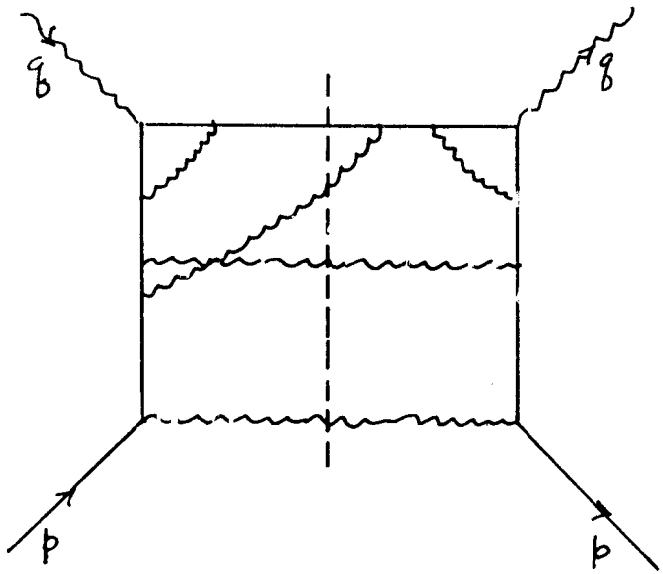

Fig. 13

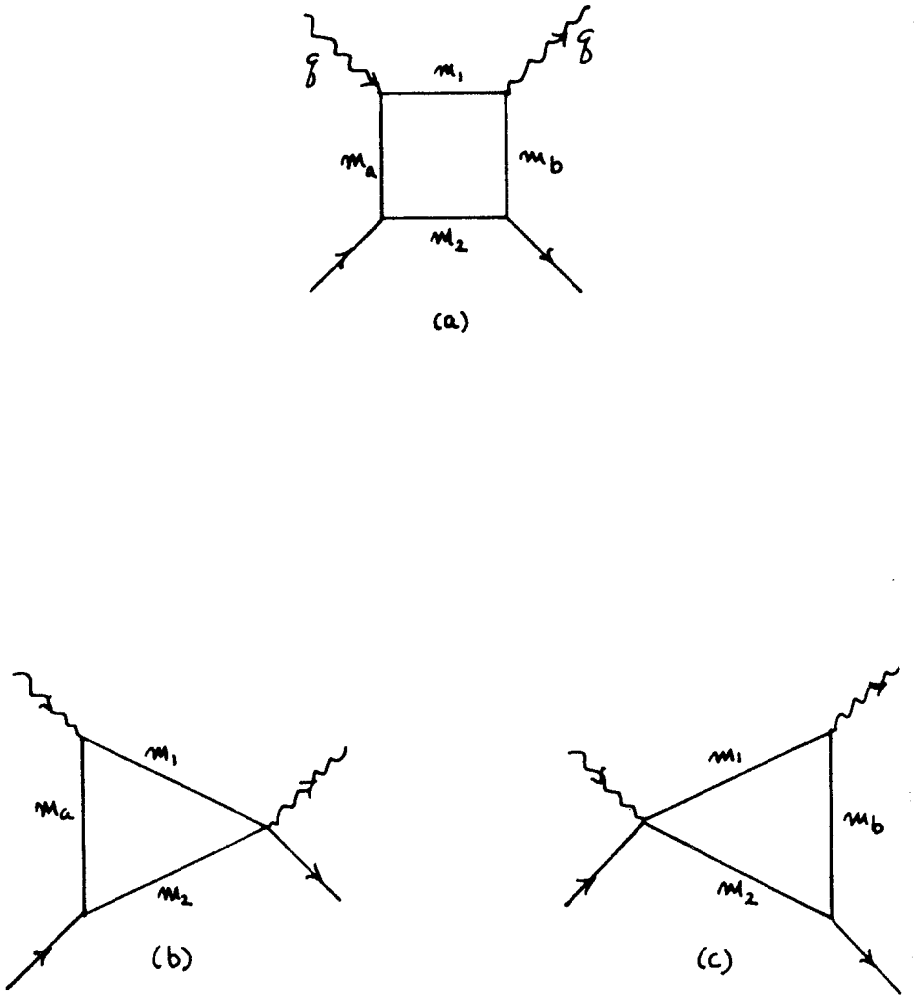

Fig. 14

REFERENCES

I. Review Talks

1) J.D. Bjorken, Electron Photon Symposium 1971, Cornell University.

2) P. Menotti, Informal Meeting on Electromagnetic Interactions, Frascati May 2-3, 1972.

3) S.D. Drell, XVI International Conference on High Energy Physics 1972, Chicago-Batavia, Vol. 2, p. 8.

4) G. Preparata, XVI International Conference on High Energy Physics 1972, Chicago-Batavia, Vol. 2, p. 130.

II. General Discussion of the Continuation Problem

5) A. Suri, Phys. Rev. D4, 570 (1971). (Contains detailed investigation of analyticity of the forward Compton amplitude.) (For the triangle singularity see J.D. Sullivan, Nucl. Phys. B22, 358 (1970).)

6) P.V. Landshoff and J.C. Polkinghorne, Phys. Rev. D6, 3708 (1972).

7) P.M. Fishbane and J.D. Sullivan, Phys. Rev. D6, 3568 (1972), Sec. II.

8) R. Gatto and G. Preparata, Nucl. Phys. B47, 313 (1972).

III. Relation Between the Current Commutator and the Annihilation Amplitude

9) J. Pestieau and P. Roy, Phys. Letters 30B, 483 (1969).

10) S.D. Drell, D.J. Levy and T-M. Yan, Phys. Rev. D1, 1617 (1972), Appendix A.

11) C.G. Callen and D.J. Gross, "Light Cone Algebra Treatment of Inclusive Reactions", Princeton Preprint, March 1972 (unpublished).

12) K.M. Bitar, Phys. Rev. D6, 2250 (1972).

13) J. Ellis and Y. Frishman, Phys. Rev. Letters 31, 135 (1973).

14) H. Fritzch and P. Minkowski, CERN Report No. TH-1575, 1972 (Revised Version).

15) R.A. Brandt and Ng Wing-Chiu, "Electron-Positron Annihilation and Hadronic Sources, ITP-SB-73-16, March 1973.

IV. Explicit Calculations of the Annihilation Amplitude (mostly perturbation theory)

16) S.D. Drell, D.J. Levy, T-M. Yan, Ref. 10.

17) N. Cabibbo, G. Parisi and M. Testa, Letters Nuovo Cimento 4, 35 (1970).

18) S-J. Chang and P.M. Fishbane, Phys. Rev. D2, 1173 (1970).

19) R. Gatto and P. Menotti, Nuovo Cimento 7A, 118 (1972).

20) P.V. Landshoff, J.C. Polkinghorne and R.D. Short, Nucl. Phys. B28, 225 (1971). (This describes a non-perturbative, covariant parton model. The kinematics and singularity structure is the same as for Feynman diagram calculations.)

21) R. Gatto, P. Menotti and I. Vendramin, Letters Nuovo Cimento 4, 79 (1972); Ann. Phys. (N.Y.) to be published.

22) V.N. Gribov and L.N. Lipatov, Yad. Fiz. 15, 1218 (1972). [Sov. J. Nucl. Phys. 15, 675 (1972).]

23) P.M. Fishbane and J.D. Sullivan, Ref. 7, and Phys. Rev. D7, 1879 (1973).

24) G. Altarelli and L. Maiani, Nucl. Phys. B51, 509 (1973).

25) A.L. Mason, Phys. Rev. D7, 3799 (1973). (Uses Callan-Symanzik equations to perform the calculation of leading logarithms. In this regard see: N. Christ, B. Hasslacher and A. Meuller, Phys. Rev. D6, 3543 (1972).)

26) R. Gatto, P. Menotti and I. Vendramin, Letters Nuovo Cimento 5, 754 (1972); Phys. Rev. D7, 2524 (1973). (Derives a presumably general relation between the threshold behavior of the annihilation and scattering amplitudes.)

27) S.D. Drell and T.D. Lee, Phys. Rev. D5, 1738 (1972). (The discussion of the annihilation amplitude as determined by their bound state model is confined to the threshold region.)

V. Group-Theoretic Derivation of the Reciprocal Relation

28) S. Ferrara, R. Gatto and G. Parisi, Phys. Letters 44B, 381 (1973).

29) E. Etim, "Gribov-Lipatov Reciprocity from Conservation Constraints and O(4) Symmetry," LNF 73/17, April 1973.

Miscellaneous References

30) See also R. Jackiw and R.E. Waltz, Phys. Rev. D6, 702 (1972).

31) S.D. Drell and T-M. Yan, Phys. Rev. Letters 24, 181 (1970).

32) G. West, Phys. Rev. Letters 24, 1206 (1970).

RECENT e^+e^- COLLIDING BEAM RESULTS*

R. F. Schwitters
Stanford Linear Accelerator Center
Stanford University, Stanford, Calif. 94305

Today we stand at a particularly exciting point in the study of electron-positron interactions. The great experiments performed at the Orsay, Novosibirsk, and Frascati storage rings have significantly broadened our understanding of the electromagnetic interaction and have shown us a richness in the structure of hadrons that few people expected where these projects were initiated. The higher energy results from the CEA BYPASS project are now in and as many, or more, questions have been raised as have been answered by the BOLD results. We therefore look forward to the new machines, SPEAR and DORIS, to answer some of these questions and presumably raise more.

In this talk, I would like to concentrate on experimental results which have appeared since the Batavia Conference. I refer the audience to the excellent review talks given at the Cornell[1] and Batavia[2] Conferences for a more complete history of the subject.

I. TESTS OF QUANTUM ELECTRODYNAMICS

Electron-positron storage rings are generally used to test the validity of QED by studying some purely electromagnetic process and looking for deviations in the experimental results from the predictions of QED at large values of the virtual mass of the relevant lepton or photon propagator. One usually normalizes the QED predictions by monitoring a small-momentum process such as small-angle Bhabha scattering or double-bremsstrahlung.

* Work supported by U. S. Atomic Energy Commission.

The CEA-BYPASS group has recently published data on the reaction $e^+e^- \to \gamma\gamma$ [3] which provides a test of QED for large space-like values of q^2 of the electron propagator. The relevant Feynman diagrams are given in Fig. 1a. They observed 34 events at a total center-of-mass energy of 4 GeV in the angular range $53^\circ \leq \theta \leq 127^\circ$. Using a double-bremsstrahlung monitor they find agreement with QED. The ratio of their experimental yield to that theoretically expected is:

$$\frac{\sigma_{EXP}}{\sigma_{QED}} = 1.05 \, {}^{+0.23}_{-0.21} .$$

A large vertical-horizontal asymmetry in the data (24 in the horizontal telescopes to 10 in the vertical telescopes) is not explained by known experimental biases or beam polarization and remains something of a mystery.

In the same apparatus, the CEA group observe 202 Bhabha (elastic e^+e^-) events which can also be used as a monitor for the $\gamma\gamma$ rate. In this case, the following comparison with QED is made:

$$\frac{[\sigma(\gamma\gamma)/\sigma(e^+e^-)]_{EXP}}{[\sigma(\gamma\gamma)/\sigma(e^+e^-)]_{QED}} = 1.21 \, {}^{+0.25}_{-0.23} .$$

The "$\gamma\gamma$" group from Frascati have reported data[4] on the "Compton" reaction $e^+e^- \to e^+e^-\gamma$ obtained at Adone in the energy range $1.4 \leq \sqrt{s} \leq 3.0$ GeV. As seen in Fig. 1b, this reaction explores the electron propagator with time-like momenta. 118 events survive their selection criteria and geometrical cuts. Kinematical distributions of these events are in excellent agreement with the predictions of QED as calculated in lowest order, using a Monte Carlo program and their measured luminosity. An example of one of these distributions is shown in Fig. 2, where the measured angles of the three final-state particles and the beam energy have been used to compute the two possible lepton-photon effective masses for each event. The comparison of the experimental effective mass distribution with the predictions of QED leads

the authors to state that there is no evidence for an excited electron that decays to $e\gamma$ with a mass below about 2 GeV. If such a particle exists in this mass range, its coupling to $e\gamma$ is less than 10^{-3}.

In a recent preprint,[5] The BCF group presents results of a high-statistics experiment which compares Bhabha scattering between wide and very small angles. They observe somewhat more than 12×10^3 events at angles roughly between 50° and 130° in the s range $1.44 \leq s \leq 9.0$ GeV^2. First-order radiative corrections must be included in the theoretical calculations in order to fit the observed collinearity distributions. They then fit the energy dependence of their events shown in Fig. 3 to the form $A s^n$ and find:

$$\frac{A_{EXP}}{A_{QED}} = 1.00 \pm 0.02 \quad \text{and} \quad n = -(0.99 \pm 0.02),$$

which is a remarkable achievement, especially considering the notorious difficulties usually encountered in luminosity monitoring to this level of precision.

It is perhaps worthwhile to make a few comments regarding breakdown parameters since no limits on breakdown parameters have been quoted in the data presented here. There is no universal choice of breakdown parameter for the lepton propagator, but a convenient parameterization leads to:

$$\frac{\sigma_{EXP}}{\sigma_{QED}} = 1 \pm \frac{2q^4}{\Lambda_\pm^4} \approx 1 \pm \frac{8E_0^4}{\Lambda_\pm^4},$$

where q^2 is the virtual lepton mass associated with the propagator, $\Lambda_\pm$ are the breakdown parameters, and E_0 is the beam energy. Since systematic errors often limit experimental precision to the 10% level, we see that a rule for estimating Λ is:

$$\Lambda_\pm \geq 2 - 3\, E_0 .$$

Note that Λ is only weakly dependent on experimental errors and one must carefully examine the precision of individual experiments when comparing QED with experiment.

In the case of the photon propagator, we know that hadron production will give rise to vacuum polarization and hence to screening or an effective photon mass. The general form of the photon propagator is:[6]

$$D_{\mu\nu}(q^2) = \frac{g_{\mu\nu}}{q^2} + \left(g_{\mu\nu} - \frac{q_\mu q_\nu}{q^2}\right) \frac{\alpha}{3\pi} \int_0^\infty \frac{d\sigma^2}{\sigma^2} \frac{R(\sigma^2)}{(q^2 - \sigma^2 + i\epsilon)}$$

where

$$R(\sigma^2) = \frac{\sigma_{e^+e^- \to \text{hadrons}}(\sigma^2)}{\sigma_{e^+e^- \to \mu^+\mu^-}(\sigma^2)} .$$

The classic experimental example of the hadronic contribution to vacuum polarization is the Orsay experiment[7] on μ pair production at energies near the ϕ-meson mass. The results of this experiment are shown in Fig. 4. Here is a very clear case of experimental deviation from simple QED which we interpret not as a breakdown of QED, but rather as a method for measuring the branching ratio of the ϕ meson to leptons!

While studying the asymptotic properties of the function R defined above and discussed in Section IV, Bjorken[8] has shown that there may be measurable deviations from simple QED for muon pair production and Bhabha scattering at "nearby" ($\sim$10 GeV) storage-ring energies, if R follows certain trends exhibited in the data known at this time. The Bhabha scattering case is particularly attractive from the experimental point of view because the deviation will be a function of production angle and one can imagine experiments with miminum systematic errors to measure the effect.

In summary, there have been no surprises in the QED studies performed on e^+e^- storage rings, and quantum electrodynamics with calcuable hadronic corrections are sufficient to explain all the known data.

II. HADRON FORM FACTORS

There have been no new data reported on the reaction $e^+e^- \rightarrow p\bar{p}$ and the Frascati point[9] at $s = 4.4\ GeV^2$ remains the only direct measurement of this reaction. The cross section is 0.91 ± 0.22 nb and is compared with the $\pi\pi$, KK cross sections discussed below by computing the square of the form factor, assuming the protons to be pseudoscalar bosons of nearly zero mass. This "form factor" is compared with the π and K data in Fig. 5, and we see that the cross section for $p\bar{p}$ production is equal to the cross section for the production of pion and kaon pairs within the experimental errors at this one energy.

There are new experimental results on the production of charged π and K pairs in e^+e^- annihilation. This process is usually described by a form factor F(s) which is related to the differential cross section by:

$$\frac{d\sigma}{d\Omega} = \frac{\alpha^2}{8s}\,\beta^3 \sin^2\theta\,|F(s)|^2 ,$$

where β is the velocity of the outgoing π or K in units of c, θ is the production angle and s center-of-mass energy squared. These are extremely difficult experiments to perform because of the small cross sections and large backgrounds due to wide-angle Bhabha scattering and cosmic rays.

The "$\mu\pi$" group from Frascati[10] reports the observation of about 30 $\pi\pi$ and KK events for center-of-mass energies between 1.2 GeV and 2.4 GeV. Fitting the total cross section for the production of these events to a power law in s, they obtain:

$$\sigma \propto s^{-m} \qquad m = 2.7 \pm 0.6 .$$

Assuming all of their events to be pion pairs, the authors compute a form factor for these data and compare it with other measurements in Fig. 5. Note that this figure represents an upper bound to the real pion form factor because of possible kaon contamination. In an attempt to measure the K contribution, they obtained data at $s = 2.25\ GeV^2$ with a trigger favorable to K's, and by using a water-filled Cerenkov counter they see 1 kaon pair along with 7 pion pairs and approximately 2000 electron-positron pairs. This result indicates that the π and K form factors are certainly comparable at this energy, the K form factor apparently being within a factor-of-2 of the pion's.

New evidence, tending to confirm the comparable magnitude of π and K pair production, comes from the BCF group.[11] Using detailed range arguments to indicate observable differences in the behavior of pions and kaons in their apparatus, they claim that approximately 1/2 (0.53 ± 0.13) of their hadron pair events, at an average s of $2.4\ GeV^2$, are K pairs and therefore the K form factor is approximately 50% larger than the π form factor at this energy. Using their value for F_K ($= 0.50 \pm 0.08$) and their ratio of kaons to the total hadron pairs, we see that the effective hadron form factor squared, computed on the assumption of pion kinematics for the BCF data is roughly 0.22 (shown as the open circle in Fig. 5), which seems somewhat low compared to the other data in Fig. 5. If the BCF group's value for F_K is correct, then the observed ratio of kaons to hadrons would have to be reduced by approximately a factor-of-two for their effective pion form factor to fall on the curve shown in Fig. 5.

In their paper,[10] the $\mu\pi$ group attempts to study the energy dependence of F_π by making various assumptions about the kaon contribution. In three fits to the data of Fig. 5 they assume: (1) $\sigma_{KK} = 0$; (2) $\sigma_{KK} = \sigma_{\pi\pi}$; (3) $|F_K|^2 = \frac{1}{3}|F_\pi|^2$. Assumptions (2) and (3) follow from considerations of vector-meson dominance and simple SU(3) breaking, respectively. The resulting values for $|F_\pi|$ are shown in Fig. 6. These three fits assume an energy dependence of the form:

$$|F_\pi|^2 \propto \frac{1}{s^n} ,$$

and the values of n obtained are $n = 1.93 \pm 0.16$ for case (1), $n = 2.70 \pm 0.16$ for case (2), and $n = 2.08 \pm 0.16$ for case (3). Thus the data rules out a constant or point-like pion form factor but can accommodate a simple pole behavior, where n = 2 and possibly

a fall-off as rapid as n = 3 favored by some recent models.[12,13] An important result of this analysis is that all of the fits give values of F_π which are significantly larger than the "ρ tail" values obtained by extrapolating the Gounaris-Sakurai[14] formula for the ρ^0 meson to these values of s.

Notably absent from the hadron pair data of Fig. 5 is any sign of a ρ' bump at $\sqrt{s}$ = 1.6 GeV, although the data are not precise enough to rule out a ρ' that decays to π pairs less than 10-20% of the time.[15]

III. VECTOR-MESON SPECTROSCOPY

While no new vector mesons have been found since the ρ', the μ-π group from Frascati[15] have attempted to study the decay properties of the ρ' by looking at final-state correlations in 23 events attributed to the reaction:

$$\rho' \to \pi^+\pi^-\pi^+\pi^- ,$$

at center-of-mass energies of 1.5, 1.6, and 1.7 GeV. The parameters used for the ρ' are

$$m_{\rho'} \approx 1.6 \text{ GeV} \qquad \Gamma_{\rho'} \approx 0.25 \text{ GeV} \qquad J^{PC} = 1^{--},\ I^G = 1^+$$

They model several possible final-state interactions with a Monte Carlo program and in comparing kinematical distributions of these models with the experimental ones, they conclude that the dominant decay is:

$$\rho'(1600) \to \rho^0(760) + \epsilon^0(800) .$$

It is not at all clear that such a conclusion has any meaning in view of the small number of events studied and the large decay widths of the particles involved. However, it is interesting to note that if the conjectured decay mode is, in fact, dominant and one assumes isotopic spin invariance to estimate neutral pion decay rates, then the measured cross section for ρ' production is consistent with a γ-ρ' coupling constant of

$$\frac{f_{\rho'}^2}{f_\rho^2} \approx 4 ,$$

which is the value predicted by the Extended Vector-Meson Dominance Model.[12]

IV. MULTI-HADRON PRODUCTION

Probably the most exciting topic in e^+e^- colliding beam physics today is the study of hadron production by single-photon annihilation of the electron-positron pair. One of the most fundamental quantities in this study is the total cross section for the production of hadrons and it is generally normalized to the purely electrodynamic cross section for the production of muon pairs. This ratio, commonly denoted by R, is therefore defined:

$$R \equiv \frac{\sigma(e^+e^- \to \text{hadrons})}{\sigma(e^+e^- \to \mu^+\mu^-)}$$

The cross section for muon pair production is calculated in lowest order QED which gives:

$$\sigma_{\mu\mu} = \frac{4}{3}\pi\frac{\alpha^2}{s} \approx \frac{21 \text{ nb}}{E_0^2(\text{GeV})} ,$$

where E_0 is the energy of the e^+, e^- beams.

This is a very small cross section and even though (as we shall see) the hadron production is comparable to or greater than $\sigma_{\mu\mu}$, the experimentalists are faced with relatively low counting-rate experiments. There is also the experimental problem that the detectors employed in measuring σ_{hadron} to date cover a relatively small fraction of the solid angle with no momentum resolution and therefore assumptions need to be made about the final states in order to estimate the efficiency of these detectors. This amounts to solving the following set of relations without independent knowledge

of the efficiencies:

$$N_p = \left[\int L\,dt\right] \sum_q \epsilon_{p,q}\sigma_q,$$

where N_p is the number of events of some observed final-state (say number of prongs) p, $\int L\,dt$ is the integrated luminosity, $\epsilon_{p,q}$ is the efficiency for detecting a final state of type q and observing it in the p class of events. σ_q is the partial cross section for the final-state q and the total cross section is given by the sum of the σ_q. These equations are usually solved by least-squares methods, with the constraint that the partial cross sections σ_q are non-negative. The particles of the final state q are usually assumed to have an invariant phase-space distribution for the purposes of efficiency calculations.

There are new data on the total hadron cross section from Frascati and CEA. The Rome-Frascati "$\gamma\gamma$" group[16] reports new results at center-of-mass energies of 2.8 GeV and 3.0 GeV. These are plotted as open boxes in Fig. 7, along with the other new data and the results known at the time of the Batavia conference. Unfortunately, the statistical and systematic errors on the new results from the $\gamma\gamma$ group make it impossible to draw quantitative conclusions. However, these data do confirm the relatively large hadron production rates observed at lower energies.

Preliminary information from the μ-π group[17] at center-of-mass energies of 2.6, 2.8, and 3.0 GeV give an average ratio of hadron production to muon pair production of 1.4 ± 0.2, which is lower than the earlier data in this energy range. The authors stress that these data are preliminary and that there may be systematic errors in the efficiency calculations, but it is nevertheless extremely interesting that their values for R are significantly lower than the earlier data and indicate the possibility of a break or discontinuity in the ratio R for values of s between 10 and about 15 GeV^2. It is obviously too early to speculate about the behavior of R in this energy range and further experiments, which can hopefully cover these energies with the same piece of apparatus, are called for.

The BOLD detector group from CEA has published its results on multihadron production at 4 GeV,[18] and the error bars have been reduced since these data were presented at the Batavia Conference. They have also obtained a preliminary value for R at s = 25 GeV^2.[19] These results are based on 88 events and approximately 100 hadron events, respectively, and the previous speaker[20] has discussed, in detail, how the experiment and data analysis were performed. Needless to say, the large multihadron production rates observed at CEA are extremely interesting, especially when compared with the preliminary data from Frascati mentioned previously. However, the large statistical and systematic errors leave some of the central questions of multihadron production unanswered.

The most important question in this subject remains: What is the energy dependence of R? The data of Fig. 7 are consistent with a linear rise in R versus s for s greater than 5 to 10 GeV^2, but can also accommodate a constant value for R at these higher energies. A linear rise in R implies that the total hadronic cross section is a constant over the energies studied and if this behavior persists at even higher energies, quantum electrodynamics will have measurable deviation, due to the hadronic contribution to the vacuum polarization, as was discussed in Section I. Presumably, a linear rise cannot continue forever, or QED as we know it will be destroyed by the time R reaches the value 137 or so! A linear rise in R at present-day storage ring energies is predicted by Drell and Chanowitz[21] who argue that we are at the verge of observing structure in the partons because of their gluon clouds formed by the exchange vector gluons with masses near 10 GeV/c^2. Unfortunately, except for some speculations about the breakdown of scaling in deep inelastic electron scattering, this is the limit of their predictive power.

The most fashionable expectation is that R is a constant. This is derived primarily from parton ideas used in the study of deep inelastic electron scattering and modern ideas of scale invariance and light-cone algebra.[22] In simple parton models, R is related to the parton charges by:

$$R = \sum_{\substack{i \\ J=1/2}} Q_i^2 + \frac{1}{4} \sum_{\substack{j \\ J=0}} Q_j^2 ,$$

where the two summations are for half-integral spin and spin-zero partons. A single triplet of quarks gives R = 2/3 which is probably ruled out by the data. Three triplets of colored quarks[23] give R = 2 and the addition of a charmed quark[23] will give R = 3 1/2, both values which are not inconsistent with the data. The Han-Nambu[24] scheme gives an asymptotic value of 4.

In another approach, Greco[12] and co-workers force a constant value of R by appropriately choosing the coupling constants of a Veneziana-like spectrum of vector mesons and derive:

$$R = 2\pi/(f_\rho^2/4\pi) \approx 2.5 .$$

This is the so-called Extended Vector-Meson Dominance Model. Sakurai,[25] using duality arguments, obtains a value for R between 3 and 5.

Any such lists of possibilities for R can go on and on; what we need at the present time is more accurate data! As a final comment, it is interesting to note that two different models[13,26] which yield constant values for R indicate that scaling should be approached from above. That is to say, if R approaches a constant (i.e., it scales) then it reaches this constant from above like 1/log s. The present data would appear to be in conflict with such a behavior.

In Fig. 8 the average multiplicities of some of the hadron data discussed here are plotted. Again, the error bars are rather large, but certain conclusions can be drawn. For example, at $s = 16\ \mathrm{GeV}^2$ the average charged multiplicity is roughly 4 so we can expect the total mean multiplicity to be approximately 6, which means the mean energy per particle is about 700 MeV, a value which is much too large for simple statistical and fireball models.[27]

The theoretical guesses for the energy dependence of the mean multiplicity range from $\langle n \rangle$ = constant to $\langle n \rangle = a + b\sqrt{s}$. Again, it is probably too early to distinguish between various models because both the models and the data are in a state of flux.

V. "2-PHOTON" PHYSICS

The final subject which I would like to touch on briefly is some preliminary experimental information on the "$2 \cdot \gamma$" reactions $e^+e^- \to e^+e^-e^+e^-$, $e^+e^-\mu^+\mu^-$, and $e^+e^-\pi^+\pi^-$, a subject that has only seen an enormous amount of theoretical work up to this time. The $\mu\pi$ group has succeeded in developing an electron-tagging system that measures the direction and energy of the outgoing electrons in a 2γ event in conjunction with a large solid-angle detector which detects the other final-state particles. The kinematics for the above-mentioned reactions are therefore over-constrained and therefore 2γ events can be unambiguously identified. In a preliminary run at Frascati[28] they observed the following numbers of events:

Reaction	Number of Events
$e^+e^- \to e^+e^-e^+e^-$	10
$e^+e^- \to e^+e^-\mu^+\mu^-$	8
$e^+e^- \to e^+e^-\pi^+\pi^-$	3

The first two reactions are in agreement with the predictions of the equivalent photon approximation[29] and the third represents the first observation of a hadronic 2γ final state.

ACKNOWLEDGMENTS

The author wishes to thank Professors M. Conversi and G. Salvini for kindly supplying unpublished and preliminary data from Frascati for inclusion in this report.

FIGURE CAPTIONS

1. Feynman diagrams describing three processes studied with e^+e^- storage rings to check the validity of Quantum Electrodynamics.
2. Experimental $e^{\pm}$, γ mass distribution from the reaction $e^+e^- \rightarrow e^+e^-\gamma$ measured at Frascati (Ref. 4). The solid curve is the prediction of QED.
3. Experimental cross section for the reaction $e^+e^- \rightarrow e^+e^-$ measured by the BCF group (Ref. 5). The solid curve is the prediction of QED.
4. Comparison of the measured cross section for the reaction $e^+e^- \rightarrow \mu^+\mu^-$ near the ϕ^o mass showing the ϕ^o contribution to the photon propagator. The dashed line is the prediction of QED neglecting the ϕ^o contribution. The solid curve is the prediction of QED including the vacuum polarization contribution of the ϕ^o meson with a particular branching ratio to leptons assumed. This figure is taken from Ref. 7.
5. The square of the pion form factor $|F_\pi|^2$ versus s taken from Ref. 10. Note that for data with $s > 2$ GeV^2, there may be K contamination and therefore this represents an upper limit for $|F_\pi|^2$. The curve is the best fit to all of the data assuming a power law behavior in s. The open circle is an estimate of $|F_\pi|^2$ including kaon contamination taken from the results of Ref. 11. The open triangle is not to be taken literally, but is included to show the near equality of the $p\bar{p}$ cross section to the $\pi\pi$ + KK cross section at $s = 4.4$ GeV^2. This point is obtained by computing $|F_\pi|^2$ from the measured (Ref. 9) $p\bar{p}$ cross section.
6. Three fits for $|F_\pi|^2$ versus s from the data of Fig. 5 under different assumptions of the kaon contamination. The curve marked "ρ^o tail" is the Gounaris-Sakurai formula (Ref. 14).
7. The ratio of the total hadronic cross section to the muon pair cross section versus s. The dashed lines represent various quark model predictions discussed in the text.
8. The mean hadron multiplicity versus s. The dashed lines are guides to the eye only.

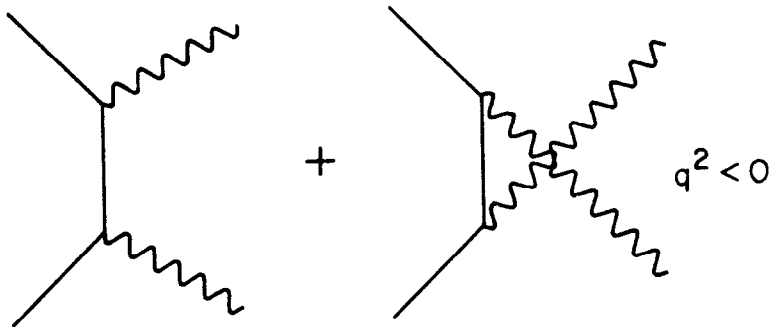

(a) TWO γ ANNIHILATION

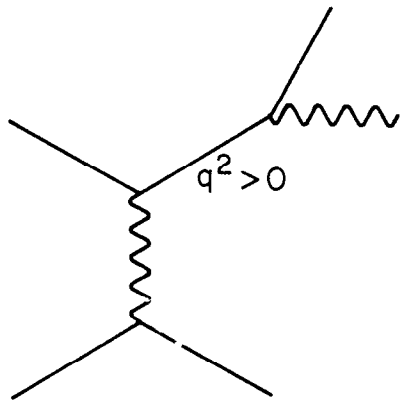

(b) "COMPTON" DIAGRAM

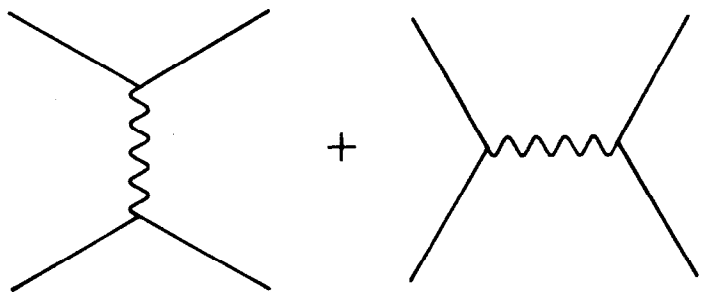

(c) BHABHA SCATTERING

2367A6

Fig. 1

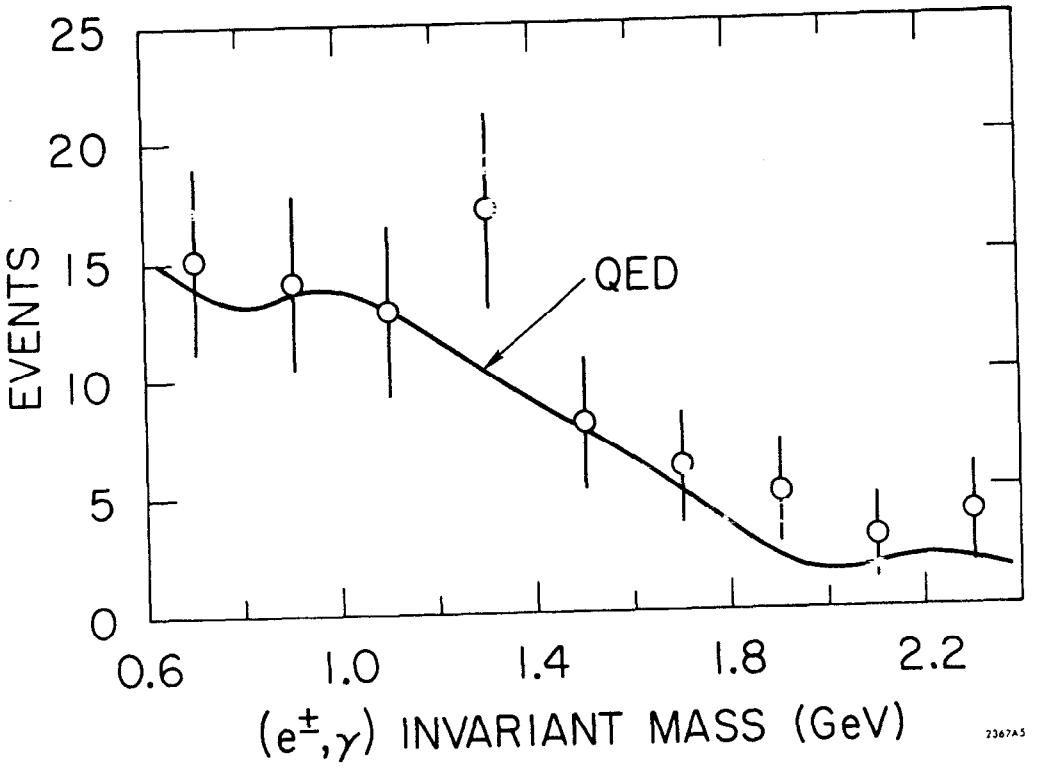
25
20
15
10
5
0
EVENTS
QED
0.6
1.0
1.4
1.8
2.2
(e±,γ) INVARIANT MASS (GeV)
2367A5

Fig. 2

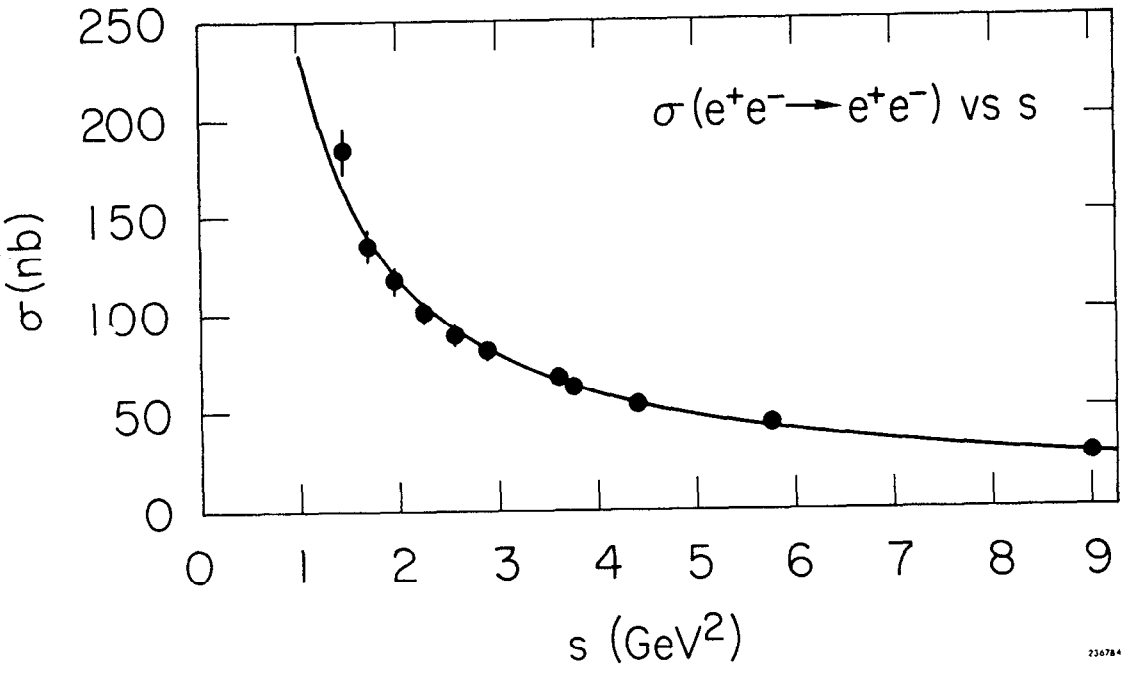
250
200
150
100
50
0
σ (nb)
σ (e+e− → e+e−) vs s
0
1
2
3
4
5
6
7
8
9
s (GeV2)
23678A

Fig. 3

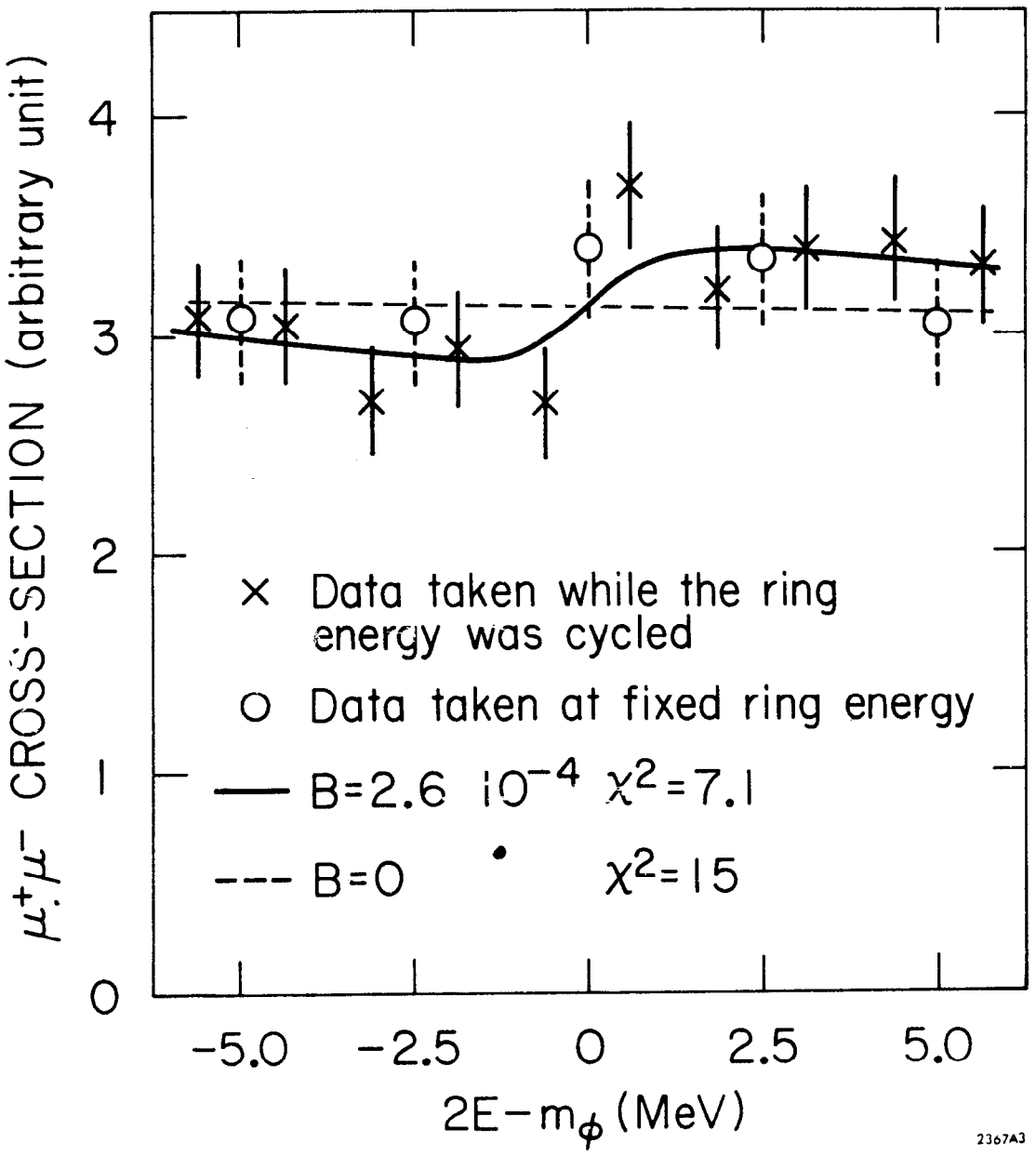
$\mu^+\mu^-$ CROSS-SECTION (arbitrary unit)
0
1
2
3
4
-5.0
-2.5
0
2.5
5.0
$2E-m_\phi$ (MeV)
× Data taken while the ring energy was cycled
○ Data taken at fixed ring energy
— B=2.6 10^{-4} χ^2=7.1
--- B=0 χ^2=15
2367A3

322

Fig. 4

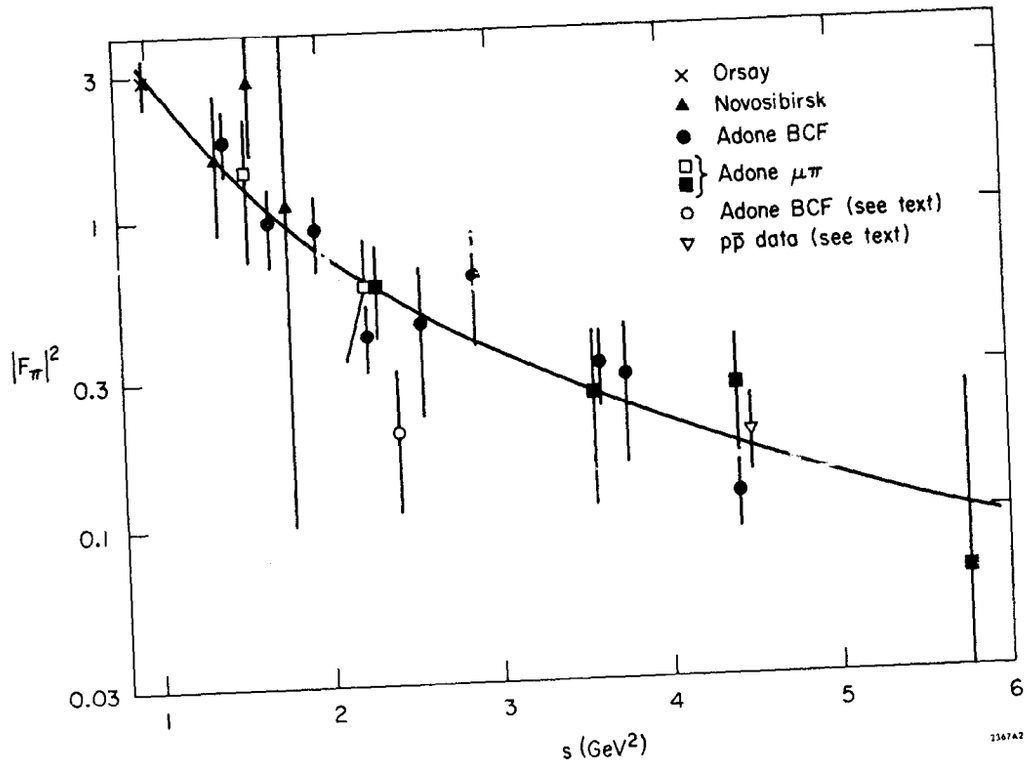
× Orsay
▲ Novosibirsk
● Adone BCF
□ ■ Adone μπ
○ Adone BCF (see text)
▽ pp̄ data (see text)
$|F_\pi|^2$
3
1
0.3
0.1
0.03
1
2
3
4
5
6
s (GeV²)
2367A2

Fig. 5

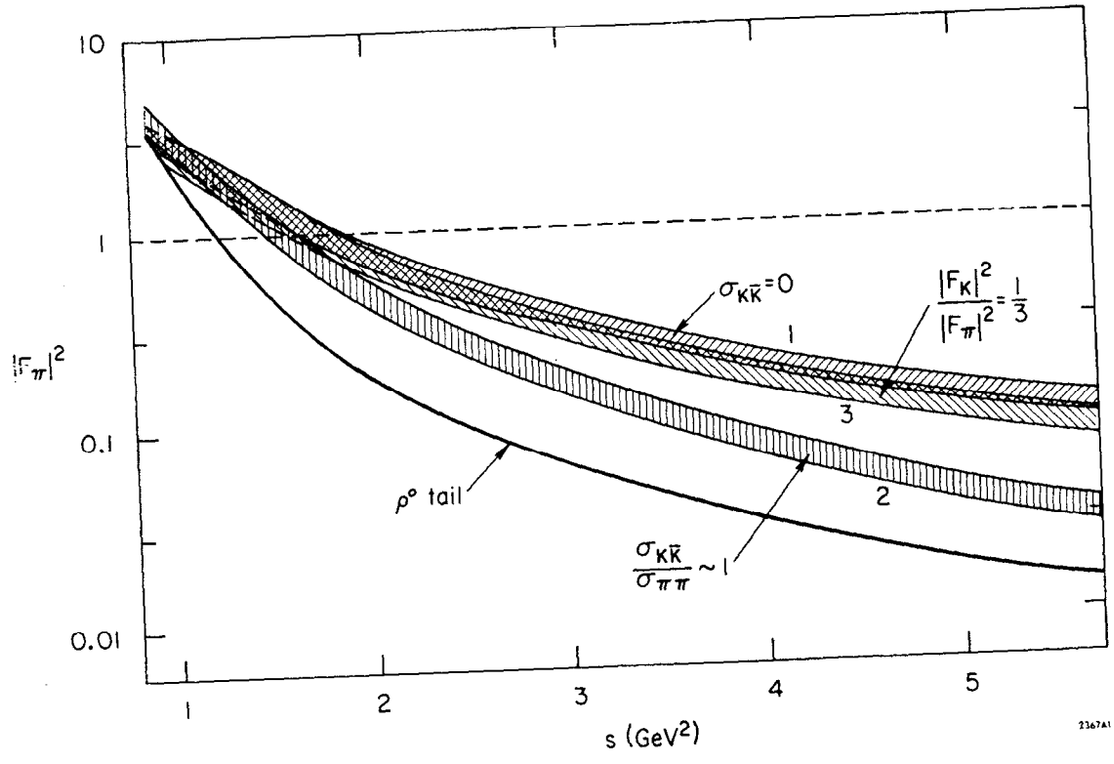
10
1
0.1
0.01
$|F_\pi|^2$
$\sigma_{K\bar{K}}=0$
1
$\frac{|F_K|^2}{|F_\pi|^2}=\frac{1}{3}$
3
2
ρ^o tail
$\frac{\sigma_{K\bar{K}}}{\sigma_{\pi\pi}}\sim 1$
1
2
3
4
5
s (GeV²)
2367A1

Fig. 6

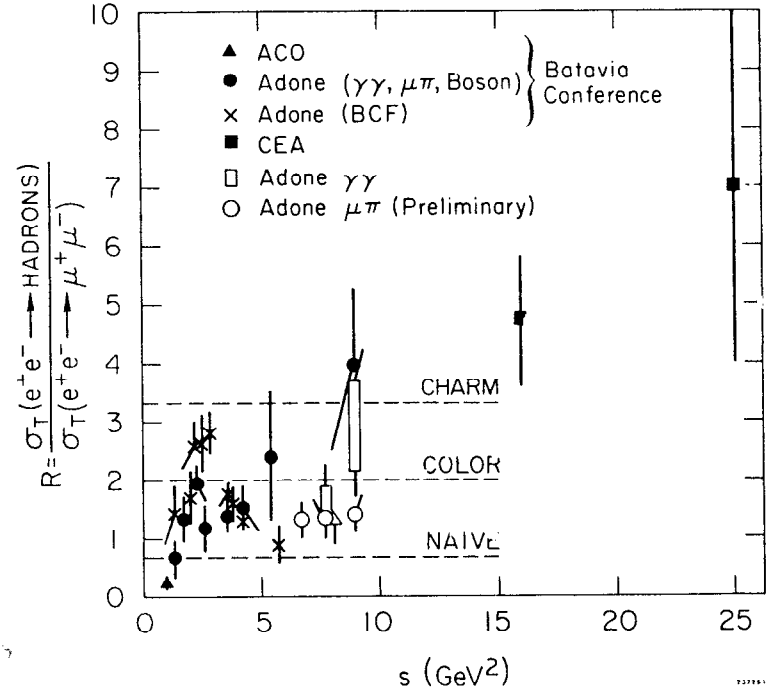
ACO
Adone (γγ, μπ, Boson)
Adone (BCF)
CEA
Adone γγ
Adone μπ (Preliminary)
Batavia Conference
CHARM
COLOR
NAIVE
R=σT(e+e−→HADRONS)/σT(e+e−→μ+μ−)
s (GeV2)

Fig. 7

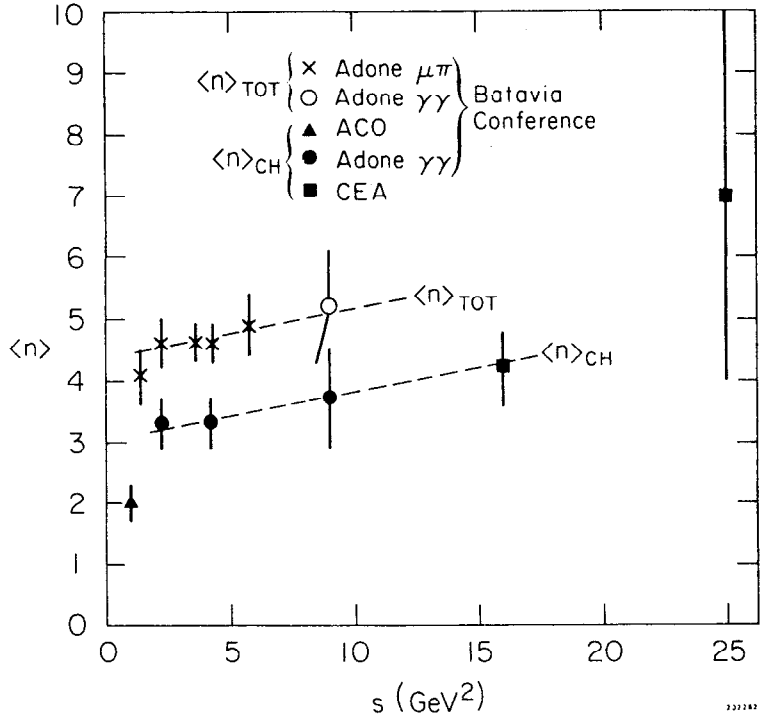
<n>TOT
Adone μπ
Adone γγ
<n>CH
ACO
Adone γγ
CEA
Batavia Conference
<n>TOT
<n>CH
<n>
s (GeV2)

Fig. 8

REFERENCES

1. Rapporteur talks on e^+e^- colliding beams in Proceedings of the 1971 International Symposium on Electron and Photon Interactions at High Energies, Cornell Univ. (1971).

   Frascati Results - C. Bernardini page 37

   Orsay Results - J. Le Francois page 51

   Novosibirsk Results - V. Siderov page 65.

2. V. Silvestrini, Proceedings of the 16th International Conference on High Energy Physics, Batavia, Ill. (1972). Vol. 4, p 1.
3. G. Hanson, et al., CEA preprint submitted to Nuovo Cimento (1973).
4. C. Bacci, et al., to be published in Phys. Letters (1973). (G. Salvini, private communication.)
5. M. Bernardini, et al., CERN preprint submitted to Phys. Letters (1973).
6. G. Källen, Helv. Phys. Acta 25, 417 (1952); and H. Lehmann, Nuovo Cimento 11, 342 (1954).
7. J. E. Augustin, et al., Phys. Rev. Letters 30, 462 (1973). See Ref. 1.
8. J. D. Bjorken, private communication.
9. M. Castellano, et al., Nuovo Cimento 14 A, 1 (1973).
10. G. Barbiellini, et al., Lettere al Nuovo Cimento 6, 557 (1973).
11. M. Bernardini, et al., Phys. Letters 44 B, 393 (1973).
12. M. Greco, CERN preprint TH.1617 (1973).
13. R. Gatto and G. Preparata, DESY preprint 73/15 (1973).
14. G. J. Gounaris and J. J. Sakurai, Phys. Rev. Letters 21, 244 (1968).
15. F. Ceradini, et al., Phys. Letters 43 B, 341 (1973).
16. C. Bacci, et al., to be published in Phys. Letters (G. Salvini, private communication).
17. F. Ceradini, et al , (M. Conversi, private communication).
18. A. Litke, et al., Phys. Rev. Letters 30, 1189 (1973).
19. A. Litke, Invited Talk at the Spring Meeting of the APS, Washington, D.C. (1973).
20. H. Newman, preceeding speaker, SLAC Topical Conference on Deep Inelastic Scattering (1973).
21. M. S. Chanowitz and S. D. Drell, Phys. Rev. Letters 30, 807 (1973).
22. S. D. Drell, SLAC-PUB-1139 (1972). (Invited talk at the parallel session on Currents I: Electron Positron Interactions, 16th International Conference on High Energy Physics, Batavia, Ill. (1972).)
23. W. A Bardeen, H. Fritzsch, and M. Gell-Mann, CERN preprint TH.1538 (1972).
24. M. Y. Han and Y. Nambu, Phys. Rev. 139 B, 1006 (1965).
25. J. J. Sakurai, UCLA preprint UCLA/73/TEP/76 (1973).
26. D. Gross and F. Wilczek, Phys. Rev. Letters 30, 1343 (1973), and D. Gross and F. Wilczek, NAL preprint NAL-PUB-73/49-THY (1973).
27. J. D. Bjorken and S. J. Brodsky, Phys. Rev. D 1, 1416 (1970).
28. F. Ceradini, et al., (M. Conversi, private communication).
29. S. J. Brodsky, et al., Cornell preprint CLNS-152 (1971).

HADRONIC FINAL STATES IN INCLUSIVE LEPTO-PRODUCTION AND COLLIDING BEAMS, i.e. FEATURES OF CURRENT FRAGMENTATION*

E.W. Colglazier +
Stanford Linear Accelerator Center
Stanford, California 94305

In his three lectures[1], Bjorken told us everything there is to know about hadronic final states in inclusive lepto-production and colliding beams - at least "at this point in time." The lessons we learned from him include: (i) how much is predicted by just assuming normalized quantities do not change (radically) as Q^2 increases at fixed W, (ii) how ones views from both the orthodox and the heretical perspectives (i.e. the predictions of various models - with no inference intended by the adjectives as to which might be correct), and (iii) how the space-time evolution is constrained by the fact that quarks don't get out. Here I shall discuss, in a mundane way and primarily for non-specialists, the features of current fragmentation in the parton model or the orthodox perspective. Using the version of the model developed primarily by Bjorken, Feynman, and co-workers.[2] I will focus on the assumptions and predictions, as well as the constraints and difficulties, with this point of view having been relieved of discussing all models by Bjorken's thorough job.

---

*Talk presented at the S.L.A.C. Summer Institute on "Deep Inelastic Scattering," July 9th - 18th, 1973
+Address after Sept. 1, 1973: Institute for Advanced Study, Princeton, New Jersey 08540

The processes of interest are the single hadronic particle inclusive lepton-hadron or lepton-lepton reactions, i.e.,

$$e\,p \to e\,h\,X,\ \nu\,p \to \mu\,h\,X,\ e^+e^- \to h\,X,\ \text{etc.}$$

The one photon (or current) approximation is assumed, so that these reactions are effectively "virtual current" - hadron scattering with one final state hadron observed. The relevant variables are ν, Q^2, and $\vec{p}_h$ for lepto-production (polarization of the current as well) and Q^2, $|\vec{p}_h|$, and θ for colliding beams (standard definition of these variables is given in Figure 1).

The first question to ask is what do we know about these processes from our ideas of strong interactions. Short range correlations or multiperipheral - type dynamics lead to limiting fragmentation or Feynman scaling and a flat central plateau in hadron-hadron scattering at high energy. If we accept this point of view (which has received experimental support at the ISR), then we should expect a similar picture in lepto-production at large W but fixed finite Q^2. A plot of the invariant inclusive cross-section $\frac{1}{\sigma_{tot}}\frac{d\sigma}{dy}$ versus the rapidity y at large W should resemble the plot given in Fig. 2. In other words, the current at small Q^2 should produce a finite fragmentation region which borders the central hadronic plateau. In the deep inelastic region when Q^2 is large, the lepton-hadron processes are possible combined scaling phenomena, perhaps exhibiting Bjorken scaling as well as Feynman scaling. The central question is what happens to the current fragmentation region in the deep inelastic regime.

Applying the ideas about strong interactions mentioned above, the kinematic bounds on the current fragmentation region at large Q^2 are easy to derive, using either Bjorken's argument[3] or Mueller-Reggeism [4,5] or the light cone.[6] The result is that the current fragmentation region extends approximately $\ln(Q^2/M^2)$ in rapidity for large Q^2 (up to a finite uncertainty; for convenience we will drop the M^2 scale) and borders the central hadronic plateau which is $\ln(w-1)$ long in rapidity for large w (see Fig.3) In the Mueller-Regge language, the explanation is as follows: The assumption of scaling for the total cross-section at large w constrains the Q^2 dependence of residues of (factorizable) Regge trajectories coupling to the photon (Fig. 4a). This constraint and the Mueller diagram for the finite target fragmentation region (Fig. 4b) imply that the normalized invariant inclusive cross-section $\frac{E}{\sigma_{tot}}\frac{d\sigma}{d^3p}$ is a function of w, $P_\perp$ and the longitudinal momentum fraction $q\cdot P_h / q\cdot P$. The w dependence disappears at very large w where the pomeron dominates. Also at very large w, the Mueller diagram for the hadronic central plateau (Fig. 4c) implies that $\frac{E}{\sigma_{tot}}\frac{d\sigma}{d^3p}$ is a function only of $P_\perp$. (It may take quite large w to develop the plateau, partially because of the logarithmic dependence, but also because of indications of a small coupling of the pomeron to the current.[7]) The Mueller-Regge expansion for the central plateau is valid only when the variables w_1 and K (see Figs. 1a and 4c) are both large, which requires being no farther from the target fragmentation boundary than $\ln(w-1)$. Since the length of the entire rapidity plot is $\ln s \approx \ln Q^2 + \ln(w-1)$, the fragmentation region of the large virtual mass current must then be $\sim \ln Q^2$ long. Unfortunately, Mueller-Reggeism alone cannot make further predictions about current fragmentation because of the unknown vertex in the appropriate Mueller diagram (Fig 4d).[5] The basic conclusion, which is independent of the language, is that the target fragmentation region and the hadronic central plateau are the same, familiar regions which appear in purely hadronic reactions. However, the current fragmentation region of length $\ln Q^2$ in rapidity is unknown and highly model dependent.

Now we shall investigate the features of current fragmentation in the parton model, for space-like Q^2 in lepto-production and, by the natural definition, for time-like Q^2 in colliding beams. The dominant feature of the parton model is that the current knocks out a parton from the target which is then moving in the direction of the incident current, i.e., in the kinematic region designated as current fragmentation. Of course, the isolated parton must then evolve, somehow, into the observed final state hadrons.

We should first state explicitly the assumptions of the parton model and, in particular, of its application to hadronic final states. The three basic assumptions can be given as follows:

(i) point-like spin 1/2 constituents of hadrons plus the standard folklore regarding their relevance to deep inelastic phenomena, i.e. scaling for total cross-sections both in lepto-production and colliding beams.

(ii) The (quark) partons don't get out, i.e. quarks have not been seen and neither have fractional quantum numbers.

(iii) ?

This third assumption used to be called short-range correlations in rapidity. However, assumption (ii) seems to place serious constraints on the space-time evolution of the dynamics; in fact, some sort of long range correlation in rapidity seems necessary. Bjorken has agonized over the problem[8]; Feynman has stated by fiat that distant partons (in rapidity) have a universal effect, not zero interaction.[9] Yet some sort of orthodox picture remains since the type of final state hadrons at a particular rapidity y only depends on the nature of the parton distribution within a finite range of y (because far away partons have a universal effect). Therefore, let us use an alternative statement for this third assumption which is at least operational:

(iii) parton fragmentation is similar to hadron fragmentation except for some differences forced by assumption (ii)

What do we mean by parton fragmentation? Let us examine the kinematics of deep inelastic lepto-production in Feynman's favorite frame[2]: the Breit frame of the current and the struck parton (Fig. 5). The parton after being hit by the current is isolated in momentum space from the remaining partons. The process by which this parton evolves into final state hadrons is descriptively called fragmentation. The assumption of an analogy with hadron fragmentation suggests we investigate the following features:

(1) limiting fragmentation (in the finite fragmentation region)
(2) existence of a plateau
(3) retention of quantum numbers
(4) dependence at the edge (near the phase space boundary)

Now we shall discuss each of these features and the resulting picture of lepto-production and e+e- annihilation.

(1) limiting fragmentation for the parton [10,11,12] (finite region in rapidity)

An isolated parton should always fragment in the same way (factorization); and only the hadron distribution within a finite rapidity distance of the phase space boundary should be dependent on the parton type (creating a finite fragmentation region). The transverse momenta of the produced hadrons should be limited; and for a hadron with a finite fraction z of the parton's momentum, the invariant distribution should be a function only of z and $p_\perp$.

Let us now see what this predicts for electroproduction. The variables are ν and Q^2 plus the longitudinal momentum p_L and the transverse momentum $p_\perp$ of the outgoing hadron. (The

azimuthal angle φ is integrated over, but there is no dependence anyway in the parton model[13]). Also, only the transverse structure functions survive in the deep inelastic limit because the quark-partons are spin 1/2. The main prediction of the parton model is that the normalized invariant inclusive distribution scales as a function of ν and z, i.e., $\frac{E}{\sigma_{tot}}\frac{d\sigma}{d^3p} \xrightarrow[\text{inelastic}]{\text{deep}} f(z, P_\perp, \nu) \xrightarrow{\text{large } \nu} f(z, P_\perp)$

The variable z (equal to K/ν and approximately $-x$ in the parton fragmentation region) is $\frac{P_L}{P_{L\,MAX}}$ in a frame where the parton moves fast (c.m., lab, Breit, etc. - z's in different frames differ slightly at finite energies). The finite fragmentation region corresponds to z finite. The ν dependence results from the density of quark-partons in the target, as is easily seen by the following formula:

$$E\frac{d\sigma}{d^3p} \propto \sum_{\substack{\text{quark}\\ \text{types}}} (\text{quark charge})^2 \times \text{quark density} \times \text{fragmentation function of quark into hadron } h$$

$$\propto \sum_{q's} Q_q^2 \times q(x) \times D_q^h(z, P_\perp)$$

In the above formula, it is probably better to integrate out the $P_\perp$ dependence (the average is limited and uninteresting) since the (limited) $P_\perp$ distribution of the struck parton is not folded in.[14] Since scaling in terms of z and ν is expected before the plateau develops, these predictions for electroproduction can be checked at relatively low values of Q^2 (e.g. $Q^2 > 1$ gev^2). Coincidence experiments from several groups [15] are already producing results which bear on the parton model predictions.

As a contrast, the predictions of another class of models are worth pointing out. J. Weis using the dual model [16] and M. Greco using a version of the vector dominance model [17] found that $\langle P_\perp^2 \rangle$ is not limited but is proportional to Q^2. From the energy-momentum sum rule, this result naturally corresponds to the normalized invariant distribution falling inversely with Q^2, i.e.,

$$\frac{E}{\sigma_{tot}}\frac{d\sigma}{d^3p} \xrightarrow[\text{inelastic}]{\text{deep}} \frac{1}{Q^2} f\left(z, \nu, \frac{P_\perp^2}{Q^2}\right)$$

Experiments at large Q^2 will easily distinguish the two predictions.

In e+e- annihilation, the variables are Q^2 and the momentum $p = |\vec{p}_h|$ and angle θ to the beam of the observed hadron. In the parton model, the timelike current produces a quark and anti-quark which fly apart (i.e. isolated in rapidity). Each subsequently fragments into hadrons which, by factorization, is identical to parton fragmentation in electroproduction. The angular distribution is, of course, determined by the spin one intermediate state; however, event by event, the hadrons are produced in jets with the dominant axis the remnant of the spreading quark-antiquark pair. Consequently, a longitudinal rapidity along the jet axis can be defined for each colliding beam event. The momenta transverse to the jet axis are obviously limited. The prediction for the invariant cross-section at high Q^2 is:

$$\frac{E}{\sigma_{tot}}\frac{d\sigma}{dp\, d\cos\theta} = f(z)(1+\cos^2\theta) \quad \text{for finite } z$$

where $z = \frac{p}{p_{max}} = \frac{2p}{Q}$ and $f(z) \propto z\sum_{q's} Q_q^2 \times D_q^h(z)$. The $(1+\cos^2\theta)$ dependence results again from the spin 1/2 nature of the quarks; folding in the average transverse momenta of the hadrons produces a

longitudinal component that disappears as $Q^2 \to \infty$ .Also, as $z \to 0$ $\left(z \sim \frac{2\langle p_\perp \rangle}{Q}\right)$ the distribution becomes isotropic. The basic experimental questions are "How high an energy is necessary to see jets?" and "When do we expect scaling?" In order to see jets, the average momentum $\langle p \rangle$ must certainly be much larger than the average transverse momentum $\langle p_\perp \rangle$ in lepto-production, and the multiplicity must be high enough such that several particles have large enough momentum to define the jet. Statistical tests can be applied to the experimental data to determine the existence of jet structure.[18] Hopefully, SPEAR at $Q^2 \cong 31$ gev^2 will be sufficient. Regarding the second and more fundamental question, it is probably already embarrassing that scaling for the total cross-section has not been observed at CEA. If the colliding beam cross-section for hadron production does not scale (constant ratio to the μ-pair production cross-section), then the naive parton model might as well be forgotten.

(2) existence of a plateau in rapidity (dz/z distribution for small z) [11,12]

Since quarks are fractionally charged, the dynamics describing an isolated quark fragmenting into hadrons cannot be completely factored from the rest of the process. The development of the plateau, e.g. between the q and $\bar{q}$ fragmentation regions in colliding beams, would preserve Feynman scaling while allowing the possibility of the fractional charge being "neutralized". Since the plateau would cover nearly all of the current region, the multiplicities from current fragmentation would be logarithmic in Q^2. Of course, Q^2 must be quite large for the plateau to develop and dominate the multiplicity because of the logarithmic relation between Q^2 and y. If scaling occurs and the multiplicity in the current fragmentation region is finite, then as Bjorken showed[1] some exclusive channel must scale (and that channel would be effectively be the partons). Thus the existence of a dz/z distribution for parton fragmentation, which is a plateau in rapidity, is desirable for several reasons. However, implementing the dynamics recognizing the constraint that quarks don't come out is quite difficult. As stressed by Bjorken,[8] this difficulty is <u>the central problem.</u>

The reason for the trouble can be related to the space-time evolution of the dynamics in familiar, calculable models which give scaling. In the cut-off field theory [19], (naive) covariant parton[20,21], ϕ^3 field theory [22], multiperipheral [23], composite proton[24], etc., models, the parton is effectively "blasted out" of the proton producing isolated quark quantum numbers in the final state.[25] The hadrons produced by the parton are separated in rapidity from the target fragments, so that there is no plateau. Consequently, as many authors have shown [19-25], the multiplicity predicted by these models is finite in e+e- colliding beams and $\ln w$ in lepto-production.

Following Bjorken [8], and the rather nice discussion of Kogut, Sinclair, and Susskind [25], we shall examine these difficulties more closely. Consider a cascade as a dynamical mechanism, as for example in e+e- annihilation. The original hope was that eventually slow partons would be produced by the cascade which could annihilate and neutralize the fractional charge. However, partons can only interact (annihilate) if they are generated in the space-time vicinity of each other. Ordinary time dilation gives an estimate of the time necessary for the cascade to begin that is proportional to Q; but large Q implies the parton has moved far away in space before the cascade starts. With standard dynamics, the cascade partons can't get back to the starting point for neutralization.

Bjorken[8] has constructed a space-time mechanism which does produce the desired result. Suppose that when the parton and anti-parton move apart a distance of approximately 1 fermi in the C.M., another pair pops out between them and polarizes the vacuum. This process continues until the parton distribution is evenly populated in rapidity producing a plateau. At a time proportional to Q, the polarization charge catches up to the initial parton and neutralizes the fractional charge. Since the parton has propagated almost freely for a long time, the naive parton picture remains. The plateau is produced, the fractional charge is removed, and the quarks disappear. Everything is very nice, but this mechanism demands long range correlations in rapidity, which seems to be the price for removing quarks from the asymptotic state.

Amazingly, this mechanism is implemented in a calculable model. As discussed by Casher, Kogut, and Susskind [26], two dimensional QED (one space and one time dimension) is a soluble model in which scaling properties of fermi fields do not require quark production in deep inelastic reactions. A vacuum polarization current neutralizes the outgoing quarks and results in massive gluon production with logarithmic multiplicities and jet alignment. However, the special properties of two dimensions seem essential; so that the extension to four dimensions is not obvious.

Another attempt to overcome the difficulties of standard models is the proposal of Preparata [27]. He constructs a field theory model of very massive quarks with definite calculational rules that include Regge behavior for quark scattering amplitudes and strong damping of off-shell quark legs that can be approximated by an essential singularity at ∞ . This later property, which is not the standard analyticity, eludes the space-time difficulties of other calculable models and produces the same results as the intuitive picture (including the plateau).

Also, the Cambridge school [28] has recently altered the covariant parton model to be compatible with a current plateau as well as other possibilities. The current region is built from two separate contributions, parton and hole fragmentation, which do not necessarily match even if both are plateaus. The close analogy with diffractive excitation models of hadronic reactions suggests some exclusive channel scales unlike the orthodox picture (also unusual is the fact that $\langle p_\perp^2 \rangle$ increases with Q^2).

(3) retention of quantum numbers in the fragmentation region

Even though the quantum numbers of quarks are fractional, they could be retained, on the average, in the fragmentation region. If true, we would be seeing "footprints" of the quarks in the final state hadrons - rather convincing evidence for a quark sub-structure even if quarks are not seen. Feynman [12] thought that the quantum number retention hypothesis would be true in general (not just in special cases of models). Farrar and Rosner [29], however, provided a devastating counter-example. Consider a simple model for e+e- annihilation in which the rapidity gap between the initial quark and antiquark is filled with isosinglet $\bar{q}$ q pairs. Adjacent quarks and antiquarks (beginning at either end) are then assumed to convert into mesons. If we measure the average quantum numbers of all the mesons to the left (insensitive to where in the neutral plateau the average is stopped), then the electric charge on the average is <u>not</u> that of the fragmenting quark unless the inserted pairs are unitary singlets (one internal pair is cut to guarantee zero triality to the left). Of course, exact SU(3) is unlikely since many more pions than kaons are expected in the plateau.

The reason for failure in the meson emission model is obvious from consideration of baryon number - since no baryons are emitted, there is no way baryon number can be retained in the fragmentation region. Moreover, the failure for electric charge then follows from the Gell Mann - Nishijima relation since the hypothesis holds for I_z and fails for $Y = B + S$ (unless there is a compensating failure for S, as in the exact SU(3) version of the meson emission model).

Bob Cahn and I initially thought baryon emission could resurrect the conjecture. It does, but the multiplicity is forced to increase as a power of Q^2. In models with logarithmic multiplicities, the hypothesis fails in general although Feynman's result could happen accidentally (so it is still worthwhile to check experimentally!). A weaker version, however, is true in general and is testable (albeit difficult).[30]

This difference between quark and hadron fragmentation concerning quantum number retention is apparent from a simple cascade formalism which I shall now describe.[30] A cascade may be thought of as a stepwise process that deposits final state hadrons at set intervals in rapidity. The formalism to be used is more general than a specific space time evolution (and the problems mentioned previously) and should only be interpreted as a mechanism for describing the quantum numbers of the final states produced by a fragmenting parton or hadron. The necessary dynamics will be put in "by hand" by guaranteeing a plateau, i.e. a constant density of emitted particles per unit step in rapidity away from the initiating end of the cascade.

As an example, consider the meson emission model as a cascade but with only p and n quarks and emitted pions (see Fig. 6). The first step of the cascade is the initial quark throwing off the first pion and producing a quark (the type depending on the pion produced) which initiates the second step. Since a particular

state after a certain number of steps is uniquely labeled by the initial quark (produced incoherently in the parton model) and the position and type of each pion in rapidity, there is no interference between states so that probabilities can be used instead of amplitudes. The quantum numbers deposited in the fragmentation region are calculable solely from knowledge of the initial quark and the one at the Nth step as $N \to \infty$. Let the probability vector at the N th step be:

$$P_N = \begin{pmatrix} \text{Prob}(p) \\ \text{Prob}(n) \end{pmatrix}$$

with a transformation matrix to the next step:

$$T = \begin{pmatrix} \text{Prob}(p \to p\pi^0) = \tfrac{1}{3} & \text{Prob}(n \to p\pi^-) = \tfrac{2}{3} \\ \text{Prob}(p \to n\pi^+) = \tfrac{2}{3} & \text{Prob}(n \to n\pi^0) = \tfrac{1}{3} \end{pmatrix}$$

where $P_{N+1} = T P_N$.

(the quark wave function for pions determines the above probabilities). The quantum numbers retained in the fragmentation region, ΔQ, equal those of the initial state, $Q(P_0)$, minus those of P_N , $Q(P_N)$, as $N \to \infty$, i.e. $\Delta Q = Q(P_0) - Q(P_\infty)$.

The eigenvalues and eignevectors of T are:

$$\lambda_1 = 1 \,, \; u_1 = \begin{pmatrix} 1 \\ 1 \end{pmatrix} \;; \quad \lambda_2 = -\tfrac{1}{3} \,, \; u_2 = \begin{pmatrix} 1 \\ -1 \end{pmatrix}$$

so that if $P_0 = \begin{pmatrix} 1 \\ 0 \end{pmatrix}$, then $P_N \xrightarrow[N \to \infty]{} \tfrac{1}{2} u_1$ .Consequently, $\Delta I_z = \tfrac{1}{2}$ but $\Delta Q_{el} = \tfrac{1}{2}$ rather than 2/3 for a p quark, which again illustrates the failure of Feynman's conjecture in the case of meson emission.

Any amount of baryon emission (e.g. $q_b \to \bar{q}_b \bar{q}_b$ + baryon) with quarks cascading independently (a discrete branching Markov process) resurrects Feynman's hypothesis but causes an avalanche of quarks ($\langle n \rangle \propto Q^{\text{power}}$). Therefore, consider the following simple cascade model with baryon emission but which is constrained to have logarithmic multiplicities:

$$T = \begin{pmatrix} \text{Prob}(q_b \to q_b + \text{meson}) & \text{Prob}(\bar{q}_b \bar{q}_b \to q + \text{anti-baryon}) \\ \text{Prob}(q \to \bar{q}_b q_b + \text{baryon}) & \text{Prob}(\bar{q}_b \bar{q}_b \to \bar{q}_b \bar{q}_b + \text{meson}) \end{pmatrix}$$

The only quantum number in the model is baryon number, and the closed system of two cascading states quarantees a plateau. The matrix T has one eigenvalue unity whose eigenvector becomes the asymptotic cascade. Unfortunately, the eigenvector carries baryon number except for a special value of the parameters (T matrix elements). Therefore, the hypothesis fails in general even with baryon emission.

The generalization of the above simple model and the extension to hadron fragmentation predicts three types of cascades, one of each triality (± 1 and 0). The properties of the transformation matrices T_0, T_{+1} and T_{-1} under charge conjugation are:

$$C T_0 C^{-1} = T_0$$
$$C T_{+1} C^{-1} = T_{-1}$$
$$C T_{-1} C^{-1} = T_{+1}$$

Consequently, the asymptotic state P_∞^0 for the zero triality cascade is an eigenvector of C(with eigenvalue +1), but not for triality ± 1. The implication for any additive quantum number Q is:

$$Q(P_{00}^{0}) = 0 \quad \text{but} \quad Q(P_{00}^{+1}) = -Q(P_{00}^{-1}) = ?$$

Therefore, quantum numbers are retained in the fragmentation region, $\Delta Q = Q(P_0)$, of a hadron but not necessarily in the fragmentation region of a quark. However, the quantity $Q(P_{00})$ is the same for all states of the same triality; so that for quarks p,n, and λ :

$$\Delta I_z(p) = +\tfrac{1}{2} \qquad \Delta B(p) = \Delta B(n) = \Delta B(\lambda)$$
$$\Delta I_z(n) = -\tfrac{1}{2} \qquad \Delta Y(p) = \Delta Y(n) = \Delta Y(\lambda) + 1$$
$$\Delta I_z(\lambda) = 0$$

(I_z works because isospin invariance of the matrix T for each triality forces the asymptotic states to have $I_z = 0$). These relations can be tested in neutrino-production where the type of quark knocked out can be determined.

Also, plateau heights, which determine the dominant contribution to the logarithmic multiplicity, are the same for all fragmenting states of the same triality (since there is a unique asymptotic cascade for each triality.) Of course, the heights are necessarily the same for triality +1 and -1 by C invariance, but there is no "a priori" relation to triality 0.

The resulting picture of lepto-production and annihilation is now easy to derive.[31-33] The description in terms of cascades is as follows.[30] In e^+e^- annihilation, the q and $\bar{q}$ produced by the virtual current cascade independently for a number of steps proportional to $\ln(Q/M)$. For large Q, the cascades will be given by approximately P_{00}^{+1} and $P_{00}^{-1} = CP_{00}^{+1}$. Thus, the heights of the cascades are the same, predicting a multiplicity

$$\langle n \rangle \sim C_{e^+e^-} \ln(Q^2/M^2)$$

and an inclusive distribution versus rapidity given in Fig.7. Of course, the quark-like quantum numbers disappear when the two cascades meet.

For deep inelastic lepto-production, we shall use the Breit frame of the virtual current and the struck parton. The target hadron cascades according to the prescription for triality zero until the cascade reaches the point at which it contains a parton of momentum $xP \sim Q/2$. The virtual current strikes this parton (assume it is a quark) and precisely reverses its motion. The hadron cascade is thus transformed into a system of triality -1 which proceeds via T_{-1} while the struck parton fragments via T_{+1}. For large Q, the cascades meet as before in e^+e^- annihilation, with C invariance guaranteeing that they have the same height and that the fractional quantum numbers are annihilated. The resultant rapidity distribution is given in Fig. 8; note that the current fragmentation region consists of a parton fragmentation region, a plateau of length

$\ln Q^2$ and a fragmentation region for the hole left by the struck parton. In the hole fragmentation region, the inclusive distribution scales as a function of two variables: zQ^2/M^2 and $p_\perp$. Also, note the similarity between the fragmentation regions for space-like and time-like currents. In particular, the current plateau heights are the same which predicts a multiplicity in lepto-production of

$$\langle n \rangle \sim c_{e^+e^-} \ln(Q^2/M^2) + c_h \ln(w-1)$$

Feynman[12], Bjorken[3], and Kogut[33] have speculated further that $c_{e^+e^-} = c_h$; so that the multiplicity in lepto-production at large s would be the same as in hadronic reactions, i.e., $\langle n \rangle \sim c_h \ln s$. Even though very large Q^2 $(\ln(Q^2/M^2) > 4)$ and w $(\ln(w-1) > 4)$ would be necessary to demonstrate the existence of both plateaus simultaneously, it should be feasible to demonstrate separately the presence of each plateau by taking first large w and small $Q^2 \sim 1\,\text{gev}^2$ to see the hadronic plateau and second small $w \sim 3$ and large Q^2 to see the current plateau. Although the multiplicity formulae depend on sufficient Q^2 and/or w to develop the plateaus, it is still very interesting at lower energies to determine experimentally the w and Q^2 dependence of the multiplicities (holding something fixed--either w, Q^2, or W) in lepto-production and annihilation and to compare with multiplicities in hadronic reactions at the same s.

Since quantum number retention is not guaranteed to be a property of parton fragmentation, the question arises as to what can be said by the parton model about quantum numbers in the current fragmentation region. The current plateau is obviously neutral, and the parton and hole fragmentation regions should balance each other. Rather than predict absolute quantum numbers in the finite fragmentation regions, the parton model does make predictions about particle ratios.[12] In electroproduction, the particle ratios are determined by the z and w dependence. The z dependence results from the quark fragmentation functions, $D_q^h(z)$, which are interrelated by charge conjugation and isospin, as for example with inclusive $\pi^\pm$ production:

$$D_p^{\pi^+} = D_n^{\pi^-} = D_{\bar{p}}^{\pi^-} = D_{\bar{n}}^{\pi^+}$$

$$D_n^{\pi^+} = D_p^{\pi^-} = D_{\bar{n}}^{\pi^-} = D_{\bar{p}}^{\pi^+}$$

$$D_\lambda^{\pi^+} = D_\lambda^{\pi^-} = D_{\bar{\lambda}}^{\pi^-} = D_{\bar{\lambda}}^{\pi^+}$$

From our knowledge of cascades, we know that as $z \to 0$

$$D_p^{\pi^+}(z) \simeq D_n^{\pi^+}(z) \propto \frac{1}{z}$$

Also, we naively expect that for finite z it is easier for a p quark than an n quark to fragment into a π^+, i.e.,

$$D_p^{\pi^+}(z) > D_n^{\pi^+}(z) \quad \text{for finite } z$$

The w dependence results from the parton density in the target about which we have several clues from existing experiments. From $\sigma_{\bar{\nu}(N+\ell)} / \sigma_{\nu(N+\ell)} \simeq 1/3$, we know that there are mainly quarks rather than antiquarks at finite x (valence picture). From

$\nu W_2^N / \nu W_2^p \to 1/4$ as $w \to 1$ we know that there are mainly p quarks in the proton as $x \to 1$. Pomeron dominance as $w \to \infty$ implies the "sea" contains equal numbers of quarks and antiquarks (dx/x distribution). From combining a neutrino and electro-production sum rule, we know that there are not many λ and $\bar{\lambda}$ quarks at finite x.[34] The last piece of information is the pertinent formula, as for example in π^+ electroproduction:

$$\frac{dN^{\pi^+}}{dz} = \frac{(\frac{4}{9}p(x) + \frac{1}{9}\bar{n}(x))\, D_p^{\pi^+}(z) + (\frac{4}{9}\bar{p}(x) + \frac{1}{9}n(x))\, D_n^{\pi^+}(z) + (\frac{1}{9}\lambda(x) + \frac{1}{9}\bar{\lambda}(x)) D_\lambda^{\pi^+}(z)}{\frac{4}{9}(p(x) + \bar{p}(x)) + \frac{1}{9}(n(x) + \bar{n}(x)) + \frac{1}{9}(\lambda(x) + \bar{\lambda}(x))}$$

Now it is trivial to get an intuitive feeling for the charge ratios in the parton fragmentation region; you can either use Bjorken's chart[2] or make up your own.[35,36]

Exact sum rules concerning quantum numbers in parton fragmentation can be derived, but they usually require an integral over all x, as in the following sum rule given by Gronau, Ravndal, and Zarmi:[12]

$$\frac{\int_0^1 (\langle n_{\pi^+} \rangle_{eN} - \langle n_{\pi^-} \rangle_{eN})\, F_1^{eN}\, dx}{\int_0^1 (\langle n_{\pi^+} \rangle_{ep} - \langle n_{\pi^-} \rangle_{ep})\, F_1^{ep}\, dx} = 2/7$$

In e+e- annihilation, the inclusive distribution is simply given by the D functions, as in π electroproduction (same for all charge states) by:[37]

$$\frac{dN^\pi}{dz} = \frac{5}{6}\left(D_p^{\pi^+}(z) + D_n^{\pi^+}(z)\right) + \frac{1}{3} D_\lambda^\pi(z)$$

or integrated over z as:

$$\langle n_{\pi^+} \rangle = \langle n_{\pi^-} \rangle = \langle n_{\pi^0} \rangle$$

(This result only depends on the isospin of the partons being 1/2). Note that this relation is true for the whole of current fragmentation and not just the plateau.

If Feynman's quantum number retention hypothesis for quarks actually occurs, a lower bound on the average quantum numbers observed in one jet of e+e- annihilation can be derived[38] (so that if this bound is violated, Feynman's conjecture is disproved experimentally.) At sufficient Q^2 for jets to be observed (and, of course, scaling), measure the quantum numbers in the left and right jets and subtract them from each other. Average the absolute magnitude of this difference and the following bounds for baryon number, electric charge, and strangeness result if Feynman's conjecture is correct:

$$\langle |B_L - B_R| \rangle \geq 2/3$$

$$\langle |Q_L^{el} - Q_R^{el}| \rangle \geq 2/3$$

$$\langle |S_L - S_R| \rangle \geq 1/3$$

(4) dependence at the edge, i.e., as $z \to 1$.

The variation of the invariant inclusive cross-section at the edge

of the fragmentation region in hadronic reactions is given by the triple-Regge formula. By arguments which are basically similar when described as an inclusive-exclusive connection,[33,39] predictions can also be made about the 1-z dependence as $z \to 1$ for parton fragmentation.

As an example of an inclusive-exclusive connection, consider the Bloom-Gilman analysis[39] of the threshold dependence of νW_2 as a function of w'. Assuming the exclusive channels in electroproduction, i.e. resonance formation, are a smooth limit of the total cross-section as $w' \to 1$, then the threshold dependence of νW_2 is related to the elastic form factor of the target. The relation is the same as that given by Drell, Yan[40], and West,[41] i.e. $p = 2m - 1$ where the form factor $F(Q^2)$ falls as $(Q^2)^{-m}$ and the threshold dependence of νW_2 is proportional to $(w'-1)^p$. In the parton model, the argument by Feynman is very similar.[12] The elastic form factor is proportional to the probability for parton configurations within the target having the struck parton at $x \sim 1$ and the rest wee (their x's $< 1/Q$). The probability for one such configuration with a dx/x distribution is $(1-x)^p$, which is proportional to νW_2 at threshold. The connection to the form factor is given by:

$$F(Q^2) \propto \int_{1-1/Q}^{1} (1-x)^p \, dx \propto \left(\frac{1}{Q^2}\right)^{\frac{p+1}{2}}$$

reproducing the previous result.

In $e^+e^- \to hX$, an identical analysis relates the 1-z dependence ($z = 2p/Q$) of the normalized invariant distribution to the time-like form factor of h. Since the power fall-off the time-like and space-like form factors is presumably the same, the Drell-Yan-West relation reappears (which guarantees as well the same power p for the 1-z dependence in annihilation as in the threshold dependence of eh.) Moreover, in the parton model, $z \to 1$ in inclusive annihilation is the edge of the parton fragmentation region. Therefore, the same dependence should always appear at the edge of parton fragmentation, as for example in inclusive lepto-production. Consequently, in $eP \to ehX$, the 1-z dependence is related by the Drell-Yan-West relation to the elastic form factor of h, corresponding in the case h is a proton or pion to $(1-z)^3$ and $(1-z)$, respectively (assuming the pion form factor falls as $1/Q^2$).[33,42]

Bjorken and Kogut[33] have arrived at a further relation that is quite remarkable. The inclusive-exclusive connection between $eP \to ehX$ and $eP \to ehP$ yields the triple-Regge formula, $p = 1-2\alpha$, where α is the Regge trajectory in the exclusive "γ^* h channel.[43] Consequently, the elastic form factor of a hadron h is related to the intercept of the Regge trajectory which couples to the virtual photon and h by:

$$F(Q^2) \propto (Q^2)^{\alpha - 1}$$

which as a rough prediction is not too bad.

Further predictions follow from incorporating spin into the inclusive-exclusive connection.[44] Assuming the same threshold dependence for σ_L and σ_T[45] plus the parton model result that $R = \frac{\sigma_L}{\sigma_T} \propto \frac{1}{Q^2} f(w)$ produces a slightly different threshold-form factor connection for the pion (which elastically couples to σ_L):

$$p = 2m - 2,$$

implying that the form factor of the pion falls faster than $1/Q^2$. However, the inclusive-exclusive connection may not be this exact.

At the very least, the inclusive-exclusive connection gives a rough idea of the variation at the edge of the parton fragmentation region.

Through an intuitive picture of parton fragmentation, we have seen how the quark parton model can make many and detailed predictions about the hadronic final states produced in deep inelastic lepto-production and e+e- colliding beams. However, the inevitable question of how to implement the dynamics, recognizing the constraint that quarks don't come out, will have to be answered "at an appropriate time."

I am very grateful to J.D. Bjorken, R.N. Cahn, G. Farrar, R.P. Feynman, and M. Kugler for sharing their insights into this subject. I would also like to thank the Aspen Center for Physics for its hospitality during completion of the written version.

Figure Captions

1.(a) Single particle inclusive lepto-production where the four-momenta of the virtual current, the target, and the observed hadron are q, P, and P_h, respectively. The components of the spatial momentum $\vec{P}_h$ (frame dependent) which are transverse and longitudinal to the virtual photon-target scattering axis are $P_\perp$ (azimuthal angle φ) and P_L, respectively.

(b) Single particle inclusive annihilation where the momenta of the virtual current and the observed hadron are q and P_h. The angle at which the hadron emerges in the center of mass is θ.

2. The invariant inclusive distribution $\frac{1}{\sigma_{tot}}\frac{d\sigma}{dy}$ versus rapidity y for high energy lepto-production at small Q^2 (i.e. $Q^2 \ll |q_{max}^2|$).

3. The invariant inclusive distribution $\frac{1}{\sigma_{tot}}\frac{d\sigma}{dy}$ versus rapidity y for high energy lepto-production in the deep inelastic region.

4.(a) Regge diagram for the virtual current-nucleon total cross-section.

(b) Mueller diagram for virtual current + nucleon $\longrightarrow$ hadron (h) + anything in the target fragmentation region.

(c) Mueller diagram for virtual photon + nucleon $\longrightarrow$ hadron (h) + anything in the central plateau region.

(d) Mueller diagram for virtual photon + nucleon $\longrightarrow$ hadron (h) + anything in the current fragmentation region.

5. Parton distribution before (a) and after (b) interaction in the Breit frame of the virtual photon and parton.

6. (a) A simple model for hadronic final states in e^+e^- annihilation. The rapidity gap between the initial quark and antiquark is filled with N isosinglet $\bar{q}q$ pairs (N $\propto$ rapidity gap). Adjacent quarks and anti-quarks (beginning at either end) are assumed to convert into pions.

(b) The above model pictured as a cascade. The first step is the initial quark throwing off the first pion and producing a quark which initiates the second step.

7. The invariant inclusive distribution $\frac{1}{\sigma_{tot}}\frac{d\sigma}{dy}$ versus rapidity y (which must be defined event by event) for high energy e^+e^- annihilation into hadrons as predicted by the parton model.

8. The invariant inclusive distribution $\frac{1}{\sigma_{tot}}\frac{d\sigma}{dy}$ versus rapidity y for high energy lepto-production in the deep inelastic region at large W as predicted by the parton model.

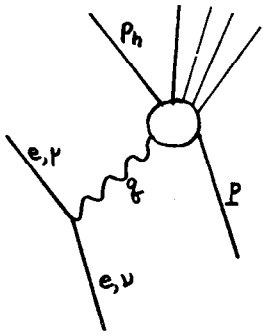

$q \cdot P = M\nu \qquad w \equiv \frac{1}{x} = \frac{2M\nu}{Q^2}$

$q \cdot q = -Q^2 \qquad w' = w + \frac{M^2}{Q^2}$

$W^2 \text{ (or } s) = 2M\nu - Q^2 + M^2$

$= (w'-1)Q^2$

$w_1 = \frac{2P_h \cdot q}{Q^2} \qquad MK = P_h \cdot P$

$z = K/\nu$

(a)

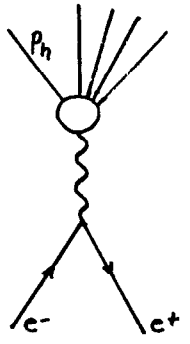

$q \cdot q = Q^2 \text{ (or } s)$

$z = w = \frac{2P_h \cdot q}{Q^2}$

(b)

Fig. 1

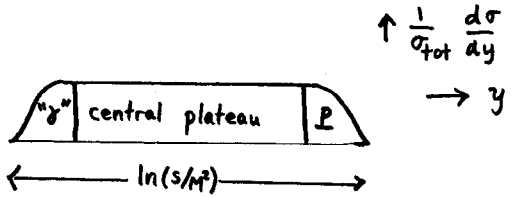

Fig. 2

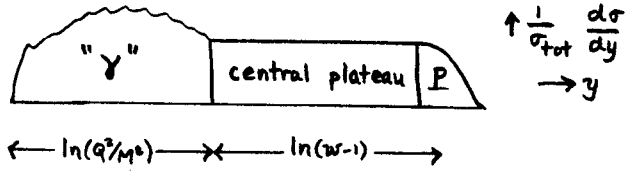

Fig. 3

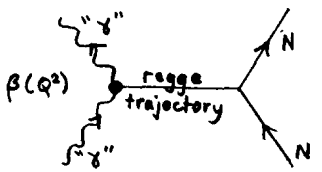

(a)

Scaling ⇒ $\beta(Q^2) \propto (Q^2)^{-\alpha}$

α = regge intercept

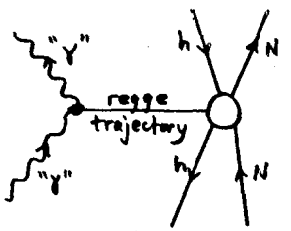

(b)

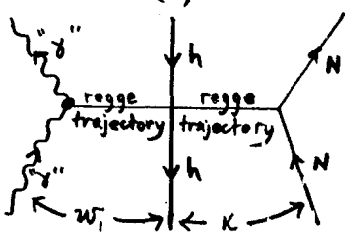

(c)

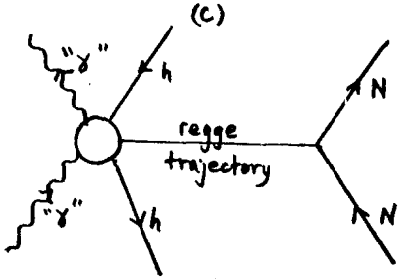

(d)

Fig. 4

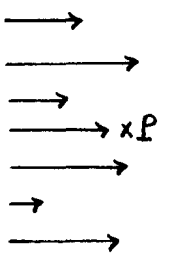

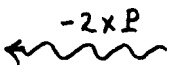

(a)

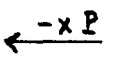

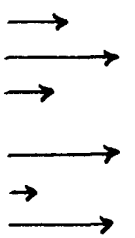

(b)

Fig. 5

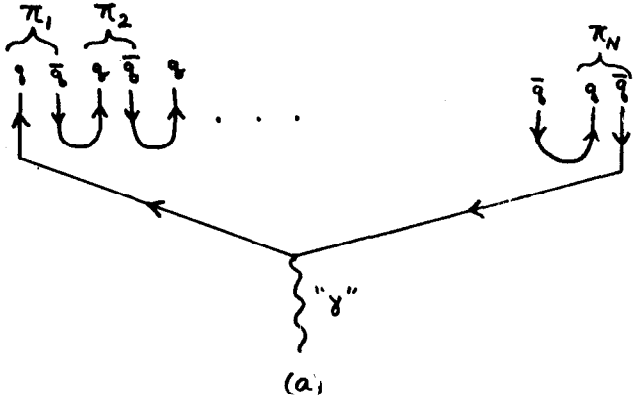

Fig. 6

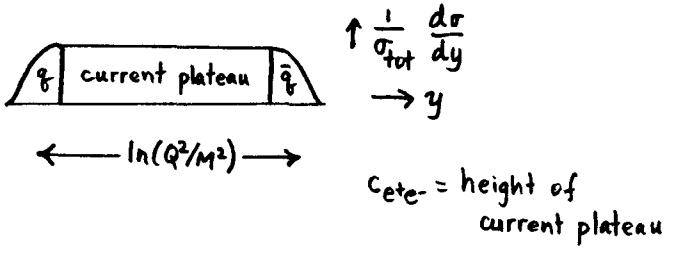

Fig. 7

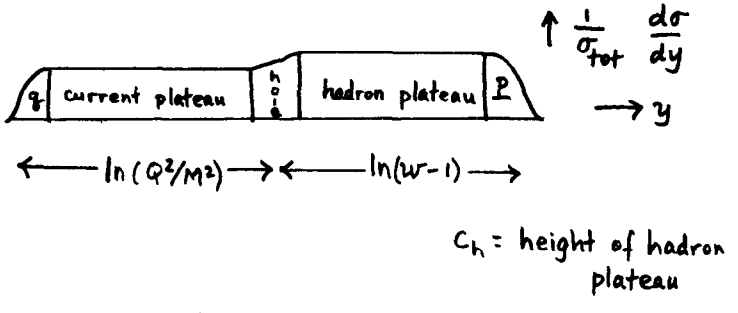

Fig. 8

References

J.D. Bjorken, Lectures delivered at the SLAC Summer Institute on "Deep Inelastic Scattering" (July 9th-18th, 1973).

The pioneering references describing this point of view are:
S.D. Drell and T.-M. Yan, Phys. Rev. Letters 24, 855 (1970).
S.M. Berman, J.D. Bjorken, and J.B. Kogut, Phys. Rev. D4, 3388 (1971) and J.D. Bjorken, Phys. Rev. D7, 282 (1973).
R.P. Feynman, Talk given at the Neutrino '72 Conference, Balatonfüred, Hungary, and Photon-Hadron Interactions, W.A. Benjamin (1972).
Other contributions are cited in the detailed references given later. Also, two other recent reviews are:
G. Altarelli, Talk given at the "VIII Recontre de Moriond", Meribel Les Allues, France, (March 4-10, 1973) and Univ. of Rome preprint 459.
J.D. Sullivan, Talk given at "Conference on Recent Advances in Particle Physics", New York (March 15-17, 1973) and Illinois preprint 73-2.

J.D. Bjorken, "Proceedings of the Fifth International Symposium on Electron and Photon Interactions at High Energies", Cornell University (1971) and "Proceedings of the Conference on Particle Physics", Irvine (1971).

S.R. Choudhury and R. Rajaraman, Phys. Rev. D5, 694 (1972).
H.D.I. Abarbanel and D.J. Gross, Phys. Rev. D5, 699 (1972).
K. Bardakci and N. Pak, Lettere al Nuovo Cimento 4, 719 (1972).
N.K. Pak, Lawrence Berkeley Report LBL-733 (unpublished).

For a review of the Mueller-Regge analysis in lepto-production and an extension to the current fragmentation region with an additional assumption (Bjorken scaling for $\frac{1}{\sigma_{tot}} E\, d\sigma/d^3p$), see R.N. Cahn and E.W. Colglazier, "Unified Mueller Picture of Deep Inelastic Inclusive lepto-production", SLAC-PUB-1194 (March 1972), to be published in Phys. Rev. D.

J. Ellis, Phys. Letters 35B, 537 (1971).
J. Stack, Phys. Rev. Letters 28, 57 (1972).
A. Schwimmer, Caltech preprint CALT-68-376 (1972).

Such a possibility could be inferred from the slow convergence of the Adler and other sum rules as well as the ratio of νW_2 for proton and neutron.

J.D. Bjorken, private communication and ref. 1.

R.P. Feynman, pg 243 of Photon-Hadron Interactions, op. cit.

10. S.D. Drell and T.-M. Yan, op. cit. For a clarification of which structure functions scale, see E. W. Colglazier and F. Ravndal, Phys. Rev. D7, 1537 (1973).

11. S.M. Berman, J.D. Bjorken, and J.B. Kogut, op. cit.

12. R.P. Feynman, op. cit.
M. Gronau, F. Ravndal, and Y. Zarmi, Nuclear Physics B51, 611 (1973).
A. Cisneros, Caltech preprint CALT-68-349 (1972).

13. F. Ravndal, Caltech preprint CALT-68-370 (1972).

14. Actually in calculable models, factorization occurs only after integration over the transverse momenta of h. See G. Altarelli and L. Maiani, Univ. of Rome preprint 421 (1973), to be published in Nuclear Physics.

15. For example, see the talks of M. Perl, K. Berkelman, G. Feldman, H. Meyer, and T. Carrol at the SLAC Summer Institute on "Deep Inelastic Scattering" (July 9th-18th, 1973).

16. J. Weis, private communication.

17. M. Greco, CERN preprint 1617 (Feb. 1973).

18. J.D. Bjorken and S.J. Brodsky, Phys. Rev. D1, 1416 (1970).

19. S.D. Drell, D.J. Levy, and T.-M. Yan, Phys. Rev. 187, 2159 (1969) and Phys. Rev. D1, 1035, 1617, 2402 (1970).
S.D. Drell and T.-M. Yan, op. cit.
N. Cabibbo, G. Parisi, and M. Testa, Nuovo Cimento Letters 4, 35 (1970).

20. P.V. Landshoff, J.C. Polkinghorne, and R.D. Short, Nucl. Phys. B19, 432 (1970).
P.V. Landshoff and J.C. Polkinghorne, Nucl. Phys. B33, 221 (1971).and Phys. Reports 5C, 1 (1972).

21. G. Altarelli and L. Maiani, op. cit.

22. H.D.I. Abarbanel, M.L. Goldberger, and S.B. Treiman, Phys. Rev. Letters 22, 500 (1969).
G. Altarelli and H. Rubinstein, Phys. Rev 187, 2111 (1969).
J.D. Dorren, Nucl. Phys. B36, 541, (1972).

23. S.S. Shei and D.M. Tow, Phys. Rev. D4, 2056 (1971).

24. S.D. Drell and T.D. Lee, Phys. Rev. D5, 1738 (1972).
T.D. Lee, Phys. Rev. D6, 1110 (1972).

25. J. Kogut, D.K. Sinclair, and L. Susskind, Institute for Advanced Study preprint COO 2220-6 (1973). A complementary result in the language of the light cone is given by: J. Stack, Univ.

of Illinois preprint 73-4 (1973).

26. A. Casher, J. Kogut, and L. Susskind, Tel-Aviv preprint 373-73 (June, 1973).

27. G. Preparata, Phys. Rev. D7, 2973 (1973).
R. Gatto and G. Preparata, DESY preprint 73-15 (May 1973).

28. R.L. Kingsley, P.V. Landshoff, C. Nash, and J.C. Polkinghorne, Cambridge preprint DAMTP 73/19(June 1973). The analogy between this model and diffractive excitation models of hadronic reactions is discussed by R.N. Cahn and J. Ellis, Talk given at A.P.S. Meeting, Berkeley (August 1973)

29. G. Farrar and J. Rosner, Phys. Rev. D7, 2747 (1973).

30. R.N. Cahn and E.W. Colglazier, SLAC-PUB-1207 (July 1973).

31. J.D. Bjorken, Phys. Rev. D7,282 (1973). This paper on "Hole Fragmentation" completed the picture of lepto-production initiated by the authors of refs. 10-12. See also C.F.A. Pantin, Nucl. Phys. B46, 205 (1972), who found the diagram in the covariant parton model corresponding to hole fragmentation but did not quite realize the existence of five regions in inclusive lepto-production.

32. R.N. Cahn, J.W. Cleymans, and E.W. Colglazier, Phys. Letters 43B, 323 (1973).

33. J.D. Bjorken and J. Kogut, SLAC-PUB 1213 (March 1973).
J. Kogut, Institute for Advanced Study preprint COO-2220-12 (1973).

34. $$\int_0^1 x\,(\lambda(x)+\bar{\lambda}(x))\,dx = \frac{9}{2}\int_0^1 \nu W_2^{e(N+P)}\,dx - \frac{15}{16}\int_0^1 \left(\frac{d\sigma}{dx}^{\nu(N+P)} - \frac{d\sigma}{dx}^{\bar{\nu}(N+P)}\right)dx$$

See the discussion of J. Cleymans and L.M. Sehgal, Aachen preprint (1973).

35. A phenomenological approach using numerical approximations to the intuitive picture allows a rough determination of the density and fragmentation functions and makes predictions about particle ratios in other processes. See, for example, J. Cleymans and L.M. Sehgal, op. cit., J. Cleymans and R. Rodenberg, Aachen preprint (1973); and J.T. Dakin and G. Feldman, SLAC-PUB 1273 (July 1973).

36. Further theoretical assumptions also yield more predictions, such as in the case of duality which has been analyzed by M. Chaichian, S. Kitakado, S. Pallua, and Y. Zarmi, CERN preprint 1626 (1973).

37. J. Ellis and C.H. Llewellyn Smith, unpublished.
M. Gronau, F. Ravndal, and Y. Zarmi, op. cit.

38. R. Cahn, private communication.

39. E. Bloom and F. Gilman, Phys. Rev. Letters 25, 1140 (1970).

40. S.D. Drell and T.-M. Yan, Phys. Rev. Letters 24, 181 (1970).

41. G. West, Phys. Rev. Letters 24, 1206 (1970).

42. R. Jaffe, unpublished.

43. Gatto and Preparata, op. cit.,derive a similar connection except that the Regge trajectory in the triple-Regge formula is quark-like.

44. F. Ravndal, Caltech preprint CALT-68-381 (1972).
P.V. Landshoff and J.C. Polkinghorne, Nucl. Phys. B53, 473 (1973).

45. Other possibilities for the threshold dependence of R are discussed by J. Gunion and R. Jaffe, MIT preprint 342 and erratum (1973).

SCATTERING AT NOT-SO-LARGE MOMENTUM TRANSFERS

R. Blankenbecler

Stanford Linear Accelerator Center

The Regge-type interactions which dominate small t reactions, cannot explore the short distance behavior of the strong interactions and hence cannot be expected to give us any "deep" understanding of what is going on at a basic level at short distances. However, it has provided a remarkably rich phenomenological description of such reactions. One is then, naturally, led to ask whether the Regge interactions are distinct from the ones which dominate high t reactions or whether they arise from essentially the same source and then should join smoothly at intermediate t. This latter possibility is very attractive since it provides a unified physical picture and perhaps a simple analytical description of large and small t. It will then predict a large number of unexpected relations between the functions (such as Regge trajectories and residues) used in the comparison of the theory with experiment and hence is very testable.

Perhaps the simplest of such theories, which cannot be discarded immediately by comparing with experiment, is the constituent interchange theory proposed by Jack Gunion, Stan Brodsky, and myself.[1, 2] There seems to be some confusion between the important aspect of the model, namely the physical picture of the dominate short range force, and the merely incidental calculational approximations that must be made in order to extract detailed predictions. The model contains three basic elements which are quite novel and essential:

(1) Constituent interchange provides a simple picture at short distances or large momentum transfers of the dominant hadron-hadron force.

(2) The basic parton interactions are soft. There are no hard vector gluons and no important parton form factor behavior.

(3) The wave functions of the hadrons fall off as inverse powers at large transverse momentum. This behavior is directly related to the fall off of the hadronic form factor.

The first element implies that the short distance forces are dominated by the heavy parton states (or at least effectively heavy) while the long range forces which control the cross sections are due to the lightest states - the hadrons. The contributions from these very coherent states should rapidly fall off as the momentum transfer increases since it becomes more and more difficult to arrange for the maximum binding interactions.

Therefore, one expects that the simplest diagrams of the type shown in Fig. 1 will dominate the large momentum transfer region. As will be discussed later, the corrections to these graphs are down by factors of s, t, or u; in the deep scattering region, where all are sufficiently large compared to masses, the correction terms can then be dropped. For the process A + B → C + D, the matrix element takes the form

$$M \sim s\, F_A(-s)\, F_C(t)\, F_D(-u) + \text{perm.}$$

This formula is not quite correct, but it is simple and has most of the characteristics of the exact formula. For a careful discussion, see ref. 2. In any case, the cross section has the form

$$\frac{d\sigma}{dt} = \left| F_A F_C F_D + \cdots \right|^2$$

Experimentally, the baryon form factor is close to a dipole and we find that the meson form factor must behave like a monopole. A careful calculation which takes spin effects into account has been performed for many different scattering processes and the result for p-p scattering is

$$\frac{d\sigma}{dt} \sim s^{-12} (1 - \cos^2 \theta_{cm})^{-5.2}$$

This can be directly compared with experiment at large angles or, better yet, forward Regge terms can be added into the trial matrix element as well as mass corrections to the above limiting form. The final result is as shown in Figure 2. The fit is quite good ($\chi^2 \sim 1.5$ per degree of freedom).

The above calculations illustrate our general philosophy, in which the theory is

applied to processes and to kinematic regimes which are simple to compute and which test the theory. We make no attempt to compute details of "typical" events, but only those rare and atypical events which depend on the detailed short ranged behavior. However, we shall test whether our physical picture of strong interactions is qualitative correct when applied to the most likely type of events but like everyone else, we cannot compute the detailed behavior.

The energy dependence of the cross section at fixed angle depends on the rate of fall of the form factors involved. The general angular dependence depends on the relative amounts of (u,t), (s,t) and (s,u) diagrams which contribute to the matrix element. This depends in turn on the quantum numbers of the constituents. For example, assuming the valence quark assignment quantum numbers, in exotic processes such as (pp) and (K^+p) elastic scattering, only the (u t) diagram can contribute and the cross sections should have both a forward and backward peak. For ($\bar{p}p$) and ($\bar{K}p$) scattering, the backward peak should be missing. The ratio (pp)/($\bar{p}p$) is predicted to be large at large angles as is the case experimentally. It should be noted that if simple vector meson exchange dominated these reactions, the ratio should be unity. The matrix element describing $\pi p \to \pi p$ can be crossed to the process $\bar{p}p \to \pi\pi$ and the comparison with experiment is very good with no new parameters!

Because the photon has a current coupling to the constituents, its effective "form factor" falls as $(-t)^{-\frac{1}{2}}$ and hence the differential cross section for photopion production should be larger than pion-nucleon scattering by one power of s at fixed angle. This is consistent with the present data (3) but a much better measurement of the energy dependence in πp scattering is needed for a precise check.

Let us now turn to a discussion of Regge effects and the natural way in which hadronic bremsstrahlung induces Regge behavior into our previous results as the momentum transfer decreases. To this end, it is convenient to sum up the results on 2 particle exclusive processes by writing them in the form of an effective scalar matrix element $M \sim G(t)(-u)^{-a}$,

where $G(t) \sim (-t)^{-2}$ and a is predicted to have the value 0 for ($\gamma p \to \gamma p$), $\frac{1}{2}$ for ($\gamma p \to \pi p$), 1 for ($\pi p \to \pi p$), and 3 for ($pp \to pp$). Therefore, when an effective $\alpha(t)$ is extracted from the data, it should approach the value $\alpha(-\infty) = -a$ for these processes. The effective trajectories for pp and $\pi^- p$ scattering have been gleaned from the data by D. Coon, Tran Thanh van, J. Gunion and myself[4]. The results are shown in Figures 3 and 4. While the errors in the πp case are large (we couldn't reliably estimate them and they are omitted from the graph), both effective trajectories are consistent with our predictions but clearly more and better checks are desired.

We are now in a position to discuss the physical processes that build up the energy dependence of the amplitudes as the momentum transfer decreases. If two particles scatter by a basic process which falls in energy, then they will clearly prefer to brems-strahlung and lose some of their longitudinal momentum so that the basic interaction can take place at a lower effective energy. On the way out, the emitted momentum will then be reabsorbed and an elastic event has occurred. Clearly, the probability of reabsorption falls as the momentum transfer increases and the basic interaction dominates again at large angles. The basic bremsstrahlung process simply generates the familiar ladder graphs (which are known to produce Regge behavior) but the rungs of the ladder are not simple particles but are more complex. The multichannel aspects must also be taken into account.

The bremsstrahlung products are predominately hadrons rather than the heavy parton states (as one would expect from uncertainty principle arguments). The wee partons of Feynman are actually the constituents of wee hadrons. This Reggeization process has been studied quantitatively (5) and we find that to lowest order, the Regge functions are

$$\alpha(t) \sim -a + g\beta(t)/(-t) + \cdots\cdots$$

$$\beta(t) \sim G(t) + \cdots\cdots ,$$

which have all the qualitative features described above including the important feature of joining smoothly onto the deep region behavior.

One also finds relations between totally unrelated Regge functions such as mesonic trajectories and residues are connected with baryonic trajectories and residues to guarantee that the forward and backward regions of meson-nucleon scattering join smoothly at 90°. This unexpected result will be discussed in detail elsewhere (5, 6).

One simple way of characterizing all the above results is in terms of a two component hadron wave function which has three simple properties. First, for the longitudinal momentum fraction $x \sim 1$, the simplest parton or "quark" constituent configuration dominates. Second, for $x \sim 0$, the hadronic bremsstrahlung components dominate. Third, the basic wave function has a power law fall off at large perpendicular momentum. These three properties seem to be sufficient for the qualitative picture of strong interactions discussed here. Quantitative results then follow in the manner described above.

The predictions of the constituent interchange model have also been worked out for several inclusive reactions(2). The diagrams that should be relevant in the deep region, which is a region in phase space near the kinematical boundary where s, t, u, and the missing mass M^2 are all large, is illustrated in Fig. 5(a). Redrawing it in the form of Fig. 5(b) shows that one should expect the structure function of particle B to enter into the reaction $A + B \to C + X$. The inclusive cross section is found to be of the form

$$sE_c \frac{d\sigma}{d^3p_c} = R_o^{A+B \to C}(s, p_\perp^2, u) + R_o^{B+A \to C}(s, p_\perp^2, u),$$

where

$$R_o = O_{eff}^{AC}(s, p_\perp^2, u)\ F_{2B}(x = -t/(M^2 - t))$$

and the operator O_{eff} arises from the effective current operator J_{eff} illustrated in Fig. 5(b). The basis interaction R_o falls rapidly in s at fixed values of $p_\perp^2$ and u. This again means that hadronic bremsstrahlung will play an important role. As illustrated in Fig. 5(c), the incident hadron A will bremsstrahlung until a hadron H with small longitudinal fraction z is present and it then interacts with the target B at a lower effective energy. However, unlike the exclusive case, z cannot get too small since otherwise H would not have enough energy left to produce particle C with its fixed $p_\perp$ value. Therefore, as $p_\perp$ increases, the Regge effects disappear. The additional contributions in the Regge regime from the hadronic bremsstrahlung graphs are of the form

$$R_1^{A+B \to C}(s, p_\perp^2, u) = \int_0^1 \frac{dz}{z} \sum_H G_{H/A}(z)\, R_o^{H+B \to C}(zs, p_\perp^2, u),$$

where $G_{H/A}$ is the probability of finding hadron H with fraction z in the incident hadron A, and one has as $z \to 0$,

$$G_{H/A}(z) \sim z^{-\alpha_A(0)}\, \beta_{AH}.$$

The z integral is cut off at its lower and upper ranges by kinematics. The separation of the inclusive cross section into R_o and R_1 is artificial; the two contributions connect smoothly together just as was found in the exclusive case.

This formula has several virtues and limitations. It should be strictly applicable to inclusive events in which hadron C is unaccompanied by any bremsstrahlung products. If such are present, they will tend to divide the perpendicular momentum and this may be expected to be a sizeable contribution at small values of $x_\perp \equiv 2p_\perp/\sqrt{s}$. However, in the region in which Regge effects are starting to become important, this effect should be small since the hadron H tends to be wee and it does not like to have sufficient energy to make many particles. In fact, any theory that lets the hadron grudgingly scatter first at large angles and then decay will not be entirely consistent since the hadron will prefer to slow down first by emitting bremsstrahlung. We also see that the interchange theory predicts a multiplicity along particle C which is much lower than one might a priori expect, but accompanying particles certainly will be present at small $x_\perp$ for exactly the same reasons that the hadronic wave function dominated at small x by multiparticle bremsstrahlung.

The above formula for the inclusive cross section has the virtue that it agrees with Feynman scaling in the fragmentation region, in the triple Regge region it has

the form given by Mueller, and in the deep region it agrees with the constituent interchange term, R_0 which eventually connects smoothly onto exclusive scattering. It therefore, provides a unified and simple description of these diverse regions of phase space. It also makes predictions about the behavior of the trajectories and residues that enter into the Regge-Mueller formulae.

In the pionization region, where $t \sim u \sim -\sqrt{s}$, and $p_\perp$ fixed, one finds ($x_F = (t-u)/s = 0$ for simplicity)

$$R \sim R_t \sim s^{\frac{1}{2}(\alpha_A + \alpha_B)} \sum_H (p_\perp)^{-N_H} \Gamma_H(2p_\perp/\sqrt{s}) ,$$

where $\Gamma_H(x_\perp)$ is a simple integral over structure functions. For the process $pp \to \pi x$, we find the important result

$$E_c \frac{d\sigma}{d^3p_c} = (p_\perp)^{-8} \Gamma(x_\perp) = s^{-4} I(x_\perp) ,$$

which has been computed and shown in Fig. 6 for simple choices of the structure functions and for the kinematic range of interest at NAL and ISR. This formula is in excellent agreement with the data recently reported in ref. 7.

As a resumè of our predictions and to help in comparing with other theories, one finds that inclusive cross sections can be written as

$$E \frac{d\sigma}{d^3p} = \frac{1}{s^4} (\alpha s)^n I_n(x_F, x_\perp) ,$$

where $x_F = 2P_3/\sqrt{s}$, and $x_\perp = 2P_\perp/\sqrt{s}$. The parameter n ranges from n = 0 for purely hadronic processes such as $pp \to hX$ (for some reactions n can be negative), to n = 1 for $\gamma p \to \pi X$, to n = 2 for $ep \to eX$, $\gamma p \to \gamma X$, and $e^+e^- \to hX$. This latter value is also the prediction for purely hadronic processes of theories which have an important vector gluon force. Such theories seemed to be ruled out by the recent data[7] if it is taken seriously. One should note that the interchange theory predicts not only the power of s but also the function $I(x_F, x_\perp)$ which accompanies it.

One very important recent development is the work using dimensional analysis by G.R. Farrar and S.J. Brodsky[8] who attempt to relate the rate of the form factor fall off to the number of constituents in the simplest most basic configuration in the hadron wave function. This approach then removes the (arbitrary) rate of fall off of the form factor and replaces it by a physically meaningful number (which must be integral). Their present theory agrees with the wave functions assumed in ref. (1) and (2) except for nucleon-nucleon scattering which falls as s^{-10} rather than s^{-12} discussed earlier. This difference arises from differences in treating the wave function needed to describe the nucleon. It shows up only in nucleon-nucleon scattering reactions. Their result follows from treating the nucleon as a three body bound state in a renormalizable theory. The old interchange results follow from a model of the nucleon as a two body bound state in a superrenormalizable theory. In order to eliminate contradictions with effective trajectories, they must postulate the absence of a strong gluon force between partons in different hadrons. In any case, this method may provide a very beautiful and simple approach to a more basic sector of the interchange theory, namely the constituent-constituent binding force problem.

In conclusion, we see that the constituent interchange theory allows one to derive relations between form factors and exclusive scattering at large angles and to connect these in a unified and simple manner to the Regge regions near the forward and backward direction. Both exclusive and inclusive scattering can be treated. The assumption that hadrons are composed of constituents with heavy average masses (they need not be eigenstates of the mass operator) and with essentially unit form factors allows one to derive the structure of the basic short range matrix element. The process of hadronic bremsstrahlung allows one to extend the predictions of the theory to include the long range forces without further explicit consideration of the constituents. The comparison with experiment is very encouraging all the way from 5 GeV/c exclusive reactions to inclusive reactions at the ISR. Few other theories can make that statement.[9]

FIGURE CAPTIONS

Fig. 1 Basic Form Factor and Scattering Diagrams in the constituent interchange model.

Fig. 2 The fit to proton-proton scattering using the interchange model plus an exponentially falling pomeron which dominates the forward direction.

Fig. 3 The effective trajectory extracted from p-p scattering data. The error bars are theoretical estimates.

Fig. 4 The effective trajectory extracted from $\pi^- p$ scattering data. The errors are too large to reliably estimate.

Fig. 5 Basic Inclusive Scattering Diagrams used in the text. The middle diagram illustrates the close connection between hadron inclusive and deep inelastic lepton scattering reactions.

Fig. 6 The predictions of the interchange model for the process $p + p \to \pi^0 + x$ if simple forms are chosen for the structure functions.

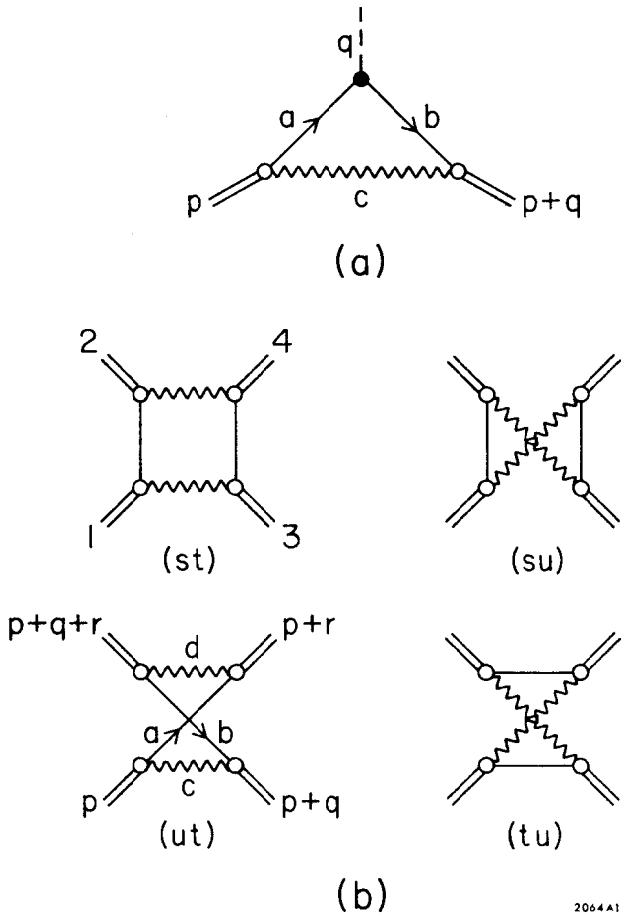

Fig. 1

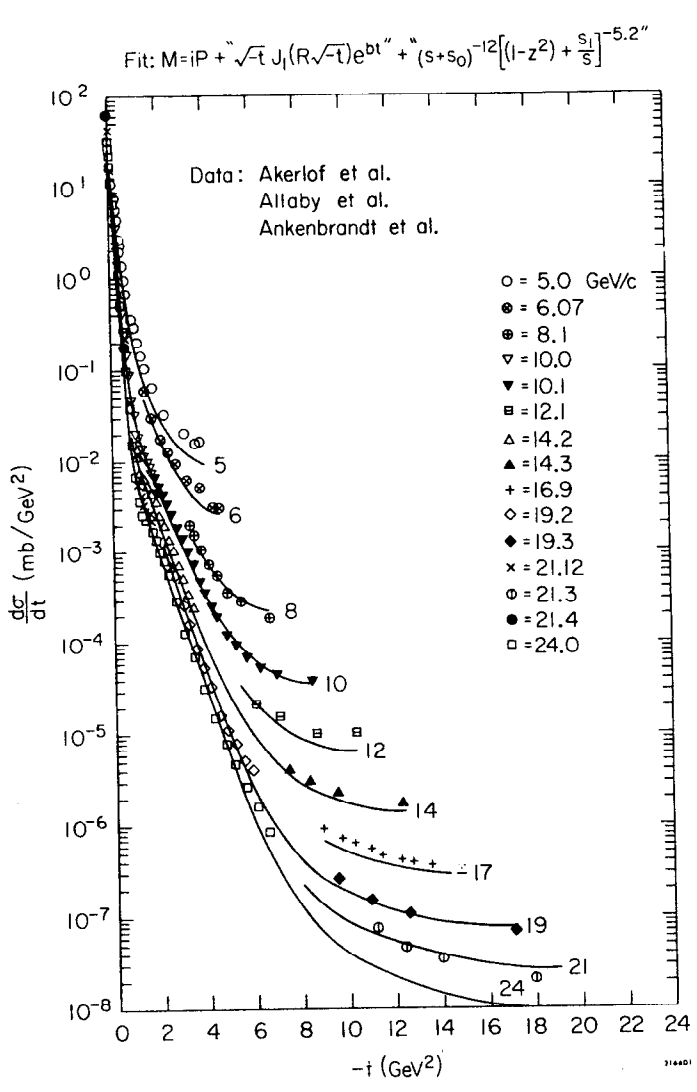
P-P Elastic
Fit: M=iP + "$\sqrt{-t}\,J_1(R\sqrt{-t})e^{bt}$" + "$(s+s_0)^{-12}\left[(1-z^2)+\frac{s_1}{s}\right]^{-5.2}$"
Data: Akerlof et al.
Allaby et al.
Ankenbrandt et al.
o = 5.0 GeV/c
⊛ = 6.07
⊕ = 8.1
▽ = 10.0
▼ = 10.1
⊟ = 12.1
△ = 14.2
▲ = 14.3
+ = 16.9
◇ = 19.2
◆ = 19.3
× = 21.12
Φ = 21.3
● = 21.4
□ = 24.0
$\frac{d\sigma}{dt}$ (mb/GeV^2)
$-t$ (GeV^2)

Fig. 2

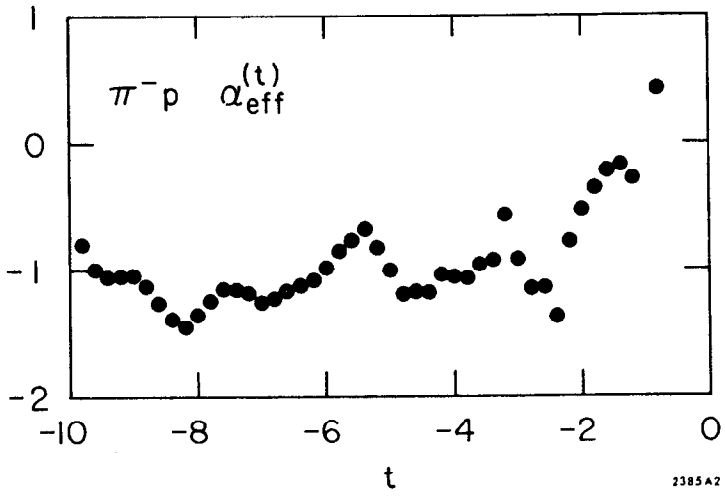
$\pi^- p$ $\alpha_{eff}^{(t)}$
t
2385A2

Fig. 3

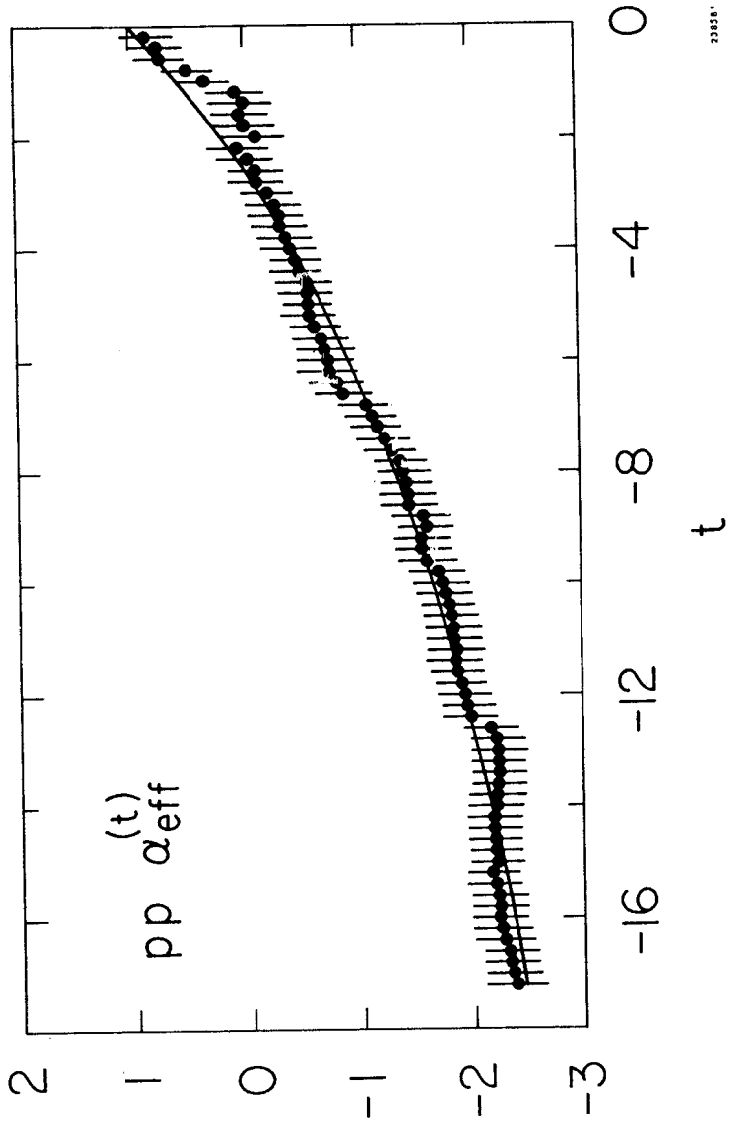

Fig. 4

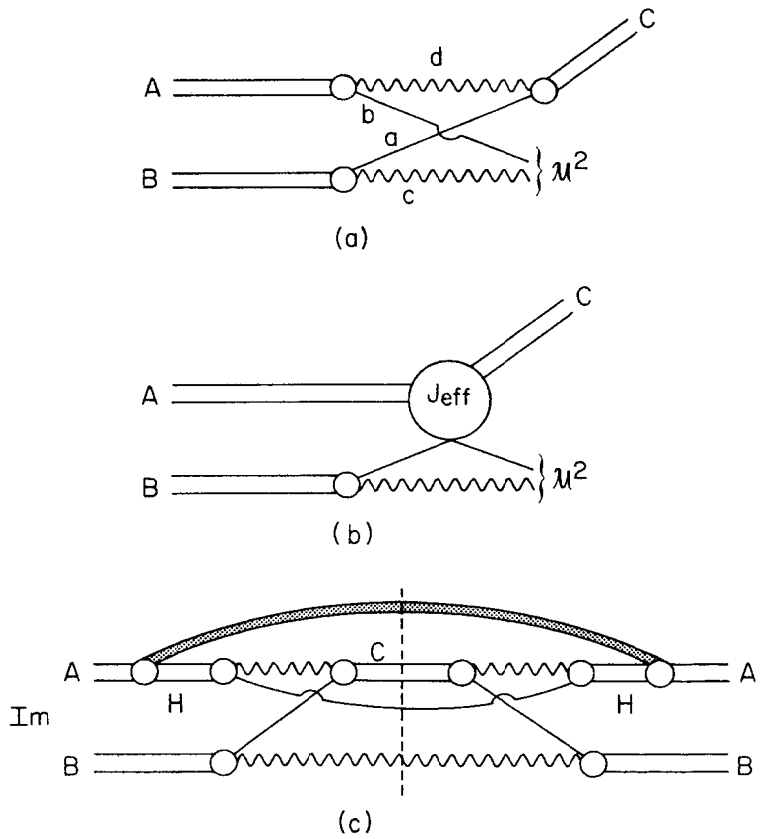

Fig. 5

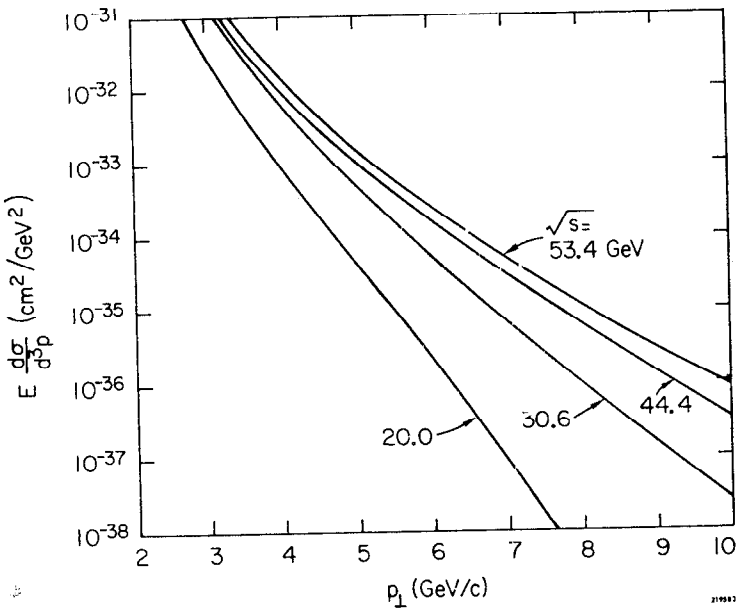

Fig. 6

REFERENCES

(1) J. F. Gunion, S. J. Brodsky and R. Blankenbecler, Physics Letters 39B, 649 (1972) ; Phys. Rev. D8, 187 (1973).

(2) S. J. Brodsky, J. F. Gunion and R. Blankenbecler, Phys. Rev. D6, 2652 (1972); Physics Letters 42B, 461 (1973).

(3) R. Anderson, et. al. Phys. Rev. Letters 30 627 (1973) and to be presented to the Bonn Conference, Sept. 1973.

(4) This paper may eventually be published.

(5) R. Savit, R. Blankenbecler, S. J. Brodsky and J. F. Gunion, "The Connection Between Regge Behavior and Fixed Angle Scattering", SLAC-PUB 1294 (to be published).

(6) R. Savit and R. Blankenbecler (to be published).

(7) F. W. Büsser et. al., CERN preprint 10 August 1973 (submitted to Phys. Letters).

(8) G. Farrar and S. J. Brodsky, SLAC-PUB-1290 (to be published).

(9) An exception to this statement for elastic scattering at least is the unique theory of T. K. Gaisser and H. M. Fried, Phys. Rev. D4 , 3330 (1971), see also H. Moreno, Phys. Rev. D5, 1417 (1972), who use soft vector gluons to "dress" the fundamental hadrons; but use a more general short ranged force. They thereby escape the obvious difficulties of simple vector meson theories and get good agreement with elastic scattering data.

NOTE: "Study of the Multiplicity as a Function of q^2 in Deep Inelastic Electron Scattering" appears herein as CLNS-240, "Measurement of Charged Hadron Multiplicities in Deep Inelastic Electron Scattering" at the request of the lecturer, K. Berkelman.

CLNS-240
AUGUST 1973

Measurement of Charged Hadron Multiplicities in Deep Inelastic Electron Scattering*

K. Berkelman, P.H. Garbincius, B. Gibbard, and P. Wanderer
Laboratory of Nuclear Studies, Cornell University

and

A.J. Sadoff
Physics Department, Ithaca College

We report measurements of the charged hadron multiplicities for electrons scattered at momentum transfers up to $Q^2 \approx 9$ GeV^2, and for s up to 16 GeV^2. Electrons are scattered in a 2.5 cm liquid hydrogen target and detected in a large-aperture spectrometer consisting of a bending magnet, proportional wire chambers, and a shower hodoscope. Charged hadrons are detected in an array of 68 scintillators almost completely surrounding the target. Data on the laboratory angular distributions will also be presented.

This is a preliminary report of an experiment which is still in progress. The results are tentative and subject to change as data taking and analysis proceeds.

*Work supported by the National Science Foundation

Introduction

Much of the recent interest in hadron collisions at high energy has focused on global features of the final states, such as the dependence of the average charged hadron multiplicity on the squared center-of-mass energy s, the relative yields in the various multiplicities, and the single-particle inclusive distributions in longitudinal and transverse momentum. One can use the experimental data to test a number of hypotheses - for example, limiting fragmentation, Feynman scaling, and short-range order in rapidity - as well to make detailed comparisons with statistical, multiperipheral, resonance, Regge, parton, and other models.[1]

We can expect the same kind of global information to be even more interesting for the hadron final states in deep inelastic electron scattering. The final-state multiplicities and inclusive spectra in the virtual-photon-nucleon collision can vary with the virtual photon mass-squared $q^2 = -Q^2 < 0$ as well as with s. Although the models which are still surviving tend to have rather similar predictions for hadron collisions, their predictions for the electroproduction final states can be quite different. To see an example of this, suppose we consider the range of predictions for the dependence of the mean charged multiplicity on Q^2.

A. Thermodynamic models. In any picture in which some kind of equilibrium is established before the final state is produced one expects the multiplicity to depend only on the total center-of-mass energy or perhaps entropy. That is, the average multiplicity should be independent of Q^2 at fixed s. Or equivalently, starting from the hypothesis of short range order in rapidity[1], the fact that the distribution of final-state hadrons in rapidity has the form of plateau, the height of which is independent of projectile, target, or the value of s, implies that the mean multiplicity, which is the integral of the plateau divided by the cross section, is just a constant times the rapidity range, which is ln s. If one tries to improve on the thermodynamic models by taking account of the Lorentz contraction of the interaction volume, a slight dependence of the multiplicity on Q^2 is introduced. For instance the Landau hydrodynamical model[2] would predict $\bar{n} = Ks^{\frac{1}{4}}/(s + M_p^2 + Q^2)^{\frac{1}{4}}$

B. Photon fragmentation models. A spacelike photon is not an ordinary projectile. It cannot just exchange a little momentum with the target and then fragment. In order to produce final-state particles on the mass shell, the virtual photon must in effect pick up a fraction $x = Q^2/2M_p\nu$ of the target nucleon, "pulverize" it, and throw it forward.[3] These pulverization fragments (or parton fragments if you prefer), having undergone a considerable change in momentum, may be expected to show up as a high multiplicity jet, the mean multiplicity increasing with x. One suggestion[3] is that $\bar{n} = Ks^{\alpha(x)}$ where $\alpha(x)$ is an increasing function of x. The argument can be phrased in terms of the rapidity distribution.[4] The photon fragmentation region is not just a rapidity range of about two units at the forward end of the rapidity scale as it would be for an ordinary projectile, but instead shows up as a plateau of width $\ln Q^2$. This photon plateau may very

well have a height K_Q greater than the height K_ω of the remaining plateau; and thus $\bar{n} = K_\omega \ln s + (K_Q - K_\omega) \ln Q^2$. Some versions of the parton model[4] share this feature of having $\bar{n}$ increase with Q^2 at fixed s.

C. Scaling models. If $\bar{n}$ were a function only of s/Q^2 instead of s and Q^2 independently, then since $\bar{n}$ must increase with s at fixed Q^2, it would have to decrease with Q^2 at fixed s. Some versions of the parton model[5] and the multiperipheral model[6] suggest $\bar{n} = K \ln \omega$. There is some experimental data[7,8,9] at $Q^2 \leq 1.4$ GeV^2 suggesting that $\bar{n}$ decreases with Q^2 at fixed s.

Until now measurements of the charged hadron multiplicity in electroproduction have been performed using volume track chambers, either a streamer chamber containing a liquid hydrogen target[7] or a liquid hydorgen bubble chamber[8]. In either case, the fact that one can tolerate only a limited number of beam particles per picture imposes a lower limit on the measurable cross section, and hence an upper limit on Q^2. To remove this restriction we have made the hadron-electron coincidence resolving time as short as possible by using scintillation counters to detect the hadrons. This enabled us to use an average incident beam intensity of typically 3×10^8 per second. The >5% beam duty cycle of a synchrotron, as opposed to a linac, is crucial too, of course.

With a finite number (68) of scintillators to cover essentially all of the solid angle around the target, we must sacrifice detailed angular resolution and any hope of measuring momenta accurately. However, for multiplicities and the gross features of the rapidity spectrum, such measurements are fortunately not necessary. We are then able to reach Q^2 values up to 9 GeV^2, much higher than in any previous coincidence electroproduction experiment, and we can explore the region of large x where the structure functions are varying significantly.

Apparatus

Figure 1 shows the layout of the experiment. The extracted electron beam from the Cornell synchrotron passed through a 2.6 cm liquid hydrogen target and on to a secondary emission monitor. Scattered electrons were detected in a spectrometer consisting of a bending magnet, eight proportional wire chambers, three planes of scintillation counters, and a lead-lucite shower telescope. After passing through the target the beam passed through the magnet gap (between the coils where the field is less) inside a heavy iron shield pipe. The scattered electron aperture covered a solid angle of 30 msterad and extended from 9° to 20° in some of the data runs, and from 14° to 25° in other runs with the detectors moved farther from the beam line. The root-mean-square resolution in Q^2 and s was typically 0.5 and 2 GeV^2, respectively. Figure 2 is a Q^2 versus s scatter plot of a sample of the events observed in the course of the experiment, including runs at 7 GeV and 11.5 GeV beam energies and at both geometries. Since there are not enough data to make a longitudinal-transverse separation, we are ignoring the possible dependence of the results on the virtual photon polarization parameter ϵ.

A single-layer array of 68 scintillation counters completely enclosed the target, except for the 3° forward cone and a 20°

backward cone. With each electron trigger, the status of each scintillator was recorded, and if it had a coincident pulse, the pulse height and time relative to the electron signal were recorded. Random triggers simultaneously sampled the accidental coincidences in the hadron scintillators.

Corrections

A. Pion contamination in the electron trigger. In order for an event to be accepted in the analysis as a scattered electron event, we require (1) that the shower counter pulse height exceed the 2.1 GeV level, (2) that the ratio of the shower pulse height (plus 2.8 GeV) and the reconstructed momentum be greater than 0.88, and (3) that the shower development start in the first 2.3 radiation lengths of the detector. This effectively eliminates any contribution from π^-, but also reduces the efficiency for counting low momentum (high s) electrons. This is tolerable, because we are not measuring cross sections. In order to be even more confident that we have removed all π^- triggers, we have excluded from the data sample all events with $s > 16$ GeV^2 (see Fig. 2). The observed average multiplicity for the rejected π^- events is about 20% less than that for the accepted electron events.

B. Target wall. The 0.013 mm kapton target wall is responsible for 5% of the observed electron rate and produces a mean multiplicity only slightly higher than does the hydrogen. This is easily corrected, using empty target data runs.

C. Radiation and multiple scattering. The electron can lose energy by radiation either in the deep inelastic process itself[10] or in the various pieces of material through which the electron must pass before being detected. This shifts by varying amounts the apparent values of Q^2 and s relative to the true values for the scattering reaction. Multiple scattering, finite target size, and wire chamber resolution have a similar effect. For each Q^2, s bin in the data we calculated by Monte Carlo the true average Q^2 and s to use in the plotting and fitting the multiplicity results for that bin.

Corrections D,E,F, discussed below have been evaluated using separate Monte Carlo calculations for each Q^2, s bin and multiplicity n. Events are generated satisfying the following requirements. (1) Each event is assumed to produce one nucleon with a 50% chance of being a proton and with a probability distribution in longitudinal and transverse momentum components which matches the existing inclusive electroproduction data[11]. (2) The remaining n-1 hadrons are pions with a 2/3 chance of being charged (charge conservation is imposed on each event, however) and with the known[11] momentum distributions. (3) Momentum and energy are conserved for each event.

D. Geometric losses. These are the hadrons that escape through the forward 3° cone, the backward 20° cone, and the 1.5-inch square hole directly above the target to accommodate the target refrigerator. We also account for those cases in which two hadrons hit the same scintillator and count as one.

E. Absorption losses. These are slow particles, mainly protons, that are absorbed or ranged out in the ~1 g/cm^2 of target and vacuum chamber wall between the point of origin and the scintillator. Fig. 3a shows a typical example of the expected distribution in apparent multiplicity after the geometric and absorption losses, calculated for $\bar{Q}^2 = 2.3$,

$\bar{s}$ = 9.5 GeV^2 and assuming an initial multiplicity of 3.

F. Conversion of gammas from π° decay. This is a significant correction, since there is about one π° per event and there is typically 5% of a radiation length of vacuum chamber wall between target and scintillators.

G. Delta rays and conversion of radiated gammas. These effects were estimated using the appropriate electrodynamic cross sections.

H. Charged decays of short-lived neutral strange particles. Following the somewhat arbitrary convention established by bubble chamber experimenters, we define the charged multiplicity to exclude the k° as a neutral particle but to include the ρ°, for example, as two charged particles. We therefore have to estimate the contribution from $K^\circ_S \to \pi^+ + \pi^-$, $\Lambda \to p + \pi^-$, and so on. There is insufficient published information on strange particle inclusive distributions in photoproduction and electroproduction on which to base such an estimate. For now, we make the guess that 5% of the events have one or more strange neutrals[8,9] and that in 80% of these events the multiplicity will be increased by two and in 20% by one.

I. Accidental coincidences. We include the effect of accidental uncorrelated counts in the hadron scintillators by making use of the information from the random-trigger events.

For the same sample Q^2 and s bin, Fig. 3b,c shows the predicted distribution (solid lines) in apparent multiplicity for each assumed value of true multiplicity n = 1,3,5,7. Figures 3b and 3c also show (dashed lines) the predictions for the next higher bin in Q^2 and in $\bar{s}$, respectively. For each of the Q^2 and s bins we now fit the experimentally observed multiplicity distribution to a linear combination of the predicted distributions (as in 3b,c) to determine the contribution of each true multiplicity. Figure 4 shows the results of these fits in those Q^2, s bins for which there is sufficient data for a meaningful plot of the multiplicity distribution.

It is fortunate that the net effect on the average multiplicity from corrections D through H very nearly cancels. Therefore the average "true multiplicity" obtained from the fits to the Monte Carlo distributions described above is, within experimental error, the same as the observed-minus-random average multiplicity obtained ignoring the corrections. This was confirmed experimentally over the entire Q^2, s range and over a range of incident electron intensity from 6 x 10^7/sec to 10^9/sec. We also took some data with doubled absorber thickness between target and scintillators. The observed average multiplicity was the same, within statistics, implying that the effect of corrections E,F, and G approximately cancels.

Although the average multiplicity is rather insensitive to corrections D through H, the proportion of events in which the number of charged hadrons is apparently even (violating charge conservation) is very sensitive to these corrections, as well as to the fraction of random counts. At low beam intensities, where randoms do not contribute, the evens comprise about 40% of the events, rather independent of Q^2 and s. Although we can correct the average data very well, there is no way to correct each event individually.

Multiplicities

Figures 5 and 6 show the measured values of the corrected average charged hadron multiplicity as a function of Q^2 and s. At each of the several fixed values of Q^2 the s dependence follows the form $\bar{n} = a + b \ln s$ (Fig. 5), as it does in photoproduction.[9] At each of the six fixed s values the data of this experiment at $Q^2 \geq 1.4$ GeV join on well with the track chamber data[7,8] at $Q^2 \leq 1.4$ GeV. It is clear from Fig. 6 that any rapid Q^2 dependence, on the same order as the s dependence, is completely ruled out by our data. In particular, any scaling behavior of the form $\bar{n} = a + b \ln \omega$ is incompatible with this experiment[12]. A best fit to the Q^2 dependence in our data,

$$\bar{n} = (-0.17\pm.06) + (1.33\pm.06) \ln s + (-.02\pm.06) \ln Q^2,$$

is consistent with no Q^2 dependence at all. In fact,

$$\bar{n} = (1.25\pm.02) \ln s$$

is an acceptable fit to all our data, over the entire Q^2, s range. This is rather close to the dependence observed in photoproduction[9] and, indeed, in all hadronic collisions[1]. The best "pulverization" fit[3] is

$$\bar{n} = (-3.3\pm.3) + (4.0\pm.1)\,(s-M^2)^{[(.2\pm.1) + (.01\pm.03)\times]}$$

Angular Distributions

Figure 7 shows distributions in hadron azimuth ϕ about the virtual photon axis, for several bins in Q^2, s. $\phi = 0$ is on the beam side of the virtual photon line in the scattering plane. To improve the statistical accuracy and reduce the sensitivity to inaccuracies in positioning the counters, we have folded the distributions about $\phi = 0$, taking advantage of the symmetry about the electron scattering plane implied by the single photon exchange hypothesis. The only correction that has been applied to these data is the subtraction of accidental coincidences and a compensation for the blind area represented by the counter through which the scattered electron passed. We have not yet corrected for losses out the 3° beam hole; such a correction will raise the yield in the first ($\phi \simeq 0$) bin. The indicated errors are statistical only.

Although we have not yet made any fits to the ϕ distributions, it appears from Fig. 7 that we may possibly have evidence for non-zero cos 2ϕ (transverse photon polarization) and cos ϕ (longitudinal-transverse interference) terms in the distribution. After we have applied more corrections to the data, we will study this possibility in more detail.

Since no hadron momenta are measured in this experiment, it is not possible to obtain inclusive longitudinal and transverse momentum spectra or center-of-mass angular distributions. Instead we display (Fig. 8) the laboratory - frame distributions in - ln tan (θ/2). It is important to note that although -ln tan (θ/2) is the same as rapidity for a $\beta \simeq 1$ particle, it is not the same in our experiment, expecially for the protons, which are generally rather slow. More analysis, corrections, comparisons with models, etc. will be necessary before we draw meaningful conclusions from these data.

Acknowledgements

We are indebted to F.M. Pipkin and collaborators for the loan of the lead-lucite shower telescope, to K.I. Greisen for the loan of eighty photomultipliers, to D.L. Hartill for aid in operating the proportional chambers and readout electronics, and to J. Klinger for help in data taking.

Figure Captions

Fig. 1 Experimental Setup.

Fig. 2 Scatter plot showing the range of Q^2 and s covered in the three data runs: 7 GeV and 11.5 GeV incident energy in the small-angle geometry and 11.5 GeV in large-angle geometry. Each dot represents one event. The density of events within the allowed experimental aperture limits, set by the inside and outside edges of the wire chambers, is determined by the scattering cross section, beam exposure, target length, and magnet gap height.

Fig. 3 Monte-Carlo generated multiplicity distributions. (a) The effect of the various corrections on the true multiplicity n for $\bar{Q}^2 = 2.3$ GeV^2, $\bar{s} = 9.5$ GeV^2, $n = 3$. (b) Predicted apparent multiplicity for n $n = 1, 3, 5, 7$ for $\bar{Q}^2$, $\bar{s} = 2.3, 9.5$ (solid line) and for $\bar{Q}^2$, $\bar{s} = 3.2, 9.7$ (dashed line). (c) Same as b, except dashed line now represents $\bar{Q}^2$, $\bar{s} = 2.3, 11.7$ GeV^2.

Fig. 4 Comparison of the observed multiplicity distribution (points with error bars), the fitted sum of Monte Carlo distributions (histogram), and the corresponding "true" multiplicities (vertical bars, reduced to 1/4 for clarity).

Fig. 5 The corrected average charged hadron multiplicity plotted against s (logarithmic scale) for several fixed Q^2 values. Only statistical errors are included Data at $Q^2 = 0$ (crosses) are from ref. 9.

Figure Captions cont.

Fig. 6 The data of Fig. 5 replotted as a function of Q^2 for several ranges of s. For comparison we have also plotted data of ref. 7 (triangles), ref. 8 (open circles), and ref. 9 (crosses).

Fig. 7 Hadron distributions in azimuth about the virtual photon direction. $\phi = 0$ is in the electron scattering plane on the beam side of the virtual photon line.

Fig. 8 Hadron distributions in $-\ln \tan(\theta/2)$, where θ is the laboratory polar angle measured with respect to the virtual photon direction.

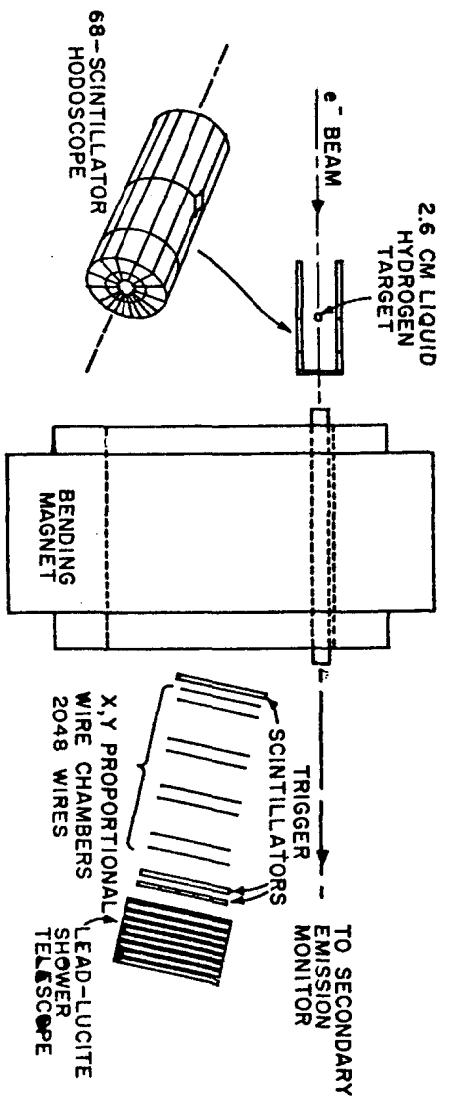

Fig. 1

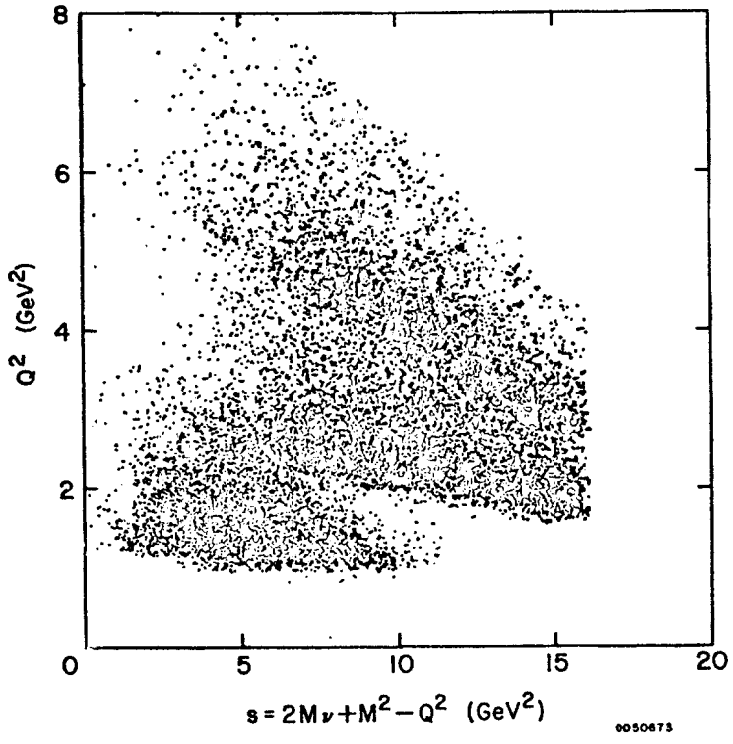
8
6
4
2
0
Q^2 (GeV^2)
5
10
15
20
$s = 2M\nu + M^2 - Q^2$ (GeV^2)
0050673

Fig. 2

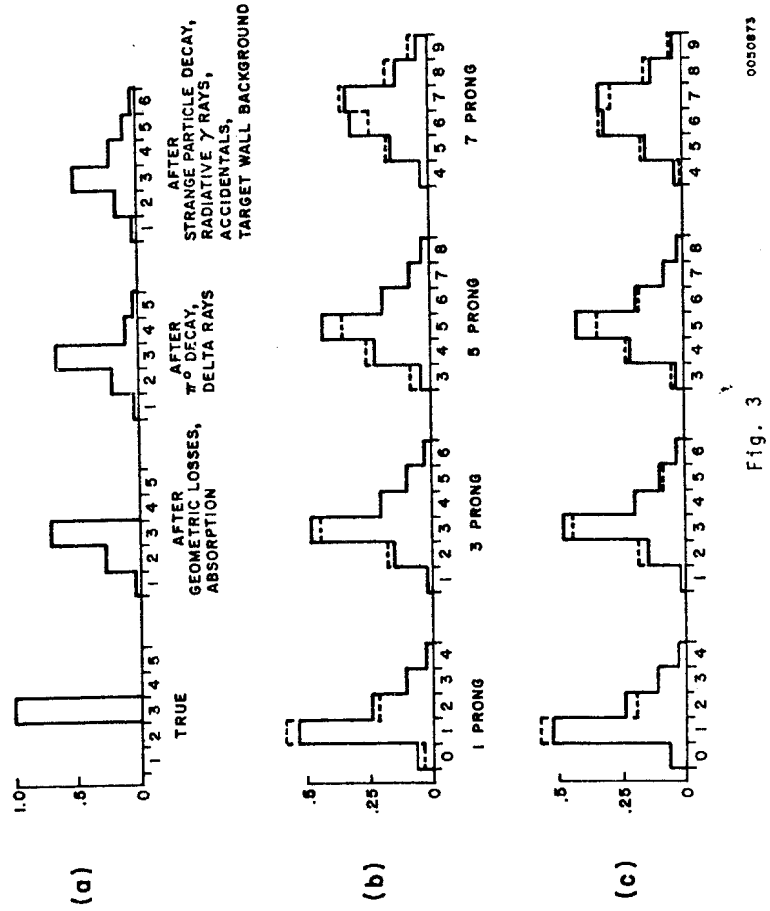
(a)
(b)
(c)
TRUE
AFTER GEOMETRIC LOSSES, ABSORPTION
AFTER π^0 DECAY, DELTA RAYS
AFTER STRANGE PARTICLE DECAY, RADIATIVE γ RAYS, ACCIDENTALS, TARGET WALL BACKGROUND
1 PRONG
3 PRONG
5 PRONG
7 PRONG
0050673

Fig. 3

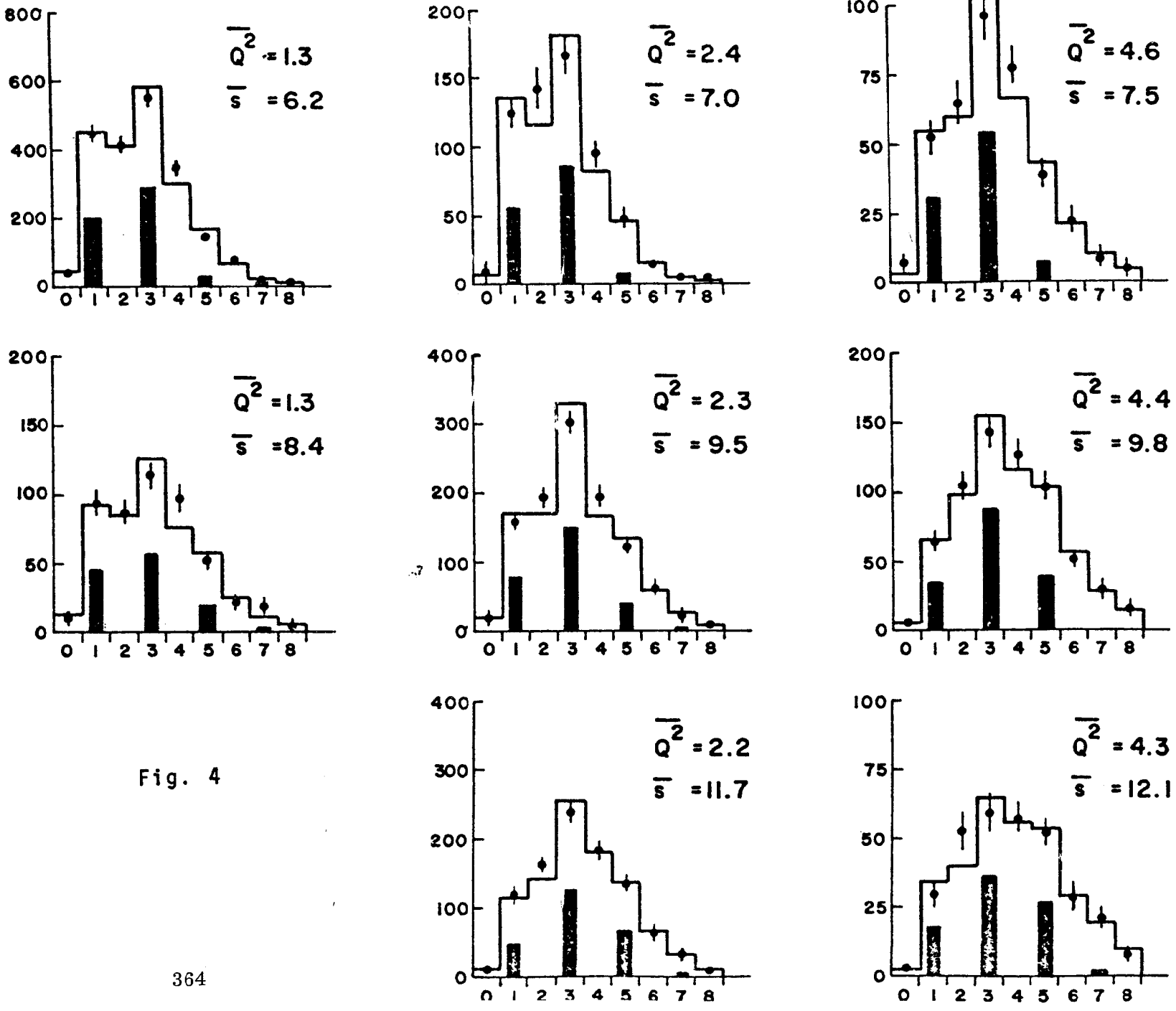
$\overline{Q^2}$ = 1.3
$\overline{s}$ = 6.2
$\overline{Q^2}$ = 2.4
$\overline{s}$ = 7.0
$\overline{Q^2}$ = 4.6
$\overline{s}$ = 7.5
$\overline{Q^2}$ = 1.3
$\overline{s}$ = 8.4
$\overline{Q^2}$ = 2.3
$\overline{s}$ = 9.5
$\overline{Q^2}$ = 4.4
$\overline{s}$ = 9.8
$\overline{Q^2}$ = 2.2
$\overline{s}$ = 11.7
$\overline{Q^2}$ = 4.3
$\overline{s}$ = 12.1

Fig. 4

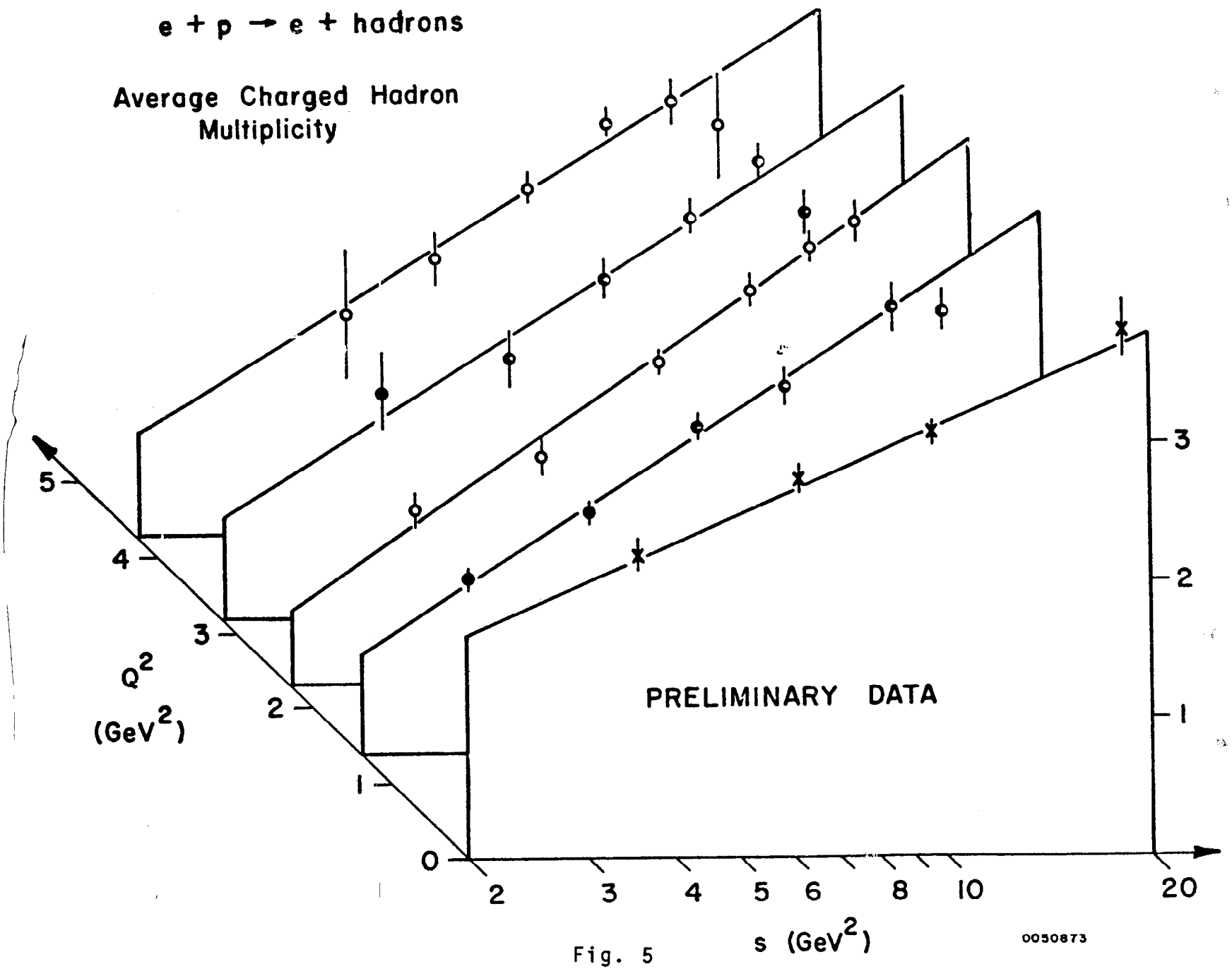
e + p → e + hadrons
Average Charged Hadron Multiplicity
PRELIMINARY DATA
Q^2 (GeV^2)
s (GeV^2)
0
1
2
3
4
5
2
3
4
5
6
8
10
20
0050873

Fig. 5

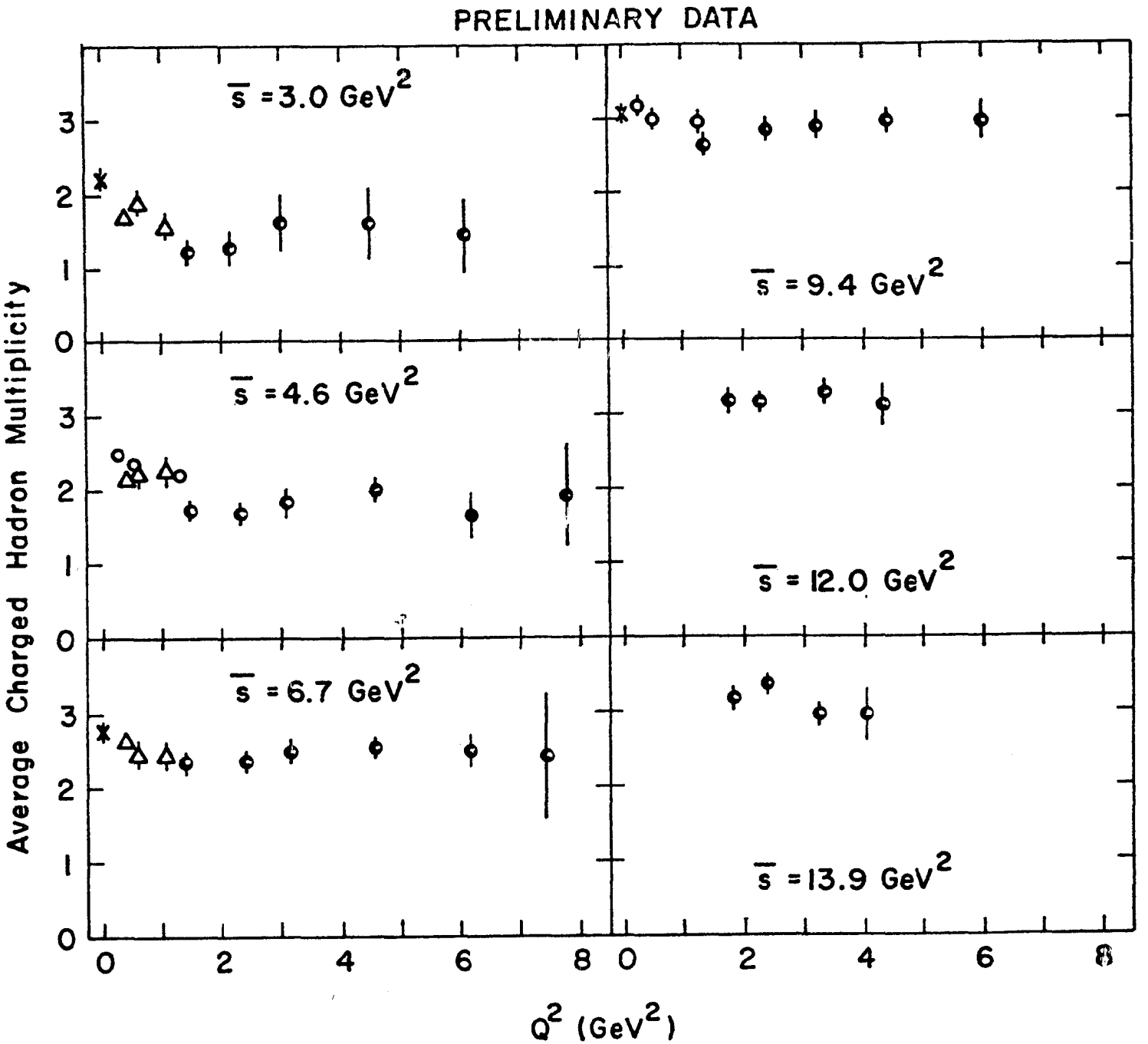
PRELIMINARY DATA
$\bar{s}$ = 3.0 GeV^2
$\bar{s}$ = 9.4 GeV^2
$\bar{s}$ = 4.6 GeV^2
$\bar{s}$ = 12.0 GeV^2
$\bar{s}$ = 6.7 GeV^2
$\bar{s}$ = 13.9 GeV^2
Average Charged Hadron Multiplicity
Q^2 (GeV^2)
0
1
2
3
4
6
8

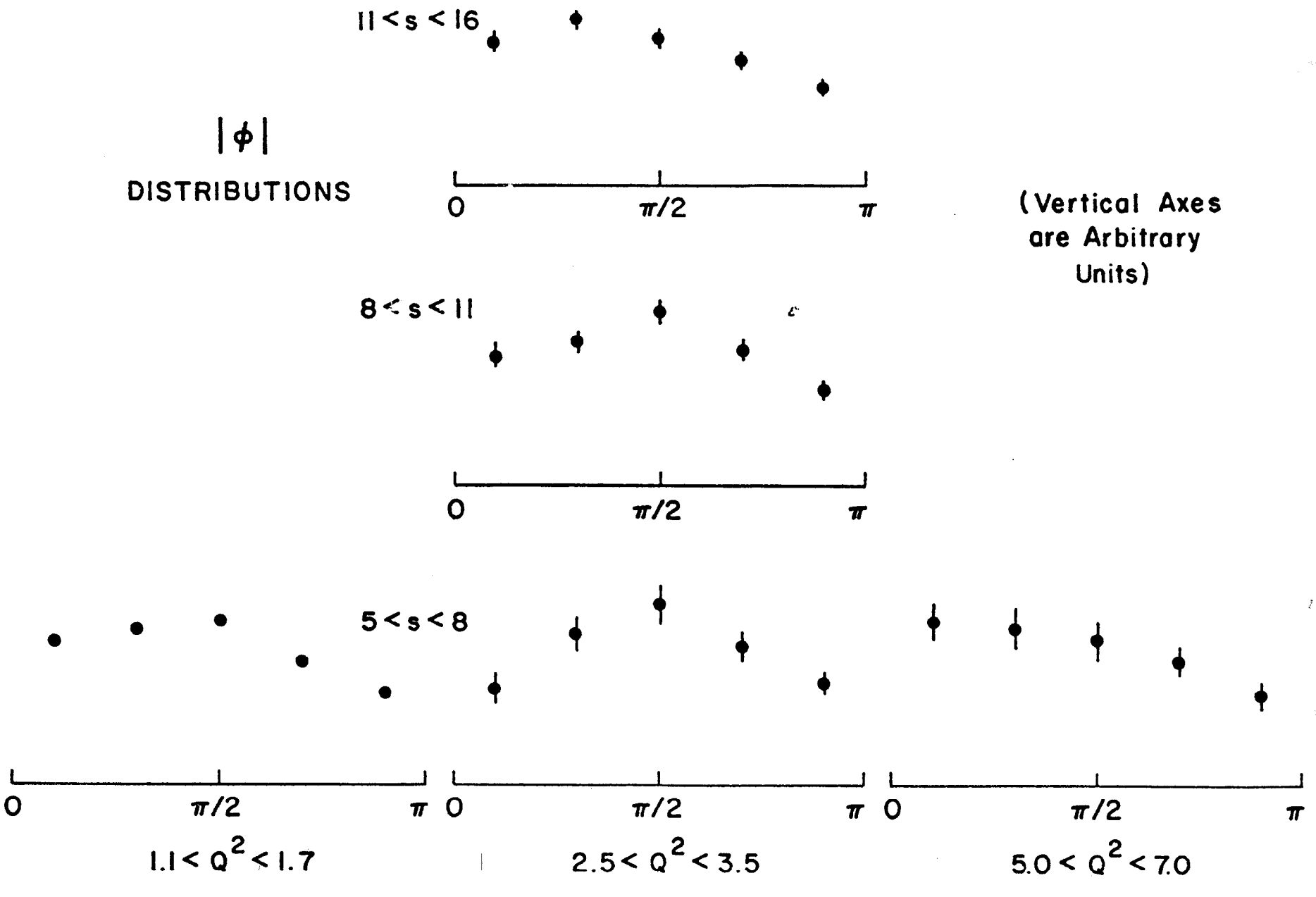
11 < s < 16
|φ|
DISTRIBUTIONS
0
π/2
π
(Vertical Axes are Arbitrary Units)
8 < s < 11
0
π/2
π
5 < s < 8
0
π/2
π
0
π/2
π
0
π/2
π
1.1 < Q² < 1.7
2.5 < Q² < 3.5
5.0 < Q² < 7.0
0050873

Fig. 7

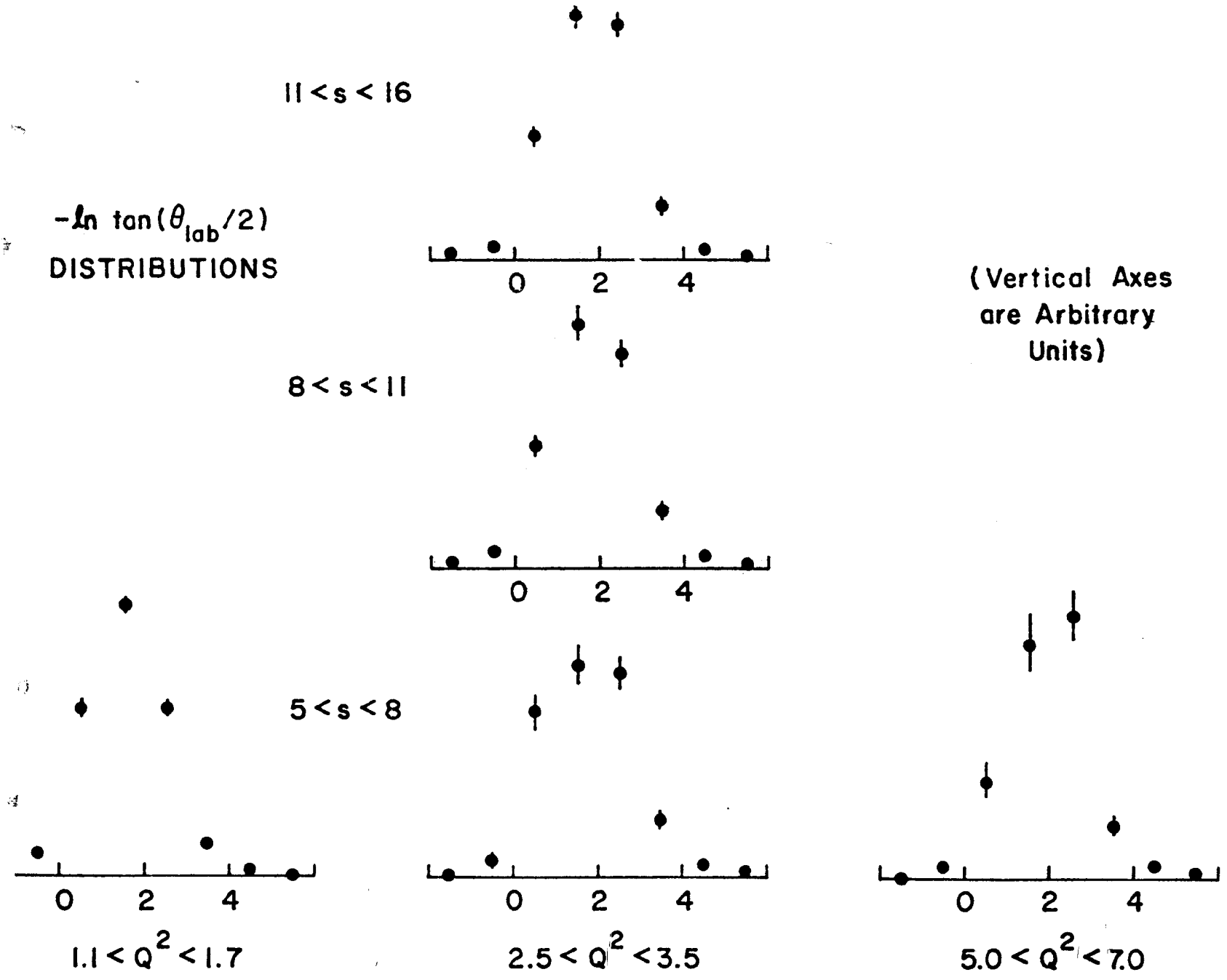
11 < s < 16
8 < s < 11
5 < s < 8
$-\ln \tan(\theta_{lab}/2)$ DISTRIBUTIONS
(Vertical Axes are Arbitrary Units)
0
2
4
$1.1 < Q^2 < 1.7$
$2.5 < Q^2 < 3.5$
$5.0 < Q^2 < 7.0$
0050873

Fig. 8

References

1. Theory and experiment for inclusive hadron reactions are reviewed by W.R. Frazer et al., Rev. Mod. Phys. 44, 284 (1972).
2. P. Carruthers and M. Duong-van (Cornell preprint CLNS-222).
3. T.T. Chou and C.N. Yang, Phys. Rev. D4, 3 (1971).
4. J.D. Bjorken and J. Kogut, Phys. Rev. (to be published); R.N. Cahn, J.W. Cleymans, and E.W. Colglazier, Phys. Letters 43B, 323 (1973).
5. S.D. Drell, D.J. Levy, and T.M. Yan, Phys. Rev. Letters 22, 744 (1969).
6. S.S. Shei and D.M. Tow, Phys. Rev. Letters 26, 470 (1971).
7. V. Eckardt et al., Nucl. Phys. B55, 45 (1973).
8. J. Ballam et al., (SLAC preprint); E.D. Bloom, Proceedings of the XVI International Conference on High Energy Physics, Chicago-NAL, 1972, vol. 2 page 66; and E.D. Bloom (private communication).
9. K.F. Moffeit et al., Phys. Rev. D5, 1603 (1972).
10. Radiation during scattering is calculated using the equivalent radiator approximation: L.W. Mo and Y.S. Tsai, Rev. Mod. Phys. 41, 205 (1969).
11. For a recent review of the data see K. Berkelman, Proceedings of the XVI International Conference on High Energy Physics Chicago-NAL, 1972, vol. 4, page 41.
12. Scaling in ω' (E.D. Bloom and F.J. Gilman, Phys. Rev. D4 2901 (1971) and in ω_w (V. Rittenberg and H.R. Rubinstein, Phys. Letters 35B, 50 (1971)) are also incompatible with the data.